

# Open Research Online

---

The Open University's repository of research publications and other research outputs

## The Biochemical Basis of Congenital Disorders of Glycosylation

### Thesis

How to cite:

Needs, Sarah (2018). The Biochemical Basis of Congenital Disorders of Glycosylation. PhD thesis The Open University.

For guidance on citations see [FAQs](#).

© 2018 The Author

Version: Version of Record

---

Copyright and Moral Rights for the articles on this site are retained by the individual authors and/or other copyright owners. For more information on Open Research Online's [data policy](#) on reuse of materials please consult the policies page.

---

[oro.open.ac.uk](http://oro.open.ac.uk)

# **The Biochemical Basis of Congenital Disorders of Glycosylation**

Sarah Needs

A thesis submitted to The Open University in partial fulfilment of the  
requirement for the degree of Doctor of Philosophy



School of Life, Health and Chemical Sciences,  
Faculty of Science, Technology, Engineering and Mathematics  
The Open University

November 2018



Sarah Needs: *Biochemical basis of congenital disorders of glycosylation*

**Supervisors**

Dr Sarah Allman<sup>1</sup>

Dr Martin Bootman<sup>1</sup>

Dr Dominic Alonzi<sup>2</sup>

**Location**

The Open University

Milton Keynes

**Submission Date**

April 2018

<sup>1</sup> The Open University, Life Health and Chemical Sciences, Milton Keynes, MK7 6AA, UK

<sup>2</sup> Oxford Glycobiology Institute, Department of Biochemistry, Oxford University, OX1 3QU,  
UK

## Declaration

The work examined in this thesis is entirely my own. Contributions made by my colleagues are acknowledged in the acknowledgments of assistance. This work has not been, and is not, currently being submitted for candidature for any other degree.

## Acknowledgements

I am deeply indebted to my supervisor Dr Sarah Allman for all her hard work and patience over the years and would like to thank her as well as Dr Martin Bootman and Dr Dominic Alonzi for all their help and support. I would also like to thank Dr Holger Kramer (Head of proteomics, MRC London Institute of Medical Sciences) for all his skill and guidance on the practical and analysis of proteomics data for CRISPR generated clones and the study of autophagosomes. Dr Daniel Berwick (LHCS, The Open University) for his guidance in the design of CRISPR guide sequences and primers.

I would also like to thank Julia Barkans, Brett Keith and George Bryant for all their help in the lab. I am grateful to the other students at The Open University for all their advice and discussions over the course of this study especially Conor McQuaid for his constantly enthusiastic discussions.

I would also like to thank my family, Jayne Needs and Fiona Needs for all their support through my studies and Anton Lindley-Decaire for all his encouragement.

## Abstract

The enzyme peptide: *N*-glycanase (EC 3.5.1.52) is an endoglycosidase which cleaves *N*-linked glycans from incorrectly folded glycoproteins exported from the endoplasmic reticulum during ER-associated degradation (ERAD). Clinical mutations in this enzyme (resulting in loss or decrease in function) are responsible for the rare congenital disorder termed N-GLY1. N-GLY1 disorder was first identified by next generation sequencing in 2012, and as such there exists little information as to the cellular effects of *N*-glycanase deficiency.

In this study, *N*-glycanase deficiency was examined in a well-characterised cell model (HEK-293). Cellular effects were examined following pharmacological inhibition of *N*-glycanase using carbobenzoxy-valyl-ananyl-aspartyl-[*O*-methyl]-fluoromethylketone (Z-VAD-fmk) and, genetic knockdown by siRNA. Attempts were also made to generate a knockout cell line using CRISPR/Cas9.

Using molecular and cellular techniques, this study has confirmed that in HEK-293, pharmacological *N*-glycanase inhibition or siRNA knockdown does not activate ER stress, oxidative stress or change the glycoprotein profile of the cell. Both treatments were associated with a small increase in ThT fluorescence associated with protein aggregates and identified that autophagy was increased in pharmacological *N*-glycanase inhibition and siRNA knockdown, and that this likely represents a protective measure. Autophagy dysregulation using ATG13 KO MEF cells found a change in the redox environment of the cell. This effect was further exacerbated in both HEK293, WT MEFs and ATG13 KO MEFs by growth in glucose-free media supplemented with galactose to reduce glycolysis as an energy source. This is suggestive of mitochondrial dysregulation, although no changes in mitochondrial membrane potential or mitochondrial content were identified. Proteomics analysis of immuno-precipitated autophagosomes induced under pharmacological *N*-glycanase inhibition and siRNA knockdown revealed increased intensity of mitochondrial proteins in these samples indicative of mitophagy which may play a role in the cellular response to impairments of *N*-glycanase function.

## Abbreviations

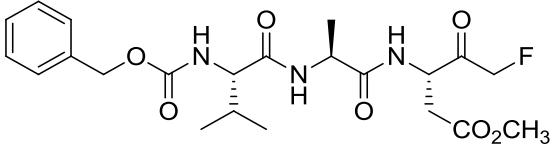
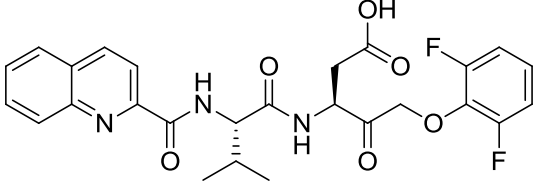
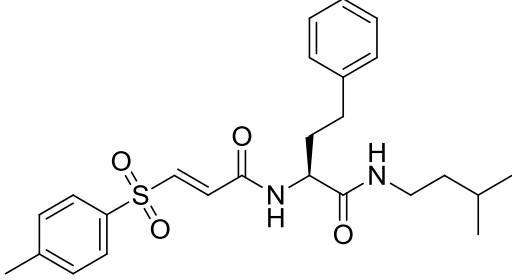
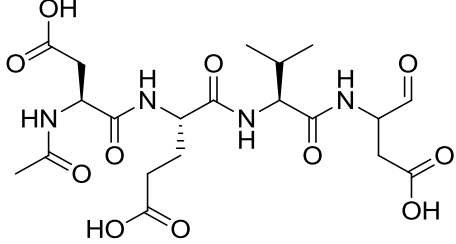
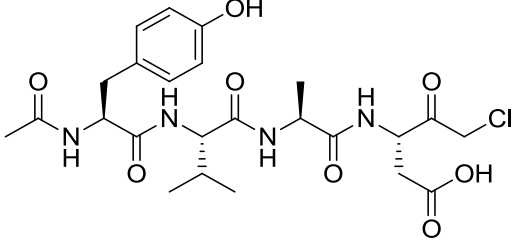
3-MA	3-methyladenine
AARE	amino acid response element
ACOT9	Acyl-CoA thioesterase 9
AGC	Automatic gain control
AKT	protein kinase B
AP	activator protein
APAF1	apoptotic protease-activating factor
APP	amyloid precursor protein
APS	Ammonium Persulfate
ATF6	Activating Transcription factor 6
A $\beta$	Amyloid- $\beta$
Bacpng	bacterial PNGase plasmid
Baf	Bafilomycin A1
BiP	Binding immunoglobulin Protein
C18-SPE	reverse phase C18 solid phase extraction
Cas9	CRISPR associated protein 9
CBR1	NADPH-Dependent Carbonyl Reductase 1
CDG	Congenital disorders of glycosylation
CFTR	Cystic Fibrosis Transmembrane Conductance Regulator
CHOP	CCAAT-enhancer-binding protein homologous protein
CID	Collision-induced dissociation
CMA	Chaperone mediated autophagy
CNX	Calnexin
ConA	Concavalin A
CRISPR	Clustered regularly interspaced short palindromic repeats
crRNA	CRISPR RNA
CRT	Calreticulin
CV	column volumes
Da	Daltons
DDVenus	Deglycosylation dependent VENUS
DISC	death-inducing signalling complex
DMSO	dimethyl sulfoxide
DSB	double stranded break
DTT	Dithiothreitol
ECL	Enhanced Chemiluminescence
EDEM	ER degradation enhancing $\alpha$ -mannosidase like protein 1
ENGase	Endo- $\beta$ -N-acetylglucosaminidase
ER	Endoplasmic Reticulum
ERK	extracellular signal-regulated kinase
ESI	Electrospray ionisation
ETS	erythroblastosis virus twenty-six
EURODIS	Rare Diseases Europe
FA	Formic acid
FASP	filter aided sample preparation
FCCP	Carbonyl cyanide-p-trifluoromethoxyphenylhydrazone
FDR	False discovery rate
fOS	Free oligosaccharides
FRAP	Fluorescence Recovery after Photo bleaching

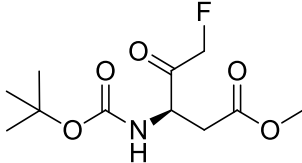
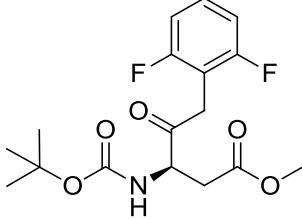
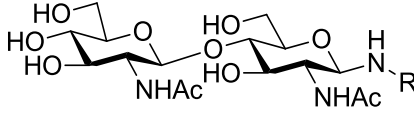
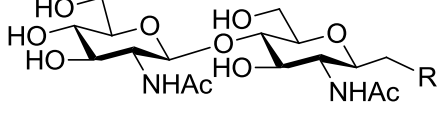
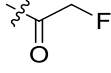
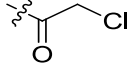
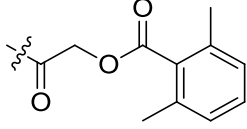
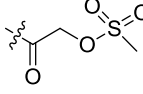
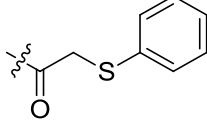
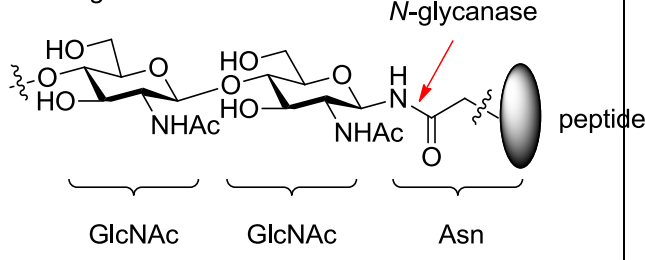


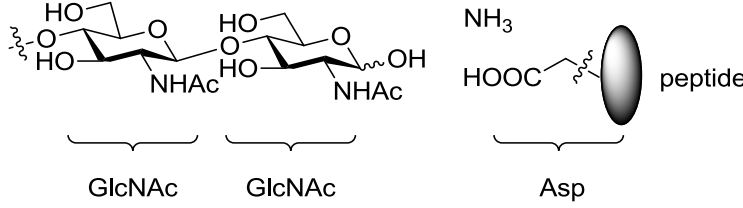
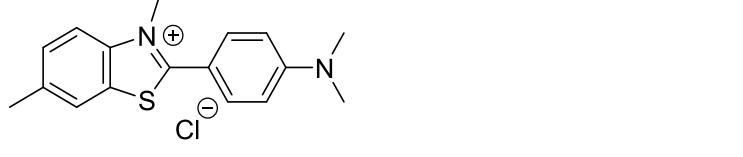
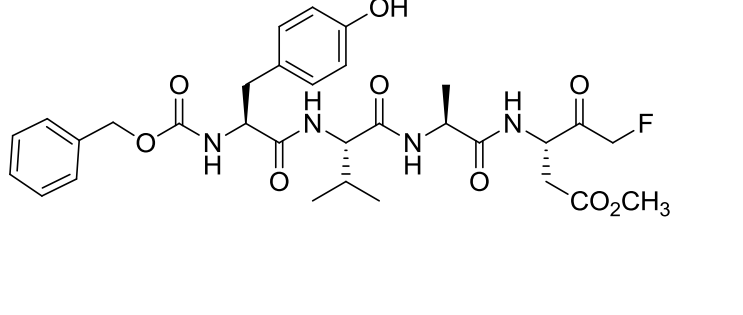
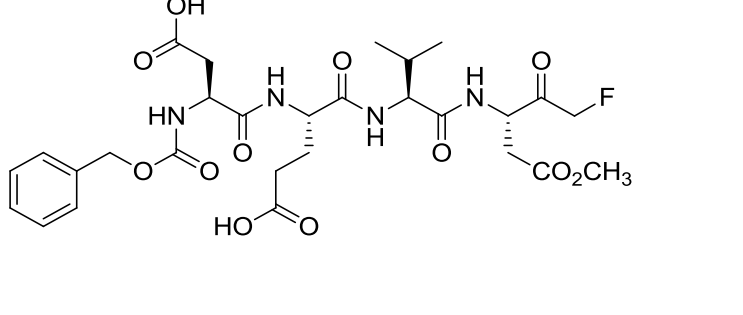
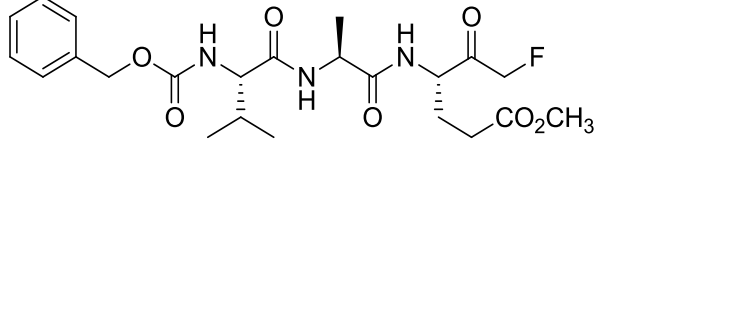
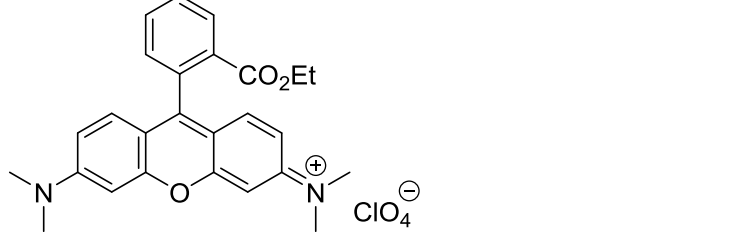
FURA-2 AM	FURA-2-acetoxymethyl ester
Glc	Glucose
GlcNAc	<i>N</i> -acetylglucosamine
GPI	Glycophosphaditylinositol
Grp78	Glucose regulated protein 78
GSH	Glutathione
HBSS	Hanks balanced salt solution
HCD	Higher-energy collisional dissociation
HCS	Heavy Chains
HDAC6	Histone deacetylase 6
HDR	Homology directed repair
HEK	Human Embryonic Kidney
HPLC	High performance liquid chromatography
IAA	Iodoacetamide
ICC	Ion charge control
IP	Immunoprecipitation
IPTG	Isopropyl $\beta$ -D-1-thiogalactopyranoside
IRE1	Inositol requiring 1
KO	Knockout
LB	Luria Broth
LC	Liquid chromatography
LC3	Microtubule-associated light chain 3
LCA	<i>lens culinaris</i>
LDS	Lithium dodecyl sulfate
LFQ	Label free quantification
LLO	Lipid-linked oligosaccharide
LTQ	Linear trap quadrupole
m/z	Mass over charge
Man	Mannose
Man2C1	Mannosidase- $\alpha$ -2C1
MAPK	mitogen-activated protein kinase
MAPKK	MAPK kinase
MHC	Major Histocompatibility Complex
MOMP	mitochondrial outer membrane permeabilisation
MS	Mass spectrometry
MS/MS	Tandem mass spectrometry
mtDNA	mitochondrial DNA
RC	respiratory chain
mTOR	Mechanistic target of rapamycin
MTT	(3-(4,5-Dimethylthiazol-2-yl)-2-5 Diphenyltetrazolium Bromide)
NGLY1	Peptide: <i>N</i> -glycanase
N-GLY1	<i>N</i> -glycanase deficiency disorder
NHEJ	Non-homologous end joining
NORD	National Centre for Rare Disorders
Nrf1	Nuclear respiratory factor 1
Nrf2	Nuclear respiratory factor 2
OGA	O-GlcNAcase
OGT	O-GlcNAc Transferase
OST	Oligosaccharyltransferase
PAGE	polyacrylamide gel electrophoresis
PAM	Protospacer adjacent motif

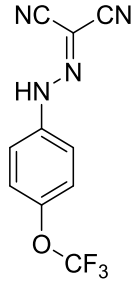
PAS	periodic acid stain
PBS	Phosphate buffered saline
PDI	Protein di-sulfide isomerase
PERK	PKR-like ER kinase
PHA-E	phaseolus vulgaris erythroagglutinin
PI3K	Phosphoinositide 3-kinase
PNGase	Peptide: <i>N</i> -glycanase
PSEN	presenilin
PSM	Proteasome gene family
PVDF	Polyvinylidene fluoride
Q-VD-OPh	5-(2,6-Difluorophenoxy)-3-[[3-methyl-1-oxo-2- [(2quinolinylcarbonyl)amino]butyl]amino]-4-oxo-pentanoic acid
Rapa	Rapamycin
RISC	RNA induced silencing complex
RNAi	RNA interference
RPM	Rotation per Minute
RSLC	Rapid separation HPLC system
RT	room temperature
RT-qPCR	Real-time- quantitative polymerase chain reaction
SDS	Sodium dodecylsulfate
SERCA	Sarcoplasmic/Endoplasmic reticulum calcium ATPase 2
sgRNA	short guide RNA
siRNA	short interfering RNA
SPS	Smart parameter setting
STK	Serine/Threonine Kinase
s-WGA	succinylated wheat germ agglutinin
TBS	Tris-buffered saline
TBST	Tris-buffered saline with Tween-20
TE	Tris-EDTA
TFA	Trifluoroacetic acid
Tht	Thioflavin T
TIDE	Tracking Indels by DEcomposition
TIM	translocase of the inner membrane
TMRE	Tetramethylrhodamine, Ethyl Ester
TOM	translocase of the outer membrane
tracrRNA	trans-activating crRNA
Ub	Ubiquitin
UDP-GT	UDP- glucuronosyltransferase
UPP	Ubiquitin-Proteasome Pathway
UPR	Unfolded protein response
V+ATPase	Vacuolar-type H <sup>+</sup> -ATPase
WGA	wheat germ agglutinin
WTCas9	Wild type Cas9
yPng1	Yeast peptide: <i>N</i> -glycanase
Z-VAD-fmk	Carbobenzoxy-valyl-alanyl-aspartyl-( <i>O</i> -methyl)-fluoromethylketone

Structures

Structure	Where?	What?
	Everywhere	Z-VAD-fmk  (cell permeable methyl ester form)
	Everywhere	Q-VD-OPh
	Chapter 3	WRR139
	Chapter 3	Ac-DEVD-CHO  (free acid form)
	Chapter 3	Ac-YVAD-cmk  (free acid form)

	Chapter 3	Boc-D-fmk
	Chapter 3	Boc-D-OPh
	Chapter 3	Chitobiose inhibitor
	Chapter 3	Chitobiose inhibitor
	Chapter 3	R-group in table 3.3
	Chapter 3	R-group in table 3.3
	Chapter 3	R-group in table 3.3
	Chapter 3	R-group in table 3.3
	Chapter 3	R-group in table
<p data-bbox="319 1579 638 1601"><i>N</i>-glycan reducing terminus</p>  <p data-bbox="821 1601 981 1624"><i>N</i>-glycanase</p> <p data-bbox="997 1702 1085 1724">peptide</p> <p data-bbox="518 1814 614 1848">GlcNAc</p> <p data-bbox="678 1814 774 1848">GlcNAc</p> <p data-bbox="869 1814 933 1848">Asn</p>	Chapter 3	Cleavage site

 <p style="text-align: center;">GlcNAc      GlcNAc      Asp</p>	Chapter 3	Cleavage – final products
	Chapter 3	Thioflavin T
	Chapter 4	Z-VAD-fmk  (note – this is the cell permeable methyl ester form)
	Chapter 4	Z-DEVD-fmk  (note – this is the cell permeable methyl ester form)
	Chapter 4	Z-VAE-fmk  (note – this is the cell permeable methyl ester form)
	Chapter 7	TMRE

 <chem>C#N=C(C#N)Nc1ccc(OC(F)(F)F)cc1</chem>	Chapter 7	FCCP
--	-----------	------

Chemdraw setting: ACS document

## Table of Contents

DECLARATION	II
ACKNOWLEDGEMENTS	III
ABSTRACT	IV
ABBREVIATIONS	V
STRUCTURES	VIII
TABLE OF CONTENTS	XII
TABLE OF FIGURES	XVI
TABLE OF TABLES	XXI
<b>CHAPTER 1</b>	<b>1</b>
1.1 STRUCTURAL AND FUNCTIONAL DIVERSITY OF PROTEINS	1
1.1.2 <i>Post-Translational Modifications</i>	2
1.1.3 <i>Phosphorylation</i>	2
1.1.4 <i>Ubiquitination</i>	4
1.1.5 <i>Glycosylation</i>	6
1.1.6 <i>GPI anchors</i>	7
1.1.6 <i>O-linked glycosylation</i>	8
1.1.7 <i>N-linked glycosylation</i>	8
1.1.8 <i>Congenital disorders of glycosylation</i>	12
1.2.1. PROTEIN FOLDING	13
1.2.3. <i>Protein folding in the ER</i>	15
1.2.4. <i>Glycoprotein folding in the ER</i>	16
1.3.1 PROTEIN DEGRADATION PATHWAYS	19
1.3.2 <i>Ubiquitin Proteasome System – ERAD</i>	20
1.3.3 <i>Autophagy</i>	24
1.3.4. <i>Proteostasis</i>	27
1.3.5. <i>Deglycosylation of misfolded proteins</i>	30
1.4.1 N-GLY1 DISORDER	33
1.4.2 <i>Molecular impact of N-glycanase deficiency</i>	35
1.4.3 <i>Deglycosylation regulates protein activity</i>	36
1.4.4 <i>N-glycanase is involved in the generation of free oligosaccharides</i>	36
1.5 AIMS AND OBJECTIVES	37
<b>CHAPTER 2.</b>	<b>38</b>
2.5.1 <i>Pharmacological inhibition of N-glycanase using Z-VAD-fmk</i>	41
2.5.2 <i>Genetic ablation of N-glycanase</i>	41
2.5.3 <i>MTT assay</i>	42
2.5.4 <i>Deglycosylation Dependent Venus (ddVENUS) assay</i>	42
2.5.5 <i>Lectin dot blots</i>	42
2.5.6 <i>Quantitation of levels Thioflavin T (ThT) fluorescence</i>	43
2.5.7 <i>Quantitation of Thioflavin T (ThT) fluorescence by flow cytometry</i>	43
2.5.8 <i>Quantitation of levels GFP-LC3 positive puncta</i>	44
2.5.9 <i>Use of CYTO-ID® autophagy detection kit with a TALI image-based cytometer</i>	44
2.5.10 <i>Assessment of transfection efficiency</i>	44
2.5.11 <i>Trypan blue exclusion measurement of cell viability</i>	44
2.5.12 <i>G418 cell survival</i>	45
2.5.13 <i>Generation of GFP-RFP-LC3 stably transfected cells</i>	45
2.5.14 <i>Quantitation of GFP-LC3 levels using in-gel fluorescence</i>	45
2.5.15 <i>Quantitation of protein levels by Western blot</i>	45
2.5.16 <i>Assessment of ER stress markers by real-time quantitative PCR (RT-qPCR)</i>	46

2.5.17 Assessment of cellular calcium handling by fluorescence imaging	48
2.5.18 Quantitation of oxidative stress by flow cytometry	49
2.5.19 Expression and purification of recombinant PNGase F	49
2.5.20 PNGase F activity assay	50
2.5.21 Generation of mAPPLE tagged Z-VAD-fmk insensitive PNGase plasmid (bacpng)	50
2.6.1 Design of guide sequences	52
2.6.2 Phosphorylation and annealing of oligonucleotides	54
2.6.3 Cloning of the sgDNA products into appropriate vectors	55
2.6.4 Transformation of plasmids into an <i>E. coli</i> expression host	55
2.6.5 Determination of sequence	55
2.6.6 PCR	55
2.6.7 Transfection of CRISPR constructs	55
2.2.7 Shotgun proteomics analysis of CRISPR clones (ThermoScientific QExactive)	56
2.7.1 Autophagosome isolation using GFP-linked magnetic beads	58
2.7.2. Autophagosome isolation using Chromotek GFP-Trap® agarose beads	58
2.7.3 In-gel trypsin digestion	58
2.7.4 Analysis of samples following in-gel digestion (Bruker AmaZon Ion Trap LCMS-MS system)	59
2.7.6 In-house FASP digestion protocol	61
2.7.7 Expedeon FASP™ protocol	61
2.7.8 Analysis of in-house and Expedeon FASP protocols (ThermoScientific LTQ Orbitrap XL)	62
2.7.9 Analysis of in-house FASP samples (ThermoScientific LTQ Orbitrap Velos)	63
2.8.1 Growth curves	64
2.8.2 Quantification of PI/Annexin V staining	64
2.8.3 Assessment of mitochondrial membrane polarisation using TMRE	65
2.8.4 Assessment of mitochondrial membrane polarisation by flow cytometry using TMRE	65
2.8.5 Determination of non-quenching concentrations of TMRE by fluorescence imaging	65
2.8.6 Assessment of levels of mitophagy by flow cytometry	65
2.8.7 Isolation of mitochondria	66
2.5 STATISTICAL ANALYSIS	66
<b>CHAPTER 3.</b>	<b>67</b>
3.1 INTRODUCTION	67
3.1.2 Pharmacological inhibition of caspases	69
3.1.3 Other targets of pharmacological caspase inhibitors	73
3.1.4 Pharmacological inhibition of N-glycanase	76
3.2 AIMS AND OBJECTIVES	82
3.3 RESULTS	83
3.3.1 No effects on cell viability are observed when cells are treated with < 100 µM Z-VAD-fmk	84
3.3.2 Z-VAD-fmk treatment shows decreased fluorescence of the deglycosylation dependent VENUS	86
3.3.3 Glycan profile of cells is not affected following treatment with Z-VAD-fmk	91
3.3.4 Thioflavin T fluorescence is transiently increases after Z-VAD-fmk treatment	95
3.3.4 Treatment with Z-VAD-fmk induces autophagy	99
3.3.5 Autophagic flux is maintained following treatment with Z-VAD-fmk	106
3.3.6 Western blot analysis LC3 in HEK cells was unsuccessful	113
3.3.8 Autophagy is protective response during N-glycanase inhibition	114
3.3.8 Z-VAD-fmk treatment of HEK cells does not induce ER stress or oxidative stress	117
3.3.9 Treatment with Z-VAD-fmk does not change O-GlcNAc modifying enzyme homeostasis	125
3.3.10 Bacterial N-glycanase (PNGase F) is insensitive to Z-VAD-fmk	127



3.3.11 <i>PNGase F was successfully cloned into a mammalian expression vector but transfection proved fatal to HEK 293 cells</i>	130
3.3 DISCUSSION	134
<b>CHAPTER 4.</b>	<b>139</b>
4.1 INTRODUCTION	139
4.2 AIMS AND OBJECTIVES	144
4.3 RESULTS	144
4.3.1 <i>No effects on cell viability are observed in cells transfected with NGLY1 siRNA</i>	145
4.3.2 <i>Knockdown of N-glycanase decreased fluorescence of the deglycosylation dependent VENUS protein</i>	146
4.3.3 <i>Glycan profile of cells transfected with NGLY1 siRNA is not affected</i>	147
4.3.4 <i>Differences in Thioflavin T fluorescence are observed following NGLY1 siRNA knockdown</i>	149
4.3.5 <i>Knockdown of N-glycanase with siRNA induces autophagy</i>	153
4.3.6 <i>Autophagy is a protective measure during N-glycanase knockdown</i>	155
4.3.7 <i>Genetic ablation of N-glycanase does not induce cellular stress</i>	156
4.3.8 <i>Expression of O-GlcNAc homeostasis enzymes are unchanged under N-glycanase knockdown</i>	162
4.4 DISCUSSION	164
<b>CHAPTER 5.</b>	<b>167</b>
5.1 INTRODUCTION	167
5.2 AIMS AND OBJECTIVES	173
5.3 RESULTS	173
5.3.1 <i>Guide sequences for N-glycanase and ENGase were cloned into WT or nickase Cas9 plasmids</i>	173
5.3.2 <i>Design of a repair template to introduce R401X mutation</i>	177
5.3.3 <i>The surveyor assay was unable to determine genetic editing in HEK 293 cells transfected with Cas9 constructs</i>	178
5.3.4 <i>Co-transfection with R401X oligo was unsuccessful</i>	180
5.3.5 <i>Transfection with PNG guide DNA in WT Cas9 plasmids lead to genomic editing in the N-glycanase gene</i>	182
5.3.6 <i>Clonally expanded cells show low viability, viable clonal cells exhibit different phenotypes to WT HEK</i>	189
5.3.7 <i>Increased sensitivity of clone 3 and 7 to cell stressors was not be rescued by pharmacological inhibition of ENGase</i>	193
5.3.8 <i>Sequencing identified no changes in gDNA sequences of Clone 3 and Clone 7 compared to WT HEK cells</i>	203
5.3.9 <i>Shotgun proteomics analysis by liquid chromatography tandem mass spectrometry (LCMS-MS)</i>	204
5.3.10 <i>Off-target effects identified by the guide sequence were significantly different in Clones 3 and 7 compared to the WT population</i>	205
5.3.11 <i>Global proteome analysis of Clone 3</i>	211
5.3.12 <i>Global proteome analysis of Clone 7</i>	213
5.4 DISCUSSION	216
<b>CHAPTER 6.</b>	<b>220</b>
6.1 INTRODUCTION	220
6.2 AIMS AND OBJECTIVES	222
6.3 RESULTS	222
6.3.1 <i>Method development</i>	223

6.3.2 TEST 2: LTQ Orbitrap XL analysis revealed increased levels of mitochondrial proteins in Z-VAD-fmk treated samples	226
6.3.3 TEST 3: LTQ Orbitrap Velos	232
6.4 DISCUSSION	249
<b>CHAPTER 7.</b>	<b>254</b>
7.1.1 Clinical presentations of N-GLY1 deficiency disorder mirror those of mitochondrial disorders	257
7.2 AIMS AND OBJECTIVES	258
7.3 RESULTS	259
7.3.1 Galactose supplemented low glucose media does not affect HEK cell proliferation	260
7.3.2 HEK cells grown in galactose show decreased MTT reduction when treated with Z-VAD-fmk for 72 h but no decrease in cell viability or proliferation	262
7.3.3 Knockdown of N-glycanase in HEK cells grown in galactose show decreased MTT reduction but no decrease in cell viability or proliferation	266
7.3.4 Galactose, low glucose media does not affect ATG13 KO or WT MEF cell proliferation	268
7.3.5 ATG13 KO MEFs show decreased formazan reduction when grown in galactose with Z-VAD-fmk treatment	269
7.3.6 WT MEFs show decreased formazan reduction when grown in galactose with Z-VAD-fmk treatment	273
7.3.7 Genetic knockdown of N-glycanase in ATG13 KO MEF and WT MEF cells in galactose supplemented DMEM reduced MTT reduction but not cell viability or proliferation	22755
7.3.8 Mitochondrial membrane potential is unaffected by inhibition and genetic ablation of N-glycanase	281
7.3.9 Measurements of mitophagy by flow cytometry were variable between experiments	294
7.3.10 Pharmacological inhibition and genetic ablation of N-glycanase does not affect mitochondrial lectin profile	298
7.5 DISCUSSION	302
<b>CHAPTER 8.</b>	<b>309</b>
8.1 INTRODUCTION	309
8.2 FINDINGS	309
8.2.1 N-glycanase knockdown and inhibition does not cause protein aggregates or cellular stress in HEK cells.	310
8.2.2 N-glycanase knockdown and inhibition increases autophagy	311
8.2.3 Nrf1 is regulated by deglycosylation	314
8.2.4 Mitochondrial involved in N-GLY1 disorder	314
8.2.4 N-glycanase and Z-VAD-fmk alters the redox environment of cells grown in galactose	315
8.2.5 Regulation of proteins by deglycosylation	318
8.2.6 Hexosamine Biosynthetic Pathway and O-GlcNAcylation	318
8.3 CONCLUSION	320
8.4 FUTURE PERSPECTIVES	321
<b>APPENDIX</b>	<b>322</b>
A.1.1 pOPH6 PNGase F plasmid (Addgene #40315)	323
A.1.2 GFP-LC3 plasmid sequence	324
A.1.3 mAPPLE-N1 plasmid map and sequence (Addgene #54567)	325
A.1.4 Sequence of bacterial PNGase mammalian expression construct BacPNG4_pCMVF	325
A.1.5 Sequence of bacterial PNGase mammalian expression construct BacPNG5_pCMVF	326
A.1.6 WT Cas9 CRISPR pSpCas9(BB)-2A-GFP (PX458) plasmid map and sequence (Addgene #48138)	326
A.1.7 WT Cas9 CRISPR pSpCas9(BB)-2A-GFP (PX458) plasmid map and sequence (Addgene #48138)	328

Table of Figures

**CHAPTER 1**

<i>Figure 1.1 Post-translation modification sites of p53</i>	2
<i>Figure 1.2 Components of the ERK1/2 signalling cascade</i>	4
<i>Figure 1.3 Linkage examples of ubiquitin chains</i>	5
<i>Figure 1.4 Modification of ubiquitin</i>	6
<i>Figure 1.5 Basic structure of a GPI-linked protein</i>	7
<i>Figure 1.6 Glycan structures of the LLO in the cytosol and ER lumen</i>	10
<i>Figure 1.7 Structures of N-glycans</i>	11
<i>Figure 1.8 Congenital disorders of glycosylation discovered over the last 30 years</i>	13
<i>Figure 1.9 Misfolded or partially folded peptides are prone to aggregation</i>	15
<i>Figure 1.10 Diagram showing the calreticulin cycle of glycoprotein folding</i>	17
<i>Figure 1.11 N-linked glycan Glc3Man9GlcNAc2</i>	18
<i>Figure 1.12 Schematic representation of ERAD</i>	21
<i>Figure 1.13 Atomic structure of human 26S proteasome</i>	23
<i>Figure 1.14 Schematic representation of autophagy</i>	24
<i>Figure 1.15 Diagram showing the protein interactions and regulation during autophagy</i>	26
<i>Figure 1.16 Proteostasis maintains the proteome in the correct conformations</i>	28
<i>Figure 1.17 Site of N-glycanase action on N-linked glycans</i>	30
<i>Figure 1.18 Protein interactions of N-glycanase</i>	31
<i>Figure 1.19 X-ray diffraction model of yeast PNGase in complex with GlcNAc2-IAC.</i>	31
<i>Figure 1.20 N-glycanase structure in fungi, yeast, mice and humans.</i>	32
<i>Figure 1.21 Symptoms of eight N-GLY1 patients</i>	34

**CHAPTER 2**

<i>Figure 2.1 PNGrx guide sequence calculation</i>	53
<i>Figure 2.2 PNGko guide sequence calculation</i>	53
<i>Figure 2.3 ENGko guide sequence calculation</i>	54

**CHAPTER 3**

<i>Figure 3.1 Structure of pro-caspase 7 and caspase 7</i>	67
<i>Figure 3.2 Extrinsic and intrinsic apoptosis pathways</i>	68
<i>Figure 3.3 Selected examples of points of action of pharmacological caspase inhibitors</i>	73
<i>Figure 3.4 Fluorescence polarisation assay of N-glycanase function</i>	77
<i>Figure 3.5 Proposed mechanism of Z-VAD-fmk binding to yPNGase</i>	78
<i>Figure 3.6 N-glycanase cleavage of protein bound N-glycans</i>	79
<i>Figure 3.7 Crystal structure of yeast N-glycanase in complex with N-GlcNAc</i>	80
<i>Figure 3.8 Products of the N-glycanase cleavage of protein bound N-glycans</i>	81
<i>Figure 3.9 MTT assay of HEK 293 cells were treated with Z-VAD-fmk or Q-VD-OPh</i>	85
<i>Figure 3.10 Schematic representation of the ddVENUS assay</i>	86
<i>Figure 3.11 Representative dot plots of the ddVENUS deglycosylation assay</i>	88
<i>Figure 3.12 ddVENUS assay for Z-VAD-fmk</i>	89
<i>Figure 3.13 Comparison of Q-VD-OPh and Z-VAD-fmk deglycosylation dependent assay</i>	90
<i>Figure 3.14 Linear range of lectin fluorescence</i>	92
<i>Figure 3.15 FITC-lectin staining of whole cell lysate treated with Z-VAD-fmk or Q-VD-OPh</i>	94
<i>Figure 3.16 Z-VAD-fmk caused a transient increase in ThT fluorescence</i>	97
<i>Figure 3.17 ThT fluorescence measured by flow cytometry</i>	98
<i>Figure 3.18 Schematic of autophagy indicating points of inhibition</i>	99
<i>Figure 3.19 GFP-LC3 HEK cells exposed to different inducers of autophagy</i>	100
<i>Figure 3.20 GFP-LC3 puncta under basal, rapamycin (5 <math>\mu</math>M) and amino acid starvation</i>	101
<i>Figure 3.21 GFP-LC3 HEK cells under different autophagy induction conditions</i>	101

<i>Figure 3.22 CytoID kit is not compatible with TALI cytometer</i>	102
<i>Figure 3.23 Z-VAD-fmk increased autophagy after 72 h</i>	104
<i>Figure 3.24 Z-VAD-fmk and Q-VD-OPh does not inhibit autophagic flux</i>	105
<i>Figure 3.25 Diagram showing the localisation GFP-RFP-LC3</i>	106
<i>Figure 3.26 JetPEI has the highest transfection efficiency in HEK cells</i>	107
<i>Figure 3.27 Fugene HD causes cell death</i>	108
<i>Figure 3.28 Survival chart of HEK cells treated with 50-1000 µg/ml G418</i>	109
<i>Figure 3.29 Representative images of HEK cells transfected with GFP-RFP-LC3</i>	110
<i>Figure 3.30 The GFP-RFP-LC3 construct behaves as predicted using Bafilomycin A1 and 3-MA</i>	110
<i>Figure 3.31 Z-VAD-fmk induces autophagy in GFP-RFP-LC3 HEK model.</i>	112
<i>Figure 3.32 Western blot and in-gel GFP-LC3 fluorescence was unable to resolve LC3I and LC3II bands</i>	113
<i>Figure 3.33 rt-qPCR measurement of ATG13 in WT MEF and ATG13 KO MEF</i>	114
<i>Figure 3.34 Z-VAD-fmk increases cell toxicity in ATG13 KO MEFS</i>	115
<i>Figure 3.35 3-MA causes cell toxicity</i>	117
<i>Figure 3.36 Diagram of unfolded protein response activation</i>	118
<i>Figure 3.37 Z-VAD-fmk or Q-VD-OPh does not activate the UPR</i>	120
<i>Figure 3.38 Thapsigargin increases cytosolic Ca<sup>2+</sup></i>	121
<i>Figure 3.39 Z-VAD-fmk or Q-VD-OPh does not affect Ca<sup>2+</sup> handling</i>	122
<i>Figure 3.40 Quantitation of Ca<sup>2+</sup> handling</i>	123
<i>Figure 3.41 Z-VAD-fmk or Q-VD-OPh does not increase ROS</i>	124
<i>Figure 3.42 Z-VAD-fmk or Q-VD-OPh does not affect OGA/OGT expression levels</i>	126
<i>Figure 3.43 Bacterial PNGase F does not contain conserved cysteine residue</i>	127
<i>Figure 3.44 PNGase F deglycosylation assay</i>	128
<i>Figure 3.45 PNGase F is not inhibited by Z-VAD-fmk</i>	129
<i>Figure 3.46 Schematic diagram showing cloning methodology</i>	130
<i>Figure 3.47 Transfection of BacPng plasmid increased cell death</i>	132
<i>Figure 3.48 BacPng plasmid caused cell death even at low concentrations</i>	133
<b>CHAPTER 4</b>	
<i>Figure 4.1 Diagram depicting the mode of action of siRNA and shRNA</i>	141
<i>Figure 4.2 Transfection of NGLY1 siRNA in HEK cells</i>	145
<i>Figure 4.3 MTT cell viability assay</i>	146
<i>Figure 4.4 ddVENUS fluorescence is reduced by 68 % 72 h post-transfection.</i>	147
<i>Figure 4.5 Log<sub>2</sub> fold change of fluorescein-labelled</i>	148
<i>Figure 4.6 ThT fluorescence in cells transfected with NGLY1 siRNA</i>	150
<i>Figure 4.7 Flow Cytometric analysis of ThT</i>	152
<i>Figure 4.8 GFP-LC3 puncta after 5 d post-transfection with NGLY1 siRNA</i>	153
<i>Figure 4.9 Representative images of HEK cells transfected with NGLY1 siRNA</i>	154
<i>Figure 4.10 GFP-LC3 puncta per cell after transfection with NGLY1 siRNA of non-targeting siRNA</i>	155
<i>Figure 4.11 MTT of ATG13 KO and WT MEFs transfected with NGLY1 siRNA</i>	156
<i>Figure 4.12 RT-qPCR analysis of CHOP, BiP, ATF4 and EDEM levels in cells transfected with NGLY1 siRNA</i>	157
<i>Figure 4.13 Traces of intracellular Ca<sup>2+</sup></i>	158
<i>Figure 4.14 HEK cells transfected with NGLY1 siRNA</i>	160
<i>Figure 4.15 HEK cells transfected with NGLY1 siRNA</i>	161
<i>Figure 4.16 OGA and OGT mRNA levels in HEK cells transfected with NGLY1 siRNA</i>	163
<b>CHAPTER 5</b>	
<i>Figure 5.1 Schematic representation of the CRISPR/Cas9 system</i>	167
<i>Figure 5.2 Process of non-homologous end-joining repair and HDR</i>	169
<i>Figure 5.3 Crystal structure of S. pyogenes Cas9</i>	170

<i>Figure 5.4 Timeline of CRISPR mediated knockout</i>	172
<i>Figure 5.5 Position of guide DNA in gDNA</i>	175
<i>Figure 5.6 PCR products of gDNA using CRISPR target primers</i>	176
<i>Figure 5.7 Guide DNA sequence allignment</i>	177
<i>Figure 5.8 Schematic representation of surveyor assay</i>	179
<i>Figure 5.9 Surveyor assay test</i>	180
<i>Figure 5.10 BsiWI digestion of gDNA post CRISPR/Cas9 transfection</i>	182
<i>Figure 5.11 Transfection rate of PNGA construct</i>	183
<i>Figure 5.12 TIDE analysis of HEK cells transfected with PNGA</i>	185
<i>Figure 5.13 Chromatogram of WT HEK and PNGA clones</i>	186
<i>Figure 5.14 Transfection rate of PNGB construct</i>	187
<i>Figure 5.15 TIDE analysis of HEK cells transfected with PNGB</i>	188
<i>Figure 5.16 Chromatogram of WT HEK and PNGB clones</i>	189
<i>Figure 5.17 N-glycanase RNA levels in clones</i>	190
<i>Figure 5.18 MTT of clones treated with 3-MA</i>	191
<i>Figure 5.19 ddVENUS assay of WT HEK cells</i>	192
<i>Figure 5.20 ddVENUS assay of clone 3</i>	192
<i>Figure 5.21 ddVENUS assay of clone 7</i>	193
<i>Figure 5.22 MTT of clones treated with lansoprazole</i>	194
<i>Figure 5.23 MTT of clones treated with MG132</i>	195
<i>Figure 5.24 MTT of clones treated with Menadione</i>	197
<i>Figure 5.25 HEK clones treated with Menadione</i>	198
<i>Figure 5.26 Growth curve of WT HEK cells</i>	200
<i>Figure 5.27 Growth curve of clone 3</i>	201
<i>Figure 5.28 Growth curve of clone 7</i>	201
<i>Figure 5.29 Doubling times of WT, clone 3 and clone 7</i>	202
<i>Figure 5.30 Chromatograms of WT, clone 3 and clone 7</i>	203
<i>Figure 5.31 TIDE analysis</i>	204
<i>Figure 5.32 Average NGLY1 intensity in WT, clone 3 and clone 7</i>	205
<i>Figure 5.33 LFQ average of IQGAP3</i>	208
<i>Figure 5.34 LFQ average of MAP1B</i>	209
<i>Figure 5.35 LFQ average of GRASP1</i>	210
<i>Figure 5.36 Volcano plot of clone 3</i>	211
<i>Figure 5.37 Volcano plot of clone 7</i>	213

## CHAPTER 6

<i>Figure 6.1 Diagram showing method development of autophagosome isolation and analysis</i>	224
<i>Figure 6.2 Proteins enriched over binding controls</i>	227
<i>Figure 6.3 Comparison of proteins identified in all conditions</i>	228
<i>Figure 6.4 Protein IDs assessed as enriched in each condition</i>	229
<i>Figure 6.5 Amino acid starvation and Z-VAD-fmk show increased mitochondria in autophagosomes</i>	230
<i>Figure 6.6 Fold over maximum LFQ intensity of mitochondrial proteins</i>	232
<i>Figure 6.7 Number of proteins identified in the GFP-Trap agarose beads and agarose bead binding control</i>	233
<i>Figure 6.8 Comparison of protein IDs found in biological replicates</i>	234
<i>Figure 6.9 Proteins enriched over binding controls</i>	235
<i>Figure 6.10 VENN diagram showing the mix of proteins</i>	236
<i>Figure 6.11 Fold over maximum LFQ intensity of mitochondrial proteins (Test 3)</i>	237
<i>Figure 6.12 Intensity of proteins involved in the negative regulation of apoptosis</i>	238
<i>Figure 6.13 Intensity of proteins involved in the positive regulation of apoptosis</i>	239

<i>Figure 6.14 STRING diagram showing interactions of proteins identified in Table 6.2</i>	241
<i>Figure 6.15 Intensity of proteins identified as co-precipitating with N-glycanase</i>	242
<i>Figure 6.16 LFQ intensities of proteasome complex proteins</i>	243
<i>Figure 6.17. ER associated protein IDs</i>	244
<i>Figure 6.18 SUM LFQ Intensity of FYCO1</i>	248
<i>Figure 6.19 Proposed action of Nrf1 activation</i>	252
<b>CHAPTER 7</b>	
<i>Figure 7.1 Mitochondrial morphology under different environmental conditions.</i>	254
<i>Figure 7.2 Methods of autophagic recruitment to mitochondria.</i>	256
<i>Figure 7.3 Galactose does not affect HEK cell proliferation.</i>	261
<i>Figure 7.4 MTT of HEK cells grown in DMEM high glucose media or galactose</i>	263
<i>Figure 7.5 PI exclusion, annexin V staining or cell number in WT HEK cells grown in glucose or galactose</i>	265
<i>Figure 7.6 MTT assay of HEK cells grown in high glucose DMEM (4.5 g/L) and galactose DMEM (10 mM) 7 d post-transfection with NGLY1 siRNA.</i>	266
<i>Figure 7.7 Galactose does not affect viability in HEK cells transfected with NGLY1 siRNA</i>	267
<i>Figure 7.8 There are no growth defects in WT MEF cells or ATG13 KO MEF cells in glucose or galactose media</i>	268
<i>Figure 7.9 MTT assay of ATG13 KO MEFs grown in DMEM high glucose media (4.5 g/L) or glucose free DMEM supplemented with galactose (10 mM)</i>	270
<i>Figure 7.10 Galactose does not affect viability of ATG13 KO MEFs treated with Z-VAD-fmk</i>	271
<i>Figure 7.11 MTT assay of WT MEF cells grown in DMEM high glucose media (4.5 g/L) or glucose free DMEM supplemented with galactose (10 mM) and treated with a) Z-VAD-fmk (0-200 <math>\mu</math>M, 72 h) b. Q-VD-OPh</i>	273
<i>Figure 7.12 Galactose does not affect viability of WT MEFs treated with Z-VAD-fmk</i>	274
<i>Figure 7.13 MTT assay of a) ATG13 KO MEF cells b) WT MEF cells grown in high glucose DMEM (4.5 g/L) and galactose DMEM (10 mM) 7 days post-transfection with NGLY1 siRNA</i>	275
<i>Figure 7.14 Galactose does not affect viability of ATG13 KO MEFs transfected with NGLY1 siRNA.</i>	277
<i>Figure 7.15 Galactose does not affect viability of WT MEFs transfected with NGLY1 siRNA</i>	279
<i>Figure 7.16 Mean TMRE fluorescence in WT HEK cells measured on TALI image based cytometer.</i>	282
<i>Figure 7.17 Mean TMRE fluorescence of HEK 293 cells treated with Z-VAD-fmk or Q-VD-OPh</i>	283
<i>Figure 7.18 mean TMRE fluorescence of HEK 293 cells transfected with NGLY1 siRNA</i>	284
<i>Figure 7.19 There is no change in TMRE fluorescence in HEK cells grown in galactose</i>	286
<i>Figure 7.20 TMRE fluorescence of HEK 293 cells grown in galactose (10 mM) supplemented DMEM transfected with NGLY1 siRNA</i>	288
<i>Figure 7.21 Median TMRE fluorescence of HEK 293 measured by flow cytometry</i>	289
<i>Figure 7.22 TMRE fluorescence of HEK 293 cells treated with FCCP (10 <math>\mu</math>M) as determined by microscopy.</i>	290
<i>Figure 7.23 TMRE fluorescence of HEK cells treated with Z-VAD-fmk or Q-VD-OPh</i>	291
<i>Figure 7.24 TMRE fluorescence of HEK 293 cells transfected with NGLY1 siRNA</i>	292

<i>Figure 7.25 MitoTracker™ Deep Red fluorescence of HEK 293 cells treated with bafilomycin or 3-MA</i>	294
<i>Figure 7.26 No increase in Mitotracker™ fluorescence intensity after 3-MA treatment with Z-VAD-fmk or Q-VD-OPh</i>	295
<i>Figure 7.27 No increase in Mitotracker™ fluorescence intensity was found after 3-MA treatment in N-glycanase knockdown</i>	296
<i>Figure 7.28 Purification of mitochondria using the Thermofisher Mitochondria isolation kit for cultured cells</i>	298
<i>Figure 7.29 Log fold change of FITC conjugated lectins</i>	300
<i>Figure 7.30 Ratios of NAD and NADH in the cytosol and mitochondria.</i>	302
<i>Figure 7.31 Schematic representation of the mitochondrial electron transport chain</i>	303
<b>CHAPTER 8</b>	
<i>Figure 8.1 Hexosamine biosynthetic pathway</i>	318
<b>APPENDIX</b>	
<i>Figure A1 pOPH6 plasmid map</i>	322
<i>Figure A2 mAPPLE-N1 plasmid map</i>	324
<i>Figure A3 WT CRISPR/Cas9 plasmid map</i>	326
<i>Figure A4 Nickase CRISPR/Cas9 plasmid map</i>	327
<i>Figure A5 PNGase gel shift assay of FITC labelled RNase B</i>	334

## Table of Tables

### CHAPTER 1

<i>Table 1.1 Effect of N-glycanase knockout in various organisms</i>	33
<i>Table 1.2 Confirmed mutations in the NGLY1 gene</i>	35

### CHAPTER 2

<i>Table 2.1. Sequence of SMARTpool NGLY1 siRNA</i>	41
<i>Table 2.2 Sequences of primers used in RT-qPCR</i>	47
<i>Table 2.3 sgDNA sequences were designed usign crispr.mit.edu</i>	51
<i>Table 2.4 Seqeuncing primers over regions of CRISPR editing</i>	53
<i>Table 2.5 R401X homology directed repair sequence</i>	55

### CHAPTER 3

<i>Table 3.1 Poly-caspase inhibition data</i>	71
<i>Table 3.2 Effects of Z-VAD-fmk in different cell lines</i>	73
<i>Table 3.3 IC50 for inhibitors of yeast N-glycanase based on chitobiose structures 8 and 9</i>	80
<i>Table 3.4 IC50 values of Z-VAD-fmk under different experimental conditions</i>	81
<i>Table 3.5 CC50 of Z-VAD-fmk for WT and ATG13 KO MEFs</i>	115

### CHAPTER 4

<i>Table 4.1 IC50 of cathepsin inhibition of caspase inhibitors</i>	139
<i>Table 4.2 Transfection strategies for siRNA</i>	141

### CHAPTER 5

<i>Table 5.1 Nomenclature of CRISPR constructs</i>	172
<i>Table 5.2 Expected band size for each mutation</i>	174
<i>Table 5.3 Conditions for homology directed repair transfection</i>	178
<i>Table 5.4 CC50 values of WT HEK cells, clone 3 and clone 7 HEK cells treated with MG132</i>	193
<i>Table 5.5 IC50 values of WT HEK cells, clone 3 and clone 7 HEK cells treated with Menadione</i>	196
<i>Table 5.6 Off-target effects of PNG guide sequence B in clone 3</i>	203
<i>Table 5.7 Off-target effects of PNG guide sequence B in clone 7</i>	204
<i>Table 5.8 Summary of proteins significantly up or downregulated in clone 3</i>	209
<i>Table 5. 9 Summary of proteins significantly up or downregulated in clone 7 compared to WT</i>	210

### CHAPTER 6

<i>Table 6.1 Autophagy receptor proteins and their targets</i>	217
<i>Table 6.2 Genes identified in co-IP experiments with N-glycanase</i>	237
<i>Table 6.3 LIR containing proteins found in enriched proteins in autophagosome isolation</i>	242



### 1.1 Structural and functional diversity of proteins

Proteins have exceptionally diverse roles, from acting as biological catalysts, to performing structural functions (such as actin in the cytoskeleton, and laminin in the extracellular matrix). This diversity of function arises from multiple factors, such as structure (Fu et al. 2000), size (Fischer et al. 2004), charge (Gitlin et al. 2006), the presence or absence of post-translational modification (PTMs) (Yu-Chieh Wang et al. 2013) and locale (Hung and Link 2011). Proteins are often classified into families and super-families which demonstrate high levels of structural and functional homology (Schlick 2002). The structures a protein can adopt are often essential to the functional role; the primary structure (the sequence of amino acids) determining the higher levels of fixed and dynamic structural organisation ultimately responsible for function. This “sequence-structure-function” paradigm has long been regarded as a cornerstone of structural biology (Shenoy and Jayaram 2010, Sadowski and Jones 2009).

The structure of a protein is generally described in terms of levels of structural organisation. First is the linear sequence of amino acids (encoded by DNA). The secondary structure involves the folding of polypeptides into  $\alpha$ -helices,  $\beta$ -sheets or random coil structures. The tertiary structure where the polypeptide is assembled to form the final conformation which can be stabilised by hydrophobic interactions and disulphide bonds (Pace et al. 2014). Perturbations in protein structure arising from mutation or damage can result in drastic functional changes. One such example is reduced oxygen binding in sickle cell anaemia;  $\beta$ -globin subunits bind heme which stabilises the protein structure and binds  $O_2$  to transport around the body. A single mutation of p.Val6Glutamic acid in the  $\beta$ -globin heme binding pocket results in polymerisation of the protein under deoxygenated conditions leading to reducing  $O_2$  binding (Thom et al. 2013, Nath and Hebbel 2015, Kassim and DeBaun 2013, Wonder et al. 2017). Likewise, changes in amino acid sequence can result in changes in the overall charge or region of a protein (such as a binding site) which may have an adverse effect on ligand binding interactions (Huang and Briggs 2002). For example, nicotinic acetylcholine receptor function relies on a ring of negatively charged amino acids on the external face; and

mutation of a single negatively charged glutamate or aspartate to a positively charged lysine results in a reduction in ion conductivity (Wilson et al. 2000).

### 1.1.2 Post-Translational Modifications

Further levels of complexity are introduced into the proteome through covalent attachment of additional modifications to protein structures. These are termed post-translational modifications (PTMs) or in some cases, co-translational modifications if they are introduced as proteins are synthesised. A variety of different post- and co-translational modifications are commonly found on protein structures, such as phosphorylation, ubiquitination, and glycosylation.

### 1.1.3 Phosphorylation

Phosphorylation allows cells to react to their environment by modifying internal pathways in response to external stimuli. It is the process of the addition of a phosphate group to a tyrosine or serine/threonine residue by tyrosine protein kinases (TPK) or a serine/threonine protein kinases (STPK) respectively. These modifications can be removed by phosphatases. It is a dynamic process with phosphate groups being cycled on and off throughout the lifespan of the protein.

Phosphorylation is extremely widespread and it is estimated that one third of all proteins (Olsen et al. 2006) are regulated via phosphorylation (Nishi et al. 2011), with many proteins bearing large numbers of potential phospho-sites. For example, the tumour suppression protein p53 is a transcription factor with a half-life of less than 20 minutes (Pant and Lozano 2014) and bears a high number of different post-translation modifications (Maclaine and Hupp 2009) including over twenty phospho-sites(Figure 1.1).

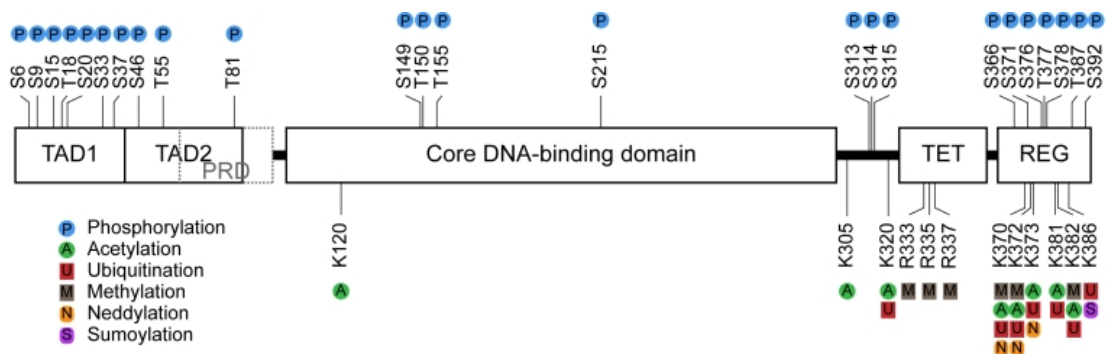


**Figure 1.1 Post-translation modification sites of p53. (Maclaine and Hupp 2009) Open access article distributed under Creative Commons Attribution Licence (CC-BY).**

Under cellular stress stimuli (such as DNA damage) p53 is phosphorylated, which serves to increase its activity as a transcription factor. Mutation studies of serine 20 to an aspartic acid residue (which mimics the presence of phospho-modified serine) found increased transcription activity (Maclaine and Hupp 2009). As well as individual proteins being regulated there are large networks of signalling cascades controlled by phosphorylation such as the mitogen-activated protein kinase MAPK cascade and, signalling induced by GPCR activation (Brzostowski et al. 2013, Cargnello and Roux 2011, Kim and Choi 2010). The MAPK cascade regulates diverse cellular functions including proliferation, apoptosis and various stress responses; often by induction of gene expression (Plotnikov et al. 2011). The MAPK cascade consists of three core kinases, MAP3K, MAPKK and MAPK (although others including MAP4K and MAPKAPK can also be involved) (Plotnikov et al. 2011). Signals are generated by sequential phosphorylation and activation of multiple kinases. Activation of extracellular receptors, including receptor tyrosine kinases (RTKs) and GPCRs results in the activation of the small GTPase Ras which recruits Raf protein kinases to the plasma membrane, which are then phosphorylated. Rafs then phosphorylate the MAPKKs, MEK 1 and MEK 2 which go on to phosphorylate ERK1/2 on both a tyrosine and threonine residue. MEK1/2 are part of a small number of dual specificity kinases, able to phosphorylate either threonine or tyrosine residue on ERK1/2. MEK1/2 also provide specificity for this cascade, as ERK1/2 is the only known target (Plotnikov et al. 2011). ERK1/2 then activates transcription factors in the nucleus and upregulates expression of several target genes including erthroblastosis virus twenty-six (ETS) and AP1 transcription factor (AP-1/FOS) both involved in cell cycle progression (Little et al. 2013).

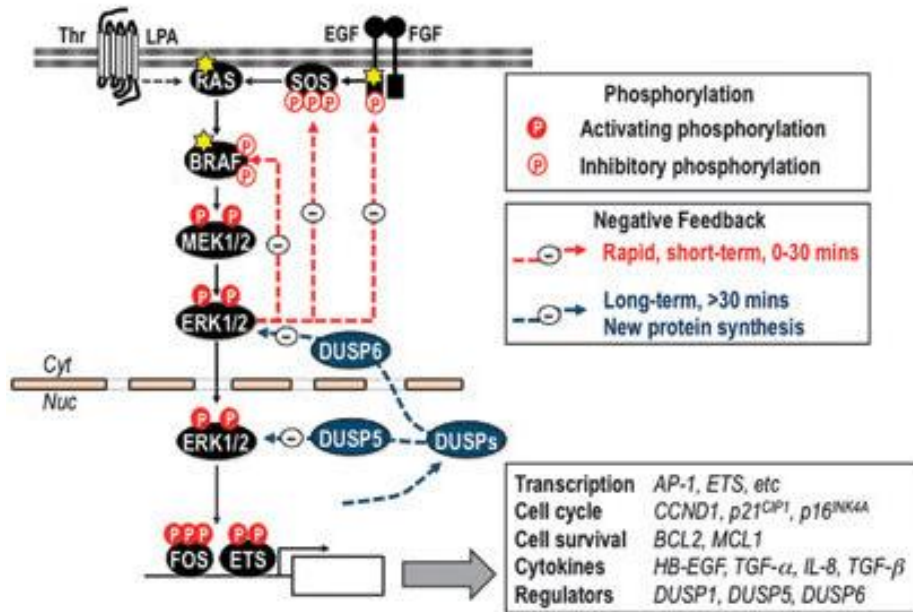
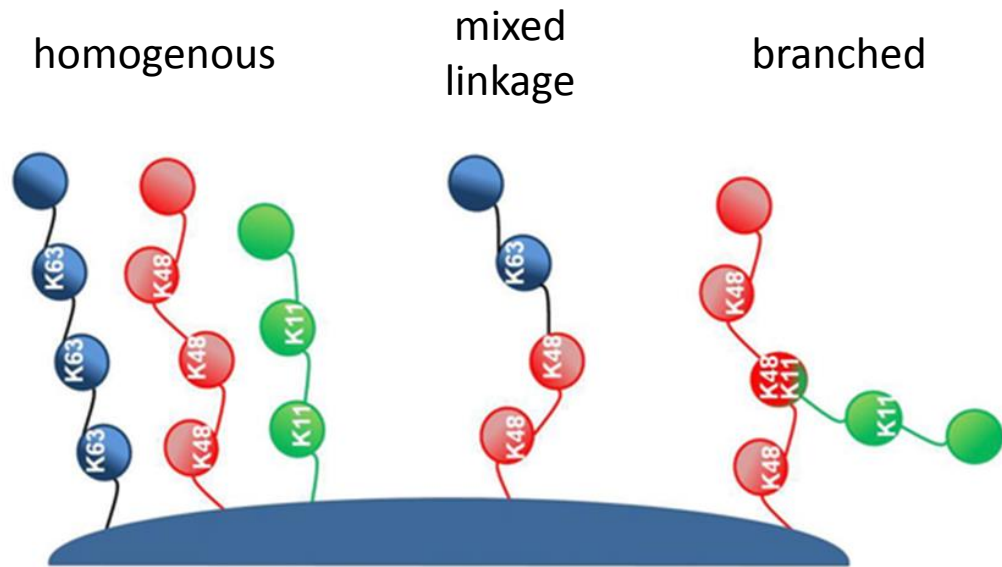


Figure 1.2 Diagram showing the key components of the ERK1/2 signalling cascade. Reprinted with permission from Nature: Oncogene (Little et al. 2013).

#### 1.1.4 Ubiquitination

Ubiquitin is a small globular protein of 76 amino acids, of which multiple copies can form chains conjugated to proteins via any of its seven lysine residues or the N-terminal methionine. This post-translational modification results in K6, 11, 27, 29, 33, 48 or 63 linked chains of ubiquitin (Figure 1.3). As well as homogenous linkages, ubiquitin chains can contain mixed linkages, which serves to increase the diversity of the signal. Proteins bearing K48 and K63 linked ubiquitin have been extensively studied as this modification is associated with protein degradation signals via the proteasome and autophagy respectively. Ubiquitination has also been implicated in other cell signalling mediated events, such as the response to DNA damage (Brinkmann et al. 2015), protein trafficking (Pizarro and Norambuena 2014) and activation of NF- $\kappa$ B (Iwai et al. 2014).



**Figure 1.3 Linkage examples of ubiquitin chains. Homogenous linkages contain ubiquitin linked via one lysine residue. Mixed linkages contain ubiquitin linked via different lysine residues. Branched chains consist of multiple ubiquitin proteins linked via different linkages to a single ubiquitin protein. (Scott et al. 2015) Open access article distributed under Creative Commons Attribution Licence (CC-BY).**

Ubiquitination is controlled by the E1, E2 and E3 proteins; these are involved in ubiquitin activation, ubiquitin transfer, and ubiquitin ligation. The ubiquitin signal is highly dynamic, and ubiquitin chains can be cycled on and off the target substrate. This removal of ubiquitin is controlled by deubiquitinating enzymes (DUBs) (Amerik and Hochstrasser 2004, He et al. 2016).

As well as ubiquitin chains acting to modulate protein function, ubiquitin itself can also bear further modifications such as acetylation and phosphorylation (Figure 1.4). Ubiquitin can also be modified by SUMOylation, the modification by the small ubiquitin-like modifier (SUMO) family further diversifying the ubiquitin signal (Henley et al. 2014). Many ubiquitin modifications have been discovered by proteomics experiments (Udeshi et al. 2013, Elia et al. 2015) however, the kinases/phosphatases and acetyltransferases/deacetylases involved in these modifications are largely unknown (Swatek and Komander 2016).

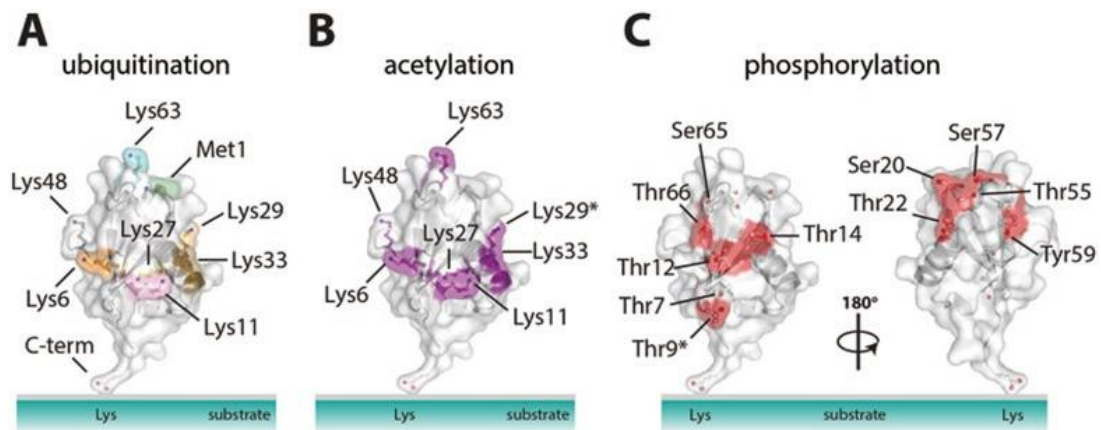


**Figure 1.4 Modification of ubiquitin (Swatek and Komander 2016). Open access article distributed under Creative Commons Attribution Licence (CC-BY).**

To decode the ubiquitin signal, proteins contain an ubiquitin binding domain (UBD) of which there are more than twenty families (Scott et al. 2015). The structure of the ubiquitin chain can lead to the specific recruitment of downstream ubiquitin-recognising proteins that modulate different cellular effects.

Ubiquitin often regulates protein function by influencing stability and protein lifespan. For example, as well as phosphorylation, p53 is also regulated by ubiquitination. Under regular conditions, the E3 ubiquitin ligase, MDM2 ubiquitinates p53 and targets it to proteasomal degradation. Knockout studies of *Mdm2* in mice have found increased cell death induced by p53 (Pant and Lozano 2014).

#### 1.1.5 Glycosylation

Glycosylation is the term used to describe the covalent attachment of carbohydrates (glycans) to biological molecules including proteins and lipids, and is one of the most common protein modifications. Although protein glycosylation is commonly described as a post translational modification (Lanctôt et al. 2006, Fabbro et al. 2015), under many conditions it is more accurately described as a co-translational modification, as the glycan is added during protein synthesis rather than following synthesis and folding events. Protein bound glycans are involved in protein folding (Ellgaard et al. 2016), molecular recognition events (Scott and Panin 2014) and cellular adhesion (Ghoshal et al. 2014). There are numerous different types of glycosylation but commonly encountered modifications are glycosylphosphatidylinositol anchors (GPI anchors), *O*-linked glycosylation and *N*-linked glycosylation.

### 1.1.6 GPI anchors

GPI anchors are glycolipid based modifications for cell surface proteins such as receptors, structural proteins and adhesion molecules (Kinoshita 2016). GPI anchors consist of a phosphatidylinositol and a glycan core made up of a single glucosamine and three mannose residues topped with phosphoethanolamine which is linked to the protein via an amide bond (Kinoshita 2016) which occurs in the ER (Fujita et al. 2011). Figure 1.5 shows the basic structure of a GPI-anchor.

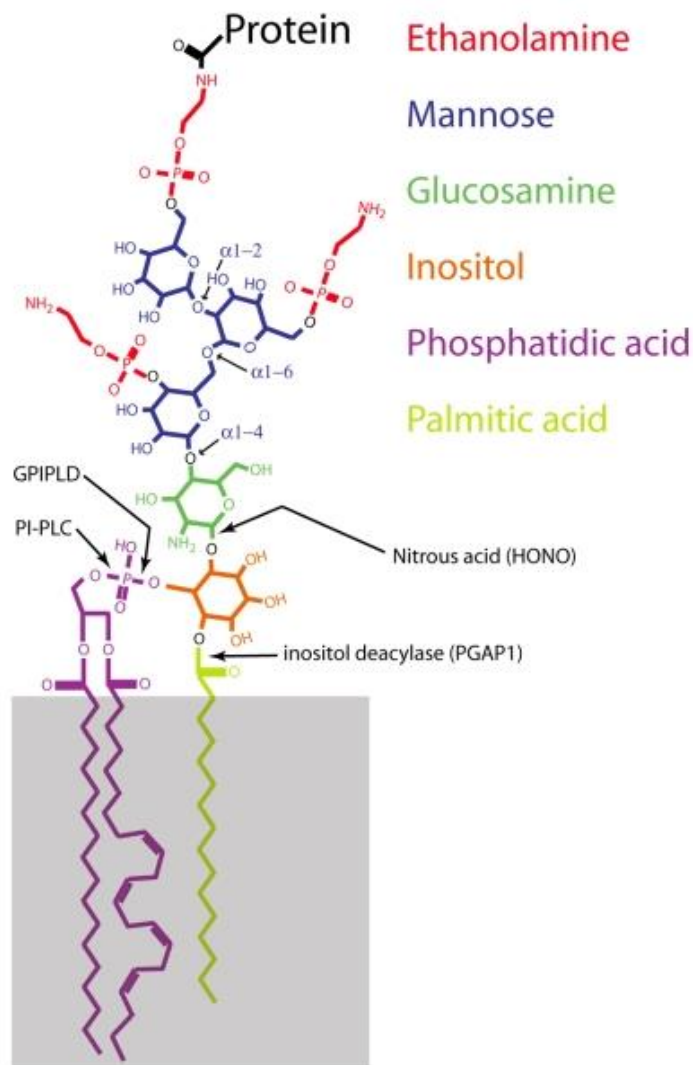


**Figure 1.5 Basic structure of a GPI-linked protein. Reprinted under the Creative Commons Attribution Licence (Zoltewicz et al. 2009)**

#### 1.1.6 *O*-linked glycosylation

*O*-linked glycans are carbohydrates covalently attached to the hydroxyl group of a serine or threonine residue via an *O*-glycosidic bond. A number of carbohydrates can be linked to serine or threonine in this manner. One of the most common structural motifs is the attachment of *N*-acetylgalactosamine (GalNAc). Such structures are classified as mucins, and glycoproteins bearing modifications of this type are important from a physiological standpoint as they often coat and protect epithelial surfaces (Stanley 2011). *O*-linked glycosylation is a complex co-translational modification; sugars are added sequentially, starting with GalNAc in the ER/cis Golgi, which is transferred to the protein substrate from the UDP-GalNAc donor by enzymes from the polypeptide *N*-acetylgalactosaminyltransferase family in the trans- Golgi, a galactose residue is added, and typically the chain is terminated by addition of two sialic acid residues (Lodish *et al.* 2000).

The simplest *O*-linked glycosylation event is the addition of a single, post-translational, *O*-GlcNAc residue to a serine or threonine residue in a protein. This process is termed *O*-GlcNAcylation and is a dynamic process; *O*-GlcNAc being attached and removed from target molecules by *O*-GlcNAc transferase (OGT) and *O*-GlcNAcase (OGA) respectively. This switchable glycan modification has been described as more akin to phosphorylation than other types of glycosylation (Bond and Hanover 2015). *O*-GlcNAc signalling has been linked to a variety of pathological states, including some neurodegenerative disorders (Wani *et al.* 2017). In p53, *O*-GlcNAcylation of serine 149 prevents phosphorylation of threonine 155 which increases stability by reducing ubiquitination (Yang *et al.* 2006).

#### 1.1.7 *N*-linked glycosylation

*N*-linked glycosylation is the addition of a glycan moiety to an asparagine residue in the consensus sequence Asn-X-Ser/Thr where X is any amino acid except proline. Compared to *O*-linked glycosylation, *N*-linked glycosylation is better understood in terms of assembly and its roles in processes such as protein folding, although other functions remain obscure. *N*-linked glycosylation is ubiquitous and is found in all three domains in life (Aebi 2013), however, only mammalian glycosylation will be reviewed here.

*N*-linked glycosylation has a key role in protein folding and the ER quality control system, where the structure of the glycan acts as a signal to indicate if a protein is correctly folded. This determines if the protein is retained or exported from the folding environment of the ER. During this folding process *N*-linked glycans may also aid folding by changing the local



environment at the site of glycosylation and play a role in the function of mature glycoproteins (Tannous et al. 2015).

*N*-linked protein glycosylation can be viewed as a sequential pathway with three main steps; production of a lipid-linked oligosaccharide (LLO), transfer of the LLO *en bloc* by oligosaccharyltransferase (OST) to a peptide with the consensus sequence Asn-X-Ser/Thr and transport to the Golgi for further processing which is summarised in figure 1.6. The first step of *N*-linked glycosylation is the production of a set of oligosaccharides joined to a lipid carrier. Activated nucleotides carrying sugars in the cytoplasm attach the sugars to a dolichol phosphate molecule embedded in the ER membrane. The sugars are attached on the cytoplasmic side of the dolichol phosphate to form an oligosaccharide formed of two *N*-acetylglucosamine residues with five mannose residues (GlcNAc<sub>2</sub>Man<sub>5</sub>). This structure is then flipped into the ER lumen (Lehrman 2015). Within the ER, further mannose and glucose residues are attached to form the core Glc<sub>3</sub>Man<sub>9</sub>GlcNAc<sub>2</sub> structure. The Glc<sub>3</sub>Man<sub>9</sub>GlcNAc<sub>2</sub> oligosaccharide is transferred *en bloc* via the oligosaccharyltransferase (OST) to an asparagine residue on the peptide (Aebi 2013).

After the glycan is covalently linked to the peptide, ER-resident glucosidases act to successively trim glucose residues from the glycan structure. Glucosidase I removes a single terminal glucose, whilst glucosidase II then removes a further glucose, leaving a glycan structure bearing a single glucose cap (Figure 1.11). Removing these moieties allow interaction with ER protein chaperones.

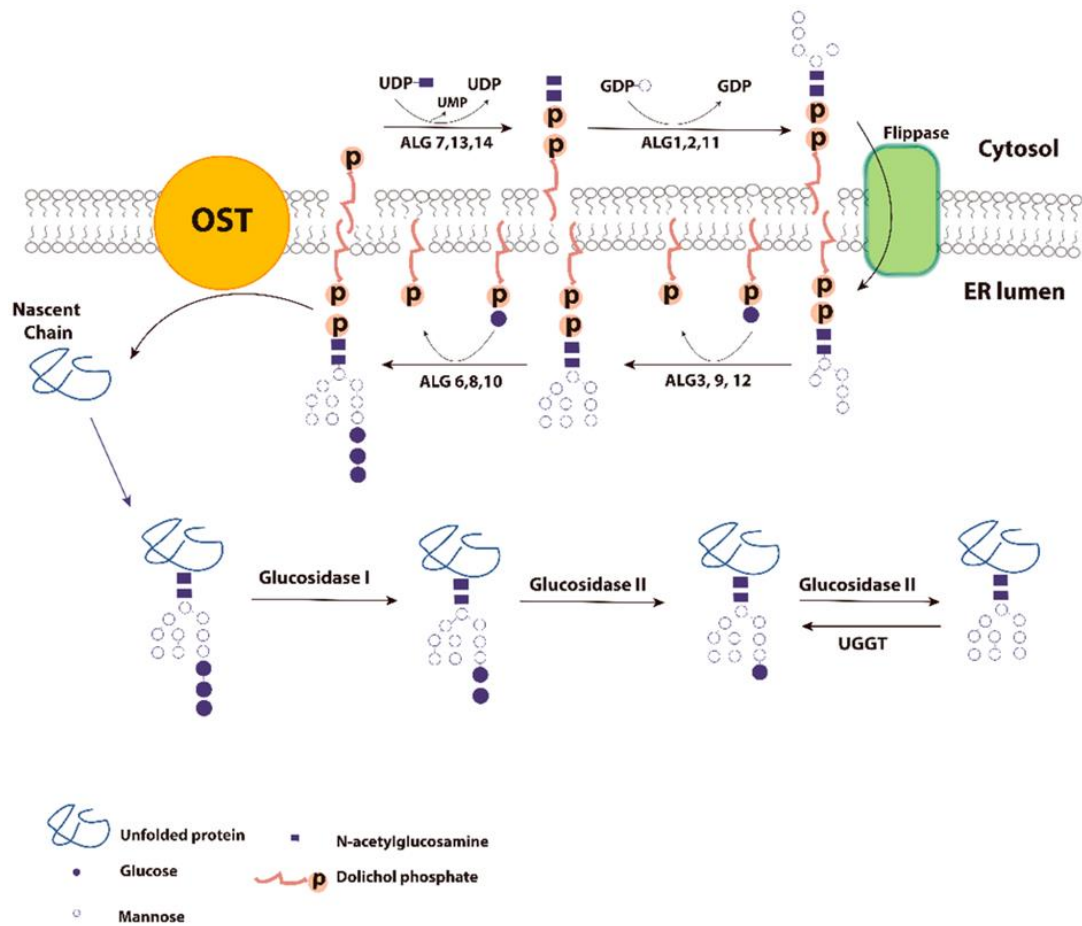


**Figure 1.6 Glycan structures of the lipid-linked oligosaccharide in the cytosol and ER luminal face. After the production of a GlcNAc<sub>2</sub>Man<sub>5</sub>, glycan structures are flipped to the ER lumen, further modified and attached to a nascent polypeptide (Wang et al. 2015). Open access article distributed under Creative Commons Attribution Licence (CC-BY).**

Once glycosylated and correctly folded, proteins are trafficked through the Golgi, where they are further elaborated. Processing by mannosidases initially occurs in the ER but continues in the cis-Golgi resulting in a number of different classes of structures. Glycans containing between five and nine mannose residues are termed high mannose glycans. Other glycans can be further processed into complex and hybrid glycans shown in figure 1.7.

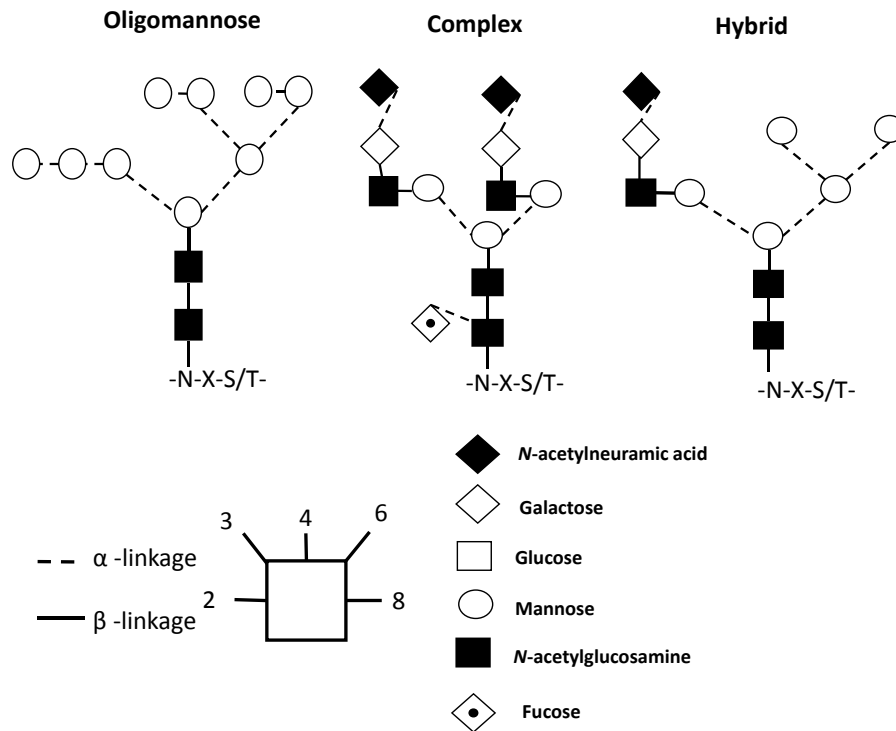


**Figure 1.7 Structures of different types of N-glycans, including oligomannose, complex and hybrid. Oxford notation.**

The cis, medial and trans-Golgi contain enzymes that modify glycan chains. Bi-antennary glycans are the most commonly found but tri- and tetra- is not uncommon. The branches are extended by galactose and sialic acid residues which are added later in the trans-Golgi by specific galactosyltransferases and sialyltransferases. Further processing of the glycans is linked with the secretory pathway and allows monitoring of protein progress (Schwarz and Aeby 2011).

Most glycoproteins are synthesised with a heterogeneous array of glycans and many bear multiple glycosylation sites. These differential glycan profiles of the same protein are termed glycoforms (Rudd and Dwek 1997) and can exhibit functional differences. It is thought that there is usually a dominant glycoform (Scott et al. 2013). Glycan heterogeneity can arise from various factors. The glycan profile of a protein may be different depending on the species, organ or tissue it is produced in (Edberg and Kimberly 1997, Raju et al. 2000). Growth conditions also influence the glycan profiles produced. For example, reducing the temperature of CHO cells (which are commonly used as an expression host in biopharmaceutical production) in culture from 37 °C to 33 °C during stationary growth has been shown to increase levels of sialylation and decrease levels of fucosylation of a secreted

human placental alkaline phosphatase (SEAP) (Nam et al. 2008). The rate of transit through the secretory pathway also effects the final glycan profile of a protein. As proteins travel through the Golgi they are in contact with different glycan modifying enzymes for different amounts of time (Hossler et al. 2007). Under disease conditions, different glycan profiles have been recorded. Control of glycan heterogeneity is especially important during the production of biopharmaceuticals as a change in expression conditions can change the properties of the therapeutic (Jefferis 2013).

#### 1.1.8 Congenital disorders of glycosylation

The importance of glycosylation can be illustrated by the fact that 1-2 % of the entire genome is dedicated to proteins involved in glycosylation (Freeze *et al.* 2009). Consequently, when mutations occur in any of these genes it results in severe, global pathological effects. Such disorders are termed congenital disorders of glycosylation (CDG), and increasing numbers of these disorders have been identified (Figure 1.8). As glycosylation occurs in all cells these disorders affect multiple organ systems especially the brain, liver and heart (Grünewald 2009, Caglayan et al. 2015, Malm and Nilssen 2008, Lefeber et al. 2011). CDGs are categorised as rare disorders according to the criteria set by Rare Diseases Europe (EURODIS), who categorise rare diseases as affecting less than 1 in 2000 people. CDGs can vary in severity from patient to patient making symptoms difficult to characterise. As of 2015, The National Centre for Rare Disorders (NORD) describes 25 CDGs related to *N*-linked glycosylation, 18 of *O*-linked glycosylation and 7 defects of glycosphingolipids and GPI anchors (NORD 2015).

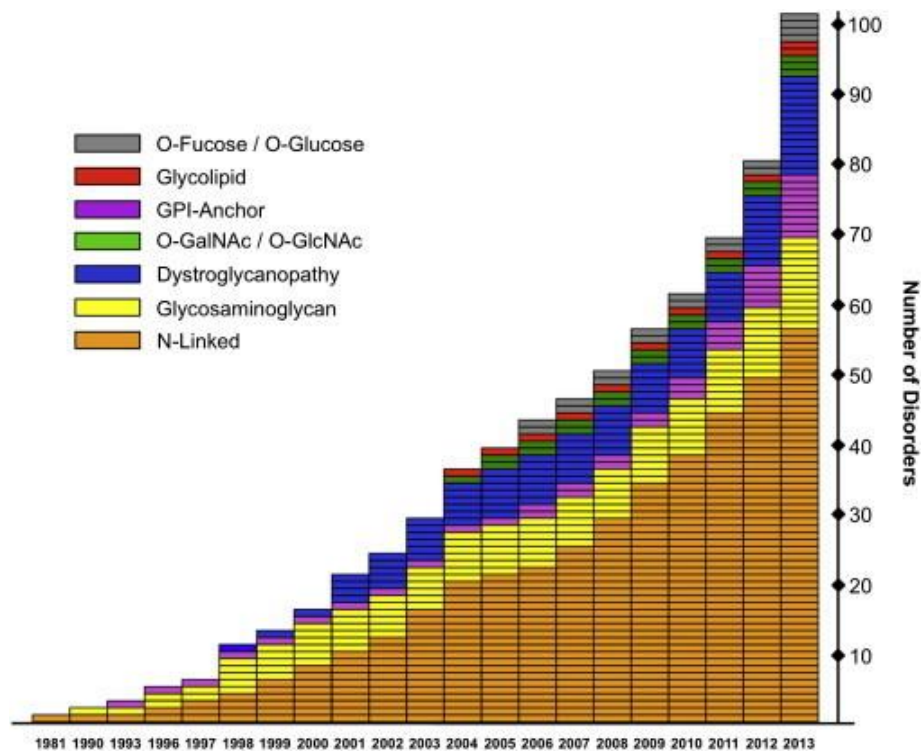


**Figure 1.8** Number of congenital disorders of glycosylation discovered over the last 30 years has increased, the majority of CDGs identified have been in *N*-linked glycosylation. Reprinted with permission from *The American Journal of Human Genetics*, 94:2, (Freeze et al. 2014).

Proteins are the major workhorses of the cell and are regulated in various ways. As mentioned, dysregulation of these processes can have major implications, not just for the protein but for the cell and body. Problems can also arise from the synthesis of proteins and strict quality control measures are in place to stop misfolded proteins from entering the proteome of the cell.

### 1.2.1. Protein folding

The primary amino acid sequence is the key determinant of the final three-dimensional structure of a protein. Folding occurs in stages, with the formation of folding intermediates which are more likely to aggregate in aqueous solutions due to exposed hydrophobic or unordered regions, which in the final conformation are hidden. Aggregation is typically driven by hydrophobic interactions and can result in amorphous structures or, in some cases (such as amyloid- $\beta$ ), a highly ordered and stable fibril structure via  $\beta$ -sheet interactions. The number of possible three-dimensional conformations a protein can adopt is wide-ranging

although, as the function of proteins relies heavily on the structure, few of these will result in a functional end product.

Correct folding relies heavily on hydrophobic interactions and weak non-covalent bonds. During folding, peptides can collapse due to these hydrophobic forces resulting in intermediate or misfolded states. The energy of this folding landscape is shown in figure 1.9. It may be energetically favourable for intermediate or misfolded structures to form aggregates through reactions with other species. Consequently, cellular mechanisms exist to reduce protein aggregation or the production of misfolded and potentially toxic protein species. *In vivo*, chaperone proteins can act to increase protein folding and prevent aggregation through binding. It is estimated that around 20 -30 % of the total protein complement of mammalian cells do not have a tertiary structure until bound to binding partners (Hartl et al. 2011).

A large number of diseases, including neurodegenerative disorders including Alzheimer's, Huntington's and Parkinson's (Irvine et al. 2008, Hashimoto et al. 2003, Gundersen 2010, Arrasate and Finkbeiner 2012), are associated with protein aggregates indicating a toxicity associated with these structures. Aggregation does not necessarily mean a protein will need to be degraded, refolding of protein aggregates via the action of protein chaperones has been observed in mammalian cells (Tyedmers et al. 2010).

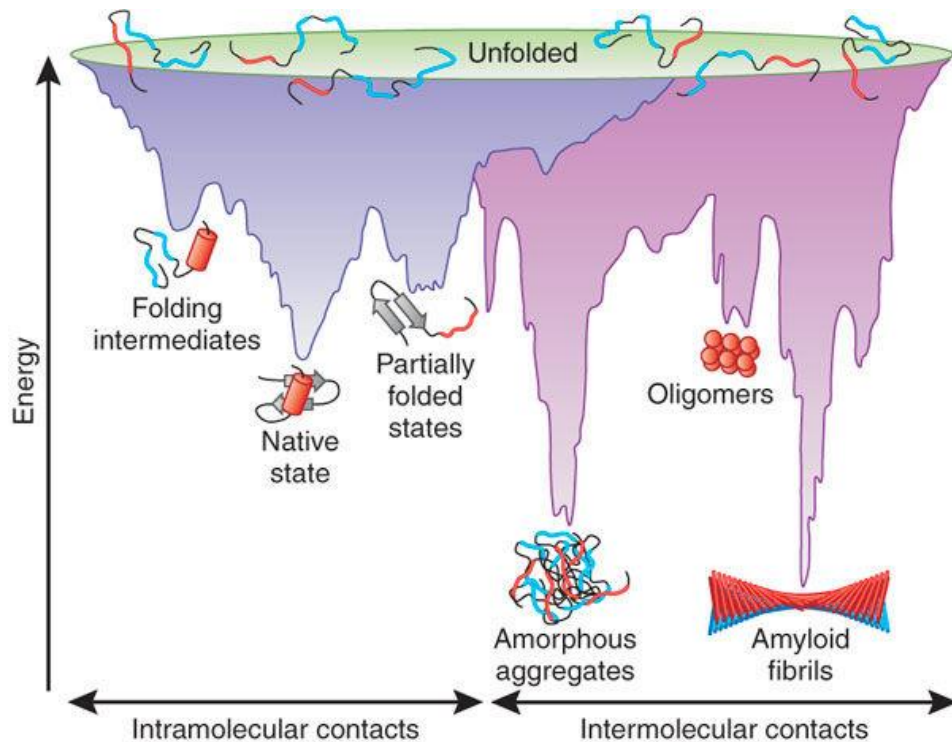


**Figure 1.9 Misfolded or partially folded peptides are prone to aggregation which is often driven by hydrophobic interactions. The purple area shows energy states moving towards a native conformation while pink shows the formation of aggregates. Reprinted, with permission of Macmillan Publishers Ltd. from (Hartl and Hayer-Hartl 2009).**

Translated peptide sequences in the cytoplasm are at a high risk of aggregation as the peptide cannot fold correctly until it has been fully synthesised. Intra-chain interactions may also block native folding. Chaperones in the cytoplasm (such as heat shock proteins (HSP) HSP70 and HSP60) recognise hydrophobic amino acid side chains and bind nascent peptides to inhibit misfolding and prevent aggregation. (Hartl and Hayer-Hartl 2009, Marciniowski et al. 2013).

### 1.2.3 Protein folding in the ER

Proteins can also contain signal sequences which target the protein to the ER secretory pathway or, to other organelles including mitochondria. The ER is involved in post- and co-translational modifications, disulphide bond formation, and the attachment of moieties such as GPI anchors which are needed for correct protein function. Similarly to protein folding in the cytoplasm, the ER contains protein chaperones (such as BiP, calnexin, calreticulin and GRP94), the action of which can increase protein solubility and decrease the tendency of structures to aggregate. Binding to these chaperones serves to retain the protein in the folding environment of the ER. Proteins containing an *N*-terminal signal sequence recognised

by the signal recognition particle (SRP) which slows translation and enables the peptide to be co-translationally transported into the ER via the SEC61 complex (Mason et al. 2000). Although these signal sequences are extremely diverse and vary in length and amino acid sequence, they are all hydrophobic. Once the ribosome nascent chain complex (RNC) binds to the SEC61 complex, translation continues and the nascent protein is delivered into the ER lumen (Nyathi et al. 2013). Once in the ER, the protein enters the quality control (QC) cycle which prevents the release of unfolded or misfolded proteins that may exert toxic effects on the cell.

#### 1.2.4. Glycoprotein folding in the ER

The calnexin/calreticulin (CNX/CRT) cycle ensures quality glycoprotein folding within the ER. This process is shown schematically in figure **1.10**.



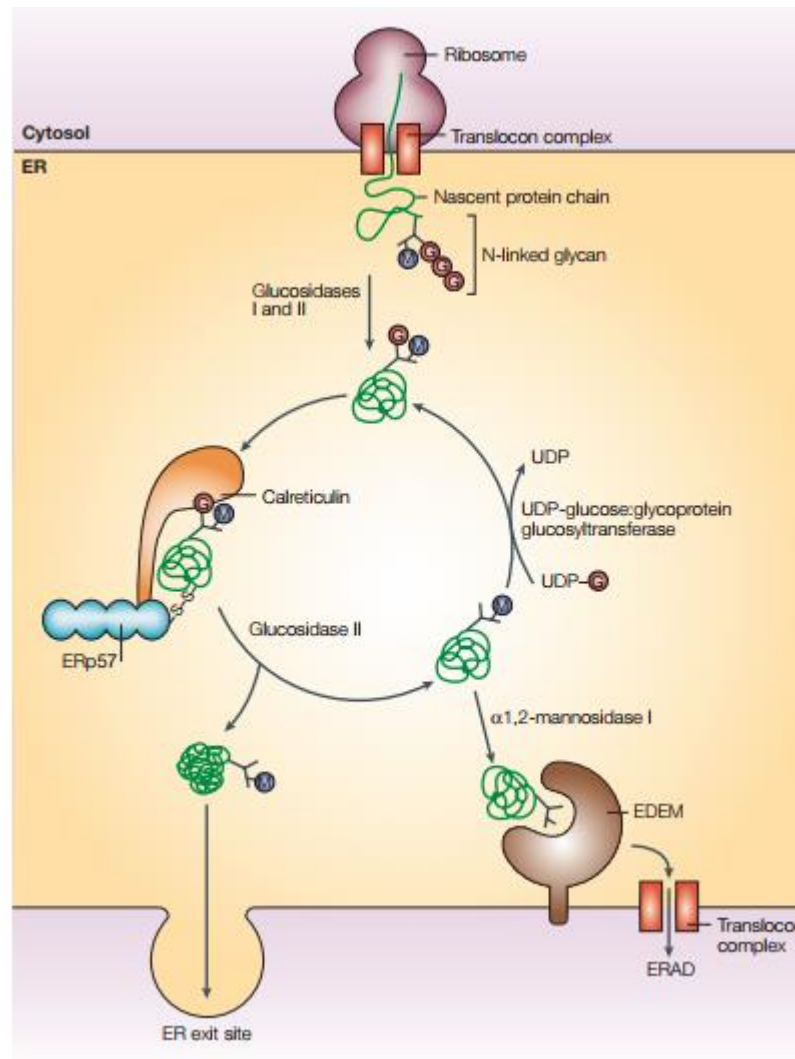


**Figure 1.10 Diagram showing the calreticulin cycle of glycoprotein folding. Reprinted with permission from Springer Nature: Nature reviews molecular cell biology (Ellgaard and Helenius 2003).**

During translation, *N*-linked glycans (Glc3Man9GlcNAc2) are transferred to proteins containing an *N*-glycan consensus site. These glycans are trimmed by ER resident glucosidase I to yield protein bound Glc2Man9GlcNAc2 which prevents rebinding to the OST complex (Ferris et al. 2014). A further terminal glucose residue is trimmed by glucosidase II allowing binding to the lectin chaperones CNX/CRT, which bind nascent mono-glucosylated glycoproteins. Generally, if the glycosylation site is within the first fifty amino acid residues the protein interacts with membrane-bound CNX, whereas if the site is after the first fifty amino acids it binds the soluble CRT (Helenius and Aeberli 2001). Upon binding to CNX or CRT, other chaperones (including ERp57) are recruited. ERp57 is an oxidoreductase that binds

stably to CNX and CRT and assists the formation of disulphide bonds in glycoproteins (Mason et al. 2000).

Glucosidase II breaks the CNX/CRT cycle by removing the terminal glucose from the Glc1Man7-9GlcNAc2 glycan, which results in the release of the protein from the chaperone. If the protein is folded correctly it leaves the CNX/CRT cycle and exits the ER. If, however, the protein is incorrectly or incompletely folded, UDP-glucuronosyltransferase (UDP-GT) catalyses the transfer of a glucose residue from the UDP-glucose donor onto Man7-9GlcNAc2 and the protein is targeted back to the CNX/CRT cycle. In this context, UDP-GT acts as a folding sensor which recognises both the specific glycan moiety and biophysical characteristics like exposed hydrophobic areas (Ritter et al. 2005). This also ensures, de-glucosylated, folded substrates are not targeted back to the CNX/CRT cycle. UDP-GT recognises the innermost GlcNAc residue of the *N*-glycan and non-native protein conformations such as exposed hydrophobic amino acid side chains (Sousa and Parodi 1995).

The rate of folding differs substantially between proteins; some proteins spend minutes, others spend hours in the CNX/CRT cycle (Helenius and Aebi 2001). If proteins fail to fold correctly following repeated recycling through the CNX/CRT cycle, they are termed terminally misfolded. Terminally misfolded proteins exit the CNX/CRT and are targeted for degradation by the proteasome in a tightly coupled process, termed ER-associated degradation (ERAD).

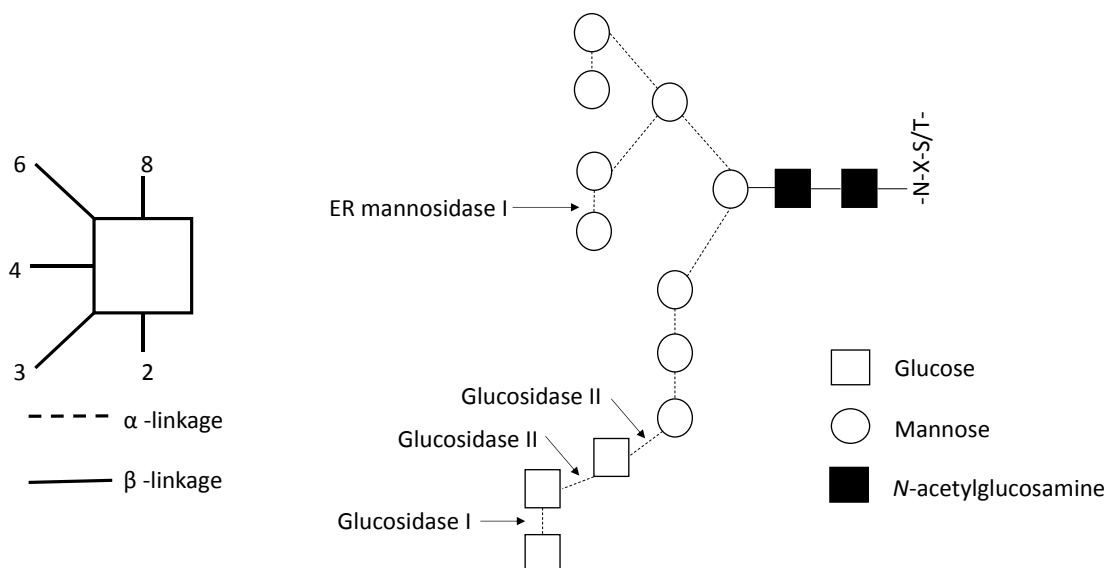


**Figure 1.11 *N*-linked glycan  $\text{Glc3Man9GlcNAc2}$ , showing the target site of glucosidase I and II and ER mannosidase I (Oxford notation).**

ER Mannosidase I is involved in the removal of proteins from the CNX/CRT cycle by catalysing the removal of a terminal mannose residue (figure 1.11). The Man<sub>8</sub>GlcNAc<sub>2</sub> glycan product of this cleavage is recognised by the ER degradation-enhancing 1, 2-mannosidase-like protein (EDEM), which directs the protein for degradation. Mannosidase I has a slow reaction time and it has been hypothesised that this may effectively act as a “timer” for ERAD substrates. If a protein remains in the CNX/CRT cycle then ER mannosidase I will eventually remove the terminal mannose and release the protein from the cycle (Avezov et al. 2008). The interaction with EDEM acts as a signal for protein degradation (Ruggiano et al. 2014, Olzmann et al. 2013, Meusser et al. 2005).

Other chaperones are also involved in the processing of glycoproteins. Malectin is an ER membrane bound protein which interacts with high mannose glycans bearing terminal glucose residues prior to the CNX/CRT cycle. During ER stress, Malectin is upregulated and may provide an extra means to halt the secretion of misfolded proteins under ER dysfunction (Galli et al. 2011).

Proteins entering the ER that are not glycosylated behave in much the same way, although the pathways which act to identify and target terminally misfolded proteins to degradative pathways are less defined. BiP is one of the most abundant ER chaperones and recognises hydrophobic regions. BiP has two domains (an ATPase activity domain and a substrate binding domain), and binds to and releases target substrates in an ATP dependent manner. Although chaperones act to increase protein solubility and reduces aggregation, folding cannot occur whilst the structure undergoing folding is bound (Mason et al. 2000).

Glycosylation is also only evident on the surface of proteins, although how this is achieved is poorly understood. Glycan transfer occurs on the nascent, unfolded polypeptide as it is translocated into the lumen of the ER. In this case it would be expected all Asn-X-Thr/Ser sequences would be targeted, however this is not the case (Medzihradzsky 2008). Initial proposals included the polarity of asparagine, serine and threonine as a mechanism to control N-linked glycosylation. Polar residues are most commonly on the exterior surface (Lodish H 2000). It may be that rapid folding of the protein restricts access of the internal consensus sequences to the OST (Stanley 2011).

### 1.3.1 Protein degradation pathways

Old or dysfunctional proteins and organelles need to be removed from the cell to maintain efficient functioning and homeostasis. There are two main degradation pathways that

maintain cellular health, the ubiquitin-proteasome system (UPS) and autophagy. The UPS is made up of a number of ubiquitin ligases, modifiers and binding proteins that recognise ubiquitin bound proteins and targets them for degradation by the proteasome. The UPS is responsible for the degradation of 80-90 % of proteins including short-lived or damaged and denatured proteins (Lilienbaum 2013). Autophagy is mainly important for degrading long-lived proteins and aggregates and organelles but both are important for maintaining pools of amino acids for making new proteins and maintaining quality control.

Dysfunction in either the UPS or autophagy results in the build-up of ubiquitin coated protein aggregates. The protein degradation pathways have been shown to have a compensatory mechanism, when one pathway is impaired the other increases its function (Kageyama et al. 2014)

### 1.3.2 Ubiquitin Proteasome System – ERAD

ER quality control and protein folding is tightly linked to the UPS. During ER quality control, misfolded proteins are identified and signalled to leave the CNX/CRT pathway. Terminally misfolded proteins targeted for degradation by ubiquitination and degraded by the 26S proteasome. This degradation process, termed ER-associated degradation (ERAD) acts to avoid the release of potentially toxic misfolded/incorrectly folded proteins into the cytosol. Signals from *N*-linked glycans divert misfolded proteins to degradation. There are four aspects of the UPS; substrate recognition, translocation from the ER, substrate targeting and degradation, which will be discussed in the context of ERAD.

Misfolded proteins are extremely diverse in nature as these are not just one protein species. Therefore the machinery dealing with them needs to either recognise the sugar chain or have a broad specificity for peptides. During protein folding in the ER, the structure of *N*-linked proteins can relay information about the folding status of polypeptides. The machinery linking recognition, retro-translocation and ubiquitination are closely coupled. This can be seen in the organisation of the large multimeric complex called the dislocon. Membrane bound ubiquitin ligases are organised around the channels for transporting proteins out of the ER, along with several different adaptors used to link glycan recognition as shown in figure 1.12.

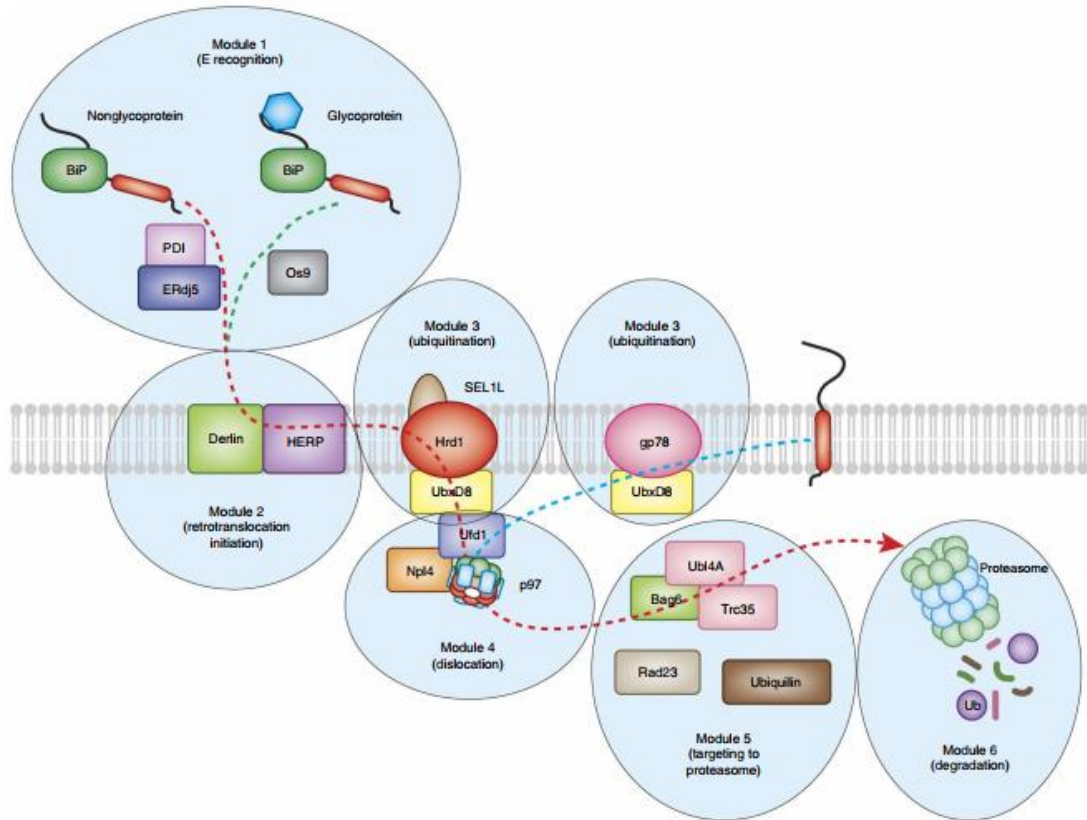


**Figure 1.12 Schematic representation of ERAD showing proteins involved in recognition, retro-translocation/dislocation, ubiquitination and targeting for proteasome degradation. Reprinted by permission from Springer Nature: Nature structural and molecular biology (Christianson and Ye 2014).**

The mammalian ER membrane contains at least 24 RING-finger E3 ubiquitin ligases involved in ubiquitinating substrate proteins, although only a few have been identified as being specifically involved in ERAD. The dislocon is a channel that exports proteins from the ER back into the cytoplasm. Proteins are targeted for degradation by the 26S proteasome by a polyubiquitin chain. Three main enzymes are needed to ubiquitinate proteins; E1, E2 and E3. Specificity comes mainly from the E3 ligases which attaches the ubiquitin moiety to the substrate peptide (Lecker et al 2006). In yeast, two E3 ligases have been identified to be involved in ERAD, Hrd1 and Doa10 which targets transmembrane/luminal regions and cytosolic, regions respectively (Hirsch et al. 2009). Homologues of Hrd1 in mammalian cells are HRD1 and gp79 (figure 1.12). Less is known about the mammalian orthologue to Doa10 but TEB4 shares similar protein structure and sequence (Hassink et al. 2005). HRD1 forms a complex with SEL1L, DERLIN, HERP and OS-9. SEL1L is an ER luminal glycoprotein which acts as a scaffold to link substrates to HRD1. SEL1L binds to OS-9 and EDEM1 and 3 (both are ER resident lectins) and ERFAD-ERp90, an ER-PDI (Olzmann et al. 2013), thus linking substrate

recognition to ubiquitination. The E3 ligase also controls the speed of degradation as the rate limiting enzyme. In HeLa cells, upon ER stress the E3 ligase HRD1 is upregulated (Kaneko et al. 2016).

Contradictory evidence has been shown for the requirement of unfolding for retro-translocation. At this point the proteins are retro-translocated into the cytosol via the ATP dependent VCP motor, also called p97 and CDC48. This is complexed with UFD1 and NPL4. Once in the cytosol a chaperone containing complex of BAG6, UBL4A and TRC35 maintain solubility of proteins containing hydrophobic regions.

The K48 ubiquitin chain is the most abundant ubiquitin chain and is used predominantly for UPS degradation of misfolded proteins. Under proteasome inhibition, K48 rapidly accumulates however, linkages 6, 11, 27 and 29 also increase, indicating involvement in proteasome degradation.

The ERAD substrates are moved to the proteasome by shuttling proteins including RAD23A/B, UBQLIN1-4 and DDI1/2 which all contain UBL and UBA domains. RAD23 contains two UBA domains which are specific for K48 linked ubiquitin (Nathan et al. 2013). RAD23 can interact with the proteasome via its UBL domain (Liang et al. 2014). The proteasome is also able to bind directly to ubiquitin chains. The 26S proteasome is a large structure of around 2.4 MDa with a 20S core subunit where linearized peptides are degraded, and one or two 19S regulatory subunits that allow binding of shuttle proteins such as Rad23 an ubiquitin chains. PSMD4 ( $\gamma$ -rpn10) and ADRM1 ( $\gamma$ -rpn13) contain a ubiquitin interacting motif (UIM) (Saeki 2017).

Prior to degradation, proteins need to be linearized. As shown in figure **1.13**, the proteasome contains a narrow channel that does not allow folded structures to enter. Degradation starts at disordered regions and unfolding starts from this point by ATPase subunits that unfold peptides (Inobe and Matouschek 2014). Unfolded proteins are able to be degraded independent of ATP with the exposed hydrophobic areas thought to replace the ubiquitin signal for targeting (Lilienbaum 2013).

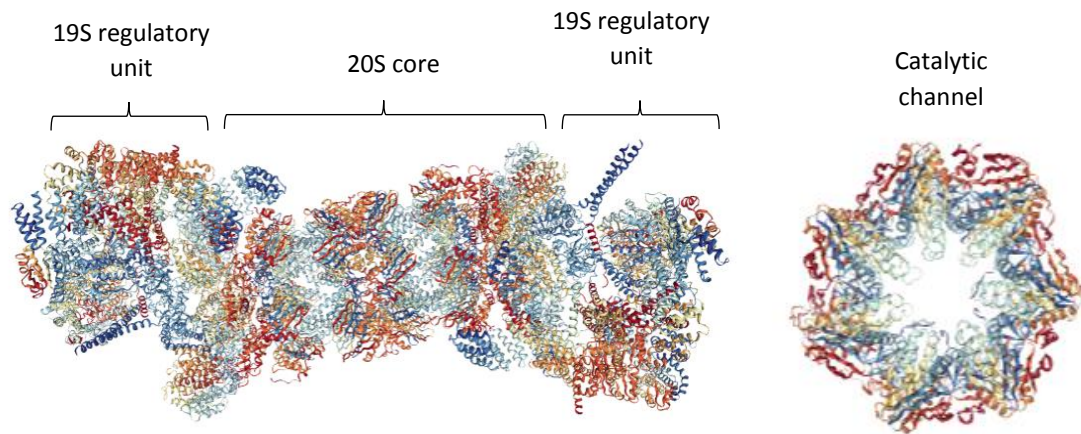


**Figure 1.13 Atomic structure of human 26S proteasome (generated from PDB ID: 5GJR (Huang et al. 2016) using NGL Viewer)**

Out of the context of ERAD, signals for degradation can arise at several levels, including during translation to recognise defective mRNA. Incorrectly incorporated amino acids are not rare. It is estimated that 5-10 % of proteins contain a wrongly incorporated amino acid (F. Wang et al. 2015). Ubiquitin linkage to substrate proteins is related to the structure of the substrate itself. E3 ligases can recognise old/damaged proteins and target them to the UPS (Kevei et al. 2017). Some substrates also contain sequence dependent affinity for the E3 ligases (known as the N-end rule) proteins with an  $\alpha$ -amino group at the N-terminus have a higher affinity for E3 ligases which targets them for degradation faster than proteins with a blocked N-terminus (Ravid and Hochstrasser 2008). For structurally disordered, small (150 aa or shorter) protein substrates, presence of a single mono-ubiquitin is enough to target to the proteasome.

The UPS usually degrades single proteins and not aggregates. These larger structures are usually tackled by the autophagy-lysosome degradation pathway. However, the role of ubiquitin in autophagy signalling is not completely understood. Ubiquitin is also found in protein aggregates, with staining most pronounced at the periphery of aggregates (Skibinski and Boyd 2012), which may perhaps be an indication that ubiquitin is conjugated to exposed surfaces after the aggregates have been formed.

### 1.3.3 Autophagy

The UPS is relatively ineffective at removing proteins which have formed aggregates since the proteins need to be unfolded and linearized for degradation (Meusser et al. 2005). The linearization of aggregated proteins takes more energy compared to partially folded proteins (figure 1.14). Autophagy is the main process cells remove organelles and larger cellular debris and protein aggregates that are resistant to proteasome degradation. There are three main types of autophagy (Galluzzi et al. 2017); macroautophagy (Feng et al. 2013), microautophagy (Li et al. 2012) and chaperone mediated autophagy (CMA) (Kaushik et al. 2011) although macroautophagy is the best characterised (and subsequent mention of autophagy in this work refers to macroautophagy). Autophagy was originally thought to be a general disposal system for cellular material, however it is becoming increasingly clear that autophagy is a highly specific and regulated process that is important for cellular homeostasis under basal and stress conditions (Zaffagnini and Martens 2016).

Autophagy is the formation of a double membrane bound vesicle, called the autophagosome (figure 1.14), which engulfs cellular debris, damaged organelles and misfolded proteins. Autophagosomes fuse with lysosomes to form autolysosomes. The cellular material originally engulfed by the autophagosome is degraded by hydrolytic enzymes in the autolysosome. The resulting material can be used to fuel anabolic processes (Hewitt and Korolchuk).

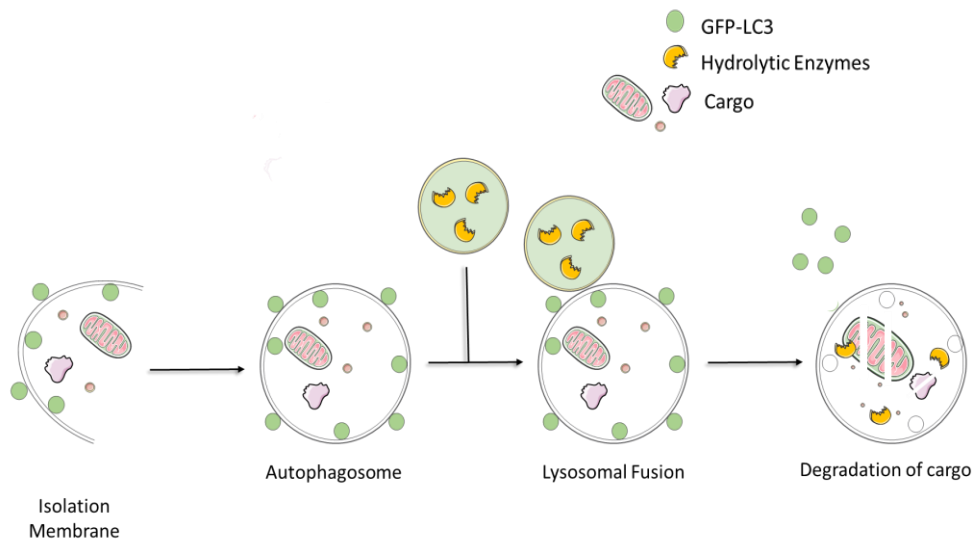


**Figure 1.14 Schematic representation of autophagy. A double membrane bound vesicle engulfs cellular material. The vesicle then fuses with a lysosome to form an autolysosome and cellular material is degraded by hydrolytic enzymes found in the lysosome.**



The canonical autophagy system is shown in Figure **1.15**. Autophagy induction is negatively regulated by the mechanistic target of rapamycin (mTOR), which is part of the mTOR complex (mTORC) (Manifava et al. 2016). Under normal conditions mTOR is not phosphorylated and actively phosphorylates ATG13, part of the ULK1 kinase complex which also contains ULK1 (or ULK2) and FIP200 leading to a suppression in autophagy activity. Under stress conditions mTOR is phosphorylated at T2446, S2448 and S2481 (Copp et al. 2009) and activity is reduced (Jung et al. 2010, Nazio et al. 2013).

Once the signal for autophagy has been initiated, the first stage of autophagy is nucleation. Nucleation has been associated with different cellular membranes including the ER (Ktistakis et al. 2016) and Golgi (Ge and Schekman 2014, Ge et al. 2013). Elongation and closure of the autophagosome membrane requires the ATG12-ATG5 complex and is necessary for the addition of phosphatidylethanolamine (PE) conjugated LC3 (LC3-II) to the autophagosome membrane (Patrice Codogno 2012).

Autophagic pathways that do not include all the components shown in figure **1.15** have also been observed. These pathways include autophagy-inducing steps that bypass the ULK1/2 complex, and are independent of ATG5 and BECLIN-1 (Patrice Codogno 2012). Although they have different signalling steps these pathways serve the same cellular function of stimulating the turnover of cellular constituents via the formation of autophagosomes.

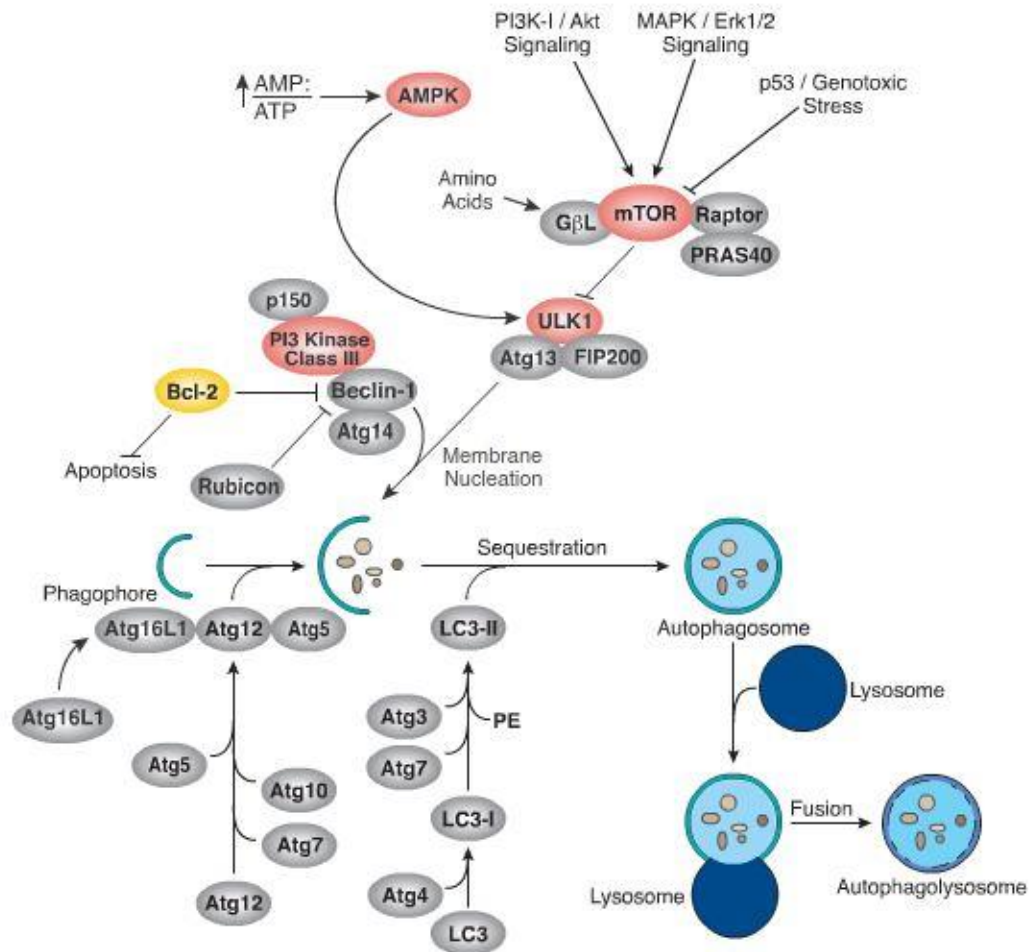


**Figure 1.15** Diagram showing the protein interactions and regulation during autophagy. Reprinted with permission from Cell Technology (Hu 2016).

The autophagosome forms at a phagophore assembly site (PAS) away from the lysosome. Upon autophagy activation, ULK1 translocates to the membrane and stimulates the production of phosphatidylinositol 3-phosphate (PI3P) which is essential to autophagic membrane dynamics. As the membrane develops, core autophagy machinery is recruited to the membrane and the ubiquitin-like LC3 is covalently attached to phosphatidylethanolamine which promotes autophagosome membrane expansion (Hanson et al. 2010), closure and fusion to lysosomes (Karanasios et al. 2016).

The selectivity of autophagic degradation is mediated by autophagic adaptor proteins. The human autophagy adaptor, p62/SQSTM1 has been implicated in the removal of protein aggregates, mitochondria and bacteria (Zaffagnini and Martens 2016). Degradation relies on the interaction between the LC3 interacting region (LIR) on adaptor proteins and LC3/GABARAP family proteins. p62 contains a number of functional domains including UB-

associated (UBA) domain, LIR and PB1 domain which allows interactions with various kinases (Johansen and Lamark 2011). The UBA domain allows interactions with mono and poly ubiquitin chains but has a preference for K63 linked ubiquitin, suggesting K63 ubiquitin targets substrates to autophagy over the UPS. Accumulation of p62 has also been seen in protein aggregates in neurodegenerative disorders. Next to BRCA1 gene 1 (NBR1) has also been associated with the recruitment of cargo for selective autophagy which also interacts with p62 via the PB1 domain, and also contains a UBA domain to allow recognition of ubiquitin and two LIR domains (Ichimura et al. 2008).

#### 1.3.4. Proteostasis

Proteostasis describes the process of maintaining a healthy pool of proteins in terms of concentration, location and function (Yerbury et al. 2016). This is managed by a number of protein chaperones and the interaction of protein degradation pathways to avoid toxicity that is associated with increased protein misfolding and aggregation. Proteostasis is often discussed in the context of ageing due to decreased activity of both the UPS and autophagy during ageing. This can be seen in the brain, a number of age-related neurodegenerative disorders are associated with increased protein aggregation.

Figure **1.16** shows a schematic representation of the proteostasis network. Misfolded or aggregated proteins are degraded by the UPS and autophagic pathways. Misfolded secretory proteins are recognised by extracellular chaperones which target them to the lysosome or are degraded by extracellular proteases (Yerbury et al. 2016).

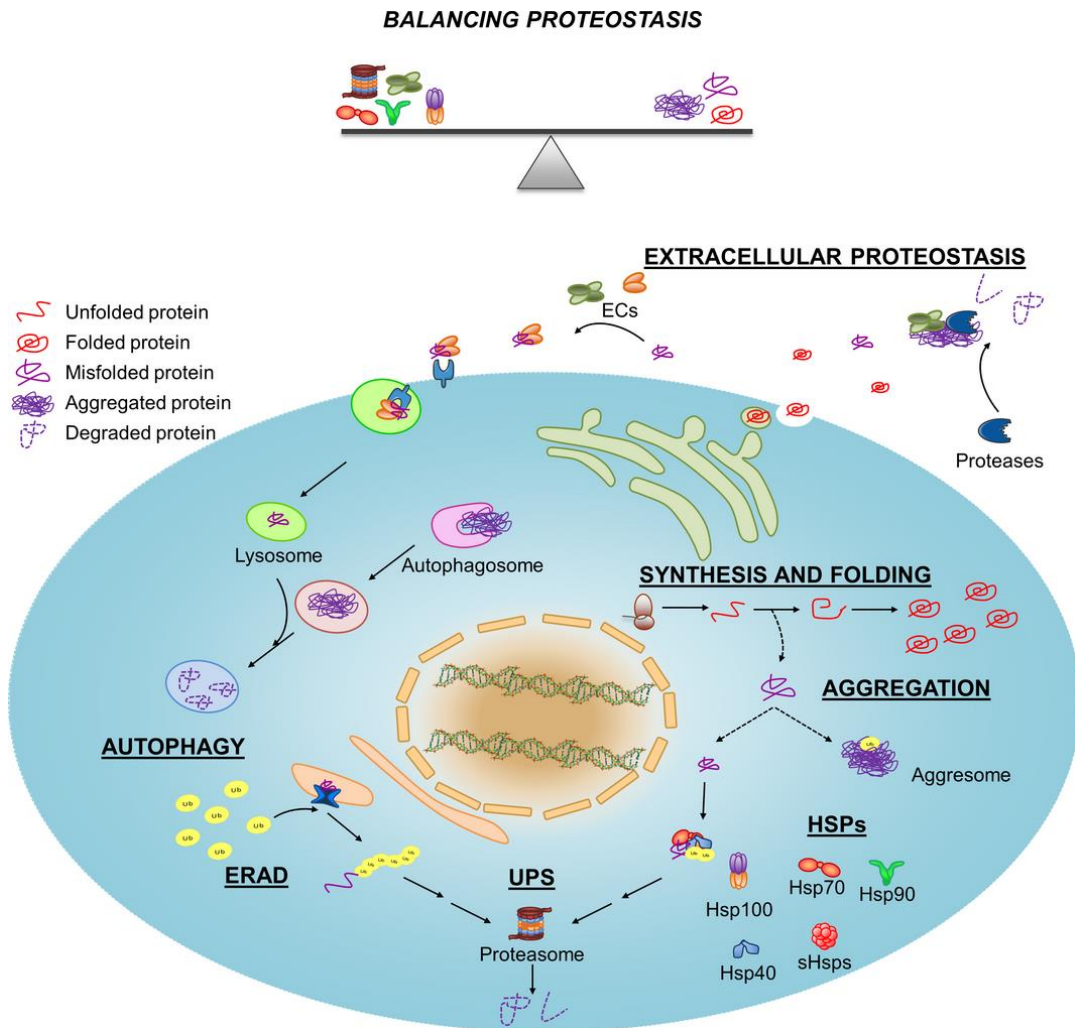


**Figure 1.16** Proteostasis maintains the proteome in the correct conformations. As proteins are synthesised and misfolded proteins are degraded via ERAD. Aggregated proteins are bound to chaperones which target them to the UPS or form larger aggregates which are degraded by autophagy. A further measure includes extracellular proteostasis that controls secreted proteins which are recognised by chaperones and targeted to the lysosome or degraded via extracellular proteases. Reprinted with permission from the *Journal of Neurochemistry* (Yerbury et al. 2016).

During aging the activity of the proteasome decreases, especially in the brain including cerebral cortex, hippocampus and spinal cord but not in the cerebellum or brainstem in rats. (Lilienbaum 2013) With this, comes an increase in the number of ubiquitinated proteins which are not removed efficiently.

Similar to the proteasome, autophagy activity decreases as we age (Lilienbaum 2013). Autophagy has been implicated in a number of diseases including cancers, neurodegenerative disorders, liver, muscle and heart disorders and ageing (Nixon 2013a). Reduced autophagy has been seen in neurodegenerative disorders including Parkinson's, Alzheimer's, Huntington's and prion diseases. Issues facing these disorders range from the different steps of autophagy including autophagosome formation, cargo recognition and trafficking to lysosomes. Correct proteostasis is especially important in post-mitotic cells such as neurons. Neurons have a large amount of axonal and dendritic cytosol and they must get rid of dysfunctional components without the aid of cellular division which can dilute cellular waste. Lysosomes are concentrated in the cell body. Autophagic vesicles clear waste by removing it at the source and trafficking back to the lysosomes. Without autophagy, ubiquitinated protein aggregates build-up, causing cell death. Autophagy is important in neurodegenerative function, loss of autophagy can cause neurodegeneration even in the absence of a disease causing mutant protein (Hara et al. 2006), in mouse models of ATG5 and ATG7 KO usually results in an embryonic lethal or neonatal lethal (Yoshii et al. 2016). The hypothesis that autophagy is necessary for the disposal of protein aggregates is supported by observations that conditional knockouts of ATG5 and ATG7 in mice, proteins important in the formation of autophagosomes, lead to the formation of protein aggregates in the liver (Takamura et al. 2011) and the development of neurodegenerative-like phenotypes (Tyedmers et al. 2010). Defects in different autophagy pathways can lead to different pathologies. The build-up of aggregates caused by reduced proteasome activity is especially toxic to neurons and cardio myocytes. These cells are post-mitotic and therefore cannot reduce stress caused by aggregates by diluting aggregates by cell division.

As well as decreased degradation activity this imbalance of proteostasis can also be the result of protein mutations that promote aggregation. In inherited forms of neurodegenerative disorders there is often an associated mutation in the aggregated protein, such as Alzheimer's which is associated with mutations in the *APP* and *PSEN 1* and *2* genes (Ryan and Rossor 2010).

Under conditions of imbalance in proteostasis or stress, cross-talk between the UPS and autophagy results in the increase or decrease in function accordingly. For example, under liver proteasome dysfunction in mice, autophagy was upregulated locally. This led to increased protein aggregates containing p62 and ubiquitin. Proteasome dysfunction inducing ER stress activates the unfolded protein response (UPR). The UPR signals through three main pathways, the ER resident PERK, IRE1 and ATF6 proteins. After activation these transcription

factors activate genes to reduce ER stress such as protein chaperones BiP and EDEM. As well as increasing protein folding elements, activation of IRE1 results in activation of JNK. This promotes autophagy by phosphorylating BCL-2, releasing BECLIN-1 to activate autophagy (Song et al. 2018) as shown in figure 1.15. While PERK activation leads to increased transcription of ATF4 which regulates transcription of ATG12 (Song et al. 2018).

### 1.3.5. Deglycosylation of misfolded proteins

As mentioned, many of the proteins traversing the degradation pathways are glycoproteins. During degradation by the proteasome, folded proteins are not able to enter the catalytic channel and it has been hypothesised that proteins bearing glycan chains are also not able to be processed in this manner. The enzyme *N*-glycanase (also known as PNGase and Peptide: *N*-glycanase, EC 3.5.1.52) is a glycan modifying enzyme which removes *N*-linked glycans at the base GlcNAc residue (provided it does not bear a core fucose modification) shown in figure 1.17.

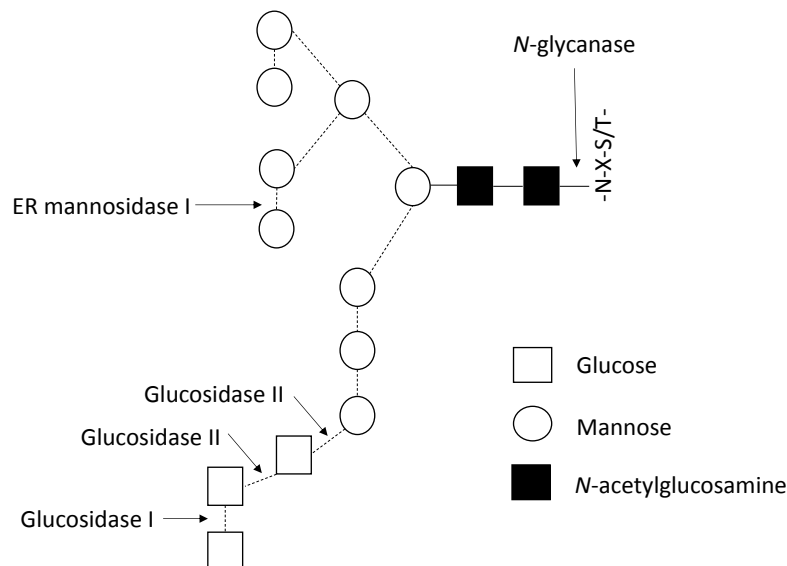


**Figure 1.17 Site of *N*-glycanase action on *N*-linked glycans**

*N*-glycanase is found in complexes associated with the dislocon and facilitates proteasome clearance by removal of *N*-linked glycans prior to degradation (Olzmann et al. 2013). Figure 1.18 shows the interaction partners of *N*-glycanase including DERLIN-1, VCP, RAD23A/B and the proteasome subunits PSMC2 and PSMC1 (Suzuki et al. 2016).

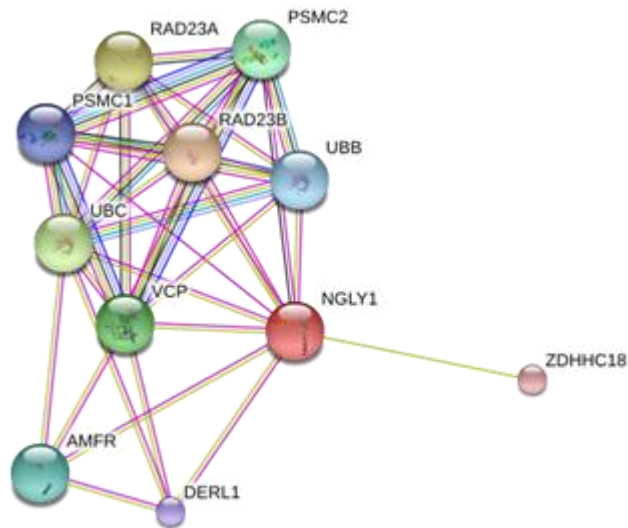


**Figure 1.18 Protein interactions for *N*-glycanase (NGLY1) (Generated by string-db.org)**

*N*-glycanase (yPng1 in yeast) activity was first identified as an important process in protein quality control and ERAD in yeast (Suzuki *et al.* 1998). *N*-glycanase has since been identified in other eukaryotes including mammals, insects and plants. It has a conserved transglutaminase-like core (TG) (Figure 1.19), which in yeast crystal studies of the protein is located in a deep cleft with three amino acids essential to enzyme function, cysteine, histidine and aspartic acid (Hirayama *et al.* 2014). Figure 1.19 shows the interaction of GlcNAc2-IAc with yeast PNGase. Mutation analysis showed that the cysteine residues were critical to activity (Suzuki 2015).

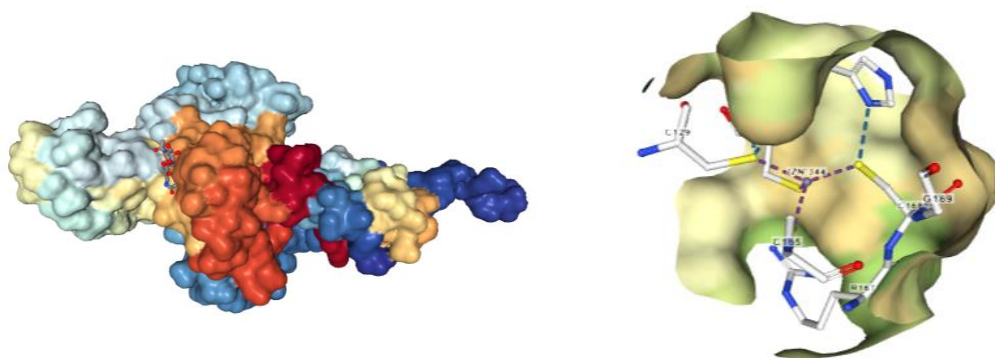


**Figure 1.19 X-ray diffraction model of yeast PNGase in complex with GlcNAc2-IAc. (Generated from PDB (Zhao *et al.* 2009)).**

*N*-glycanase is found throughout the body with studies in mice isolating *N*-glycanase in several organs including the brain, kidneys, liver and spleen with varying activity levels (Kitajima et al. 1995). In higher eukaryotes the enzyme also contains a ubiquitin binding (PUB) domain present at the *N*-terminus which is responsible for interactions with ERAD components on the ER membrane (Hirayama et al. 2014). This indicates that the link between  $\gamma$ Png1 to the proteasome is important for efficient clearance of ERAD substrates which is mediated by Rad23.

Mammalian *N*-glycanase is around twice the size of its yeast and bacterial homologues (Suzuki 2015). The domains found in *N*-glycanase are shown in figure 1.20. This also shows sites of mutations on human *N*-glycanase associated with disease.

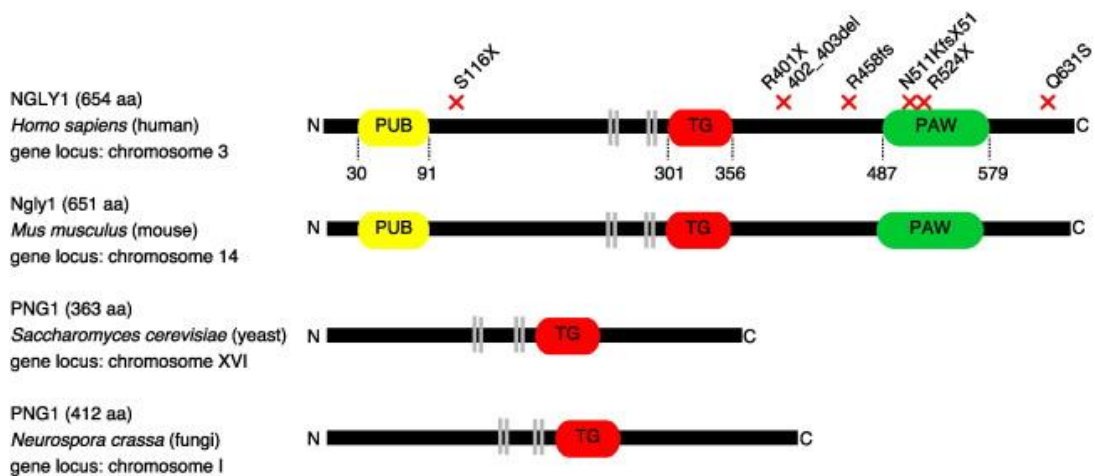


**Figure 1.20 Schematic of *N*-glycanase structure in fungi, yeast, mice and humans. Red crosses indicate mutations associated with disease in human *N*-glycanase. Reprinted from Gene, 577, (Suzuki et al. 2016) with permission from Elsevier.**

*N*-glycanase has been shown to have a role during ERAD (Chantret et al. 2010, Hosomi and Suzuki 2015, Huang et al. 2015) (Suzuki et al. 2000). In yeast PNGase KO cells it was found that the ERAD glycoprotein substrate, mutant carboxypeptidase Y protein (CPY) exhibited a decreased rate of degradation (Suzuki et al. 2000), leading to hypothesis that glycoproteins cannot be efficiently degraded if the glycan chain is still attached to the protein. However, in mammalian cells the degradation rate of other proteasome degradation dependent proteins including class I HCs and TCR $\alpha$  did not show a decreased rate of degradation under inhibition of *N*-glycanase (Misaghi et al. 2004, Hirsch et al. 2003).



### 1.4.1 N-GLY1 disorder

Due to the varying pathologies and differences in severity, along with the high number of individual CDGs, speed and accurate methods of diagnosis are currently limited (Lefeber et al. 2011). The apparently low frequency of CDGs may indicate severity, with a low survival rate and underdiagnoses. N-GLY1 deficiency disorder is the first disorder of deglycosylation identified and is caused by a mutation in the *NGLY1* gene. *N*-glycanase is an enzyme involved in the degradation of terminally misfolded *N*-linked glycoproteins. A variety of effects of reduced *N*-glycanase activity have been described in model organisms (Table 1.1).

**Table 1.1 Effect of *N*-glycanase knockout in various organisms**

Organism	Observed phenotypes	References
<i>S. cerevisiae</i>	Defect in ERAD; no growth/viability defects	(Suzuki et al. 2000, Kim et al. 2006, Hosomi et al. 2010)
<i>N. crassa</i>	Temperature sensitive growth with strong polarity defects	(Maerz et al. 2010)
<i>A. thaliana</i>	No obvious defect	(Maeda and Kimura 2014, Zielinska et al. 2012)
<i>D. discoideum</i>	Slow growth and development; defect in cell aggregation during multicellular development	(Gosain et al. 2012)
<i>C. elegans</i>	Abnormal axon branching of VC4/VC5 egg-laying neurons, defective egg laying	(Habibi-Babadi et al. 2010)
<i>D. melanogaster</i>	Severe developmental delay	(Funakoshi et al. 2010) (Owings et al. 2018)
<i>M. musculus</i>	Embryonically lethal (C57BL/6), reduced body weight.	(Fujihira et al. 2017)

In humans, the congenital disorder of deglycosylation (CDDG) termed N-GLY1 was first described in a publication in 2012 (Need et al. 2012). Similar to CDGs, N-GLY1 has a complex and varied clinical presentation. Symptoms include global developmental delay (observed

in all documented cases), movement disorders, hypotonia and alacrimia (Enns et al. 2014, Lam et al. 2016, Caglayan et al. 2015, He et al. 2015). A summary of symptoms observed in eight N-GLY1 patients is shown in figure 1.21.

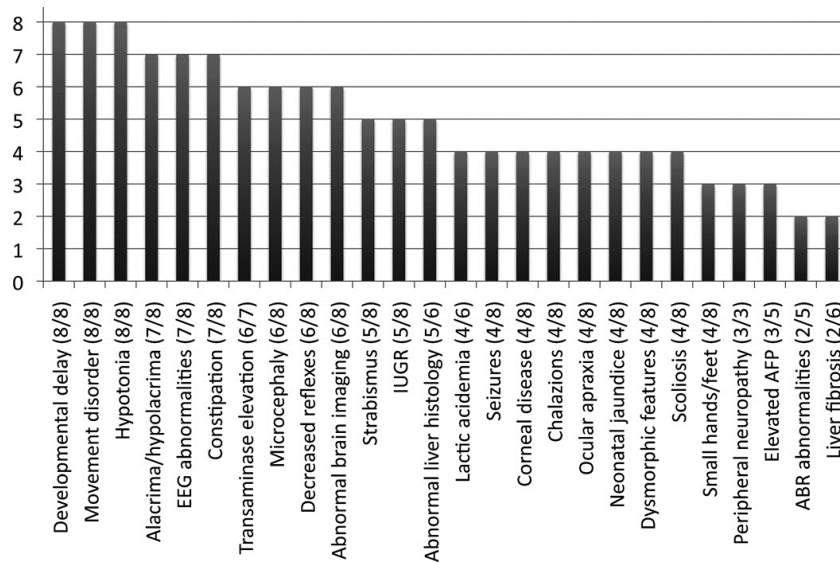


**Figure 1.21 Symptoms observed in eight N-GLY1 patients with prevalence indicated underneath. Reprinted by permission from Macmillan Publishers Ltd: Genetics in Medicine (Enns et al. 2014).**

N-GLY1 disorder results from mutations in the *NGLY1* gene which encodes *N*-glycanase 1 and as of 2017, a minimum of 46 patients have been described in the literature (Lam et al. 2016, Enns et al. 2014, Caglayan et al. 2015). The most common mutation identified was c1201A>T/pR401X as a homozygous mutation in 5/8 patients and heterozygous mutation in 1/8 patients in the first description of the symptoms of N-GLY1 deficiency (Enns et al. 2014). Several other mutations have also been identified summarised in Table 1.2.

**Table 1.2 Confirmed mutations in the NGLY1 gene, c indicates chromosomal mutation and p indicates the effect of the protein sequence in amino acids. Information taken from (Enns et al. 2014, Lam et al. 2016, Caglayan et al. 2015)**

Chromosomal mutations (maternal/paternal allele)	Effect on protein maternal/paternal
c1201A>T homozygous	pR401X
c1891del/c1201A>T	pQ631S/pR401X
c1370dupG homozygous	pR458 frameshift
c1205_1207del/c1570G>A	p402_403del/pR542X
c953T>C/1169G>C	pL318P/pR390P
c931G>A/730T>C	pE311K/pW244R
c1604G>A/ c1910delT	pW535/ pL637
c622C>T/ c930C>T	pQ208/ pG310G (splice site)
c347C>G/ c881+5G>T	pS116/ pIVS5+5G>T

Patients with the c1201A>T mutation were assessed as moderately to severely impaired which is a higher severity compared to those with other mutations (Enns et al. 2014). Using dermal fibroblasts derived from N-GLY1 patients, it was found that *N*-glycanase mRNA levels were reduced by 30-97%. The c1201A>T mutation in *NGLY1* was the most detrimental resulting in 87-97% reduction in NGLY1 mRNA as measured by qPCR (He et al. 2015).

#### 1.4.2 Molecular impact of *N*-glycanase deficiency

The molecular impact of *N*-glycanase deficiency has been examined in cellular, model organisms and murine models. *N*-glycanase has shown to be involved in the degradation of *N*-glycoproteins during ERAD (Chantret et al. 2010, Hosomi and Suzuki 2015, Huang et al. 2015) but has also been linked to other functions in the cell such as generation of free oligosaccharides (fOS) and Nrf1 activation (Owings et al. 2018, Tomlin et al. 2017).

#### 1.4.3 Deglycosylation regulates protein activity

Deglycosylation has recently been identified as a process of post-translational modification and has been identified in the stabilisation of tyrosinase-derived peptides for presentation to MHC Class I molecules and Nrf1 activation. Generation of the HLA-A\*0201 epitope (which is presented as asparagine or aspartic acid isoform) is formed by glycosylation in the ER then subsequent deglycosylation by *N*-glycanase (Altrich-VanLith et al. 2006). Likewise, the nuclear respiratory factor (NRF1) is present as an ER-anchored glycoprotein. Under basal conditions NRF1 is quickly degraded by the proteasome. Under proteasome dysfunction NRF1 is cleaved, deglycosylated by *N*-glycanase and transported to the nucleus where it acts to upregulate genetic factors related to proteasomal degradation. In *N*-glycanase deficient cells, NRF1 is excluded from the nucleus (Tomlin et al. 2017). Other protein species are likely to be regulated in this manner.

#### 1.4.4 *N*-glycanase is involved in the generation of free oligosaccharides

Removal of the *N*-glycans from a peptide results in the conversion of the peptide asparagine residue to aspartic acid and, the release free oligosaccharides (fOS) bearing terminal  $\alpha$  1-amino-GlcNAc. There are two main sources of fOS in cellular systems; those released from misfolded proteins and those acting as glycan donors for nascent proteins during protein folding in the ER. The structures released from misfolded proteins by *N*-glycanase are usually Man<sub>9</sub>-7GlcNAc<sub>2</sub> structures. Those acting as donors to nascent proteins by OST complex are mainly Glc<sub>3</sub>Man<sub>9</sub>GlcNAc<sub>2</sub>. In mammalian cells the Glc<sub>3</sub>Man<sub>9</sub>GlcNAc<sub>2</sub> structures are trimmed in the ER by ER  $\alpha$ -glucosidases I and II and  $\alpha$ -mannosidase to form Man<sub>8</sub>GlcNAc<sub>2</sub> which is exported into the cytosol. Cytosolic fOS are further catabolised by ENGase and Man<sub>2</sub>C<sub>1</sub> to produce Man<sub>5</sub>GlcNAc<sub>1</sub>. These are then broken down by lysosomes. The biological role of fOS in normal cellular health is currently undetermined, although perturbations in fOS distribution and levels can be indicative of certain cell stress (Alonzi et al. 2008, Alonzi et al. 2013).

In yeast, the majority of fOS are generated by the yeast *N*-glycanase, *ypng1* (96%) (Hirayama et al. 2014), whereas significantly lower total levels of fOS are generated by *N*-glycanase action in mammalian cells. Upon *N*-glycanase ablation in human HepG2 cells the total fOS levels were measured by pulse-chase radiolabelling methods, and an inhibition of total fOS of 25 % for *N*-glycanase inhibition by Z-VAD-fmk treated cells and 12 % following siRNA knockdown (Chantret et al. 2010) was observed in an ENGase deficient background.

Knockdown by siRNA of *N*-glycanase resulted in a reduction in Glc1Man9GlcNAc2 and Man9GlcNAc2 fOS species, but levels of Man8GlcNAc2 remained the same in an ENGase deficient background. Similar results were also seen in cells pre-treated with Z-VAD-fmk (Chantret et al. 2010). Under *N*-glycanase knockdown fOS can also be generated by ENGase. Suzuki et al. (2015) identified cytosolic endo- $\beta$ -*N*-acetylglucosaminidase (ENGase) (EC:3.2.1.96) as a glycosyl hydrolase acting in the absence of *N*-glycanase activity. This study used an ERAD glycoprotein substrate, ricin A nontoxic mutant (RTA $\Delta$ m) which contains an ER targeting and retention KDEL sequence. Following expression of RTA $\Delta$ m in WT, ENGase<sup>-/-</sup>, NGLY1<sup>-/-</sup>, or double knockout MEF cells the ratio of deglycosylated/glycosylated RTA $\Delta$ m found 10 % of the protein was deglycosylated in the double knockout. Whereas *N*-glycanase deficient cells had increased, around 35 % of the deglycosylated form. ENGase deficient cells exhibited 29 % deglycosylated RTA $\Delta$ m, indicating other glycan processing enzymes have the capacity to effect the deglycosylation of proteins.

### 1.5 Aims and Objectives

N-GLY1 deficiency is a relatively new disorder and little is known about the molecular effects of *N*-glycanase deficiency in cells. *N*-glycanase has already been shown to participate in ER-associated degradation and it is clear from multiple disorders that precisely functioning proteostasis is pivotal to cellular health. An understanding of which is necessary for new treatment targets of not only N-GLY1 disorder but also protein misfolding and aggregation disorders.

This thesis is divided into these objectives found in each chapter: Chapter 3 – the effect on cellular pathways under inhibition of *N*-glycanase using Z-VAD-fmk, Chapter 4 – the effect on cellular pathways under genetic ablation of *N*-glycanase using siRNA, Chapter 5- the pursuit of a stable *N*-glycanase knockout using CRISPR gene editing techniques to study long term effects of *N*-glycanase deficiency, Chapter 6 – identification of cargo and autophagy related proteins under *N*-glycanase inhibition and siRNA knockdown and Chapter 7- the effect on mitochondrial function.

## 2.1 Introduction

This chapter details the reagents, materials and methods employed in this thesis.

## 2.2 Reagents

Z-VAD-fmk (CAS: 187389-52-2, catalogue no. A1902) and Q-VD-Oph (CAS: 1135695-98-5 catalogue no. A1901), 3-MA (CAS: 5142-23-4, catalogue no. A8353) were purchased from APExBIO. MTT (Invitrogen™ Molecular Probes™, CAS: 298-93-1, catalogue no. 10133722), DMSO (Fisher Bioreagents™, CAS: 67-68-5, catalogue no. 10103483), menadione (MP Biomedicals, CAS: 58-27-5, catalogue no. 11453490), RPMI media (Gibco™, catalogue no. 31870025), FBS (Gibco™, catalogue no. 15140122), L-glutamine (Gibco™, catalogue no. 25030081), 1% penicillin/streptomycin (Gibco™, catalogue no. 15140122), Trypsin-EDTA (0.25%) phenol red (Gibco™, catalogue no. 25200056), MG132 (Alfa Aesar™, CAS: 133407-82-6, catalogue no. 15465519), Thioflavin T (ACROS Organics™, CAS: 2390-54-7, catalogue no. 211760250), MEM Amino Acids Solution (Gibco™, catalogue no. 11130036) and MEM Non-Essential Amino Acids (Gibco™, catalogue no. 11140050), Bafilomycin A1 (Tocris Bioscience™, CAS: 88899-55-2, catalogue no. 13429173), Novex™ Wedgewell™ Tris-Glycine Mini Gels (Invitrogen™, catalogue no. XP04120BOX), FURA-2 AM (Invitrogen™ Molecular Probes™, CAS: 108964-32-5, catalogue no. 10308392), Thapsigargin (Invitrogen™ Molecular Probes™, CAS: 67526-95-8, catalogue no. 10226822), DH5 $\alpha$ ™ Competent Cells (Invitrogen™, catalogue no. 18265017), Phusion High-Fidelity DNA Polymerase (ThermoScientific™, catalogue no. 10402678), MS Grade Trypsin Protease (Thermo Scientific™ Pierce™, catalogue no. 13464189), Dead Cell Apoptosis Kit with Annexin V FITC and PI, for flow cytometry (Invitrogen™ Molecular Probes™, catalogue no. 10267392), Mitochondria Isolation Kit for Cultured Cells (ThermoScientific™, catalogue no. 89874), MitoTracker™ Deep Red FM (Invitrogen™ Molecular Probes™, catalogue no. 12010156), along with general consumables, buffer components, salts and solvents, were purchased from Fisher Scientific. RNase B (CAS: 9001-99-4, catalogue no. J61996, EC 3.1.4.22) was purchased from Alfa Aesar™.

JetPEI® HTS DNA transfection reagent (Polyplus-transfection®, catalogue no. 89129-914), JetPRIME® DNA and SiRNA transfection reagent (Polyplus-transfection®, catalogue no.

89129-920) was purchased from VWR. Fluorescein (FITC) conjugated lectin panels, Lectin Kit 1 (catalogue no. FLK-2100) and Lectin Kit II (catalogue no. FLK-3100) were purchased from Vector Laboratories.

Bio-Rad Protein Assay Dye Reagent Concentrate (for assessment of protein concentration via the Bradford method) (catalogue no. 5000006), LDS sample buffer (catalogue no. 1610747), 10x Tris/Glycine/SDS electrophoresis running buffer (catalogue no. 1610732), Clarity™ ECL Western Substrate solution (catalogue no. 170506), Bio-Rad Criterion™ Empty Cassettes (catalogue no. 3459904) were purchased from Bio-Rad.

SMARTpool: ON-TARGETplus NGLY1 siRNA (Dharmacon™, catalogue no. L-016457-01) and ON-TARGETplus non-targeting control (Dharmacon™, catalogue no. D-001810-01), DharmaFECT 1 (catalogue no. T-2001-01) were purchased from Dharmacon™. Sequences of NGLY1 siRNA are shown in Table 2.1.

RT-qPCR primers (Table 2.2) and cloning primers (Table 2.3) were purchased from Eurofins Genomics.

Sequencing primers (Table 2.5) and guide DNA sequences (Table 2.4) for CRISPR mediated knockout of *N*-glycanase were purchased from Sigma Aldrich.

One-Step Luna® Universal qPCR Master Mix (catalogue no. M3003), Monarch PCR and DNA cleanup kit (catalogue no. T1030S), BamHI (catalogue no. R0136S), XhoI (catalogue no. R0146S), T4 DNA ligase (catalogue no. M0202S) were purchased from New England Biolabs Inc®.

RNeasy Mini Kit (catalogue no. 74104), DNeasy Blood and Tissue Kit (catalogue no. 69504), QIAquick Gel Extraction Kit (catalogue no. 28704), QIAprep Spin Miniprep Kit (catalogue no. 27104) was purchased from Qiagen.

ROSBrite™ 570 (catalogue no. 160000-AAT) was purchased from Stratech.

Midori green Direct DNA stain (catalogue no. S6-0018) was purchased from GeneFlow.

GFP-Trap agarose beads (catalogue no. gta-20), agarose beads (catalogue no. bab-20) and spin columns (sct-20) was purchased from Chromotek.

CYTO-ID autophagy detection kit (catalogue no. ENS-51031-K200) was purchased from Enzo Life Sciences.

### 2.3 Plasmids

The pOPH6 plasmid encoding for bacterial PNGase F was a kind gift from Shaun Lott (Addgene plasmid # 40315).

The N-terminal mAPPLE tag mammalian expression vector, mAPPLE-N1 was a kind gift from Michael Davidson (Addgene plasmid # 54567).

Construct encoding for GFP-LC3 (sequence presented in appendix **A.1.2**) was a kind gift from Martin Bootman. Construct encoding for the tandem LC3 reporter, GFP-RFP-LC3 was a kind gift from Martin Bootman.

The deglycosylation dependent VENUS (ddVENUS) plasmid was a kind gift from J.E. Grotzke, (Grotzke et al. 2013).

Plasmids containing the CRISPR WT and Nickase Cas9, pSpCas9(BB)-2A-GFP (PX458) from Addgene (Addgene plasmid # 48138) and pspCas9n(BB)-2A-GFO (PX461) (Addgene plasmid # 48140) respectively, were kind gifts from Feng Zhang.

All plasmids were transformed into DH5 $\alpha$  *E. coli* with the exception of the pOPH6 plasmid encoding bacterial PNGase F which was also transformed into BL21 DE3 *E. coli*.

### 2.4 Cell culture

Cells were maintained in RPMI media supplemented with FBS (10 %), L-glutamine (2 mM) and penicillin/streptomycin (1 %). To subculture, media was removed and the cell monolayer washed with warm PBS. The PBS was removed and warm 0.25% EDTA-Trypsin was added until all cells detached (approx. 2 min). Fresh media was added and the cells were split at 1:10 dilution. Cells were maintained at 37 °C at 5% CO<sub>2</sub>. Cells were frozen at 80 % confluency. As before, cells were detached from flasks by trypsin and trypsin inactivated by the addition of fresh media. Cells were pelleted by soft centrifugation (4 °C, 1000 rpm, 5 min). The supernatant was discarded and the pellet re-suspended in freezing media (1 ml, 90 % FBS, 10 % DMSO) and aliquoted into cryovials. Vials were frozen overnight at -80 °C in a freezing container. After 24 h, cryovials were moved to liquid nitrogen for long-term storage.

### 2.5 Characterisation of the effects of pharmacological inhibition and genetic ablation of N-glycanase

The methods described in this section were employed to characterise the effects on cell viability, N-glycanase activity, glycoprotein profile, Thioflavin T fluorescence, autophagy



calculation by imaging, CYTO ID, western blot or in-gel fluorescence. Markers for the unfolded protein response and OGA/OGT expression levels were calculated by real-time qPCR, primers sequences can be found in Table 2.2. ER Ca<sup>2+</sup> handling and ROS levels were also examined following treatment with Z-VAD-fmk or, siRNA knockdown of *N*-glycanase. Finally, generation of a bacterial PNGase F, cloned into a mammalian expression vector is outlined.

### 2.5.1 Pharmacological inhibition of *N*-glycanase using Z-VAD-fmk

Where pharmacological inhibitors were employed, cells were plated at 20 000 in 12-well plates or glass cover slips where appropriate and left to adhere for 24 h prior to treatment with Z-VAD-fmk or Q-VD-OPh.

### 2.5.2 Genetic ablation of *N*-glycanase

The sequence of the SMARTpool NGLY1 siRNA used in throughout is presented in Table 2.1. Where siRNA was employed, cells were plated at 10 000 in 12-well plates or glass cover slips where appropriate and left to adhere for 24 h prior to transfection with NGLY1 siRNA (25 nM) or the corresponding ON-TARGETplus Non-targeting control siRNA (25 nM).

**Table 2.1 Sequence of SMARTpool NGLY1 siRNA**

ON-TARGET plus SMARTpool siRNA	Sequence	Molecular Weight (g/mol)	Extinction coefficient (L/mol·cm)
1	GCGAGUGGGCCAAUUGUUU	13444.9	362408
2	CUGCCGAGCUGUAGGGUUU	13459.8	359649
3	CCAUAAUUGUGGAGCUUGU	13414.9	375402
4	GGAGAAUGGCGUGUGGAAA	13444.8	364277

### 2.5.3 MTT assay

Cells were plated in a 96 well plate (Greiner) at a density of 2000 cells per well. Cells were incubated with treatments as indicated per experiment. Following treatment, media was aspirated and replaced with fresh media (100  $\mu$ l) containing MTT (final concentration 0.2 mg/ml). Plates were incubated at 37 °C for 2 h. Following incubation, media containing MTT was carefully removed and DMSO (100  $\mu$ L) was added to each well. The plates were then shaken for 20 min at RT. The absorbance was read using a BMG Labtech FLUOstar OPTIMA plate reader at 570 nm. Treatment with menadione (20  $\mu$ M, 24 h) was included as a positive control to confirm decreased absorbance in non-viable cells.

### 2.5.4 Deglycosylation Dependent Venus (ddVENUS) assay

HEK 293 cells plated in 12 well plates (Greiner) at a density of 80 000 cells per well were transfected with ddVENUS plasmid DNA (2  $\mu$ g per well) using JetPEI® HTS DNA transfection reagent (Polyplus-transfection®) in accordance with the manufacturer protocol. After 24 h, Z-VAD-fmk (0-300  $\mu$ M) was added and the cells incubated for a further 24 h. For genetic ablation of *N*-glycanase, HEK 293 cells were transfected with SMARTpool: ON-TARGETplus NGLY1 siRNA (25 nM) or an ON-TARGETplus non-targeting control (25 nM) using JetPRIME® DNA and SiRNA transfection reagent (Polyplus-transfection®) as per the manufacturer instructions. Cells were analysed 3d post-transfection.

The proteasome inhibitor, MG132 (8  $\mu$ M) was added for 6 h before the cells were trypsinised, collected by centrifugation and re-suspended in HBSS (500  $\mu$ l). Cells were kept on ice before measurement. Fluorescence intensity was measured by flow cytometry on a BD FACSCalibur (BD Biosciences) and analysed using BD CellQuest™. A minimum of 10 000 cells were analysed for each condition. A non-transfected well was used as a control to determine background fluorescence. Cells were analysed using the FL1 filter at 400 V. The non-transfected cells were gated out of analysis and the median fluorescence intensity of transfected cells was plotted.

### 2.5.5 Lectin dot blots

Cells were treated as described in the data. Wells were trypsinised and washed twice in ice-cold PBS and lysed in 1% triton in PBS at 4 °C with constant agitation for 30 min. Lysate was centrifuged at 15 000 g for 15 min. Protein concentration was determined by Bradford assay. Protein solution was spotted (2  $\mu$ l) with an equal final concentration of 1, 0.5 and 0.25  $\mu$ g onto nitrocellulose membrane and allowed to air dry for 1 h. Membranes were blocked in

0.1 % PBS-T for 1 h. Membranes were exposed to fluorescein-labelled lectins (Vector laboratories) and incubated for 2 h at RT at a final concentration of 2 µg/ml. Membranes were washed with PBS-T (3 x 10 min) and imaged using Syngene Gel:Doc imaging system. Images were analysed using Syngene GeneTools software for dot blot fluorescence analysis. Post-imaging protein concentration was confirmed by visible, total protein amido black staining. Nitrocellulose membranes were incubated in amido black staining solution (0.1 % amido black, 40 % methanol, 5% acetic acid) for 15 s and de-stained (40 % methanol, 10% acetic acid) for 20 min at RT. Membranes were imaged using a Syngene Gel:Doc imaging system and analysed using Syngene GeneTools software for dot blot absorbance analysis.

#### 2.5.6 Quantitation of levels Thioflavin T (ThT) fluorescence

HEK cells were plated at 40 000 cells per well in a 12 well plate and treated with either Q-VD-OPh or Z-VAD-fmk (50 µM, 24-72 h) or a vehicle control (DMSO). For genetic ablation, HEK cells were transfected with SMARTpool: ON-TARGETplus NGLY1 siRNA (Dharmacon™, catalogue no. L-016457-01) or ON-TARGETplus non-targeting control (Dharmacon™, catalogue no. D-001810-01) (25 nM, 3-5 d). Cells were incubated with ThT (1 µM, 0.5 h).

Following ThT staining, cells were washed three times in imaging buffer (121 mM NaCl, 5.4 mM KCl, 0.8 mM MgCl<sub>2</sub>, 1.8 mM CaCl<sub>2</sub>, 6 mM NaHCO<sub>3</sub>, 5.5 mM D-glucose, 25 mM HEPES, pH 7.4 supplemented with Gibco MEM Amino Acids Solution and MEM Non-Essential Amino Acids. Coverslips were imaged using a Leica DMI6000 fluorescence microscope under 63x oil immersion objective. A minimum of three images (ex 485 nm, em 520 nm) were taken per condition. Areas were selected in bright field to ensure ThT fluorescence was unbiased. Images were analysed using ImageJ. The images were background subtracted by selection of areas adjacent to cells and subtracting the mean fluorescence from the image. The perimeter of the cells were defined and, the mean fluorescence per cell was calculated.

#### 2.5.7 Quantitation of Thioflavin T (ThT) fluorescence by flow cytometry

Flow cytometry was also used to determine ThT fluorescence. HEK cells were treated with either Q-VD-OPh or Z-VAD-fmk (50 µM, 24-72 h) or a vehicle control (DMSO). For genetic ablation, HEK cells were transfected with SMARTpool: ON-TARGETplus NGLY1 siRNA or an ON-TARGETplus non-targeting control (25 nM, 3-5 d). Cells were loaded with Thioflavin T (5 µM, 30 m) at 37 °C in complete media. Cells were detached with trypsin and washed in HBSS three time by centrifugation. Cells were re-suspended in HBSS (500 µl) and analysed using BD FACSCalibur on the FL1 channel (ex 488 em 530), at 440 V, 10 000 cells were counted per condition.

#### 2.5.8 Quantitation of levels GFP-LC3 positive puncta

GFP-LC3 HEK cells were plated on uncoated 16 mm glass coverslips at (40 000 cells per well) and treated with Z-VAD-fmk or Q-VD-OPh (50  $\mu$ M, 24-72 h) or a vehicle control. For genetic ablation, HEK cells were transfected with SMARTpool: ON-TARGETplus NGLY1 siRNA or an ON-TARGETplus non-targeting control (25 nM, 3-5 d). Cells were imaged on the oil immersion 63x objective. A minimum of three areas per coverslip were imaged and were selected under bright field. The number of GFP-LC3 positive puncta were counted manually and, the average number of puncta per cell was calculated per condition. To measure flux, GFP-LC3 HEK cells were treated with Bafilomycin A1 (100 nM, 1 h) or 3-MA (5 mM, 1 h) at 37 °C at 5% CO<sub>2</sub>. Cells were re-imaged and the number of GFP-LC3 puncta was calculated.

#### 2.5.9 Use of CYTO-ID® autophagy detection kit with a TALI image-based cytometer

HEK cells were plated in a 12 well plate at a density of 20 000 cells and left to adhere for 24 h. After 48 h cells were treated with Bafilomycin A1 (100 nM) or amino acid starvation (121 mM NaCl, 5.4 mM KCl, 0.8 mM MgCl<sub>2</sub>, 1.8 mM CaCl<sub>2</sub>, 6 mM NaHCO<sub>3</sub>, 11 mM D-glucose, 25 mM HEPES, 2 mM L-Glutamine, pH 7.4) for 4 h or amino acid starvation with Bafilomycin A1 treatment. Cells were detached with trypsin, collected and washed (3X HBSS). Cells were then incubated with ENZO CYTO-ID® autophagy detection kit stain (ENZ-51031-K200) as per the manufacturer instructions. Following staining, cells were washed in HBSS (3X HBSS). Sample was loaded into TALI cellular analysis slides (25  $\mu$ l). Cells were analysed under the green channel and the mean fluorescence per region plotted. Nine regions were imaged per condition.

#### 2.5.10 Assessment of transfection efficiency

To identify the most effective transfection condition in HEK 293 cells, the transfection efficiencies for several transfection reagents were tested using the GFP-RFP-LC3 plasmid. Transfections were undertaken as per manufacturer instructions in triplicate and efficiency assessed by fluorescence imaging 48 h post-transfection.

#### 2.5.11 Trypan blue exclusion measurement of cell viability

Trypan blue exclusion was used to determine cell viability. Cells were detached from cell culture plates with trypsin, which was deactivated by the addition of complete media. Equal volumes of cell suspension and 0.4 % trypan blue solution were added. The cell suspension was loaded onto a haemocytometer and the percentage of cells with dye inclusion evident was determined.

#### 2.5.12 G418 cell survival

HEK cells were plated at 20 % confluency in a 48 well plate and treated with up to 2 mg /ml G418 over 11 days. Wells were classified as either viable or non-viable. Non-viable wells were determined by eye at >80 % of the cells unattached to the well bottom.

#### 2.5.13 Generation of GFP-RFP-LC3 stably transfected cells

Stable transfection of GFP-RFP-LC3 construct in HEK293 cells was carried out in accordance with the following protocol. HEK cells were seeded at 60% confluence into a 10 cm cell culture dish (Greiner) and left to adhere overnight. The cells were transfected with GFP-RFP-LC3 construct using JetPEI® HTS DNA transfection reagent as per manufacturer's instructions. After 48 h, the dish was split into 6 x 10 cm dishes supplemented with G418 (1mg/ml) diluted in PBS in complete media. Once distinct colonies could be observed, individual colonies were transferred into single wells in a 48 well plate using a sterile P1000 filter pipette tip. Expression was examined by fluorescence microscopy (Leica DMI6000, 20x objective) once cells reached confluency. Colonies expressing fluorescence under green (ex 485 nm, em 520 nm) and red channel (ex 541-551, em 565-605 nm) were expanded. Fluorescence was compared to the GFP-LC3 HEK cells under the same excitation conditions. These were further characterised, and cell populations that showed 50 % positive green and red cells were with cells that showed equivalent GFP signal as the GFP-LC3 HEK cells were used in future experiments and a stock was frozen down and cells were characterised with Bafilomycin and 3-MA. Autophagy calculation was done as described by section 2.5.8, however, the red and green channels were merged and yellow and red puncta were counted manually.

#### 2.5.14 Quantitation of GFP-LC3 levels using in-gel fluorescence

Cells were treated as indicated in the experiment. Cells were trypsinised and collected by centrifugation and washed 3 times in ice-cold PBS. Cells were lysed in 1 % Triton X 100 for 30 min at 4 °C and centrifuged at 16 000 g for 20 min at 4 °C. The protein lysate concentration was calculated by Bradford Assay. Lysate was added to 4X LDS-loading dye (3:1 lysate:dye) to a final concentration of 10-20 µg/20 µl. Samples were run on 4:15% Tris-Glycine Mini Gels at 150 V for 1 h in Tris/Glycine/SDS running buffer (BioRad). The gel was removed and imaged using the GFP filter on a Syngene Gel:Doc.

#### 2.5.15 Quantitation of protein levels by Western blot

Cells were treated as indicated in the experiment. Cells were trypsinised and collected by centrifugation and washed 3 times in ice-cold PBS. Cells were lysed in 1 % Triton X 100 for 30 min at 4 °C and centrifuged at 16 000 g for 20 min at 4 °C. The protein lysate concentration

was calculated by Bradford Assay (BioRad Cat#5000006). Lysate was added to 4X LDS-loading dye 3:1 lysate:dye to a final concentration 10-20 µg/20 µl. Samples were boiled at 95 °C for 10 m. The protein lysate concentration was calculated by Bradford Assay (BioRad Cat#5000006). Lysate was added to 4x LDS-loading dye 3:1 lysate:dye to a final concentration 10-20 µg/20 µl. Samples were run on 4:15% Tris-Glycine Mini Gels at 150 V for 1 h in Tris/Glycine/SDS running buffer (BioRad). The gel was soaked in cathode buffer (25 mM Tris-Base pH 9.4, 40 mM Glycine, 10 % MeOH) for 15 minutes. PVDF membrane was cut to size and soaked in Methanol for 30 s, washed in dH2O for 2 min and soaked in Anode II buffer (25 mM Tris-Base, pH 10.4, 10 % MeOH) for 5 m. To create the sandwich, two filter papers were soaked in Anode I (0.3 M Tris-Base pH 10.4, 10 % MeOH) and placed on the Bio-Rad Semi-Dry Transfer apparatus, followed by a filter paper soaked in anode II buffer, the PVDF membrane, the gel and 3 filter papers in cathode buffer. Air bubbles were gently rolled out and excess buffer removed from the semi-dry plate. The gel was transferred for 1 h at 74 mA. Transfer efficiency was tested using Ponceau S staining and Coomassie staining of the gel after transfer. The membrane was blocked in 5 % semi-skimmed milk solution in TBS with 0.1 % Tween 20 (TBS-T) for 1 h at RT. Anti-GFP antibody (Santa Cruz, mouse monoclonal anti-GFP antibody (#18A11): sc-69779) was incubated at 1/200 dilution at 4 °C overnight. The membrane was washed 3 times at 10 min each in TBS-T followed by incubation of secondary antibody for 2 h at RT (1/8000 dilution, Vector Laboratories, HRP Horse anti-mouse IgG antibody peroxidase, cat#PI-2000). Membranes were soaked in Clarity Western ECL substrate solution (Bio-Rad) as per manufacturer's instructions. Excess solution was removed by touching the corner of the membrane to a tissue and the membrane was imaged using the Syngene Gel:Doc.

#### 2.5.16 Assessment of ER stress markers by real-time quantitative PCR (RT-qPCR)

RT-qPCR was used to determine changes in ER stress markers, *N*-glycanase downregulation for siRNA mediated knockdown, OGA and OGT expression in HEK cells and the presence of ATG13 in ATG13 KO and WT MEF cells. The sequences of all primers used can be found in Table **2.1**. RT-qPCR was carried out using the MJ Opticom real time PCR machine.

For analysis of ER stress markers, cells were treated with Z-VAD-fmk or Q-VD-OPh (50 µM, 24-72 h) or a vehicle control and MG132 (5 µM, 18 h). For genetic ablation of *N*-glycanase, HEK cells were transfected with SMARTpool: ON-TARGETplus ngly1 siRNA or an ON-TARGETplus non-targeting control (25 nM, 3-5 d). For the analysis of OGA and OGT expression, cells were treated with Z-VAD-fmk or Q-VD-OPh (50 µM, 24-72 h) or a vehicle

control. For genetic ablation of *N*-glycanase, HEK cells were transfected with SMARTpool: ON-TARGETplus ngly1 siRNA or an ON-TARGETplus non-targeting control (25 nM, 3-5 d). For the analysis of ATG13 expression levels in ATG13 KO and WT MEF cells, no treatment was added. For confirmation of siRNA knockdown of *N*-glycanase, HEK cells were transfected with 10-40 nM siRNA using JetPrime™ or DharmaFECT® according to manufacturer's instructions. Control samples were transfected with 40 nM non-targeting siRNA with either DharmaFECT® or JetPrime™. Quantities were normalised to GAPDH and percentage knockdown was calculated from the non-targeting control.

RNA was extracted using RNeasy Mini Kit. RNA (100 ng) was used with the One-Step Luna® Universal qPCR Master Mix per manufacturer's instructions. Samples were heated to 55 °C, 10 min to convert RNA to cDNA followed by an initial denaturation 98°C, 5 min followed by denaturation at 95 °C, 30 s, annealing at 58 °C, 30s, extension at 72°C, 30 s for 42 cycles. The threshold was taken over the global minimum over 10 standard deviations and analysed using the double delta Ct method. GAPDH was employed as a housekeeping gene and an untreated control was used as the baseline. A melting curve was undertaken post run to confirm specificity of primers from 50-90 °C reading every 0.5 °C.

**Table 2.2 Sequences of primers used in RT-qPCR**

Species	Gene	Sequence
Human	GAPDH Forward	5'-AGGGCTGCTTTAACTCTGGT-3'
	GAPDH Reverse	5'-CCCCACTTGATTTTGGAGGGA-3'
	BiP (Grp78) Forward	5'-ACGTGGAATGACCCGTCTGT-3'
	BiP (Grp78) Reverse	5'-AACCACCTTGAACGGCAAGA-3'
	CHOP Forward	5'-ACCAAGGGAGAACCAGGAAACG-3'
	CHOP Reverse	5'-TCACCATTCGGTCAATCAGAGC-3'
	ATF4 Forward	5'- TTGAGGATAGTCAGGAGCGT -3'
	ATF4 Reverse	5'-TGGAACACACAGCTACAGCA-3'
	EDEM Forward	5'-CAAGTGTGGGTACGCCACG-3'
	EDEM Reverse	5'-AAAGAAGCTCTCCATCCGGTC-3'
	OGA Forward	5'-TTCCTGAAGGCTAATGGCTCCCG-3'
	OGA Reverse	5'-ATGTCACAGGCTCCGACCAAGT-3'
	OGT Forward	5'-CATCGAGAATATCAGGCAGGAG-3'
	OGT Reverse	5'-CCTTCGACACTGGAAGTGTATAG-3'
	NGLY Forward	5'-GGTTTGAAGCTCGCTATGTTTGGGATTAC-3'
NGLY1 Reverse	5'-CTTGTACAGACATCTTCACATGCATCAC-3'	
Mouse	ATG13 Forward	5'- AGGGCGGGAGAGATCGTTTG-3'
	ATG13 Reverse	5'- CAGCACAGGTCGCAGAGAGA-3'

#### 2.5.17 Assessment of cellular calcium handling by fluorescence imaging

GFP-LC3 HEK cells were plated on uncoated 16 mm glass coverslips at (40 000 cells per well) and treated with Z-VAD-fmk or Q-VD-OPh (50  $\mu$ M, 24-72 h) or a vehicle control. For genetic ablation, HEK cells were transfected with SMARTpool: ON-TARGETplus ngly1 siRNA or an ON-TARGETplus non-targeting control (25 nM, 3-5 d). Cells were incubated in FURA-2 AM (1  $\mu$ M) in imaging buffer supplemented with Gibco MEM Amino Acids Solution and MEM Non-essential Amino Acids Solution for 20 min at 37°C. Cells were washed three times in imaging buffer and incubated for a further 20 m. Coverslips were imaged using a Leica DMI6000 fluorescence microscope on the 20x objective. Calcium was mobilised from the ER using Thapsigargin (1  $\mu$ M) after 180 s. Images were taken every 20 s for 12 m. Time lapse videos



were analysed using ImageJ. Cytosolic areas of cells were selected plus a background region for 340 and 380 nm. A minimum of 20 cellular regions were analysed per coverslip. The 340/380 ratio was calculated. The area under the curve, baseline average of first eight images and peak height were calculated using GraphPad Prism 7.

#### 2.5.18 Quantitation of oxidative stress by flow cytometry

Flow cytometry was used to determine RosBrite 570 fluorescence. HEK cells were treated with either Q-VD-OPh or Z-VAD-fmk (50  $\mu$ M, 24-72 h) or a vehicle control (DMSO). For genetic ablation, HEK cells were transfected with SMARTpool: ON-TARGETplus ngly1 siRNA or an ON-TARGETplus non-targeting control (25 nM, 3-5 d). Cells were loaded with RosBrite 570 (5  $\mu$ M, 30 m) at 37 °C in complete media. Cells were detached with trypsin and washed in HBSS three time by centrifugation. Cells were re-suspended in HBSS (500  $\mu$ l) and analysed using BD FACSCalibur on the FL2 channel (ex 488 em 585-642), at 440 V, 10 000 cells were counted per condition.

#### 2.5.19 Expression and purification of recombinant PNGase F

Overnight cultures were grown at 37 °C in LB media supplemented with ampicillin (100  $\mu$ g/ml). The overnight culture (0.8 % final volume) was used to inoculate fresh LB media supplemented with ampicillin (100  $\mu$ g/ml). Large scale cultures (500 ml) were grown at 37 °C until OD<sub>600</sub> 0.5-0.7. Protein expression was induced by the addition of IPTG (1 mM final concentration). Following induction, cultures were left to grow overnight with shaking (30 °C, 210 rpm). PNGase F was purified using a variation of the methodology described by Loo *et al.* (2002). Cells were pelleted at 600 g and washed in half the original volume of ice-cold PBS, and the cell pellet re-suspended in 2% culture volume of chilled sucrose (0.5 M) in Tris-HCl at (0.1 M, pH 8). The resultant lysate was pelleted at 8000 g (20 min, 4°C) and re-suspended in 2% original culture volume chilled sdH<sub>2</sub>O. The suspension was incubated on a tube roller (4 °C, 20 min). MgCl<sub>2</sub> (200  $\mu$ l of 1 M solution) was added to a final concentration of 20 mM and incubated on a tube roller for a further 20 minutes. The suspension was pelleted by centrifugation (8000g, 20 min, 4°C). The supernatant was filtered through a Nalgene PES 0.45  $\mu$ m syringe filter (725-2545) before being manually loaded on a nickel affinity column (HisTrap HP histidine tagged protein purification column, 5 ml, cat#17524701) by syringe pre-equilibrated with 20 ml wash buffer (20 mM HEPES, 300 mM NaCl, 20 mM imidazole). Contaminants were washed with 2 column volumes of wash buffer. Protein material was eluted with 4 column volumes of elution buffer (20 mM HEPES, NaCl (300 mM) and imidazole (300 mM)). Fractions were analysed for target protein by SDS-Page

gel (Novex 12 % Tris-Glycine Mini Gels Cat#XP00122BOX). Fractions containing target protein were dialysed (10 kDa) overnight into 2 L storage buffer (20 mM Tris-HCl, 50 mM NaCl, 5 mM Na<sub>2</sub>EDTA, pH 7.5 at 4 °C). The dialysed samples were concentrated by centrifugation (3000 g) to 35 mg/ml and stored at 4 °C.

#### 2.5.20 PNGase F activity assay

Activity of purified recombinant PNGase F was tested using RNaseB as a substrate. RNase B (20 µg, Alfa Aesar) was added to denaturing buffer (1 µl, 0.5% SDS in 40 mM DTT) to a final volume of 10 µL. Samples were heated (95 °C, 10 min). The mixture was cooled on ice and PNGase F (5 µg) was added, with 50 mM sodium phosphate (pH 7) to a final volume of 20 µL. The sample was incubated at 37 °C while shaking for 1.5 h. Digestion was stopped with the addition of 4 x LDS loading dye. Samples were analysed on a denaturing SDS-PAGE gel (4:15%, polyacrylamide gel set in BioRad Criterion Empty Cassettes).

#### 2.5.21 Generation of mAPPLE tagged Z-VAD-fmk insensitive PNGase plasmid (bacpng)

PCR based cloning was used to clone PNGase F from the poPH6 plasmid to be inserted into a mammalian expression vector with a C-terminal linked mAPPLE fluorescent marker, mAPPLE-N1. This would allow transfection of a Z-VAD-fmk insensitive PNGase into HEK cells. The poPH6 plasmid (1 ng) underwent PCR with the Phusion High-Fidelity DNA polymerase with the forward and reverse cloning primers found in Table 2.3 using the following protocol: Initial denaturing (95 °C, 3 min), 98 °C (20 s), annealing (60 °C for 15 s), extension (72 °C for 30 s) for 34 cycles. The resulting product was excised from the gel and extracted using QIAquick Gel Extraction Kit. The isolated PCR product and N1-mAPPLE plasmid were double digested with BamHI and XhoI. The mAPPLE-N1 plasmid (1 µg) or PCR product (1 µg) was digested with 10 units of restriction enzyme in 1xNEB Buffer 3.1 at (37 °C, 4 h) in a final volume of 50 µL. Digestion was confirmed by 1.5 % TAE agarose gel. The PNGase F PCR product was ligated into the mAPPLE-N1 plasmid using T4 DNA ligase. Vector DNA (50 ng) and insert DNA (50 ng) was incubated with 10X T4 DNA ligase buffer (2 µL) and T4 DNA ligase (1 µL) in nuclease free water (20 µL) for 48 h at 4°C. The reaction mixture (2 µL) was transformed into DH5α<sup>TM</sup> Competent Cells (50 µl). *E. coli* were plated on agar plates supplemented with Kanamycin (50 µg/ml). The plasmid was extracted from *E. coli* using QIAprep Spin Miniprep Lit. Plasmid DNA was digested with BamHI and XhoI as before and colonies exhibiting the correct predicted sized bands were submitted for sequence analysis and termed bacpng 1-6.

**Table 2.3 Cloning primers for generation of bacterial PNGase F into N1-mAPPLE mammalian expression vector**

Forward cloning primer	5'-GCAG <u>CTCGAG</u> ACCATGGCTCCGGCAGATAATAC-3'
Reverse cloning primer	5'-GATG <u>CGGATCC</u> AAGTTTG-3'

## 2.6 Generation of CRISPR targeting plasmids

Plasmid maps for CRISPR plasmids are available in Appendix, figure **A.3** and figure **A.4**.

### 2.6.1 Design of guide sequences

Guide sequences were designed using [crispr.mit.edu](http://crispr.mit.edu) web tool (using the nickase analysis) and are presented in Table **2.4**.

**Table 2.4** sgDNA sequences were designed usign [crispr.mit.edu](http://crispr.mit.edu)

Batch #	Oligo name	Length	Sequence 5'-3'
HA09093690	PNGrx-sgB-T	25	CACCGTACTTCGAGACACTATTAAT
HA09093691	PNGrx-sgB-B	25	AAACATTAATAGTGTCTCGAAGTAC
HA09093692	PNGrx-sgA-T	25	CACCGTTCTTTAACCTTAGTTCTTC
HA09093693	PNGrx-sgA-B	25	AAACGAAGAACTAAGGTTAAAGAAC
HA09093694	ENGko-sgB-T	25	CACCGGGCGTGGAAGCCCCGCTTGG
HA09093695	ENGko-sgB-B	25	AAACCCAAGCGGGGCTTCCACGCC
HA09093696	ENGko-sgA-T	25	CACCGCAAGTAAAAGCTGATTGGTT
HA09093697	ENGko-sgA-B	25	AAACAACCAATCAGCTTTTACTTGA
HA09093698	PNGko-sgB-T	25	CACCGACTAGACTCTTGCCTGTCAG
HA09093699	PNGko-sgB-B	25	AAACCTGACAGGCAAGAGTCTAGTC
HA09093700	PNGko-sgA-T	25	CACCGGGCTGTGTTTCCAATCCGGA
HA09093701	PNGko-sgA-B	25	AAACTCCGGATTGGAAACACAGCCC

For the PNGko guide, sequences were selected from gDNA 4801-5041. For the RX mutation gDNA 49602-49842 were used (which overlapped the R401X mutation site). The ENGase mutation was calculated for gDNA 2729-2969. Figure **2.1-2.3** shows the design tool, [crispr.mit.edu](http://crispr.mit.edu) out for PNGrx, PNGko and ENG guide sequences respectively indicating the number of off-target effects for both WT and Nickase variety Cas9 plasmids.

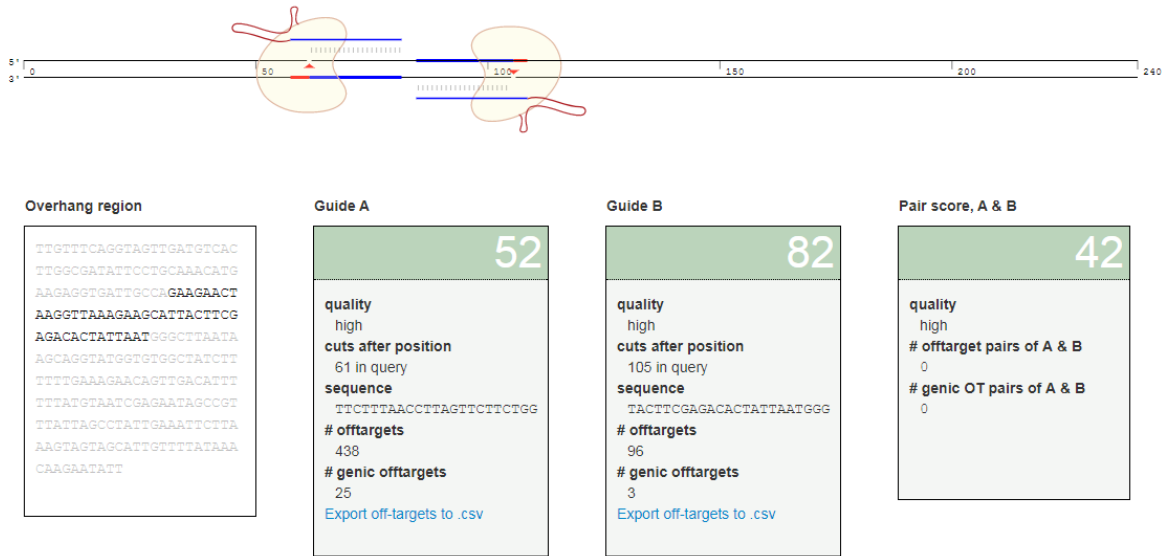


Figure 2.1 PNGrx guide sequence calculation. Diagram showing the schematic position of guide sequences A and B with off target effects.

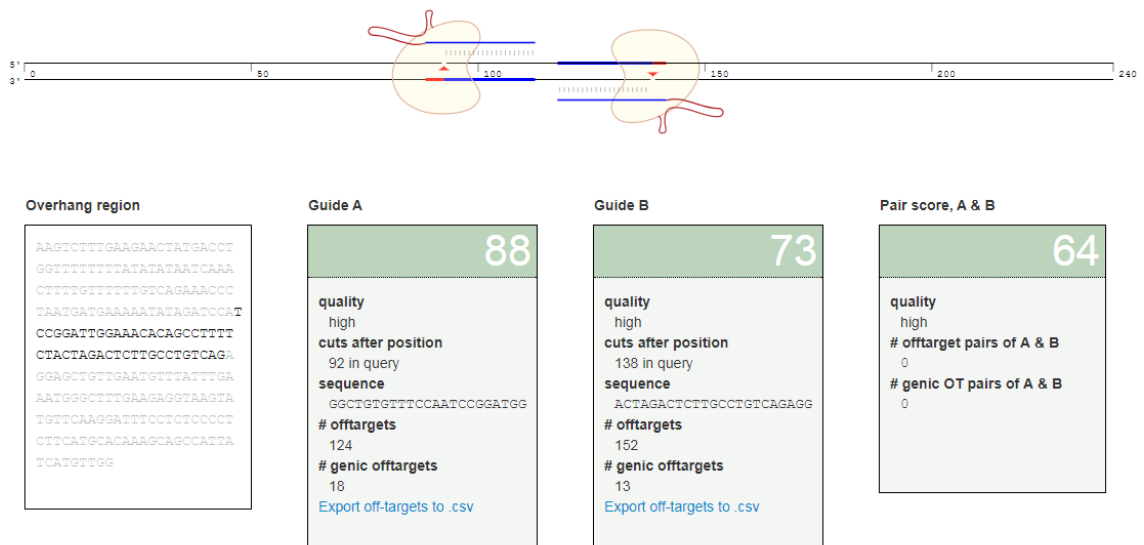
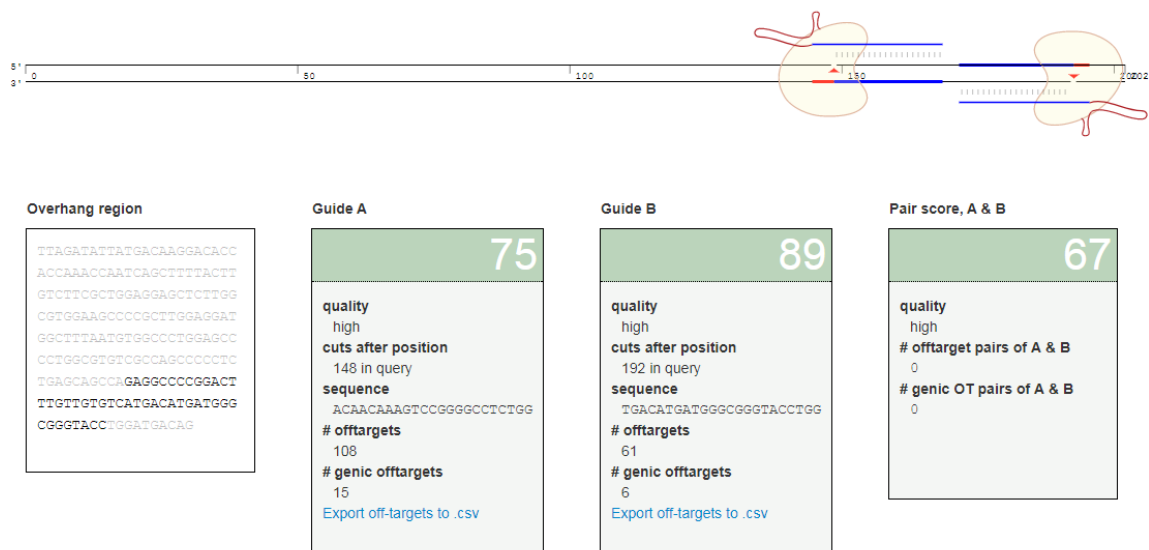


Figure 2.2 PNGko guide sequence calculation Diagram showing the schematic position of guide sequences A and B with off target effects.



**Figure 2.3 ENGko guide sequence calculation. Diagram showing the schematic position of guide sequences A and B with off target effects.**

Table 2.5 lists the PCR/sequencing primers used to amplify gDNA regions around the expected CRISPR/Cas9 mutation sites.

**Table 2.5 Sequencing primers over regions of CRISPR editing supplied by Sigma Aldrich**

Batch #	Primer Name	Length	Sequence 5'-3'	Tm
HA09093684	PNGko-seq-F	21	GTACCTTAACAGCACAGAATG	59.15
HA09093685	PNGko-seq-R	19	CCTACTACAGACAGGTAGC	45.40
HA09093686	PNGrx-seq-F	18	TCTTGACCCTGGGAAGTG	55.3
HA09093687	PNGrx-seq-R	20	GTCAGGTACTACCAACTG	45.31
HA09093688	ENGko-seq-F	22	GAATACCGATCCACCTTCACAC	59.15
HA09093689	ENGko-seq-R	22	CTGGTCTCAAACCTCCTGAGGTC	58.79

### 2.6.2 Phosphorylation and annealing of oligonucleotides

Oligonucleotides were phosphorylated and annealed to form double stranded oligonucleotides. Two corresponding single stranded oligonucleotides were annealed by adding polynucleotide kinase (1  $\mu$ l), 10X T4 ligation buffer (1  $\mu$ l), the top and bottom oligonucleotides (1  $\mu$ l of 100  $\mu$ M stock) were added to a final volume of 8  $\mu$ l in ddH<sub>2</sub>O in a PCR tube. The oligonucleotides were phosphorylated and annealed using a thermocycler at 37 °C for 30 min, 95 °C for 5 min, 25 °C for 5 min. The annealed oligonucleotides were diluted 1:200 in ddH<sub>2</sub>O.

### 2.6.3 Cloning of the sgDNA products into appropriate vectors

The phosphorylated and annealed sgDNA product was cloned into both pSpCas9(BB)2A-GFP and pSpCas9n(BB)2A-GFP. Plasmid DNA was diluted to 50 ng/ml (2 µl) and mixed with the annealed oligonucleotides (2 µl), 10X tango buffer (2 µl), DTT (10 mM, 1 µl), ATP (10 mM, 1 µl), Bpi1 (1 µl), T7 ligase (0.5 µl) to a final volume of 20 µl in ddH<sub>2</sub>O. The ligation reaction was incubated for 1 h at 37 °C, 5 min 21 °C. Linear DNA was eliminated by Plasmidsafe exonuclease activity. The ligation reaction (11 µl) was added to 10X PlasmidSafe buffer (1.5 µl), ATP (10 mM, 1.5 µl) and PlasmidSafe exonuclease (1 µl). The reaction was incubated at 37 °C for 30 min followed by 70 °C for 30 min.

### 2.6.4 Transformation of plasmids into an *E. coli* expression host

Plasmids were transformed by heat shock into *E. coli* DH5α. Briefly, plasmid product (15 µl) was incubated with *E. coli* DH5α (100 µl) for 10 min on ice. Cells were heat shocked at 42 °C for 45 s and placed on ice for 2 min. Pre-warmed SOC media (900 µl) was added to the bacteria and incubated at 37 °C for 1 h. Cells were plated on LB agar containing 100 µg/ml ampicillin and incubated overnight at 37 C.

### 2.6.5 Determination of sequence

Plasmids were extracted by Qiagen maxi prep kit per manufacturer's instruction. Plasmid construct and transformation was confirmed by DNA sequencing. Two colonies were picked for each transformation and Qiagen maxi prep was performed according to manufacturer's instructions. Plasmid DNA was sent to MRC PPU DNA sequencing and services at Dundee University using U6-Fwd primer or sequencing primers described in Table 3. Sequences available in appendix **A.2**.

### 2.6.6 PCR

Genomic DNA was extracted from HEK 293 cells using Qiagen DNeasy Blood and Tissue kit and PCR was done using the Phusion High fidelity polymerase kit. PCR products were separated by 1.5% agarose gel in TAE buffer (40 mM Tris, pH 7.6, 20 mM acetic acid, 1 mM EDTA) at 150 V for 1 h. DNA was stained with Midori Green. Images were taken on the Synegne G:Box imaging system.

### 2.6.7 Transfection of CRISPR constructs

CRISPR plasmids were transfected using JetPei™ according to the manufacturers guidelines (2:1 mixture of transfection reagent:plasmid DNA, incubated in 150 mM NaCl solution at RT

for 0.5 h). For CRISPR transfections including the specific mutation oligo, for every 1 µg of plasmid DNA, 1 µl of 10 mM oligo was added to the DNA.

**Table 2.6 R401X homology directed repair sequence**

R401X oligonucleotide insertion sequence	5'- TAATCTTGTTAAGTATTTGTATTCTGTTATTTGTTTCAGGTAGTTGATGTCAC TGGCGATATTCCTGCAAACATGAAGAGGTGATTGCCAGAAGAAGCTAAGGTT AAAGAAGCATTACTTCGAGACACTATTAATGGGCTTAATAAGCAGGTATGGT GTGGCTATCTTTTTGAAAGAACAGTTGACATTTTTTATGTAATC-3'
---	---

### 2.2.7 Shotgun proteomics analysis of CRISPR clones (ThermoScientific QExactive)

Following desalting of protein digests by reverse phase C18 solid phase extraction (C18-SPE), samples were resolubilised in 0.1 % TFA (20 µl) by shaking (30 min, 1200 rpm) and sonication (10min). The solutions were centrifuged (17,000 g, 10 min, 5 °C) and transferred to LC-MS sample vials. Peptides were separated using an Ultimate 3000 RSLC nano liquid chromatography system (Thermo Scientific) coupled to a Q-Exactive mass spectrometer (Thermo Scientific) via an EASY-Spray source. Injected sample volumes were loaded onto a trapping column (Acclaim PepMap 100 C18, 100 µm × 2 cm) at 8 µL/min in 2 % acetonitrile, 0.1% TFA. Peptides were then eluted on-line to an analytical column (EASY-Spray PepMap C18, 75 µm × 75 cm). Peptides were separated using a ramped 80 minute gradient, 4-70 % of buffer B (buffer A: 2% acetonitrile, 0.1% FA; buffer B: 80% acetonitrile, 0.1% FA). Eluted peptides were analysed by the Q-Exactive operating in positive polarity using a data-dependent acquisition mode. Ions for fragmentation were determined from an initial MS1 survey scan at 70,000 resolution (determined at m/z 200), followed by HCD (Higher-energy collisional dissociation) of the top 12 most abundant ions at a MS2 resolution of 17,500 (determined at m/z 200). MS1 and MS2 scan AGC targets set to 1e6 and 1e5 for a maximum injection time of 50 ms and 110 ms respectively. A survey scan m/z range of 350 – 1800 m/z was used, with a normalised collision energy set to 27 %, underfill ratio – 1%, charge state exclusion enabled for unassigned, +1, +8 and >+8 ions. LC-MS/MS analysis was carried out in technical duplicate runs.



Data was processed using the MaxQuant software platform (v1.5.8.3), with database searches carried out by the in-built Andromeda search engine against the Swissprot Human database. A reverse decoy database approach was used at a 1% false discovery rate (FDR) for peptide-spectrum matches and protein identification. Search parameters included: maximum number of missed cleavages set to 2, fixed modifications: cysteine carbamidomethylation and variable modifications: methionine oxidation, protein N-terminal acetylation. Label-free quantification was enabled with an LFQ minimum ratio count of 2. For data analysis protein and peptide identifications and relative quantification outputs from Maxquant were further processed in Excel, with protein and peptides hits to the 'reverse database', 'potential contaminants' (peptide list only) and 'Only identified by site' field removed.

## 2.7 Proteomics analysis of autophagosomes

This section describes the protocols used for isolation of autophagosomes and settings associated with mass spectrometer analysis.

### 2.7.1 Autophagosome isolation using GFP-linked magnetic beads

GFP-LC3 HEK cells were cultured as before, washed twice with ice cold PBS and collected. Pellets were re-suspended in ice cold 0.25 M sucrose, 1 mM EDTA, 20 mM HEPES, pH 7.4 and lysed by dounce homogenisation and vortexed every 10 minutes for 30 minutes on ice. Cells were centrifuged at 10 000g for 20 minutes at 4 °C and the pellet washed twice in 0.1% BSA in PBS and re-suspended in PBS. Autophagosomes were isolated using BioRad SureBeads Protein G magnetic beads coupled to anti-GFP antibody at 2-4 µg antibody per 1 mg beads. Protein concentration was determined by Nanodrop and visual inspection under a fluorescence microscope.

### 2.7.2. Autophagosome isolation using Chromotek GFP-Trap® agarose beads

GFP-LC3 HEK cells were cultured as before and washed twice with ice cold PBS and collected. Cells were lysed in 1 % Triton in PBS by dounce homogenisation and incubated for 30 min at 4°C. Lysate was centrifuged at 6000 g for 10 min at 4 °C. The supernatant was removed and centrifuged again at 20 000 g for 20 min at 4 °C. The supernatant was discarded and the pellet re-suspended in PBS (500 µl) and added to filter spin column with GFPTrap® agarose beads (50 µl) or agarose bead control (50 µl) washed 3x in PBS. Samples were tumbled for 1 h at 4°C. Samples were then centrifuged at 2 500 g for 2 min and, the flow through was discarded. Samples were washed 7x in ice-cold PBS-T by centrifugation. Samples were eluted by 0.2 M glycine, pH 2.5 (50 µl) for 1 min with constant vortexing. Beads were centrifuged into a fresh, low protein binding tube. Elution was repeated and samples pooled. Samples were neutralised by the addition of 1 M phosphate buffer (pH 7.4).

### 2.7.3 In-gel trypsin digestion

Autophagosomes were enriched by anti-GFP immunoprecipitation of GFP-LC3 in HEK cells treated with basal control, amino acid starvation, rapamycin (5 µM) and Z-VAD-fmk (50 µM, 72 h) followed by Bafilomycin treatment (100 nM, 4 h). The eluent was run on a 12 % Tris:Glycine SDS Page gel. Bands were cut into 1mm<sup>2</sup> squares and washed overnight in wash solution (50% MeOH, 5% acetic acid, 200 µl), the wash solution was changed after 24 h and incubated for 2-3 h at RT while shaking. The wash solution was removed and acetonitrile (200 µl) was added to dehydrate the gel for 5 min at RT. This step was then repeated. DTT

solution (10 mM in 100 mM ammonium bicarbonate, 30  $\mu$ l) was added and samples were reduced for 30 min. DTT was removed and iodoacetamide (50 mM, 30  $\mu$ l) was added to alkylate cysteine residues for 30 min. This solution was then removed and acetonitrile (200  $\mu$ l) was added for 5 min. The acetonitrile was removed and ammonium bicarbonate (50 mM, 200  $\mu$ l) was added for 10 min. The trypsin reagent was prepared on ice by adding ice-cold 50 mM ammonium bicarbonate (2 ml) to sequencing grade modified trypsin (20  $\mu$ g). Trypsin solution (30  $\mu$ l) was added to each gel piece and incubated at RT for 10 min before centrifugation to remove excess trypsin. Ammonium bicarbonate (50 mM, 5  $\mu$ l) was added to stop the gel pieces drying out and the gel pieces were incubated at 37° C overnight. Any liquid left in the tube was removed and, ammonium bicarbonate (50 mM, 50  $\mu$ l) was added for 10 min. The supernatant was collected and extraction buffer I (50% acetonitrile, 5% formic acid, 50  $\mu$ l) was added. The samples were incubated for 10 min, then the supernatant was collected. Extraction buffer II (85% acetonitrile, 5% formic acid, 50  $\mu$ l) was added for 10 min and the supernatant collected and pooled. The combined supernatants were dried in a vacuum centrifuge. The pellet was re-suspended in 2% acetonitrile and 0.1% formic acid (20  $\mu$ l) and transferred to LC-MS sampling tubes.

#### 2.7.4 Analysis of samples following in-gel digestion (Bruker AmaZon Ion Trap LCMS-MS system)

Protein samples were combined with reducing SDS-PAGE sample buffer, heat denatured and resolved on a Tris-Glycine 4:12% gel. Following Coomassie blue staining, each lane was excised to generate five equally sized sections which were cut into 1 – 2 mm<sup>3</sup> gel pieces and placed into 1.5 ml sample tubes. Gel pieces were rinsed twice with wash solution for 18 h in total (200  $\mu$ L, 50% methanol, 5% acetic acid). The solutions were removed and gel pieces were dehydrated in acetonitrile (200  $\mu$ L, 5 min). The supernatant was removed and gel pieces were dried in a vacuum centrifuge for 3 min. Disulfide reduction was performed with 10 mM DTT (30  $\mu$ L) for 0.5 h, followed by alkylation with 100 mM iodoacetamide (30  $\mu$ L) for 0.5 h. Supernatants were removed from the gel samples and dehydration with acetonitrile and evaporation performed as described above. Gel pieces were washed with 100 mM ammonium bicarbonate (200  $\mu$ L, 10 min). Supernatants were removed and dehydration performed with acetonitrile and evaporation as above. The gel samples were then rehydrated on ice with freshly prepared trypsin solution (30  $\mu$ L, 20 ng/ $\mu$ L sequencing grade trypsin in 50 mM ammonium bicarbonate). After rehydration excess trypsin solution was removed and 50 mM ammonium bicarbonate (10  $\mu$ L) was added to prevent dehydration of gel pieces. Gel samples were digested at 37 °C for 18 h. The gel pieces were then extracted

sequentially with 50 mM ammonium bicarbonate (60  $\mu$ L), 50 % acetonitrile, 5 % formic acid (FA) (60  $\mu$ L) and 85 % acetonitrile, 5 % FA (60  $\mu$ L). The combined extracts were evaporated in a vacuum centrifuge and were redissolved in 5% acetonitrile, 0.1% FA (20  $\mu$ L) on an ultrasonic bath and transferred into LC-MS sample vials.

For the LC-MS/MS analysis of in-gel digested protein material, liquid chromatography was performed using an Ultimate 3000 nano-HPLC system (Dionex, Sunnyvale, CA, USA) comprising a WPS-3000 micro auto sampler, a FLM-3000 flow manager and column compartment, a UVD-3000 UV detector, an LPG-3600 dual-gradient micro-pump, and an SRD-3600 solvent rack controlled by Hystar (Bruker Daltonics, Billerica, MA, USA) and DCMS link 2.0 software. Samples were concentrated on a trapping column Dionex (Sunnyvale, CA, USA, 300 $\mu$ m i.d., 0.1cm) at a flow rate of 20  $\mu$ L/min. For the separation with a C18 Pepmap column (75  $\mu$ m i.d., 15 cm, Dionex), a flow rate of 250 nL/min was used as generated by a cap-flow splitter cartridge (1/1000). Peptides were eluted by the application of a 0.5 h multi-step gradient using solvents A (98% H<sub>2</sub>O, 2% acetonitrile, 0.1% FA) and B (80% acetonitrile, 20% water, 0.1% FA).

Composition (% solvent B)	Run time (min)
<b>2-10</b>	0-3
<b>10-25</b>	3-18
<b>25-50</b>	18-30
<b>50-90</b>	30-30.2

The liquid chromatography was interfaced directly with a 3D high capacity ion trap mass spectrometer (amaZon; Bruker Daltonics) utilizing 10  $\mu$ m i.d. distal coated SilicaTips (New Objective, Woburn, MA, USA) and nano-ESI mode. SPS parameter settings on the ion trap were tuned for a target mass of 850 m/z, compound stability 100 % and a smart ICC target of 250,000. MS/MS analysis was initiated on a contact closure signal triggered by HyStar software (version 3.2). Up to five precursor ions were selected per cycle with active exclusion (0.5 min) in collision-induced dissociation (CID) mode. CID fragmentation was achieved using helium gas and a 30 %-200 % collision energy sweep with amplitude 1.0 (ions are ejected from the trap as soon as they fragment).

Raw LC-MS/MS data were processed and Mascot compatible files were created using DataAnalysis 4.0 software (Bruker Daltonics). Database searches were performed using the

Mascot algorithm (version 2.4) and the UniProt\_SwissProt database with mammalian taxonomy restriction (v2015.11.26, number of entries 549,832). The following parameters were applied: 2+, 3+ and 4+ ions, peptide mass tolerance 0.3 Da, 13C = 2, fragment mass tolerance 0.6 Da, number of missed cleavages: two, instrument type: ESI-TRAP, fixed modifications: Carbamidomethylation (Cys), variable modifications: Oxidation (Met).

#### 2.7.6 In-house FASP digestion protocol

Autophagosomes were isolated as before. Spin filters (30 kDa) were conditioned with mQ water (50  $\mu$ L) and centrifuged at 12 000 g for 2 min. Protein lysates were loaded onto the filter and centrifuged at 12 000 g for 5 min. UA buffer (8M urea in 0.1M Tris/HCl, pH5) (200  $\mu$ L) was added and centrifuged at 12 000 g for 15 min. This was repeated twice. DTT (10 mM, 100  $\mu$ L) in UA was added and shaken for 1 min followed by static incubation for 30 min at 40  $^{\circ}$ C. The sample was centrifuged at 12 000 g for 10 min. Iodoacetamide solution in UA (50 mM, 100  $\mu$ L) was added to the filter and shaken for 1 min before being incubated for 20 min at RT. UA (100  $\mu$ L) was added and centrifuged at 12 000 g for 15 min. This was repeated twice. Ammonium bicarbonate (50 mM, 100  $\mu$ L) was added and centrifuged at 12 000 g for 10 min. This was repeated twice. The trypsin reagent was prepared on ice by adding ice-cold 50 mM ammonium bicarbonate (2 ml) to sequencing grade modified trypsin (20  $\mu$ g). The trypsin solution (200  $\mu$ L) was added at 6 ng/ $\mu$ L in ammonium bicarbonate (50 mM) and shaken for 1 min and incubated overnight at 37  $^{\circ}$ C. The spin filter was transferred to a new collection tube and centrifuged at 12 000 g for 10 min. NaCl solution (0.5 M, 50  $\mu$ L) was added to the filter and centrifuged for a further 10 min. TFA (1 %, 50  $\mu$ L) was added and the samples were desalted using C18 tips.

#### 2.7.7 Expedeon FASP™ protocol

The Expedeon FASP™ kit (Expedeon, catalogue no. 44250) was used per manufacturer instructions. Briefly, autophagosomes were isolated as before. Lysate solution (30  $\mu$ L) was added to a urea sample solution (200  $\mu$ L) then transferred to a spin filter and centrifuged at 14 000 g for 15 min. 10 x iodoacetamide stock (10  $\mu$ L) was added to a urea solution (90  $\mu$ L) and added to the filter. The samples were vortexed for 1 min and incubated (protected from light) for 20 min at RT then centrifuged at 14 000 g for 10 min. The filter was washed three times with urea solution (100  $\mu$ L) and centrifuged at 14 000 g for 15 min. Followed by three ammonium bicarbonate (50 mM, 100  $\mu$ L) washes and centrifuged at 14 000 g for 10 min. Digestion solution (75  $\mu$ L) was added to the filter and vortexed for 1 min. The tubes were wrapped in parafilm and incubated overnight at 37  $^{\circ}$ C. Spin filters were transferred to a new

collection tube and ammonium bicarbonate solution (40  $\mu$ l) was added and centrifuged at 14 000 g for 10 min. This step was repeated and the samples pooled. NaCl solution (0.5 M, 50  $\mu$ L) was added and centrifuged at 14 000 g for 10 min. The pooled eluate was acidified with TFA (1 %, 50  $\mu$ L). Samples were desalted using C18 tips.

#### 2.7.8 Analysis of in-house and Expedeon FASP protocols (ThermoScientific LTQ Orbitrap XL)

Following desalting of protein digests by reverse phase C18 solid phase extraction (C18-SPE), samples were resolubilised in 0.1 % trifluoroacetic acid (TFA) (20  $\mu$ l) by shaking (30 min, 1200 rpm) and sonication (10 min). The solutions were centrifuged (17,000 g, 10 min, 5 °C) and transferred to LC-MS sample vials. Sample aliquots were injected and separated using an Ultimate 3000 RSLC nano liquid chromatography system (Thermo Scientific) coupled to a LTQ Orbitrap XL mass spectrometer (Thermo Scientific) via a Proxeon nano-spray source. Injected sample volumes were loaded onto a trapping column (Acclaim PepMap 100 C18, 100  $\mu$ m  $\times$  2 cm) at 8  $\mu$ L/min in 2 % acetonitrile, 0.1 % TFA. Peptides were eluted on-line to an analytical column (Acclaim Pepmap RSLC C18, 75  $\mu$ m  $\times$  50 cm) and separated using a stepped 90 minute gradient, 4-25% of buffer B for 60 minutes, 25-65 % buffer B for 30 minutes (buffer A: 2 % acetonitrile, 0.1 % FA; buffer B: 80 % acetonitrile, 0.1 % FA). Eluted peptides were analysed by the LTQ Orbitrap XL operating in positive polarity using a data-dependent acquisition mode. Ions for fragmentation were determined from an initial MS1 survey scan at 30,000 resolution (determined at m/z 200), followed by Ion Trap CID (collision-induced dissociation) of the top 6 most abundant ions. MS1 and MS2 scan AGC targets set to 1e6 and 1e4 for a maximum injection time of 500 ms and 100 ms respectively. A survey scan m/z range of 350 – 1800 was used, with a normalised collision energy set to 35 %, charge state rejection enabled for singly charged precursor ions and a minimum threshold for triggering fragmentation of 500 counts.

Data was processed using the MaxQuant software platform (v1.5.8.3), with database searches carried out by the in-built Andromeda search engine against the Swissprot Human database. A reverse decoy database approach was used at a 1 % false discovery rate (FDR) for peptide-spectrum matches and protein identification. Search parameters included: maximum number of missed cleavages set to 2, fixed modifications: cysteine carbamidomethylation and variable modifications: methionine oxidation, protein N-terminal acetylation. Label-free quantification was enabled with an LFQ minimum ratio count of 2. For data analysis protein and peptide identifications and relative quantification outputs from

MaxQuant were further processed in Excel, with protein and peptides hits to the 'reverse database', 'potential contaminants' (peptide list only) and 'Only identified by site' field removed.

#### 2.7.9 Analysis of in-house FASP samples (ThermoScientific LTQ Orbitrap Velos)

Following desalting of protein digests by reverse phase C18 solid phase extraction (C18-SPE), samples were resolubilised in 0.1% trifluoroacetic acid (20 µl) by shaking (30 min, 1200 rpm) and sonication (10 min). The solutions were centrifuged (17,000 g, 10 min, 5°C) and transferred to LC-MS sample vials. Sample aliquots were injected and separated using an Ultimate 3000 RSLC nano liquid chromatography system (Thermo Scientific) coupled to a LTQ Orbitrap Velos mass spectrometer (Thermo Scientific) via the EASY-Spray ion source. Injected sample volumes were loaded onto a trapping column (Acclaim PepMap 100 C18, 100 µm × 2 cm) at 8 µL/min in 2 % acetonitrile, 0.1 % TFA. Peptides were eluted on-line to an analytical column (EASY-Spray PepMap C18, 75 µm × 50 cm) and separated using a stepped 90 minute gradient, 4-25 % of buffer B for 60 minutes, 25-65 % buffer B for 30 minutes (buffer A: 2 % acetonitrile, 0.1 % FA; buffer B: 80 % acetonitrile, 0.1 % FA). Eluted peptides were analysed by the LTQ Orbitrap Velos operating in positive polarity using a data-dependent acquisition mode. Ions for fragmentation were determined from an initial MS1 survey scan at 15,000 resolution (determined at m/z 200), followed by Ion Trap CID (collision-induced dissociation) of the top 10 most abundant ions. MS1 and MS2 scan AGC targets set to 1e6 and 1e4 for a maximum injection time of 500 ms and 100 ms respectively. A survey scan m/z range of 350 – 1600 was used, with a normalised collision energy set to 35 %, charge state rejection enabled for singly charged precursor ions and a minimum threshold for triggering fragmentation of 500 counts. LC-MS/MS analysis was carried out in technical duplicate runs.

Data was processed using the MaxQuant software platform (v1.5.8.3), with database searches carried out by the in-built Andromeda search engine against the Swissprot Human database. A reverse decoy database approach was used at a 1 % false discovery rate (FDR) for peptide-spectrum matches and protein identification. Search parameters included: maximum number of missed cleavages set to 2, fixed modifications: cysteine carbamidomethylation and variable modifications: methionine oxidation, protein N-terminal acetylation. Label-free quantification was enabled with an LFQ minimum ratio count of 2. For data analysis protein and peptide identifications and relative quantification outputs from MaxQuant were further processed in Excel, with protein and peptides hits to the 'reverse

database', 'potential contaminants' (peptide list only) and 'Only identified by site' field removed.

## 2.8 Characterisation of mitochondrial function under inhibition and genetic ablation of *N*-glycanase

This section describes the characterisation of mitochondrial function following the characterisation of MTT reduction in both glucose and galactose containing media with confirmation of cell viability by measurement of PI exclusion, annexin V staining and cell number confirmation. Mitochondrial membrane potential and mitochondrial content and mitochondrial glycoprotein analysis was performed after treatment with either Z-VAD-fmk, Q-VD-OPh or NGLY1 siRNA transfection.

### 2.8.1 Growth curves

Cells were grown in either high glucose DMEM media or glucose free media supplemented with galactose (10 mM) or a glucose:galactose 50:50 mix for 6 d prior to experimentation. Cells were then plated at 1000 cells per well in a 48 well plate. Cells were detached using trypsin-EDTA solution (100  $\mu$ l) and diluted with complete media (400  $\mu$ l). Cell suspensions were counted by haemocytometer. Four individual wells were counted for each cell line at each time point.

### 2.8.2 Quantification of PI/Annexin V staining

Cells were grown in either high glucose DMEM media or glucose free media supplemented with galactose (10 mM) for 6 d prior to experimentation and plated into 12 well plate. HEK cells were treated with either Q-VD-OPh or Z-VAD-fmk (50  $\mu$ M, 24-72 h) or a vehicle control (DMSO). For genetic ablation, HEK cells were transfected with SMARTpool: ON-TARGETplus NGLY1 siRNA or an ON-TARGETplus non-targeting control (25 nM, 3-5 d). Menadione (20  $\mu$ M, 18 h) was used as a positive control for cell death and apoptosis inducer. Samples were trypsinised to detach cells and washed three times in PBS. Cells were incubated with the Molecular Probes™ Dead Cell Apoptosis Kit with Annexin V FITC and PI, for flow cytometry. Cells were re-suspended in 1x annexin binding buffer (100  $\mu$ l). FITC annexin V (5  $\mu$ l) and Propidium iodide (PI) (1  $\mu$ l, 100  $\mu$ g/ml) was added for 15 min at RT. Samples were diluted with annexin binding buffer (400  $\mu$ l) and red/green signal was analysed using a TALI image based cytometer. The percentage of annexin V positive and PI negative cells were calculated. Cell number was also recorded.



### 2.8.3 Assessment of mitochondrial membrane polarisation using TMRE

To measure mitochondrial depolarisation, HEK cells were plated in 12 well plates and treated as described. Cells were trypsinised, washed twice in PBS and incubated for 20 min with TMRE (100 nM, 0.5 h). Cells were depolarised using FCCP (20  $\mu$ M). The cell suspension (25  $\mu$ l) was loaded onto TALI cytometer slides and measured using the red filter. The threshold was set at unstained HEK 293 cells and the average RFU was plotted. The delta measurement was calculated as the difference between untreated and FCCP treated samples.

### 2.8.4 Assessment of mitochondrial membrane polarisation by flow cytometry using TMRE

To measure mitochondrial depolarisation HEK cells were plated in 12 well plates and treated as described in the data. Cells were trypsinised and washed twice in PBS and incubated with TMRE (50 nM, 20 min). Cells were depolarised using FCCP (20  $\mu$ M). Cells were detached with trypsin and washed in HBSS three times by centrifugation. Cells were re-suspended in HBSS (500  $\mu$ l) and analysed using BD FACSCalibur™ on the FL2 channel (ex 488 em 585-642), at 440 V, 10 000 cells were counted per condition. Median cellular fluorescence was plotted.

### 2.8.5 Determination of non-quenching concentrations of TMRE by fluorescence imaging

HEK cells were plated on uncoated 16 mm glass coverslips at (40 000 cells per well). Cells were incubated with increasing amounts of TMRE (25-400 nM) in imaging buffer supplemented with Gibco MEM Amino Acids Solution and MEM Non-essential Amino Acids Solution for 20 min at 37°C. Cells were washed three times in imaging buffer. Coverslips were then imaged using a Leica DMI6000 fluorescence microscope on the 20x objective. TMRE was mobilised from the mitochondria using FCCP (10  $\mu$ M) after 180 s. Images were taken every 20 s for 12 min. Time lapse videos were analysed using ImageJ. Cytosolic areas of cells were selected plus a background region. A minimum of 20 cellular regions were analysed per coverslip.

### 2.8.6 Assessment of levels of mitophagy by flow cytometry

HEK cells were treated as indicated, in the presence or absence of Bafilomycin (50 nM, 18 h). Cells were trypsinised and washed twice in PBS and loaded with Mitotracker™ Deep Red FM (75  $\mu$ M) for 30 minutes at 37 °C in complete media. The signal from Mitotracker™ Deep Red was collected at 440 V using FL3 (ex 635 nm em 670 nm LP). Median fluorescence was plotted.

### 2.8.7 Isolation of mitochondria

Mitochondria were isolated using ThermoScientific Mitochondria Isolation Kit for Cultured Cells as per the manufacturer instructions. Cells were grown as previously described and washed in PBS. The cells were scraped and collected by centrifugation at 1000 rpm for 5 min. Cells were counted and re-suspended at  $20 \times 10^6$  in Reagent A (800  $\mu$ l) and incubated for 2 min on ice. Reagent B (10  $\mu$ l) was added and incubated for a further 5 min on ice vortexing every minute. Reagent C (800  $\mu$ l) was added and centrifuged at 700 g for 10 min at 4 °C. The supernatant was collected and centrifuged for a further 15 min at 12 000 g at 4 °C. The presence of mitochondria in the isolated fraction was determined by immunoblotting as described in section 2.5.15. Protein samples were treated as before and incubated with the mouse monoclonal Tim23 Antibody (H-8): sc-514463 at 1/200 dilution or mouse monoclonal  $\beta$ -actin (C-4): sc-47778 at 1/1000 dilution.

### 2.5 Statistical Analysis

Data was tested for normal distribution using the Shapiro-Wilk normality test. For data comparing conditions and time a Two-way ANOVA was done followed by Tukey's or Dunnett's post hoc test as indicated in the figure legend. For samples comparing one condition, a One-way ANOVA was performed followed by a Tukey's or Dunnett's post hoc. For all tests \* $p < 0.05$ , \*\* $p < 0.01$ , \*\*\* $p < 0.001$  \*\*\*\* $p < 0.0001$ . For shotgun proteomics analysis of cell lines, significance was tested using multiple t-tests with Benjamini-Hochberg correction.

### 3.1 Introduction

Caspases are a class of important cysteine proteases which are involved in the regulation of cell death, cytokine release and inflammation (Shi 2004) and can be broadly classified according to function. Mammalian caspases 3, 6, 7, 8 and 9 have been linked to apoptotic pathways whereas caspases 1, 4, 5 and 12 have been linked to inflammation (Jimenez Fernandez and Lamkanfi 2015). The functional roles of caspases 2, 10 and 14 are less well defined, and as such, they are more difficult to categorise (McIlwain et al. 2013). Caspases implicated in apoptosis are designated as either initiator caspases (caspases 8 and 9) or effector (sometimes-termed executioner) caspases (caspases 3, 6 and 7). In resting states, all caspases exist as inactive zymogens, and are activated by either dimerization or cleavage. Initiator caspases are responsible for the initial cleavage (and hence activation) of the effector caspases 3, 6 and 7, which once cleaved, can themselves effect cleavage of other effector caspases. In the inactive form, (prior to cleavage) the active site of effector caspases (such as caspase 7, shown in figure 3.1) is hidden. Upon cleavage, the enzyme undergoes conformational change in the active site which exposes the catalytic groove (Shi 2004). Initiator caspases (caspases 2, 8, 9, 10) also undergo cleavage, however, unlike effector caspases this does not lead to increased catalytic activity. Initiator caspases are activated by dimerization through interactions with adaptor proteins (Chang and Yang 2000).

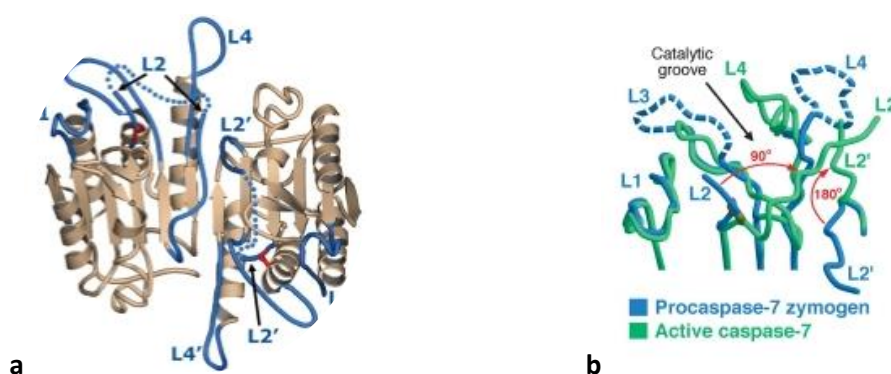


**Figure 3.1 Structure of pro-caspase 7 and caspase 7. a) Inactivated pro-caspase 7 b) close up of position of the surface loops at inactivated and activated caspase 7. Reproduced from (Shi 2004) under Creative Commons Attribution Licence (CC-BY).**

Two main apoptotic pathways are recognised in humans, termed intrinsic and extrinsic apoptosis respectively (Brentnall et al. 2013, Nair et al. 2014). These two pathways are presented schematically in figure 3.2.

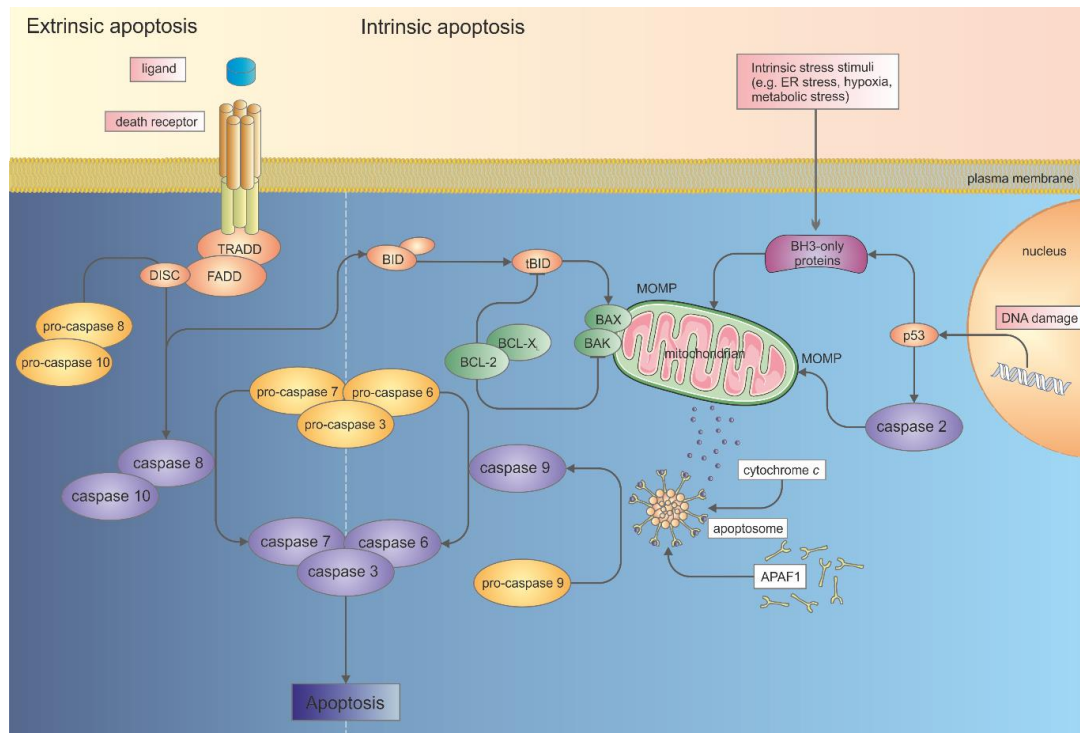


**Figure 3.2 Extrinsic and intrinsic apoptosis pathways.**

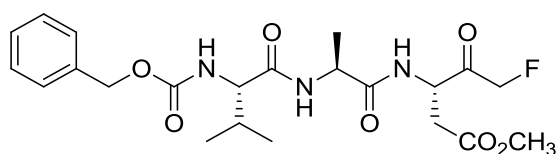
Intrinsic apoptosis can be independently mediated by stress factors (such as cytochrome *c*) released following permeabilisation of the mitochondrial membrane. Mitochondrial outer membrane permeabilisation (MOMP) can be triggered by exposure to intrinsic stress stimuli, which can include hypoxic insult and ER stress arising from the accumulation of misfolded proteins. Caspase-9, which exists in the cell in an inactive monomeric form, is activated by dimerization (Pop et al. 2006). This dimerization is mediated by the interaction of caspase-9 CARD pro-domain with the apoptotic protease-activating factor containing 1 (APAF1) apoptosome (Bao and Shi 2007, Su et al. 2017). The activation of caspase 9 in turn activates the effector caspases 3, 6 and 7 and results in the induction of apoptosis.

The extrinsic pathway involves the activation of caspase 8 via ligand-activated death receptors on the plasma membrane (TNF family receptors) and the death-inducing signalling complex (DISC). DISC has also been linked to the activation of caspase 10 (Bao and Shi 2007). The activation of caspase 8 may result in either the direct induction of apoptosis by the

activation of effector caspases, or through the activation of intrinsic apoptosis pathways. Intrinsic apoptosis pathways are activated through the interaction of activated caspase-8 with BID (a BCL-2 family member). Once cleaved, BID is translocated to the mitochondria and activates BAX and BAK. This results in MOMP, the concomitant activation of caspase 9, activation of the effector caspases and ultimately apoptosis.

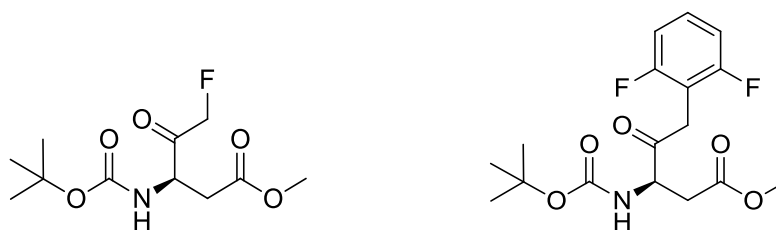
### 3.1.2 Pharmacological inhibition of caspases

Carbobenzoxy-valyl-alanyl-aspartyl-(*O*-methyl)-fluoromethylketone (Z-VAD-fmk<sup>1</sup>, **1**) is a poly-caspase inhibitor used extensively as a tool to study apoptosis in cell culture (Cowburn et al. 2005, Fransolet et al. 2015, Karl et al. 2014, Niu et al. 2016, Yang et al. 2004).



**1**

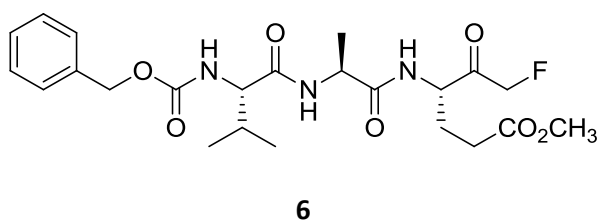
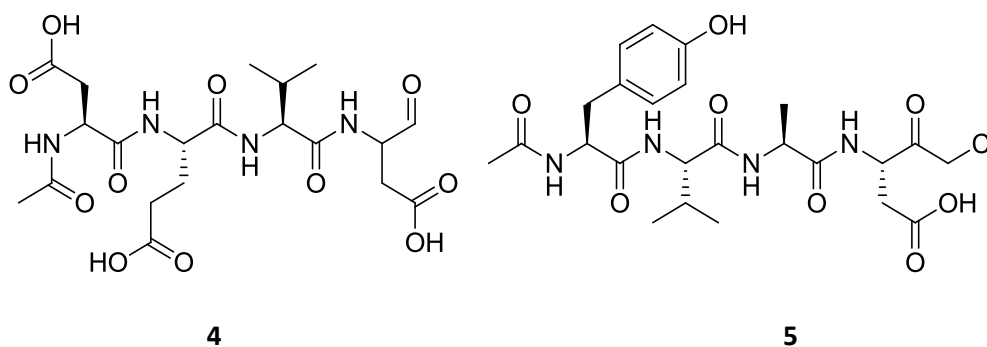
Synthetic caspase inhibitors such as Z-VAD-fmk **1** are competitive inhibitors which act as pseudo-substrates and react with the catalytic cysteine residue in the active site (Callus and Vaux 2006). They are predominantly based upon partially protected peptidic structures bearing non-native functionality and vary in length from single amino acids (such as Boc-D-fmk **2** and Boc-D-OPh **3**) to tetrapeptide structures. The protecting groups serve to improve properties such as stability (resistance to proteolytic cleavage) and cell permeability, whereas the non-native electrophilic functional groups interact with the nucleophilic cysteine residue in the enzyme active site.



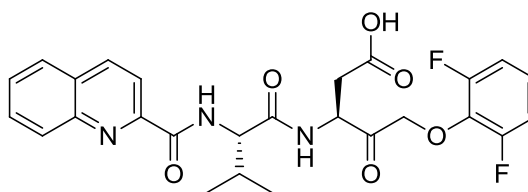
<sup>1</sup> It is noted that in the literature, Z-VAD-fmk is used interchangeably to describe both the cell permeable methyl ester form, carbobenzoxy-valyl-alanyl-aspartyl-(*O*-methyl)-fluoromethylketone (CAS: 187389-52-2) and the free acid carbobenzoxy-valyl-alanyl-aspartyl-fluoromethylketone (CAS: 634911-81-2). Throughout this thesis, Z-VAD-fmk is used to denote the methyl ester form **1** (CAS: 187389-52-2).

**2****3**

Aldehyde functionalised caspase inhibitors, such as Ac-DEVD-CHO **4**, tend to exhibit reversible inhibition profiles. In contrast, halomethylketones, such as Z-VAD-fmk **1** and Z-VAE-fmk **6** and the chloromethylketone Ac-YVAD-CMK **5** (along with similar diazomethylketone, acyloxymethylketone and phenoxyethylketone bearing structures), act as irreversible inhibitors by binding covalently to the active site cysteine residue.



Pharmacological inhibitors of caspases often show activity across multiple protein targets within this class. Table 3.1 shows the inhibition profiles of three structurally distinct peptidyl caspase inhibitors, (Z-VAD-fmk **1**, Ac-DEVD-CHO **4** and the difluorophenoxy methylketone inhibitor, quinolyl-valyl-O-methylaspartyl-[2,6-difluorophenoxy]-methyl ketone, Q-VD-OPh **7**) is commonly employed in cell-based studies.



**7**

**Table 3.1 Poly-caspase inhibition data for four commonly used pharmacological caspase inhibitors**

	Z-VAD-fmk 1	Z-VAE-fmk 6	Ac-DEVD-CHO 4	Q-VD-OPh 7
<b>Caspase 1</b>	<i>No data found</i>	<i>No data found</i>	<i>No data found</i>	IC <sub>50</sub> 25-400 nM ( <i>in vitro</i> ) (Caserta et al. 2003)
<b>Caspase 2</b>	IC <sub>50</sub> = 200 nM ( <i>in vitro</i> ) (Chauvier et al. 2006)	<i>No data found</i>	<i>No data found</i>	IC <sub>50</sub> = 80 nM ( <i>in vitro</i> ) (Chauvier et al. 2006)
<b>Caspase 3</b>	K <sub>i</sub> = 18.4 μM ( <i>in vitro</i> ) (Zhigang Wang et al. 2010)	K <sub>i</sub> = 1200 μM ( <i>in vitro</i> ) (Sadhukhan et al. 2006)	K <sub>i</sub> = 2 nM ( <i>in vitro</i> ) (Garcia-Calvo et al. 1998)	IC <sub>50</sub> 25-400 nM ( <i>in vitro</i> ) (Caserta et al. 2003)
<b>Caspase 7</b>	<i>No data found</i>	<i>No data found</i>	K <sub>i</sub> = 2 nM ( <i>in vitro</i> ) (Garcia-Calvo et al. 1998)	<i>No data found</i>
<b>Caspase 8</b>	K <sub>i</sub> = 0.45 μM ( <i>in vitro</i> ) (Zhigang Wang et al. 2010)	K <sub>i</sub> = 27.8 μM ( <i>in vitro</i> ) (Sadhukhan et al. 2006)	<i>No data found</i>	IC <sub>50</sub> 25-400 nM ( <i>in vitro</i> ) (Caserta et al. 2003)
<b>Caspase 9</b>	K <sub>i</sub> = 17.1 μM ( <i>in vitro</i> ) (Zhigang Wang et al. 2010)	K <sub>i</sub> = 14.16 μM ( <i>in vitro</i> ) (Sadhukhan et al. 2006)	<i>No data found</i>	IC <sub>50</sub> 25-400 nM ( <i>in vitro</i> ) (Caserta et al. 2003)

Both the leaving group and the peptide chain can influence the specificity and efficacy of the inhibitor. Studies comparing Boc-D-fmk **2** and Boc-D-OPh **3** found lower concentrations of Boc-D-OPh **3** were needed to inhibit caspases 2, 3, 7, 8, 9 and 10 compared to Boc-D-fmk **2** (Chauvier et al. 2006). Q-VD-OPh **7**, which bears a hydrophobic quinoline substituent (Chauvier et al. 2006), is a more potent inhibitor of caspase 2 than Boc-D-OPh **3** both *in vitro* and *in vivo* with Boc-D-fmk **2** showing nearly double the inhibitory effect of Q-VD-OPh **7** for caspases 2, 7, 8 at 25 μM *in vitro* (Chauvier et al. 2006). In cellular models treated with 100 μM caspase inhibitors, Q-VD-OPh **7** abolished caspase 3, 7 and 9 activity by greater than 90 %, whereas Boc-D-OPh reduced caspase 3 and 9 activity by around 80 % (Chauvier et al.



2006). Some selected examples of pharmacological inhibitors of caspases and their targets are shown in figure 3.3.

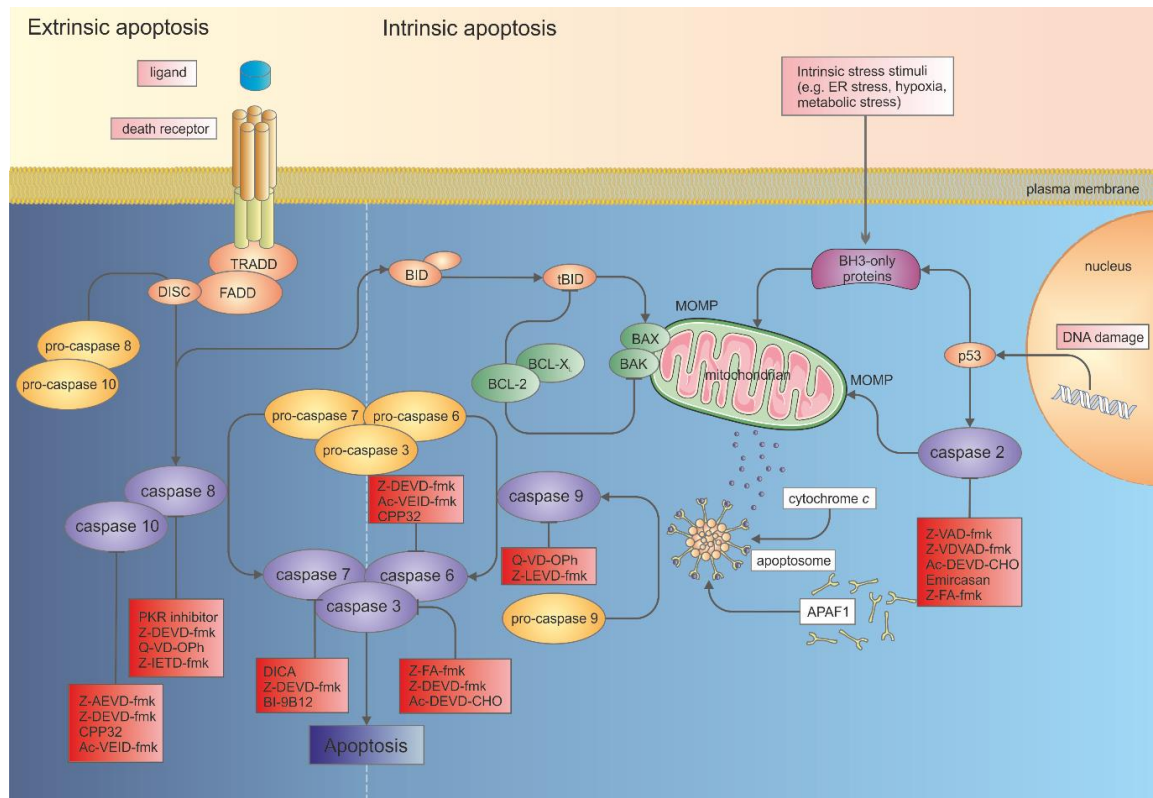


**Figure 3.3 Selected examples of points of action of pharmacological caspase inhibitors**

### 3.1.3 Other targets of pharmacological caspase inhibitors

Although pharmacological inhibition is a useful tool to probe cellular processes, many inhibitors exhibit a spectrum of effects that may or may not be related to the primary mechanism or target of inhibition. For example, in addition to the inhibition of caspase proteases, Z-VAD-fmk **1** has also been shown to inhibit a number of other non-caspase cysteine proteases, including cathepsin B, H and L (Schotte et al. 1999, Chauvier et al. 2006), and picornaviral 2A proteinases (Deszcz et al. 2004).

Q-VD-OPh **7** has also been shown to act as an inhibitor of cathepsin H, albeit to a lesser extent than Z-VAD-fmk **1** (at 1  $\mu$ M Z-VAD-fmk abolishes almost 75 % of cathepsin H activity whereas Q-VD-OPh **7** only decreases cathepsin H activity by 50 %) (Chauvier et al. 2006). Both the nature of the functionalisation and the peptide backbone have been linked to differing inhibitory profiles or effectiveness. Boc-D-fmk **3** (100  $\mu$ M) has been shown to be a less potent inhibitor of cathepsin B than Z-VAD-fmk **1**; the former resulting in < 10 % reduced activity,

whereas treatment with Z-VAD-fmk **1** (100  $\mu$ M) resulted in a > 80 % reduction in activity. Table **3.2** details examples of studies where treatment of cells with Z-VAD-fmk **1** has resulted in the observation of effects not expected with inhibition of caspases and apoptosis.

**Table 3.2 Effects of Z-VAD-fmk in different cell lines other than caspase inhibition and inhibition of apoptosis**

Cell line	Treatment	Observation
<b>Mouse macrophage J774A.1</b>	Z-VAD-fmk (100 $\mu$ M, 8 h)	Induction of autophagy and necrotic cell death. Increase of TNF $\alpha$ secretion. (Martinet et al. 2006a).
<b>L929 mouse fibrosarcoma</b>	Z-VAD-fmk (10 $\mu$ M, 24 h)	Necroptosis mediated by increased TNF $\alpha$ production (Wu et al. 2011).
<b>Photoreceptors of Male Sprague-Dawley rats</b>	Z-VAD-fmk (300 $\mu$ M) with Necrostatin-1 (400 $\mu$ M) 72 h	<i>In vivo</i> activation of autophagy and subsequent necrosis (Dong et al. 2013)
<b>3T9 MEF</b>	Z-VAD-fmk (50 $\mu$ M) with Etoposide (85 $\mu$ M) 12 h	Increase in number of cells with mitochondrial membrane depolarisation. Increase of ROS and cytochrome c release (Rodríguez-Enfedaque et al. 2012)
<b>Neutrophils (primary human)</b>	Z-VAD-fmk (>100 $\mu$ M, 0.5 h)	Increase of TNF $\alpha$ induced cell death (Cowburn et al. 2005).
<b>Neutrophils (primary human)</b>	Z-VAD-fmk (1-30 $\mu$ M, 0.5 h)	Inhibition of TNF $\alpha$ induced ROS production Blockage of TNF $\alpha$ induced apoptosis (Cowburn et al. 2005).
<b>B16-F10 melanoma</b>	Z-VAD-fmk (50 $\mu$ M, 72 h)	<i>In vitro</i> induction of necrosis (Werthmoller et al. 2015).
<b>C57/BL6 mice</b>	Z-VAD-fmk (2mg/kg, 72 h)	<i>In vivo</i> decrease of tumour growth and reduction of infiltration (Werthmoller et al. 2015).

<b>Porcine Renal tubular epithelial cells (LLC-PK<sub>1</sub>)</b>	Z-VAD-fmk (20 µM) with cisplatin (50 µM) 0-30 h	Blockage of autophagic flux Decrease of cell viability Inhibition of calpain and cathepsin activity (Herzog et al. 2012).
<b>MEF</b>	Z-VAD-fmk (20 µM) mouse recombinant TNF (30 ng/mL) and cyclohexamide (10 µg/mL) 24 h	Observation of necrosis <i>in vitro</i> Increase of ROS production (Lin et al. 2004)
<b>L929</b>	Z-VAD-fmk (10 µM) or ALLM (calpain inhibitor) (10 µM) with oridonin (50 µM) 24 h	<i>In vitro</i> treatment failed to rescue oridonin damage. (Cheng et al. 2008)
<b>L929</b>	Z-VAD-fmk (20 µM) 5-10 h	Autophagic cell death observed <i>in vitro</i> (Chen et al. 2011)

Several studies have shown that Z-VAD-fmk exerts toxic effects and, that treatment with the inhibitor results in necrosis *in vitro* (Werthmoller et al. 2015, Dong et al. 2013, Wu et al. 2011, Martinet et al. 2006b). These studies have also shown necrosis is often accompanied by autophagic features, indicating possible autophagy mediated cell death (Martinet et al. 2006a, Dong et al. 2013). Treatment of the macrophage cell lines, J774A.1 and RAW264.7 with Z-VAD-fmk resulted in increased autophagy markers followed by activation of caspase 8 and necrosis (Lin et al. 2004). Increased secretion of TNF $\alpha$  in macrophages following Z-VAD-fmk treatment has also been observed, which could result in increased cell death in these cell lines through an increase in ROS production (Kim et al. 2010). However, another study looking to clarify the effect of TNF $\alpha$  mediated necrosis following treatment with Z-VAD-fmk found no increase in cellular ROS (Cowburn et al. 2005). In this study, necrosis was only observed following treatment with high concentrations of Z-VAD-fmk (> 100 µM). Lower concentrations (1-30 µM) resulted in the inhibition of TNF $\alpha$  induced cell death (Cowburn et al. 2005).

The effects of Z-VAD-fmk treatment on L929 murine fibrosarcoma cells also include changes in the levels of markers linked to autophagy (Chen et al. 2011). Upon treatment with Z-VAD-fmk increased levels of the autophagy marker LC3 II and induction of necrosis was found

(Chen et al. 2011). Autophagic flux was determined to be intact and knockdown of BECLIN-1 and ATG5, important factors involved in the function of autophagy, rescued the cell death phenotype. These results suggest that autophagy activation was implicit in cell death (Chen et al. 2011).

Contradictory evidence has been presented in other studies. A 2008 study (Wu et al. 2008b) demonstrated that Z-VAD-fmk treatment resulted in the induction of necrosis, whereas treatment with the autophagy inducer rapamycin or serum starvation blocked cell death. Treatment with chloroquine, an autophagy inhibitor, increased the sensitivity of L929 cells to Z-VAD-fmk induced necrosis. Cell death was determined to result from the inhibition of lysosomal cathepsin B which blocked autophagic flux by inhibiting maturation of autolysosomes. Using a GFP-mRFP-LC3 tandem reporter construct as a tool, a block in lysosomal maturation was reported following treatment with Z-VAD-fmk (Herzog et al. 2012). This study also reported reduced cathepsin activity of RTEC cells treated with Z-VAD-fmk (10  $\mu$ M, 12 h), whereas (Chen et al. 2011) found no inhibition of cathepsin B or calpain following treatment of Z-VAD-fmk (20  $\mu$ M, 6-12 h) in L929 cells.

It may be hypothesised that, if Z-VAD-fmk toxicity is due to cathepsin inhibition, then similar results should be observed with cathepsin inhibitors. However, (Wu et al. 2008a) showed that treatment with cathepsin inhibitors either alone or, in combination with other caspase inhibitors, Z-IETD-CHO (an inhibitor of caspase 8) or Z-DEVD-CHO (an inhibitor of caspase 3) did not reduce cell viability. These results suggest that other factors other than caspase inhibition and cathepsin inhibition lead to necrosis in these cell types.

In combination, these studies indicate that a number of different effects are observed with Z-VAD-fmk, both when employed alone and in conjunction with other cell stressors. These effects appear to show some dependency upon treatment regimens and cell type. In this study, the effects of Z-VAD-fmk will be compared with pan-caspase inhibitor Q-VD-OPh to gain insight into the effects of Z-VAD-fmk in cells.

#### 3.1.4 Pharmacological inhibition of *N*-glycanase

In 2004, Z-VAD-fmk was identified as an inhibitor of yeast *N*-glycanase (Misaghi et al. 2004) following a high-throughput screen of over 100 000 compounds. This study employed a fluorescence based screening platform based upon the commonly used RNase B deglycosylation assay used to assess the activity of glycosidases capable of cleaving mammalian *N*-glycans. In the standard assay, bovine pancreatic RNaseB (a globular

glycoprotein of ~15 kDa containing a single *N*-linked glycosylation site at Asn<sup>34</sup>) (Prien et al. 2009) is incubated with *N*-glycanase, which results in the cleavage of the carbohydrate moiety. The extent of deglycosylation can be quantified by SDS-Page, the molecular mass of the deglycosylated protein being less than its glycosylated counterpart.

Figure 3.4 shows the modified assay, which utilises FITC-labelled RNase B as a substrate for yeast *N*-glycanase. Under conditions of inhibition of *N*-glycanase, RNase B remains glycosylated. Glycosylated structures are detected by the binding of Concanavalin A (ConA), a lectin originally extracted from the jack-bean, *Canavalia ensiformis* which exhibits binding towards glucosyl and mannosyl residues. Binding of ConA to fluorescein labelled RNase B increases fluorescence polarisation, allowing detection of inhibited yeast *N*-glycanase.

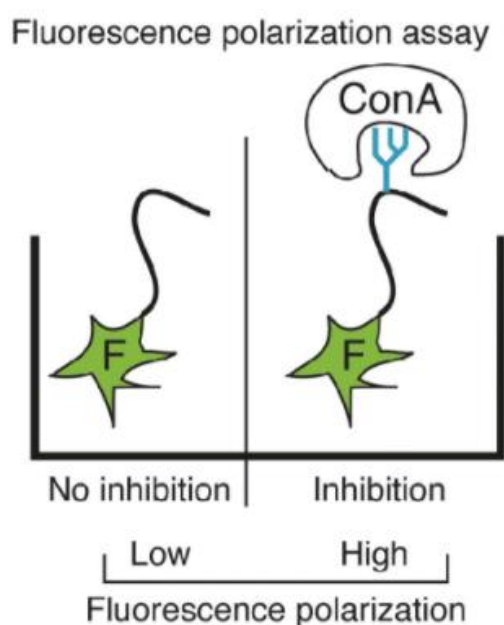


**Figure 3.4 Schematic diagram of the fluorescence polarisation assay of *N*-glycanase function. Reprinted from (Misaghi et al. 2004), p1677, with permission from Elsevier.**

After initial identification of Z-VAD-fmk as an inhibitor of yeast *N*-glycanase, further studies were set out to confirm this. MALDI-MS analysis of yeast *N*-glycanase (yPng1) treated with Z-VAD-fmk (and subsequently dialysed to remove excess Z-VAD-fmk) resulted in the detection of an intact mass of 43 613 Da. This indicates 1:1 binding stoichiometry when compared with the native protein mass of (43 208 Da), and demonstrates irreversible binding as the inhibitor was not removed after dialysis. Yeast *N*-glycanase treated with Z-VAD-fmk proved unable deglycosylate RNase B (Misaghi et al. 2004). Further studies using yPng1 bearing a C191A mutation of the active site cysteine demonstrated that no mass increase by

MALDI-MS was observed and therefore the active site cysteine, C191 residue is critical to inhibitor binding.

As with cysteine proteases (such as caspases), Z-VAD-fmk interacts with the cysteine residue to form a stable thioether bond. The binding mechanism proposed by Misaghi *et al.* (2004) is shown in figure 3.5. Upon binding of the aspartyl side chain, the enzyme undergoes conformational changes resulting in the aspartic acid, histidine and cysteine residues of the active site catalytic triad being drawn closer together, and the deprotonation of the cysteine thiol. Rotation of the inhibitor at the aspartyl chain brings the electrophilic carbon atom in close proximity to activate the cysteine. Nucleophilic attack of the cysteine results in the formation of a carbon-cysteine thioether bond.

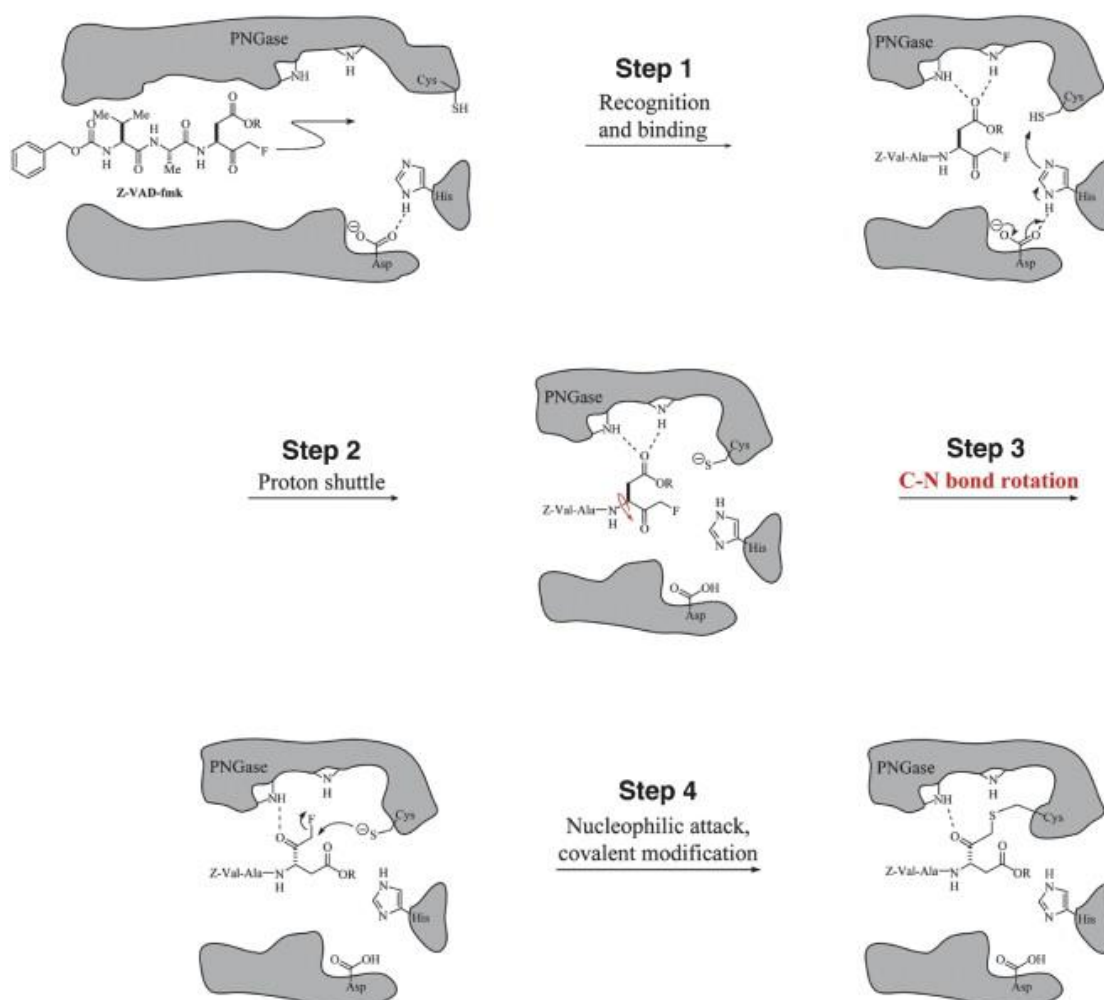
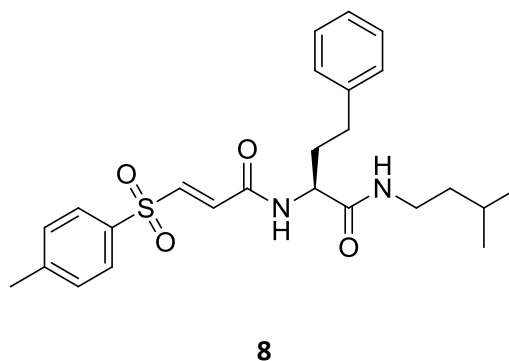
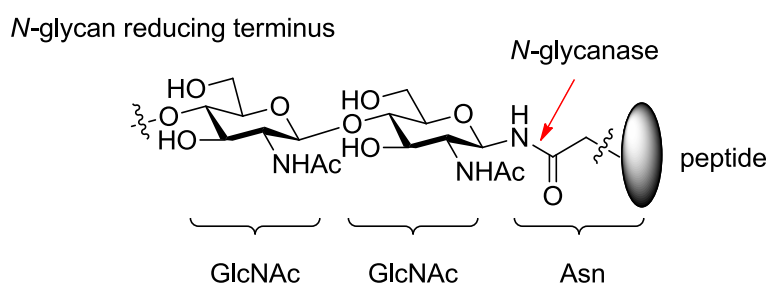
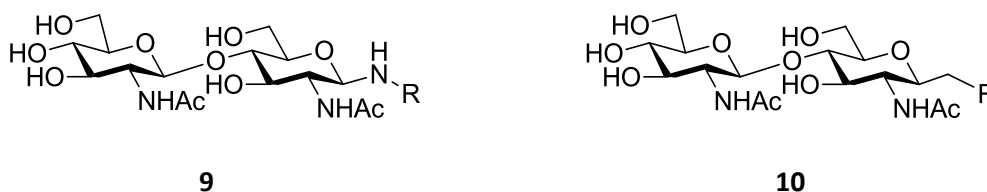


Figure 3.5 Proposed mechanism of Z-VAD-fmk binding to yeast PNGase. Reprinted from (Misaghi *et al.* 2004), p1677, Copyright (2004), with permission from Elsevier.

Few inhibitors of *N*-glycanase have been identified and characterised. Known inhibitors can be divided into two distinct structural classes. Peptidyl inhibitors include Z-VAD-fmk, **1** and the peptide vinyl sulfone WRR139 **8** ( $IC_{50} = 5.5 \mu M$ ) (Tomlin et al. 2017). WRR139 was initially identified from a screen of peptide-based thiol reactive electrophiles using a deglycosylation-dependent VENUS (ddVENUS) fluorescence assay as a reporter (Grotzke et al. 2013, Tomlin et al. 2017). Other peptide vinyl sulfones examined in this study demonstrated no inhibitory activity towards *N*-glycanase.



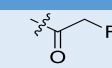
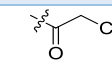
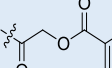
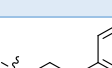
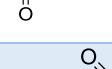
The other distinct structural class of inhibitors are those based on the *N,N'* diacetylchitobiose core (Witte et al. 2009). *N,N'* diacetylchitobiose based inhibitors (such as those based on structures **9** and **10**) mimic the natural *N*-glycan substrates of *N*-glycanase, the point of enzymatic cleavage is shown in figure **3.6**.



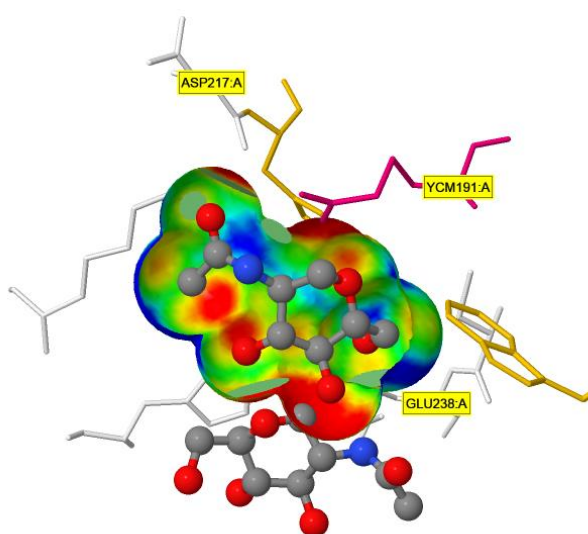
**Figure 3.6** *N*-glycanase cleavage of protein bound *N*-glycans

Table 3.3 shows examples of synthetically produced *N*-glycanase inhibitors based on the *N,N'* diacetylchitobiose core (containing *N,N'* diacetylchitobiose and leaving group) and the corresponding IC<sub>50</sub> values for the *in vitro* inhibition of yeast *N*-glycanase.

**Table 3.3 IC<sub>50</sub> for inhibitors of yeast *N*-glycanase based on chitobiose structures 8 and 9 (determined *in vitro* using an RNase B deglycosylation assay) adapted from (Witte et al. 2009)**

R	Inhibitor 8	Inhibitor 9
	IC <sub>50</sub> (μM) = 563 ± 50	IC <sub>50</sub> (μM) = > 1000
	IC <sub>50</sub> (μM) = 1.6 ± 0.5	IC <sub>50</sub> (μM) = 0.74 ± 0.1
	IC <sub>50</sub> (μM) = > 1000	IC <sub>50</sub> (μM) = > 1000
	IC <sub>50</sub> (μM) = > 1000	IC <sub>50</sub> (μM) = > 1000
	IC <sub>50</sub> (μM) = 1.2 ± 0.1	Not determined

Whereas *N,N'* diacetylchitobiose based inhibitors are thought to bind to the carbohydrate binding site of *N*-glycanase (Figure 3.7), Z-VAD-fmk associates with the peptide binding site (Witte et al. 2009).



**Figure 3.7 Crystal structure of yeast *N*-glycanase in complex with *N*-GlcNAc (generated from PDB ID: 3ESW (Zhao et al. 2009) using JsMol)**



Unlike *N,N'* diacetylchitobiose based inhibitors, Z-VAD-fmk is not structurally similar to the natural *N*-glycan substrates and is therefore not an immediately intuitive inhibitor of *N*-glycanase. However, the natural *N*-glycan substrates are bound to asparagine residues and once cleaved, leave an aspartic acid (as shown in Figure 3.8). The aspartyl side chain of Z-VAD-fmk and the presence of a peptide chain therefore may be sufficient for *N*-glycanase to recognise the inhibitor.

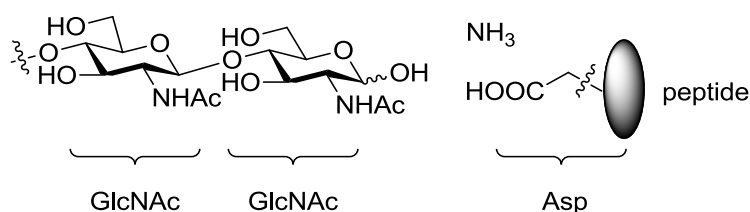


**Figure 3.8** Products of the *N*-glycanase cleavage of protein bound *N*-glycans

The selectivity of inhibitors such as Z-VAD-fmk **1** and WRR139 **2** for *N*-glycanase may be attributed to the structure of the peptidyl portion of the molecule. Similar peptidyl inhibitors of caspases such as Q-VD-OPh **6** do not demonstrate activity against *N*-glycanase (Tomlin et al. 2017). As previously shown in Table 3.1 Q-VD-OPh has a similar caspase inhibition profile as Z-VAD-fmk (Chauvier et al. 2006), yet does not inhibit *N*-glycanase. Previously reported  $IC_{50}$  of *N*-glycanase for yeast and human *N*-glycanase under different experimental conditions are shown in Table 3.4.

**Table 3.4**  $IC_{50}$  values of Z-VAD-fmk under different experimental conditions

Condition	$IC_{50}$
Yeast <i>N</i> -glycanase ( <i>in vitro</i> ) (Misaghi et al. 2004)	$IC_{50} = 50 \mu M$
Human <i>N</i> -glycanase in US2 expressing U373 astrocytoma cells (Misaghi et al. 2004)	$IC_{50} = 7 \mu M$
Human <i>N</i> -glycanase in K562 (human immortalised myelogenous leukaemia RRID:CVCL_0004) (Tomlin et al. 2017)	$IC_{50} = 4.4 \mu M$

An IC<sub>50</sub> of 50 µM was reported for yeast *N*-glycanase *in vitro* (Misaghi et al. 2004). The IC<sub>50</sub> value for human *N*-glycanase was determined in US2 expressing U373 astrocytoma cells using pulse chase in the presence of the proteasome inhibitor ZL3VS (100 µM). In the absence of Z-VAD-fmk, all Major Histocompatibility Complex (MHC) heavy chains (HCs) were deglycosylated within 0.5 h, whereas complete inhibition of deglycosylation was observed at 30 µM of Z-VAD-fmk. It is noted that in this study, inhibition of deglycosylation did not impede proteasome degradation of class I HCs (Misaghi et al. 2004). In a study carried out by (Tomlin et al. 2017), the IC<sub>50</sub> values of Z-VAD-fmk and WRR139 were established in K562 (human immortalised myelogenous leukaemia) cells. IC<sub>50</sub> values were determined for Z-VAD-fmk and WRR139 (4.4 µM and 5.5 µM respectively) using the ddVENUS assay with detection of the fluorescence signal by FACS (Tomlin et al. 2017). In this study, cells were treated with Z-VAD-fmk (24 h) followed by MG132 (6 h, 5 µM).

### 3.2 Aims and objectives

This aim of this chapter is to characterise the cellular effects of Z-VAD-fmk. As *N*-glycanase deficiency can be regarded as a disorder of ERAD, much of this chapter will examine effects linked to protein degradation; including the accumulation of misfolded proteins (which often arise from dysfunction in proteostasis) and potential stress responses (such as ER stress and oxidative stress responses). Furthermore, since Z-VAD-fmk has been linked to the induction of autophagy, the effect of Z-VAD-fmk on autophagic induction and autophagic flux will be investigated in an attempt to elucidate whether this is linked to caspase inhibition or to the inhibition of *N*-glycanase.

Throughout this chapter, Q-VD-OPh has been employed as a control for caspase inhibition due to the similarities in the caspase inhibition profile observed with these two pharmacological inhibitors.

### 3.3 Results

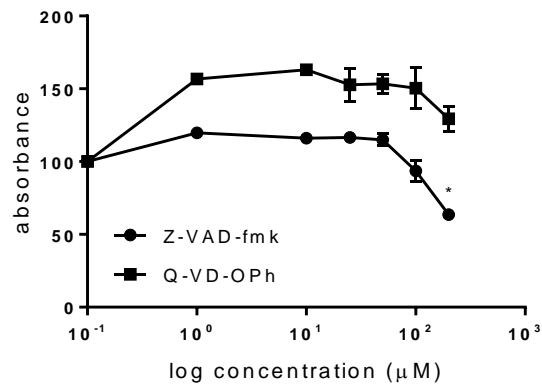
In this section, the effects of Z-VAD-fmk on HEK cells are characterised and the results summarised below. Firstly, the effects on cell viability were established using an MTT cytotoxicity assay. The effects of Z-VAD-fmk on HEK cells was further characterised by examination of the inhibition profile of *N*-glycanase using a deglycosylation dependent fluorescence assay. Due to the role of *N*-glycanase in glycan processing and quality control, the glycan profile following Z-VAD-fmk treatment has been examined using lectin dot blots to quantify specific glycan moieties.

It has also been proposed that a deficiency in *N*-glycanase can result in the accumulation of GlcNAc-positive protein aggregates. However, no conclusive evidence has been presented which indicates the presence of aggregates in cell culture models. In this study, cells were examined for evidence of protein aggregation using Thioflavin T. As protein aggregates also have a role in ER stress and the activation of the unfolded protein response (UPR), and Z-VAD-fmk has been shown to act as an inhibitor of *N*-glycanase. Genes upregulated during the UPR were examined under Z-VAD-fmk inhibition. ER calcium levels have also been noted in ER stress responses, as stress can lead to increased 'leakiness' in ER calcium channels. ER calcium was quantified using Fura-2 following the inhibition of SERCA channels by Thapsigargin. As protein aggregation has also been linked to increased oxidative stress, oxidative stress was measured by flow cytometry fluorescence intensity of ROS Brite 57. The activation of autophagy has been also linked to proteasome function, and increased autophagy has been observed in various cell lines following Z-VAD-fmk treatment. To study the effect of Z-VAD-fmk on autophagy, GFP-LC3 HEK293 cells were treated with Z-VAD-fmk. In order to determine if any changes in the level of autophagy could be attributed to caspase inhibition or the inhibition of other cellular targets, cells were also treated with Q-VD-OPh as a comparison. Finally, a bacterial *N*-glycanase (Z-VAD-fmk insensitive) was cloned into a mammalian expression vector, in an attempt to rescue any effects of Z-VAD-fmk which could perhaps be attributed to *N*-glycanase inhibition.

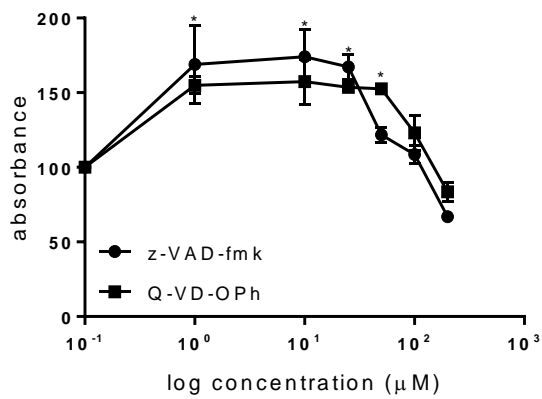
### 3.3.1 No effects on cell viability are observed when cells are treated with < 100 $\mu$ M Z-VAD-fmk

To confirm that Z-VAD-fmk treatment was not inducing any cytotoxic effects, HEK cells were treated with 1-200  $\mu$ M Z-VAD-fmk at 24, 48 and 72 h. Cell viability was assessed using the MTT (3-(4,5-dimethylthiazol-2-yl)-2,5-diphenyltetrazolium bromide) based assay, shown in Figure **3.9**. No cytotoxic effects were observed for Z-VAD-fmk at concentrations  $\leq$  100  $\mu$ M, although there was a decrease in viability above 200  $\mu$ M at 48 h (Figure **3.9b**) and 72 h (Figure **3.9c**) at 63.5 % and 73.5% respectively (compared to 129 % and 109 % with Q-VD-OPh at 200  $\mu$ M).

a



b



c

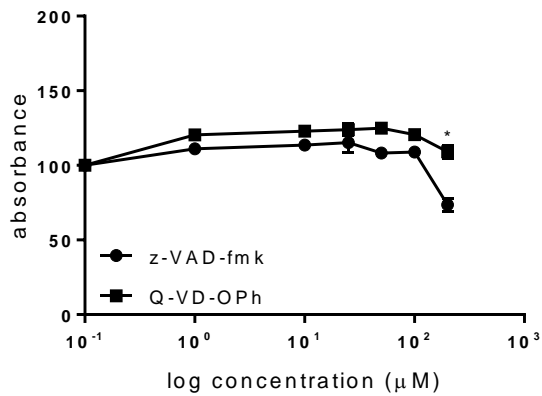
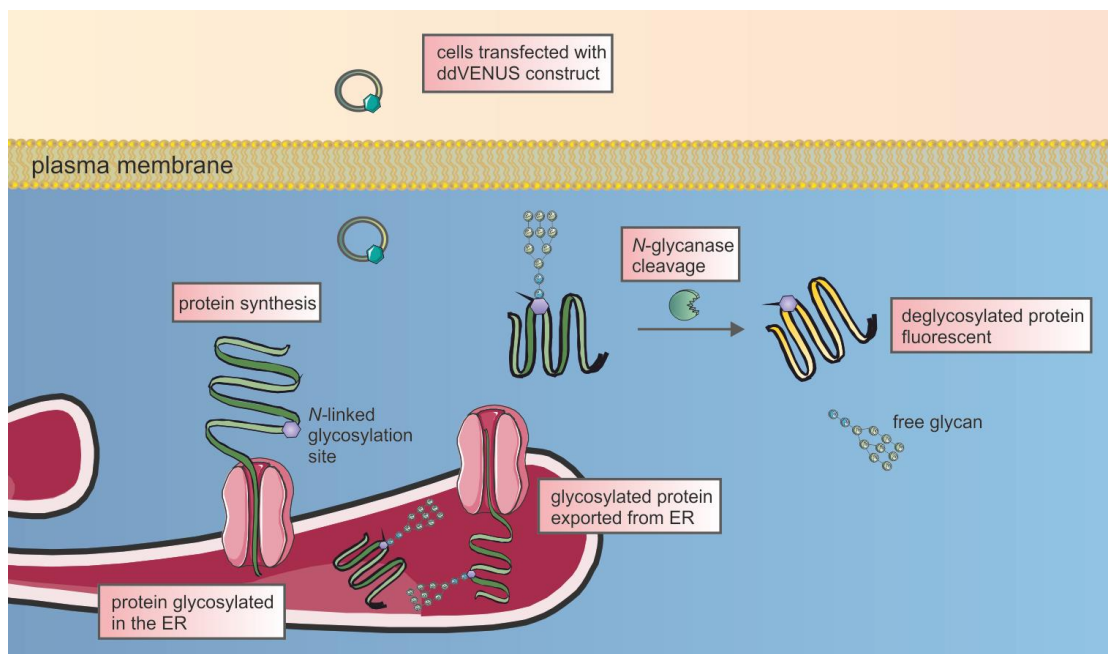


Figure 3.9 MTT assay of HEK 293 cells were treated with Z-VAD-fmk or Q-VD-OPh for a) 24 h b) 48 h c) 72 h. Data was normalised to the vehicle. One-way ANOVA, followed by a Dunnett's post hoc test against the vehicle.  $n=3$ ,  $P < 0.05$ , error bars  $\pm$  SEM.

### 3.3.2 Z-VAD-fmk treatment shows decreased fluorescence of the deglycosylation dependent VENUS

A deglycosylation dependent VENUS (ddVENUS) fluorescence assay was employed to quantify the effects of Z-VAD-fmk on *N*-glycanase function. This assay was originally developed by Grotzke *et al.* (2013) as a tool to probe ERAD function (Grotzke *et al.* 2013). Following publication, the assay was employed to detect deglycosylation activity of *N*-glycanase (Tomlin *et al.* 2017, He *et al.* 2015). In these studies, cells were transfected with the ddVENUS plasmid which encodes a modified VENUS protein bearing a single *N*-glycosylation consensus site and an ER targeting sequence which acts as a substrate for ERAD. The protein is co-translationally modified on translocation into the ER, and the glycosylated form exported into the cytosol. Following retro-translocation into the cytosol, the glycan is cleaved by *N*-glycanase which results in the release of a free glycan and the fluorescence form of the VENUS protein. When glycosylated, the protein exhibits little basal fluorescence. The VENUS fluorescence also requires co-treatment of a proteasome inhibitor to prevent degradation by the proteasome. The principle of the assay is shown schematically in Figure 3.10.



**Figure 3.10 Schematic representation of the ddVENUS assay. The ddVENUS construct is transfected into cells. Upon protein synthesis, the *N*-linked glycosylation site is glycosylated. The glycoprotein is translocated to the cytoplasm where it (upon deglycosylation) gives a fluorescent signal.**

The ddVENUS fluorescence assay describe above (Grotzke et al. 2013, He et al. 2015, Tomlin et al. 2017) has been used in the literature to confirm Z-VAD-fmk as an inhibitor of *N*-glycanase activity and, confirm activity in patient fibroblasts. In these studies, patient fibroblasts were transfected with the ddVENUS construct and treated with MG132 (6 h). Positively transfected cells were gated and the number of positive cells were calculated and compared to a Venus construct fluorescence. Patients with N-GLY1 with no detectable levels of *N*-glycanase protein (as determined by immunoblotting) exhibited between 40-80 % reduction in median fluorescence of ddVENUS (He et al. 2015).

In this study, HEK cells were transfected with the ddVENUS construct and after 24 h were treated with Z-VAD-fmk (1-300  $\mu$ M, 24 h) followed by MG132 (8  $\mu$ M, 5 h) to prevent degradation of the VENUS fluorescent signal. Cells were gated as shown in Figure **3.11a**. Cells were then sorted against the FL1 filter. Un-transfected cells were gated out of the analysis (Figure **3.11b**) and the median fluorescence of samples were calculated for Gate R2. The fluorescent intensity was plotted for the transfected cells. Figure **3.11c** shows the fluorescence of the vehicle control and Figure **3.11d** shows samples treated with Z-VAD-fmk (200  $\mu$ M, 24 h). The histogram presented in Figure **3.11e** shows the shift to the left upon treatment with Z-VAD-fmk (200  $\mu$ M, 24 h) (pink) compared to the vehicle control (green).

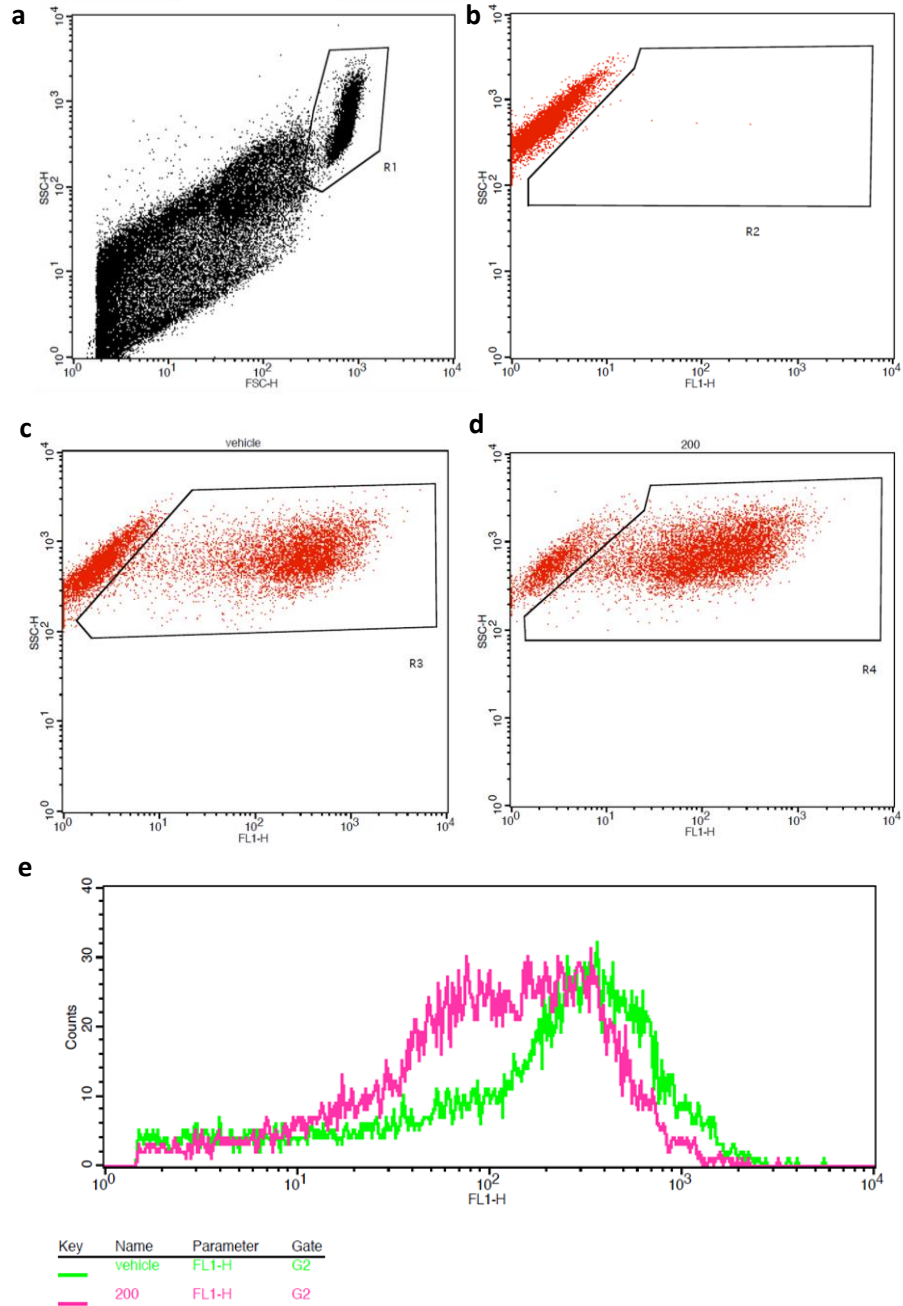


**Figure 3.11** Representative dot plots of the ddVENUS deglycosylation assay a) whole cell sample showing position of cell gating against forward and side scatter b) Un-transfected cells in gate R1 against side scatter and FL1 filter c) Vehicle control HEK cells transfected with the ddVENUS construct and treated with MG132 for 6 h d) treated with 200  $\mu$ M Z-VAD-fmk for 24 h and MG132 for 6 h. e) representative histogram of ddVENUS fluorescence of the vehicle control (green) and Z-VAD-fmk (200  $\mu$ M, pink).



To calculate the range of Z-VAD-fmk inhibition of deglycosylation, ddVENUS was transfected in HEK cells and treated with Z-VAD-fmk (1-300  $\mu\text{M}$ , 24 h). The median fluorescence was calculated and normalised to the vehicle control (Figure 3.12). The  $\text{IC}_{50}$  was calculated at 68.72  $\mu\text{M}$ .

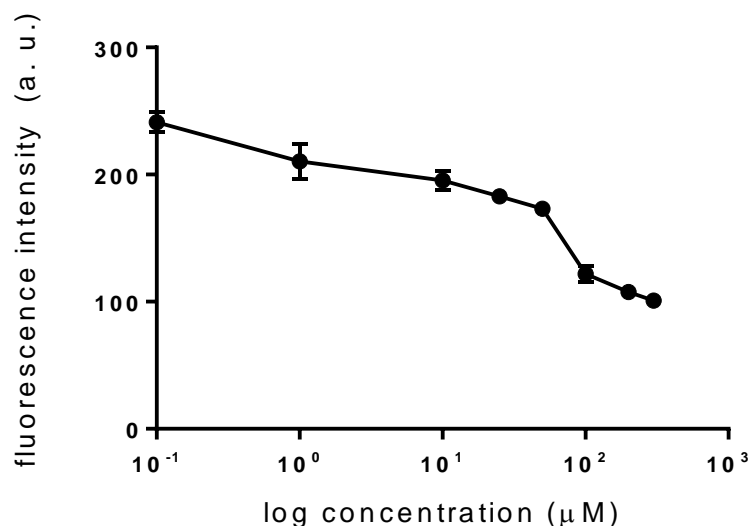


**Figure 3.12 ddVENUS assay for Z-VAD-fmk.** HEK cells were transfected with ddEVNUS construct and treated with 1-300  $\mu\text{M}$  Z-VAD-fmk for 24 h followed by 8  $\mu\text{M}$  MG132 for 6 h. The median ddVENUS fluorescence was calculated. Error bars  $\pm$  SEM,  $n=3$ , R square = 0.908,  $\text{IC}_{50}$  68.72.

To confirm that Q-VD-OPh did not affect the deglycosylation of ddVENUS, transfected HEK cells were treated with either Q-VD-OPh or Z-VAD-fmk (50  $\mu\text{M}$ , 24 h). The median fluorescence intensity was calculated and normalised to the vehicle control. Treatment with Z-VAD-fmk exhibited a decrease in 72 % of the fluorescence of the control whereas Q-VD-OPh showed a non-significant 12 % average increase (Figure 3.13).

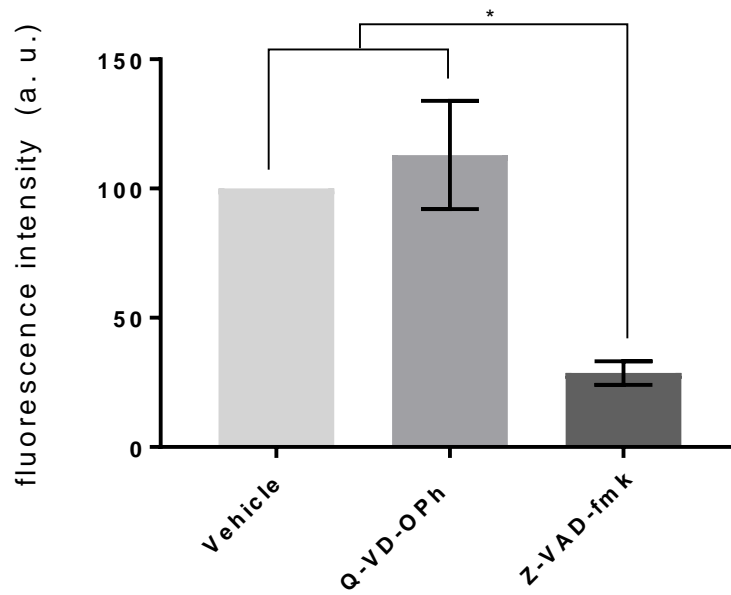


**Figure 3.13 Comparison of Q-VD-OPh and Z-VAD-fmk deglycosylation dependent assay.** HEK cells were transfected with the ddVENUS construct and treated with 50  $\mu$ M Z-VAD-fmk or Q-VD-OPh for 24 h, and 8  $\mu$ M MG132 for 6 h. The median ddVENUS fluorescence was calculated and normalised to the vehicle. One-way ANOVA followed by Tukey's post hoc. Error bars  $\pm$  SEM,  $n=3$ ,  $P < 0.05$ . Q-VD-OPh = 112 %, Z-VAD-fmk = 28 %.

### 3.3.3 Glycan profile of cells is not affected following treatment with Z-VAD-fmk

Due to the role of *N*-glycanase in glycan processing, the potential for changes in cellular glycan profile were examined. This was investigated using fluorescein labelled lectin dot blots. Lectins are proteins which exhibit specific binding to different carbohydrates. To investigate the global glycan profile of treated cells the following lectins were used: *lens culinaris* agglutinin (LCA), *concanavalin A* (ConA), *phaseolus vulgaris erythroagglutinin* (PHA-E), succinylated wheat germ agglutinin (sWGA) and wheat germ agglutinin (WGA). ConA and LCA have a broad specificity to high mannose glycans, whereas LCA specifically recognises  $\alpha$ -linked mannose. ConA also recognises  $\alpha$ -linked mannose residues and was used as a control for LCA staining. PHA-E recognises complex glycan structures and galactose. WGA and sWGA both have a specificity for terminal *N*-GlcNAc residues. WGA has also been shown to bind terminal sialic acid residues, whereas sWGA binds solely to terminal *N*-GlcNAc without interacting with sialic acids. In order to first establish the linear range of the assay, whole cells were lysed using 1 % triton in PBS and cleared by centrifugation. The resultant protein solution was spotted onto nitrocellulose membrane at 0.25, 0.5, 1 and 2  $\mu$ g (total protein concentration, as established by Bradford assay). Membranes were incubated with 2  $\mu$ g/mL of each FITC-labelled lectin at 4 °C overnight. The fluorescence intensity of the bound lectin was quantified using Syngene GeneTools software. The blots were then stained with amido black to establish the total protein levels and the extent of staining quantified using Syngene GeneTools. Figure **3.14** shows the fluorescence signal intensity against protein concentration for each lectin.

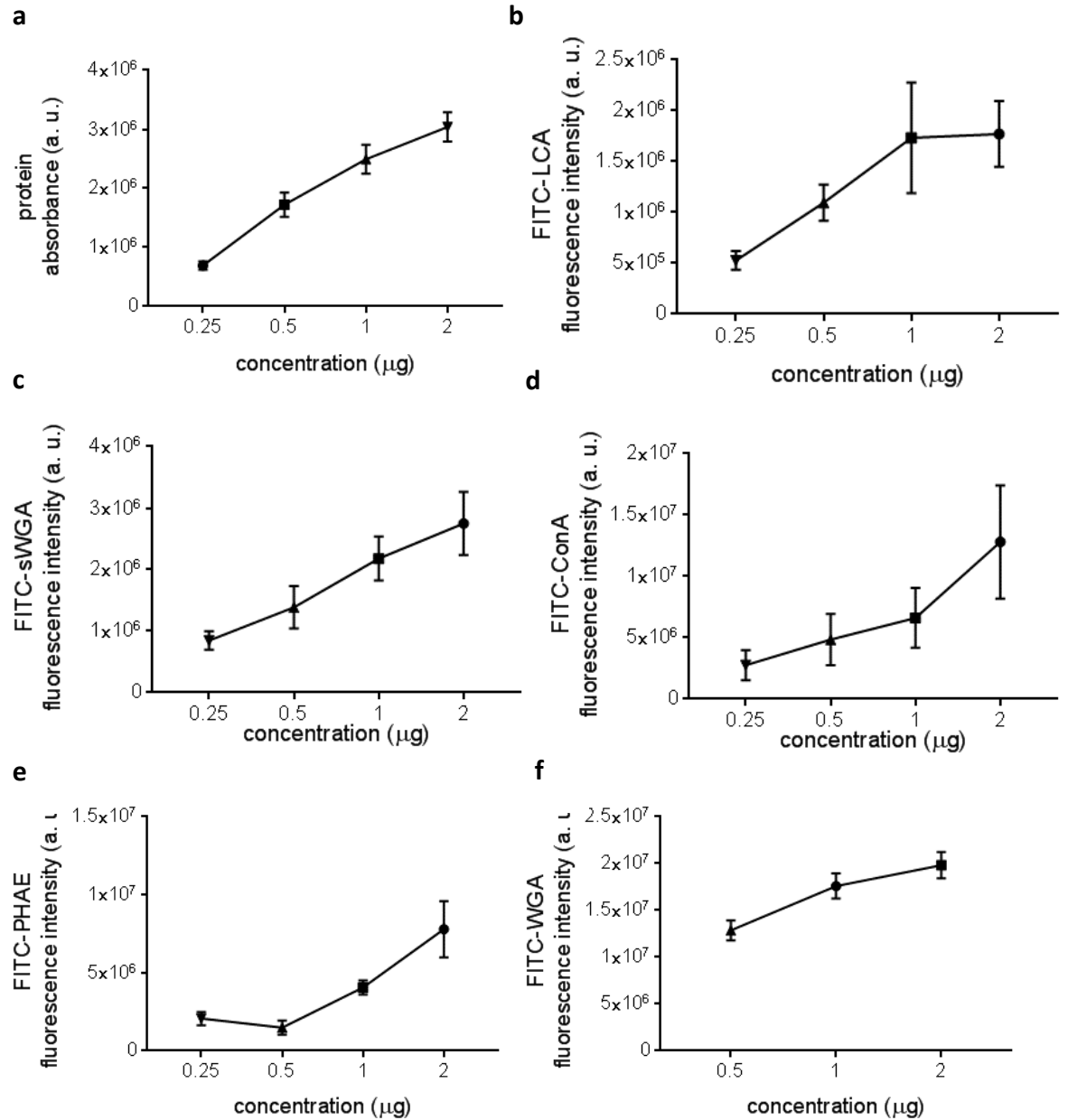


**Figure 3.14** Linear range of lectin fluorescence. Lectin fluorescence intensity presented against protein concentration and protein concentration measured by amido black staining. a) Protein stained by amido black and measured by absorbance. b) FITC-LCA labelling, c) FITC-sWGA labelling, d) FITC-ConA labelling e) FITC-PHA-E labelling, f) FITC-WGA labelling. Error bars  $\pm$  SEM, n=3.

All lectin fluorescence intensities were calculated as within the linear range of the assay at 1  $\mu\text{g}$  total protein concentration, with the exception of LCA (which was calculated at 0.5  $\mu\text{g}$ ). Following the establishment of suitable protein concentrations within the linear range of the assay, cells treated with Z-VAD-fmk and Q-VD-OPh (50  $\mu\text{M}$ , 24 - 72 h) were examined, and the results presented in Figure **3.15 (a-e)**. No significant difference was observed in the lectin binding profiles for ConA, PHA-E, LCA, sWGA and WGA upon treatment with either inhibitor. These results are in accordance with previous studies which have examined the binding of sWGA and ConA to proteins from *N*-glycanase KO MEF cells (Huang et al. 2015, Fujihira et al. 2017), which also demonstrated no observable difference with these two lectins (Huang et al. 2015).

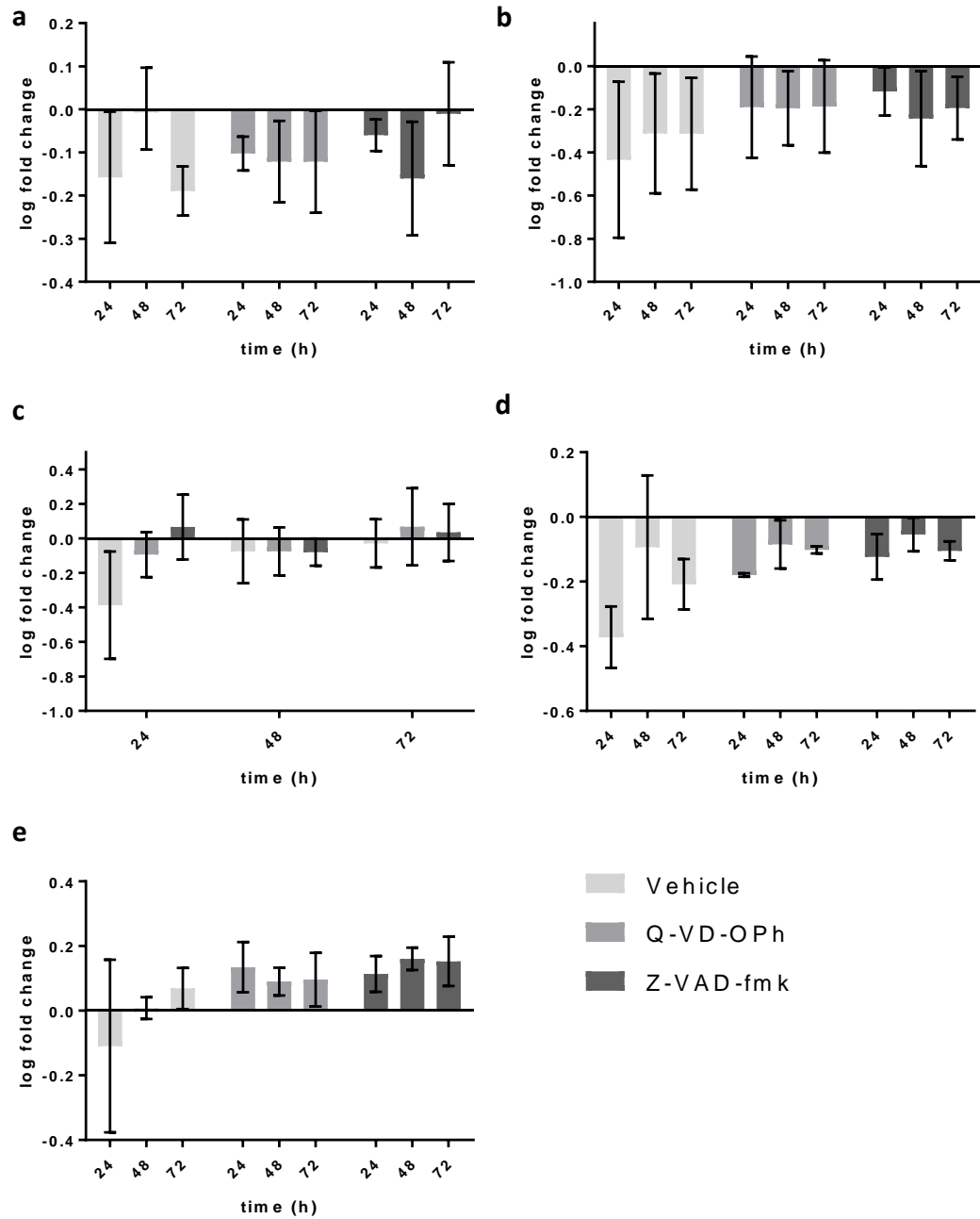
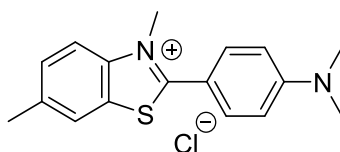


**Figure 3.15** FITC-lectin staining of whole cell lysate treated with Z-VAD-fmk or Q-VD-OPh (50  $\mu$ M, 24-72 h). Log<sub>2</sub> fold change of a) FITC-ConA b) FITC-LCA c) FITC-PHAE d) FITC-WGA e) FITC-sWGA fluorescence normalised to untreated control. Total protein concentration (1  $\mu$ g except LCA which is 0.5  $\mu$ g). Error bars  $\pm$  SEM,  $n=3$ , Two way ANOVA.

### 3.3.4 Thioflavin T fluorescence is transiently increases after Z-VAD-fmk treatment

Thioflavin T (ThT, **11**) is a fluorescent benzothiazole which has been shown to exhibit preferential binding to  $\beta$ -sheet motifs. It is commonly employed as a tool in the study of neurodegenerative diseases (such as Alzheimer's disease) where it has been used to visualise protein aggregates including amyloid plaques (Beriault and Werstuck 2013, Biancalana and Koide 2010, Lindberg et al. 2015, Veloso and Kerman 2013).



**11**

It has been proposed that misfolded proteins have a higher level of exposed  $\beta$ -sheets than correctly folded proteins and, that this may increase the aggregation through hydrophobic interactions.  $\beta$ -sheets are highly hydrophobic and readily bind to other exposed  $\beta$ -sheets (Nault et al. 2013). The intensity of ThT fluorescence can provide a relative measure of their abundance.

Analysis of ThT fluorescence can be problematic. It is well documented that protein aggregates have been associated with ER stress (Ogen-Shtern et al. 2016, Genereux and Wiseman 2015, Hyrskyluoto et al. 2014, Lawless and Greene 2012). Studies have found a positive correlation between ThT fluorescence intensity and ER stress markers (Teixeira et al. 2006) such as GRP78 and GADD153 following treatment with the known ER stress inducer Thapsigargin (Beriault and Werstuck 2013). The authors of this study concluded ThT can be used as a real-time measure of ER stress. Under Thapsigargin induced stress, ThT fluorescence was also found to be localised to ER targeting anti-KDEL sequences (Ming Yuan Li et al. 2015) indicating fluorescence localisation to misfolded proteins in the ER (Beriault and Werstuck 2013).

In cellular models, it has been suggested that deficiency in *N*-glycanase results in other glycan processing enzymes acting upon the *N*-linked glycans still present upon misfolded proteins during ERAD. Suzuki et al. (2015) identified cytosolic endo- $\beta$ -*N*-acetylglucosaminidase (ENGase) (EC:3.2.1.96) as a glycosyl hydrolase acting in the absence of *N*-glycanase activity. This study used an ERAD glycoprotein substrate, ricin A nontoxic mutant (RTA $\Delta$ m), which

contains an ER targeting and retention KDEL sequence. Following expression of RTA $\Delta$ m in WT, ENGase KO, NGLY1 KO, or double knockout MEF cells the ratio of deglycosylated/glycosylated RTA $\Delta$ m found 10 % of the protein was deglycosylated in the double knockout. Whereas *N*-glycanase deficient cells had increased, around 35 % deglycosylated form. ENGase deficient cells had 29 % deglycosylated RTA $\Delta$ m. Indicating other enzymes are able to deglycosylate proteins. Furthermore, cells expressing ENGase found increased RIPA insoluble fractions compared to the double knockout in which the deglycosylated form of rta $\Delta$ m was stabilised supporting the role of protein aggregates in *N*-glycanase deficient cells (Huang et al. 2015).

In this study, ThT fluorescence was used to quantify endogenous levels of protein aggregates under *N*-glycanase inhibition and was quantified using a combination of fluorescence imaging and flow cytometry. HEK cells were treated with Z-VAD-fmk or Q-VD-OPh (50  $\mu$ M, 24-72 h) and stained with ThT (1  $\mu$ M, 0.5 h). ThT fluorescence increased after 48 hours of 50  $\mu$ M Z-VAD-fmk treatment, and then decreased back to near control levels after 72 h (Figure **3.16a**). Figure **3.16b** shows representative images of ThT that did not present distinct aggregated structures and showed fluorescence profiles localised to the perinuclear space. This suggests that no large aggregates are formed following pharmacological inhibition of *N*-glycanase, but these patterns could be a result of a build-up of misfolded proteins or a slowing in ER translocation upon *N*-glycanase inhibition; ThT has been shown to co-localise with KDEL sequences in the ER (Beriault and Werstuck 2013). This is in accordance with other studies which have examined *N*-glycanase deficiency which have not reported evidence of distinct protein aggregates in cell culture models (Fujihira et al. 2017, Huang et al. 2015) or in histological slices acquired from *N*-glycanase KO mice visualised with Congo red or periodic acid stain (PAS) (Fujihira et al. 2017).



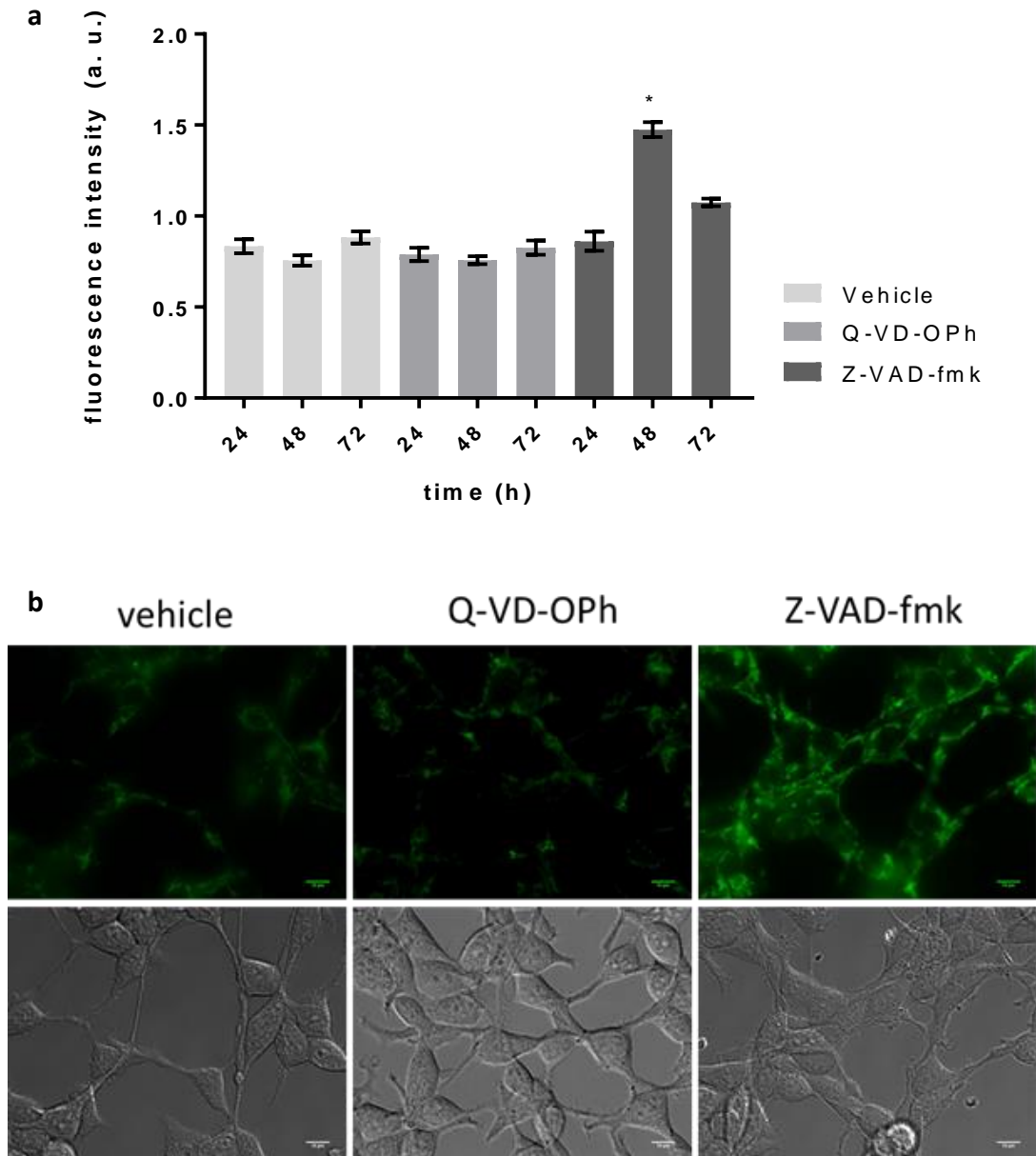


**Figure 3.16** Z-VAD-fmk caused a transient increase in ThT fluorescence. HEK cells treated with Z-VAD-fmk (50  $\mu$ M, 24-72 h) showed transient increase in fluorescence (48 h) with no change in vehicle or Q-VD-OPh (50  $\mu$ M, 24-72 h). Cells were stained with ThT (1  $\mu$ M, 0.5 h), washed twice with imaging buffer. **a**) Fluorescence intensity per cell was calculated and normalised to an untreated control. A minimum of three images were taken per coverslip and three biological replicates were analysed for each condition. Error bars  $\pm$  SEM,  $n=3$ ,  $P < 0.05$ . Two way ANOVA, Tukey's post hoc **b**) Representative images of HEK cells stained with ThT (1  $\mu$ M). Scale bar indicates 8  $\mu$ m.

ThT fluorescence intensity was also quantified using flow cytometry (Figure 3.17). HEK cells were treated with either Z-VAD-fmk or Q-VD-OPh along with the proteasome inhibitor MG132, a known inducer of protein aggregates (Kim et al. 2011, Cheng et al. 2013, Velentzas et al. 2013). A significant increase in ThT fluorescence in cells treated with MG132 compared with all other treatments except Z-VAD-fmk at 48 h was observed. The cells treated with Z-VAD-fmk at 48 h exhibited significantly higher levels of fluorescence than those treated with Z-VAD-fmk at 72 h and Q-VD-OPh at 48 h and 72. Figure 3.17b shows a representative histogram of the data collected by flow cytometry.

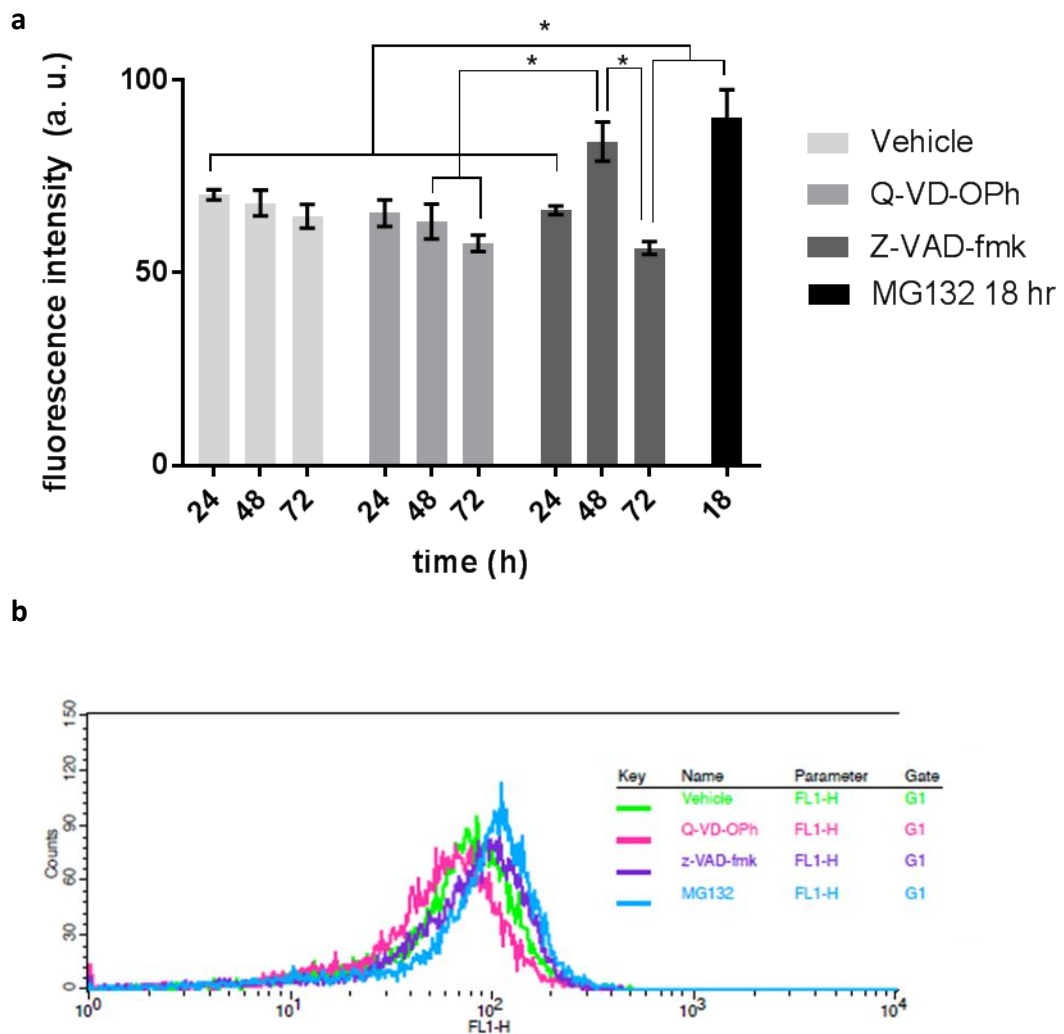


**Figure 3.17** Z-VAD-fmk caused a transient increase in ThT fluorescence as measured by flow cytometry. **a)** Flow Cytometric analysis of HEK cells visualised with ThT after treatment with Z-VAD-fmk or Q-VD-OPh (50  $\mu$ M, 24-72 h) or MG132 (100 nM). 10 000 cells were calculated per condition (three biological replicates). Two-way ANOVA, Tukey's post hoc. Error bars  $\pm$  SEM,  $P < 0.05$ ,  $n=3$ . **b)** Representative histogram of ThT fluorescence measured by flow cytometry (48 h).

### 3.3.4 Treatment with Z-VAD-fmk induces autophagy

HEK cells stably transfected with a GFP-LC3 construct were employed to examine autophagy. LC3 is expressed on the outer and inner membranes of autophagosomes and, when linked to GFP, allows autophagosomes to be visualised as distinct bright puncta. To confirm if cells expressing this construct can be used to examine the effects of pharmacological *N*-glycanase inhibition, cells were first treated with agents with known and predictable actions on autophagy. Modulators of autophagic activity include Bafilomycin A1 and 3-MA (Mauvezin and Neufeld 2015). Bafilomycin A1, an inhibitor of the lysosomal vacuolar-type H<sup>+</sup>-ATPase (V+ATPase), inhibits the acidification of autolysosomes and prevents autophagosome degradation. This ultimately results in an observable accumulation of autophagosomes in the cell shown in Figure 3.19. 3-MA is an inhibitor of class I and III PI3K, one of the major signalling pathways controlling mTOR activity. 3-MA inhibits autophagy by suppressing the production of PI3P which is involved in the recruitment of autophagy related proteins for phagophore membrane (R. Chen et al. 2014). Treatment with 3-MA is expected to result in a reduction in the number of autophagosomes present. The effects of these modulators are presented schematically in (Figure 3.18).

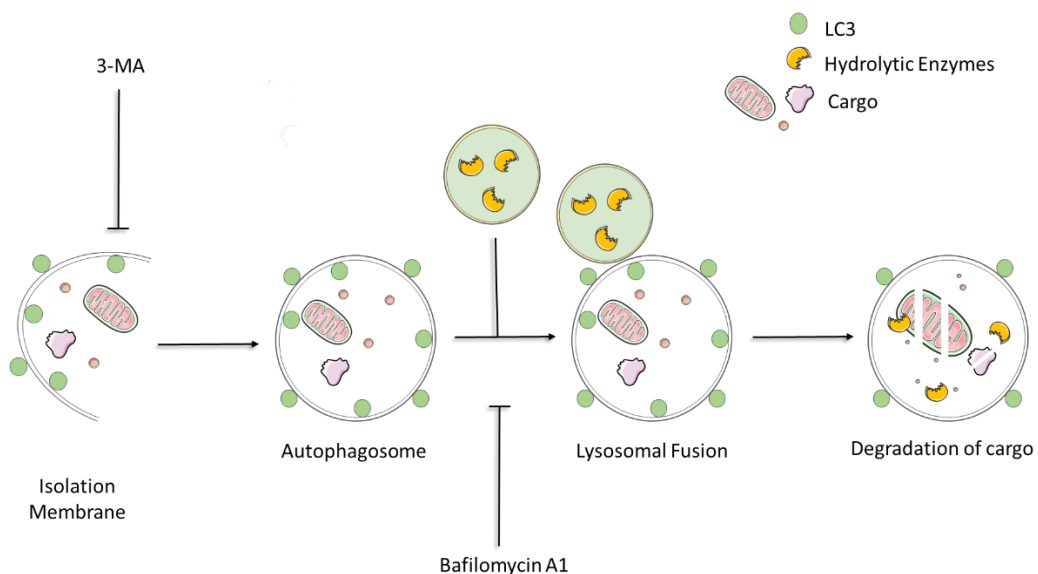


**Figure 3.18 Schematic representation of autophagy indicating points of inhibition of 3-MA and bafilomycin A1. Bafilomycin A1 is an inhibitor of the lysosomal V+ATPase which inhibits fusion of autophagosomes to lysosomes and inhibits autophagosome degradation. 3-MA inhibits PI3P production and recruitment of autophagy related proteins to the phagophore membrane, consequently inhibiting the formation of autophagosomes.**

In order to induce autophagy, cells were either treated with rapamycin, an inhibitor of mTOR that induces autophagy (Harder et al. 2014, L. Q. Wang et al. 2015) or exposed to amino acid starvation conditions (R. Chen et al. 2014), and co-treated with Bafilomycin A1. Autophagosomes were visualised as green punctate structures, representative images shown in Figure 3.19.

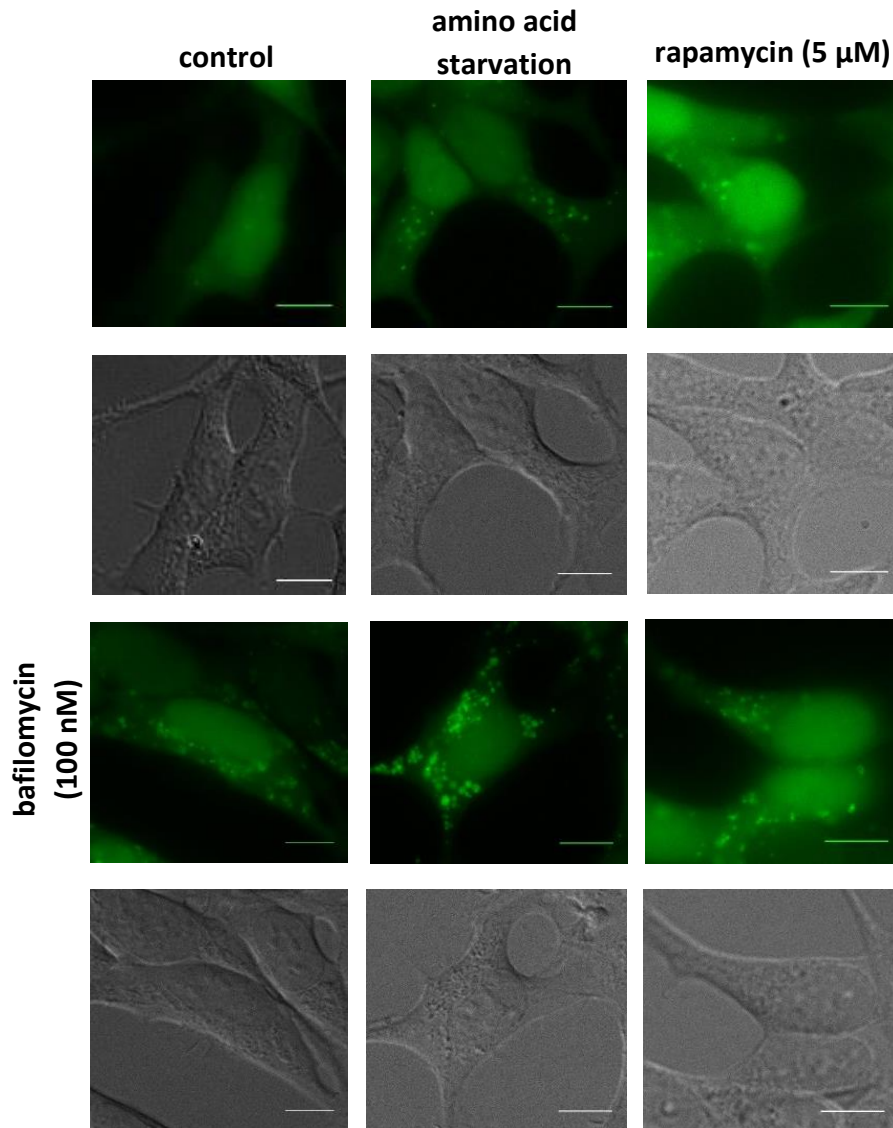


**Figure 3.19** Representative images of GFP-LC3 HEK cells exposed to different inducers of autophagy (rapamycin treatment and amino acid starvation) and co-treated with Bafilomycin A1. Scale bar indicates 10 μm.

GFP-LC3 HEK cells treated with rapamycin and exposed to amino acid starvation conditions show increased numbers of puncta compared to untreated cells. Figure 3.20 shows the quantification of the average number of puncta per cell.

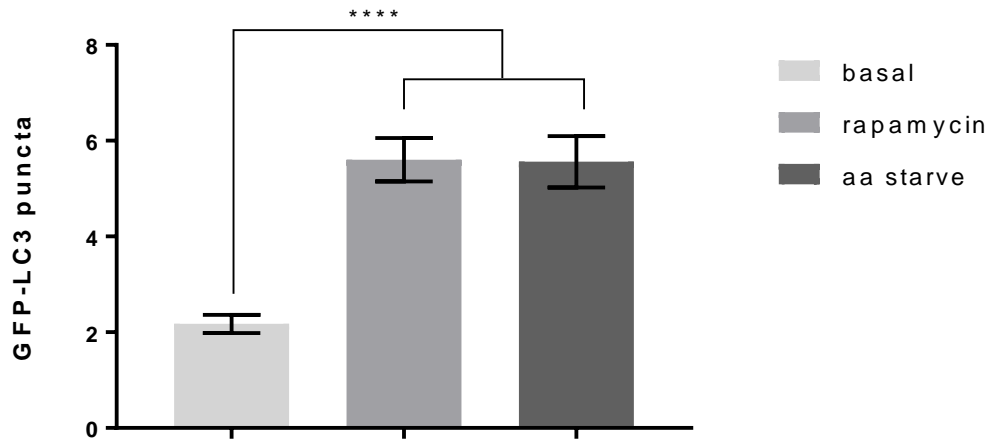


**Figure 3.20** Number of GFP-LC3 puncta under basal, rapamycin (5  $\mu$ M) and amino acid starvation conditions. One-way ANOVA, Dunnett's post hoc. Error bars  $\pm$  SEM,  $n=3$ , \*\*\*\*  $P < 0.0001$

Co-treatment with Bafilomycin A1 results in a further increase in the number of punctate structures observed (Figure 3.21)

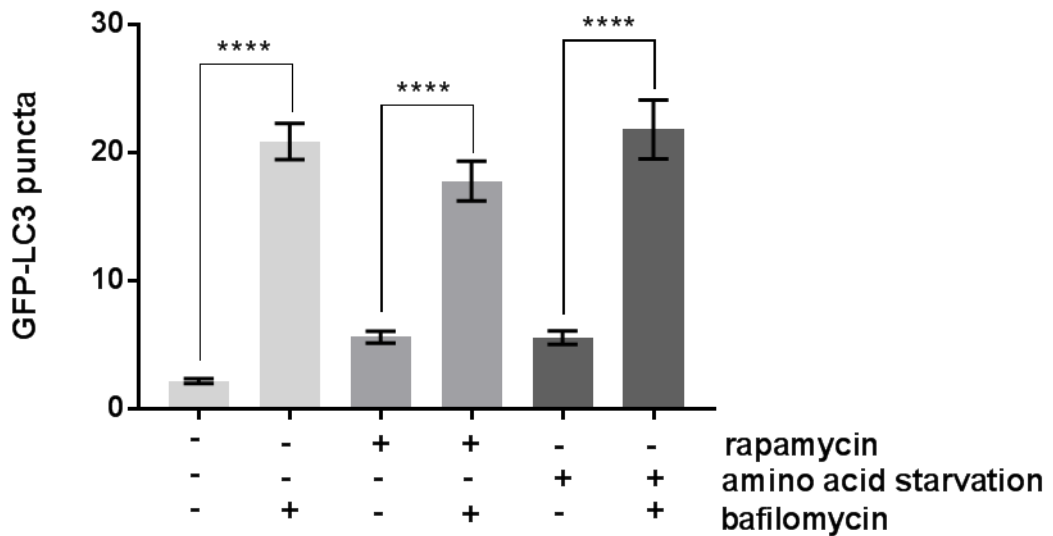


**Figure 3.21** Quantitation of puncta in GFP-LC3 HEK cells under different autophagy induction conditions. Rapamycin (5  $\mu$ M) treatment and amino acid starvation co-treated with Bafilomycin A1 (100 nM, 1 h). A minimum of 3 images were taken per coverslip. Error bars  $\pm$  SEM,  $n=3$ , \*\*\*\* indicates  $P < 0.0001$ . Two-way ANOVA, Dunnett's post hoc.

A number of commercial assays for autophagy are available, including the CytoID® Autophagy Detection Kit (Enzo) which is based upon the selective accumulation of a proprietary cationic amphiphilic dye in autophagic vesicles. The suitability of this kit was also examined using the TALI image based cytometer (Invitrogen). HEK cells were exposed to amino acid starvation, co-treated with Bafilomycin A1 and incubated with CytoID® as per the manufacturer’s protocol. Green fluorescence was recorded on a TALI image based cytometer. However, no significant differences were observed between any of the conditions. Figure 3.22a shows the histograms obtained and representative images. The mean fluorescence intensity per cell is presented in Figure 3.23b. On the basis of these results, the use of GFP-LC3 expressing HEK cells was deemed more suitable than the CytoID® Autophagy Detection Kit and was therefore used in subsequent experiments.

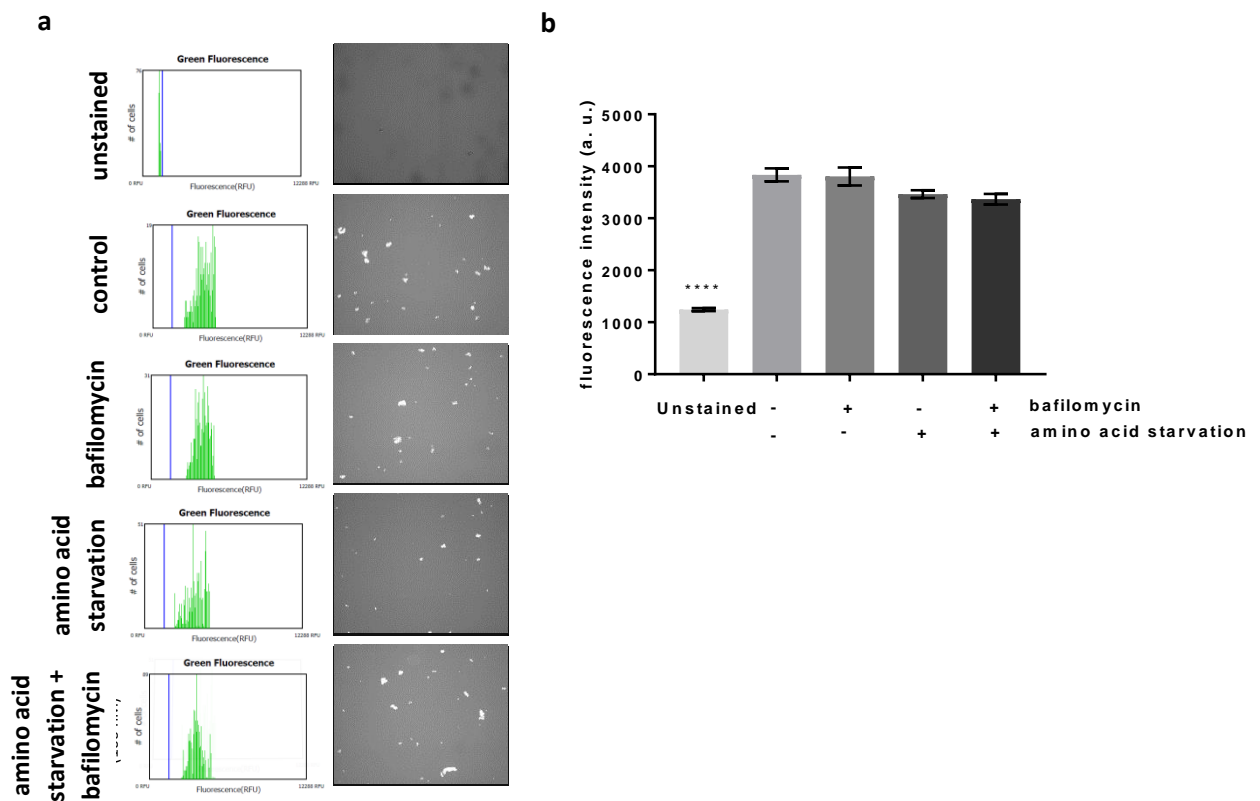


**Figure 3.22** CytoID kit is not compatible with TALI cytometer a) Representative histograms and images acquired on a TALI image-based cytometer (Invitrogen) of HEK cells stained with CytoID® autophagy detection kit (Enzo) b) mean fluorescence intensity per cell (CytoID® autophagy detection kit). A minimum of 9 images were taken per condition, one-way ANOVA, Tukey’s post hoc, error bars  $\pm$  SEM.

Figure **3.23a** shows the number of GFP-LC3 positive puncta observed following treatment with Q-VD-OPh or Z-VAD-fmk (50  $\mu$ M). A significant increase in GFP-LC3 puncta was observed after 72 h. No similar increase was observed in cells treated with vehicle or with broad spectrum caspase inhibitor, Q-VD-OPh. Figure **3.23b** shows representative images of the GFP-LC3 HEK cells.

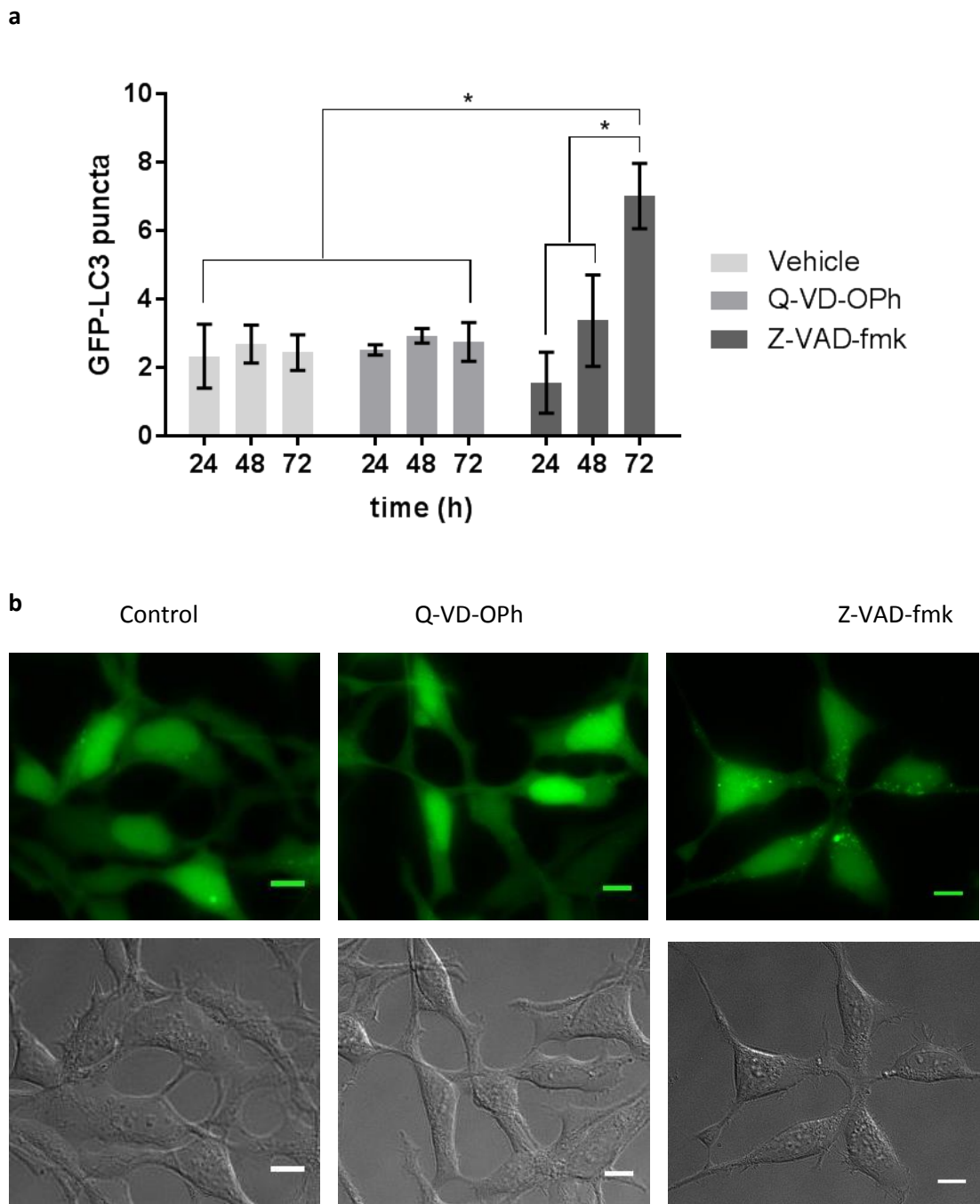


**Figure 3.23** Z-VAD-fmk increased autophagy after 72 h. **a)** GFP-LC3 puncta are increased after 72 h treatment with Z-VAD-fmk (50  $\mu$ M), no increase was seen under vehicle or Q-VD-OPh (50  $\mu$ M). Minimum of three images per coverslip. Error bars indicate  $\pm$  SEM,  $n=3$ ,  $P < 0.05$ , Two-way ANOVA, Tukey's post hoc **b)** Representative images of treatment of Z-VAD-fmk or Q-VD-OPh after 72 h. Scale bar indicates 10  $\mu$ m.



As an increase in the number of puncta observed could result from other effects, such as aberrant vesicle trafficking or blockage of lysosomal fusion, it was necessary to examine autophagic flux. HEK cells were treated with Bafilomycin A1 and 3-methyladenine (3-MA). As well as being present on the membrane of autophagosomes, LC3 has been shown to have a functional role in the clearance of protein aggregates and can form interactions with ubiquitinated aggregates via p62 (L. Wang et al. 2013, Bjørkøy et al. 2005) (Pankiv et al. 2007). To determine if puncta observed in the GFP-LC3 HEK cells reflect genuine autophagy, and not protein aggregation, cells were treated with 3-MA, an early stage autophagy inhibitor. If the LC3 puncta visible in the Z-VAD-fmk treated cells were due to LC3 binding protein aggregates, a greater number of LC3 puncta would be expected in the presence of 3-MA compared to that of the control conditions. As shown in Figure 3.24, 3-MA inhibits LC3 puncta formation during Z-VAD-fmk treatment. Treatment with Bafilomycin A1 results in an increase in the number of GFP-LC3 puncta observed. The results suggest that autophagic flux is maintained, as well as the LC3 puncta observed in the Z-VAD-fmk treated HEK cells are autophagosomes, and not a consequence of protein aggregation.

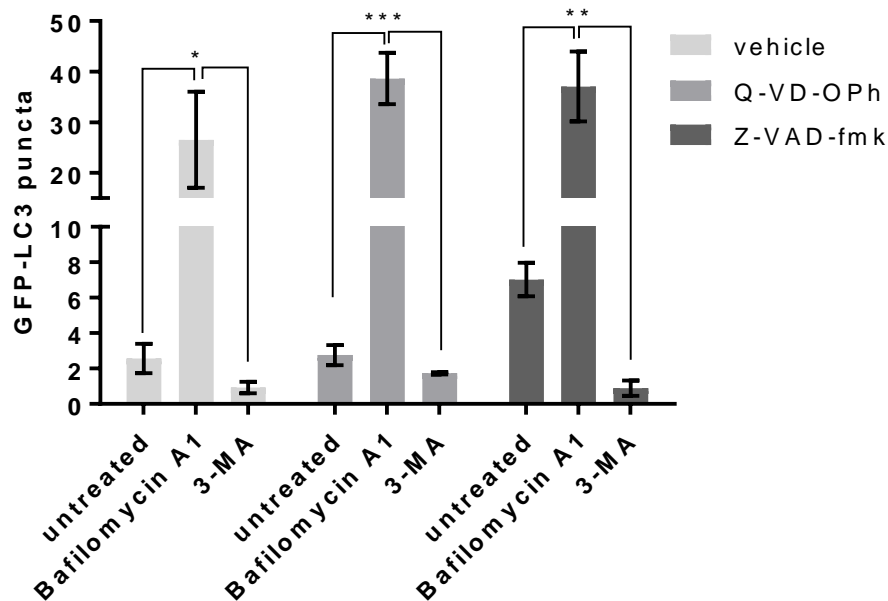


**Figure 3.24** Z-VAD-fmk and Q-VD-OPh do not inhibit autophagic flux. GFP-LC3 puncta per cell after treatment with Z-VAD-fmk or Q-VD-OPh (50  $\mu$ M, 72 h) followed by Bafilomycin A1 treatment (1 h, 100 nM) or 3-MA (1 h, 5 mM). Error bars indicate  $\pm$  SEM, \* indicates  $P < 0.05$ , \*\* indicates  $P < 0.01$ , \*\*\* indicates  $P < 0.001$ . One way ANOVA within each condition, Tukey's post hoc.

### 3.3.5 Autophagic flux is maintained following treatment with Z-VAD-fmk

A tandem RFP-GFP reporter for LC3 has also been employed as a tool for quantitation of autophagic flux (Kimura et al. 2007). GFP is acid sensitive (Roberts et al. 2016) so, as autophagosomes fuse with lysosomes, the GFP signal is quenched by the acidic environment. RFP is not as sensitive to acidic environments so is not quenched during autophagosome and lysosome fusion. LC3 puncta that show GFP and RFP co-localisation (yellow) indicate autophagosomes, whereas RFP puncta (red) alone indicate autolysosomes where the GFP signal has been quenched. Cells with a functional autophagic pathway show a combination of yellow (RFP+GFP) and red (RFP only) puncta. A diagram showing the localisation and quenching of GFP-RFP-LC3 is shown in Figure 3.25.

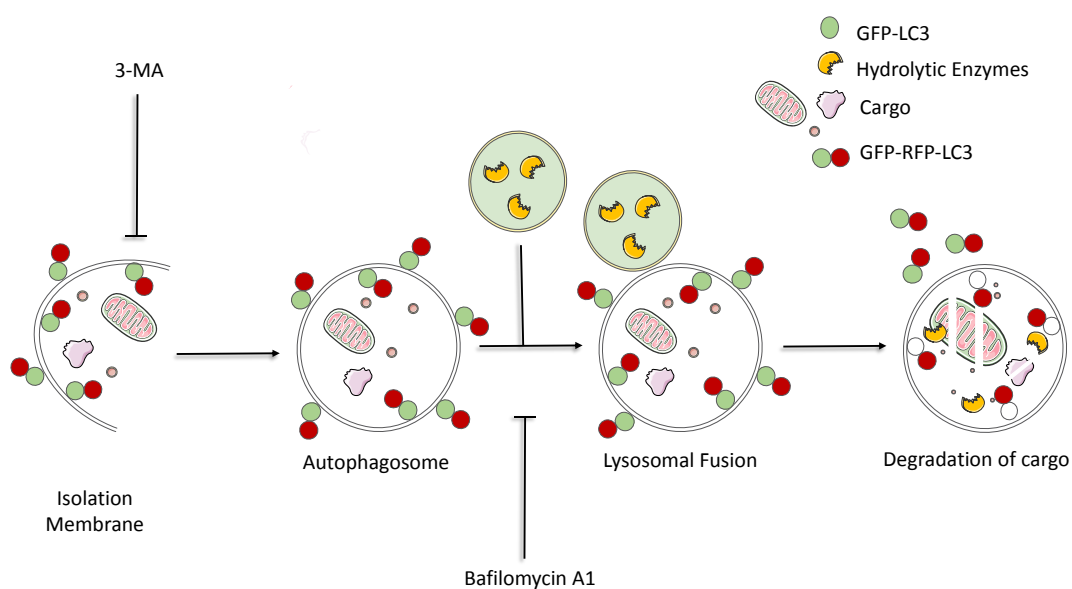


**Figure 3.25 Diagram showing the localisation GFP-RFP-LC3 on autophagosome membranes through maturation and degradation.**

The tandem RFP-GFP-LC3 reporter was transfected into HEK293 cells. Various transfection reagents were tested to optimise transfection efficiency. After 48 h, transfection efficiency was determined by the percentage of GFP positive cells. Figure 3.26a shows the percentage of transfected cells under different transfection reagents, representative images for each reagent are shown in Figure 3.26b. JetPei was found to give to most transfection with >70% efficiency and was chosen for subsequent transfections.

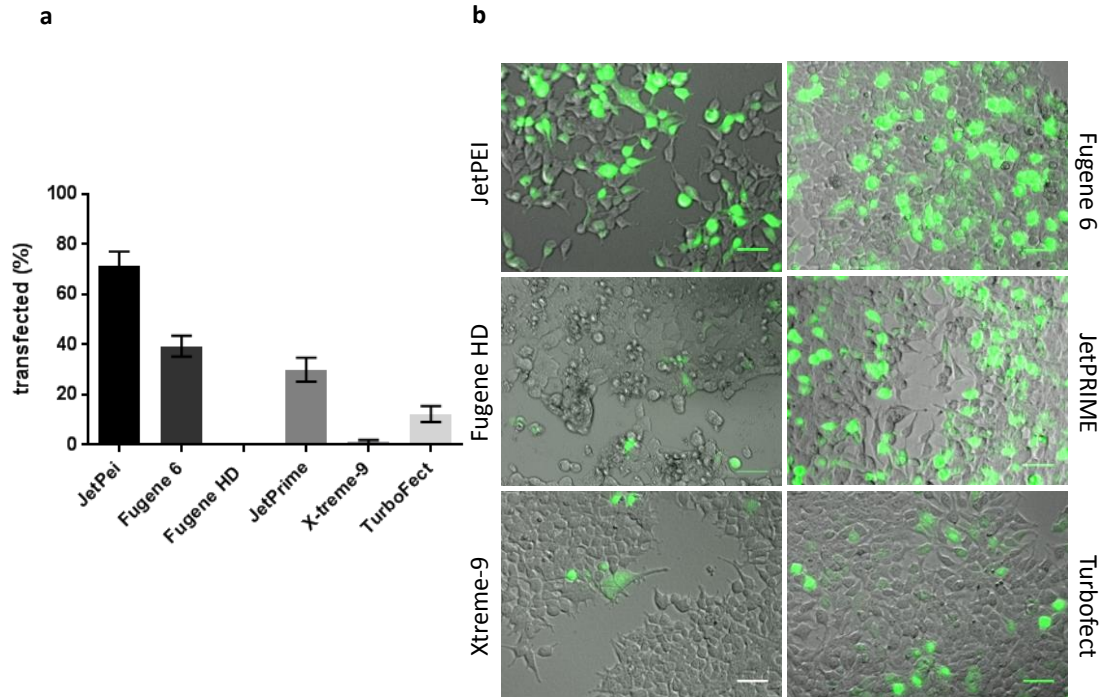


**Figure 3.26** JetPEI has the highest transfection efficiency in HEK cells a) Percentage of transfected cells after 48 hours. HEK cells were transfected with the GFP-RFP-LC3 construct and imaged under the GFP filter. A minimum of three images were taken per condition. Error bars  $\pm$  SEM b) Representative images demonstrating transfection efficiency for each transfection reagent (composite images showing bright-field image overlaid with GFP signal). Scale bar indicates 10  $\mu$ m.

It was observed that a number of the transfection reagents exhibited varying levels of cellular toxicity. Cell viability was quantified using trypan blue exclusion. The percentage of viable cells was calculated and shown in Figure 3.27. Whilst most reagents were found to be non-toxic, Fugene HD displayed significantly more cell death compared to the other reagents with only 45 % viability.

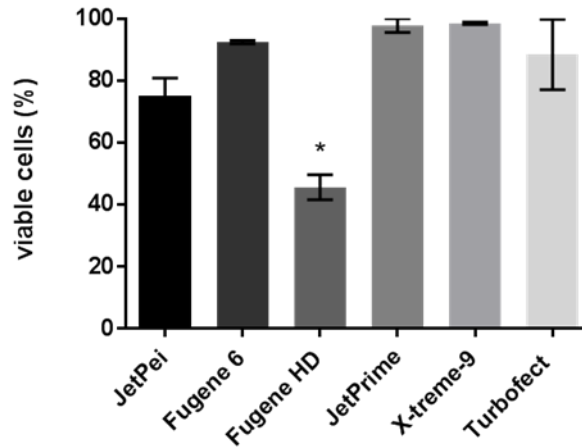


**Figure 3.27 Fugene HD causes cell death. Trypan blue exclusion of non-viable cells. One-way ANOVA, Tukey's post hoc, error bars  $\pm$  SEM,  $n=3$ ,  $P < 0.05$**

To generate a stable cell line, successfully transfected cells were selected for with the mammalian antibiotic marker G418. To determine the lowest level of G418 to induce death of non-transfected cells after 6 days in culture, cells were plated in 24 well plate and subjected to increasing concentrations of G418. Cell death was assessed by eye when cells detached from the cell culture plate. Figure 3.28 shows the survivability of HEK cells in G418.

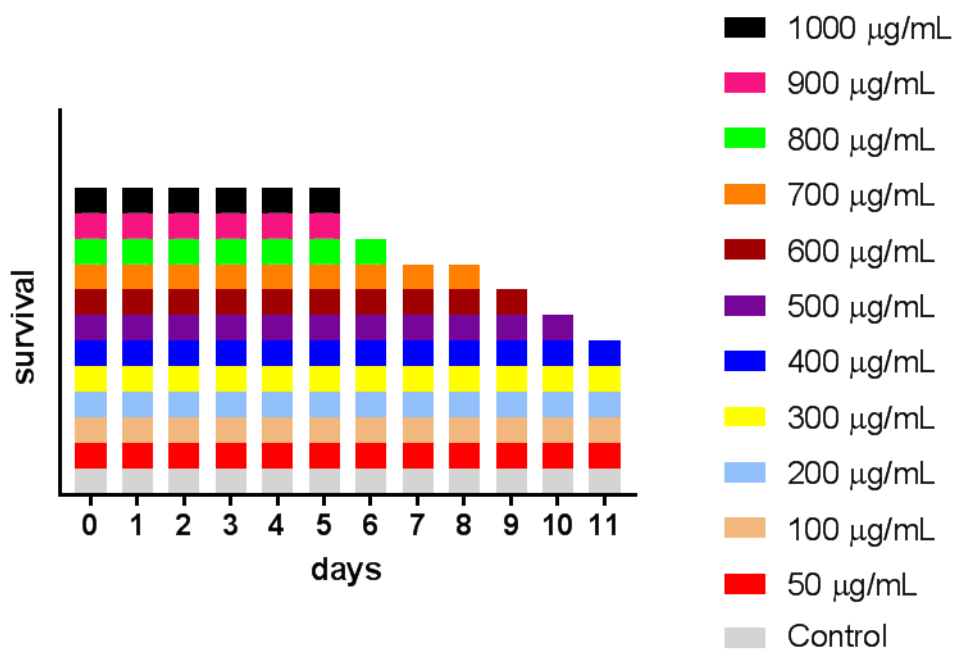


**Figure 3.28 Survival chart of HEK cells treated with 50-1000 µg/ml G418. Cells were plated in 48 well plate and treated with G418. Survival was determined when > 90 % of the cells were detached from the well.**

To generate a stable cell line, HEK cells were transfected with the GFP-RFP-LC3 construct and treated with 800 µg/ml G418 for 7 d. Cells were then serially diluted to generate single clones. However, HEK cells under this condition showed increased cell death and the cells that survived were mostly polyclonal lines. A well was selected that had similar fluorescence intensity to the GFP-LC3 HEK cells under the same excitation conditions. To test the appropriateness of this construct HEK cells transfected with GFP-RFP-LC3 were treated with Bafilomycin for 1 h. Representative images are presented in Figure 3.29.

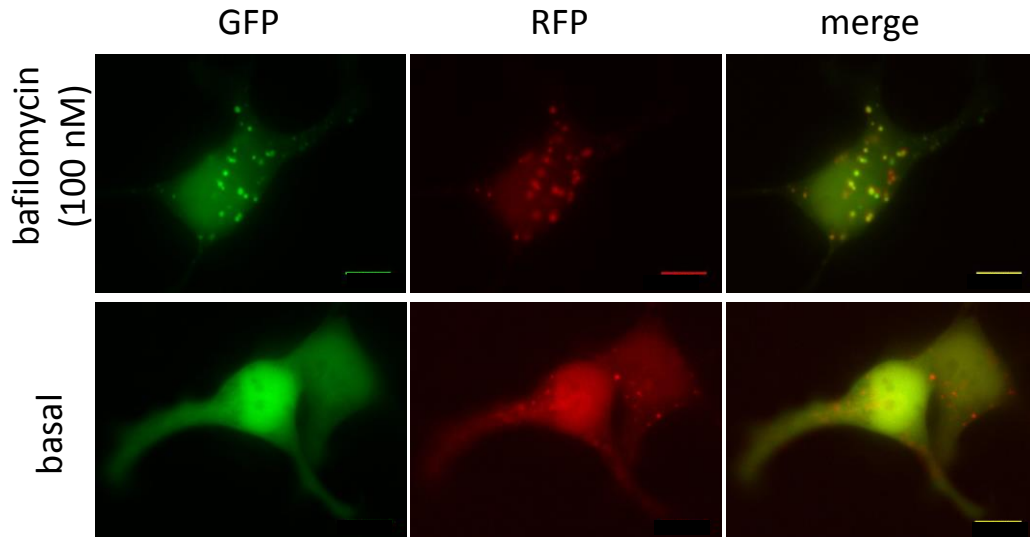


**Figure 3.29** Representative images of HEK cells transfected with GFP-RFP-LC3 construct treated with Bafilomycin A1 (100 nM, 1h) and basal (untreated cells). Scale bar indicates 10  $\mu$ m.

As Bafilomycin blocks lysosomal degradation and acidification of lysosomes, only green and red co-localised puncta were observed with few RFP signals. The addition of 3-MA blocks autophagosome formation, resulting in an overall decrease in both the GFP and RFP signal (Figure 3.30).

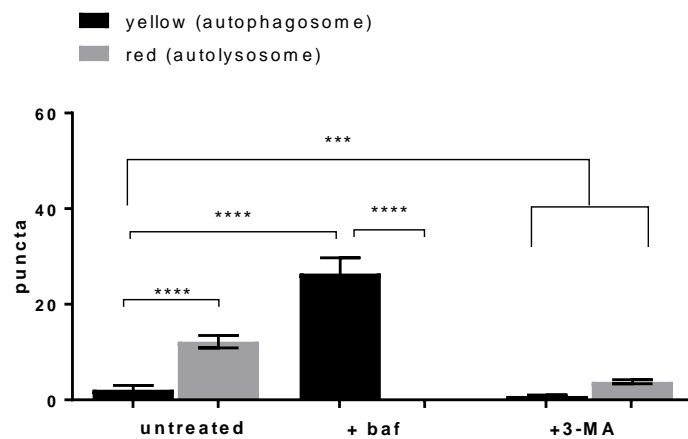


**Figure 3.30** The GFP-RFP-LC3 construct behaves as predicted using bafilomycin A1 and 3-MA. A minimum of three images were taken per coverlip. Two-way ANOVA, Tukey's post hoc, error bars  $\pm$  SEM, n=2, \*\*\*\* indicates  $P < 0.0001$ , \*\*\* indicates  $P < 0.001$ .

HEK cells expressing the tandem GFP-RFP-LC3 reporter showed a significant increase in the number of autophagosomes at 48 h and 72 h when treated with Z-VAD-fmk (50  $\mu$ M). At every time point, red puncta were observed. The presence of red punctate structures indicates that autophagosome and autolysosome fusion remained active and, that autophagic flux was maintained (Figure **3.31a**). Representative images of cells treated with vehicle control and Z-VAD-fmk at 72 h are shown in Figure **3.31b**.

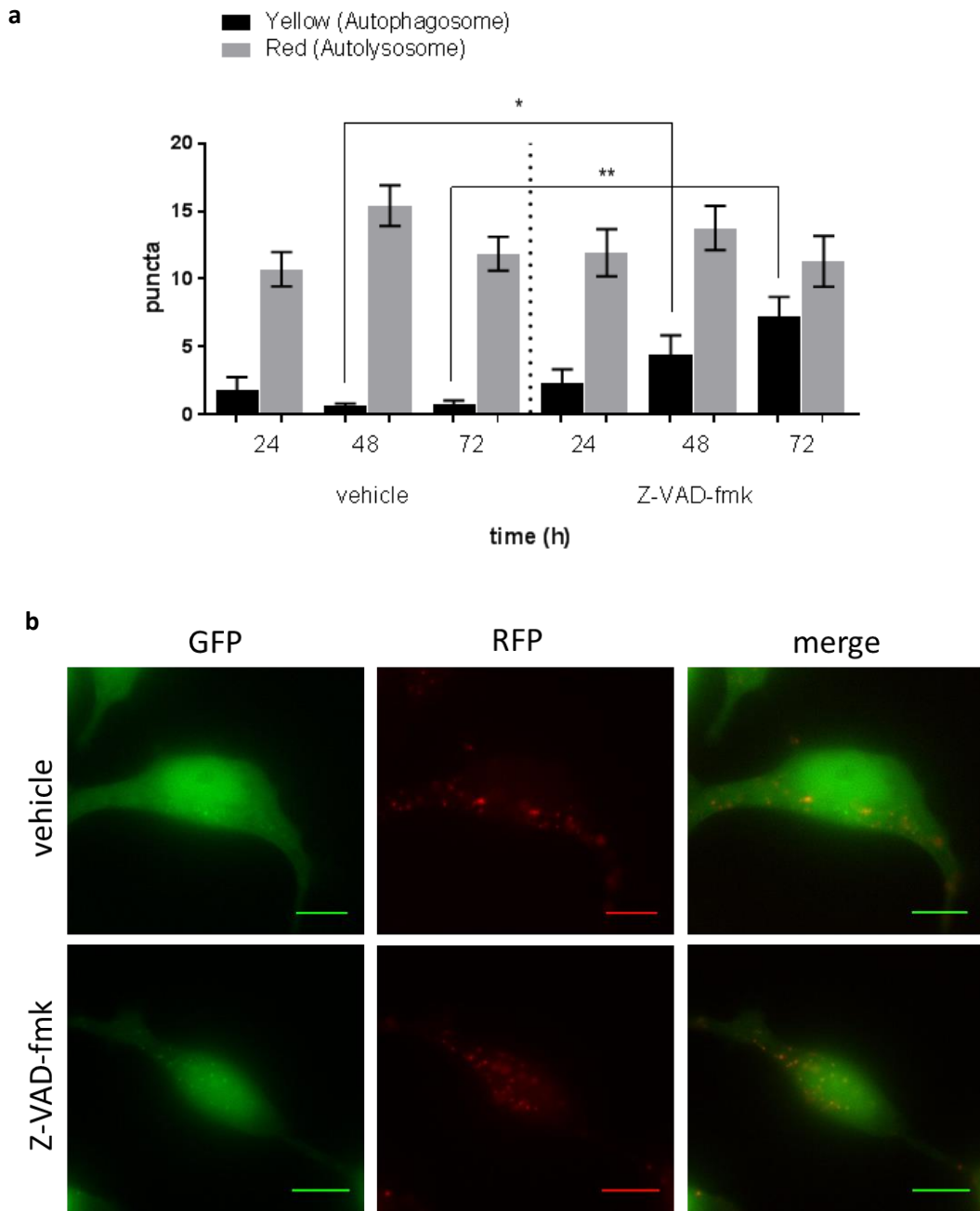


**Figure 3.31 Z-VAD-fmk induces autophagy in GFP-RFP-LC3 HEK model. a) Quantitation of punctate structures. A minimum of three images were recorded per coverslip and two biological replicates. Two-way ANOVA between autophagosome and autolysosome quantitation, followed by Tukey's post hoc b) Representative images of HEK cells transfected with GFP-RFP-LC3 construct treated with Z-VAD-fmk (50  $\mu$ M, 72 h). Scale bar indicates 10  $\mu$ m.**



### 3.3.6 Western blot analysis LC3 in HEK cells was unsuccessful

Western blot analysis of LC3 is a common method used to quantify relative levels of LC3, LC3I and LC3II in cells (Streeter et al. 2016, Chen et al. 2011, Barth et al. 2010, Pugsley 2017). In order to examine if this method was applicable in this case, samples of cleared HEK cell lysate (5 – 50 µg total protein concentration) were prepared for analysis. Attempts were also made to determine the levels of LC3I and LC3II in GFP-LC3 HEK cells by monitoring the in-gel fluorescence of GFP (thus negating any potential issues with transfer efficiency, antibody specificity and antibody binding efficiency). For this method, cells were lysed with 1 % Triton X-100 and analysed SDS-page gel. Figure **3.32a** shows the in-gel fluorescence of GFP-LC3 HEK lysate (10 or 20 µg per well) treated with Bafilomycin or amino acid starvation. LC3 I was observed to be much brighter than the LC3 II band, which did not allow the intensity of LC3 II to be quantified. Western blot against GFP produced similar results (Figure **3.32b**), the LC3I band was clearly visible. Treatment with Bafilomycin A1 increased the intensity of the LC3II signal, however it was not possible to resolve the bands clearly, resulting in difficulty in quantifying both the levels of LC3I and LC3II.

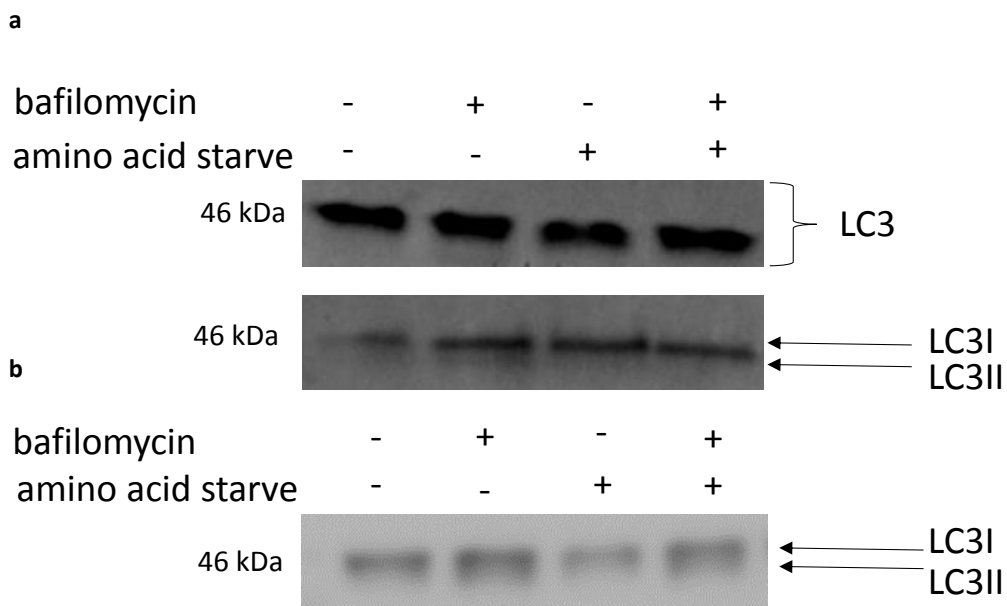


**Figure 3.32** Western blot and in-gel GFP-LC3 fluorescence was unable to resolve LC3I and LC3II bands.a) in-gel fluorescence of GFP-LC3, top 20 µg total protein loaded, bottom panel shows 10 µg total protein loaded per well b) anti-GFP western blot (10 µg total protein loaded).

### 3.3.8 Autophagy is protective response during N-glycanase inhibition

Autophagy was shown to be increased under Z-VAD-fmk treatment. The role of autophagy under these conditions was examined using an ATG13 deficient cell line (a kind gift from Prof. Nicholas Ktistakis, Babraham Institute, Cambridge). ATG13 is an autophagy factor critical to autophagosome formation (Kaizuka and Mizushima 2016, Suzuki et al. 2003). ATG13 KO MEFs were first confirmed as deficient by RT-qPCR for murine ATG13 mRNA. A significant difference in ATG13 mRNA compared to the WT MEF line was observed (Figure 3.33).

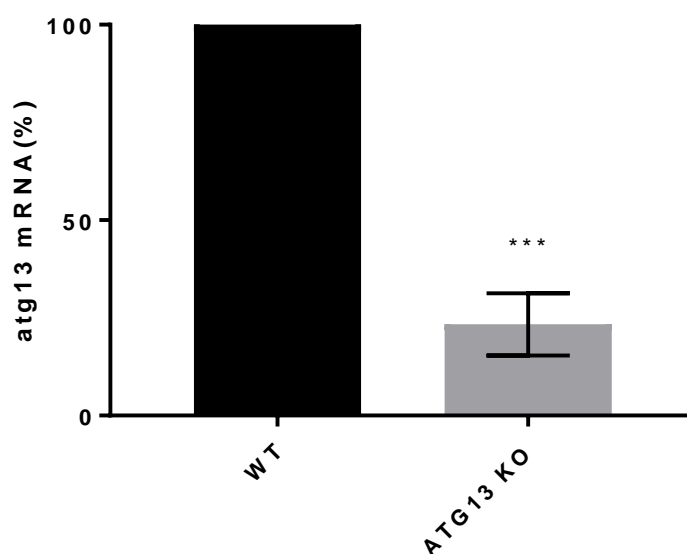


**Figure 3.33** rt-qPCR measurement of ATG13 in WT MEF and ATG13 KO MEF. Student's t-test,  $P < 0.001$ , error bars  $\pm$  SEM,  $n=3$ .

The cell viability of ATG13 KO MEF cells and corresponding WT MEF cells was measured by MTT assay in the presence of Z-VAD-fmk (Figure 3.34a) or Q-VD-OPh (Figure 3.34b) after 24 h. It was observed that Z-VAD-fmk treatment in ATG13 deficient MEF cells was toxic within 24 h. However, following treatment with the corresponding caspase inhibitor, Q-VD-OPh, no toxicity was observed. This suggests that the toxicity observed was due to N-glycanase inhibition rather than caspase inhibition and, that autophagy acts as a protective measure under N-glycanase inhibition. The calculated  $CC_{50}$  values are summarised in Table 3.5.

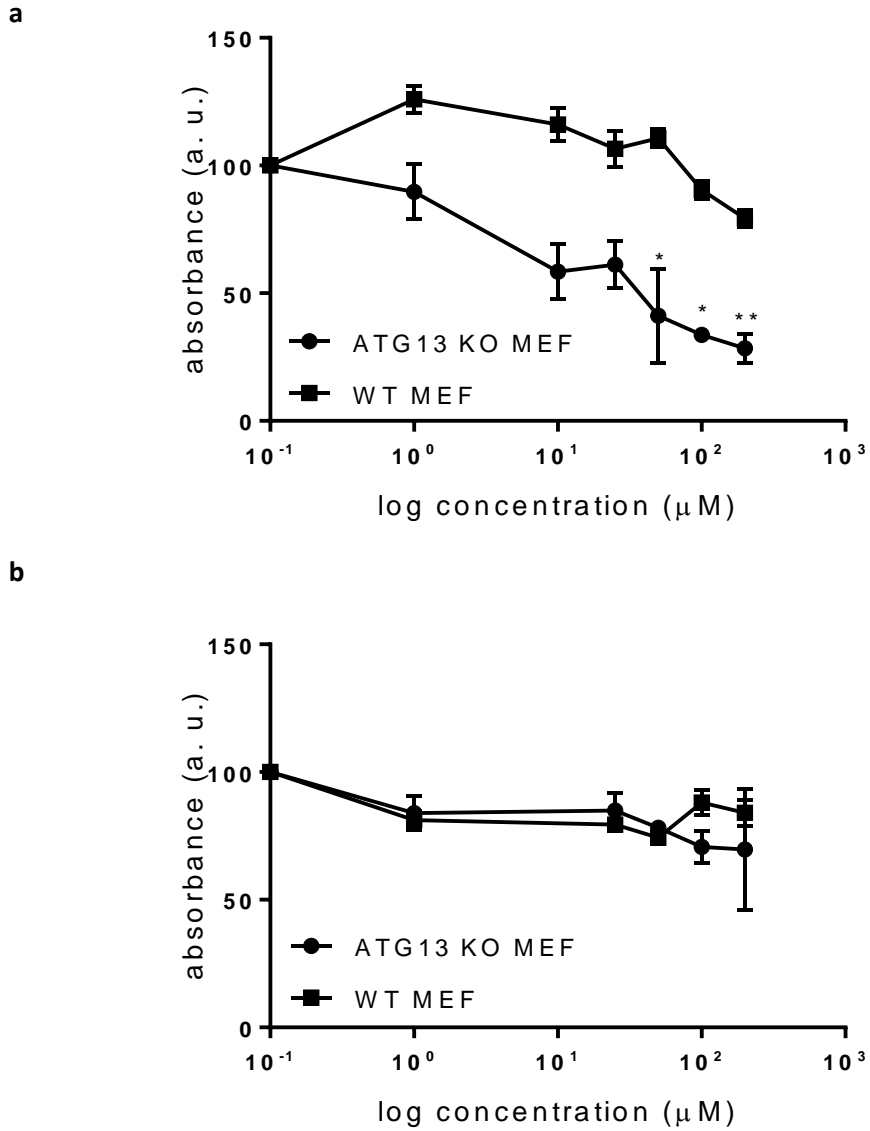


**Figure 3.34 Z-VAD-fmk increases cell toxicity in ATG13 KO MEFS. MTT of ATG13 KO MEF and WT MEF treated with a) Z-VAD-fmk (1-200 μM) or b) Q-VD-OPh (1-200 μM) for 24 h. One way ANOVA, Dunnett's post hoc. Error bars ± SEM,  $n = 3$ ,  $P < 0.05$ .**

**Table 3.5 CC<sub>50</sub> of Z-VAD-fmk for WT and ATG13 KO MEFs**

Cell line	CC <sub>50</sub> (μM)
<b>ATG13 KO MEF</b>	14.96 ± 12.53
<b>WT MEF</b>	289.30 ± 88.08

To further confirm the effect of autophagy modulating Z-VAD-fmk toxicity, the autophagy inhibitor 3-MA was used to block autophagy in HEK cells and the viability measured after Z-VAD-fmk treatment. The viability of HEK cells treated with 3-MA alone was first determined by MTT assay for 24 h and had a CC<sub>50</sub> value of 21.64 ± 18.67 mM (Figure 3.35a). Unlike genetic manipulation, pharmacological inhibitors can often not be used for long periods. HEK cells were treated with Z-VAD-fmk (50 μM) over 72 h, then treated with 3-MA (10 mM) for 6 h. Viability was measured by MTT assay (Figure 3.35b). There were no significant differences observed between the 3-MA treated and untreated conditions. A small significant difference between Z-VAD-fmk treated cells at 24 and 72 h was noted, although neither of these were significantly different from the vehicle control. This may be due to initial treatments with Z-VAD-fmk and Q-VD-OPh resulting in an initial increase in absorbance at low concentrations.

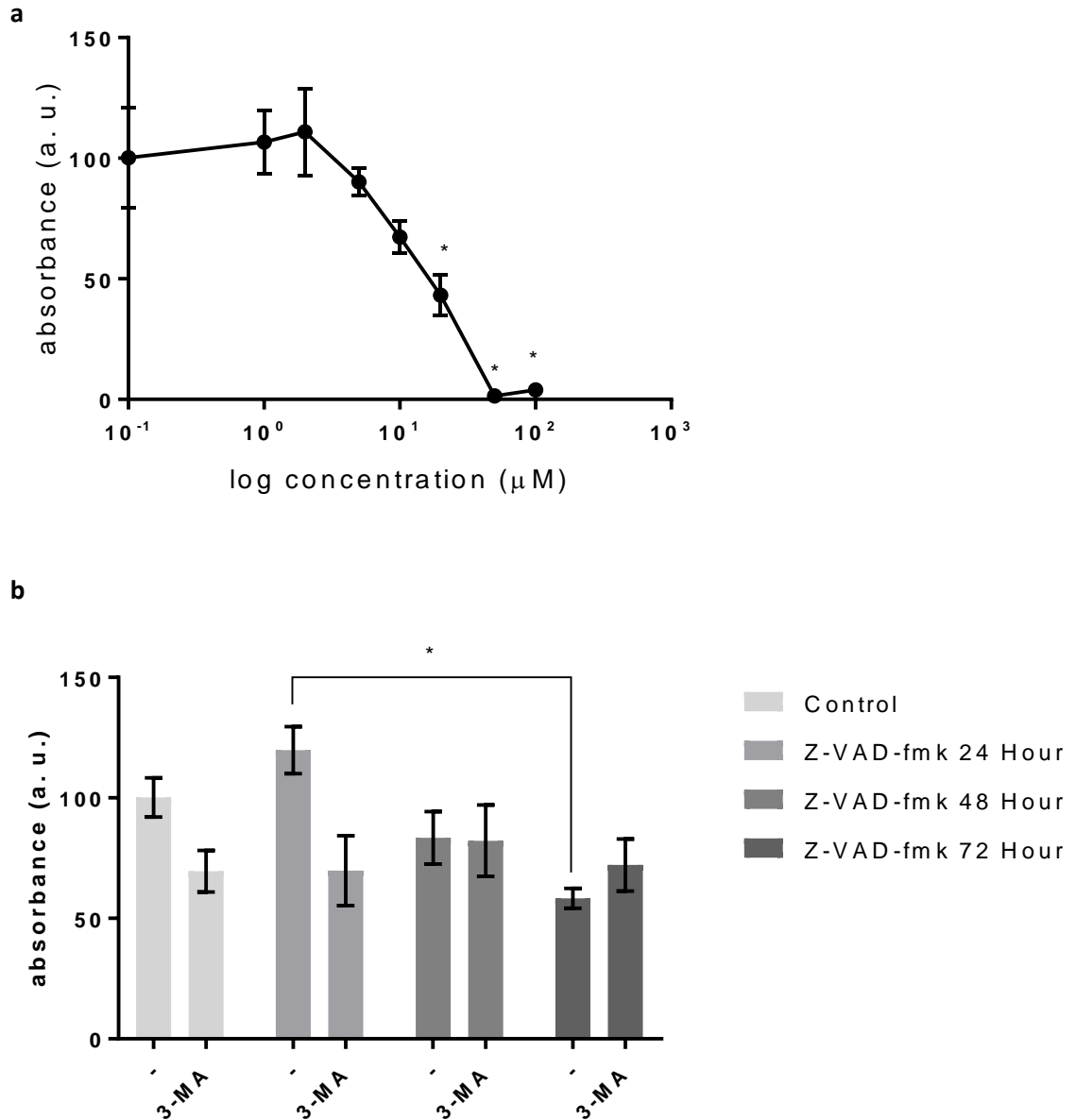


**Figure 3.35 3-MA causes cell toxicity. a) MTT of HEK cells treated with 3-MA (24 h). One-way ANOVA, Dunnett's post hoc, error bars  $\pm$  SEM,  $n=3$ ,  $P < 0.05$ . b) MTT of cells treated with Z-VAD-fmk (50  $\mu\text{M}$ , 24-72 h) followed by 3-MA (10 mM, 6 h). Two-way ANOVA, Tukey's post hoc. Error bars  $\pm$  SEM,  $n=3$ ,  $P < 0.05$ .**

### 3.3.8 Z-VAD-fmk treatment of HEK cells does not induce ER stress or oxidative stress

The UPR is activated by the accumulation of unfolded proteins in the ER and is often linked to changes in degradation pathways including autophagy (Senft and Ronai 2015, Sovolyova et al. 2014). Increased ThT fluorescence has been linked with increased  $\beta$ -sheet motifs commonly associated with misfolded or unfolded protein structures (Beriault and Werstuck 2013, Groenning et al. 2007). As NGLY1 deficiency is regarded as a defect of ERAD (Enns et

al. 2014), and as there is some evidence to suggest a build-up of misfolded proteins resulting from lower enzyme activity, there have been suggestions that inhibition of or deficiency in *N*-glycanase can result in ER stress (Martinet et al. 2006b, Misaghi et al. 2005). Little direct evidence, however, has been presented for this.

The UPR has been well-defined and the components involved well characterised (Kennedy et al. 2015, Shapiro et al. 2016, Taylor 2016, Nishitoh 2012). To test whether Z-VAD-fmk inhibition of *N*-glycanase activated the UPR, RT-qPCR was performed using several markers upregulated during the UPR. During the accumulation of misfolded proteins, the UPR is activated by three key ER membrane proteins: PERK, ATF6 and IRE1 (**Figure 3.36**) which result in the activation of ATF4, cleavage of ATF6 and splice activation of XBP1. This results in increased transcription of various chaperones and proteins involved in protein folding and secretion with the aim of reducing ER 'load'. These chaperones include BiP, CHOP and EDEM.

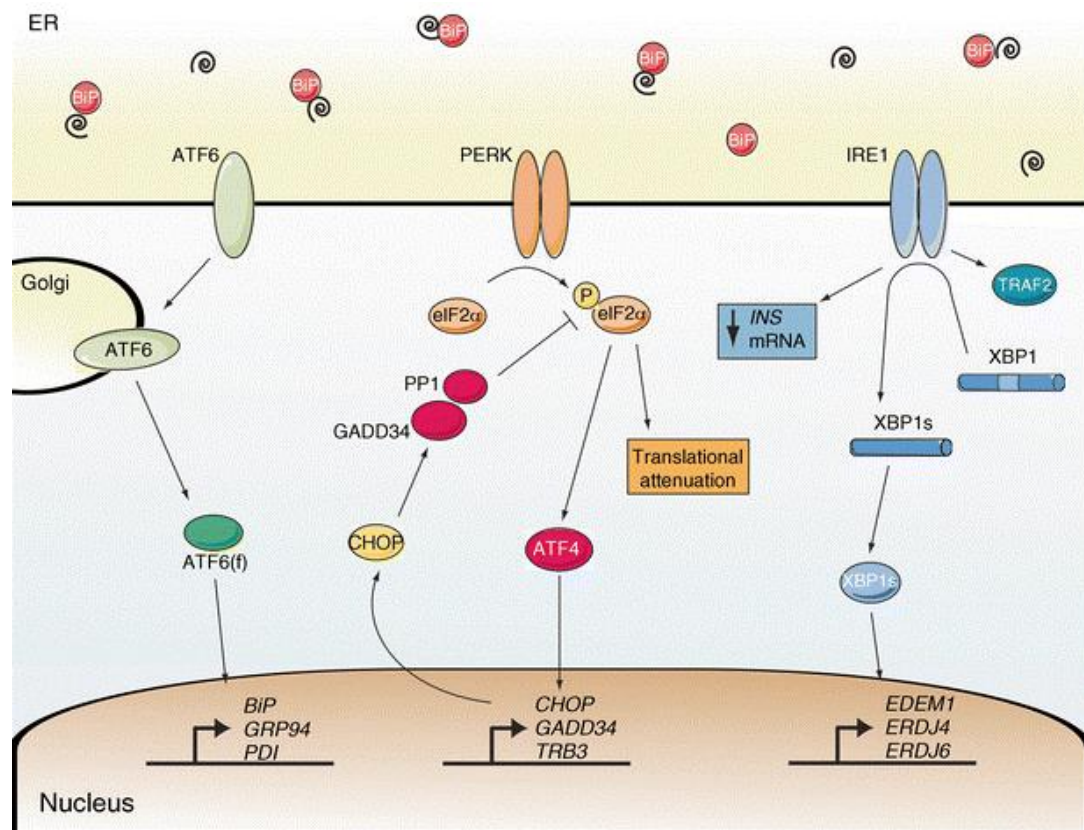


**Figure 3.36** Diagram of unfolded protein response activation. The three main arms of the UPR: ATF6, PERK and IRE1 are shown in the ER membrane followed by increased expression of several effectors including BiP, CHOP and EDEM1. Reprinted by permission from Springer Nature: *Diabetologia* (Eizirik et al. 2013).

During ER stress, BiP (a well-characterised ER chaperone important in protein quality control) disassociates from the ER transmembrane sensors, PERK, IRE1 and ATF6 leading to their activation and, concomitant activation of the UPR response. This results in an increase in transcription of BiP by cleaved ATF6 (Wang et al. 2009, Haze et al. 1999). Other ERAD associated proteins, such as EDEM are also upregulated. Under severe or prolonged ER stress, cells can undergo apoptosis. This mechanism is controlled by CHOP, JNK and caspase-12 (Li et al. 2014). CHOP and ATF4 were included specifically because they have been shown to regulate the transcription of several ATG proteins (B'chir et al. 2013). ATF4 binds to C/EBP-ATF response element (CARE) to affect transcription. During amino acid starvation, these are referred to as amino acid response elements (AARE). ATF4 and CHOP bind to the p62 AARE to induce transcription of p62 and precedes its induction in amino acid starved cells (B'chir et al. 2013).

Z-VAD-fmk and Q-VD-OPh treated cells were analysed for up-regulation of the UPR associated proteins CHOP, BiP, ATF4 and EDEM. Figure **3.37** shows the  $\log_{10}$  fold change in mRNA expression of each gene. No significant increase in any of the markers was observed. The proteasome inhibitor MG132 was used as a positive control, inhibition of the proteasome results in activation of the UPR (Obeng et al. 2006, Nakajima et al. 2011). Treatment with MG132 results in up-regulation of a significant increase in ER stress markers CHOP, BiP and ATF4 however, EDEM was not significantly upregulated after MG132 treatment.

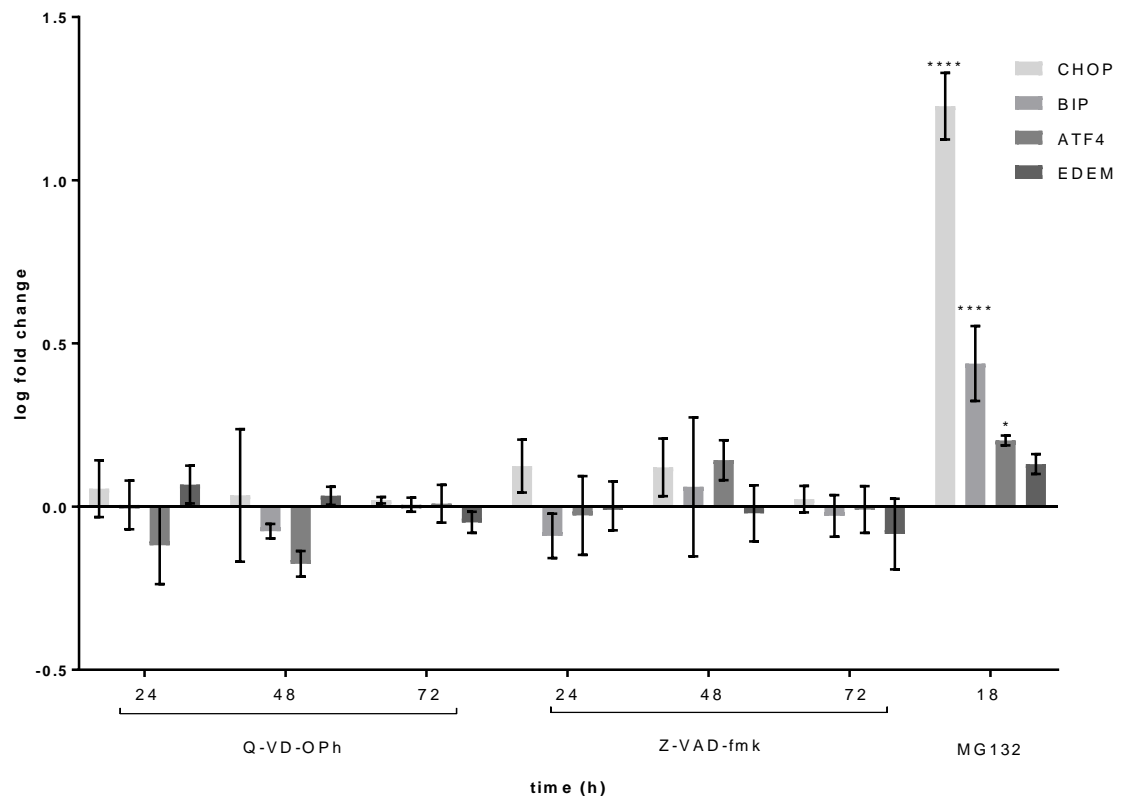


**Figure 3.37 Z-VAD-fmk or Q-VD-OPh does not activate the UPR. rt-qPCR analysis of CHOP, BiP, ATF4 and EDEM levels in cells treated with Z-VAD-fmk or Q-VD-OPh (50  $\mu$ M, 24-72 h). mRNA levels normalised to GAPDH and an untreated control using  $\Delta\Delta$ Ct method. Log<sub>2</sub> fold change is presented with error bars  $\pm$  SEM,  $P < 0.05$ ,  $n=3$ . Two-way ANOVA, Tukey's post hoc within each mRNA target.**

The sensors for detection of misfolded proteins are located on the ER luminal side of the ER and the signal is then transduced to the cytosol (Wang et al. 2016). As misfolded proteins are exported from the ER into the cytosol to be degraded by the proteasome the ER may not invoke mechanisms to respond to misfolded proteins which are not accumulating or delayed in the ER lumen. In conclusion, it does not appear that activation of ER stress and the UPR is associated with activation of autophagy in HEK cells exposed to Z-VAD-fmk treatment.

As well as being a site of protein folding and secretion, the ER is a major cellular  $\text{Ca}^{2+}$  store. Perturbations in the ER homeostasis are often marked by changes in  $\text{Ca}^{2+}$  handling within the organelle, especially ER 'leakiness' (Kania et al. 2015, Hammadi et al. 2013, Mekahli et al. 2011). To determine the baseline calcium levels in the cell, HEK cells were loaded with the ratiometric dye Fura-2-AM (1  $\mu$ M), then treated with various concentrations of Thapsigargin



(10.0, 5, 1, 0.5  $\mu\text{M}$ ). Thapsigargin (an inhibitor of SERCA) to block reuptake of  $\text{Ca}^{2+}$  into the ER. Treatment with Thapsigargin results in an increase in cytosolic  $\text{Ca}^{2+}$  levels. Calcium traces are presented in Figure 3.38. Treatment with higher concentrations of Thapsigargin resulted in a more rapid and sharper increase in cytosolic  $\text{Ca}^{2+}$  concentration (as shown by a higher amplitude). The area under the curve, which reflects the total increase in cytosolic  $\text{Ca}^{2+}$  concentration remained the same for each concentration of Thapsigargin examined, despite differences in the rate of increase and initial onset. For subsequent studies a 1  $\mu\text{M}$  concentration of thapsigargin was employed, to allow for any changes in both rate and initial onset of effects to be examined.

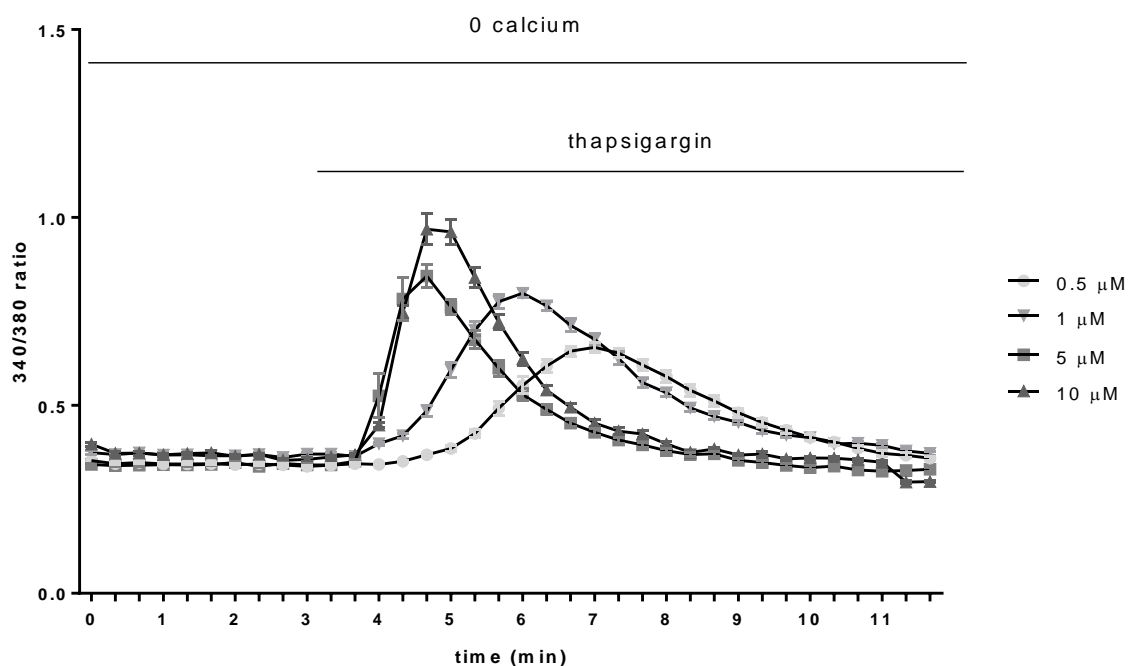


**Figure 3.38 Thapsigargin increases cytosolic  $\text{Ca}^{2+}$ .** HEK cells loaded with Fura-2 AM (1  $\mu\text{M}$ ) in  $\text{Ca}^{2+}$  free imaging buffer. After 3 min, Thapsigargin (10, 5, 1, 0.5  $\mu\text{M}$ ) was added.  $n=1$ , average of 16 cells, error bars  $\pm$  SEM.

HEK cells were treated with either Z-VAD-fmk (24-72 h, 50  $\mu\text{M}$ ) or Q-VD-Oph (24-72 h, 50  $\mu\text{M}$ ) and loaded with Fura-2 (1  $\mu\text{M}$ ). Baseline ER calcium levels were calculated from the first eight readings, the height of the peak was used as a measure of the rate of release. Total peak area was used as a measure of the total release from the ER. Figure 3.39 shows the traces of three independent experiments for each treatment. No significant difference in the levels of ER  $\text{Ca}^{2+}$  release was observed in HEK cells treated with Z-VAD-fmk (compared to vehicle and cells treated with Q-VD-Oph (50  $\mu\text{M}$ )) (Figure 3.40a-c).

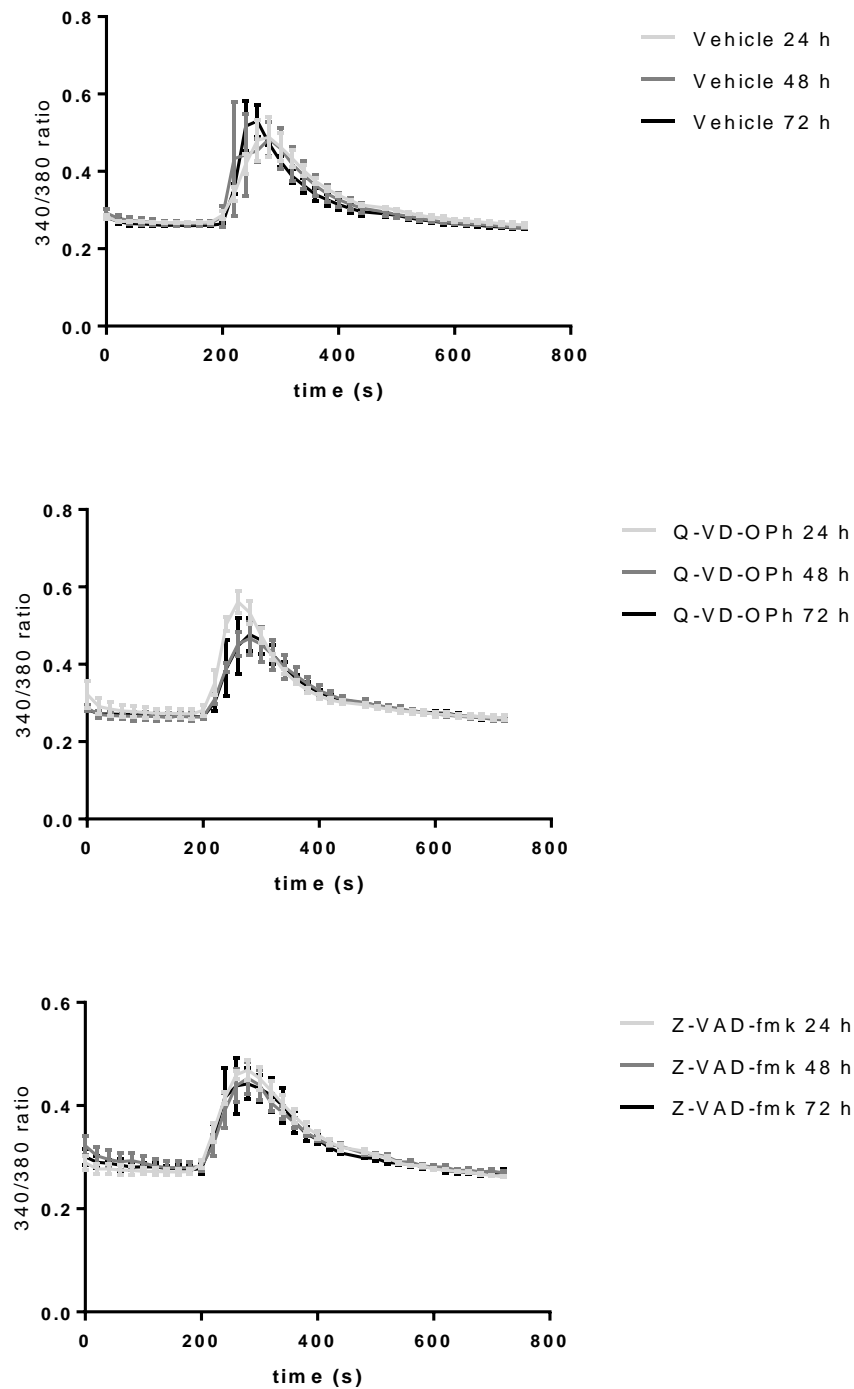


**Figure 3.39** Z-VAD-fmk or Q-VD-OPh does not affect Ca<sup>2+</sup> handling. Traces of HEK cells treated with Z-VAD-fmk or Q-VD-OPh (50  $\mu$ M, 24-72 h), loaded with Fura-2 AM (1  $\mu$ M, 0.5 h) and treated with Thapsigargin (1  $\mu$ M, 180 s). Error bars  $\pm$  SEM,  $n=3$ .

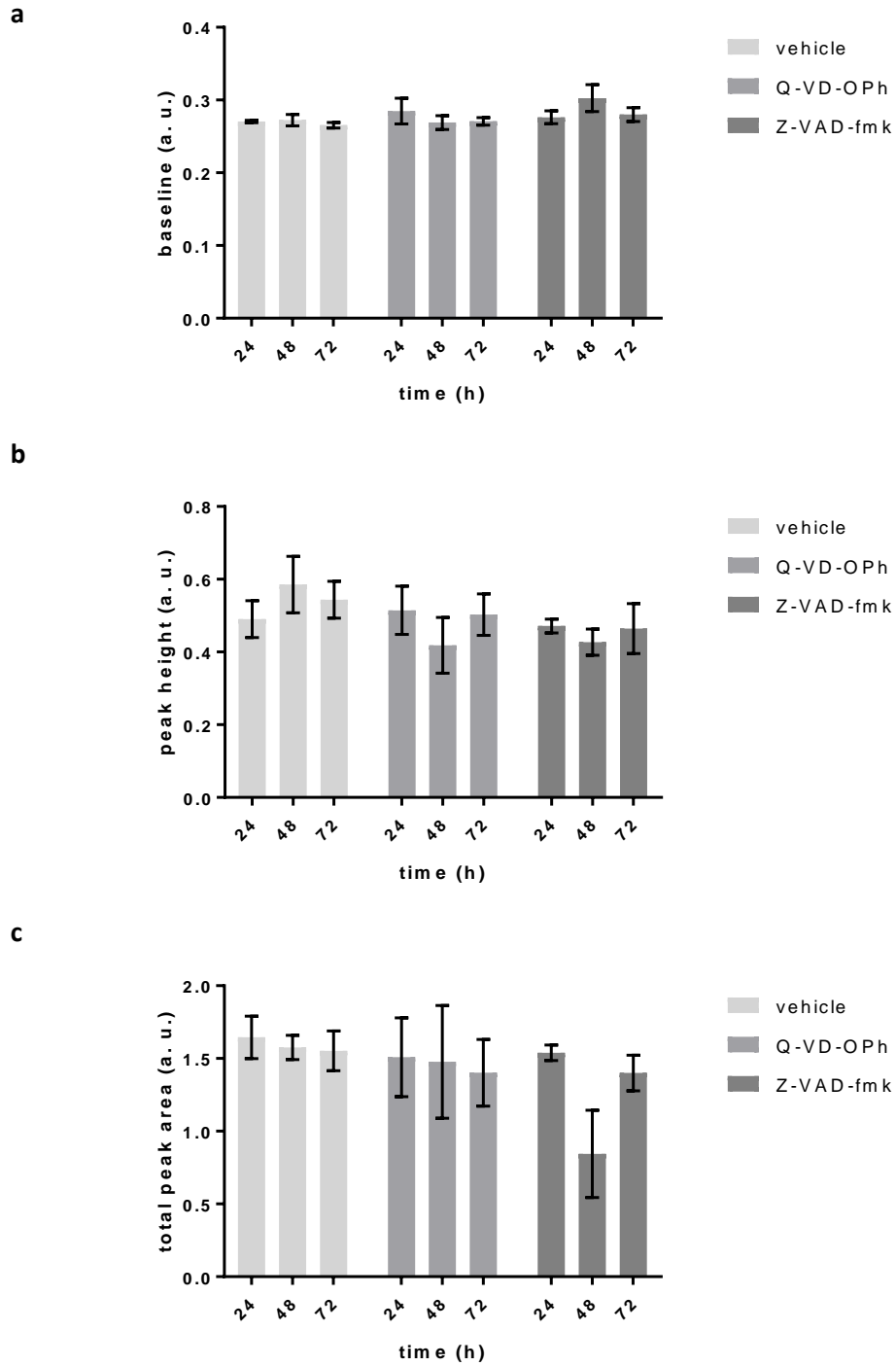


**Figure 3.40 Quantitation of Ca<sup>2+</sup> handling.** HEK cells treated with Z-VAD-fmk or Q-VD-OPh (50  $\mu$ M, 24-72 h). a) shows the baseline Ca<sup>2+</sup> levels calculated from the first eight readings b) shows peak height c) total peak area of the traces. Two-way ANOVA. Error bars  $\pm$  SEM,  $n=3$ .

Certain ER stress events have been shown to be linked to oxidative stress. Oxidative stress has been defined as a dysfunction in the homeostasis between reactive oxidant species production and antioxidant defences (Betteridge 2000) and is initiated by the presence of reactive oxygen species (ROS), such as hydrogen peroxide, nitric oxide, superoxide, hydroxyl and monoxide radicals. In the ER, glutathione (GSH) is responsible for reducing erroneous disulphide bond formation during protein folding. When protein folding in the ER is disrupted (for example, by accumulation of misfolded proteins) the increased need to reduce disulfide bonds leads to a reduction in antioxidant capacity and subsequent oxidative stress. Therefore, if there is a higher level of misfolded protein in the ER an increase in levels of ROS may be expected.

The level of ROS was measured by flow cytometry using the cell-permanent fluorogenic probe ROS Brite™ 570 (ATT Bioquest). Menadione, which has been reported to induce apoptosis via ROS (Loor et al. 2010, Kim et al. 2014, Criddle et al. 2006) was used a positive control for ROS production (Figure 3.41). There were no significant differences found in HEK cells treated with Z-VAD-fmk or Q-VD-OPh compared to the vehicle and untreated cells. Menadione (5  $\mu$ M, 18 h) produced a significant increase in ROS Brite fluorescence.

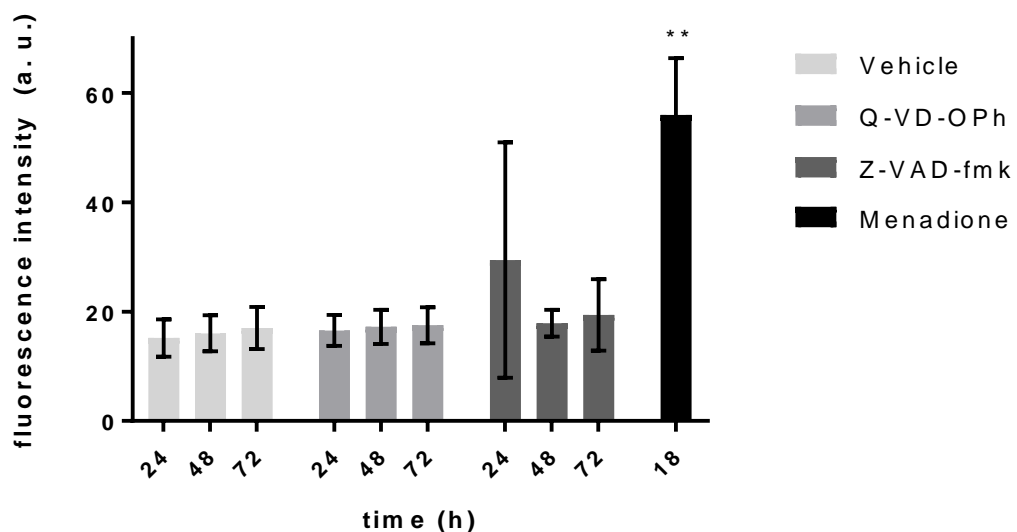


**Figure 3.41 Z-VAD-fmk or Q-VD-OPh does not increase ROS. HEK cells treated with Z-VAD-fmk or Q-VD-OPh (50  $\mu$ M, 24-72 h). Cells were stained with ROS Brite 570 (5  $\mu$ M, 0.5 h). Two-way ANOVA, Tukey's post hoc, error bars  $\pm$  SEM,  $n=3$ , \*\*  $P < 0.01$ .**

### 3.3.9 Treatment with Z-VAD-fmk does not change O-GlcNAc modifying enzyme homeostasis

It has been reported that in NGLY1 deficient MEF cells, ENGase is able to act on *N*-glycanase substrates. This results in proteins modified with a single *N*-GlcNAc residue (Huang et al. 2015, Fujihira et al. 2017). It has been hypothesised that this increase in *N*-GlcNAc modifications may interfere with *O*-GlcNAc signalling. Increased levels of *O*-GlcNAc have been shown to influence the expression of the *O*-GlcNAc modifying enzymes such as *O*-GlcNAcase (OGA) which adds *O*-GlcNAc and, *O*-GlcNAc transferase (OGT) which removes it. Inhibition of OGA using Thiamet G, results in an increase in *O*-GlcNAc and OGA (as determined by western blot) (Zhang et al. 2014). It was also confirmed that treatment with Thiamet G also resulted in increased mRNA transcript level of OGA after 6 h in HELA, SH-SY5Y and K562 cell lines.

Therefore, if there is an increase in the levels of protein bound *N*-GlcNAc in the cell as a result of ENGase action, this may have an impact upon the systems responsible for cellular *O*-GlcNAc cycling (particularly OGA). To investigate this hypothesis, RT-qPCR was employed to measure the levels of mRNA associated OGA and OGT in HEK cells treated with Z-VAD-fmk (50  $\mu$ M) and Q-VD-OPh (50  $\mu$ M). Figure **3.42a and b** shows the  $\log_{10}$  fold change in mRNA OGA and OGT levels respectively after treatment with Q-VD-OPh or Z-VAD-fmk. No significant changes were observed.

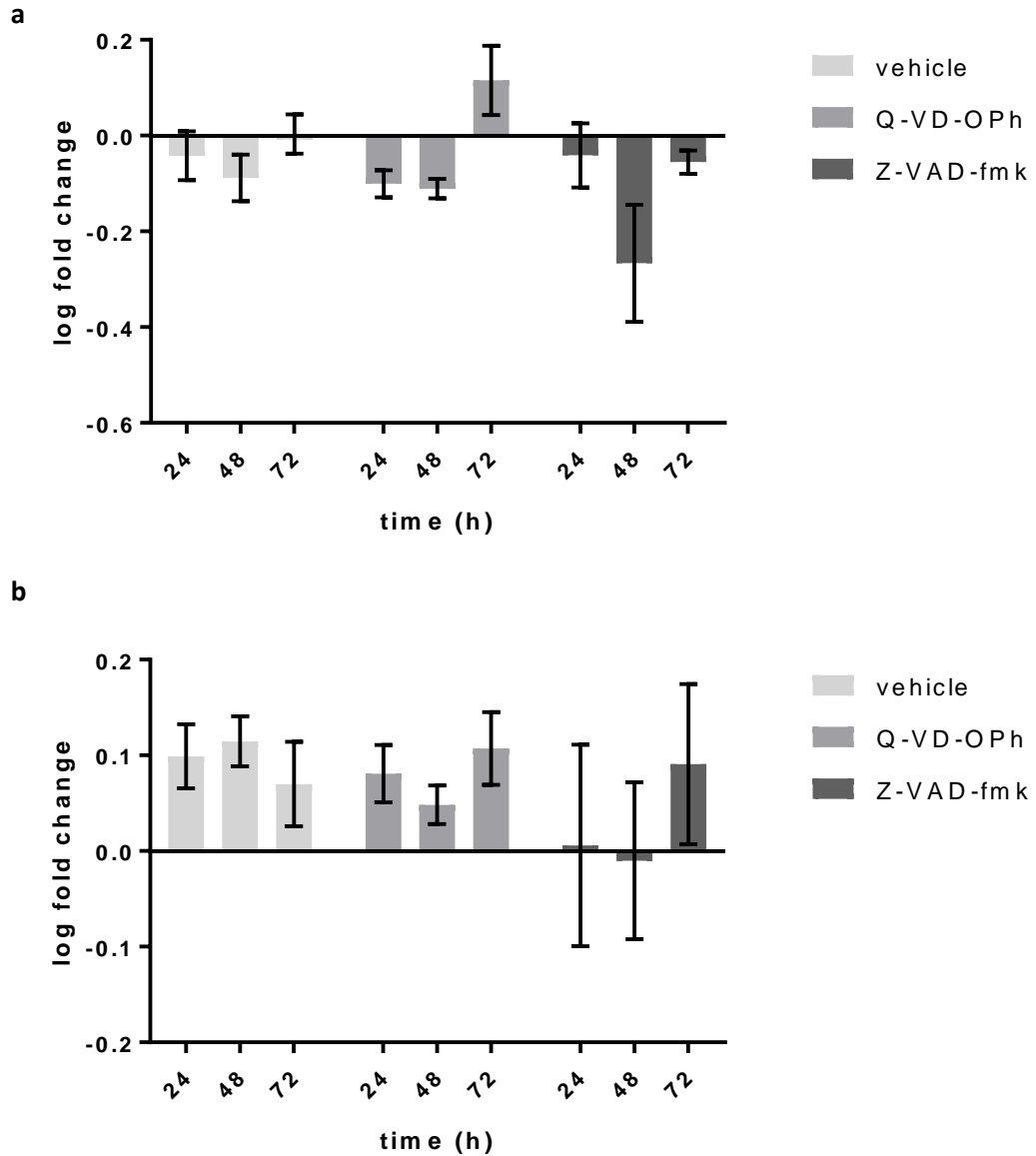


**Figure 3.42** Z-VAD-fmk or Q-VD-OPh does not affect OGA or OGT expression levels. Log<sub>2</sub> fold change of a) OGA and, b) OGT mRNA expression levels in HEK cells treated with Z-VAD-fmk or Q-VD-OPh (50  $\mu$ M, 24-72 h). OGA and OGT levels were normalised to GAPDH and an untreated control. Two-way ANOVA, error bars  $\pm$  SEM,  $n=3$ .

### 3.3.10 Bacterial *N*-glycanase (PNGase F) is insensitive to Z-VAD-fmk

Bacterial *N*-glycanase (PNGase F) is commonly employed in the biopharmaceutical industry in workflows where removal of protein bound *N*-glycans is advantageous, for example, in protein structural studies (where glycans can interfere with protein crystallisation) or, in biopharmaceutical quality control analysis. Unlike the mammalian orthologue, bacterial PNGase F is not inhibited by Z-VAD-fmk. Z-VAD-fmk is proposed to covalently bind to the cysteine in the active site of mammalian *N*-glycanase (Misaghi et al. 2004), thus inhibiting the enzyme. This conserved cysteine residue is present in human, mouse and yeast *N*-glycanase enzymes but is not present in bacterial forms of the enzyme (as highlighted in Figure 3.43).



**Figure 3.43 Bacterial PNGase F does not contain conserved cysteine residue in active site. Alignment of yeast, mouse and bacterial PNGase F amino acid sequences (generated using Clustal Omega). The conserved cysteine residue of yeast and mouse *N*-glycanase (marked) is not found in bacterial PNGase F (Flavobacterium).**

In order to explore if over-expression of a Z-VAD-fmk insensitive *N*-glycanase could rescue the effects observed following treatment with Z-VAD-fmk, efforts were made to clone bacterial PNGase F into a suitable mammalian expression vector for transfection into HEK cells. The bacterial construct was first characterised to confirm the Z-VAD-fmk insensitivity. Recombinant PNGase F (a kind gift from Shaun Lott (Addgene plasmid #40315) bearing a hexa-histidine tag was expressed and purified in *E. coli* BL21 (DE3). Recombinant PNGase F contained an Outer Membrane Protein A3 (OmpA3) leader sequence to localise the protein

to the periplasm to allow purification by osmotic shock (Confer and Ayalew 2013) (Missiakas and Raina 1997). The enzymatic activity of the isolated protein was confirmed using an RNase B deglycosylation assay. Figure 3.44 shows the glycosylated RNase B around 17 kDa. Deglycosylated RNase B migrates at around 15 kDa.

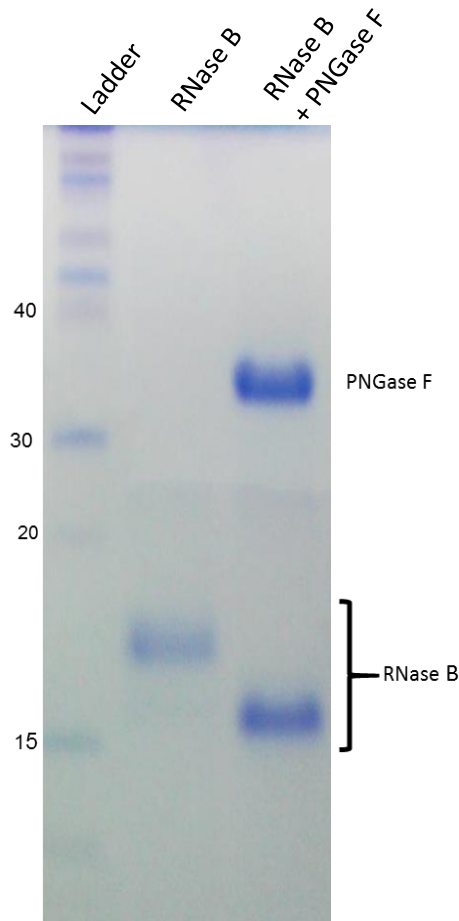


**Figure 3.44 PNGase F deglycosylation assay. PNGase F was incubated with denatured RNase B (24 h at 37 °C) and samples were analysed by SDS-PAGE (4-15 % Tris-Glycine).**

In order to confirm the expressed protein was insensitive to Z-VAD-fmk, purified recombinant bacterial PNGase F was incubated with increasing concentrations of Z-VAD-fmk (1 h, room temperature). RNase B was then added and the reaction mixture incubated at 37 °C for 1 h. The samples were then analysed by SDS-Page, and it was observed that there was no inhibition of deglycosylation (Figure 3.45).



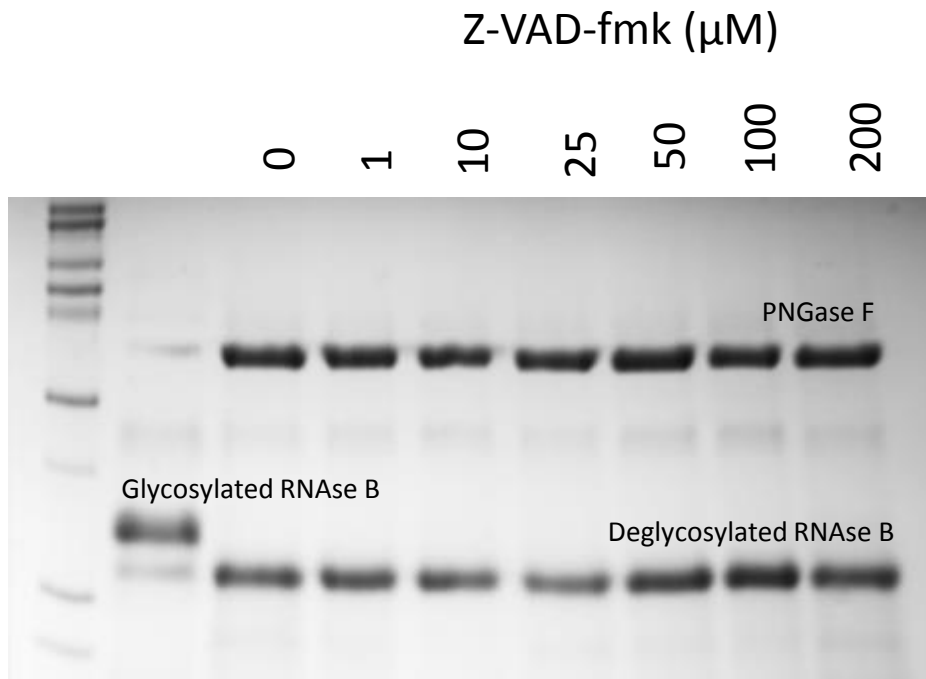


**Figure 3.45 PNGase F is not inhibited by Z-VAD-fmk. Purified bacterial PNGase F was tested for Z-VAD-fmk sensitivity using the RNase B deglycosylation assay. Bacterial PNGase F was incubated with Z-VAD-fmk (1-200  $\mu\text{M}$ ) for 1 h prior to RNase B deglycosylation assay.**

3.3.11 PNGase F was successfully cloned into a mammalian expression vector but transfection proved fatal to HEK 293 cells

Z-VAD-fmk is not a specific inhibitor for *N*-glycanase but is commonly employed and an inhibitor of caspases. To provide further evidence that the effects seen in these studies were due to the inhibition of *N*-glycanase (rather than caspase inhibition) the Z-VAD-fmk insensitive bacterial PNGase was cloned into a mammalian expression vector, with a view to examining if over-expression of a Z-VAD-fmk insensitive *N*-glycanase could successfully rescue the observed phenotypes. Bacterial PNGase F was cloned by PCR and ligated into a (N1-mAPPLE, Addgene cat#54567) mammalian expression vector containing an N-terminal N1-mAPPLE fluorescent tag. The cloning strategy is shown schematically in Figure 3.46.

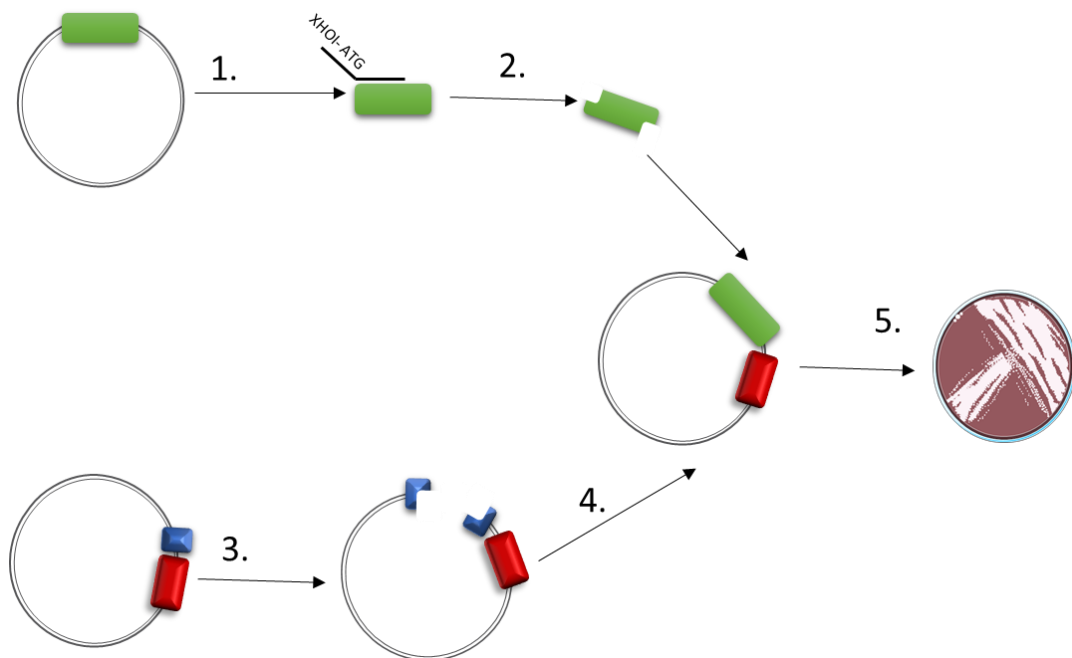


**Figure 3.46 Schematic diagram showing the cloning protocol for generation of Z-VAD-fmk insensitive N1-mAPPLE tagged protein in N1-mAPPLE.**

The cloning strategy is described in detail below.

1. Primers were generated to clone the PNGase F from the POPH6 bacterial expression vector. Primers were designed with a four base pair match to the 5' end with the addition of a XHOI restriction site, a new ATG sequence and an eighteen base pair matching at the 3' end.
2. The PCR product was extracted from the agarose gel and digested with XHOI and BAMHI

3. N1-mAPPLE plasmid was co-digested with BAMHI and XHOI to generate complementary sticky ends.
4. The digested N1-mAPPLE plasmid was purified and extracted from an agarose gel. The N1-mAPPLE backbone was added to the digested PNGase F and ligated using T4 ligase (48 h, 4 °C).
5. Plasmid was transformed into DH5 $\alpha$  *E. coli*. Several single colonies were isolated, termed bacterial PNGase (bacpng) 1-6 plasmid and sequenced.

Plasmids were sequenced to confirm the incorporation of the bacterial PNGase F insert into N1-mAPPLE backbone (Appendix **A2**). Transfection of the Z-VAD-fmk insensitive plasmid into HEK cells, however, proved inefficient compared with the control transfection of HEK cells with the empty N1-mAPPLE vector, with only 20 % transfection efficiency compared to the N1-mAPPLE backbone (Figure **3.47**).

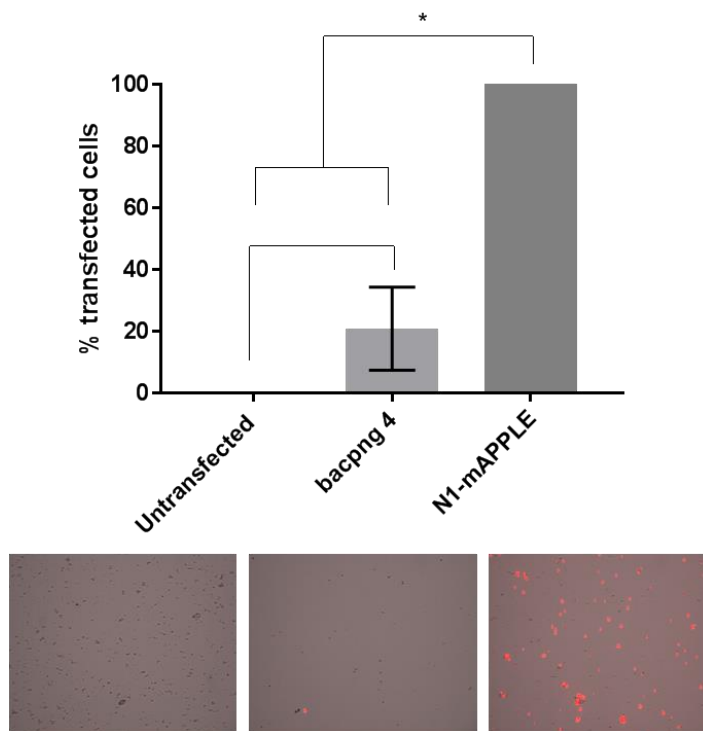


**Figure 3.47** Transfection of BacPng plasmid caused increased cell death and poor transfection. HEK cells were transfected with plasmid DNA (3  $\mu$ g) per well in a 12 well plate. The transfection efficiency of the N1-mAPPLE backbone was set at 100 % and the transfection efficiency of the Z-VAD-fmk insensitive PNGase plasmid was normalised to this. One-way ANOVA, Tukey's post hoc, error bars  $\pm$  SEM,  $P < 0.05$ . Lower panel contains representative images of cells using the TALI cytometer for (left to right) un-transfected cells, cells transfected with the vector containing the bacterial PNGase insert and cells transfected with N1-mAPPLE backbone.

It was noted that transfection with the Z-VAD-fmk insensitive PNGase plasmid resulted in decreased cell viability and little transfection even at low plasmid levels. Figure 3.48 shows that cell viability was decreased in HEK cells transfected with bacterial PNGase plasmid compared to the backbone control. The effect of Z-VAD-fmk could not be investigated by the introduction of a Z-VAD-fmk insensitive bacterial PNGase due to the poor transfection efficiency and the decrease in cell viability post transfection.

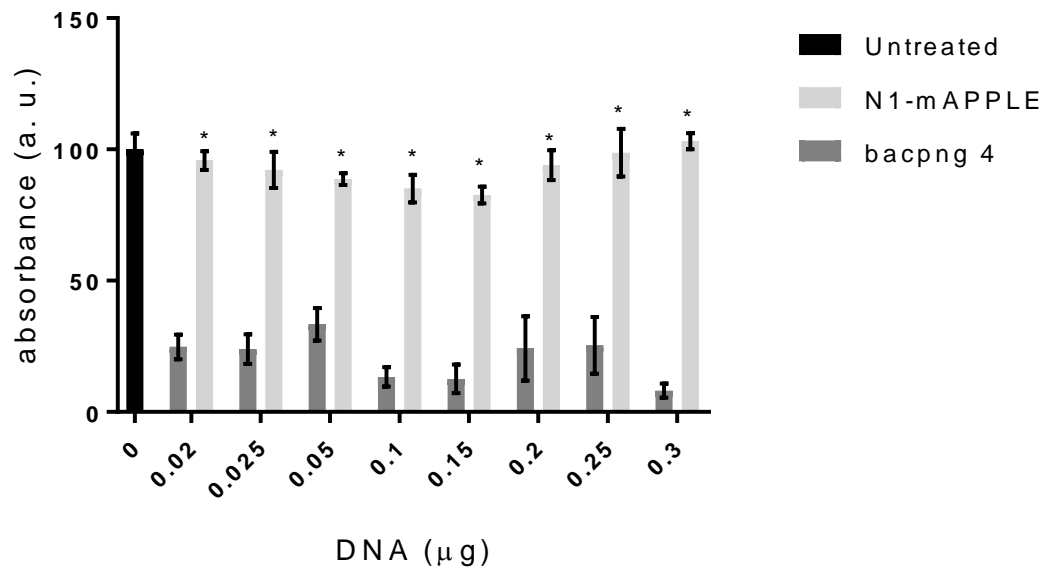


**Figure 3.48 BacPng plasmid caused cell death even at low concentrations. MTT assay of HEK cells transfected with increasing amounts of N1-mAPPLE plasmid DNA or BacPng4 plasmid DNA. Absorbance was normalised to vehicle control. Two-way ANOVA, Tukey's post hoc test, error bars  $\pm$  SEM,  $n=3$ ,  $P < 0.05$ .**

### 3.3 Discussion

Z-VAD-fmk has been reported to exhibit a broad spectrum of cellular effects. Commonly employed in cell culture as a pan-caspase inhibitor, it has also been shown to act as an inhibitor of *N*-glycanase. The aim of this chapter was to characterise the effects observed upon Z-VAD-fmk treatment of HEK 293 cells, compared to those observed upon treatment with Q-VD-OPh. Q-VD-OPh has a similar caspase inhibition profile, but does not act as an inhibitor of *N*-glycanase.

The effects of treatment with both pharmacological agents on cell viability, *N*-glycanase activity, glycan profile, ER stress, ER Ca<sup>2+</sup> handling and ROS levels was determined. There is some debate as to whether effects noted in *N*-glycanase deficiency are related to ERAD dysfunction. One of the hypotheses linked to effects noted in *N*-glycanase deficiency is that inhibition is not directly related to the dysfunction of ERAD but instead, changes in *O*-GlcNAc homeostasis. This was examined by testing the expression levels of the enzymes OGA and OGT. In addition, the effects Z-VAD-fmk and Q-VD-OPh on protein aggregation and autophagy were also examined. Finally, a Z-VAD-fmk insensitive bacterial PNGase was cloned into a mammalian expression vector with the aim of rescuing effects of Z-VAD-fmk by increasing levels of Z-VAD-fmk insensitive PNGase.

To establish a suitable working range, cell viability assays (using MTT) were carried out using Z-VAD-fmk and Q-VD-OPh. MTT assays are commonly used as a measure of viability, but results can be misinterpreted. Other studies have reported that treatment with Z-VAD-fmk results cell death in different cell lines (Table 3.2) (Martinet et al. 2006b, Wu et al. 2011, Dong et al. 2013, Cowburn et al. 2005, Werthmoller et al. 2015, Herzog et al. 2012, Chen et al. 2011). However, no decrease in MTT reduction was observed in the concentration range examined in HEK cells. MTT reduction can be influenced by factors such as changes in the cellular redox environment, and are often cell line specific (Berridge et al. 2005).

There are very few options available to directly quantify cellular *N*-glycanase activity. Initial studies identifying Z-VAD-fmk as an inhibitor of  $\gamma$ Png1 used purified yeast PNGase and a glycoprotein substrate, RNase B. In this assay, enzymatic deglycosylation was identified by gel shift. This method was later adapted by other studies to examine *N*-glycanase activity in MEF cell extracts. In these instances, cell lysate was incubated with RNase B and, both the glycosylated and deglycosylated forms detected by western blot (Suzuki 2005, Huang 2015, Fujihira et al. 2017)}. A similar assay was attempted in this study employing FITC-conjugated RNase B as the substrate to allow in-gel fluorescence detection. The FITC label did not

interfere with deglycosylation of RNase B by PNGaseF as shown in Appendix A5. However, upon incubation with HEK lysate for 18-72 h, no deglycosylation was observed using this method. The method has only been reported twice in the literature, both in MEF cell lines (Huang et al. 2015, Fujihira et al. 2017) indicating a possible cell dependency.

Inhibition of *N*-glycanase activity can reportedly be measured using the ddVENUS assay developed by Grotzke *et al.* 2013. The ddVENUS assay was originally developed to study ERAD (Grotzke et al. 2013) but was first used as a measure of *N*-glycanase activity in He *et al.* 2015. This assay has been used several times since to measure the activity of *N*-glycanase in multiple models (Tomlin et al. 2017, Kong et al. 2018). In HEK cells, this assay exhibited a higher level of background fluorescence compared to other published models and had a higher calculated IC<sub>50</sub> value compared to other cell types. This may be due to cell dependent or differences in experimental design. In the study by (Tomlin et al. 2017) Z-VAD-fmk was added to K562 cells for 7 h whereas in HEK cells, incubation times below 18 h found no change in fluorescence. Furthermore, this method has not been validated against other glycan processing enzymes (such as ENGase) against which a number of inhibitors have been identified (Y. Bi et al. 2017).

The glycan profile of cells treated with both pharmacological agents was also examined. Previous studies have looked at the lectin profile of MEF cells *N*-glycanase KO cells (Huang et al. 2015, Fujihira et al. 2017). FITC-ConA staining of *N*-glycanase KO MEF glycoproteins showed similar levels of fluorescence intensity compared to WT and ENGase KOs, however, double KOs showed an increase in fluorescence indicating more high mannose bound glycoproteins (Huang et al. 2015), although this was not quantified. Measurements of *O*-GlcNAc by western blot in *N*-glycanase KO, ENGase and double KO MEF cells found no differences in *O*-GlcNAc levels (Fujihira et al. 2017). This study looks at the overall glycoprotein population against a panel of different lectins in HEK cells using two high mannose binding lectins, two GlcNAc binding lectins and a complex structure binding lectin. No differences in lectin binding were observed. This is perhaps not surprising, as it may be hypothesised that inhibition of *N*-glycanase would preferentially influence proteins to be degraded rather than interfere in the glycosylation of correctly folded proteins. In addition, if proteins were not being degraded efficiently only an increase in *N*-linked high mannose glycans would be expected. A lectin dot blot is a simple method for determining glycan populations and is more commonly used as a qualitative technique rather than a means of absolute quantitation. To increase resolution, proteins can be separated by SDS-Page prior to blotting.

One hypothesis which has been mooted to explain the effects noted in *N*-glycanase deficiency is the possibility of *N*-GlcNAc positive aggregates interfering with *O*-GlcNAc mediated signalling pathways. Literature reporting changes in OGA and OGT found (after exposure to Thiamet G) there was a significant increase in OGA but no change in OGT; indicating OGA would be more of a measure of disruption of *O*-GlcNAcylation than OGT. No positive control, however, was used in this study to identify if OGA would be increased following Thiamet G inhibition (Zhang et al. 2014).

To explore potential changes in *O*-GlcNAc mediated signalling, gene expression of *O*-GlcNAc modifying enzymes OGA and OGT was employed. This method is likely to only detect large, global changes in *O*-GlcNAc levels, and no change in OGA or OGT post Z-VAD-fmk or Q-VD-OPh treatment was observed in HEK cells. There is not likely to be any significant change in *O*-GlcNAc when these results are considered alongside the lectin blots of WGA and sWGA. This does not completely rule out a disruption in *O*-GlcNAcylation, but is suggestive that any effects are more likely to involve a specific substrate rather than a global change in population.

ERAD dysfunction is often accompanied by ER stress, and this has been suggested as a consequence of *N*-glycanase inhibition (Martinet et al. 2006a, Misaghi et al. 2005). In this study, ER stress was measured by quantification of expression levels of well-characterised UPR markers and, assessment of ER Ca<sup>2+</sup> handling. Together these results can be used to identify ER stress in a cellular model. Cells treated with Z-VAD-fmk and Q-VD-OPh were analysed for up-regulation of the UPR associated proteins CHOP, BiP, ATF4 and EDEM. No significant increase in any of these markers was observed. As many studies have found associations with Ca<sup>2+</sup> handling and stress, ER Ca<sup>2+</sup> handling was also examined. In this study, Ca<sup>2+</sup> levels were measured using the ratiometric dye Fura-2 and leak was induced using the SERCA inhibitor Thapsigargin (Gerasimenko et al. 2014, Lomax et al. 2002, Kopach et al. 2005). No significant differences were found in the levels of ER Ca<sup>2+</sup> release in HEK cells treated with Z-VAD-fmk. In addition, ROS are often present during numerous types of cellular stress and, in this study, was examined by flow cytometry. ROS was measured using flow cytometry analysis of the fluorescence intensity of the ROS indicator ROS Brite 570. There were no significant differences found in HEK cells treated with Z-VAD-fmk or Q-VD-OPh when compared to the vehicle and untreated cells. Combined, these results suggest that treatment with Z-VAD-fmk does not induce significant ER stress.



Increased ER stress and increased ROS has been linked to the presence of protein aggregates. A recent study has suggested the presence of aggregates in *N*-glycanase KO cells in culture (Huang et al. 2015), although it should be noted that this involved transfection of a model ERAD substrate (which has the potential to cause stress in itself by increasing protein load). Other studies have found links between *N*-glycanase and aggregation determined by Congo Red visualisation (Fujihira et al. 2017) a technique commonly used to detect amyloid fibril aggregates (Gregoire et al. 2012). In this study, the presence of protein aggregates was examined through quantification of ThT fluorescence and these results further validated using flow cytometry. By using a general stain, endogenous protein aggregates can be studied in live cells. An increase in ThT fluorescence intensity per cell was identified in both methods, although no distinct aggregates were found. By using flow cytometry methods it could also be confirmed that there were no discrete sub-populations more susceptible to Z-VAD-fmk treatment. These results could perhaps be attributed to increased soluble misfolded proteins or, by an increase in ER luminal size and binding to proteins that have not folded correctly yet in the lumen. To fully identify if there is a role for protein aggregates in this model, another method would need to be used (for example, examination of the presence of ubiquitinated proteins or a measure of ER content).

Activation of autophagy is often accompanied by a stress signal (Guo and White 2016). Despite the absence of discrete protein aggregates and lack of ER stress markers, there was an induction of autophagy at 72 h in cells treated with Z-VAD-fmk (but not Q-VD-OPh). Autophagy was assessed by the production of GFP-LC3 positive-puncta in a stably-transfected HEK cell-line. A stable cell line was used over transient transfections due to a more homogenous population and a higher number of cells expressing the construct. Although both methods cause increased levels of LC3 (which can promote aggregates) using a stable cell line avoids potential stress resulting from transfection. The increase in levels of autophagy resulting from Z-VAD-fmk treatment was also confirmed using a GFP-RFP-LC3 construct. The effects on autophagy following Z-VAD-fmk treatment were consistent across both cell lines. Efforts to further confirm autophagy activation using immunoblotting were unsuccessful.

Further support for the induction of autophagy following Z-VAD-fmk treatment (but not Q-VD-OPh treatment) comes from the use of genetic KO MEFs. ATG13 KO MEF cells showed increased cell toxicity measured by MTT in the presence of Z-VAD-fmk but not to Q-VD-OPh. Although not a direct measurement of autophagy, this serves to confirm Z-VAD-fmk has toxic

effects on cells which cannot undergo autophagy, and is suggestive of a mechanism whereby autophagy is protective under conditions of Z-VAD-fmk exposure.

To examine if the effects observed on Z-VAD-fmk treatment on autophagy and ThT fluorescence could be rescued by over expression of a Z-VAD-fmk insensitive form of the enzyme, a Z-VAD-fmk insensitive PNGase construct suitable for mammalian expression was constructed. Cloning and sequence analysis of the plasmid found correct incorporation of bacterial PNGase F into the backbone plasmid. However, transfection of the plasmid into HEK cells resulted in high levels of cell death. It is possible that these toxic effects were a result of large quantities of the enzyme being produced, or the incompatibility of bacterial proteins with the expression host (similar levels of toxicity were observed when transfection was tested with a plasmid from another bacterial colony which had the same sequences and the effects were the same indicating it is not just a single plasmid effect but general to transfections of bacterial PNGase).

Pharmacological inhibitors are rarely specific and as previously explored, Z-VAD-fmk has a high number of potential targets. These include multiple caspases, *N*-glycanase and various lysosomal cathepsins. To further confirm that the effects found under Z-VAD-fmk treatment were linked to *N*-glycanase inhibition, the effects following genetic ablation of *N*-glycanase were examined using siRNA.

#### 4.1 Introduction

The interplay between autophagy and apoptosis is key to cellular maintenance and survival. Autophagy has been implicated in apoptosis in several cases (termed autophagic cell death) (Button et al. 2015). Caspases can also play a role in the regulation of autophagy via interactions with BECLIN-1. Caspase 3 mediates BECLIN-1 cleavage, decreasing autophagy and promoting apoptosis (Zhu et al. 2010, Wirawan et al. 2010, Button et al. 2015). Therefore, inhibition of caspases may increase levels of active BECLIN-1 inducing autophagy. To induce apoptosis, the c-terminal fragment of BECLIN-1 localises to the mitochondria and induces the release of cytochrome c (Li et al. 2011).

Cathepsin inhibition halts autophagic flux through lysosomal dysfunction. Several caspase inhibitors including Z-VAD-fmk have been identified as inhibitors of cathepsins (Schotte et al. 1999). Cathepsins are lysosomal proteases involved in cargo degradation (Turk et al. 2012). The  $IC_{50}$  of cathepsins by Z-VAD-fmk and other caspase inhibitors with similar structures (Z-DVED-fmk **12** and Z-YVAD-fmk **13**) are shown in Table 4.1. The  $IC_{50}$  was determined using crude lysate from rat liver incubated with inhibitors (30 min, 25 °C). Active cathepsins were labelled with 125I-DCG-04 which covalently binds the active site of cathepsins. Loss of labelling indicates inhibition of the cathepsins by the caspase inhibitors (Rozman-Pungerčar et al. 2003). The same group also examined at cathepsin inhibition in a cell culture model. In Jurkat T cells treatment with Z-VAD-fmk (100  $\mu$ M, 24 h) followed by addition of Z-FR-AMC and Z-RR-AMC (cathepsin B substrates) the amount of AMC released was measured. Z-VAD-fmk treatment resulted in a loss of more than 50 % activity. In HEK293 cells, treatment resulted in a loss of 88-96 % cathepsin activity (Rozman-Pungerčar et al. 2003). This crossover of inhibition is likely due to the cysteine residue in the active sites of both caspases and cathepsin.

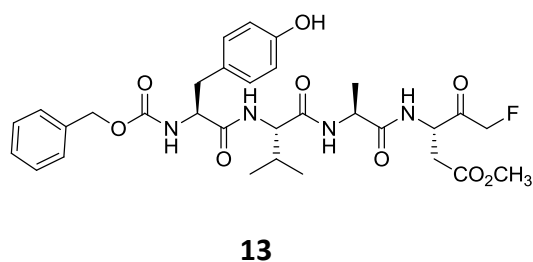
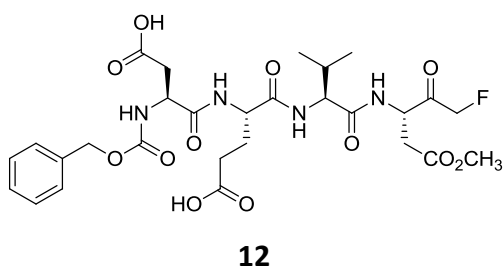


**Table 4.1 IC<sub>50</sub> of Cathepsin inhibition of caspase inhibitors**

	Z-DEVD-fmk 11	Z-YVAD-fmk 12	Z-VAD-fmk 1
<b>Cathepsin X</b>	0.63 $\mu$ M	0.65 $\mu$ M	1.9 $\mu$ M
<b>Cathepsin B</b>	0.62 $\mu$ M	1.4 $\mu$ M	3.1 $\mu$ M
<b>Cathepsin C</b>	100-170 $\mu$ M	100-170 $\mu$ M	<i>Data not found</i>
<b>Cathepsin J</b>	100-170 $\mu$ M	100-170 $\mu$ M	<i>Data not found</i>
<b>Cathepsin H</b>	>200 $\mu$ M	>200 $\mu$ M	>200 $\mu$ M

Lysosomes are an important component of autophagy as well as antigen signalling and cellular stress signalling (Man and Kanneganti 2016). Lysosomes fuse with autophagosomes to produce autolysosomes which contain cathepsins, as well as other hydrolytic enzymes and degrades cargo. Inhibition of cathepsins results in an increase in LC3II due to the protein not being degraded completely in multiple cells types (Jung et al. 2015, Herzog et al. 2012). Treatment with Z-VAD-fmk (50  $\mu$ M, 72 h) found an increase in autophagosomes although this was not found with pan-caspase inhibition (Q-VD-OPh, 50  $\mu$ M, 72 h) but also no increased ROS production which could be due to inhibition of BECLIN-1 cleavage.

Exploring the effects Z-VAD-fmk on *N*-glycanase is therefore complicated, as Z-VAD-fmk has been shown to exert inhibitory effects on a number of other proteins implicated in the regulation of autophagy and apoptosis (including caspases, cathepsins and proteinases). In order to determine if the effects of Z-VAD-fmk treatment are specifically linked to the inhibition of *N*-glycanase in HEK cells, siRNA was used as tool to selectively reduce the levels of *N*-glycanase expression in the cell.

RNA interference (RNAi) is a powerful tool which can be employed to effect transient reduction in levels of specific proteins within the cell. This mechanism relies upon the capacity of anti-sense RNA to inhibit gene expression (Kim and Rossi 2008) and can be employed in an experimental setting to selectively silence or knock-down the expression of a target gene, allowing the assessment of the individual contribution of genes to a specific observed cellular effect. RNAi is an umbrella term for different mechanisms of RNA based gene regulation via the degradation of specific mRNA. RNAi is mediated by double stranded RNA (dsRNA) including siRNA and shRNA.

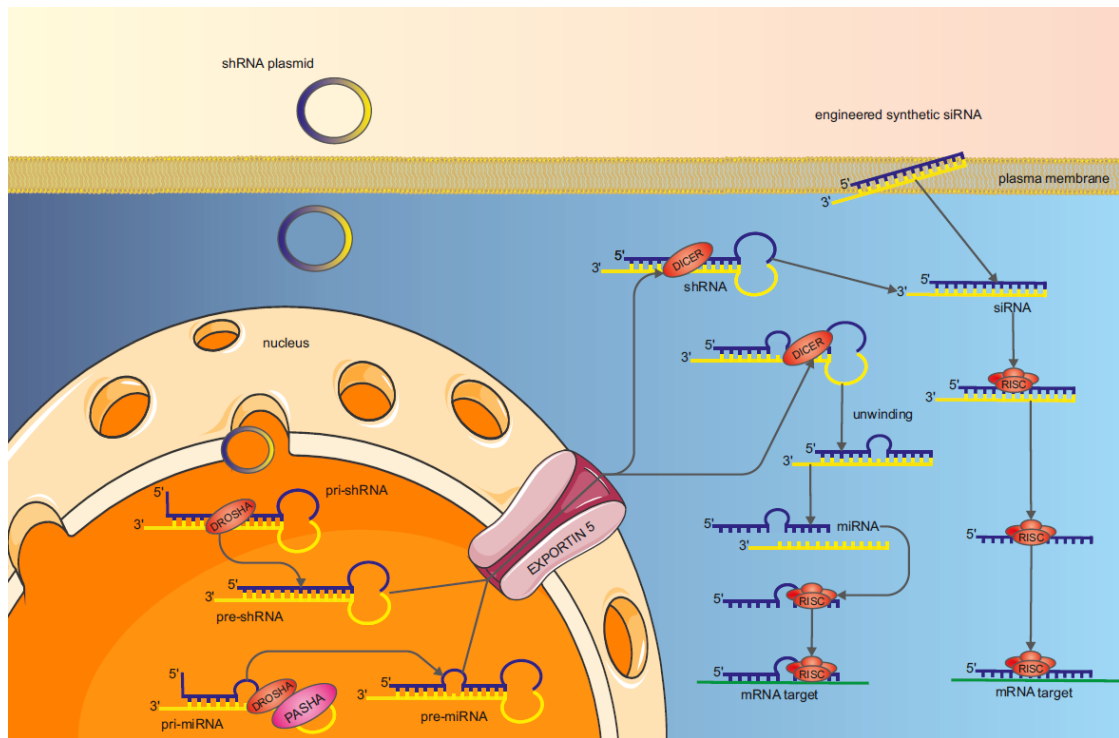


**Figure 4.1** Diagram depicting the mode of action of siRNA and shRNA gene silencing.

Eukaryotic cells contain micro RNAs (miRNA), an endogenous system of gene silencing via mRNA degradation. Figure 4.1 shows the processing of synthetic miRNA which start as large primary RNA (pri-mRNA) which are processed in the nucleus by Drosha and Pasha to produce ~ 65-75 nucleotides long hairpin pre-miRNAs (Redfern et al. 2013, Tan et al. 2011). These are exported into the cytoplasm by Exportin 5 where they interact with the Dicer complex containing TRBP and PACT which are involved in miRNA processing (Wilson et al. 2015). Dicer further processes these dsRNA molecules in shorter, around 22 nucleotide long mature miRNA. The guide RNA sequence can then interact with the RNA-induced silencing complex (RISC). The RISC complex is composed of many different proteins. Guide RNA sequences are loaded onto Argonaute proteins, the catalytic enzyme required for miRNA processing (Redfern et al. 2013). Under experimental conditions, synthetic double stranded RNA is introduced into cells in the form of siRNA or shRNA. This can be achieved by a variety of methods, including by electroporation, viral mediated delivery or the use of cationic liposome based transfection agents or by modified siRNA that can be taken up by cells in a passive manner (Jie Wang et al. 2010). Exogenous siRNAs are usually around 21-23 base pairs of dsRNA with symmetric 2-3 base pair overhangs. The siRNA structures also contain a 5' phosphate group and a 3' hydroxyl group (Pham and Sontheimer 2005). Once inside the cell the siRNA forms a complex with RISC. RISC is composed of proteins including Argonaute 2,

Dicer and the Tar RNA binding protein (TRBP) (Daniels et al. 2009). Collectively, this forms the minimal RNA-induced silencing complex (RISC) assembly. The siRNA is unzipped and the anti-sense strand is retained as a guide. This guide RNA binds to complementary target mRNA creating a new dsRNA which is degraded by Dicer complex (Bartlett and Davis 2006, Hannus et al. 2014). Without the mRNA of a protein it cannot be translated resulting in a knockdown of the protein.

There are a number of factors that interfere with the efficacy of siRNA silencing. Efficient siRNA knockdown relies on efficient delivery into cells, the efficiency of the siRNA molecules to knockdown the target gene and the specificity of that pool. The first is that the efficient delivery of siRNA into cells is dependent upon the method of transfection. Different transfection strategies are available as shown in Table 4.2. Transfection is a common way of introducing exogenous DNA into cell culture, and has been employed in this study. However, the method used can impact cellular health and metabolic efficiency. If cells are not amenable to common transfection methods, electroporation or viral mediated methods may be used as alternatives.

**Table 4.2 Transfection strategies for siRNA**

Cellular Uptake Strategy	Advantages	Disadvantages
<b>Transfection (Cationic liposomes / polymer)</b>	<ul style="list-style-type: none"> <li>• Fast</li> <li>• Many cell types</li> <li>• Use for plasmid DNA, ssDNA, siRNA and shRNA</li> </ul>	<ul style="list-style-type: none"> <li>• Not all cells are favourable to transfection methods</li> </ul>
<b>Electroporation</b>	<ul style="list-style-type: none"> <li>• Recommended for difficult to transfect cells</li> </ul>	<ul style="list-style-type: none"> <li>• Increased cell death</li> </ul>
<b>Viral-mediated</b>	<ul style="list-style-type: none"> <li>• Good for difficult to transfect cells</li> <li>• Used for stable transfections</li> </ul>	<ul style="list-style-type: none"> <li>• Undertaken under Biosafety 2 conditions</li> </ul>

Increased siRNA concentration increases the amplitude and duration of siRNA mediated knockdown *in vitro* and *in vivo* (Bartlett and Davis 2006, Caffrey et al. 2011, Hannus et al.

2014). As well as concentration, the doubling time of the cell line can affect the duration of gene silencing. Fast doubling times (~ 1 day) have a silencing duration of approximately 7 days. In non-dividing cells knockdown is predicted to last around 21 days (Bartlett and Davis 2006). Indicating dilution via cell division of the siRNA impacts the ability to knockdown target proteins significantly.

Small interfering RNA is not completely specific to the target gene and off target effects are sometimes seen which can lead to complications in interpretations if other mRNAs are also being knocked down. Off-target effects can be due to partial complementarity to other mRNA sequences apart from the intended target, inflammatory response caused by delivery technique used such as lipid transfection reagents or changes in endogenous microRNA processing by saturation of the machinery with synthetic siRNA (Jackson and Linsley 2010).

Increased doses of siRNA correlates with increased number of off-target gene silencing (Caffrey et al. 2011). Pooling siRNAs can also help to reduce off-target effects. All the siRNA sequences target the specific gene but will have different levels of off-target effects meaning that there is efficient target knockdown but less off-target silencing (Jackson and Linsley 2010). The siRNA used in this study was a pool of four different siRNA species targeting *N*-glycanase each with different levels of off-targeting. A blast search of the siRNA sequences have shown the highest sequence homology of 78 % homology of sequence 1 and 3 targeting adhesion G protein-coupled receptor D2 (ADGRD2) and RUN domain containing 3B (RUNDC3B) respectively and sequences 2 and 4 with 73 % targeting GRIP and coiled-coil domain containing 2 (GCC2) and GDNF family receptor alpha 1 (GFRA1) respectively.

Factors involving the stability or the introduction of secondary structures in the siRNA molecule can affect interactions with the target mRNA decreasing silencing. However, there are now a number of companies dedicated to the design of siRNA products that remove secondary structures and increase intracellular stability.

Other than sequence design and transfection optimisation, factors innate to the target or cell line effects the efficiency of gene silencing that are still not well understood. For example, knockdown studies using the KRT7 gene found knockdown of greater the 90 % In HeLa cells but only around 30 % decrease in HEK 293 cells compared to controls (Hong et al. 2014). Although the reason for these differences is still unclear, one reason could be changes in target concentration or life-span of the target in different cell types.

## 4.2 Aims and Objectives

The aim of this chapter is to look at the effect of genetically downregulating *N*-glycanase in HEK cells. This will allow confirmation of the cause of the effects of treatment with the pharmacological agent Z-VAD-fmk and enable the further characterisation of the effects of *N*-glycanase deficiency in a standard cell culture model.

## 4.3 Results

In this section, the effects of siRNA mediated knockdown in HEK cells were characterised. The efficiency of siRNA mediated knockdown was assessed by quantification of *N*-glycanase mRNA levels. The effects on cell viability were established by MTT cytotoxicity assay. *N*-glycanase activity was measured using the ddVENUS fluorescence assay 72 h post transfection. The effect on the glycoprotein population was assessed by lectin binding profile of whole cell lysates. Evidence of protein aggregates was studied using the  $\beta$ -sheet binding dye, ThT **11**. The level of autophagy following *N*-glycanase deficiency was studied through quantification of the number of GFP-LC3 positive puncta in HEK cells.

Protein aggregates or dysfunction in protein degradation as hypothesised to occur in *N*-glycanase deficiency (Huang et al. 2015, Martinet et al. 2006b, Misaghi et al. 2005) also play a role in the activation of ER stress and the unfolded protein response (UPR). Genes upregulated during the UPR were tested under siRNA knockdown of *N*-glycanase. Another measure of ER functioning and stress is  $\text{Ca}^{2+}$  handling in the ER. Stress can lead to a 'leakiness' in ER  $\text{Ca}^{2+}$  channels. ER  $\text{Ca}^{2+}$  was quantified by the ratiometric Fura-2 under inhibition of SERCA channels by Thapsigargin. Protein aggregation has also been linked in other disorders with increased oxidative stress. Oxidative stress was measured by flow cytometry fluorescence intensity of the ROS indicator, ROS Brite 570.

As in the previous chapter, the effect on *O*-GlcNAc modifying enzymes was examined. Evidence has been presented that supports the hypothesis that under *N*-glycanase deficiency, another glycan processing enzyme ENGase can act on the glycans of misfolded proteins leaving *N*-GlcNAc positive proteins and this may lead to *O*-GlcNAc dysfunction in cells (Huang et al. 2015). *O*-GlcNAc modifying enzymes, OGA and OGT were used as an indicator of changes in *O*-GlcNAc signalling homeostasis.



#### 4.3.1 No effects on cell viability are observed in cells transfected with NGLY1 siRNA

To test the efficiency of *N*-glycanase knockdown, HEK cells were transfected using Dharmafect™ or jetPRIME® with 10-40 nM ON-TARGET plus siRNA smart pool (Dharmacon L-016457-01-0005) containing four sequences of siRNA targeting *N*-glycanase. RNA was extracted 48 h post-transfection and *N*-glycanase mRNA was measured by RT-qPCR. The control was a non-targeting siRNA control of 40 nM transfected with either Dharmafect™ or jetPRIME®. Transfection using Dharmafect™ resulted in a reduction in *N*-glycanase mRNA by 16 %, 48.4 % and 47.4 % at 10 nM, 25 nM and 40 nM respectively (figure 4.2). JetPRIME® transfection resulted in a reduction of *N*-glycanase mRNA by 64 %, 79 % and 71 % at 10 nM, 25 nM and 40 nM respectively (figure 4.2). To minimise off-target effects, the minimum amount to still provide maximal knockdown was used, 25 nM siRNA with jetPRIME® was used for subsequent tests.

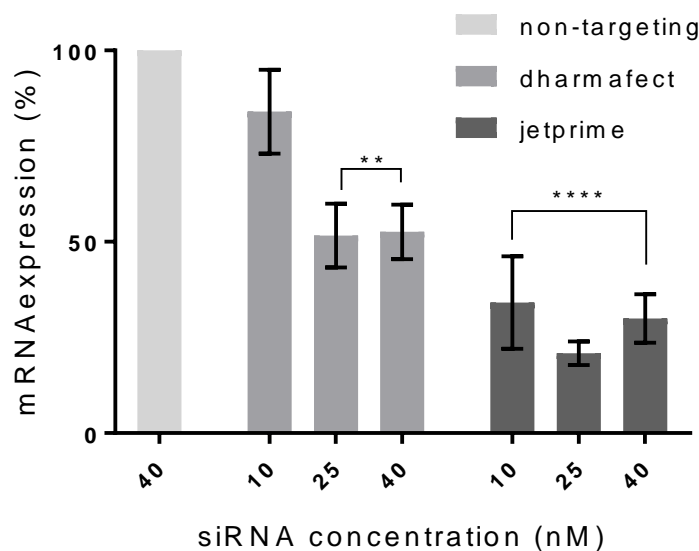


**Figure 4.2** Transfection of NGLY1 siRNA in HEK cells. Data represents the % KD compared to a non-targeting control. Two-way ANOVA, Dunnett's post hoc compared to non-targeting siRNA. \*\*  $P < 0.01$ , \*\*\*  $P < 0.001$ , Error bars  $\pm$  SEM,  $n=3$ .  $IC_{50}$  calculated for Dharmafect = 29.73 nM.  $IC_{50}$  calculated for JetPRIME® = 1.4 nM from three concentrations.

Z-VAD-fmk did not show a decrease in cell viability, although this could be due to its role in caspase inhibition. Cell viability was assessed using an MTT assay comparing siRNA knockdown to a non-targeting control matched to the same time post-transfection. Figure 4.3 shows no significant decrease in cell viability after 7 d post-transfection when compared to day 0.

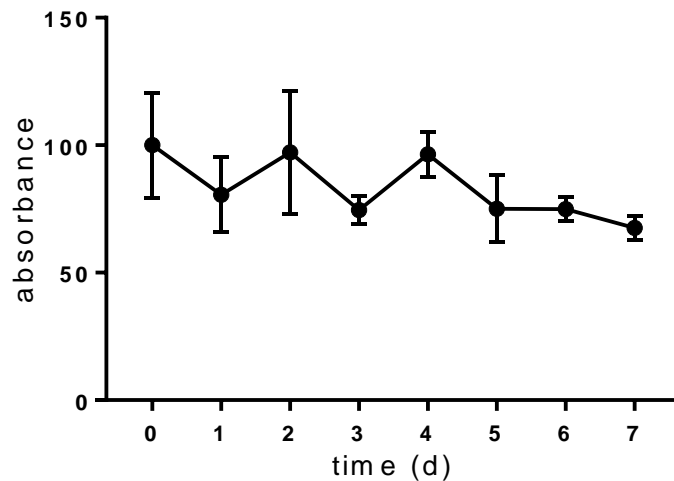


**Figure 4.3 MTT cell viability assay. HEK cells transfected with 25 nM NGLY1 siRNA over 7 days. Data normalised to non-targeting control of the same time and Day 0 represented as 100 %. One-way ANOVA. No significant differences were found compared to time 0.**

#### 4.3.2 Knockdown of *N*-glycanase decreased fluorescence of the deglycosylation dependent VENUS protein

The levels of mRNA do not always reflect protein and activity levels. Western blotting can determine the level of specific proteins in a sample, however, western blotting of *N*-glycanase proved unsuccessful. The deglycosylation dependent activity of the ddVENUS fluorescence assay was used to determine effective knockdown of *N*-glycanase activity. Fluorescence signal in HEK cells was measured three days post-transfection. Figure 4.4 shows the significant reduction in fluorescence intensity as a percentage compared to the non-targeting control. There was a significant different in median fluorescence intensity with a 68 % reduction.

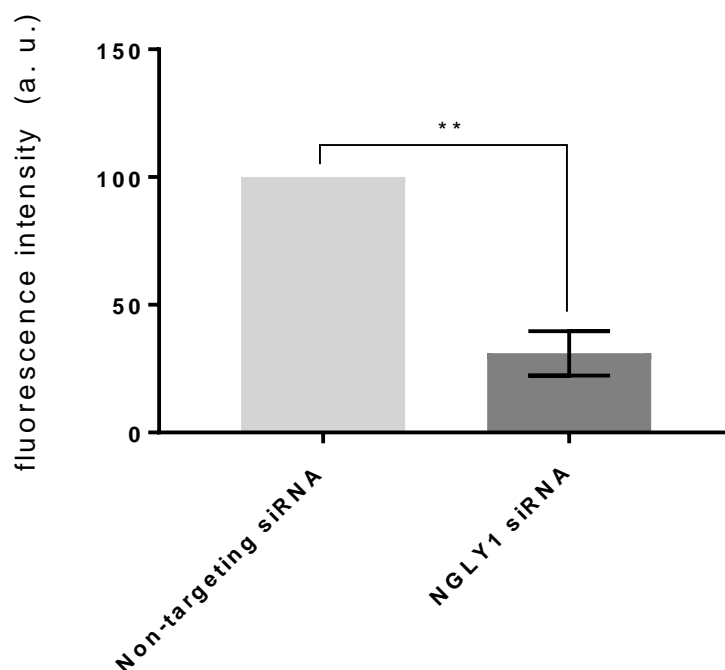


**Figure 4.4 ddVENUS fluorescence is reduced by 68 % 72 h post-transfection. HEK cells were transfected with NGLY1 siRNA or non-targeting siRNA (25 nM) with JetPRIME® for 3 d followed by transfection with ddVENUS construct with JetPEI. After 72 h fluorescence intensity was analysed by flow cytometry. Data represents percentage of fluorescence normalised to non-targeting control. Students t-test, \*\* P < 0.01, error bars  $\pm$  SEM,  $n=3$ .**

#### 4.3.3 Glycan profile of cells transfected with NGLY1 siRNA is not affected

Due to *N*-glycanase role as a glycan processing enzyme, the glycoprotein profile was tested using lectin dot blots. HEK cells were transfected with *N*-glycanase or non-targeting siRNA over 5 d. Cells were collected, lysed and whole cell lysates were applied to a nitrocellulose membrane and incubated with ConA, LCA, PHA-E, WGA and sWGA. Figure 4.5 shows the fluorescence intensity of each fluorescein labelled lectin binding to 1  $\mu$ g of whole cell lysate. There was no significant difference in lectin binding compared to the non-targeting controls.

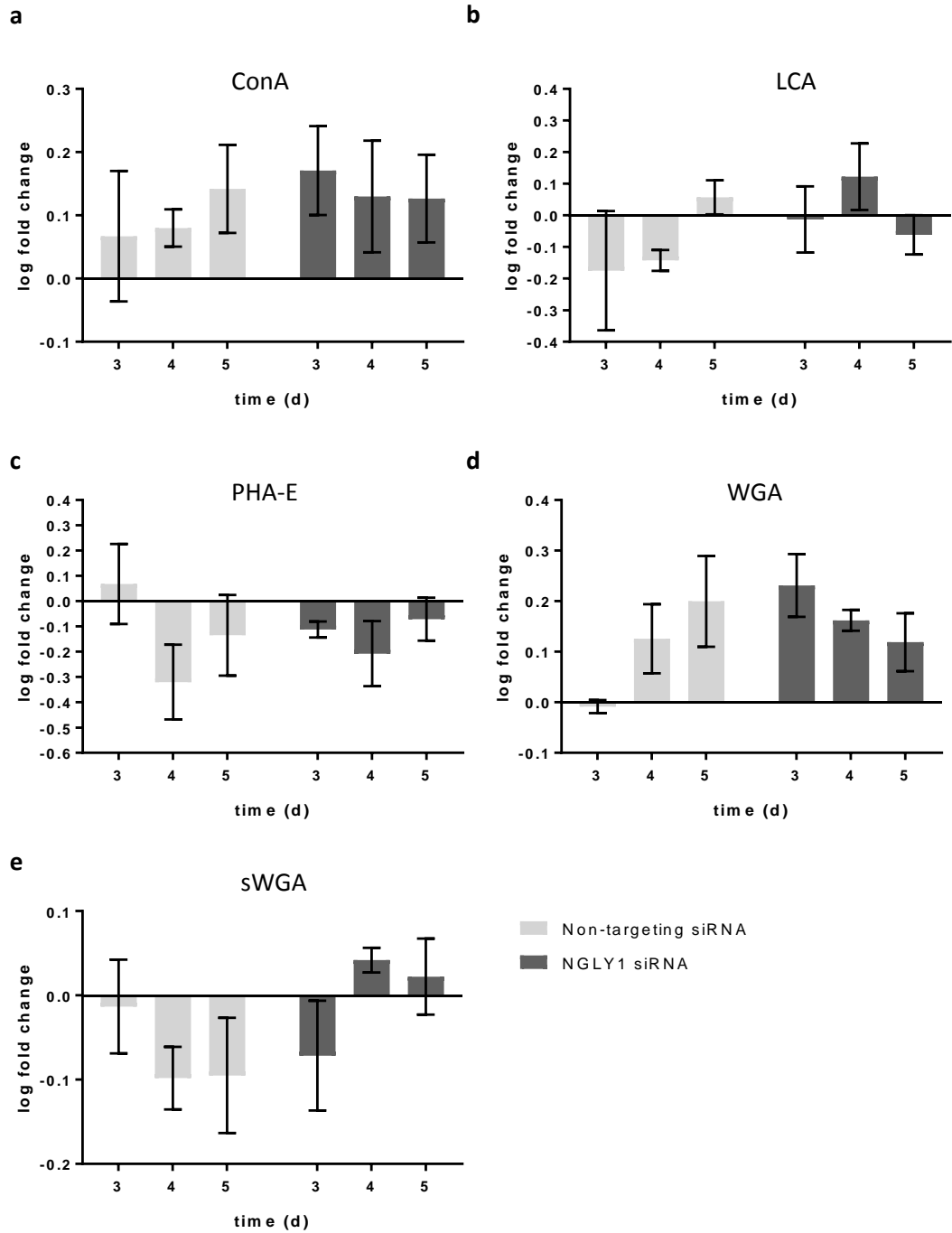


**Figure 4.5** Log<sub>2</sub> fold change of fluorescein-labelled a) ConA, b) LCA, c) PHA-E, d) WGA, e) sWGA biondign to 1  $\mu$ g of whole cell lysate. Fluorescence normalised to untransfected control. Error bars  $\pm$  SEM,  $n=3$ , Two way ANOVA,  $P > 0.05$ .

#### 4.3.4 Differences in Thioflavin T fluorescence are observed following NGLY1 siRNA knockdown

Inhibition of *N*-glycanase using Z-VAD-fmk exhibited a transient increase in ThT fluorescence after 48 h, decreasing to basal levels at 72 h. To determine whether this was an effect caused by decreased *N*-glycanase activity and not caspase/cathepsin inhibition, the staining of ThT was studied after siRNA knockdown of *N*-glycanase. HEK cells were transfected with *N*-glycanase siRNA or the non-targeting control for 3-5 d followed by incubation with ThT (1  $\mu$ M, 30 min) and imaged. Figure **4.6a** shows the fluorescence intensity per cell was normalised to an untreated control. There was a significant difference between non-targeting 4 d and *N*-glycanase siRNA 4 d. However, there was increased variation within the non-targeting control group with significant differences occurring between days 3, 4 and 5. It is the variation in the non-targeting controls which caused this significance leading to unreliable results. This could be due to the transfection causing cellular stress and the cells recovering at different rates over time or variations in transfections on different days. Figure **4.6b** shows representative images of ThT staining day 4 post-transfection.

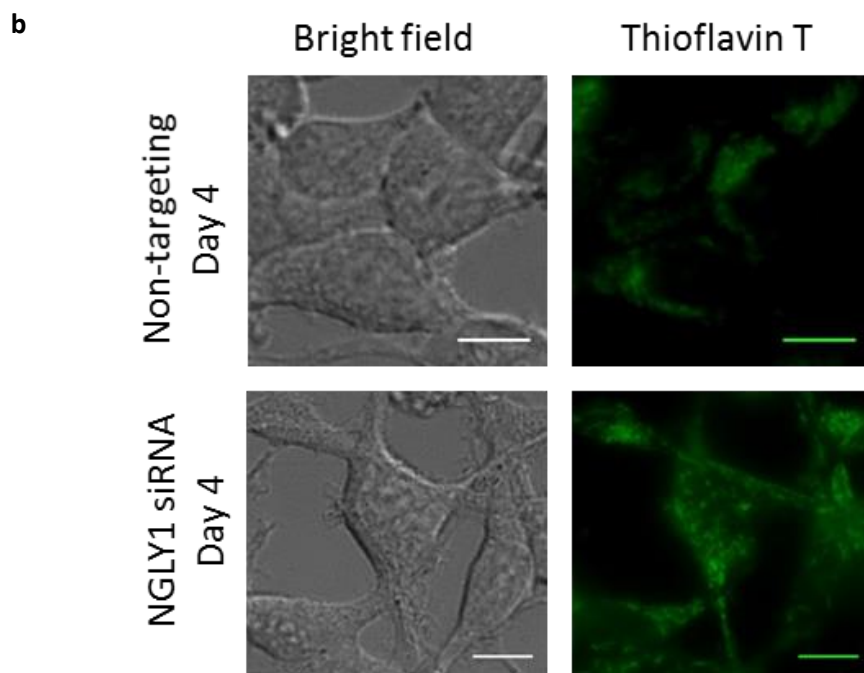
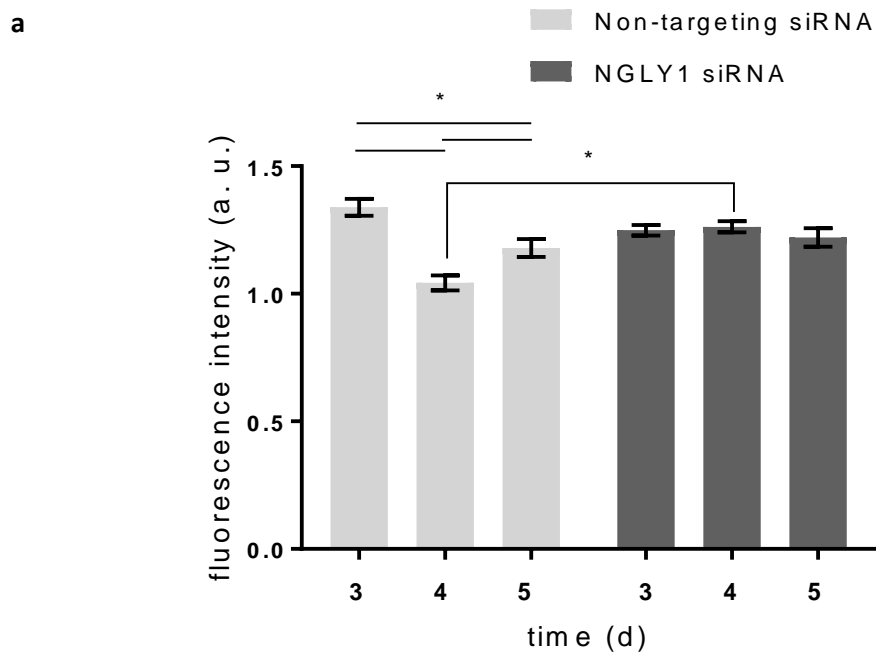


**Figure 4.6** ThT fluorescence in cells transfected with NGLY1 siRNA or non-targeting siRNA over 3-5 d. **a)** HEK cells were stained with ThT (1  $\mu$ M, 0.5 h). Fluorescence intensity per cell was calculated and normalised to an untreated control. A minimum of three images were taken per coverslip and three biological replicates were analysed for each condition. Error bars  $\pm$  SEM,  $n=3$ ,  $P < 0.05$ . Two-way ANOVA, Tukey's post hoc **b)** Representative images of HEK cells 4 d post-transfection with the non-targeting control or NGLY1 siRNA.

Flow cytometry analysis of ThT was also employed to confirm changes seen in fluorescence microscopy, allowing an increased number of cells to be analysed with 10 000 cells gated per condition with three biological replicates. Figure **4.7a** shows the flow cytometric analysis of ThT which included the treatment with the proteasome inhibitor MG132 (100 nM, 18 h) to induce the formation of protein aggregates. There was no significant increase in fluorescence within or between the siRNA groups. However, there was a slight increase in ThT intensity after day 5 of 21 % of the siRNA knockdown which resulted in a non-significant difference between ngly1 siRNA day 5 and MG132. A representative histogram of the ThT fluorescence at day 5 post-transfection is shown in Figure **4.7b**.

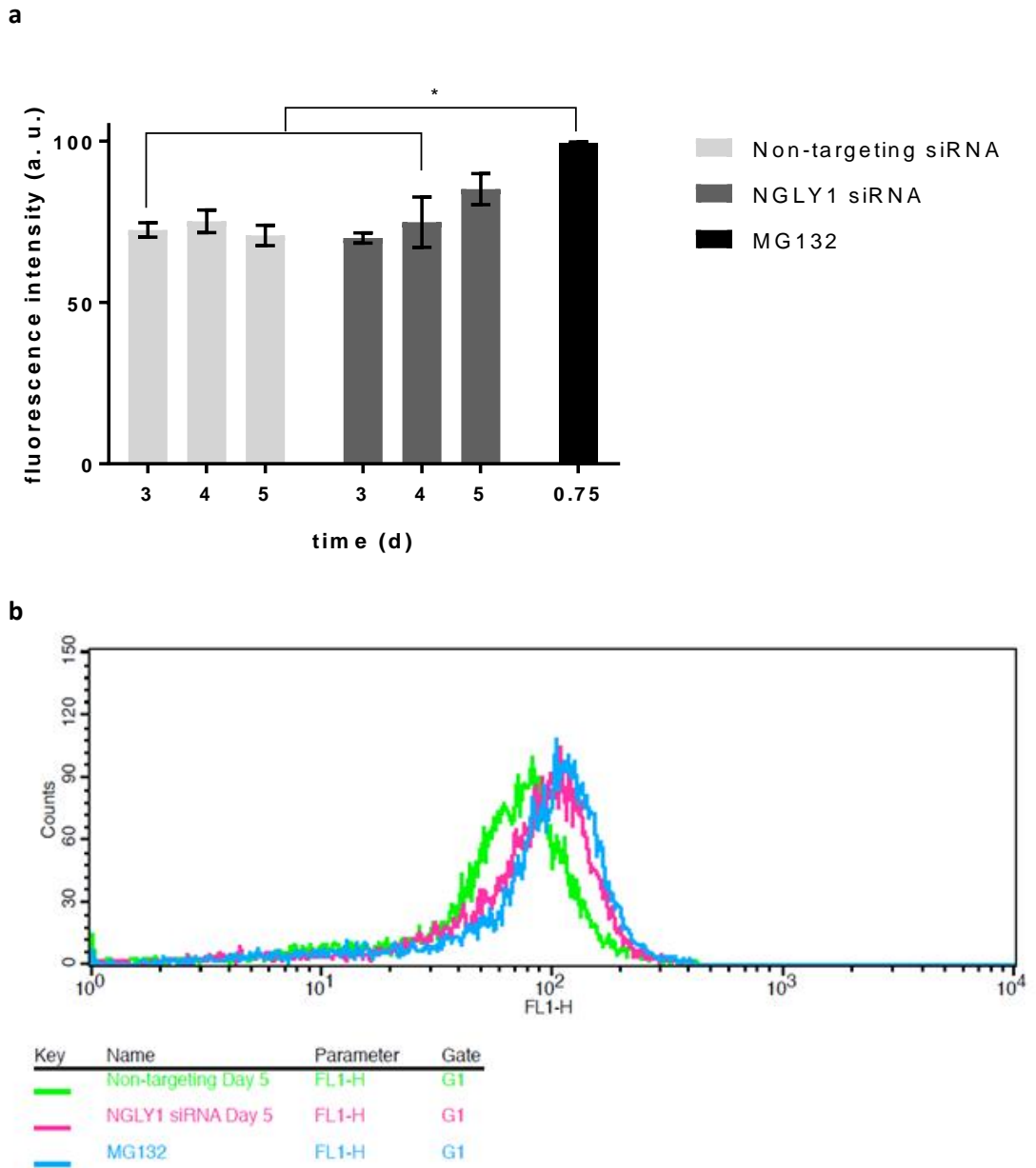


**Figure 4.7** Flow Cytometric analysis of ThT after transfection with 25 nM NGLY1 siRNA or non-targeting siRNA over 3-5 days or MG132 (100 nM, 18 h). **a)** 10 000 cells were calculated per condition with three biological replicates. Median fluorescence intensity of ThT is presented. A significant increase in ThT fluorescence of cells treated with MG132 compared to non-targeting siRNA days 3-5 and NGLY1 siRNA days 3 and 4 was found. MG132 acts as a positive control to increase misfolded proteins. Two-way ANOVA, Tukey's post hoc Error bars  $\pm$  SEM,  $P < 0.05$ ,  $n=3$ . **b)** Representative histogram of ThT fluorescence of Ngly1 siRNA, non-targeting siRNA (25 nM, 5 d) and MG132 (100 nM, 18 h).



#### 4.3.5 Knockdown of *N*-glycanase with siRNA induces autophagy

In order to establish whether siRNA knockdown of *N*-glycanase results in an increase in levels of autophagy, GFP-LC3 labelled autophagosomes were quantified. Figure 4.8 shows the quantitation of GFP positive puncta 3-5 d post-transfection with *N*-glycanase siRNA and non-targeting siRNA control. Five days post-transfection with *N*-glycanase siRNA there was a significant increase in the number of GFP positive puncta compared to the non-targeting siRNA control (with an increase of an average of 2 puncta per cell to 5.8 puncta per cell).

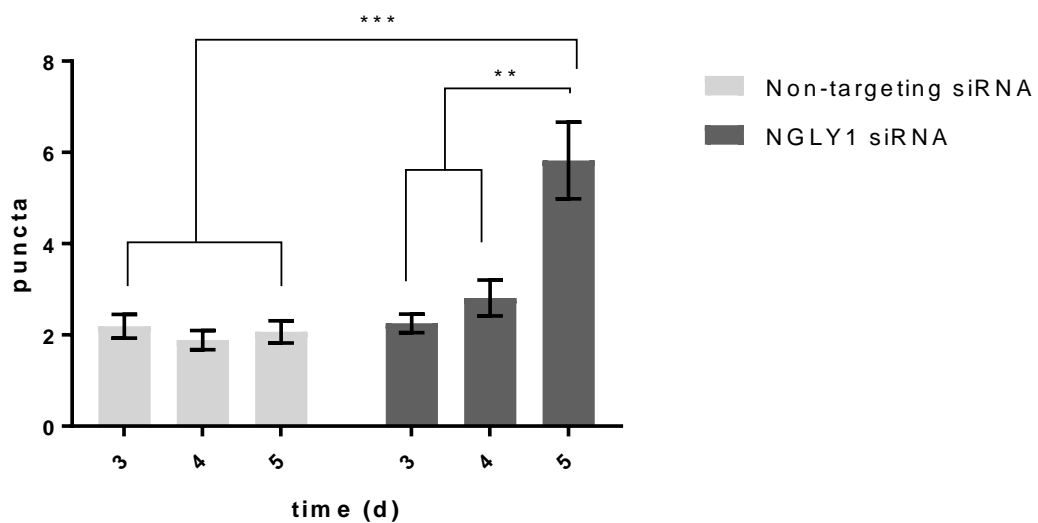


**Figure 4.8** GFP-LC3 puncta are increased after 5 d post-transfection with NGLY1 siRNA (25 nM). Quantitation of the average GFP-LC3 puncta per cell, minimum of three images per coverslip with three biological replicates. Error bars indicate  $\pm$  SEM, \*\*  $P < 0.01$ , \*\*\*  $P < 0.001$ , Two way ANOVA, Tukey's post hoc.

**Figure 4.9** shows representative images of GFP-LC3 HEK cells 5 d post-transfection with both *N*-glycanase and non-targeting siRNA control. This shows an increase in GFP-LC3 puncta in the *N*-glycanase knockdown.

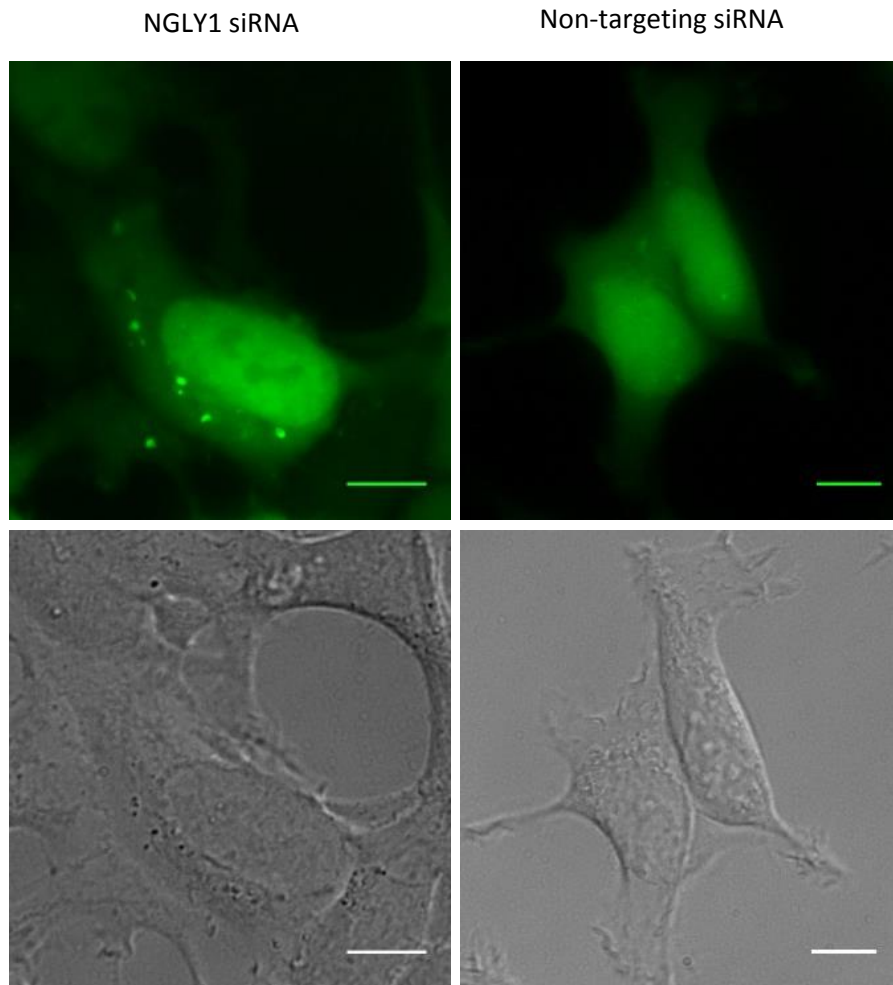


**Figure 4.9** Representative images of HEK cells transfected with NGLY1 siRNA or non-targeting siRNA after 5 days. Scale bar indicates 10  $\mu\text{m}$ .

To determine if the puncta observed are due to a blockage in autophagosome degradation, autophagic flux was examined using the autophagic modifiers Bafilomycin A1 and 3-MA. Figure 4.10 quantified the number of puncta following Bafilomycin and 3-MA treatment. A significant increase in GFP positive puncta following Bafilomycin treatment was observed in both the non-targeting control cells and *N*-glycanase siRNA cells. Following treatment with 3-MA a significant drop the average number of GFP-LC3 positive puncta per cell is observed. This indicates that autophagic flux is not inhibited and the increase in autophagosomes represents a true increase in autophagic activity.

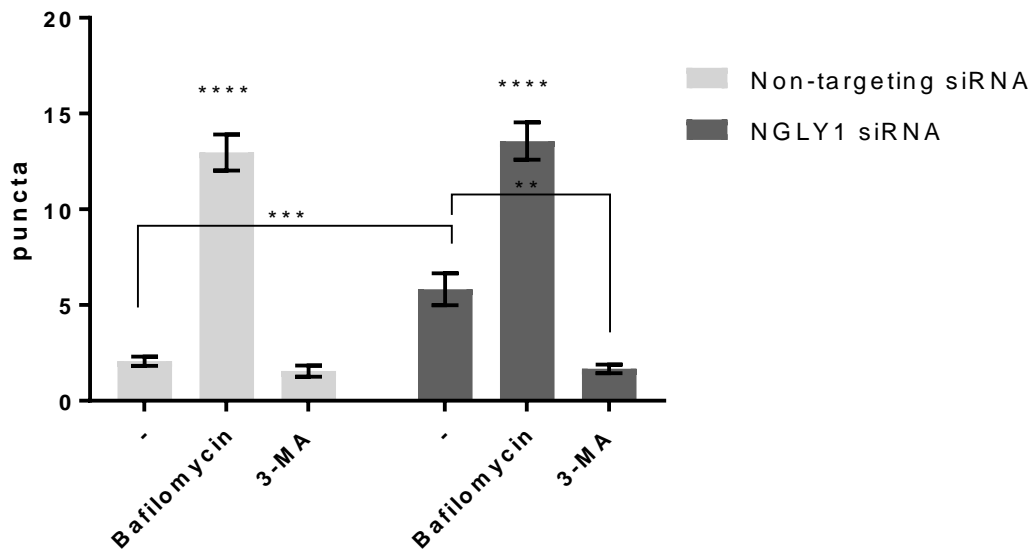


**Figure 4.10 GFP-LC3 puncta per cell after transfection with NGLY1 siRNA of non-targeting siRNA (25 nM, 5 d) with Bafilomycin A1 (100 nM, 1 h) or 3-MA (5 mM, 1 h). Error bars  $\pm$  SEM, \*\* indicates  $P < 0.01$ , \*\*\* indicates  $P < 0.001$ , \*\*\*\* indicates  $P < 0.0001$ . Two-way ANOVA, Tukeys post hoc.**

#### 4.3.6 Autophagy is a protective measure during *N*-glycanase knockdown

ATG13 KO MEFs were sensitive to Z-VAD-fmk treatment and resulted in decreased formazan absorbance. In order to examine if ATG13 KO MEF cells showed sensitivity to genetic ablation of *N*-glycanase, cell viability was assessed by MTT assay. ATG13 KO MEF cells and corresponding WT MEFs were transfected with *N*-glycanase siRNA or the non-targeting control. Figure 4.11 shows the formazan absorbance for each cell type was normalised to the formazan absorbance of the non-targeting siRNA and absorbance was compared to day 0 post-transfection. A significant decrease was observed following day 3; WT MEFs absorbance at 97% compared to day 0 with ATG13 KO MEFs at 62 % of the control and a final reduction to 46 % by day 7 while WT MEFs were at 86 %. These results demonstrate that functional autophagy is important for survival under *N*-glycanase knockdown.

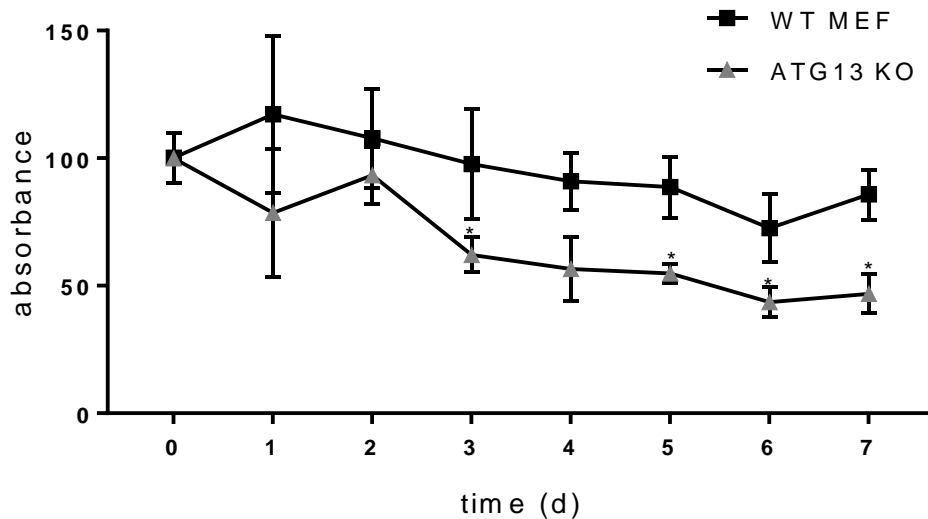


**Figure 4.11 MTT of ATG13 KO and WT MEFs transfected with NGLY1 siRNA or non-targeting control (25 nM). Values normalised to cells transfected with non-targeting siRNA (25 nM) and percentage of Day 0. One-way ANOVA, Dunnett's post hoc, error bars  $\pm$  SEM,  $n=3$ ,  $P < 0.05$ .**

#### 4.3.7 Genetic ablation of *N*-glycanase does not induce cellular stress

*N*-glycanase is closely involved in ERAD by removing glycan chains from misfolded proteins destined to be degraded by the proteasome. Disruption or slowing of this process has been hypothesised to result in ER stress responses (Misaghi et al. 2005, Martinet et al. 2006b). This hypothesis is based upon the observations that the ERAD substrate RTA $\Delta$ m is stabilised under *N*-glycanase deficiency (Huang et al. 2015) indicating the possibility of aggregates and therefore activation of the UPR. Recent evidence from murine models however has found no evidence for ER stress in the absence of *N*-glycanase activity concluded by the absence of protein aggregation staining of Congo red and PAS (Fujihira et al. 2017) but no measure of protein markers associated with ER stress. In order to evaluate if ER stress/activation of the UPR occurs under *N*-glycanase genetic ablation two approaches were employed. The levels of characteristic ER stress markers (CHOP, BiP, ATF4 and EDEM) were examined by RTq-PCR. In addition, ER Ca<sup>2+</sup> homeostasis following genetic ablation of *N*-glycanase activity was also quantified. A last measure of stress measured was oxidative stress (which has been reported to be linked to ER stress (Mota et al. 2015, Dandekar et al. 2015, Rinnerthaler et al. 2015).

Total RNA was extracted from cells 3, 4 and 5 days post transfection with *N*-glycanase or non-targeting siRNA or a positive control for the UPR, MG132 (100 nM, 18 h) and RT-qPCR was

used to determine levels of CHOP, BiP, ATF4 and EDEM. Figure 4.12 shows the  $\log_{10}$  fold change in expression compared to the non-targeting control. There was no significant difference in mRNA levels of these stress markers in cells exposed to *N*-glycanase siRNA. The proteasome inhibitor MG132 (100 nM, 18 h) was used as a positive control (Velentzas et al. 2013)). Significant upregulation of the ER stress markers, CHOP, BiP and ATF4, was observed in the presence of MG132. The results obtained suggest that siRNA knockdown of *N*-glycanase does not induce ER stress and activation of the UPR.

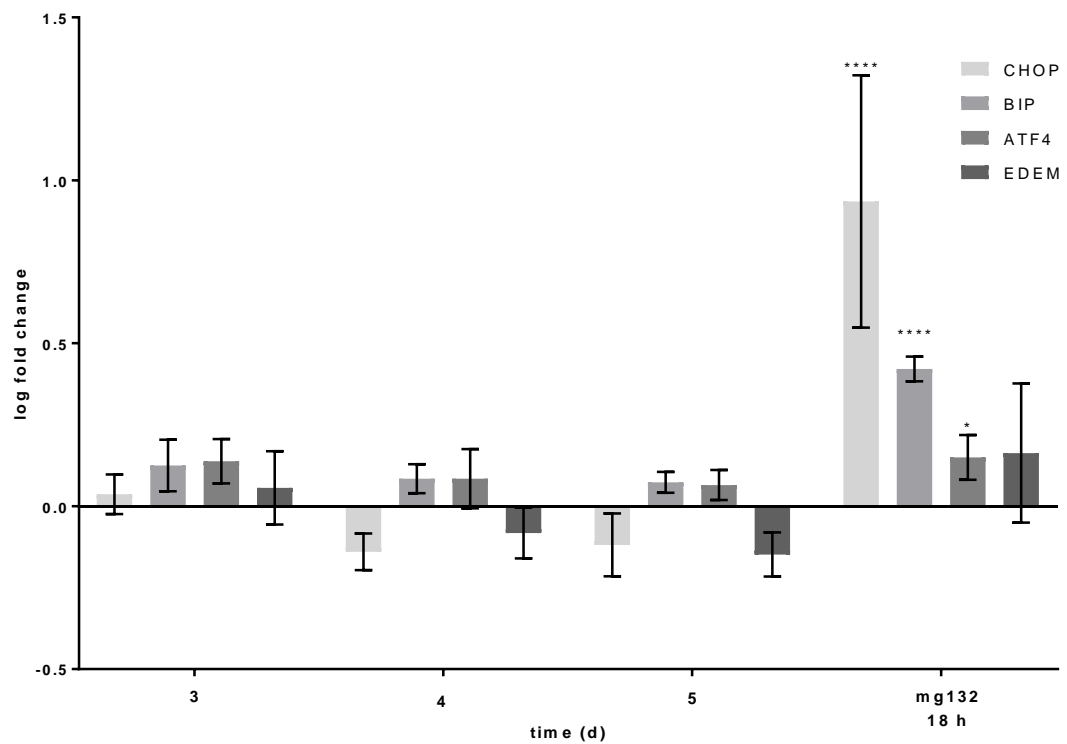


**Figure 4.12 RT-qPCR analysis of CHOP, BiP, ATF4 and EDEM levels in cells transfected with NGLY1 siRNA or non-targeting siRNA (25 nM, 3-5 d). mRNA levels normalised to GAPDH and a non-targeting siRNA control.  $\log_{10}$  fold change is presented with error bars  $\pm$  SEM, \*\*\*\*  $P < 0.0001$ ,  $P < 0.05$ ,  $n=3$ . Data analysed using  $\Delta\Delta C_t$  method. One-way ANOVA followed by Dunnett's post hoc comparing experimental to MG132 positive control.**

Changes in ER  $\text{Ca}^{2+}$  homeostasis provide an additional means of quantifying ER stress. Treatment of cells with Thapsigargin, a sesquiterpene lactone which acts as a potent non-competitive inhibitor of SERCA, results in inability of the ER to replenish ER  $\text{Ca}^{2+}$  stores. As Thapsigargin also induces the influx of calcium ions from the extracellular media into cytosol (Huang et al. 2011), the quantification of ER  $\text{Ca}^{2+}$  profile was carried out in calcium-free imaging buffer supplemented with EDTA (1 mM) (Cameron et al. 2016, Gigout et al. 2005). Figure 4.13 shows HEK cells after siRNA knockdown of *N*-glycanase and non-targeting siRNA loaded with Fura-2 AM (1  $\mu\text{M}$ ) and incubated in calcium free media for 5 min prior to imaging. ER  $\text{Ca}^{2+}$  leak was simulated by the addition of Thapsigargin (1  $\mu\text{M}$ ) after 180 s. As intracellular  $\text{Ca}^{2+}$  increases the fluorescence 340/380 ratio increases.

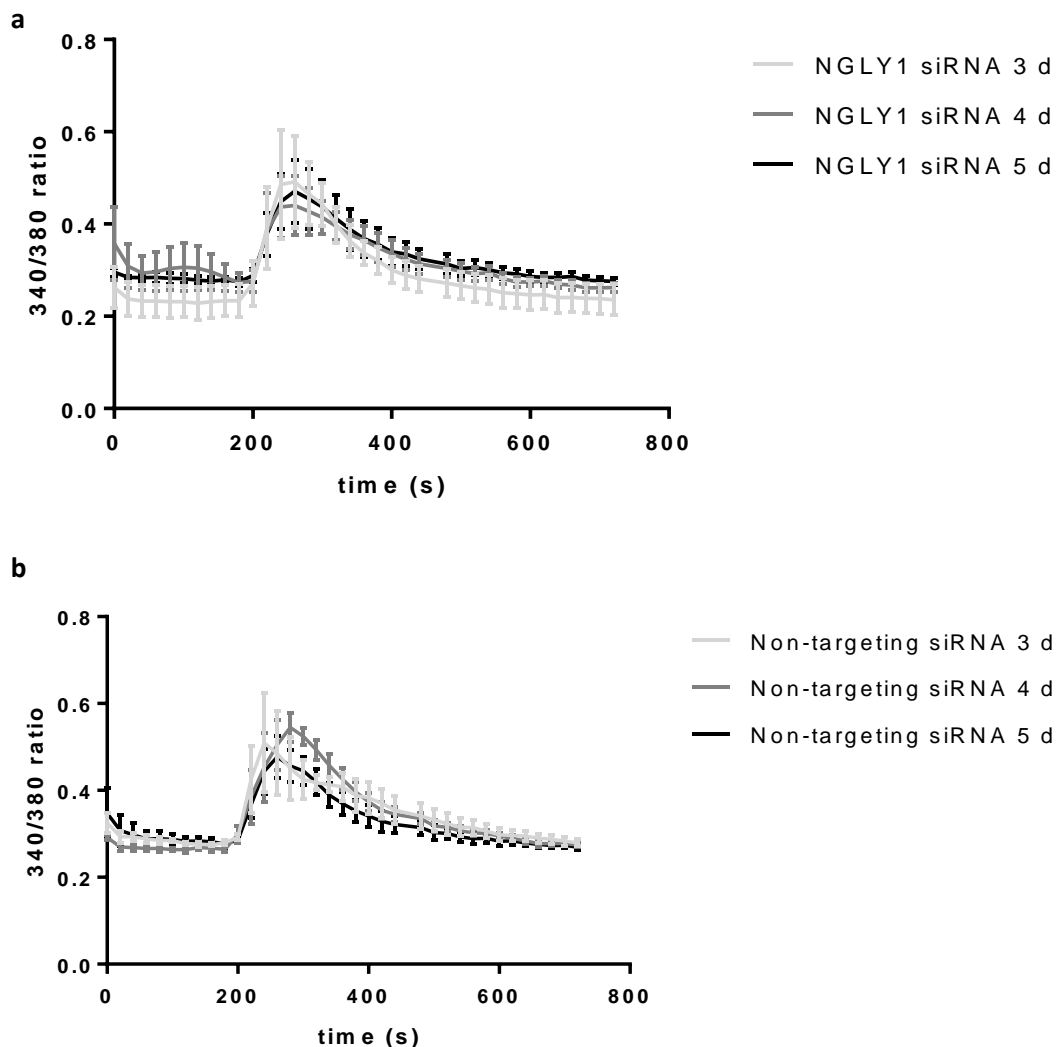
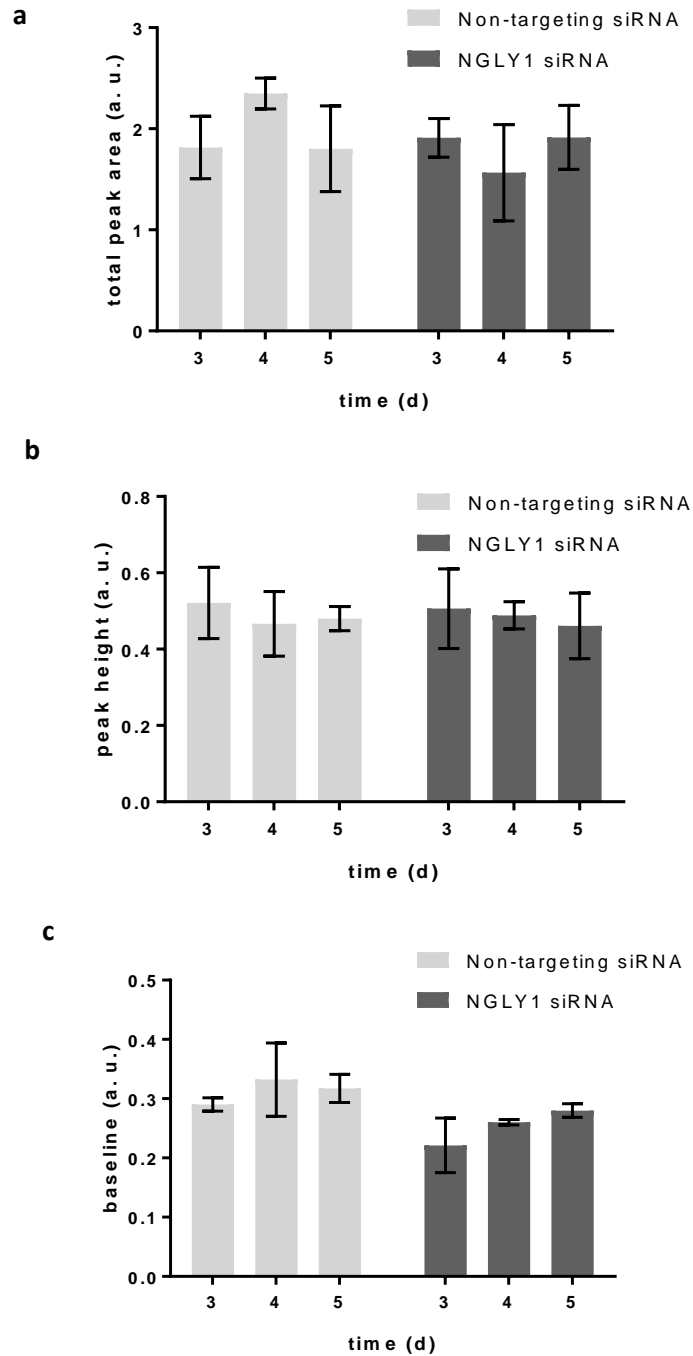


Figure 4.13 Traces of intracellular  $\text{Ca}^{2+}$  in calcium free buffer after the addition of Thapsigargin (1  $\mu\text{M}$ ) at 180 s. HEK cells transfected with either, a) NGLY1 siRNA or, b) non-targeting control (25 nM, 3-5 d). Error bars  $\pm$  SEM,  $n=3$ .

To quantify any differences in  $\text{Ca}^{2+}$  handling the total peak area, peak height and baseline measurements were quantified (Figure 4.14). Figure 4.14a shows the total peak area was measured by taking the area under the curve (AUC). This gives a measure of the total  $\text{Ca}^{2+}$  released from the ER. There was no significant differences in *N*-glycanase targeted siRNA compared to the non-targeting control. Due to no changes in the AUC, the faster  $\text{Ca}^{2+}$  mobilises from the ER the taller the Fura-2 peak. There were no significant changes compared to the non-targeting control (figure 4.14b). The baseline level of Fura-2 fluorescence was recorded for 3 min prior to the addition of Thapsigargin (1  $\mu\text{M}$ ). The measuring of basal not only gives information about the role of ER  $\text{Ca}^{2+}$  but also of basal  $\text{Ca}^{2+}$  levels during rest (figure 4.14c). There were no significant differences measured in baseline cytosolic  $\text{Ca}^{2+}$  levels in *N*-glycanase knocked down cells compared to the non-targeting control.



**Figure 4.14** HEK cells transfected with NGLY1 siRNA or non-targeting siRNA (25 nM, 3-5 d). total peak area was calculated by the AUC. Height of peak was calculated by the highest reading. Baseline calcium levels were calculated from the average of the first eight readings in calcium free imaging buffer. Error bars  $\pm$  SEM,  $n=3$ . Two-way ANOVA, no significant differences.



Mitochondria, as the main energy source of the cell are good indicators of cellular health, and functioning can be affected by other organelles (Marchi et al. 2014, Malhotra and Kaufman 2011). The mitochondria are a major source of ROS leading to oxidative stress (Zorov et al. 2014). Oxidative stress has been defined as a dysfunction in the homeostasis between reactive oxidant species production and antioxidant defences (Betteridge 2000). Oxidative stress is initiated by the presence of increased reactive oxygen species (ROS), such as hydrogen peroxide, nitric oxide, superoxide, hydroxyl and monoxide radicals. ROS levels were quantified by flow cytometry using the ROS indicator ROS Brite™ 570 shown in figure 4.15. There were no significant differences between *N*-glycanase targeting siRNA and the non-targeting control. However, when comparing within the *N*-glycanase siRNA treatment, there was a significant increase after day 3 with an increase from an average of 16 FI units to 21 for days 4 and 5. This is a small increase and is not significant compared to the non-targeting siRNA controls.

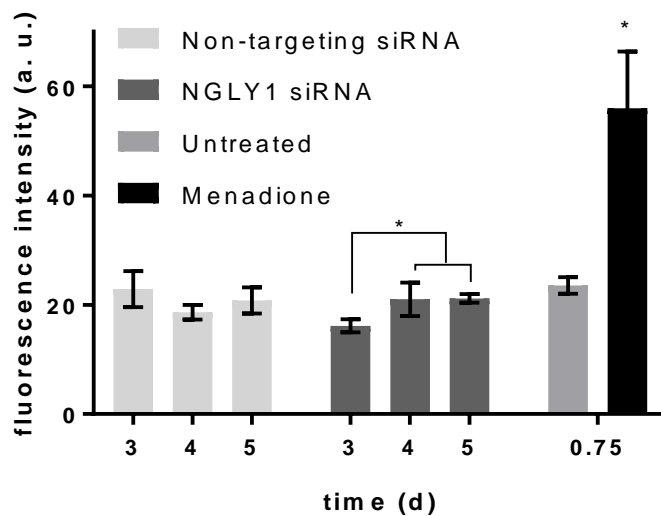


**Figure 4.15** HEK cells transfected with NGLY1 siRNA or non-targeting siRNA (25 nM, 3-5 d) and incubated with Ros Brite 570 (5  $\mu$ M, 30 min). Two-way ANOVA, Tukey's post hoc. \*  $P < 0.05$ , Error bars  $\pm$  SEM,  $n=3$ .

#### 4.3.8 Expression of *O*-GlcNAc homeostasis enzymes are unchanged under *N*-glycanase knockdown

Increased levels of *O*-GlcNAc impacts the expression of the enzymes that control them. OGT and OGA which catalyses the addition and removal of *O*-GlcNAc respectively. Thiamet G, an inhibitor of OGA has been used to study the increase of *O*-GlcNAc and expression levels of OGA and OGT. Inhibition of OGA results in an increase in *O*-GlcNAc and OGA measured by western blot (Zhang et al. 2014). It was further confirmed that Thiamet G increased mRNA transcript level of OGA after 6 h in HELA, SH-SH5y and K562 cell lines (Zhang et al. 2014). If there is an increase in GlcNAc being detected in the cell this may have an impact on the GlcNAc modifying enzymes, especially on OGA levels.

To assess changes in *O*-GlcNAc signalling, mRNA levels were measured by RTq-PCR. HEK cells were transfected with *N*-glycanase or control siRNA and total RNA extracted after 3, 4 and 5 d. Figure **4.16a** shows the  $\log_{10}$  fold change in expression levels of OGA and in figure **4.16b**, OGT levels. Expression was analysed using the  $\Delta\Delta C_t$  method using GAPDH as the housekeeping gene and compared to an untreated control. There were no significant differences in OGT or OGA mRNA expression levels after knockdown over day's 3-5 post transfection. This indicates that *O*-GlcNAc homeostasis is not altered under *N*-glycanase knockdown.

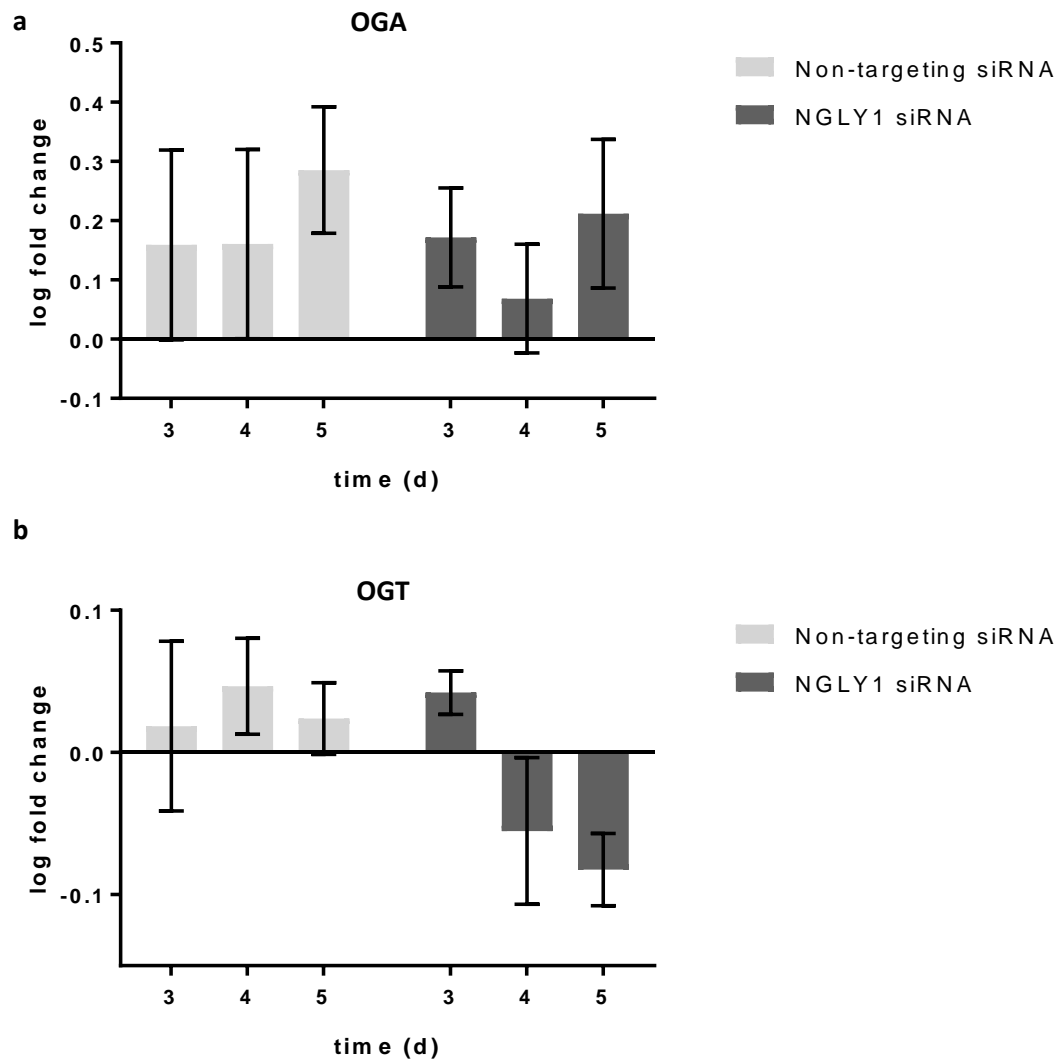


**Figure 4.16 OGA and OGT mRNA levels in HEK cells transfected with NGLY1 siRNA or non-targeting siRNA (25 nM, 3-5 d). a) OGA levels, b) OGT levels. GAPDH was used as the housekeeping gene and values normalised to an untreated control. Fold change was calculated using the  $\Delta\Delta C_t$  method. Two way ANOVA. Error bars  $\pm$  SEM.**

#### 4.4 Discussion

The main situations in which off-target effects of siRNA may be observed include partial complementary binding to other mRNA targets and, saturation of endogenous microRNA machinery by synthetic siRNA leading to changes in endogenous processing (Fischer-Kierzkowska et al. 2011). In this study, a pool of four different siRNA sequences targeting *N*-glycanase were used simultaneously. It has been shown that pools of siRNAs targeting the same gene minimise off-target effects compared to single siRNA (Hannus et al. 2014). The greater the number of siRNA sequences in each siPool means a lower concentration per individual sequence thus diluting the sequence specific off-target effects of each sequence (Hannus et al. 2014).

The results from this series of experiments can be compared to the effects of treatment with the pharmacological inhibitor, Z-VAD-fmk treated cells. Kinetics of *N*-glycanase inhibition varies between experiments as Z-VAD-fmk is a much faster inhibitor compared to mRNA degradation. The effects of Z-VAD-fmk and *N*-glycanase siRNA have similar effects on HEK cells despite this difference in time-course. Both treatments resulted in a significant decrease in the fluorescence of the ddVENUS construct, indicating inhibition and KD of *N*-glycanase. In addition, both treatments showed no significant loss in cell viability measured by MTT assay < 100  $\mu$ M Z-VAD-fmk or, over 7 d post-transfection with siRNA. There were no significant changes in the lectin binding profile of whole cell lysates under either pharmacological or genetic inhibition of *N*-glycanase, indicating no major defects in the glycosylation of proteins.

Under Z-VAD-fmk inhibition there was a consistent transient increase in ThT after 48 h with decrease to basal levels at 72 h. Transfection of *N*-glycanase siRNA resulted in increased variation in ThT fluorescence resulting in a significant increase in ThT fluorescence compared to non-targeting control at 4 d measured by microscopy. Significant variation was also seen between days 3, 4 and 5 of the non-targeting control indicating transfection may have an effect. ThT measured by flow cytometry showed no significant changes in ThT fluorescence compared to the non-targeting control, although 5 d post-transfection showed an increase in ThT fluorescence closer to the positive control than the rest of the samples. There were changes in ThT under genetic ablation but variation between samples was more than with Z-VAD-fmk.

Under Z-VAD-fmk inhibition increased autophagosome number coincided with the reduction in ThT, suggesting that autophagy was activated by increased misfolded proteins. *N*-

glycanase knockdown also found an increase in autophagosome number after 5 d compared to the non-targeting control, suggesting that increased autophagy levels can be linked to reduction in *N*-glycanase activity (rather than other effects of Z-VAD-fmk). Although the interaction with ThT is less clear due to the increased variation, increased presence of misfolded proteins is not likely to be the only explanation for increased autophagosomes. Again, stress signals that may be induced after increased protein aggregation or increased ER-load were studied. Both *N*-glycanase KD and Z-VAD-fmk found no increase in UPR-associated gene upregulation, Ca<sup>2+</sup> ER handling or ROS levels. This supports the evidence that *N*-glycanase deficiency in HEK cells does not cause classical protein aggregates or the concomitant cellular response and, is likely to not be a major cause of aggregates in unstressed, highly proliferative cells.

OGA and OGT expression levels were analysed by rt-qPCR. There was no change in OGA or OGT indicating no global change in *O*-GlcNAcylation. This was also confirmed by sWGA and WGA lectin dot blots.

This chapter aimed to compare the results from Z-VAD-fmk treated HEK cells and siRNA mediated knockdown of *N*-glycanase to unpick the effects Z-VAD-fmk and the effects of *N*-glycanase deficiency in a cell culture model. It can be concluded that *N*-glycanase deficiency can be linked to an increase in autophagy in HEK cells and could potentially explain phenotypes in other cell lines which have used Z-VAD-fmk as a caspase inhibitor. For example, L929 cells have been reported to exhibit cell toxicity following Z-VAD-fmk treatment (Cheng et al. 2008, Chen et al. 2011, Wu et al. 2008b). L929 has a dividing time of 120 h, which compared to the HEK cells (which have a doubling time of 21.3 h) in this study could indicate that division helps cells deal with the effects of *N*-glycanase inhibition and, that this can be managed by increased levels of autophagy. In L929 cells, stress resulting from aggregates or dysfunctional organelles cannot be ameliorated by division as quickly and it has been reported that autophagy has led to autophagic cell death (Chen et al. 2011, Wu et al. 2008b).

Both Z-VAD-fmk and siRNA mediated gene silencing of *N*-glycanase are transient methods to examine *N*-glycanase deficiency. Short-term inhibition or siRNA knockdown can give information of the importance of *N*-glycanase in cellular functions. However, transfections with siRNA may vary from experiment to experiment depending on the efficiency of siRNA introduction to the cell and nucleic-acid complexing. Gene silencing mediated by siRNA also has an increased knockdown time as the cell has to first degrade the active protein present

in the cell (which could have a half-life of around 30 h). This can lead to difficulty in measuring modest changes that are time dependent. Furthermore, short term inhibition does not look at how cells adapt over long periods of time. To examine this, efforts were then made to use CRISPR-mediated genome editing to create a stable KO of *N*-glycanase. Such a tool would enable the study of *N*-glycanase deficiency over a longer period of time, which may more closely resembling the clinical disorder.

### 5.1 Introduction

The Type II Clustered Regularly Interspaced Short Palindromic Repeats (CRISPR) system is an integral part of the prokaryotic and archaea adaptive immune defence system against viral infection (Rath et al. 2015a, Carter and Wiedenheft 2015, Barrangou and Marraffini 2014). The CRISPR region is an area of DNA found on both chromosomes and plasmids, made up of short repeated sequences which are separated by spacers (Figure 5.1). During infection, pathogenic DNA is incorporated into the spacers and transcribed into CRISPR RNAs (crRNA). The crRNA hybridise with transactivating CRISPR RNA (tracrRNA) and form a complex with the endonuclease CRISPR associated protein 9 (Cas9).

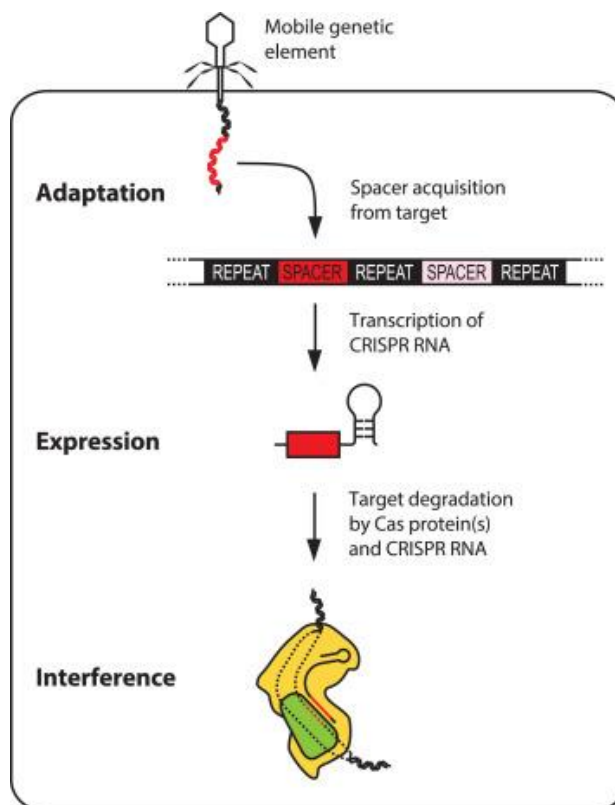


**Figure 5.1 Schematic representation of the CRISPR/Cas9 system (Rath et al. 2015b) Open-access article distributed under the terms of the Creative Commons Attribution Licence (CC BY).**

The crRNA targets the Cas9 to the pathogenic DNA subject to the presence of a protospacer adjacent motif (PAM) (usually NGG where N is any amino acid) (Sander and Joung 2014, Louwen et al. 2014). Since the pathogenic DNA has been incorporated into the prokaryotic genome, upon the next infection with the same pathogen the CRISPR defence system is ready to go and provides memory to the immune system making it adaptive. As the targeting of the CRISPR/Cas9 system depends on short RNA sequences which share homology with target DNA, it can be exploited in the laboratory as a method for generating programmable genetic mutations in cells. There are three types of CRISPR systems, type I, II and III. The most commonly used is Type II (from *Streptococcus pyogenes*) (Li et al. 2016, Ran et al. 2013) as it requires the fewest number of proteins to be functional and is thus easier to apply to a laboratory setting.

To create a mutation, the Cas9 endonuclease is used to make a cut in the DNA at a point determined by a short guide RNA (sgRNA) approximately 3-4 base pairs upstream of a PAM sequence. The sgRNA binds to complementary gDNA and brings the Cas9 endonuclease into contact with the DNA to create a double stranded break (DSB). As DNA can become damaged by the sometimes harsh environment of the cell (such as exposure to stressors like radiation damage and oxidative stress) DNA repair mechanisms are needed to maintain DNA stability. The cell has two methods of DNA repair following DSBs; non-homologous end joining (NHEJ) and homology directed repair (HDR) (Figure 5.2). NHEJ repair is the most commonly used repair mechanism for DSBs in human cells (Williams et al. 2014). DSBs are recognised by the Ku70/80 heterodimer that recruits other NHEJ proteins to the site of the break including a DNA ligation complex. Repetitive cutting and repairing of a site results in insertion and deletion mutations (indels). For the incorporation of specific mutations, homology directed repair (HDR) is employed. A donor template containing the desired mutation with homology arms on either side (up to 100 bp) of the expected cut site is introduced into the cell. Repair events result in the insert of a precise sequence.



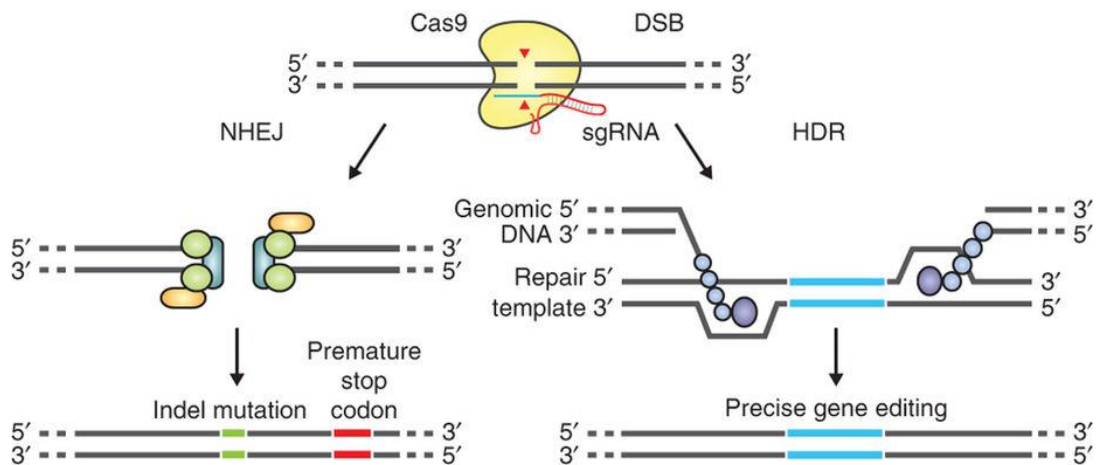


**Figure 5.2 Process of non-homologous end-joining repair and homology directed repair.** Reprinted with permission from Macmillan Publishers Ltd (Ran et al. 2013).

WT Cas9 has two domains which exhibit nuclease activity, the RuvC1 and HNH domains shown in Figure 5.3 which together result in the cleavage of both strands of gDNA resulting in a double-strand break (DSB). Three *S. pyogenes* Cas9 variants are commonly used. The wildtype (WT Cas9) creates a double stranded break in DNA, whereas a ‘nickase’ variant (Cong et al. 2013, Sander and Joung 2014) creates single stranded breaks. The third variant exhibits no endonuclease activity. In a laboratory setting, the endonuclease activity negative Cas9 allows targeting of DNA without cleavage. In this case Cas9 can act as a silencer, promoter or visualizer of the target region.

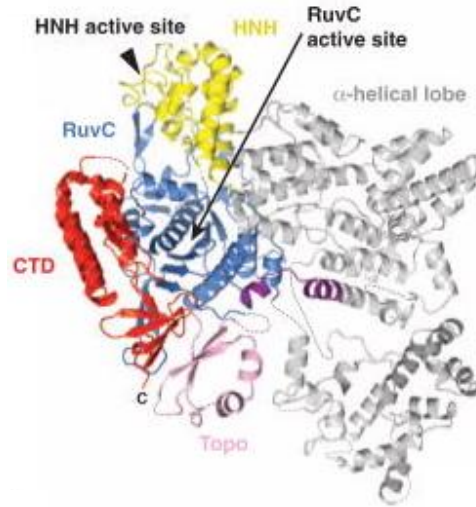


**Figure 5.3 Crystal structure of *S. pyogenes* Cas9 showing RuvC and HNH active site. Reprinted with permission from AAS (Jinek et al. 2014)**

The nickase variant contains a mutation in one of the two nuclease active sites of the WTCas9. This mutation results in an endonuclease which produces single stranded breaks in the DNA. Single strand DNA breaks are the most commonly found DNA damage and (Caldecott 2008) are repaired by higher fidelity methods less likely to create indels compared to NHEJ. WT Cas9 results in blunt DSB, however, to create a DSB using nickase Cas9, two nickase Cas9 variants need to be introduced with different but nearby guide sequences. This results in the formation of ‘sticky ends’. Although it is unknown how NHEJ treats sticky end DSB repair there is evidence to suggest longer sticky end DSBs (5 bp vs 3 bp overhang) enhances mutagenesis (Caldecott 2008). The nickase Cas9 systems also show more specificity than the WT counterparts because nickase uses two guide sequences rather than one. This makes it less likely that two sequences which share enough homology are near enough to create a DSB apart from at the target site, therefore decreasing off target effects compared to the WT Cas9. If there is sequence homology in other parts of the genome, these will only create single stranded breaks which are then repaired by the high fidelity HDR pathway which is less likely to introduce mutations.

The timeline for generating CRISPR mediated genetically edited cells is shown in Figure 5.4. Design of guide sequences have been simplified by use of online bioinformatics resources (Lei et al. 2014, Brazelton et al. 2015) that calculate sequences next to PAM sites and

calculate off target effects. Cloning of guide sequences into the Cas9 plasmids is typically in the order of one week, whereas isolating clonal cells and expansion can take up to a month.

CRISPR methods have several advantages over other techniques employed for targeted gene editing. CRISPR Cas9 is easily targeted depending on the guide sequence, as a new oligo can be synthesised and ligated in to the plasmid. This is significantly less time consuming than construction of transcription activator-like effector nucleases (TALENs) genes. The cut site for Cas9 is also reliable and predictable; Cas9 effects cleavage three base pairs upstream from the PAM site between the seventeenth and eighteenth nucleotide of the guide sequence on the target gene. Targeting does require a PAM site to be immediately downstream of the target site which may cause problems. Guide sequences can also potentially target other areas of the genome but off-target effects can be reduced using shorter guide sequences or nickase Cas9 variants.

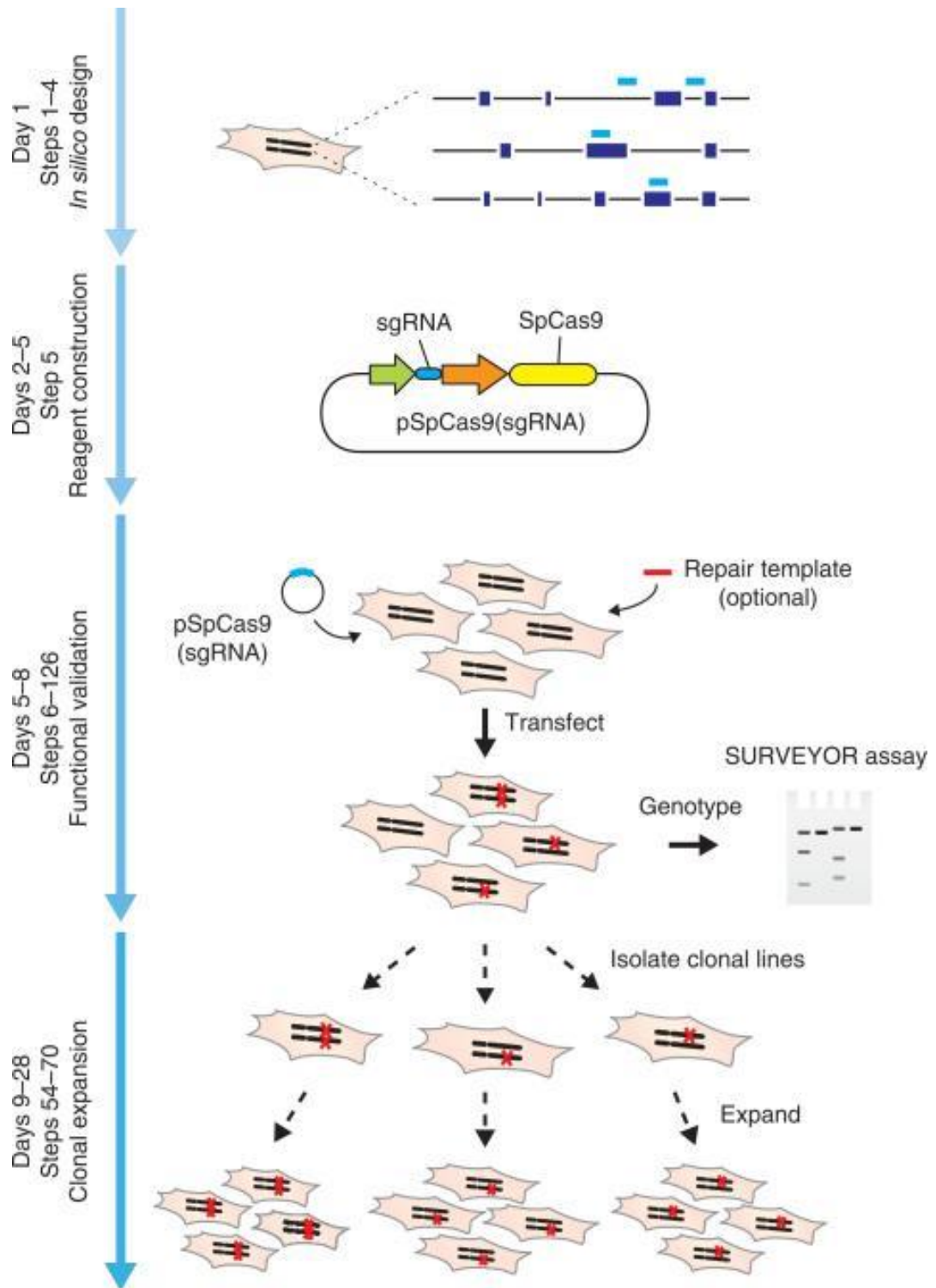


Figure 5.4 Timeline of CRISPR mediated knockout protocol. Reprinted by permission from Macmillan Publishers Ltd (Ran et al. 2013).

## 5.2 Aims and Objectives

Whereas previous work studying the effect of inhibition and deficiency of *N*-glycanase has used methods resulting in short-term perturbation (pharmacological inhibition or siRNA knockdown), the aim of this chapter is to generate a genetic knockout of *N*-glycanase for the use in examining any effects related to long-term *N*-glycanase deficiency. To explore effects which may be associated with long-term *N*-glycanase deficiency, CRISPR plasmids containing WT Cas9 (or the nickase variant) and guide sequences to target the *N*-glycanase gene were used in an attempt to create both general knockouts and the specific R401X *N*-glycanase mutation in cells. Based on the findings that a double knockout of *N*-glycanase and ENGase have a less severe phenotype (Huang et al. 2015), attempts were made to create an ENGase knockout cell line.

## 5.3 Results

In this chapter, the generation of guide DNA sequences for introduction into the WT and nickase Cas9 plasmids for the knockout of *N*-glycanase and ENGase will be discussed. Also discussed will be the efficiency of genomic editing in HEK 293 cells and determination of *N*-glycanase activity in CRISPR Cas9 transfected cells and potential phenotypic differences. The WT and nickase Cas9 plasmids used in this work were developed by Ran et al. (2013), are human codon-optimised to increase translation of the Cas9 protein and contain a nuclear localisation sequence to target the Cas9 to the nucleus. The nickase construct used in this study contains an aspartate to alanine point mutation (D10A) (Ran et al. 2013).

### 5.3.1 Guide sequences for *N*-glycanase and ENGase were cloned into WT or nickase Cas9 plasmids

WT Cas9 and nickase plasmids were generated containing guide sequences for *N*-glycanase and ENGase. Plasmids were created using two different guide sequences for each target (denoted A and B). Two sets were used to target *N*-glycanase. The constructs denoted PNG were designed to target areas close to the beginning of the protein. The constructs denoted RX were designed to target the area of the gene containing the most commonly found clinical mutation, R401X/c.1201A>T. In addition to the targeting Cas9 to form indel mutations, an insertion oligonucleotide containing the R401X mutation was designed for use with the RX plasmids for HDR editing. For each area, two sequences were designed, A and B. In WT Cas9

plasmids each one can be transfected to generate a DSB. However, they were also designed to target areas in close proximity so as when cloned into a nickase Cas9 plasmid backbone and co-transfected together a DSB could be effected (Table 5.1). Guide sequences were also generated for ENGase, another glycan processing enzyme (Huang et al. 2015) implicated in deglycosylation of misfolded glycoproteins in the absence of *N*-glycanase. As ENGase and *N*-glycanase double KO had a less severe phenotype it would be useful to also create an ENGase and *N*-glycanase KO cell line. Sequences of the targeting DNA can be seen in Figure 5.5. Plasmid maps can be found in Appendix A.2, Figure A3 and A4.

**Table 5.1 Nomenclature of CRISPR constructs**

Cas9	Mutation	Guide Sequence
<b>WT</b>	PNG	A or B
	RX	
	ENG	
<b>Nickase</b>	PNG	A and B co-transfected
	RX	
	ENG	

Primers were designed over the region of editing to facilitate sequencing of the area. Figure 5.5 shows the areas of interest in *N*-glycanase and ENGase sequences. Magenta indicates the position of the primers while blue indicates guide sequence B and green indicates guide sequence A and yellow shows the position of the PAM site. For the RX mutation sequence, red text indicates the overlap region of the designed insertion oligo.

PNG

GTACCTTAACAGCACAGAATGTAATTTACTGTTTTACTTATAGTAAAAACAACCATTGGTTTAGGG  
 AAGAAAGAAAATCAGGTGACTATAAAGGTATACCTAGGTCATGTTTGTGAAAGTAAAGTCTTTGAA  
 GAACTATGACCTGGTTTTTTTTATATATAATCAAACCTTTGTTTTTGTGAGAAACCCTAATGATGA  
 AAAATATAGATCCA<sup>TCCGGATTGGAAACACAGCC</sup>TTTTCT<sup>ACTAGACTCTTGCCTGTCAG</sup>AGGAGCT  
 GTTGAATGTTTTATTGAAATGGGCTTTGAAGAGGTAAGTATGTTCAAGGATTTCCCTCCTCCCTCTTC  
 ATGCACAAAGCAGCCATTATCATGTTGGTGAATAATTGTTTGAATAAGATAATGTTTTTTAATTTAT  
 CATTTTGGGAATCAGTAGAAGTAGTATTTCTTCATTGATTGGACATTTAAAAATCACAACAAGTAT  
 AGTTTAAAAATTCAGTAAAAATGTAACAACGCTCCACAGAGAAATTCCTACGAGTCTCAGTTCCTTAA  
 AATAAGGTCATACATGCAACCCAAGGACCAATGTGGTTCACCTTTAGGCTTTTAGCTAAAAACCTGA  
 TTTGTGAGCACACATGAATACTAATAGAGTCTA<sup>GCTACCTGTCTGTAGTAGG</sup>

PNGRX

TCTTGACCCTGGGAAGTGAGACTGCAGTGAGCTGAGATCACGCCACTGCACTCTAGCCTGGACAACA  
 GAGCGAGACTTCGCTCCAAAAAATGCATTTAAAAATTACATACATTCTAGGTATTTAGTAAGTAA  
 AGGTTGATGGTTGTAATCTGTAAAGTATTTGTATTCTGTTATTTGTTTCAGGTAGTTGATGTCACT  
 TGGCGATATTCCTGCAAACATGAAGAGGTGATTG<sup>CCA</sup>GAAGA<sup>ACTAAGGTTAAAGA</sup>GCAT<sup>TACTTG</sup>  
<sup>GAGCACTATTAA</sup>GGGCTTAATAAGCAGGATGGTGTGGCTATCTTTTTTGAAGAACAGTTGACA  
 TTTTTATGTAATCGAGAATAGCCGTTTATTAGCCTATTGAAATTCCTAAAGTAGTAGCATTGTTTT  
 ATAAACAAGAATATTTAATATCTTTTTGAATATTAAGAATAAAAAATATTCTTTTTGTTCATTGA  
 AAATTTGCGGACTCATTTAAATATTATGAGTATTTTGGATTAAACTGTCTCATTTCAAAGTTCT  
 TTGAAACAAAATTT<sup>CAGTATTGGTAGTACCTGAC</sup>

ENGase

GAATACCGATCCACCTTCACACCTGGGGCTTTGGGGCAGGTCAGCCCCTGCCCTCTCATGTTCCCT  
 TCTCTGTTATTGTTAAAAATGTTTCGATTAATCCTATAATAGTTTCCATTAATTGCTCAATGTTTCTG  
 TCCTCGGACCAGTTAGATATTATGACAAGGACACCACAA<sup>ACCAATCAGCTTTTACTTG</sup>TCTTCGCT  
 GGAGGAGCTCTT<sup>GGCGTGAAGCCCGCTT</sup>GGA<sup>GGATGGCTT</sup>AATGTGGCCCTGGAGCCCTGGCG  
 TGTCGCCAGCCCCCTCTGAGCAGCCAGAGGCCCGGACTTTGTTGTGTCATGACATGATGGGCGGGT  
 ACCTGGATGACAGGTGAGGACCTGGCCTTACATTGATGTTGCTTACATTGTTCTCCTTTGCTGGGGT  
 GGGGGCTGGAGGGGCGGGAGAGAGTGCCATGTGTAGAAAGAGCACTGGGCGGGGAGTCAGGAGACGG  
 GCATTGGAGGGATGGCACTAACTGCGAGAAGAAGGCAGGCCCAAGTGTTCATCTGTA AAAAAGGGAA  
 GACTGGGCTGGGCTTGGTGGCTCACACCTATAATCCCAGCACTTTGGGAGGTCAAGGCAGGTGGGTC  
 ACCT<sup>GACCTCAGGAGTTT</sup>GAGACCAG

**Figure 5.5 Position of the guide DNA sequences in genomic DNA of *N*-glycanase and ENGase. Magenta indicates primer sequences, Blue indicates guide sequence A, green indicates guide sequence B and yellow indicates PAM sequences.**

Primers were initially tested on WT HEK gDNA to ensure specificity (sequences can be found in Chapter 2, Table 2.4). Sequences were amplified using the KAPA High Fidelity polymerase (Kapa Biosystems) at 60 °C annealing temperature for all primers and run on a DNA agarose gel stained with Midori green (Figure 5.6). Despite a non-specific band in the PNGRX annealing temperature resulted in specific amplification of the sections. This allows amplification of the sequences that will be mutated and thus ensures that they can be sequenced to detect genome changes.

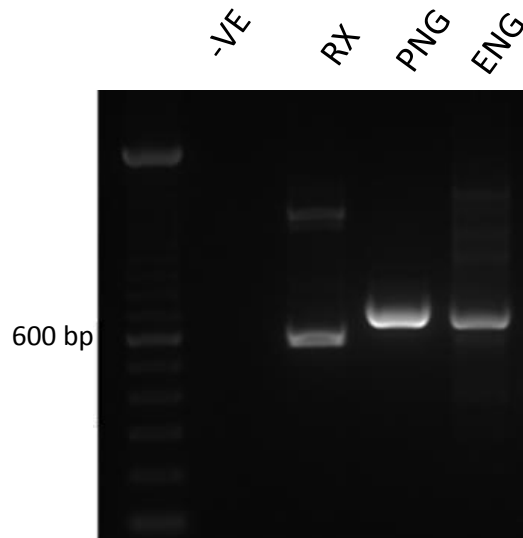


Figure 5.6 PCR products of HEK gDNA amplified with sequencing primers. Primers are specific for the sequence.

Table 5.2 Expected band size for each mutation

Mutation	Expected band size
<b>RX</b>	570
<b>PNG</b>	655
<b>ENG</b>	629



### 5.3.2 Design of a repair template to introduce R401X mutation

An oligonucleotide was designed in order to introduce the R401X (A1201T) mutation, the most common deleterious mutation associated with NGLY1 disorder. This sequence was designed with homology arms of at least 50 bp each side of the mutation. A restriction enzyme site (BSiWI) was introduced in this sequence, to ensure that there existed a means of analysing the resultant oligonucleotide insertion. Figure 5.7 shows the design of the oligonucleotide sequence for the insertion of the R401X (A1201T) mutation. The bottom sequence indicates the genomic DNA sequence of *N*-glycanase. The top sequence (shown in red) indicates the oligonucleotide. The primer positions for sequencing are shown in pink, whereas the guide sequences are highlighted in blue and green. PAM sites are displayed in yellow. The oligonucleotide contains a site for the restriction enzyme, BSiWI (shown as blue text). The important A to T mutation which gives rise to the A>T 1201 (R401X) clinical mutation is within the BSiWI cut site, and is underlined.

PNGRX

```

TCCTGACCCTGGGAAGTGAGACTGCAGTGAGCTGAGATCACGCCACTGCACTCTAGCCTGGACAACAG
AGCGAGACTTCGTCTCCAAAAAATGCATTTAAAAATTACATACATTCTAGGTATTTAGTAAGTAAAG

      5' -TAATCTTGTTAAGTATTTGTATTCTGTTATTTGTTTCAGGTAAGTTGATGTCACTTGG
GTTGATGGTTGTAATCTTGTTAAGTATTTGTATTCTGTTATTTGTTTCAGGTAAGTTGATGTCACTTGG
      BsiWI
CGATATTCCTGCAAACATGAAGAGGTGATTGCGTACGGAACTAAGGTTAAAGAAGCATTACTTCGAGA
CGATATTCCTGCAAACATGAAGAGGTGATTGCCAGAAGAACTAAGGTTAAAGAAGCATTACTTCGAGA

CACTATTAATGGGCTTAATAAGCAGGTATGGTGTGGCTATCTTTTTTAAAAGAACAGTTGACATTTTT
CACTATTAATGGGCTTAATAAGCAGGTATGGTGTGGCTATCTTTTTTAAAAGAACAGTTGACATTTTT

TATGTAATC-3'
TATGTAATCGAGAATAGCCGTTTATTAGCCTATTGAAATTCCTTAAAGTAGTAGCATTGTTTTATAAAC

AAGAATATTTAATATTCCTTTTTGAATATTAAGAATAAAAAATATTCCTTTTTGTTTCATTGAAAATTTT
GCGGACTCATTTTTAAATATTATGAGTTATTTGGATTAAACTGTCTCATTTCAAAGTTCTTTGAAACA
AAATTTCAGTATTGGTAGTACCTGAC
  
```

**Figure 5.7** Sequence of the repair template for use with RX plasmids to increase the homology directed repair pathway. Black indicates the gDNA of *NGLY1*. Red indicates the oligonucleotide sequence. Green indicates guide sequence A. Blue highlight indicates guide sequence B. Yellow indicates PAM sequence. Pink indicates primer sequences. Blue text indicates the BsiWI restriction enzyme site in the oligonucleotide. The underlined T indicates the mutation forming the A>T 1201 (R401X) clinical mutation.

### 5.3.3. The surveyor assay was unable to determine genetic editing in HEK 293 cells transfected with Cas9 constructs

HEK cells were transfected with plasmids containing the WT Cas9 with the guide sequences A or B or the nickase pair using JetPei (3 µg total DNA per well in a 6 well plate). After 48 h, transfection efficiency was determined by observing the GFP signal. If transfection was found to be above 75%, genome stability was assessed using a surveyor assay. The surveyor assay is a technique used to measure mutations and contains an endonuclease which recognises mismatched DNA. Genomic DNA is amplified from WT control cells and test cells. The samples are mixed, denatured and hybridised. If mutations have occurred in the test sample there will be a mixed sample with some hetero-duplexes which contain mismatched sequences. The endonuclease can cut at these sites and the DNA can be analysed by agarose gel. WT sequences will have no cut sites but if the CRISPR method has been successful, the test sample can contain multiple fragments. This process is presented schematically in Figure **5.8**.

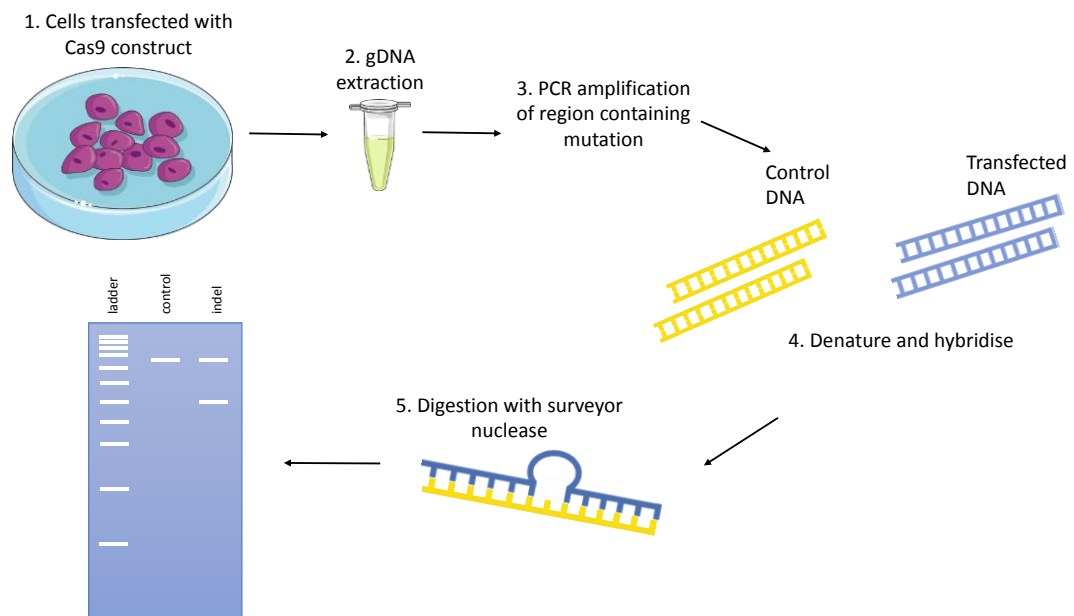


**Figure 5.8 Schematic representation of the surveyor assay. Cells are transfected with Cas9 construct. The genomic DNA is extracted after several days and the area for genomic editing occurs is amplified by PCR. WT and edited DNA are denatured and hybridised together to form heteroduplexes. If the transfected DNA contains indel mutations this will form a mismatch in the sequence, which the surveyor nuclease recognises and makes a cut. The results can be visualised on DNA agarose gels.**

After transfection with the Cas9 RX and PNG constructs the surveyor assay did not detect mutations in this system. Figure 5.9 shows the results of the surveyor assay carried out on gDNA from isolated WT cells, HEK transfected with RXA plasmid, RXB plasmid and RXAB nickase pair from (left to right). Increased levels of transfected DNA were used to see if there were any low levels of cut DNA present. The results from this assay do not show evidence of DNA cleavage. It is possible that the mutation rate was very low (as to be barely detectable against the background of uncleaved DNA) or, that the endonuclease did not cut.

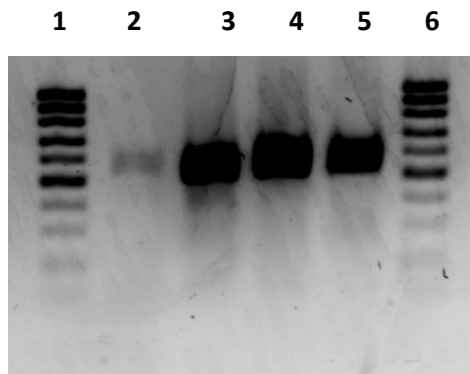


**Figure 5.9** Surveyor assay results from WT DNA (lane 2), WT Cas9 PNgRx guide sequence A (lane 3), WT Cas9 PNgRx guide sequence B (lane 4) and nickase Cas9 guide sequences A and B (lane 5). MW markers (lanes 1 and 6)

#### 5.3.4. Co-transfection with R401X oligo was unsuccessful

To create the R401X mutation, an oligonucleotide sequence with the change from A > T at 1201 was generated. Double stranded DNA breaks around the area of the target mutation following co-transfection with the oligosaccharide should promote homology mediated repair. As well as the clinical mutation, a restriction enzyme site for BsiWI was designed into the oligonucleotide sequence. On incorporation into the genome, the area is amplified by PCR and incubated with BsiWI which results in a cut in edited cells but not in WT sequences. A successful cut will generate fragments of 237 bp and 333 bp compared to the 570 WT sequence. WT Cas9 guide sequences A and B were transfected and or nickase Cas9 guide sequence A and B co-transfected into HEK 293 cells and co-transfected with single stranded oligosaccharide. The established protocols for this systems (Ran et al. 2013) recommend 1  $\mu$ l of oligo (10  $\mu$ M) per 0.5  $\mu$ g plasmid DNA transfected. The conditions per transfection are summarised in Table 5.3.

**Table 5.3 Conditions for homology directed repair transfection**

Transfection reagent	Plasmid DNA ( $\mu\text{g}$ )	Oligo volume ( $\mu\text{L}$ )	Digestion conditions
<b>JetPEI</b>	0.5	1	18 h 55 °C
		5	
	1	1	
		5	
<b>JetPRIME</b>	0.5	1	
		5	
	1	1	
		5	

Under all conditions tested the DNA agarose gels showed no evidence of successful cleavage. A representative gel of HEK 293 cells transfected with 1  $\mu\text{g}$  plasmid DNA with 5  $\mu\text{L}$  oligo by JetPEI and digested with BsiWI at 55 °C for 18 h is shown in Figure 5.10. As the incorporation of the cut site could not be confirmed, further transfections were studied using the PNG mutation guide sequences rather those targeting the clinical mutation.

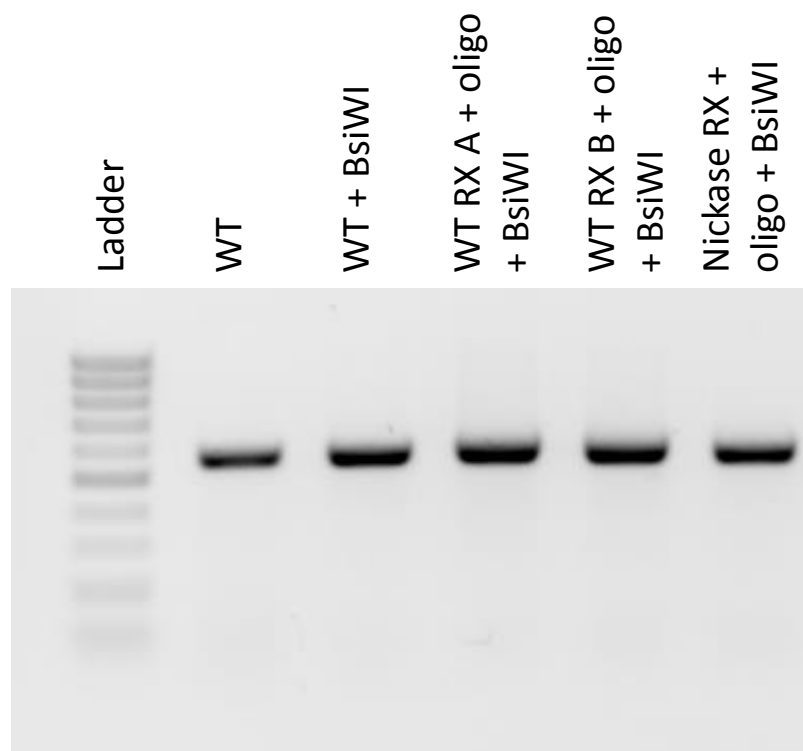


**Figure 5.10 Representative gel of HEK 293 cells transfected (JetPEI) with 1  $\mu$ g plasmid DNA with oligo (5  $\mu$ L) and digested with BsiWI (55  $^{\circ}$ C, 18 h).**

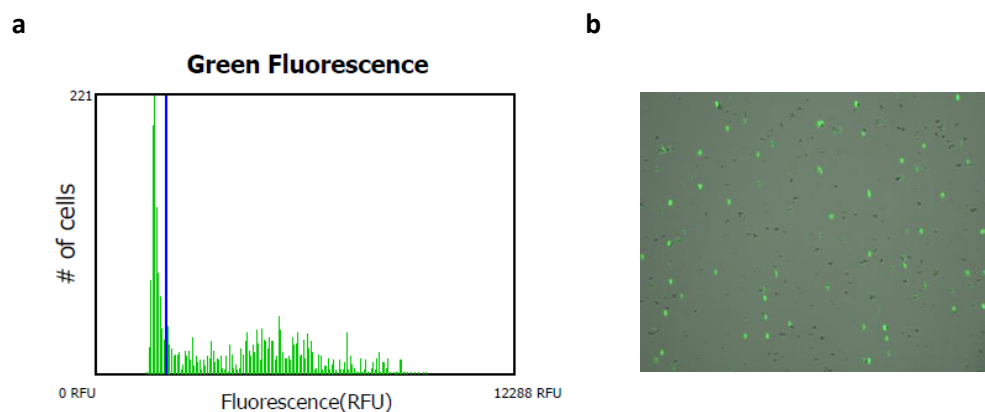
#### 5.3.5. Transfection with PNG guide DNA in WT Cas9 plasmids lead to genomic editing in the *N*-glycanase gene

HEK cells were transfected with the PNG plasmids and the transfection efficiency was determined by recording the number of GFP positive cells with respect to the total population. gDNA was extracted 48 h post transfection and, the area of editing was amplified by PCR. The PCR product was sequenced and the raw sequencing files compared to those obtained from WT DNA using the Tracking of Indels by Decomposition (TIDE) analysis web tool (Brinkman et al. 2014). TIDE analysis looks at the difference of a mixed population of cells, calculates where the expected cut site is from the guide DNA sequence and calculates the percentage of edited sequences. For the first round of tests HEK cells were transfected with PNG plasmids, however, the quality of the DNA extracted was not suitable for the analysis. For analysis using the TIDE web tool, high quality sequencing is essential for detection of genomic editing as the tool relies upon peak fidelity and confidence levels of a

chromatogram to determine changes from a control sequence. Initially DNA was extracted from agarose gels but by removing this step and applying a nucleotide removal kit (NEB) increased DNA quality was achieved. The sequence prior to the PAM site is expected to be unmodified. For a good quality sequence, the percentage of aberrant sequences before the cut site is expected to be below 10 %. After the cut site, the control sequence should remain below 10 % aberrant sequences and this level should be increased in the test sample.

Previous research (Richardson et al. 2016) has shown that by co-transfecting non-homologous DNA, such as bacterial plasmids, salmon sperm DNA and oligonucleotides with no homology for the target genome, the percentage of indels significantly increases. This method also increases the number of homozygous indels. A study testing different non-homologous DNA with CRISPR mutations found HEK cells transfected with just the Cas9 plasmid with guide DNA it was found to have around 60 % editing efficiency, all of which were heterozygous. With the addition of non-homologous oligonucleotides, editing efficiency increased to 40% heterozygous and 60% homozygous mutations (Richardson et al. 2016).

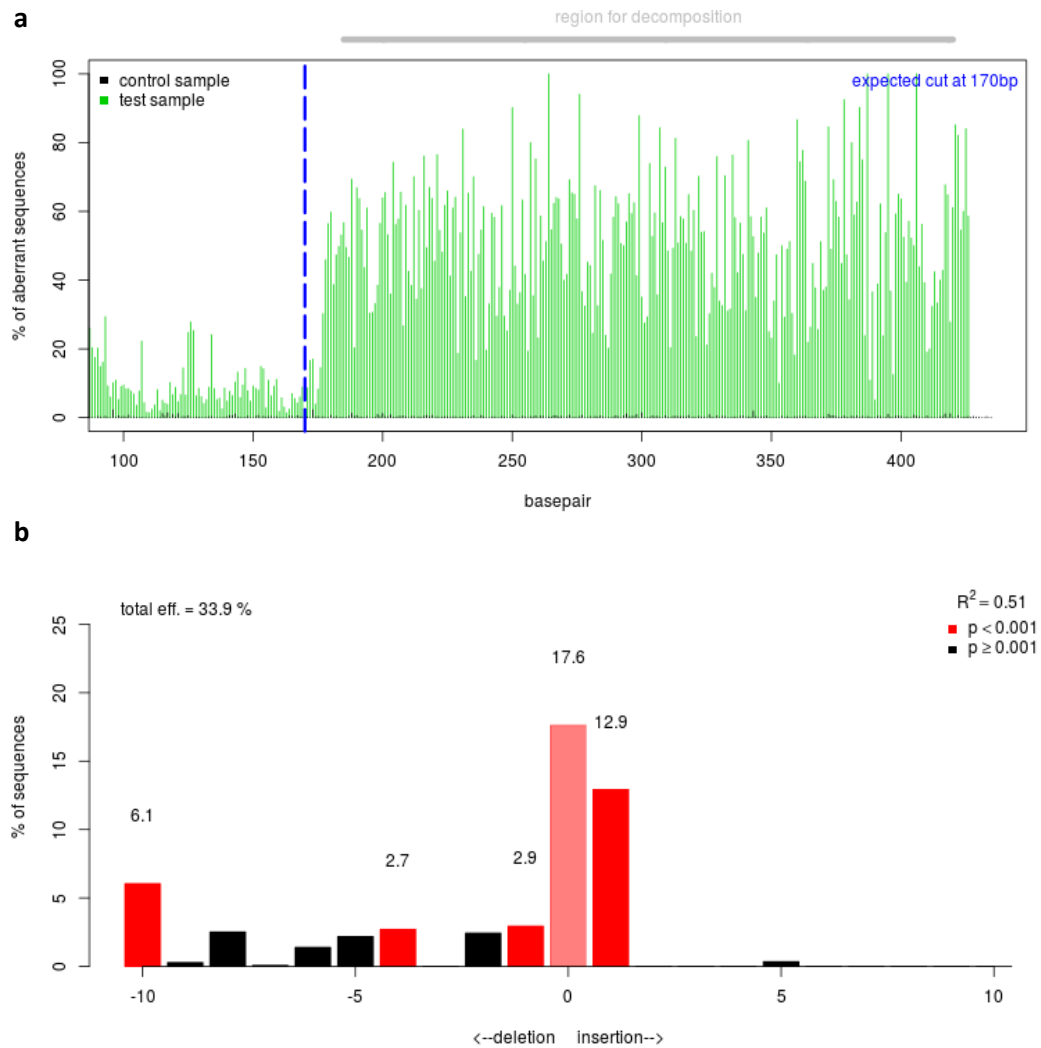
To ensure a high level of efficacy, HEK cells were co-transfected with PUC18 plasmid with either the PNG A or B WT Cas9 constructs (3 µg of DNA per well, 6 well plate). After 48 h DNA was extracted and the target site amplified and sequenced. Transfection efficiency for WT Cas9 PNG A was assessed using the TALI image based cytometer (Figure 5.11).



**Figure 5.11** Transfection of HEK cells with WT Cas9 construct guide sequence A after 48 h as assessed by quantification of the fluorescence signal a) representative histogram produced by TALI image based cytometer b) corresponding representative image of transfection generated by TALI image based cytometer.

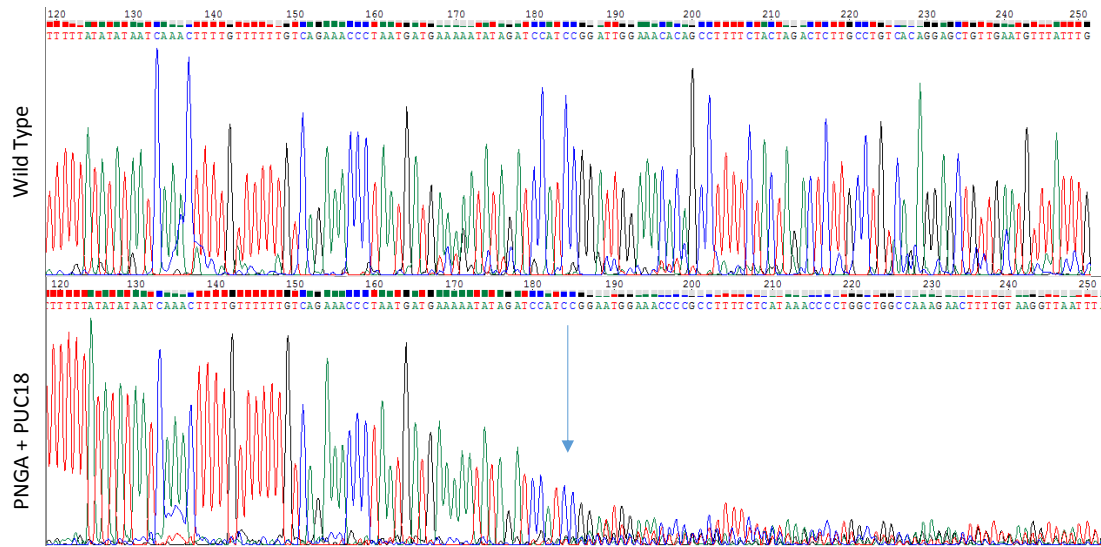
The sequence data obtained for HEK cells transfected with WT Cas9 PNG guide sequence A and co-transfected with PUC18 plasmid were analysed by TIDE analysis. Figure **5.12a** shows the TIDE analysis and Figure **5.12b** shows the quantitation of indels formed. The graph indicates the number of insertion or deletion of nucleotides and the percentages of sequences that show these indels. WT HEK sample is represented in black and has a low level of aberrant sequences across the decomposition window while the test sample has a significant increase after the expected cut site, indicating genomic editing. There was a total efficiency of 33.9 %, with the highest possible editing being a +1 bp insertion of a cytosine residue.





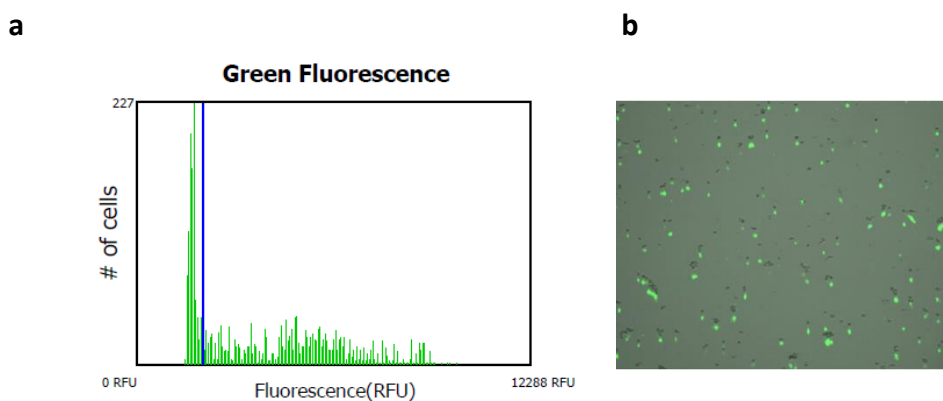
**Figure 5.12 TIDE analysis of HEK 293 cells transfected with WT Cas9 PNG guide sequence A**  
**a) TIDE decomposition window for WT Cas9 PNG guide sequence A sequence. b) quantitation of insertion and deletion percentages.**

Under these conditions 12.9 % of the sequences were found to have a +1 bp insertion. Of these insertions, the most common insertion was a cytosine at 93.5 %. The original chromatograms of the wild type HEK cells transfected with PUC18 and cells transfected with WT cas9 with guide sequence A and co-transfected with PUC18 are shown in figure 5.13. The arrow indicates the predicted cut site where after this the quality of the sequence decreases.



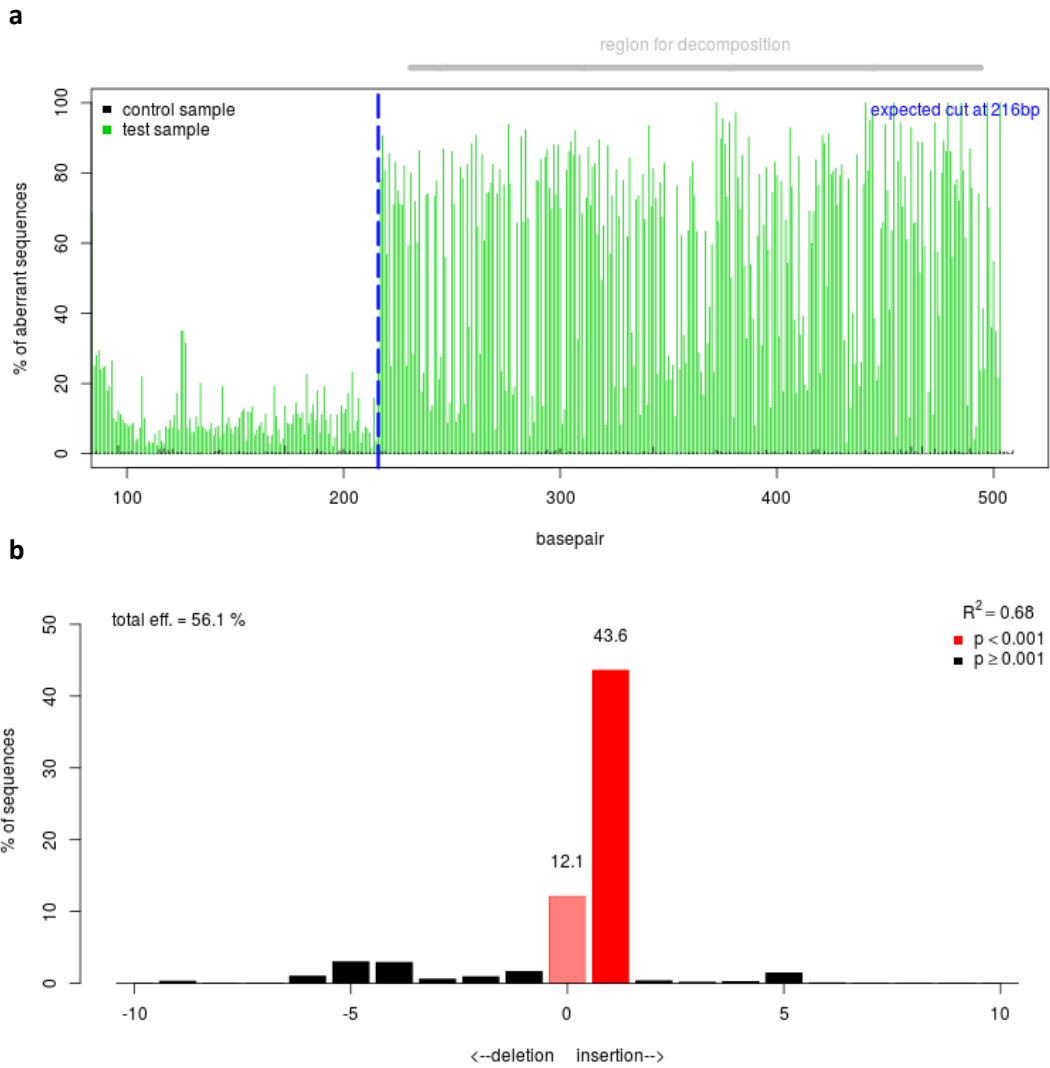
**Figure 5.13 Chromatograms from sequencing data HEK cells transfected with PUC18 (WT) and mixed population of WT Cas9 PNG guide sequence A and co- transfected with PUC18 cells.**

The same experiment was performed using WT Cas9 PNG guide sequence B construct co-transfected with PUC18. Figure 5.14 shows the transfection efficiency of HEK cells transfected with guide sequence B.



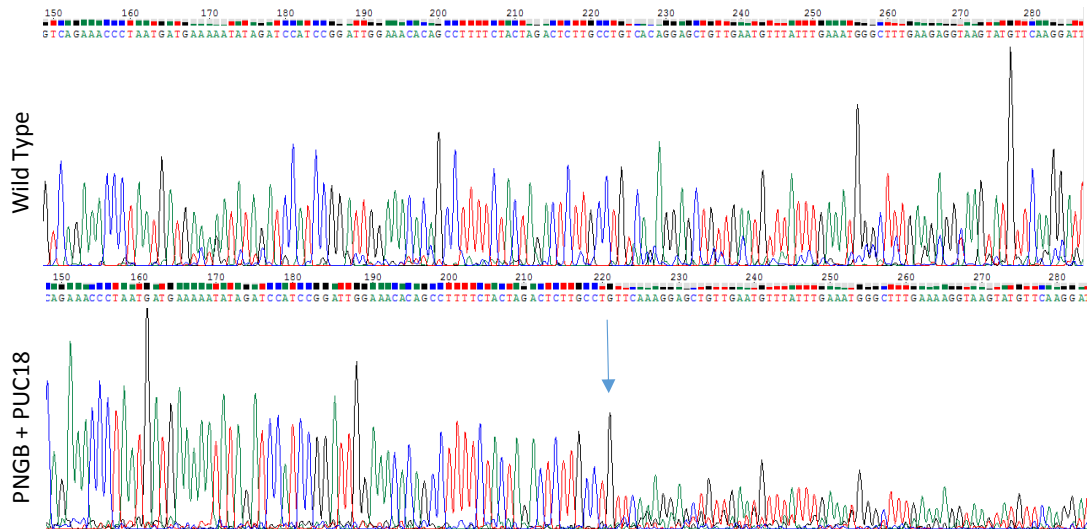
**Figure 5.14 Transfection of HEK cells with WT Cas9 construct guide sequence B after 48 h a) panel histogram generated by TALI image-based cytometer b) representative image of transfection imaged using a TALI image-based cytometer**

Figure **5.15a** shows the TIDE analysis for WT and Cas9 PNG sequence B and the indel quantitation in figure **5.15b**. There was a total efficiency of 56.1 %, the greatest mutation a +1 bp, with a 65.8 % being a thymine residues. Before the expected cut site at 216 bp only a low level of aberrant sequences with a significant increase after the cut site are observed, and a low level throughout indicating good sequence quality.



**Figure 5.15 TIDE analysis of HEK 293 cells transfected with WT Cas9 PNG guide sequence B.a) TIDE decomposition window for WT Cas9 PNG guide sequence B sequence. b) Percentage of sequences found for mutations.**

Chromatograms used for the TIDE analysis are shown in Figure 5.16. The cut site is estimated at 216 bp. In the PNGB + PUC18 chromatogram there is a clear decrease in sequence quality. This indicates a mixed population of sequences compared to the WT sequence.



**Figure 5.16 Chromatograms showing HEK cells transfected with PUC18 (WT) and mixed population of WT Cas9 cells (PNG guide sequence B co- transfected with PUC18).**

### 5.3.6 Clonally expanded cells show low viability, viable clonal cells exhibit different phenotypes to WT HEK

Individual cells were isolated to ensure a clonal final population. HEK cells were diluted in two concentrations (5 or 1 cell per well in 96 well plates). Wells were analysed daily to identify wells containing a single cell. Many of the singly diluted cells did not survive. Of the single cells which proliferated under these conditions, colonies were expanded. Several clones proved to be non-viable after sub-culturing.

Some mutations can cause degradation of the mRNA associated with the target protein. Of the surviving colonies (numbered 1-12) generated from the WT Cas9 PNG B transfection (which showed the greatest editing efficiency) RNA was extracted and mRNA of *N*-glycanase was examined. The results are presented in Figure 5.17. Little difference in mRNA was observed between the clones, with the greatest change being a ~3 fold increase in clone 9. Levels of mRNA do not always indicate levels of active protein (Greenbaum et al. 2003), in this instance both immunoblotting and immunofluorescence (both anti-NGLY1 antibodies: ab73984 and ab197107) techniques failed to produce definitive results.

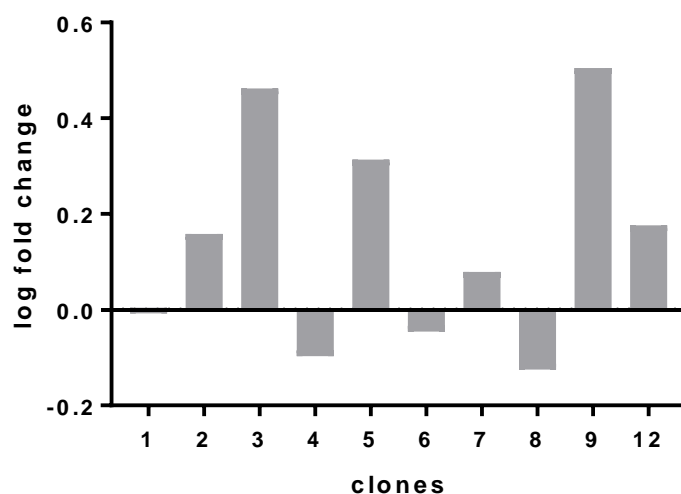


**Figure 5.17** RT-qPCR of *N*-glycanase mRNA in clonally isolated HEK cells transfected with PNG WT Cas9 guide sequence B and PUC18. Data normalised to GAPDH and PUC18 transfected WT HEK cells. *n*=1.

Since autophagy impaired cells had lower viability compared to WT cells under Z-VAD-fmk inhibition and *N*-glycanase knockdown, cells lacking a functional *N*-glycanase may be more susceptible to autophagy inhibition. Clones were treated with 3-MA at a concentration previously established as non-toxic to WT cells (5 mM, 24 h), and compared to the vehicle. Clones 3, 4, 5, 6 and 7 exhibited increased sensitivity to 3-MA compared to the WT (Figure 5.18). A decrease in formazan absorbance (indicating reduced cell viability) of 43, 42, 33, 56 and 37 % was observed for clones 3, 4, 5, 6 and 7 respectively.

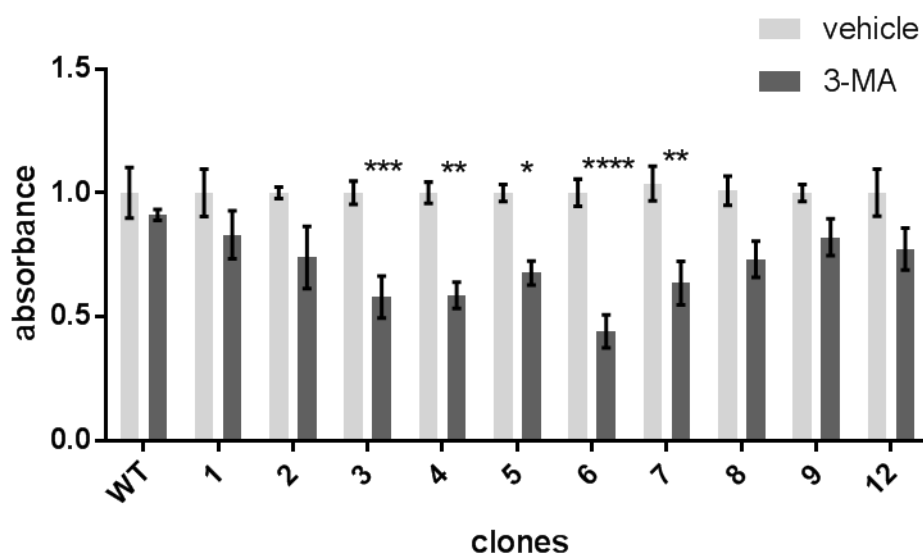


**Figure 5.18 MTT assay against clones isolated from a population of cells transfected with WT Cas9 PNG guide sequence B. Cell were treated with 3-MA (5 mM, 24 h). Student's t-test between vehicle and 3-MA treated. Error bars  $\pm$  SEM,  $n=3$ , \*  $P < 0.05$ , \*\*  $P < 0.01$ , \*\*\*  $P < 0.001$ , \*\*\*\*  $P < 0.0001$ .**

Clones 3 and 7 from WT Cas9 PNG B populations latterly survived expansion and repeated sub-culture. In order to quantify any potential changes in deglycosylation activity using fluorescence, clones 3 and 7 were transfected with the ddVENUS construct. The transfected cells were treated with increasing amounts of Z-VAD-fmk (1-300  $\mu$ M). The  $IC_{50}$  for WT HEK was previously established as 68.14  $\mu$ M (Figure 5.19). Clone 3 and 7 had decreased  $IC_{50}$  values of 5.67 and 59.97  $\mu$ M respectively, however the lowest level seen in WT HEKs was a decrease in fluorescence by 58 % whereas in clone 3 and 7 the lowest decrease was recorded as 52 % and 32 % respectively (Figures 5.20 and 5.21). This indicates a lower sensitivity to Z-VAD-fmk and decreased *N*-glycanase activity. Furthermore, the fit of the curve was reduced in clones 3 and 7. To measure the goodness of fit  $R^2$  was measured with 1 indicating a perfect fit and 0 indicating a horizontal line being the best fit. WT HEK cells had a  $R^2$  of 0.92 indicating a good fit while clones 3 and 7 had  $R^2$  values of 0.47 and 0.44 respectively indicating that the data does not follow a trend as well as WT HEKs. Furthermore, this assay has not been validated against other glycan processing enzymes. A number of proton pump inhibitors have been identified as ENGase inhibitors (Bi et al. 2017). This assay, if it is to be used as an assay for specifically *N*-glycanase activity needs to be validated against other deglycosylated enzymes.

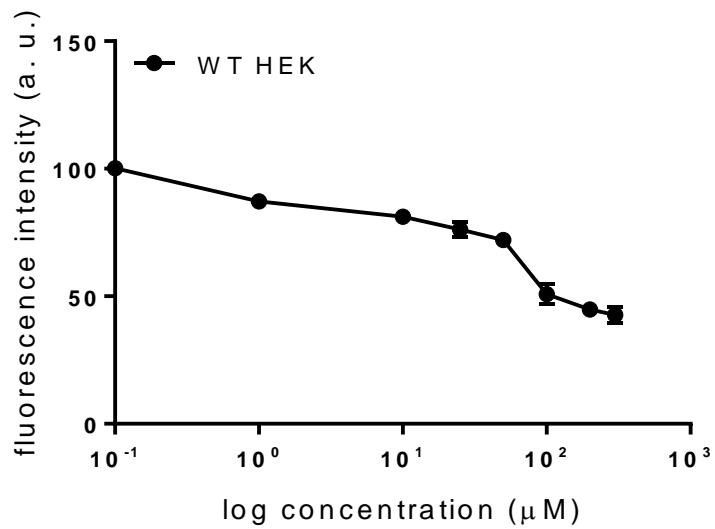


Figure 5.19 ddVENUS assay of WT HEK cells. HEK cells were transfected with ddEVNUS construct and treated with Z-VAD-fmk (1-300  $\mu\text{M}$ , 24 h) followed by MG132 (8  $\mu\text{M}$ , 6 h). The median ddVENUS fluorescence was calculated. Error bars  $\pm$  SEM,  $n=3$ ,  $R^2$  0.92,  $\text{IC}_{50}$  68.14  $\mu\text{M}$ .

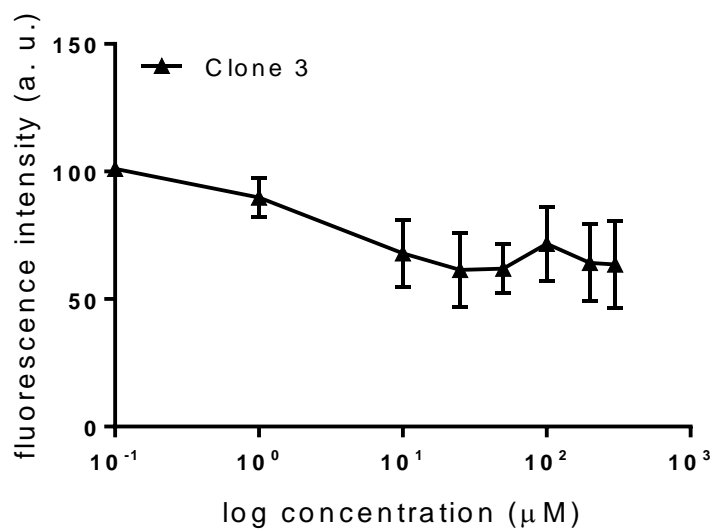
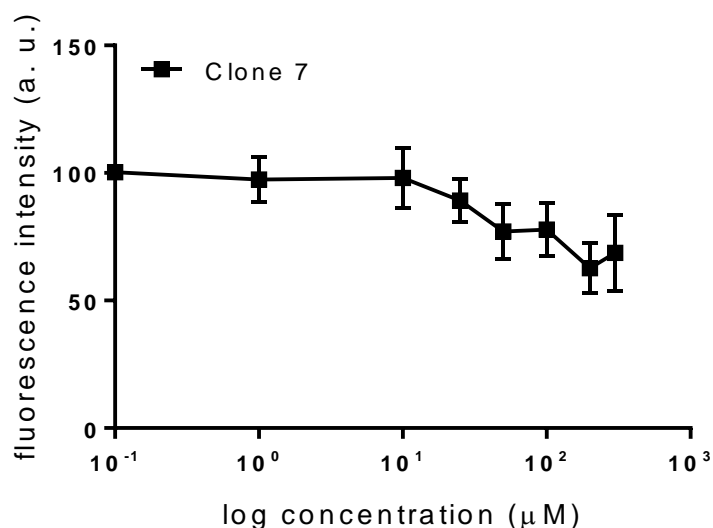


Figure 5.20 ddVENUS assay of Clone 3 HEK cells. Clone 3 HEK cells were transfected with ddEVNUS construct and treated with Z-VAD-fmk (1-300  $\mu\text{M}$ , 24 h) followed by MG132 (8  $\mu\text{M}$ , 6 h). The median ddVENUS fluorescence was calculated. Error bars  $\pm$  SEM,  $n=3$ ,  $R^2$  0.47,  $\text{IC}_{50}$  5.67  $\mu\text{M}$ .





**Figure 5.21 ddVENUS assay of Clone 7 HEK cells. Clone 7 HEK cells were transfected with ddEVNUS construct and treated with Z-VAD-fmk (1-300 μM, 24 h) followed by MG132 (8 μM, 6 h). The median ddVENUS fluorescence was calculated..Error bars ± SEM,  $n=3$ ,  $R^2$  0.44,  $IC_{50}$  59.97 μM.**

5.3.7. Increased sensitivity of clone 3 and 7 to cell stressors was not rescued by pharmacological inhibition of ENGase

ENGase knockout in conjunction with N-glycanase deficiency has been identified as resulting in less severe phenotypes in murine models compared to N-glycanase knockout alone (Huang et al. 2015, Fujihira et al. 2017). A number of proton pump inhibitors (such as lansoprazole and omeprazole) have been identified as ENGase inhibitors; the  $IC_{50}$  of lansoprazole determined to be 24.38 μM in vitro using human ENGase (Bi et al. 2017). Based on these findings, if clone 3 and 7 have a deficiency in N-glycanase it may be postulated inhibition of ENGase may result in an increase cell viability under conditions of cellular stress. The cell viability of the WT and clonal cells for lansoprazole was determined using MTT assay.  $IC_{50}$  values of 123.1, 174.1 and 52.1 μM were recorded for WT HEK, clone 3 and clone 7 respectively (Figure 5.22).

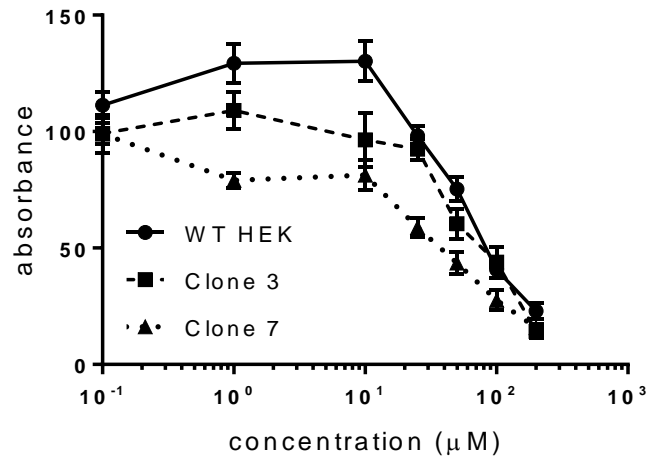


**Figure 5.22** MTT of HEK cells with lansoprazole. HEK 293 cells were treated with lansoprazole (24 h). Data normalised to the average of the vehicle.  $n=3$ , error bars  $\pm$  SEM. Bottom panel shows representative images (bright-field, 20X objective) of cells treated with lansoprazole (25  $\mu$ M, 24 h).

HEK cells were treated with increasing concentrations of the proteasome inhibitor MG132 in the presence or absence of lansoprazole (10  $\mu$ M) for 24 h to determine the effect of MG132 and lansoprazole co-treatment on WT cells and clones 3 and 7. MG132 has been identified as resulting in increased cell toxicity in N-glycanase deficient cells as it has been linked to Nrf1 activation in WT cells (Tomlin et al. 2017). Nrf1 is responsible for upregulation of proteasome proteins under proteasome inhibition. Cells deficient in N-glycanase are unable to induce proteasome gene transcription and therefore exhibit increased sensitivity to proteasome inhibition. HEK cells were treated with increasing concentrations of MG132 (Figure 5.23a). No significant decrease in formazan absorbance compared to the WT was observed for clones 3 and 7. A significant increase was observed for clone 3 ( $CC_{50}$  of 24 nM compared to the WT 14 nM). HEK cells were treated with increasing concentrations of MG132 with or without a non-toxic level of lansoprazole (10  $\mu$ M) (Figure 5.23b-d). A summary of  $CC_{50}$  values is presented in Table 5.4.

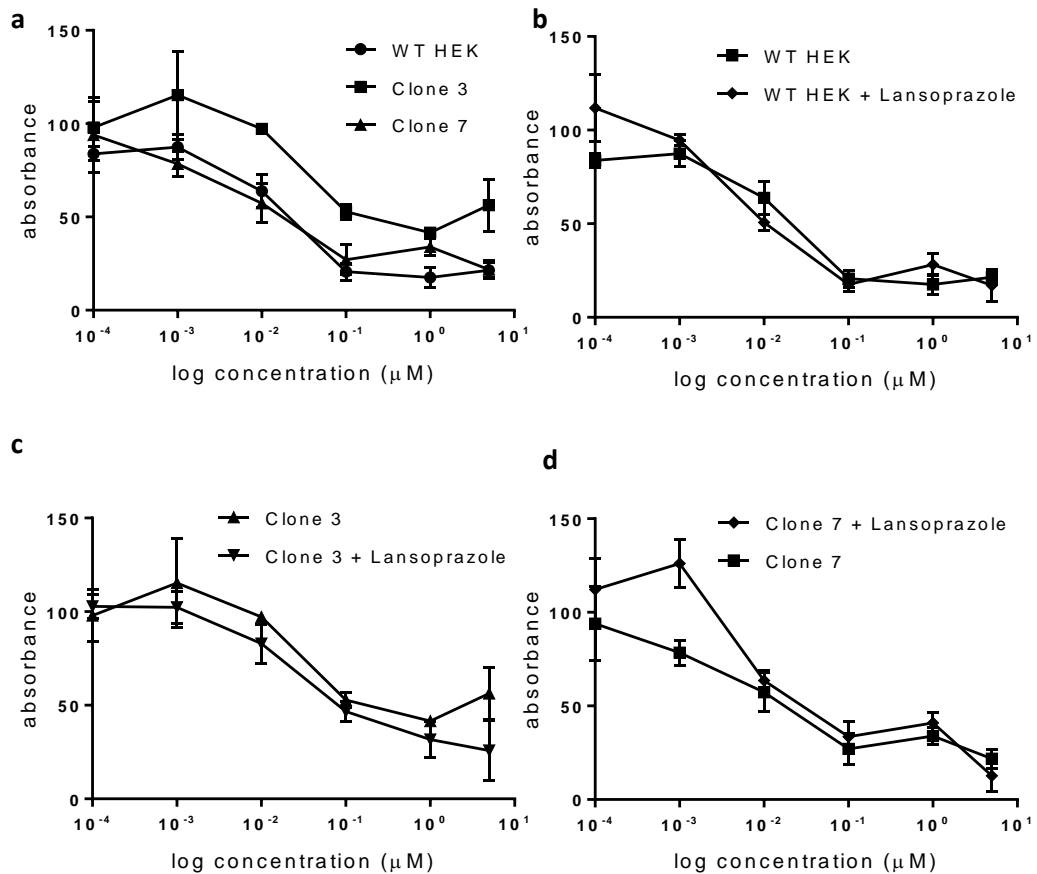


**Figure 5.23** MTT of HEK cells treated with MG132 (24 h) in the presence or absence of lansoprazole (10 μM). a) WT HEK, clone 3 and clone 7 cells treated with MG132 (0.1-15 μM, 24 h), b) HEK cells treated with MG132 (0.1-15 μM, 24 h) or without lansoprazole (10 μM), c) Clone 3 HEK cells treated with MG132 (0.1-15 μM, 24 h) or without lansoprazole (10 μM), d) Clone 7 HEK cells treated with MG132 (0.1-15 μM, 24 h) or without lansoprazole (10 μM). Data was normalised to the average of the vehicle. Two-way ANOVA, Dunnett's post hoc.  $n=3$ , error bars  $\pm$  SEM.

**Table 5.4 CC<sub>50</sub> values of WT HEK cells, clone 3 and clone 7 HEK cells treated with MG132(24 h) in the presence or absence of lansoprazole (10 μM)**

Condition	CC <sub>50</sub> (nM)	Fold change (WT)	Fold change (lansoprazole)
WT HEK	14		0.4
WT HEK + Lansoprazole (10 μM)	5.4		
Clone 3	24	1.7	1.6
Clone 3 + Lansoprazole (10 μM)	38		
Clone 7	6	0.4	1.6
Clone 7 + Lansoprazole (10 μM)	10		

No significant decreases in formazan absorbance compared to the WT were observed, which suggests that clones 3 and 7 are not deficient in *N*-glycanase. There was also no significant difference in formazan absorbance in WT HEKs and clone 3 between MG132 and MG132 co-treated with lansoprazole. A small difference in the viability of clone 7 when treated with MG132 (10 nM) (Figure 5.23d) was noted.

The experiment was repeated using Menadione, which serves to induce apoptosis through mitochondrial dysfunction and increased ROS production (Monteiro et al. 2013). HEK cells were first treated with Menadione to establish cell viability in the presence of the inhibitor (Figure 5.24a).

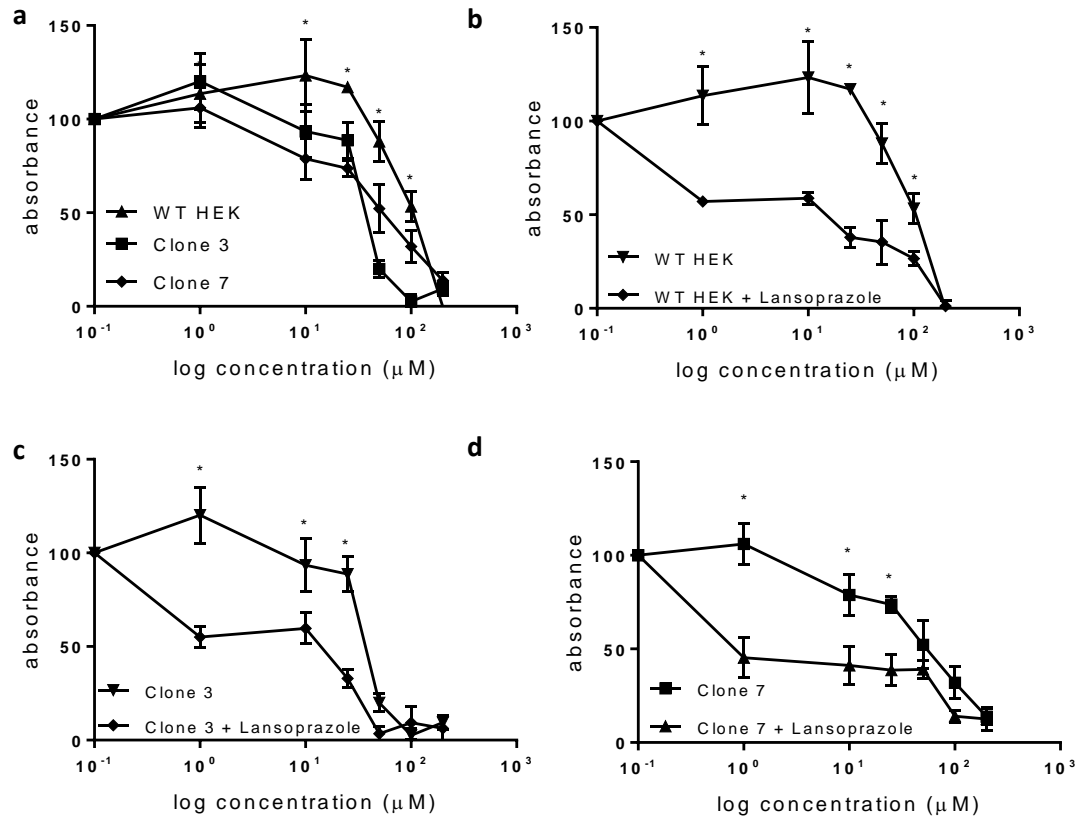


**Figure 5.24** MTT of HEK 293 cells treated with menadione (24 h) with or without lansoprazole. a) HEK 293, clone 3 and clone 7 cells were treated with menadione (1-200 μM, 24 h). b) HEK cells were treated with menadione (1-200 μM, 24 h) in the presence or absence of lansoprazole (10 μM) c) Clone 3 HEK 293 cells were treated with menadione (1-200 μM, 24 h) in the presence or absence of lansoprazole (10 μM). d) Clone 7 HEK 293 cells were treated with menadione (1-200 μM, 24 h) in the presence or absence of lansoprazole (10 μM). Data was normalised to the average of the vehicle. Two-way ANOVA, Dunnett's post hoc. Error bars ± SEM,  $n=3$ ,  $P < 0.05$ .

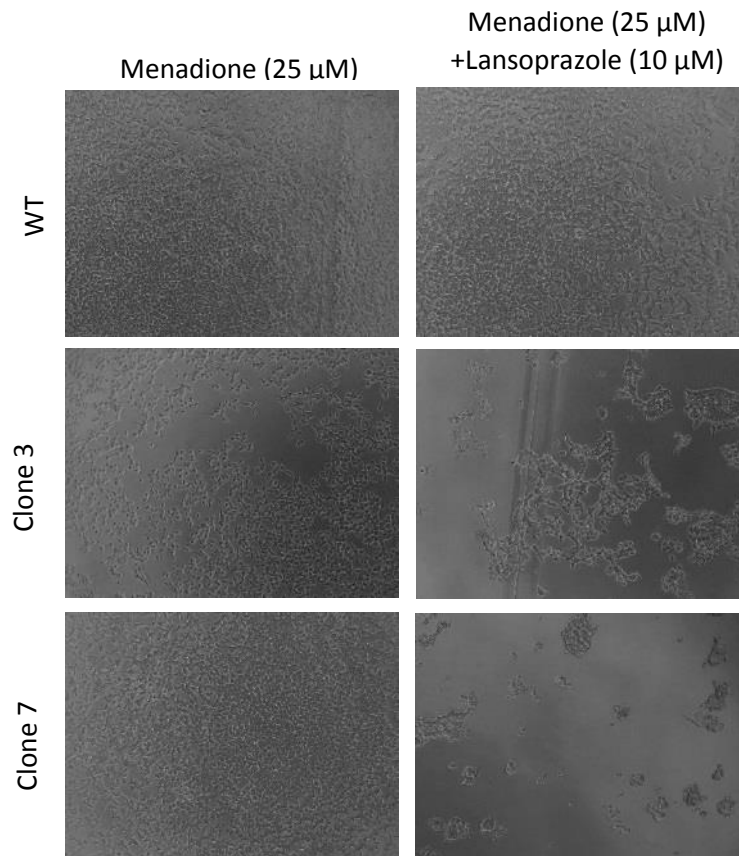


**Figure 5.25** Representative images (bright field, 20X objective) of WT, clone 3 and clone 7 cells treated with Menadione (25  $\mu$ M, 24 h) in the presence or absence of lansoprazole (10  $\mu$ M).

A summary of the  $IC_{50}$  are presented in Table 5.5. Clones 3 and 7 showed significantly lower formazan absorbance compared to the WT (0.12 and 0.2 fold change respectively compared to the WT). These results suggest that clones 3 and 7 are more susceptible to mitochondrial damage than WT HEK cells. All cell lines also had a significant decrease in formazan absorbance following the addition of lansoprazole (10  $\mu$ M).

**Table 5.5 IC<sub>50</sub> values of WT HEK cells, clone 3 and clone 7 HEK cells treated with Menadione (25  $\mu$ M) in the presence or absence of lansoprazole (10  $\mu$ M)**

Condition	CC <sub>50</sub> (nM)	Log <sub>2</sub> Fold change (WT)	Log <sub>2</sub> Fold change (lansoprazole)
WT HEK	361.16		-4.06
WT HEK + Lansoprazole (10 $\mu$ M)	23.23		
Clone 3	43.51	-3.06	-1.12
Clone 3 + Lansoprazole (10 $\mu$ M)	20.16		
Clone 7	74.15	-2.32	-3.84
Clone 7 + Lansoprazole (10 $\mu$ M)	5.8		

To further investigate mitochondrial function in these cell lines, cells were grown under high glucose (DMEM media with L-glutamine and Pen/Strep with high glucose (4.5g/L, 25 mM)) or galactose media (DMEM: no glucose supplemented with 10 mM D-galactose) or a 50:50 mix. To avoid recording changes in growth due to initial changes in acute availability of carbohydrates for metabolism, cells were grown for six days under each different media conditions to allow them to stabilise prior to measuring growth rates. Many highly proliferating cell lines are grown under high glucose levels in laboratories and, as a result of this, have adapted to produce energy via aerobic glycolysis and not oxidative phosphorylation (OXPHOS) (Aguer et al. 2011, Marroquin et al. 2007, Rodriguez-Enriquez et al. 2001). Substituting galactose for glucose in media is thought to push cells to produce energy via OXPHOS; increasing mitochondrial load and thus increasing sensitivity to mitochondrial toxicants (Marroquin et al. 2007). If clone 3 and 7 have defects in mitochondrial function or are sensitive to mitochondrial toxicants (possibly due to reduced N-glycanase activity) there may be a change in phenotype when grown in galactose. Cells were plated at 2000 cells per well in a 24 well plate, and were counted post subculture over 15 days. The doubling times were calculated for the linear phase of the growth curves. WT

HEK cells exhibited comparable growth rates in high glucose media, the 50:50 mix and the media supplemented with galactose (Figure 5.26). This indicates that the galactose does not inhibit the growth of WT HEK cells. This confirms the observations (Cannino et al. 2012) that galactose supplementation does not significantly increase the doubling times of WT HEK cells. The doubling times of clones 3 and 7 under each condition are presented in Figures 5.27 and 5.28.

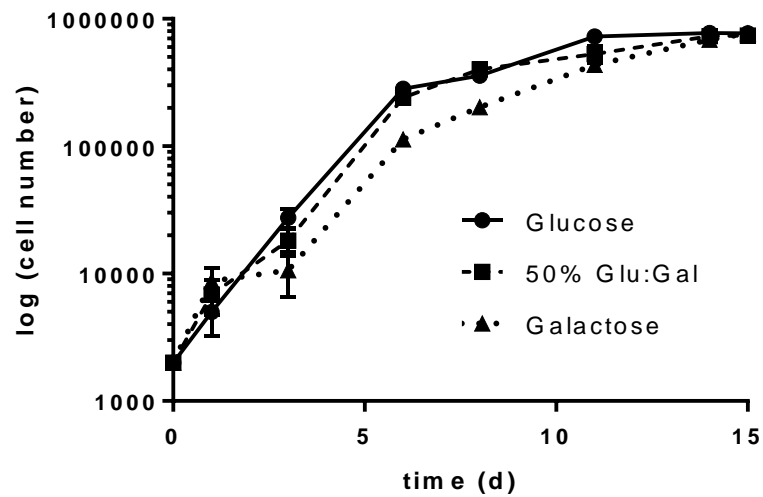


Figure 5.26 Growth curve of WT HEK in high glucose (4.5 g/L), Galactose (10 mM) or 50:50 glucose: galactose media. Cells were counted by haemocytometer and are expressed as log (cell number) per well post sub-culturing. Error bars  $\pm$  SEM,  $n=4$ .



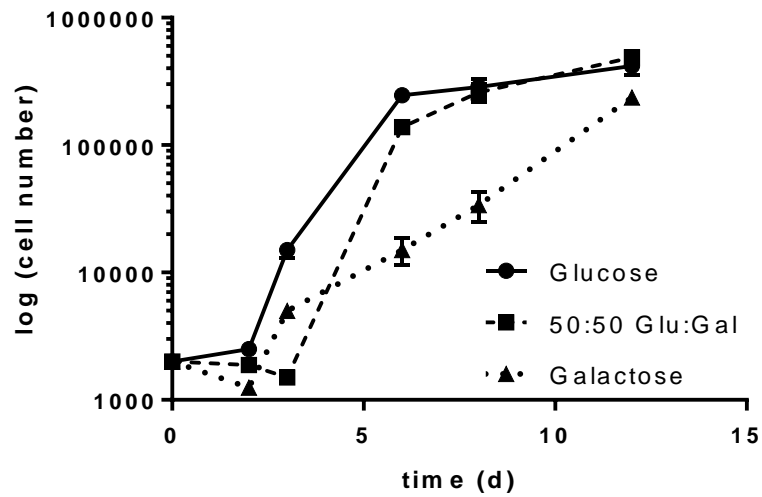


Figure 5.27 Growth curve of Clone 3 HEK in high glucose (4.5 g/L), Galactose (10 mM) or 50:50 glucose: galactose media. Cells were counted by haemocytometer and are expressed as log (cell number) per well post sub-culturing. Error bars  $\pm$  SEM, n=4.

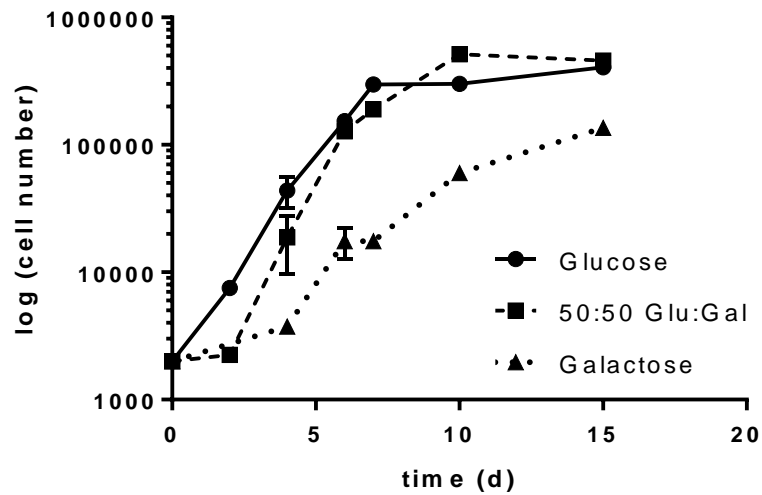
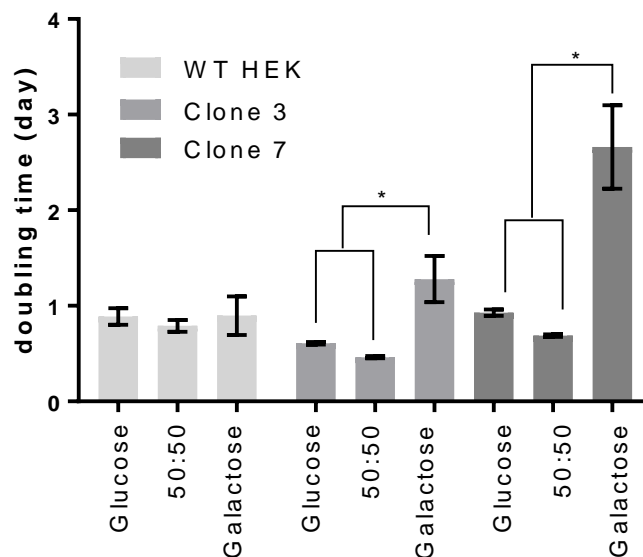


Figure 5.28 Growth curve of Clone 7 HEK in high glucose (4.5 g/L), Galactose (10 mM) or 50:50 glucose: galactose media. Cells were counted by haemocytometer and are expressed as log (cell number) per well post sub-culturing. Error bars  $\pm$  SEM, n=4.

The WT HEK, clone 3 and clone 7 were found to have doubling times of 21.0, 22.0 and 14.4 h respectively when grown in media supplemented with glucose. When grown in media supplemented 50:50 with glucose and galactose, the doubling times were 18.9, 16.3 and 11.0 h for the WT HEK cells, clone 3 and clone 7 respectively. However, when cells were grown in galactose supplemented media (10 mM), growth times for clones 3 and 7 were significantly increased (63.9 h and 30.7 h respectively) whilst that of the WT HEK cells remained similar. These results are further summarised in Figure 5.29.



**Figure 5.29** Clones 3 and 7 had significantly longer doubling times when grown in the absence of glucose. Doubling times calculated from the linear range of the growth curve. Error bars  $\pm$  SEM,  $n=4$ ,  $P < 0.05$ . One-way ANOVA within cell types, Tukey's post hoc.

### 5.3.8 Sequencing identified no changes in gDNA sequences of Clone 3 and Clone 7 compared to WT HEK cells

Whilst carrying out functional assays to characterise the properties of the surviving clones, sequencing was carried out on the amplified region spanning the predicted cut site. The PCR product was confirmed as a single band by agarose gel. Extra nucleotides and contaminants were removed using Monarch® PCR and DNA Clean-up Kit (NEB) and the product sequenced by Source Bioscience (Oxford, United Kingdom). The chromatograms for WT HEK cells, clone 3 and clone 7 spanning the target cut site at 216 are shown in Figure 5.30.

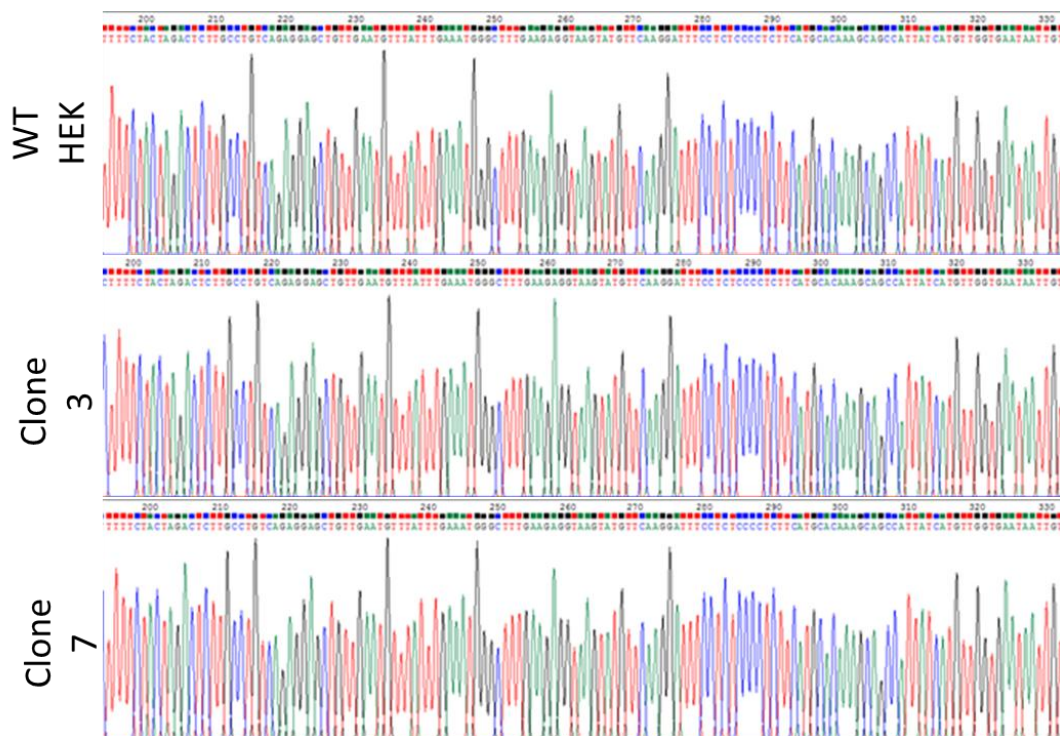


**Figure 5.30 Chromatograms of WT HEK and clone 3 and clone 7 genomic DNA sequences spanning the expected cut site at position 216.**

Although the sequences showed perfect alignment, TIDE analysis was carried out as there may be heterozygous mutations found. HEK cells are pseudo-triploid and can have up to five copies of a gene (Lin et al. 2014). The TIDE analysis and summary of any changes of the sequence are summarised in Figure 5.31. There were no significant changes between clone 3 and clone 7 compared to the WT sequence detected. Any changes detected in the chromatograms compared to the WT sequence were extremely small, with less than 1 % of the sequences having any changes.

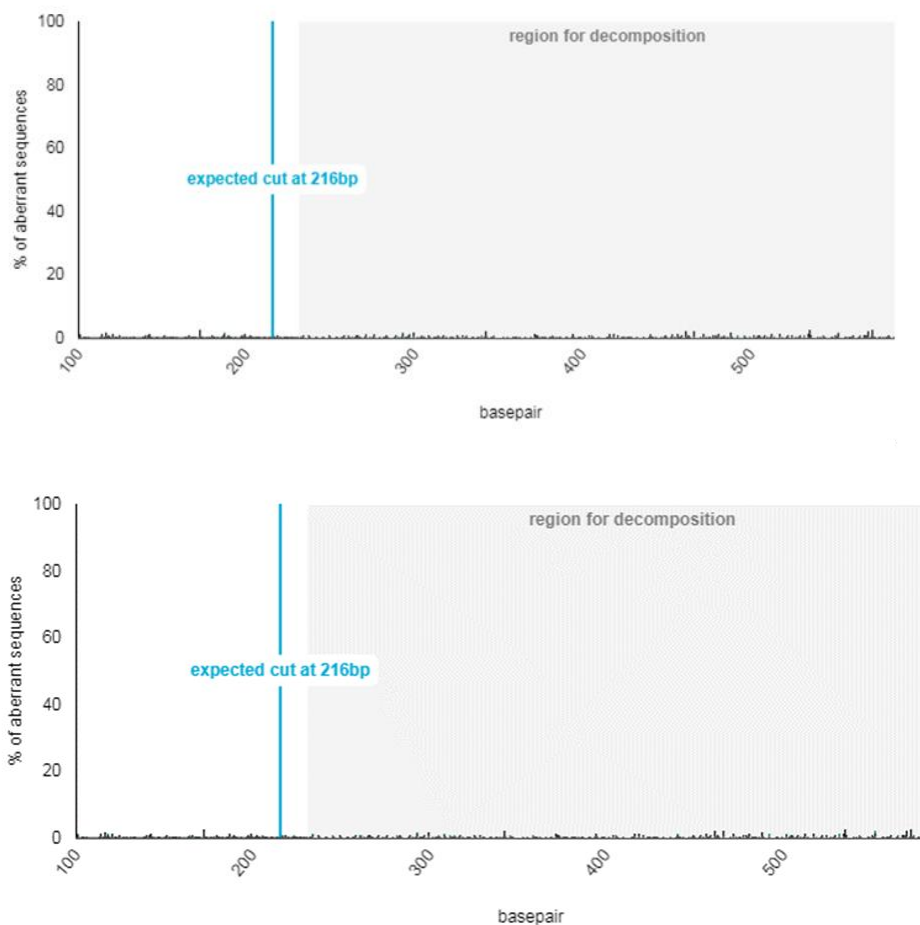


**Figure 5.31 TIDE analysis of a) clone 3 HEK cell compared to WT HEK cells and b) clone 7 HEK cells compared to WT HEK cells.**

### 5.3.9 Shotgun proteomics analysis by liquid chromatography tandem mass spectrometry (LCMS-MS)

Although no difference was identified in the sequence of *N*-glycanase there are significant phenotypic differences between the cell lines. Shotgun proteomics was performed to examine differences in protein levels between the clonal populations and the WT. Shotgun proteomics refers to the characterisation of a mixture of peptides cleaved by proteolysis. In this study, shotgun proteomics was used to profile the proteome of clone 3, clone 7 and WT HEK cell lines described above. Shotgun (bottom-up) proteomics analysis by liquid chromatography tandem mass spectrometry was employed to investigate if changes in the phenotype could be explained by differences in the proteome. Such methods provide a wide coverage of the proteome, particularly important for the detection of proteins of low abundance, or those which are under-represented in sampling and provides a means to

examine up/down regulation of proteins. In this method, three biological replicates of each cell pellet were lysed, digested by FASP and analysed by Ultimate 3000 RSLC nano liquid chromatography system coupled to a Q-Exactive mass spectrometer with two technical replicates. Peptides were mapped onto proteins using MaxQuant against Swissprot Human database with an FDR of 1 % and intensities were assessed by label free quantification.

The average LFQ intensity for *N*-glycanase is shown in figure 5.32. As previously shown (figure 5.30) there were no changes in *N*-glycanase sequence and no significant differences in intensity between cell lines.

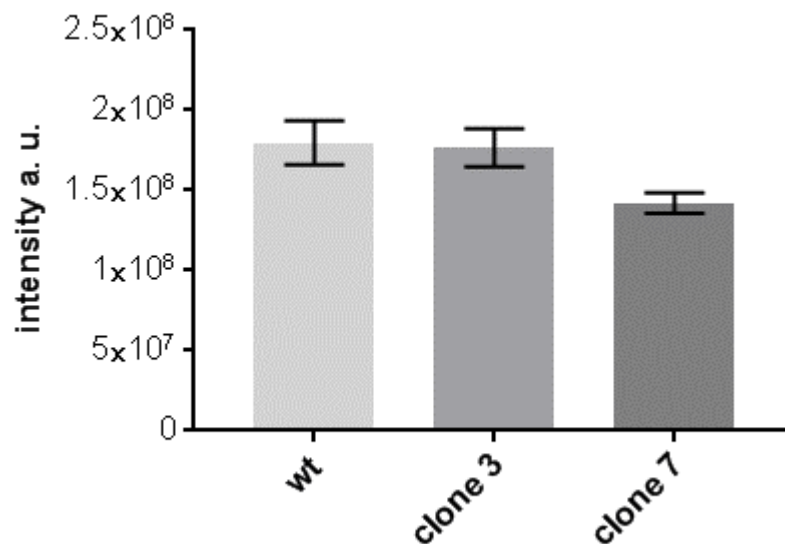


**Figure 5.32 Average intensity of *N*-Glycanase 1 in WT, clone 3 and clone 7 cell lines. One-way ANOVA**

5.3.10 Off-target effects identified by the guide sequence were significantly different in Clones 3 and 7 compared to the WT population

To elaborate on the causes of phenotypic differences of the cell lines, the off-target effects of the CRISPR/Cas9 targeting sequence were examined. Off-target effects occur when the guide sequence of the target gene closely matches the sequence of another part of DNA and is able to bind. The CRISPR design web tool calculates potential off-target effects allowing up to four mismatched bases (Zhang 2017). PNG B WT guide sequence has an estimated 12 genic off-target effects listed in Table 5.6. The intensity levels of these off-target sequences was examined. Of the off-target effects identified all had 4 mismatches. Off-target genes

were searched for in the proteomics dataset and the LFQ intensity for each was plotted. Of the 12 possible off-target genes only 7 were identified in the dataset and 2 were significantly different in clone 3. *P*-value was calculated using multiple student's t-test with Benjamini-Hochberg FDR between the WT and clone 3.

**Table 5.6 Off-target effects of PNG guide sequence B including the log<sub>2</sub> fold change in clone 3 compared to the WT population. Multiple t-tests with Benajmini-Hochberg FDR correction. NA indicates protein was not identified through proteomics analysis**

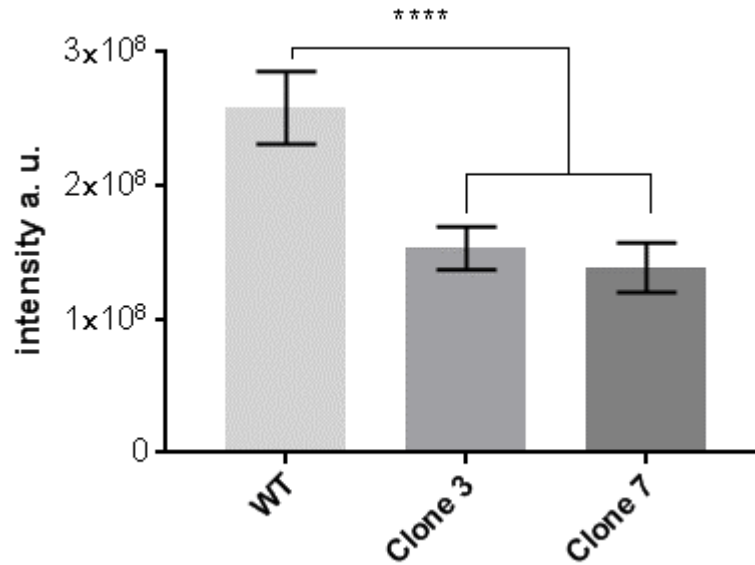
	Off-target genes	Number of mismatches	Log <sub>2</sub> fold change clone 3	<i>P</i> -value
1	UNC79	4	NA	NA
2	GPRASP1	4	-0.4737	0.103446
3	SDE2	4	0.183099	0.050965
4	IFT122	4	-0.26224	0.781510
5	WDR90	4	NA	NA
6	FAM96A	4	0.287852	0.504386
7	MAP1B	4	-0.34819	0.000036
8	IQGAP3	4	-0.75487	0.000010
9	GSKIP	4	-0.32019	0.454528
10	ZNF276	4	NA	NA
11	EPG5	4	NA	NA
12	SSTR3	4	NA	NA

Comparing the off-target for clone 7 in Table 5.7, again only 2 targets were significantly different with IQGAP3 (figure 5.33) common to both clone 3 and clone 7. Due to the different off target effects it is likely that clone 3 and clone 7 have different genetic mutations.

**Table 5.7 Off-target effects of PNG guide sequence B including the log<sub>2</sub> fold change in clone 7 compared to the WT population. Multiple t-tests with Benjamini-Hochberg FDR correction. NA indicates protein was not identified through proteomics analysis.**

	Off-target genes	Number of mismatches	Log <sub>2</sub> fold change clone 7	P-value
1	UNC79	4	NA	NA
2	GPRASP1	4	-0.37933	0.000849
3	SDE2	4	-0.03929	0.652650
4	IFT122	4	-2.13538	0.331070
5	WDR90	4	NA	NA
6	FAM96A	4	0.505333	0.652222
7	MAP1B	4	-0.0769	0.183848
8	IQGAP3	4	-0.89716	0.000004
9	GSKIP	4	0.143625	0.688025
10	ZNF276	4	NA	NA
11	EPG5	4	NA	NA
12	SSTR3	4	NA	NA

The average LFQ values for each significant different off-target effect is shown, and the position of the off-target binding site. IQ Motif Containing GTPase Activating Protein 3 (IQGAP3) was decreased in both clone 3 and clone 7. IQGAP3 is preferentially located in epithelial cells at cell-cell contact sites. Dysregulation has been associated with a number of cancers including breast, liver and gastric, pancreatic cancer (Hu et al. 2016, Qian et al. 2016, Oue et al. 2017, Xu et al. 2016). IQGAP3 has also been associated with cell proliferation, KO studies in epithelial cells inhibits proliferation and ERK activity (Nojima et al. 2008, Cagnol and Chambard 2010). In Eph4 cultures, IQGAP3 reduces expression upon cell contact, slowing proliferation. In RNAi KD experiments cell proliferation was decreased by around a third (Nojima et al. 2008). Under cell culture conditions, HEK cells and clones 3 and 7 grow at similar rates in glucose containing media and were collected at the same time which should reduce effects of cell culture technique on protein expression. However, if IQGAP3 contains a mutation in clone 3 and clone 7, this may explain differences in cell proliferation under different conditions.

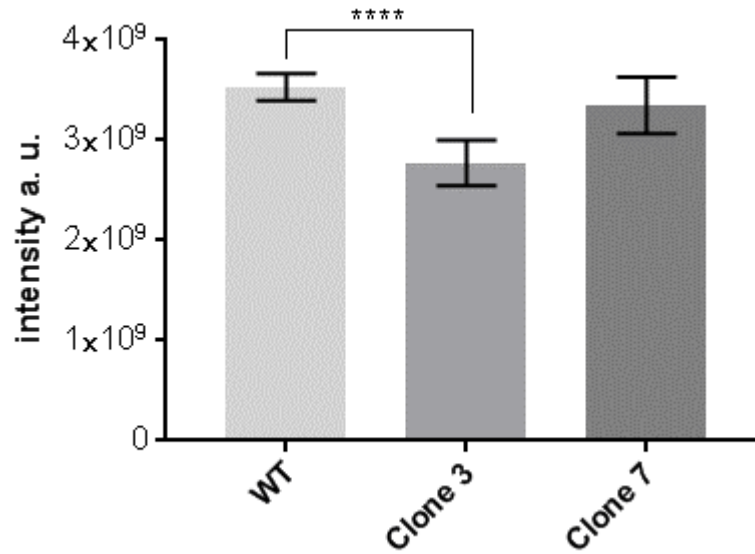


9644-GGCTGCAGGTAAGGACTAGGCTCTGCCCTGCCAGGAGTAGGCTCAATGCGTATGGGAGGG-9704

**Figure 5.33** LFQ averages of IQGAP3 in WT, clone 3 and clone 7. Error bars  $\pm$  SEM,  $n=3$ . One-way ANOVA, Tukey's post hoc. \*\*\*\* P < 0.0001. Highlighted genomic sequence indicates off target binding site, underlined sequence indicates exon. Binding site is within an intron on IQGAP3.

Microtubule Associated Protein 1B (MAP1B), shown in figure 5.34 interacts with the cytoskeleton and is involved in the trafficking of cellular components including proteins, vesicles and organelles (Bodaleo et al. 2016, Jiménez-Mateos et al. 2006). This was significantly decreased in clone 3 but only had a minor decrease of 0.12 fold change in clone 7.

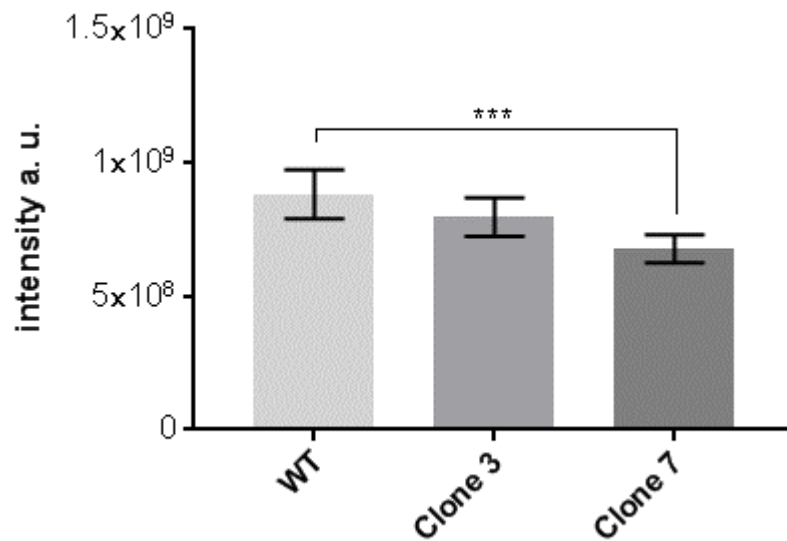




91760-CTGAAAATGGGCCAACTGAAGTGGACTACAGTCCTTCTGACATGCAGGACTCCAGTTTAT-91820

**Figure 5.34 LFQ averages of MAP1B in WT, clone 3 and clone 7 Error bars  $\pm$  SEM,  $n=3$ . One-way ANOVA, Tukey's post hoc. \*\*  $P < 0.0001$ . Highlighted genomic sequence indicates off target binding site, underlined sequence indicates exon. Binding site is within an exon.**

Most of the literature on GRIP1 associated protein 1 (GRASP1) is associated with neuronal function, but is likely to be involved in vesicular trafficking/fusion as GRASP1 KO results in endosome recycling dysfunction at synapses (Hoogenraad and van der Sluijs 2010, Ye et al. 2000). These changes in vesicle trafficking proteins may be involved in the increased sensitivity to autophagy blockers (figure 5.35).



5400-CTGGTTCTGAAAAGAAGATGAAGCCATTCAGAGGCTACTGACAGAGAAGAGTCCAGGCC-5460

**Figure 5.35** LFQ averages of GRASP1 in WT, clone 3 and clone 7. Error bars  $\pm$  SEM,  $n=3$ . One-way ANOVA, Tukey's post hoc. \*\*\*  $P < 0.001$ . Highlighted genomic sequence indicates off target binding site, underlined sequence indicates exon. Binding site is within an exon on GRASP1.

To identify off-target mutations, the DNA around the site of the potential cut-site would be amplified and sequenced. Although there are significant decreases in these highlighted proteins, it does not identify gene-editing. Differences could result from mutation sites on other proteins that do not have a significantly different protein concentration and dysfunction could cause knock-on effects. However, as a screening trial to identify mutations, it is best to start with those that are significantly different.

### 5.3.11 Global proteome analysis of Clone 3

As well as off-target effects, the global proteasome for each cell line was analysed in comparison to the WT population. Figure 5.36 shows the up and downregulated proteins of clone 3 compared to the WT. The dotted line indicates a  $p$ -value of 0.05. Protein IDs highlighted in red indicate a greater than 4 fold change compared to the WT.

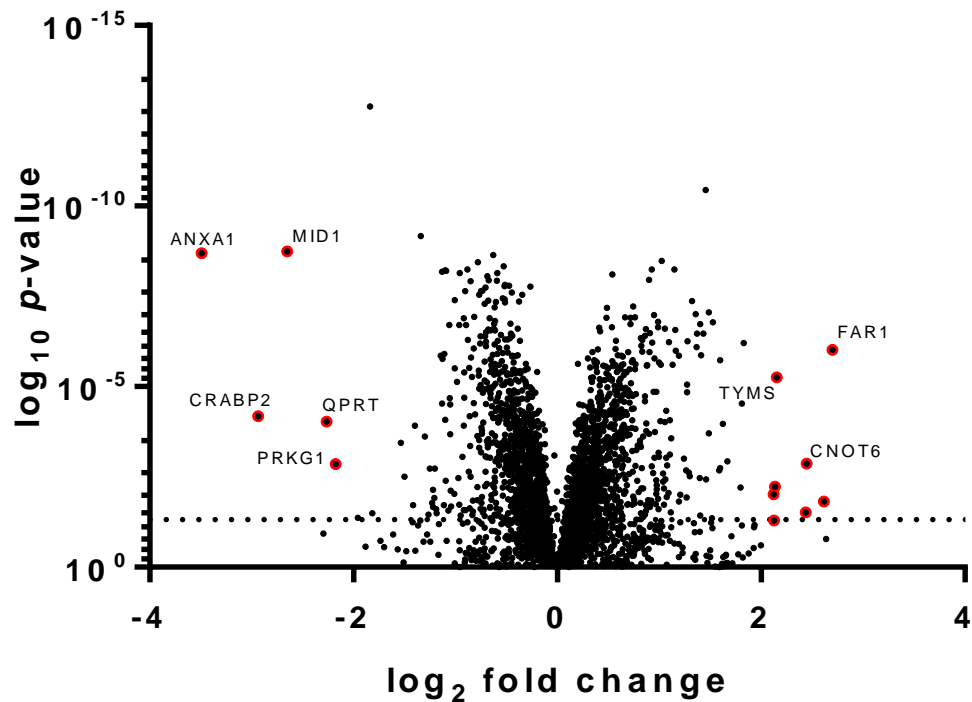


**Figure 5.36** Volcano plot of protein intensity identified in clone 3 were compared to intensity in WT samples by Student's t-test with Benjamini-Hochberg correction.  $P$ -value was plotted against  $\log_2$  fold change in expression. Black and red circles indicate protein ID's where  $p < 0.05$  and a greater than  $\log_2 2$  fold change difference.

Proteins that were significantly different and were greater 4-fold different are summarised in Table 5.8 with key functions highlighted. A number of these proteins are associated with cell cycle and metabolism which link to decreased cell proliferation under low glucose conditions. Furthermore, GPC4 is a GRIPS family protein which could be involved in the interaction with GRASP1 but are not known interactors. STRING database analysis did not identify a significant number of interactions. However, CNOT6 and PRKG1 do show an interaction and ANXA1 with the off-target ID, SSTR3.

**Table 5.8 Summary of proteins significantly up or downregulated in clone 3 compared to WT. Gene names marked in red indicate proteins shared in both clone 3 and clone 7.**

Gene Name (clone3)	p-value	Log <sub>2</sub> fold change	Function	Reference
<b>GPC4</b>	0.03047	2.436071	GRIPS family, cell cycle and growth regulation	(Karihaloo et al. 2004)
<b>BTBD2</b>	0.015382	2.613466	Binding partner to topoisomerase I	(Xu et al. 2002)
<b>FAM117B</b>	0.009688	2.122745	Lateral Sclerosis	(Hadano et al. 2001)
<b>ZFAND5</b>	0.005952	2.134269	Anchors Ub proteins to proteasome	(McCourt et al. 2018)
<b>PRKG1</b>	0.001383	-2.1752	Serine/threonine kinase, NO/cGMP signalling pathways	(Durnin et al. 2017)
<b>CNOT6</b>	0.001352	2.446814	mRNA degradation, transcriptional regulation.	(Wahle and Winkler 2013)
<b>QPRT</b>	9.24E-05	-2.26403	Catabolism of quinolinate	(Ullmark et al. 2017)
<b>CRABP2</b>	6.52E-05	-2.93548	Retinoic acid binding protein	(Percicote et al. 2018)
<b>TYMS</b>	5.55E-06	2.154701	Methylation of DNA, required for DNA replication and repair	(Krushkal et al. 2016)
<b>FAR1</b>	9.49E-07	2.699748	Reduction of fatty acids to alcohols.	(Rizzo 2014)
<b>ANXA1</b>	2.01E-09	-3.48942	Anti-inflammatory response	(He et al. 2017)
<b>MID1</b>	1.8E-09	-2.65142	E3 Ub ligase	(Du et al. 2013)

### 5.3.12 Global proteome analysis of Clone 7

Figure 5.37 shows the up/downregulated proteins of clone 7 compared to the WT. The dotted line indicates 0.05, any protein ID above this line indicates a  $p$ -value  $> 0.05$  calculated by a multiple t-tests with Benjamini-Hochberg correction. Protein IDs highlighted in red indicate a greater than 4 fold change compared to the WT. Clone 7 showed decreased cell proliferation in galactose supplemented media and increased cell toxicity when treated with lansoprazole and 3-MA. There is a phenotypic difference that is not due to targeted mutation of *N*-glycanase.

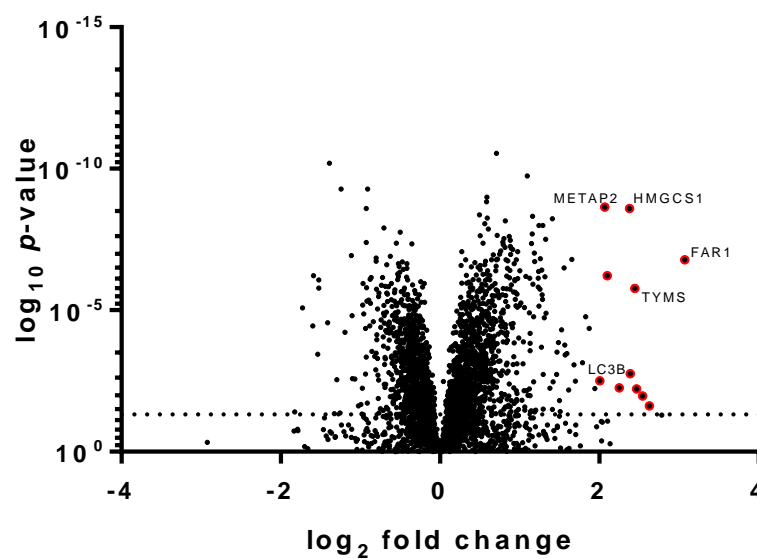


**Figure 5.37** Volcano plot of protein intensity identified in clone 7 were compared to intensity in WT samples by Student's t-test with Bonferroni correction. P-value was plotted against log<sub>2</sub> fold change in expression. Black and red circles indicate protein ID's where  $p < 0.05$  and a greater than log<sub>2</sub> 2 fold change difference.

Based on STRING analysis there was no significant interactions between proteins significantly upregulated in clone 7. Only MAP1B is shown as an interactor of MAP1LC3B which is upregulated in clone 7. This could indicate increased autophagy and play a role in clone 7 sensitivity to 3-MA. Again, GPC4 was upregulated which may be involved in GRASP1 pathway and CDC123 involved in cell cycle.

**Table 5.9 Summary of proteins significantly up or downregulated in clone 7 compared to WT. Gene names marked in red indicate proteins identified in both clone 3 and clone 7.**

Gene names (clone 7)	p-value	Log <sub>2</sub> fold change	Function	Reference
<b>GPC4</b>	0.023856	2.630387	GRIPS family, cell cycle and growth regulation	(Karihaloo et al. 2004)
<b>CAMLG</b>	0.010717	2.542715	Calcium signalling	(Jakobsen et al. 2008)
<b>CNOT6</b>	0.00608	2.469235	mRNA degradation, transcriptional regulation.	(Wahle and Winkler 2013)
<b>FAM117B</b>	0.005504	2.252368	Lateral Sclerosis	(Hadano et al. 2001)
<b>MAP1LC3B</b>	0.003133	2.004566	Autophagy marker	(Barth et al. 2010)
<b>ZFAND5</b>	0.001765	2.388114	Anchors Ub proteins to proteasome	(McCourt et al. 2018)
<b>TYMS</b>	1.7E-06	2.448217	Methylation of DNA, required for DNA replication and repair	(Krushkal et al. 2016)
<b>CDC123</b>	6.03E-07	2.100386	Required for entry into S-phase	(Perzlmaier et al. 2013)
<b>FAR1</b>	1.67E-07	3.0744	Reduction of fatty acids to alcohols.	(Rizzo 2014)
<b>HMGCS1</b>	2.56E-09	2.37906	Forms HMG-CoA	(Mathews et al. 2014)
<b>METAP2</b>	2.27E-09	2.069096	Removes N-terminal methionine from nascent proteins.	(Frottin et al. 2016)

Identification of the increased DNA repair protein, TYMS, is probably not surprising as both clone 3 and clone 7 were transfected with Cas9 designed to break DNA. Proteins involved in cell cycle and metabolic processes could be involved in the changes in growth in galactose media. This could also indicate OXPHOS dysregulation. FAM117B is involved in the KEAP1 complex which plays a role in the Nrf2 antioxidant response (Hast et al. 2013) which could also be involved in mitochondrial function. However, to categorically identify the cause of these changes, mutation sites need to be sequenced.

## 5.4 Discussion

This chapter describes the steps and strategies towards establishing a stable *N*-glycanase deficient cell line using CRISPR mediated genomic editing targeted towards both *N*-glycanase. Firstly, the tools used to initiate genome editing were described following by the efficacy of delivery and editing efficiency measured by TIDE analysis. From initial transfections clonal populations were isolated and characterised using various methods to try to identify the mutations achieved. Unfortunately, difficulties, in the detection of gene-editing lead to delayed analysis of clonal populations, leading to increased sub-culturing of unknown populations. Because of this, attempts to create a cell line deficient in *N*-glycanase resulted in the isolation of only two populations of cells with phenotypic differences from the WT cell line despite no detectable differences in the *NGLY1* gDNA. Although gene editing technologies are becoming a more common method to create stable cell-culture models, as a technique it presents a number of logistical challenges. Isolation of single colonies and confirmation of genomic changes were the main challenges of this project.

This study used CRISPR plasmids specifically designed to introduce sgDNA into cell culture models. This is a fast and easy way of creating a high number of different targeting plasmids as only the 25-nucleotide targeting sequence needs to be made for different targets. The availability and use of online guide sequence design tools further streamlines this approach. Other methods can use direct transfection of the Cas9 protein complexed with guide sequence (Liang et al. 2015), however, plasmid transfection is a common method and has been demonstrated to a high efficiency in HEK cells. Transfection efficiency was followed by GFP signal. While transfection of plasmids alone showed a good transfection efficiency, the addition of the HDR repair template decreased transfection efficiency. Methods to enrich transfected cells, such as FACs sorting based on the GFP signal would reduce the number of cells needed to be screened during clonal isolation. Co-transfection of the oligo alongside the RX plasmids did not yield incorporation of the restriction site into the genome. HDR occurs less frequently than NHEJ during S and G2 phase and only results in incorporation of around 0.5-20 % using just Cas9 plasmids and an oligo. However, methods are emerging that increase the efficiency of HDR. Inhibition of the NHEJ protein DNA ligase IV has been found to increase incorporation of oligo in a dose dependent manner in MeJuso cells with an increase in efficiency of up to 19-fold compared to an untreated control



(Maruyama et al. 2015). Another study has reported cold-shock treatment significantly increases HDR in mc-iPSCs (Guo et al. 2018) which could be used in conjunction with the introduction of non-homologous DNA method used in this study.

Difficulties in the analysis of genome editing of mixed cells proved problematic in this system. The commonly used surveyor assay did not show obvious annealing of and cutting of different species. No positive control was present so it is unclear whether this was due to low-zero genome editing or incorrect experimentation. Genome editing was assessed by TIDE analysis. This involves the comparison of high quality sequences, which required optimisation and would be more costly to screen a large number of individual populations compared to other PCR based assays. A simpler method uses PCR with the primer based over the Cas9 restriction site (Harayama and Riezman 2017). As the cut site of Cas9 is very predictable this is not difficult to do. Loss of binding of the primer indicates mutation and indicates populations to analyse further.

Further difficulties developed from the clonal isolation of populations. Many of the clonally derived cells resulting from transfection with PNG-B plasmid did not survive isolation and several populations perished after several subcultures. For isolation of single cells, serial dilutions in 96-well plates were used. Many cells do not survive isolation, as was evident in this system. This is not likely due to any mutations caused, *N*-glycanase KO models are not known to be lethal apart from the case of one mouse model (Fujihira et al. 2017). Other methods of isolation that have shown to improve cell health include the use of conditioned media. Media collected from healthy cells can be centrifuged to remove debris and used to dilute transfected cells. This media contains molecules secreted from cells during growth and can help maintain cells at a low density. Colony picking is another method of isolating clonal populations that reduces the risk of cell death due to isolation. Cells are plated in a large tissue plate at a low density so that instead of a monolayer, colonies form. Colonies can be picked using cloning rings or the tip of a pipette tip. However, this can be difficult to see individual colonies. An agarose-cloning method is similar to this but involves pouring a layer of agarose and media mixture onto the cells (Mathupala and Sloan 2009). Once the agarose has solidified colonies can be picked with truncated pipette tips and transferred to a multi well plate. This increases cell picking as the plate can be moved without dislodging colonies, prevents cells from drying and aids in sticking to the pipette tips. Isolation is

one of the most important steps and as shown in Figure 5.4, isolation and expansion of clonal populations is the most-time consuming step.

The characterisation of mutations in monoclonal populations proved difficult. Although TIDE analysis was used successfully for mixed populations, sequences for individual cell lines following clonal selection were not of sufficient quality to categorically identify mutations or WT sequences. Furthermore, the nature of HEK cells can complicate analysis. HEK cells are pseudo-triploid and the more copies of a gene, the less likely a difference in one will be seen by chromatogram. HEK cells also have a high degree of diversity, even within clonal populations, differences in karyotype have been observed (Lin et al. 2014). Due to difficulty in sequencing, surviving clones 3 and 7 were characterised to identify any phenotypic differences. Initially, N-glycanase mRNA levels were tested to try and identify KO but no clones exhibited significant decrease in mRNA, but this does not discount a reduction in protein levels. Western blot proved unsuccessful due to high levels of background. Phenotypic characterisation by cell viability in response to autophagy inhibitor 3-MA, the proteasome inhibitor MG132 and ROS activator Menadione and cell proliferation studies in different growth media did not identify mutations in the cell lines but were used to identify if any phenotypic differences were present during optimisation of sequencing was performed. Once sequencing was optimised, it was identified there was no editing in the N-glycanase gene. However, the phenotypic differences in the cells was intriguing and shotgun proteomics of the cell lines was performed.

This method is used to identify changes in protein intensity compared to the WT population. One caveat of these phenotypic changes and proteomics analysis is that clone 3 and clone 7 have undergone clonal expansion, however, the WT cells represent a mixed population. To properly control for these experiments, several isolated colonies of WT cells would need to be analysed to identify if these changes could be due to individual population differences. As mentioned, HEK cells are very diverse (Lin et al. 2014). With that in mind, shotgun proteomics allowed measurement of N-glycanase levels in cells and also allowed identification of possible mutations in off-target effects. To further characterise the use of these cells, off-target mutations need to be analysed. This can be done by amplifying the expected mutation site and sequencing the gDNA.

Significant differences in the intensity levels of four out of twelve of the genic off-target effects have already been identified.

In conclusion, this chapter identified that plasmid inducible CRSIPR/Cas9 gene editing is possible and the efficacy of the PNGB guide sequence. Further optimisation of HDR using a donor repair sequence is needed as are more robust methods for clonal expansion.

## 6.1 Introduction

Under basal conditions, autophagy maintains a healthy pool of proteins and organelles (Nixon 2013b). Under conditions of cellular stress or nutrient starvation, autophagy has been shown to selectively target different organelles such as mitochondria, ER, ribosomes and peroxisomes (Ding and Yin 2012, Overbye et al. 2007, Cebollero et al. 2012, Waite et al. 2016). Studies have used different approaches to identify core autophagic proteins (along with factors specific to different conditions and disorders) including bioinformatics, protein identification by tandem mass spectrometry (proteomics) and microscopy co-localisation (Dengjel et al. 2012, Pugsley 2017).

In yeast cells, eighteen autophagy related proteins have been identified in starvation induced autophagy and these play roles throughout autophagosome initiation, elongation and membrane closure (Suzuki et al. 2017) and are conserved throughout eukaryotic cells. However, autophagy pathways have been described that do not require all these factors, termed non-canonical mechanisms. For example, BECLIN-1, ULK1 or AMPK independent autophagy (Codogno et al. 2011, Cheong et al. 2011, Alers et al. 2012) have all been identified. Another important facet of autophagy are autophagy receptor proteins, which recognise selective cargo by binding target cargo and recruiting autophagic membranes, usually via an LC3-interacting domain (LIR) (Jacomin et al. 2016, Johansen and Lamark 2011). Table 6.1 shows a number of known autophagy receptors and specific targets for degradation.

**Table 6.1 Autophagy receptor proteins and their targets**

Autophagy receptor protein	Target	Reference
<b>P62</b>	ubiquitin	(S. Chen et al. 2014)
<b>NCO4</b>	ferritin	(Mancias et al. 2014)
<b>NDP52</b>	bacteria via ubiquitin	(Verlhac et al.)
<b>NBR1</b>	mitochondria	(Johansen and Lamark 2011)
<b>OPTN</b>	mitochondria via ubiquitin	(Wong and Holzbaur 2014)
<b>BNIP3/NIX</b>	mitochondria	(Gao et al. 2015)
<b>CCPG1</b>	ER	(Smith et al. 2018)
<b>TRIM20 and TRIM21</b>	inflammasome	(Kimura et al. 2015)
<b>PHB2</b>	mitochondria	(Wei et al. 2017)

Proteomics approaches employ tandem mass spectrometry as a tool to quantitatively study how the proteome changes. This method has been used to identify core autophagy proteins under different conditions or effects on the cellular proteome by autophagic events (Dengjel et al. 2012, Zimmermann et al. 2010, Mathew et al. 2014, Li et al. 2017, Overbye et al. 2007). Dengjel et al. (2012) examined the core autophagy proteins in MCF-7 cells under known autophagy inducing conditions to identify core proteins shared by different stimuli (Dengjel et al. 2012). To achieve this, autophagy was induced by amino acid starvation, rapamycin and then an untreated control group all treated with concanamycin A (to prevent degradation of autophagosomes) (Merkulova et al. 2014, Dengjel et al. 2012). Autophagosomes were isolated either by iodixanol density gradient or immunoprecipitation of GFP-LC3. Of the 728 biologically relevant proteins, 94 were identified in all stimuli, 42 of which are known interactors of autophagy related proteins including LC3, p62 and GABARAPL2 (Dengjel et al. 2012). Under the conditions described in this study, only autophagosome membrane proteins were identified as of interest. However, the cargo of autophagosomes can also give an insight in to the type of selective autophagy or changes in function under different conditions.

Different conditions can result in the removal of different cellular compartments. Starvation induces a bulk removal of cytosolic components, however, certain stressors such as those resulting from damaged organelles and protein aggregates require selective recognition and degradation of targets. In some cases, increased autophagosome production does not

always correlate to increased cargo degradation (Martinez–Vicente et al. 2010). Several studies have found increased autophagy in Huntington’s disease, but have found that cargo is not efficiently recognised (Tang and Sulzer 2014, Martinez–Vicente et al. 2010, S. Chen et al. 2014). In a study using two Huntington’s disease mouse models along with human lymphoblast’s from Huntington patients, proteolysis in autophagic compartments was found to be impaired (Martinez–Vicente et al. 2010). Electron microscopic images of the neurons of Huntington’s disease mouse models indicated increased double membrane bound vesicles compared to controls, but these structures had decreased electron density without identifiable cargo. To confirm this, autophagosomes from mice livers were isolated by differential centrifugation and cargo and membrane proteins were separated by hypotonic shock. The fractions were separated by bi-dimensional electrophoresis and revealed markedly less proteins in the lumen of the autophagosomes in the HD mice compared to controls (Martinez–Vicente et al. 2010), indicating a defect in cargo recognition. These results suggest that an increase in autophagosomes alone is not enough to correctly identify organelle and protein cargo for autophagic degradation.

## 6.2 Aims and Objectives

An increase in the number of autophagosomes was identified following Z-VAD-fmk and genetic KD of *N*-glycanase. To gain insight into autophagy processes in this system, autophagosomes were purified from cellular material, digested with trypsin and examined by liquid chromatography-tandem mass spectrometry (LC-MS/MS) to identify the proteins. This method will allow the detection of not just autophagy related proteins but also cargo proteins. Z-VAD-fmk and *N*-glycanase KD induced autophagy will be compared to other known methods of autophagy induction including amino acid starvation, rapamycin and basal autophagy.

## 6.3 Results

In this chapter, autophagosomes induced by Z-VAD-fmk and *N*-glycanase KD by siRNA were compared to autophagy induction by amino acid starvation, rapamycin and basal autophagy in HEK293 cells. The first section of the chapter describes the method development of autophagosome analysis, identifying how the method of sample preparation, mass spectrometry equipment and data analysis software used was refined. The latter part of this chapter looks at identification of biologically relevant proteins to examine differences between *N*-glycanase inhibition/KD compared to other autophagy models. Proteins were

identified as enriched by having a greater than twofold increase in intensity over the binding control and assigned by a minimum of two razor or unique peptides. Enriched proteins were analysed using Go Ontology terms identified by either DAVID Bioinformatics Functional annotation tool (Huang et al. 2008) or STRING database (Szklarczyk et al. 2017). The dataset was also examined for LC3 interacting proteins against iLIR database (Jacomin et al. 2016) to identify autophagy adaptor proteins involved in different conditions.

### 6.3.1. Method development

To study the composition of autophagosomes formed under *N*-glycanase inhibition compared to other forms of autophagy induction, stably transfected GFP-LC3 HEK293 cells were utilised. Autophagy was induced by Z-VAD-fmk treatment for 72 h or *N*-glycanase KD by siRNA for 5 d, rapamycin for 6 h, amino acid starvation for 6 h and an untreated control. All samples were then treated with Bafilomycin (100 nM, 4 h) to enrich autophagosomes and prevent degradation of cargo. Autophagosomes were purified by immunoprecipitation of GFP-LC3 and prepared for proteomics analysis. Figure 6.1 summarises the development of the autophagosome analysis methodology by the isolation method of autophagosomes, the method of proteomics sample preparation, the mass spectrometry equipment used and the method employed for data processing and analysis. The isolation method was optimised, to ensure efficient and specific isolation of autophagosomes are needed for meaningful analysis of proteins. As MS detection relies on the detection of peptides from which protein IDs are assigned, an efficient digestion protocol is needed. Mass spectrometers also have different sensitivity. In this study, increasingly sensitive mass spectrometers were used, along with increasingly stringent data analysis software.

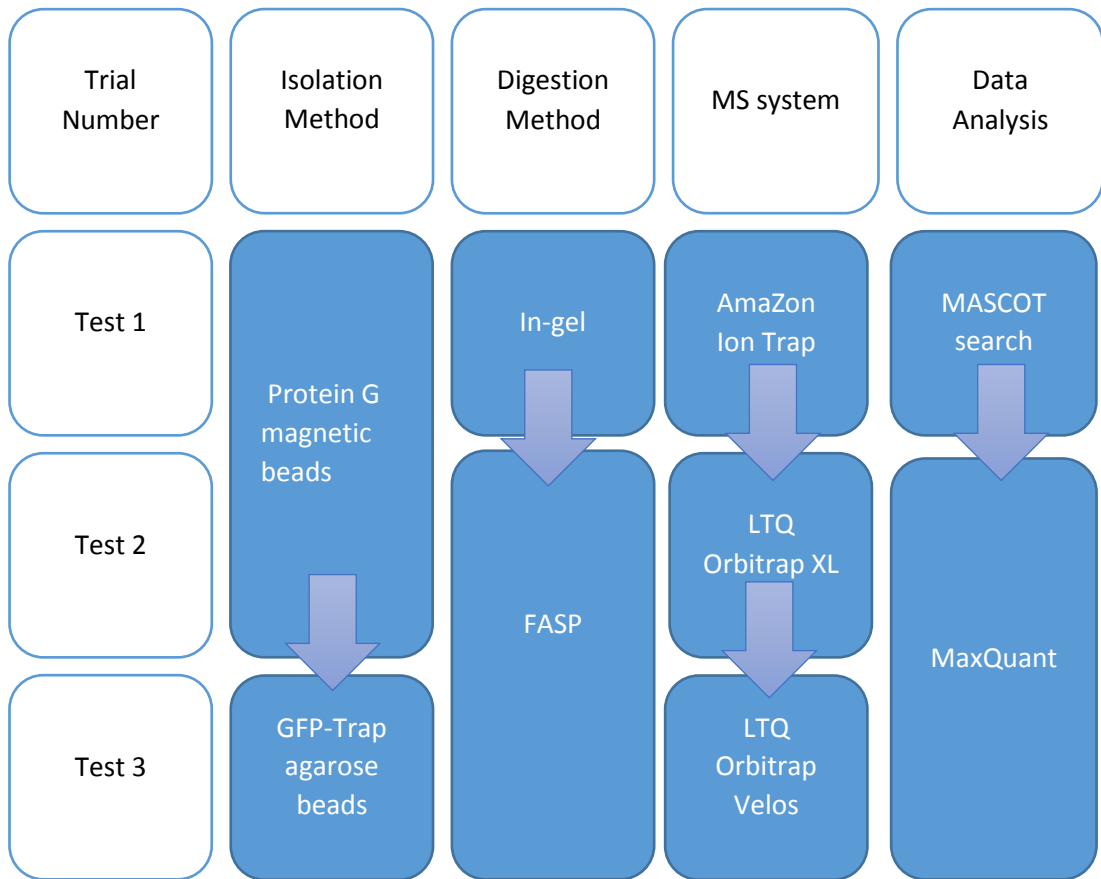


**Figure 6.1** Diagram showing method development of autophagosome isolation and analysis.

The initial test (Test 1) isolated autophagosomes using anti-GFP conjugated Protein G magnetic beads (Surebeads BioRad). Protein G is an Ig binding, bacterial protein isolated from *Streptococci sp.* that binds to the non-variable Fc region (Yang et al. 2003), allowing conjugation of different antibodies to the same bead. The aim is to co-precipitate intact autophagosomes rather than LC3 alone. For this reason, a non-ionic detergent was used to lyse cells that preserves protein-protein interactions along with a protease inhibitor cocktail to avoid protein degradation. The anti-GFP antibody (BioLegend FM264G rat anti-GFP, 2 µg) was attached to 1 mg of magnetic beads as per manufacturers' instruction followed by incubation with cellular lysate. All tests contained a mock IP as a binding control. Although the magnetic beads were conjugated to a specific antibody, other proteins can associate with the antibody or the magnetic beads non-specifically. To control for this, magnetic beads were conjugated with a rat IgG for FLAG proteins (BioLegend L5 Rat anti-FLAG, 2 µg). In this system, proteins identified at comparable intensities on the anti-FLAG conjugated beads as the anti-GFP conjugated beads, were identified as contaminating proteins and then excluded from analysis, proteins with intensity of twofold or greater were identified as enriched. After



isolation of GFP-LC3 tagged autophagosomes, samples were prepared for LC-MS/MS analysis. Proteomics relies on the analysis of peptides to identify proteins and proteins need to be digested with a specific protease (usually trypsin) prior to analysis. Test 1 used an in-gel digestion technique where IP samples are separated and visualised by SDS-PAGE before being digested. For digestion, each lane was split into five and analysed separately to increase the number of peptides identified in each condition. Proteins were digested with trypsin to generate tryptic peptides. Protein digests were then analysed using a Bruker AmaZon Ion Trap LC-MS/MS system. Peptides were assigned protein IDs using the MASCOT algorithm (Matrix Science) by searching against the SwissProt database restricted to human proteins. In this test, only a limited number of proteins were identified, on average only 74 proteins were identified in the anti-GFP pull down experiments and 53 identified in the anti-FLAG mock IP. However, LC3 was identified in all anti-GFP IP samples, indicating that the immunoprecipitation was successful.

To increase the number of protein identifications, several changes were made to the initial protocol. The starting material was increased 6-fold, along with the concentration of antibody per mg of beads and total amount of beads was doubled. The method of digestion was changed to a FASP tryptic digestion protocol (Wisniewski et al. 2009) to decrease potential loss of material occurring in in-gel digestion which can leave peptides trapped in the gel matrix. The previous study also found a high number of protein identifications in the binding control. Wash steps were increased from three to seven to remove non-specific proteins. Samples were prepared by the FASP method using a comparison between an in-house protocol and a commercial FASP kit (Expedeon). Although this method may reduce material loss during digestion, a single injection is used per sample instead of five used for the in-gel digestion protocol resulting in fewer peptides per sample. The mass spectrometer was also changed to a more sensitive model to increase protein identification. The LTQ Orbitrap XL has a higher scan speed and higher mass accuracy (due to the Orbitrap mass analyser) allowing more peptides to be identified successfully. The raw data were processed and analysed using the MaxQuant software which allows for label free quantification (LFQ) to identify and quantify proteins which are up or downregulated between experimental conditions (Wisniewski et al. 2009). This optimised approach increased the number of proteins identified, but still produced high background levels.

To further improve autophagosome purification (test 3), starting material was increased to 80 million GFP-LC3 HEK293 cells per sample. Protein lysates from GFP-LC3 HEK293 cells underwent a further centrifugation step to remove cytosolic LC3. In tests 1 and 2 lysates

underwent a soft spin to remove cell membranes. After lysis and soft spin, the supernatant of test 3 was removed and centrifuged at 17 000 g for 20 min at 4 °C to pellet autophagosomes. The supernatant was removed and the pellet was gently re-suspended in ice-cold sterilised PBS (Dengjel et al. 2012) and the immunoprecipitation was performed using this sample.

GFP-Traps® (ChromeTek) were also used in place of GFP antibody coupled magnetic beads. GFP-Traps® are manufactured with GFP antibodies derived from the *Camelidae* family, which lack any light chains and the non-variable region (nanobodies) are coupled to agarose beads. These were used in conjunction with centrifugal filters (pore size 20 µm) designed to retain the beads but not unbound proteins. Peptides were analysed using an LTQ Orbitrap Velos, and MaxQuant was used to process and analyse mass spectrometry raw data.

### 6.3.2 TEST 2: LTQ Orbitrap XL analysis revealed increased levels of mitochondrial proteins in Z-VAD-fmk treated samples

To identify the best FASP protocol a commercial kit was tested against an in-house method. This experiment was performed with two technical replicates per LC-MS/MS analysis. These methods performed comparably in terms of the number of proteins identified. To limit the impact of stochastic peak picking and thereby limitations to consistent protein identification in the data-dependent (DDA) LC-MS/MS analysis approach, the protein IDs for technical replicates and for both FASP digestion protocols were pooled. The normalised raw and LFQ protein intensities that were found in both samples were averaged. Contaminating proteins are expected to be present in both the FLAG sample and GFP sample in comparable quantities. Proteins identified with a greater than two-fold change were classed as enriched and protein intensity scatterplots as a function of log<sub>2</sub>-fold change for experiment/control are shown in figure 6.2. The value for LC3 has been highlighted in all plots.

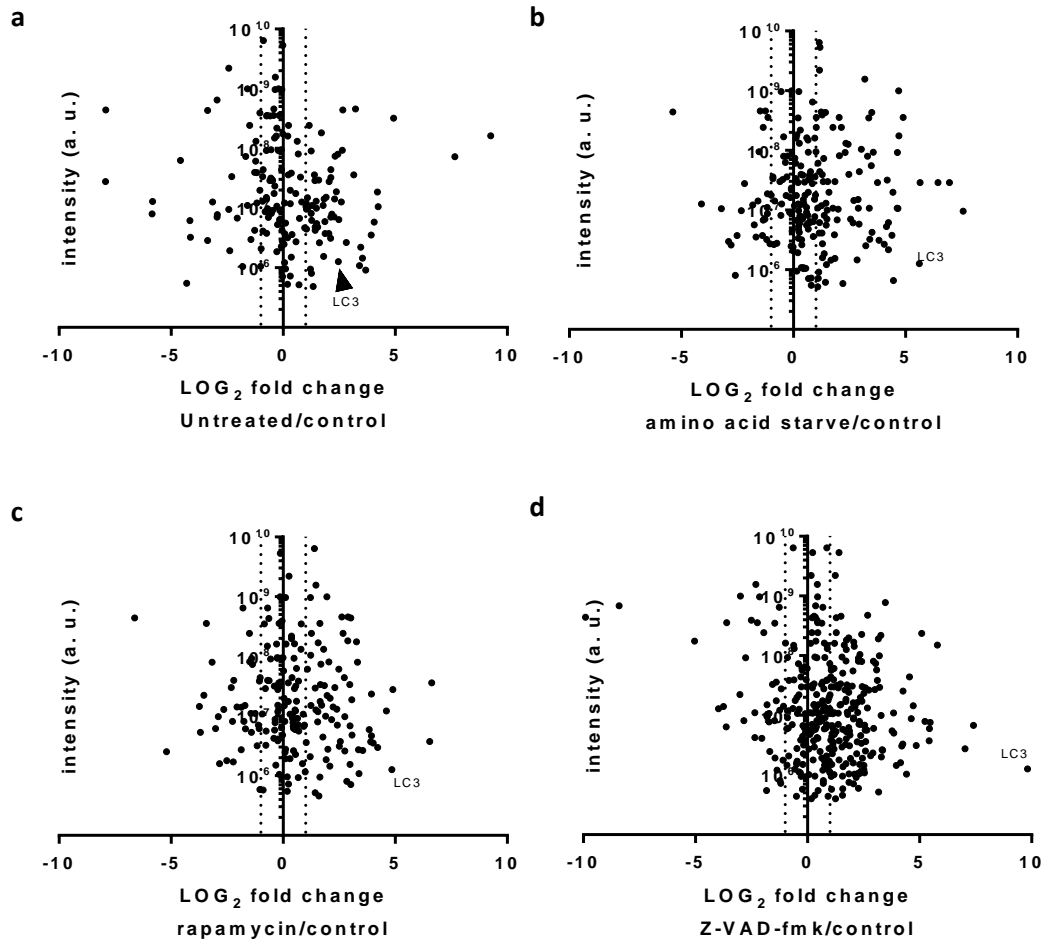


**Figure 6.2** Proteins enriched over binding controls. Log<sub>2</sub> fold change of raw protein intensity in proteins from GFP-IP compared to binding control a) untreated b) amino acid starvation c) rapamycin d) Z-VAD-fmk treated cells.

A number of proteins present in the experimental conditions were absent from the binding control. Proteins are identified by assigning peptide fragments to the ID. To avoid inclusion of ambiguously identified IDs, proteins assigned using only a single peptide were excluded from analysis (Cottrell 2011).

Proteins were compared between groups. Twenty-four proteins were found to be shared in all four conditions (Figure 6.3). As expected, LC3 along with ATG proteins, ATG7 and ATG3, were found in all conditions. ATG3 and ATG7 are involved in the attachment of LC3 to phosphatidylethanolamine (PE) which drives autophagosome maturation (Nath et al. 2014). Pro-LC3 is cleaved by ATG4B resulting in LC3 I, ATG7 binds to the C-terminus of LC3 I, ATG3 binds and ATG7 dissociates. ATG3 catalyses the addition PE to form LC3 II (Gao et al. 2013).

It is usual to see these proteins together, several co-IP experiments examining LC3 have also identified ATG7 and ATG3 in mammalian cells (Komatsu et al. 2007, Behrends et al. 2010, Tanida et al. 2001). Furthermore, ATG7 has been identified in p62 positive aggregates (Gao et al. 2013). Figure 6.3b shows a small cluster of ribosomal proteins were identified in all four groups. Ribosomes are commonly found in many proteomics samples as they are very abundant proteins. However, degradation of ribosomes has also been reported under starvation conditions and rapamycin treatment (Heinrichs 2008, Waite et al. 2016).

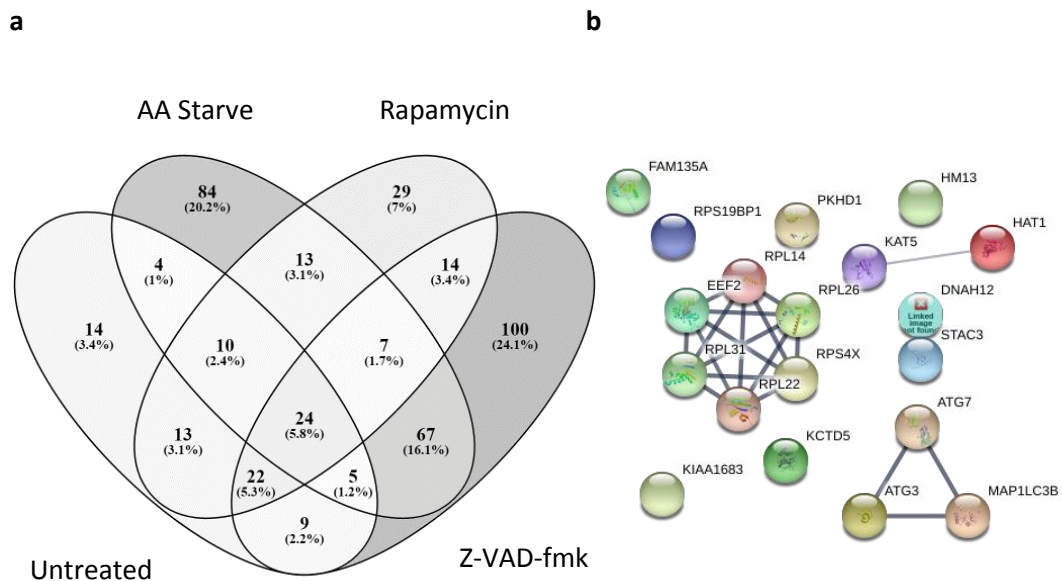


**Figure 6.3 Comparison of proteins identified in all conditions. a) VENN diagram showing overlap of enriched protein IDs. b) STRING diagram of proteins shared by all groups (Szklarczyk et al. 2017).**

Protein identifications found to be enriched in each group were pooled and analysed by DAVID Bioinformatics Functional Annotation Tool (Huang et al. 2008) to identify enriched cellular components. Of the highest, extracellular exosomes contained a high number of HSP and vesicle or vesicle trafficking proteins such as RAB family proteins, Clathrin and MAP

proteins which are also associated with other processes. The dataset also contained a high number of heat shock proteins (HSPs), histones and ribonuclear proteins.

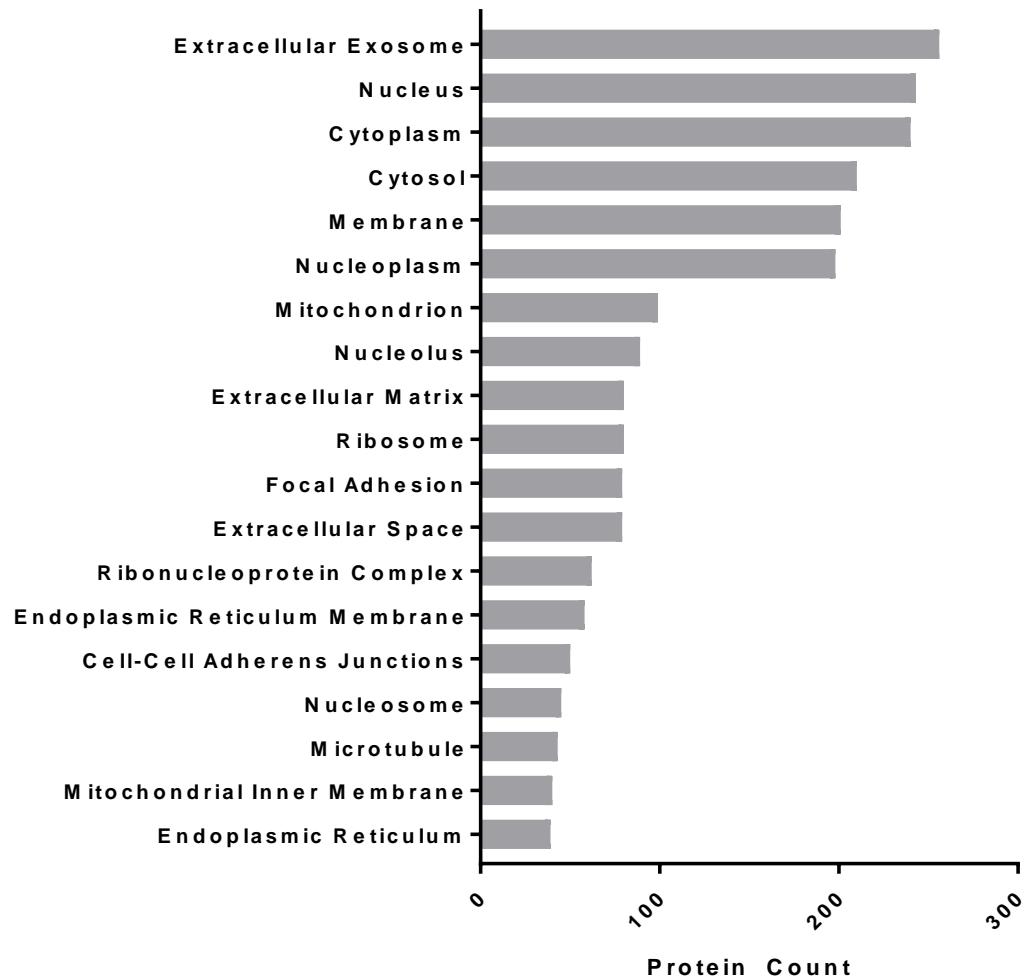


**Figure 6.4 Protein IDs assessed as enriched in each condition were pooled to identify enriched protein groups across the experiment. Protein IDs were annotated using DAVID Bioinformatics Tool (Huang et al. 2008) against Gene Ontology: Cellular Components.**

Of the enriched protein IDs across all four conditions, 13 % were identified as mitochondrial based on the Go Ontology (GO) term GO:0005739 mitochondrion. The sum LFQ intensity of all mitochondrial proteins is shown in Figure 6.5 and found a significant increase in mitochondrial protein intensity in amino acid starved and Z-VAD-fmk treated cells compared to the untreated control. This indicates more mitochondria were in autophagosomes

induced by amino acid starvation and Z-VAD-fmk treatment. Amino acid starvation has previously been linked to the induction of mitophagy in multiple cell models (Bartolomé et al. 2017, Mauro-Lizcano et al. 2015).

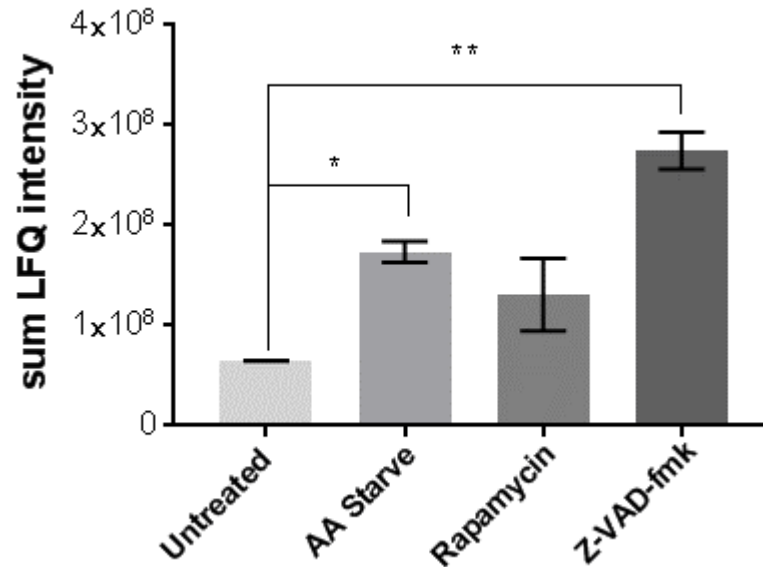


**Figure 6.5 Amino acid starvation and Z-VAD-fmk show increased mitochondria in autophagosomes. Sum LFQ intensity of mitochondrial proteins identified. Average of two technical replicates. One-way ANOVA, Tukey's post hoc.**

The protein identifications are summarised in Figure 6.6. This shows the fold over maximum intensity. In this display the protein ID with the highest intensity across all conditions equals 1 while 0 indicates an absent ID. Z-VAD-fmk treated cells had the highest intensity and number of proteins identified. The majority of these proteins represent mitochondrial membrane proteins such as translocases of the inner and outer membrane proteins (TIMM and TOMM proteins). The majority of the proteins identified in the untreated and Rapamycin treated cells represent ribosomal proteins such as Mitochondrial ribosomal protein L14 and L16 (MRPL14 and 16).

Interestingly, an autophagy receptor implicated in mitophagy was identified in both amino acid starvation and Z-VAD-fmk, PHB2 (Lahiri and Klionsky 2017, Wei et al. 2017). Mitophagy is the specific removal of mitochondria via the autophagic machinery and maintains a healthy pool of mitochondria, the entire protein content of mitochondria are turned over every few days indicating a basal level of mitochondria degradation by autophagy (Chan et al. 2015). Whole mitochondria are engulfed in double membrane vesicles and degraded via lysosomes. This process uses the same core machinery as canonical autophagy. There are two main

types of mitophagy, ubiquitin mediated mitophagy (involving the PINK1/Parkin system) and receptor mediated removal, which involves mitophagy adaptor proteins such as NIX, BNIP3, PHB2 and FUNDC1 and the recruitment of autophagy membranes.

Ubiquitin mediated mitophagy causes stabilisation of PINK1 on the outer mitochondrial membrane (OMM) upon mitochondrial membrane depolarisation. PINK1 phosphorylates ubiquitin at Ser65 (Kondapalli et al. 2012) which activates parkin, an ubiquitin ligase which attaches ubiquitin chains to OMM proteins such as MFN1 and MFN2 to amplify the PINK1 signal. Autophagy receptors including NBR1 and P62 all have LIR and UB domains to further recruit autophagic machinery (M. Lazarou et al. 2015). There are two main mitochondrial receptor families which mediate mitophagy, NIX and BNIP3 family and FUNDC1. NIX and BNIP3 are not highly expressed under normal conditions but are upregulated under hypoxic conditions and are localised to both mitochondrial and ER membranes (Zhang et al. 2008). Under hypoxic conditions hypoxia-inducible factor 1 (HIF-1) upregulates BNIP3 and NIX (Zhang et al. 2008) and under starvation conditions FOXO3 binds to BNIP3 and NIX promoter regions (Bakker et al. 2007). Both proteins contain a LIR domain, allowing recruitment of LC3. FUNDC is also located on the OMM. The N-terminus contains a LIR domain and faces the cytoplasm. Similarly to BNIP3 and NIX, removal of the LIR domain results in abolishment of LC3 binding and defects in mitophagy. Prohibitin 2 however, is located on the inner mitochondrial membrane (IMM). Prohibitin 2 can increase PINK1/Parkin mitophagy by binding autophagy membranes once the membrane has been recruited but can also bind directly to LC3 upon OMM rupture (Wei et al. 2017).

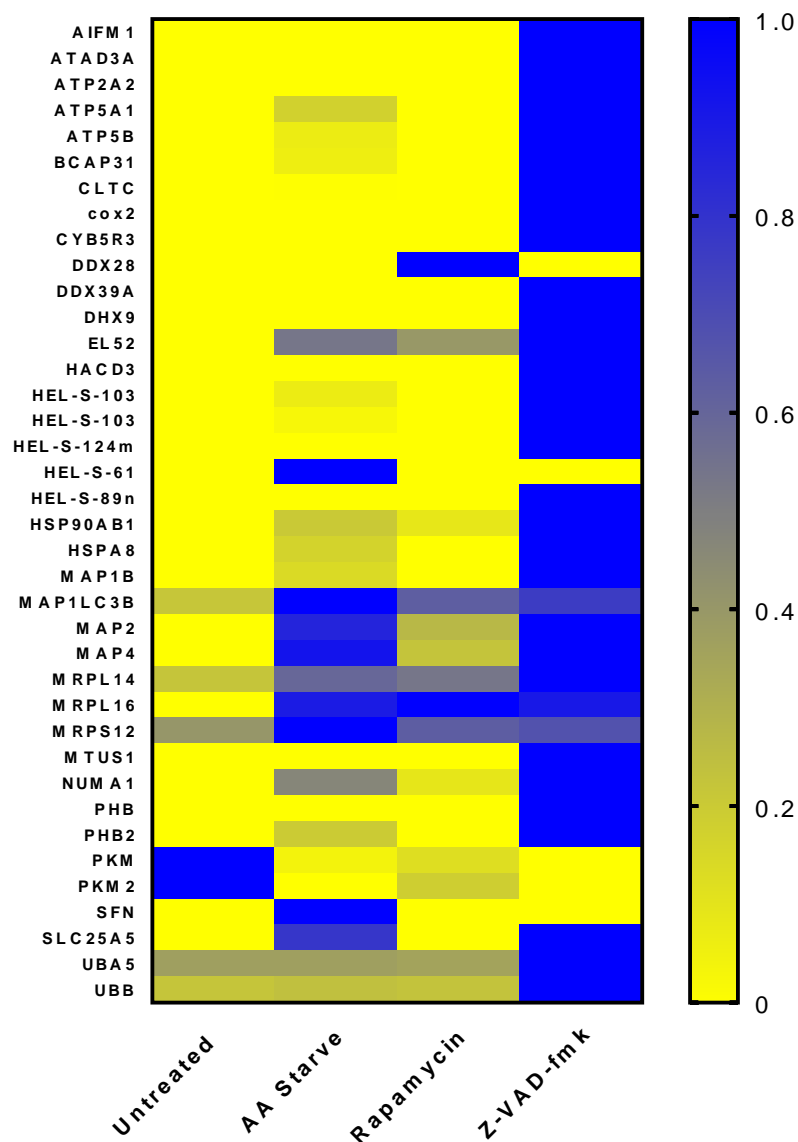


**Figure 6.6** Fold over maximum LFQ intensity of mitochondrial proteins. 1 indicates highest intensity, 0 indicates absent. Average of two technical replicates where 0 values were discounted.

### 6.3.3 TEST 3: LTQ Orbitrap Velos

The final autophagosome-IP proteomics experiment (Test 3) used GFP-Trap® isolation of GFP-LC3 in combination with FASP digestion from cells treated with amino acid starvation, Z-VAD-fmk, *N*-glycanase siRNA KD cells and an untreated control. This experiment was performed with three biological replicates. Overall, this method identified 1018 unique



protein IDs. As well as an increased number of proteins identified in each test condition, there was a decrease found in the agarose bead binding controls shown in Figure 6.7.

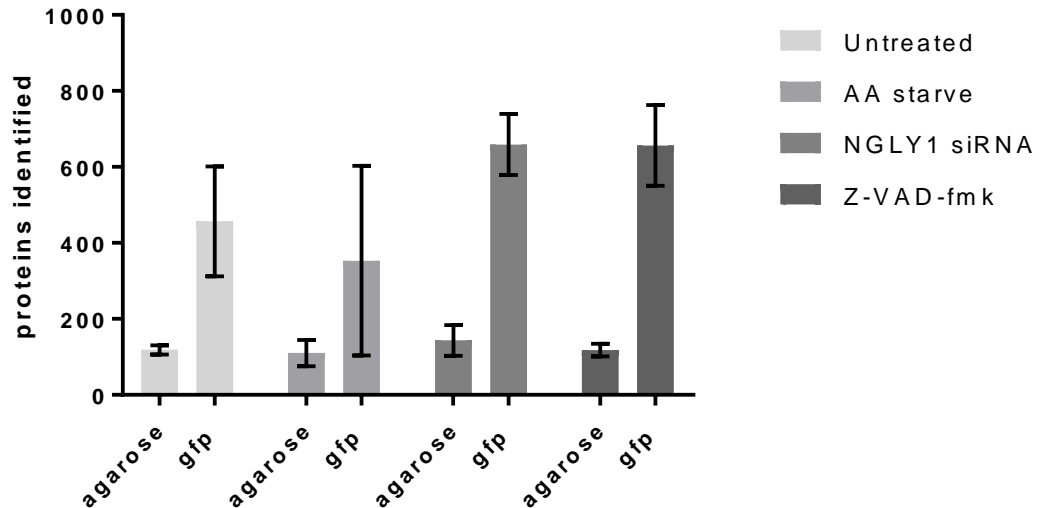


**Figure 6.7** Number of proteins identified in the GFP-Trap agarose beads and agarose bead binding control for cells treated with Z-VAD-fmk (50  $\mu$ M, 72 h), transfected with NGLY1 siRNA (25 nM, 5 d), amino acid starvation for 4 h or untreated cells. All conditions were treated with Bafilomycin (100 nM) for 4h before collection. Error bars  $\pm$  SEM,  $n=3$ ,  $P < 0.05$ .

The proteins identified in each group were compared within biological replicates of sample. Figure 6.8 shows the number of proteins shared between replicates. There is a good level of reproducibility between all biological replicates in *N*-glycanase siRNA transfected samples and Z-VAD-fmk treated cells, with 79 % and 60 % of proteins identified in all three replicates respectively. Untreated cells and amino acid starved samples showed increased variation with only 28 % and 8 % of protein identifications shared across all replicates respectively. However, in the untreated control the majority of proteins, 76 %, were identified in two or more replicates. For this reason, when averaging data, 0 values were excluded so as to not reduce protein intensity in the case of a missing value from a replicate.

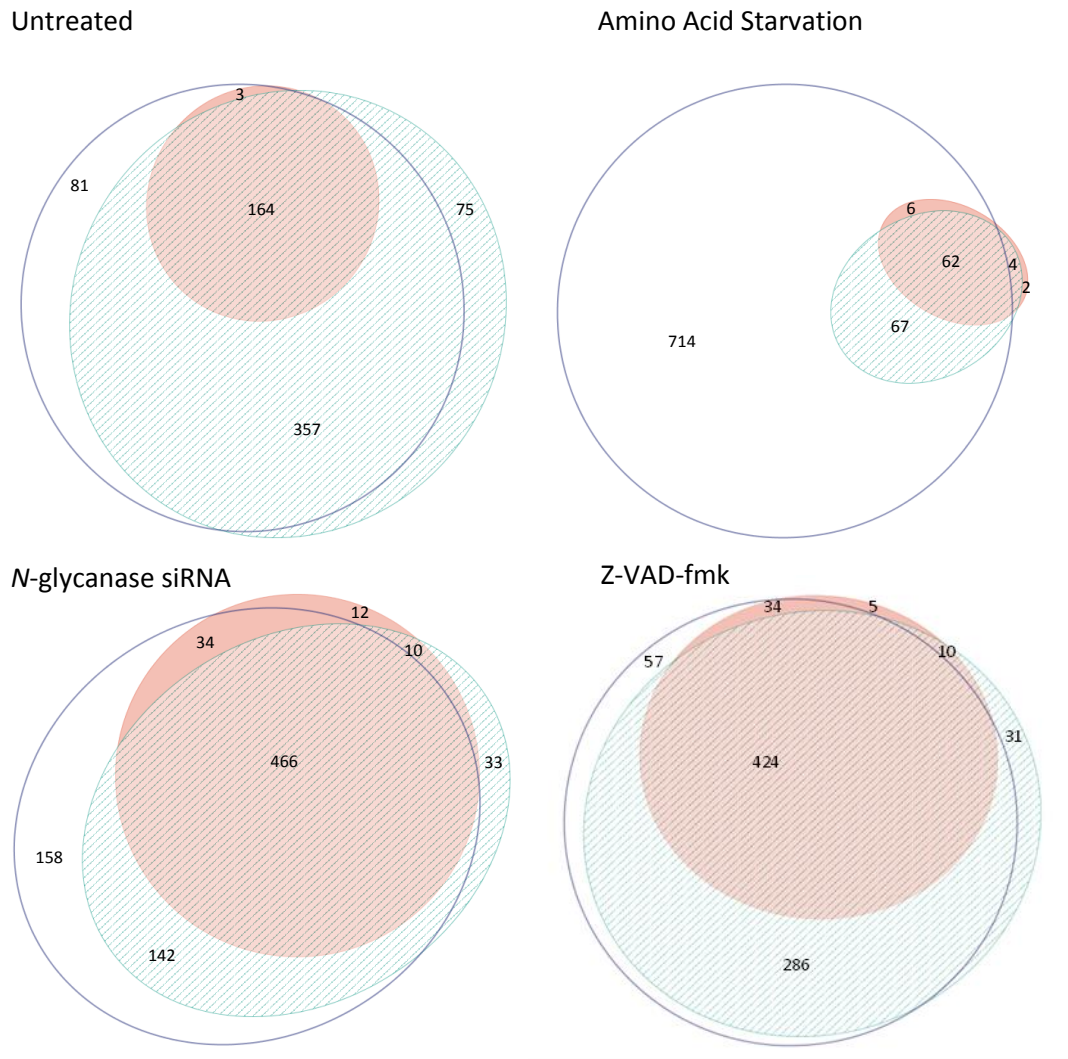


**Figure 6.8 Comparison of protein IDs found in biological replicate of cells treated with Z-VAD-fmk (50  $\mu$ M) for 72 h, transfected with NGLY1 siRNA (25 nM) for 5 d, amino acid starvation for 4 h or untreated cells with 2 or more razor and unique peptides. All conditions were treated with Bafilomycin (100 nM) for 4h before collection. Proportional VENN diagrams show the total number of proteins identified in each group. Pink indicates replicate 1, Blue striped indicates replicate 2 and clear indicates replicate 3.**

Proteins were identified as enriched if the experimental intensity was twofold or higher than the binding control. The majority of proteins identified were only present in the experimental IP and absent in the binding control. Proteins are identified by assigning peptide fragments to the ID. To avoid inclusion of ambiguously identified IDs, proteins assigned using only a

single peptide were excluded from analysis. Protein intensity scatterplots as a function of  $\log_2$ -fold change for experiment/control are shown in Figure 6.9. A number of autophagy related enriched proteins are highlighted. In all samples LC3B shows increased enrichment compared to the control samples which indicates success of the GFP-LC3 IP. Other enriched proteins include ATG3, p62, FYCO1 and MAP1B involved in autophagy and vesicle transport. ATG3 is involved in the conjugation of LC3-PE for autophagosome maturation (Nath et al. 2014). The autophagy receptor, p62 links ubiquitinated substrates to the autophagic membrane via a LIR domain (Peng et al. 2017). MAP1B and FYCO1 links vesicles via the microtubule network and FYCO1 links specifically LC3 via a LIR domain to microtubules to facilitate transport (Amaya et al. 2015).

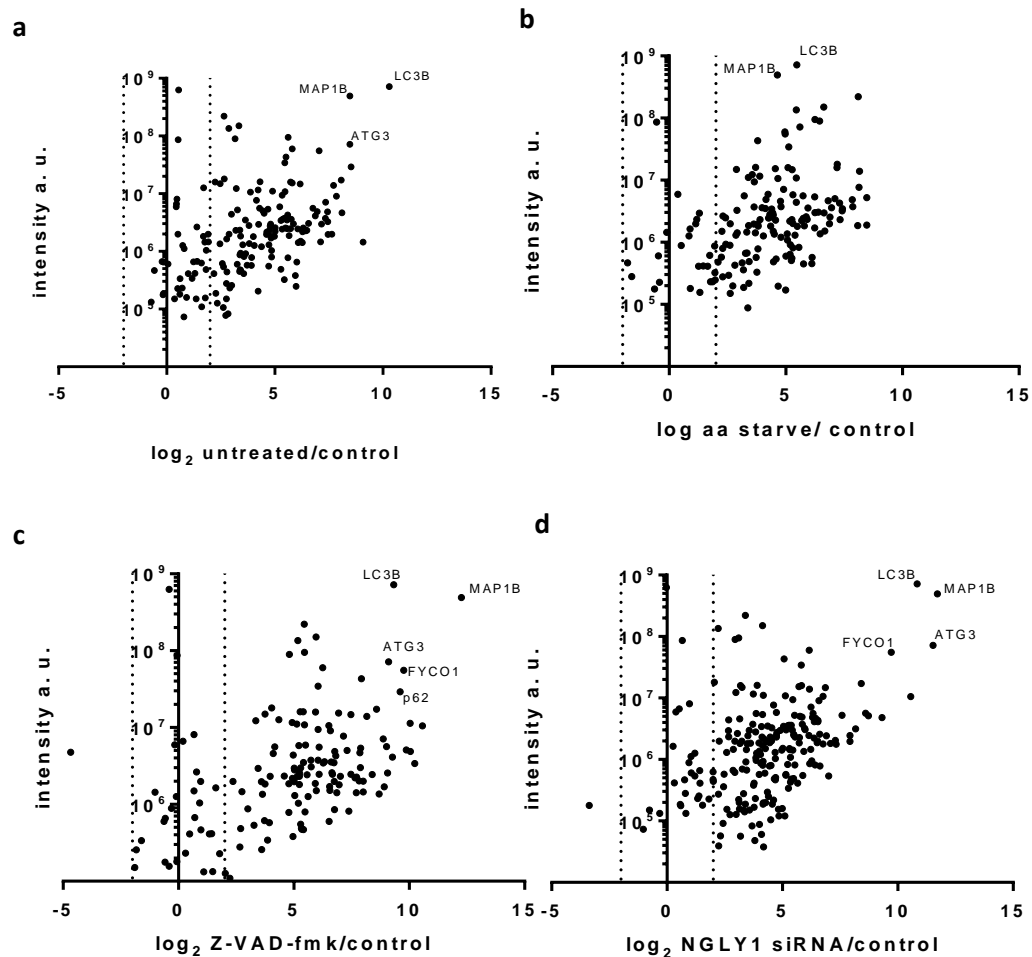


**Figure 6.9** Proteins enriched over binding controls a) untreated cells b) amino acid starvation c) cells treated with Z-VAD-fmk (50  $\mu$ M, 72 h) d) Cells transfected with NGLY1 siRNA (25 nM, 5 d). Proteins with greater than two-fold increase were identified as enriched.

Proteins identified as enriched over the binding control and containing one or more peptide assignment were analysed. Based on the averages of three biological replicates, excluding 0 values, the protein IDs were compared between the four conditions. The majority of the proteins identified in this experiment were identified in all three conditions shown in figure 6.10. This suggests that the core machinery and proteins involved in basal, amino acid starvation, Z-VAD-fmk and *N*-glycanase KD induced autophagy are very similar.

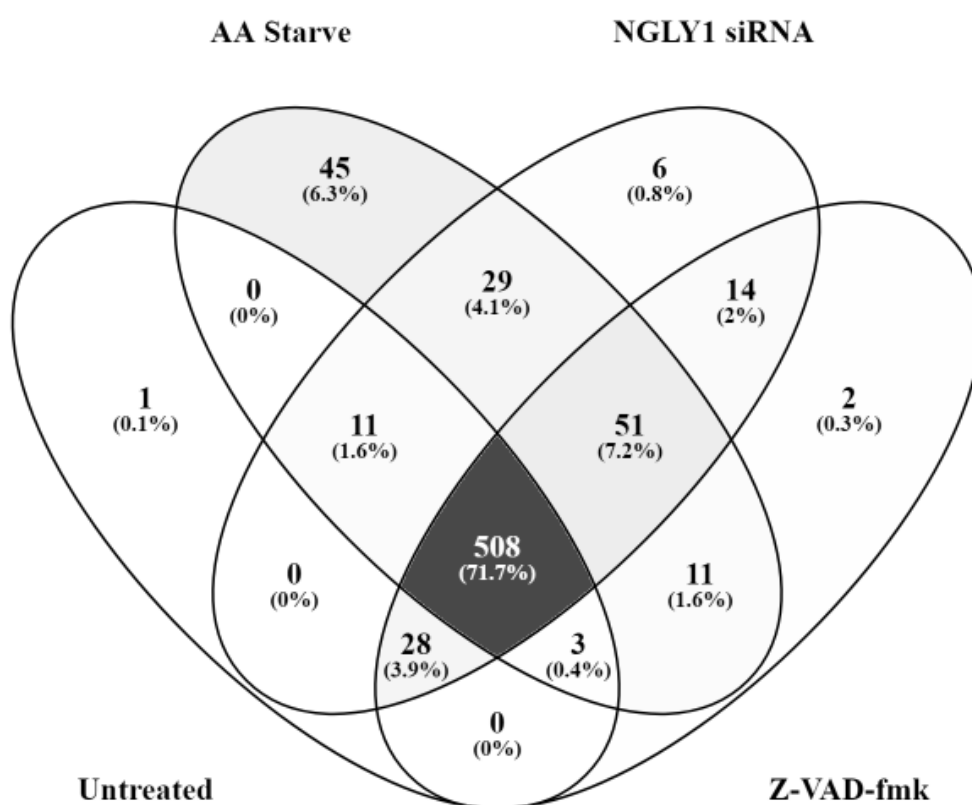


**Figure 6.10 VENN diagram showing the mix of proteins in Untreated cells, amino acid starvation, NGLY1 siRNA and Z-VAD-fmk treated cells. 71.7 % of proteins were identified in all four conditions.**

Due to the increased number and intensity of mitochondrial proteins identified in Z-VAD-fmk and amino acid starvation induced autophagy compared to the untreated control, the mitochondrial proteins were analysed in Test 3. Figure 6.11a summarises the mitochondrial proteins identified in each sample. The heat map shows the fold over max LFQ intensity, 1 indicates the highest intensity while 0 indicates ID is missing from the sample. LFQ intensity

is based on the average of three biological replicates, excluding 0 values. The sum LFQ intensities for the overall mitochondrial content is shown in Figure 6.11b. Due to the variation within amino acid starved condition replicates (Figure 6.8), the intensity of proteins is significantly decreased compared to Z-VAD-fmk and NGLY1 siRNA. Although there is no global change in LFQ intensity in Z-VAD-fmk and NGLY1 siRNA compared to the untreated control, there are individual proteins differences shown by the fold over max intensity levels in Figure 6.11a.

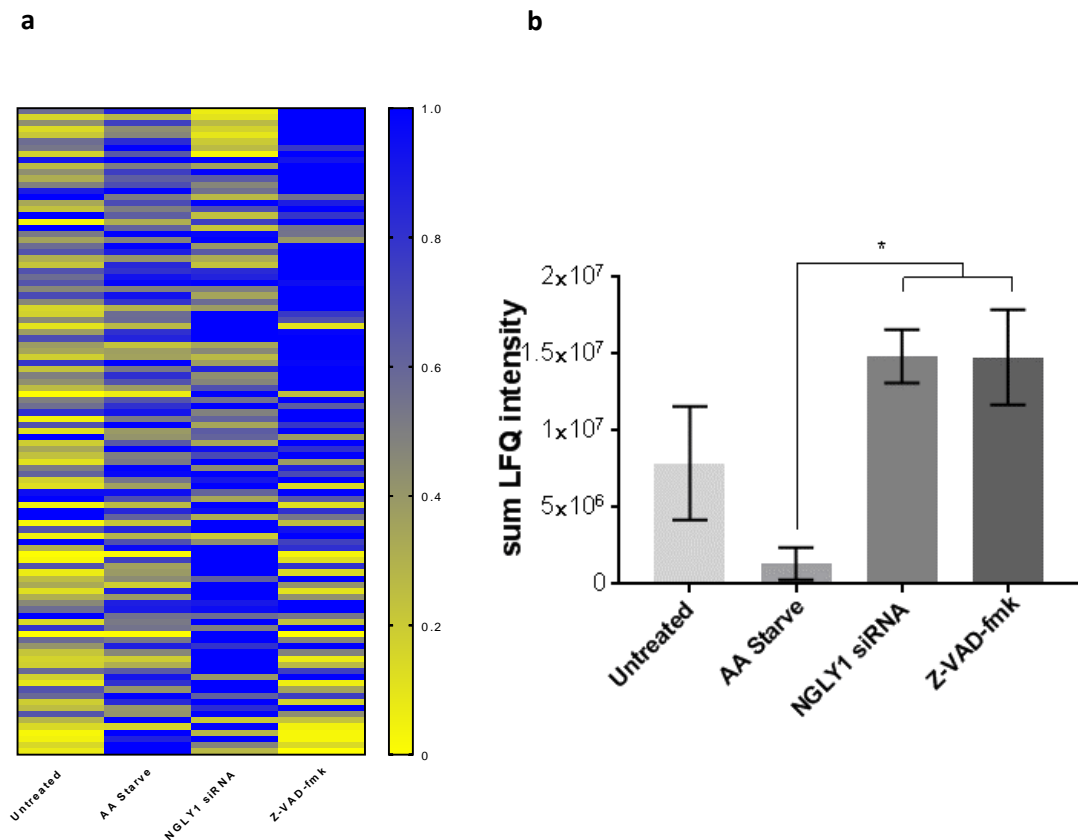


**Figure 6.11** Fold over maximum LFQ intensity of mitochondrial proteins (Test 3) Average intensity of three biological replicates, excluding 0 values. 0 indicates absence from all three replicates, 1 indicates the highest intensity in that condition for that protein b) Average of the Sum LFQ intensities of each biological replicate, excluding 0 values. Error bars  $\pm$  SEM. One-way ANOVA, Tukey's post hoc.

To identify individual differences/patterns, mitochondrial proteins were further examined. Mitochondria are central to cell survival and sensitive to changes in the cellular environment. During the activation of apoptosis, a number of mitochondrial effects have been observed including increased permeability of the OMM and release of apoptotic factors including cytochrome c and apoptosis-inducing factor Mitochondria associated 1 (AIFM1) (Wang and

Youle 2009). Proteins involved in both the positive and negative regulation of apoptosis (GO:0043066 and GO:0043065 respectively) were identified. Figure 6.12a shows the fold over maximum LFQ intensity of proteins involved in the negative regulation of apoptosis.

The majority of the proteins identified in this group are heat shock proteins, DNAJA3, DNAJA1, HSPA5, HSPA9, HSPD1, that act as chaperones for misfolded proteins to mediate stress and exert an anti-apoptotic effect (Lanneau et al. 2008). The interaction of these proteins are shown in Figure 6.12b (Szklarczyk et al. 2017) with HSPs highlighted in red. Several antioxidant response proteins were also identified including peroxiredoxin (PRDX2 and PRDX3 and PARK7 which acts as a redox sensitive chaperone, highlighted in blue in figure 6.12b (Taipa et al. 2016). Glutathione S-Transferase P (GSTP1) also exerts a protective role and detoxifies hydrophobic proteins by conjugating them to glutathione (Aynacioglu et al. 2004). Similarly to Test 2, the autophagy receptor, PHB2, was also identified. The majority of HSPs were also identified as binding to ubiquitin protein ligases, highlighted in green (figure 6.12b), indicating ubiquitin targeting of cargo. There were no significant difference in protein intensity between groups for individual proteins.

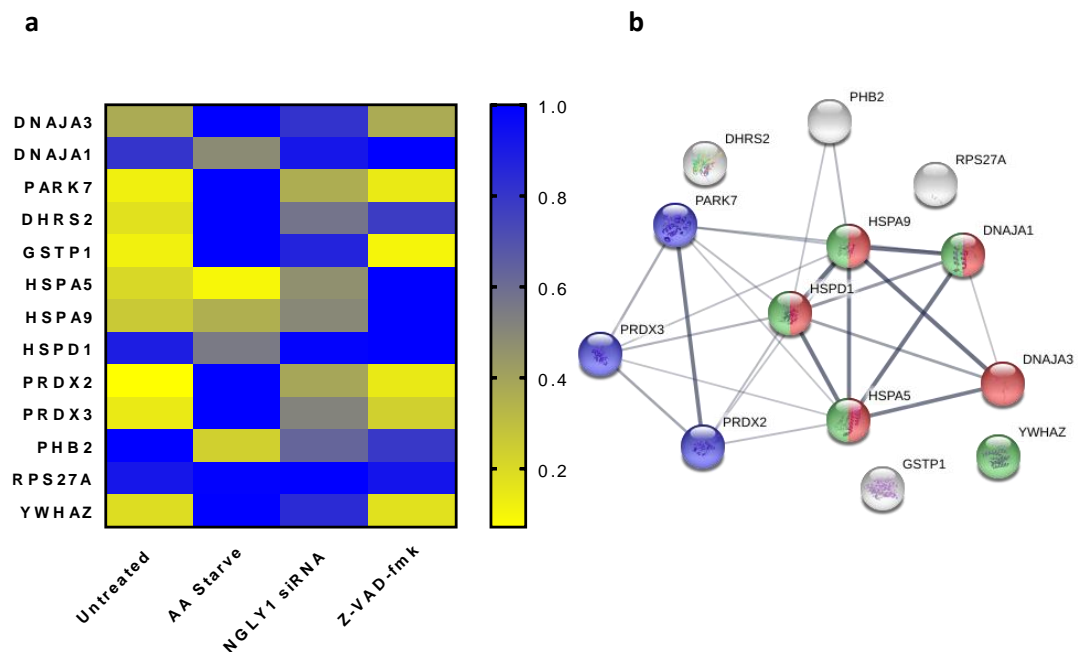


Figure 6.12 Intensity of proteins involved in the negative regulation of apoptosis.a) Summary of the fold over maximum intensity of mitochondrial proteins identified in the negative control of apoptosis (GO:0043066) b) String diagram showing interaction of proteins. Red: unfolded protein binding, blue: PRDX activity and green: ubiquitin protein ligase binding.

Several of the HSPs were also identified in the positive regulation of apoptosis (Figure 6.13a). Complement 1q-binding protein (C1QBP) is a component of the mPTP complex regulating OXPHOS and IMM permeability. Reduction of C1QBP promotes apoptosis (Kai Li et al. 2015). BAX is also involved in the permeabilisation of the OMM signalling apoptosis leading to the release of cytochrome c and apoptosis inducing factor mitochondria associated 1 (AIFM1). Many of these factors are present on the mitochondria at all times, however, BAX is recruited to the mitochondria following stress (Maes et al. 2017). There were no significant differences in intensity across the groups although there is a trend to increased identification and intensity in NGLY1 siRNA and Z-VAD-fmk treated cells of pro-apoptotic proteins, BAX and AIFM1. The interaction of these proteins are shown in Figure 6.13b (Szklarczyk et al. 2017). The level of interactions show that these proteins were not just identified in the same biological process but are also functionally related to each other in the cell.

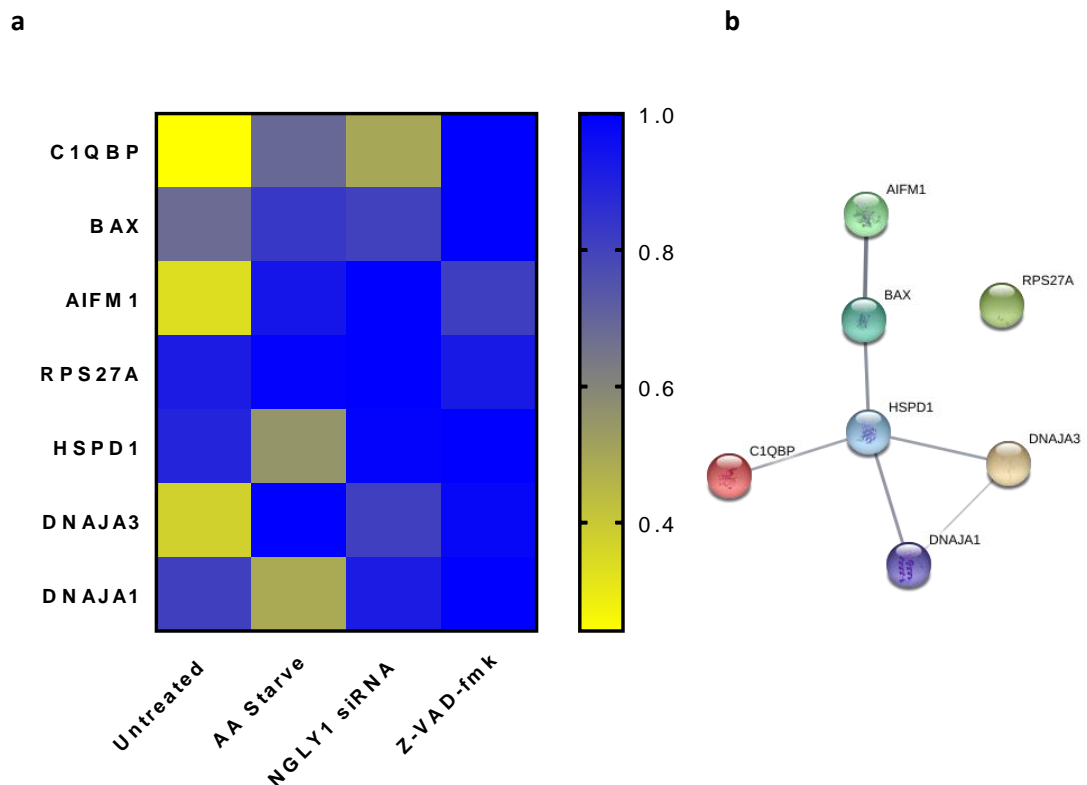


Figure 6.13 Intensity of proteins involved in the positive regulation of apoptosis a) Summary of fold over maximum intensity of mitochondrial proteins identified in the negative control of apoptosis (GO:0043065) b) String diagram showing interaction of proteins. Average of three biological replicates, excluding 0 values.

It was noted that this dataset shared a number of protein IDs with proteins found in co-immunoprecipitation datasets of *N*-glycanase (Jäger et al. 2011). Table 6.2 summarises genes with possible interactions with *N*-glycanase by co-IP collated from the UCSC Genome Browser (Kuhn et al. 2013).

**Table 6.2 Genes identified in co-IP experiments with *N*-glycanase (Kuhn et al. 2013, Jäger et al. 2011). Gene IDs highlighted in green indicate presence in autophagosome isolation.**

ACBD3	AP1M1	APP	ATL3	ATP2A2	ATP2A3	BCAP31
C20orf24	CALR	CAPN1	CHAF1B	CHI3L2	CKAP4	CLGN
CLN6	CTSD	DERL1	DHCR24	DNAJB11	EMC1	ENDOD1
ERGIC2	ERGIC	ERLEC1	FAF1	FLOT1	GANAB	GLG1
HM13	HSPH1	ITGAL	ITGB2	ITM2B	KIR3DL1	KIR3DL2
LDLR	LMAN1	LMAN2	MESDC2	NPLOC4	NSFL1C	OS9
PDIA3	PDIA6	PGRMC1	PHB	PHB2	PIP4K2A	PRKCSH
PSMC1	PSMC2	PTPLAD1	RABGAP1	RAD23A	RAD23B	RAN
RER1	RHOC	RNF5	SDF2	SDF2L1	SEC61A1	SEC62
SEH1L	SEL1L	SPAG5	SPCS2	SPCS3	SRPK2	SSR4
SUN1	SURF4	TIMM13	TIMM8A	TIMM8B	TMEM38B	TRBC1
TRBV12-3	UBC	UFD1L	UGGT1	UGGT2	VAPA	VCP
RPN1						

Of these, 19 were also identified in the autophagosome isolation and mainly consisted of ER proteins. Figure 6.14 shows the interactions of these proteins. ER proteins are highlighted in blue, the proteasome complex in yellow, the Golgi apparatus in green and mitochondrial intermembrane space protein transporter in red (Szklarczyk et al. 2017). As a member of ERAD (Chantret et al. 2010, Suzuki 2015, Suzuki et al. 2001, Suzuki et al. 2016), *N*-glycanase would be expected to co-precipitate with ER resident proteins and members of the proteasome. Inhibition and *N*-glycanase KD may change the interaction profile of these proteins. While inhibition leaves the protein in the cell but reduces activity, siRNA mediated KD stops the translation of new proteins, also removing non-deglycosylation functions of the protein.



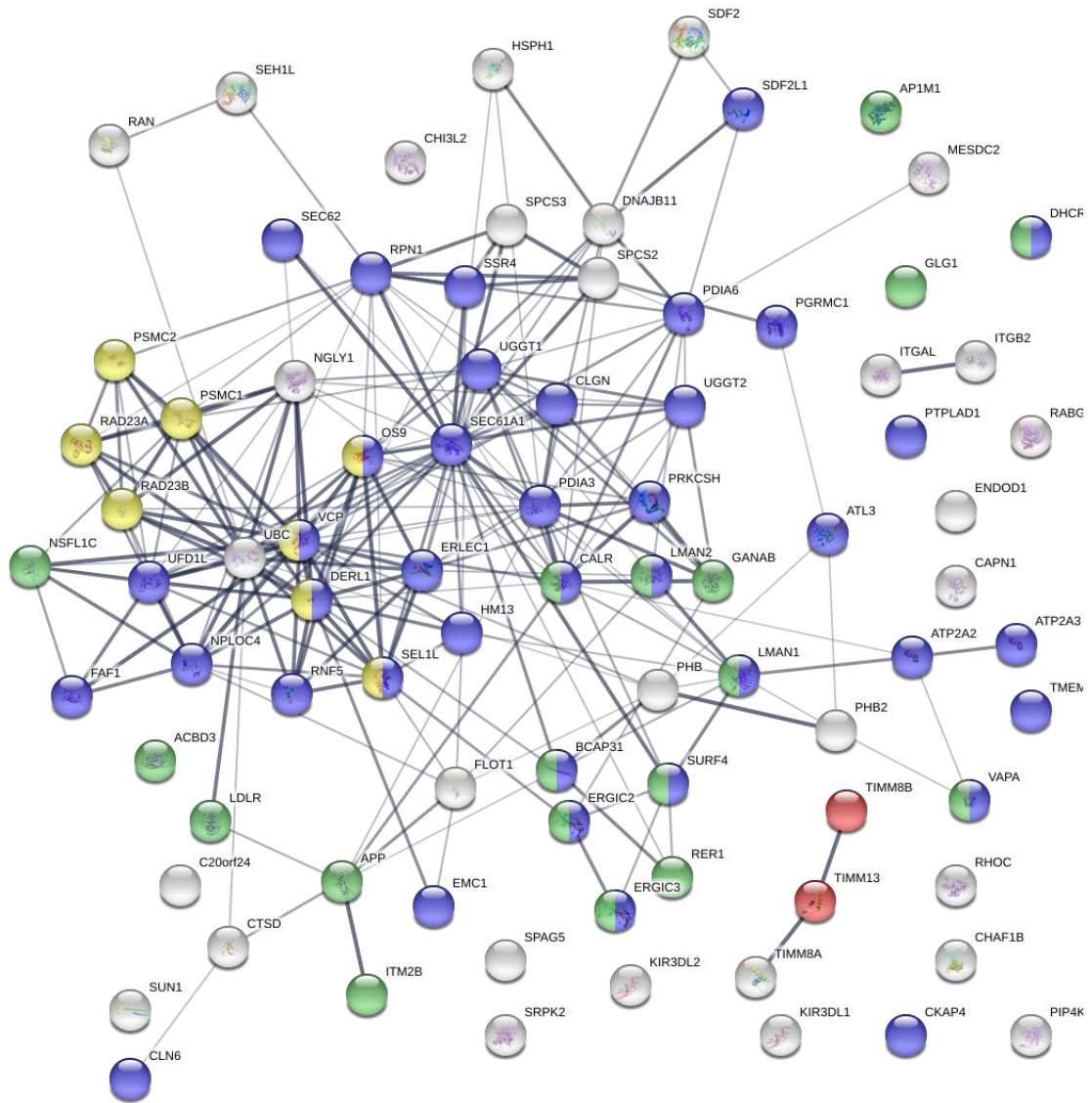


**Figure 6.14** STRING diagram showing interactions of proteins identified in Table 6.2. Blue: Endoplasmic reticulum, Yellow: Proteasome complex, Green: Golgi apparatus, Red: Mitochondrial intermembrane space protein transporter complex (Szklarczyk et al. 2017). Line thickness indicates confidence of interaction.

The proteins identified as possible *N*-glycanase interactors were studied. The average (excluding 0) fold over maximum intensity is summarised in Figure 6.15a. Using multiple t-tests with Benjamini-Hochberg correction, a significant difference in PSMC2 was identified between the untreated control and *N*-glycanase siRNA KD (Figure 6.15b). Proteasome 26S subunit ATPase 2 (PSMC2) is a subunit of the regulatory particle of the 26S proteasome. PSMC2 has received interest due to its increased expression in osteosarcoma cell lines (Song et al. 2017), KD of which halted cell cycle and increased apoptosis in osteosarcoma cell lines

(Song et al. 2017) thereby inhibiting tumour growth. This also identifies PSMC2 as an integral part of the 26S proteasome.

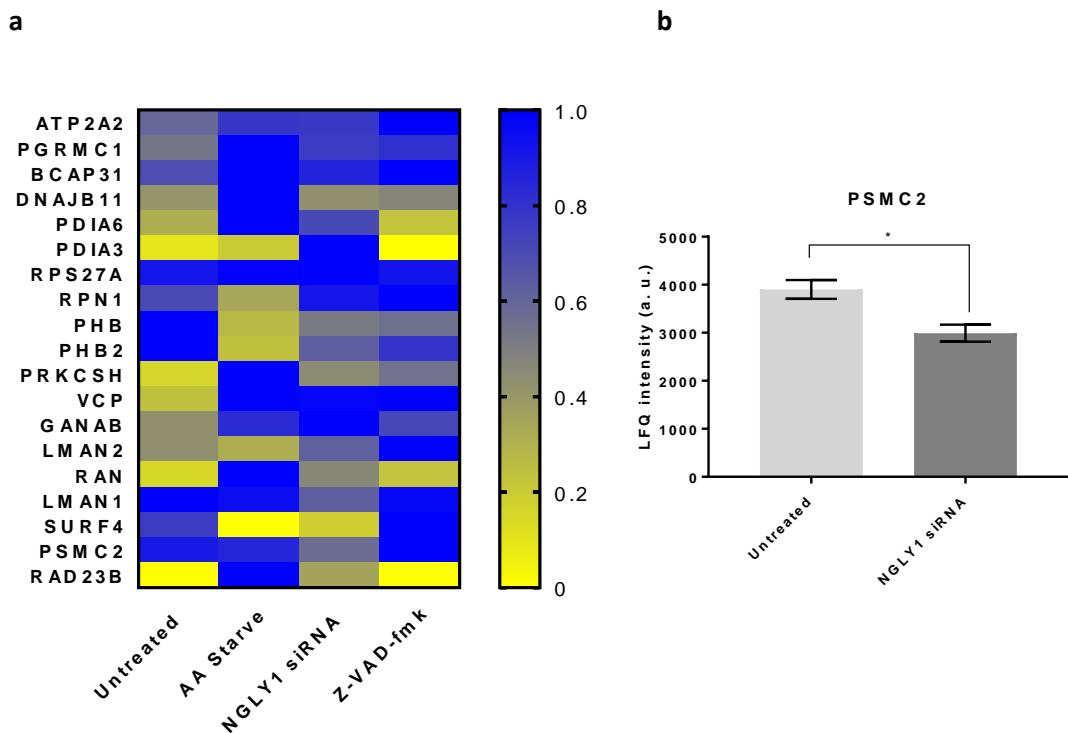


**Figure 6.15** Intensity of proteins identified as co-precipitating with *N*-glycanase. **a)** Fold over maximum intensity, average of three biological replicates excluding 0 values. **b)** Average LfQ intensity of PSMC2 of three biological replicates excluding 0 values in Untreated and NGLY1 siRNA KD.  $P < 0.05$ .

Due to the significant decrease in PSMC2 identified in figure **6.15b**, other proteins identified as partners in the proteasome complex identified from the GO term GO:0000502 were examined. RAD23B also identified a significant decrease in *N*-glycanase siRNA treated cells compared to the untreated control (Figure **6.16a**). RAD23B is a ubiquitin receptor for the proteasome joining ubiquitinated substrates for proteasomal degradation (Wade and Auble 2010). This trend of decreased proteasome subunits was found in both Z-VAD-fmk and *N*-glycanase siRNA mediated KD for PSCM3 and PSCM5 (Figure **6.16b** and **6.16c**) although no significant differences were identified. No obvious decrease was observed in VCP and PSMC6 (Figure **6.16d** and **6.16e**).

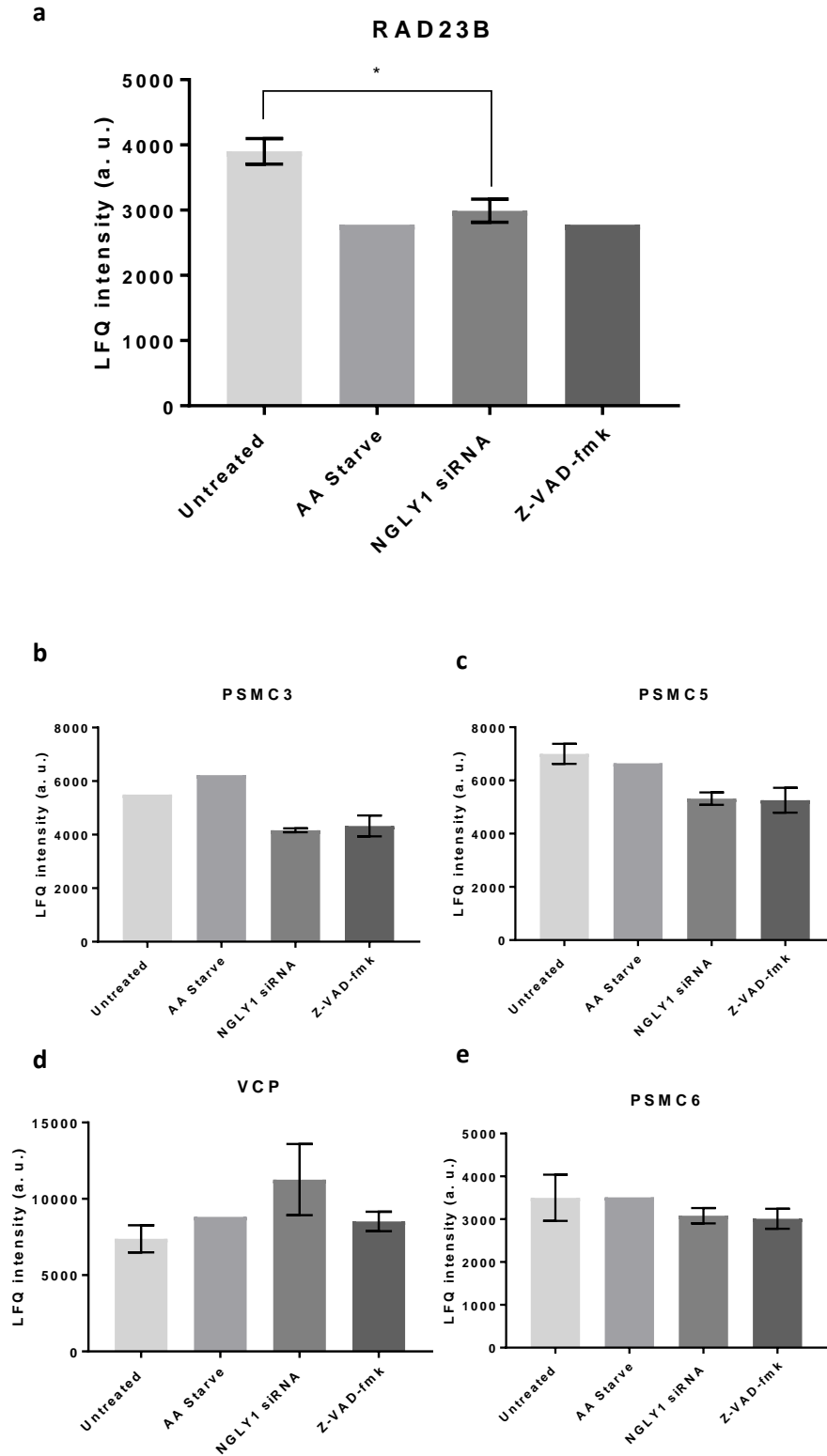


**Figure 6.16** LFQ intensities of proteasome complex proteins. Average of three biological replicates excluding 0 values a) RAD23B b) PSMC3 c) PSMC5 d) VCP e) PSMC6. Error bars  $\pm$  SEM. One-way ANOVA, Tukey's post hoc.

Since the proteasome is extensively linked to the ER via ERAD, the levels of ER-associated proteins was examined. Proteins were identified based on inclusion in the GO term GO:0005789, endoplasmic reticulum (figure 6.17a). There was no significant change in ER protein associated intensity in *N*-glycanase KD and Z-VAD-fmk treated cells (figure 6.16b) indicating the change in the proteasome complex is not a general effect for ER components. Similarly to mitochondrial based proteins, the amino acid starvation condition has a high degree of variation due to the two of the replicates containing reduced protein number.

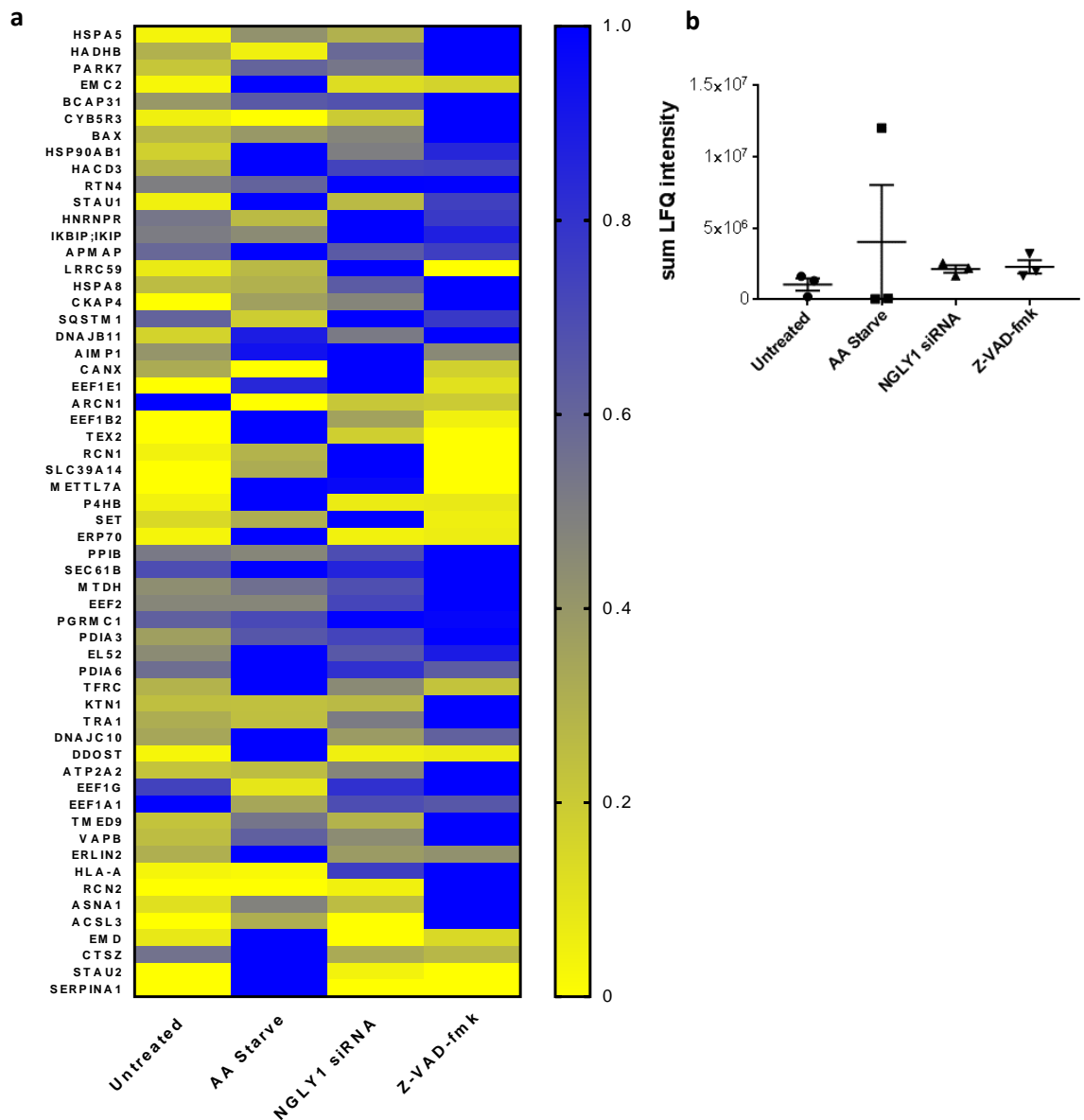


Figure 6.17 ER associated protein IDs a) fold over maximum intensity of the average of three biological replicates (excluding 0 values) b) SUM LFQ intensity per condition, average three biological replicates, excluding 0 values. Error bars  $\pm$  SEM. One-way ANOVA.

In order to identify other processes involved in selective autophagy, the dataset was tested for proteins containing LC3 interacting regions (LIRs). Selective autophagy is controlled by autophagy receptor proteins, most of which recruit cargo to autophagosome via a LIR domain (Johansen and Lamark 2011). Protein IDs were checked against the iLIR database and IDs that were found in *N*-glycanase siRNA, Z-VAD-fmk or untreated cells are summarised in **Table 6.3**. (Jacomin et al. 2016). The number of razor and unique peptides indicates the number of peptides identified to assign an ID across all conditions. Not all proteins were identified in all samples and, the number of replicates is also included.

**Table 6.3 LIR containing proteins found in enriched proteins in autophagosome isolation. The number of razor and unique peptides indicates how many peptides assigned to a protein were identified summed across all samples/conditions.**

Uniprot ID	Gene Name	LIR pattern	Razor + unique peptides	Number of replicates identified in
Q9BQS8	<b>FYCO1</b>	ADYQAL	67	Z-VAD-fmk-3 siRNA-3 Untreated- 3 AA Starve- 1
E9PGC8	<b>MAP1A</b>	AEYDSV	41	Z-VAD-fmk-3 siRNA-3 Untreated- 3
Q99623	<b>PHB2</b>	PGYIKL	11	Z-VAD-fmk-3 siRNA-3 Untreated- 3 AA Starve- 2
Q13043	<b>STK4</b>	GDYEFL	10	Z-VAD-fmk-2 siRNA-2 Untreated- 1
Q13501	<b>P62</b>	DDWTHL	17	Z-VAD-fmk-3 siRNA-3 Untreated- 2
O75367	<b>H2AFY</b>	DGFTVL	9	Z-VAD-fmk-1 siRNA-2 Untreated- 2 AA Starve- 1
Q96AG4	<b>LRRC59</b>	KEYDAL	8	Z-VAD-fmk-3 siRNA-3 Untreated- 2 AA Starve- 1
Q13188	<b>STK3</b>	GDFDFL	6	Z-VAD-fmk-2 siRNA-1
D6R9P3	<b>HNRNPAB</b>	RGFVFI	5	Z-VAD-fmk-2 siRNA-2 AA Starve- 1
J3KN66	<b>TOR1AIP1</b>	GDFEPL	5	Z-VAD-fmk-2 siRNA-3 Untreated- 2

P42696	<b>RBM34</b>	PVYVPV	5	Z-VAD-fmk-2 siRNA-2 AA Starve- 1
H7C5Q2	<b>ACOT9</b>	ATFVMV	4	Z-VAD-fmk-2 siRNA-2 Untreated- 1 AA Starve- 1
F6S6P2	<b>BAG6</b>	AEYVEV	3	Z-VAD-fmk-2 siRNA-2 Untreated- 2
Q03252	<b>LMNB2</b>	AEYQEL	3	Z-VAD-fmk-1 AA Starve- 1
H7BYX6	<b>NCAM1</b>	LEFILV	2	Z-VAD-fmk-1 siRNA-1 AA Starve- 1
E7EU81	<b>GOLGB1</b>	KEYEIL	2	Z-VAD-fmk-2
P16152	<b>CBR1</b>	PVYLAL	2	Z-VAD-fmk-1 siRNA-1 AA Starve- 1
Q6P2E9	<b>EDC4</b>	ADFLSL	2	Z-VAD-fmk-2 AA Starve- 1

FYCO1 was identified as significantly increased in Z-VAD-fmk sample compared to untreated control and *N*-glycanase siRNA treated cells shown in Figure 6.18. FYCO1 is involved in the linkage of autophagosomes to microtubules for transport. This increase in FYCO1 in Z-VAD-fmk treated cells and to a lesser extent, *N*-glycanase siRNA, may be due to an overall increase in autophagy. An increased autophagosome number may indicate a greater need to transport autophagosomes to lysosomes for degradation. Amino acid starvation cells only contained a single replicate identifying FYCO1. None of the other LIR domain containing proteins showed significant differences.

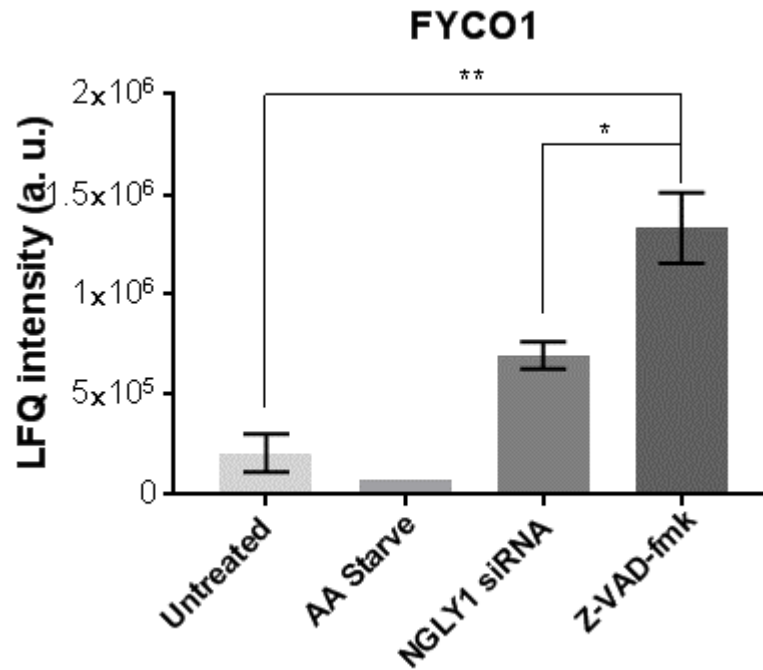


**Figure 6.18 SUM LFIQ Intensity of FYCO1 average of three biological replicates excluding 0 values. Error bars  $\pm$  SEM. One-way ANOVA, Tukey's post hoc. \* indicates  $P < 0.05$ , \*\* indicates  $P < 0.01$ .**

Three of the LIR containing proteins are localised to the mitochondria according to the human protein atlas (HPA). Acyl-CoA thioesterase 9 (ACOT9), Leucine-Rich Repeat-Containing Protein 59 (LRRC59) and Prohibitin 2 (PHB2). Due to the localisation of these proteins there may be link to mitophagy. However, this would need to be further validated experimentally.



## 6.4 Discussion

This chapter aimed to identify autophagy-associated and cargo proteins involved in the activation of autophagy under Z-VAD-fmk treatment and siRNA KD of *N*-glycanase. In order to examine autophagosomes, GFP-LC3 immunoprecipitation was used and proteomics analysis of the IP protein mixture was performed. LC3 is the most commonly used marker for identification of autophagosomes and previous studies have successfully used this as a target for IP of autophagosomes (Dengjel et al. 2012, Hanna et al. 2012, Martinez-Lopez et al. 2013). Firstly, this chapter looks at the method development of autophagosome isolation and analysis, followed by functional analysis of clusters assigned by Gene ontology terms. From the final test it was found there was an increase of mitochondrial proteins in Z-VAD-fmk and *N*-glycanase KD samples compared to the untreated control with increased intensity of proteins associated with the control of apoptosis. Conversely, a significant decrease in the proteasome subunit PSMC2 and proteasome ubiquitin receptor, RAB23B was found in *N*-glycanase KD compared to the untreated control. This trend was also identified in Z-VAD-fmk and other proteasome markers including PSMC3 and PSMC5. However, there were no differences identified in ER associated proteins, suggesting this effect was only based on the proteasome rather than ERAD. Finally, LIR containing proteins were examined to determine selective autophagy across the samples and found a significant increase in the microtubule associated protein FYCO1 in Z-VAD-fmk treated cells compared to the untreated control.

Autophagosomes represent a small fraction of the cellular proteome and efficient and specific IP is necessary for meaningful analysis. GFP-LC3 was used as the target for IP which is the most common marker for autophagosomes. However, GFP-LC3 is also present in the cytosol. Initial tests used a simple lysate clearance, however, the antibody used for the IP could be binding to cytosolic LC3 I instead of autophagosomes. To try and remove this, final samples were pre-cleared of large debris by centrifugation followed by a hard centrifugation to pellet autophagosomes. However, this method may be too harsh for autophagosome structures which may become damaged and lyse, releasing cargo that is of interest in this study. Other methods of autophagosome isolation could have been used such as purification of autophagosomes by density gradient centrifugation followed by immunoprecipitation (Dengjel et al. 2012) to increase the specific binding to autophagosomes.

Proteins were identified as relevant using enrichment over the binding control. Experimental proteins with an intensity of twofold or higher in the corresponding binding control were used for analysis. For proteins only found in the experiential control, identifications only

associated with a single razor and unique peptide were excluded from analysis. This is because a single peptide can be mapped onto several proteins. By removing single peptide matches, remaining identifications have a minimum of two peptides (Cottrell 2011) representing more stringent identification criteria.

Several approaches were used to identify functional clusters from the enriched dataset. Several databases were used to identify Gene Ontology terms including STRING database (Szklarczyk et al. 2017) and the DAVID Functional annotation tool (Huang et al. 2008) to identify. The Harmonizome was used to identify protein interactions including non-validated text mining (Papanikolaou et al. 2015) interactions (Rouillard et al. 2016a). This is especially useful when examining proteins with little literature on their protein interaction networks and is able to use open access repositories from high-throughput experiments to identify possible protein interactions. LIR containing proteins were identified against the iLIR database (Jacomin et al. 2016).

To identify functional clusters of proteins they were annotated using Gene Ontology (GO) terms. GO terms are widely used and can be separated into various groupings depending on what is of interest, such as cellular components, biological process etc. However, GO terms have a high level of redundancy. Figure 6.5 shows the GO cellular components annotations. GO terms can show a high level of redundancy; for mitochondria, two sections for mitochondrion and mitochondrial inner membrane and for nuclear proteins three sections are given over to nucleus, nucleolus and nucleosome which contain multiple copies of the same protein IDs. This means groups that may be of interest but contain a lower protein count can get lost in the analyses. This has been identified as an issue of the GO terms used and protocols aiming to reduce redundancy have been developed (Jantzen et al. 2011). STRING database also uses GO terms to categorise protein groups.

In Test 2, increased numbers of mitochondrial proteins were identified in Z-VAD-fmk treated cells compared to the untreated control and the amino acid starved cells. This trend was partially replicated in Test 3 with increased protein IDs and intensity in both N-glycanase KD and Z-VAD-fmk compared to the untreated control, although this was not significant. Increased mitochondrial proteins present in autophagosome isolation may be suggestive of selective mitophagy. Mitophagy can be signalled by a variety of effects and is essential to maintain pools of healthy mitochondria for energy production and cellular homeostasis. One of the most common signals for mitophagy is oxidative stress, although no increase in

reactive oxygen species was detected in the previous Chapters 3 and 4 under Z-VAD-fmk or *N*-glycanase siRNA KD.

Many of the proteins identified as involved in mitophagy (such as PHB2 and proteins involved in regulation of apoptosis such as C1QBP and AIFM1) are already present in mitochondria and may be identified as increased because of increased mitochondrial uptake via increased levels of autophagy. As such, this cannot be regarded as indicative of activation based on this data alone. To identify if mitophagy is truly occurring, further validation is required. As well as cargo leading to changes in the autophagosome composition, initiation site may also play a role. Several organelles have been implicated in the donation of membranes for autophagosomes including the ER, Golgi and mitochondria (Hailey et al. 2010, Karanasios et al. 2016, Noda 2017) and should also be considered as a potential source of organelle identified membrane proteins. There is little literature based on the protein composition of autophagosomes and whether donated membranes retain many of the membrane proteins associated with them and contradictory evidence of the origins of autophagy membranes also exists (Cook et al. 2014, Nascimbeni et al. 2017, Ding and Eskelinen 2014).

Interestingly, a decrease in proteins involved in the proteasome complex was identified. Recently, the *N*-glycanase dependent regulation of the transcription factor, Nuclear respiratory factor 1 (Nrf1) has been identified (Tomlin et al. 2017). Nrf1 is involved in the transcription of proteasomal proteins, mitochondrial proteins and redox proteins (Biswas and Chan 2010). Nrf1 and 2 are part of the CNC-bZIP family and bind antioxidant response elements (AREs), a sequence to initiate transcription of target genes (Digaleh et al. 2013). During Nrf1 synthesis the protein is held in the ER membrane with the majority of the protein within the ER lumen (Radhakrishnan et al. 2014). Activation depends on p97/VCP, known interactors of *N*-glycanase (Zhao et al. 2007, Christianson et al. 2011) which flips Nrf1 from the ER lumen to the cytoplasmic face allowing the proteasome access to break down the cytoplasmic face of the protein. It has been identified that *N*-glycanase is responsible for Nrf1 activation via a deglycosylation dependent activation route (Tomlin et al. 2017). KO of *N*-glycanase halts translocation to the nucleus following proteasome inhibition (Tomlin et al. 2017). The proposed activation of Nrf1 is shown in Figure **6.19**.

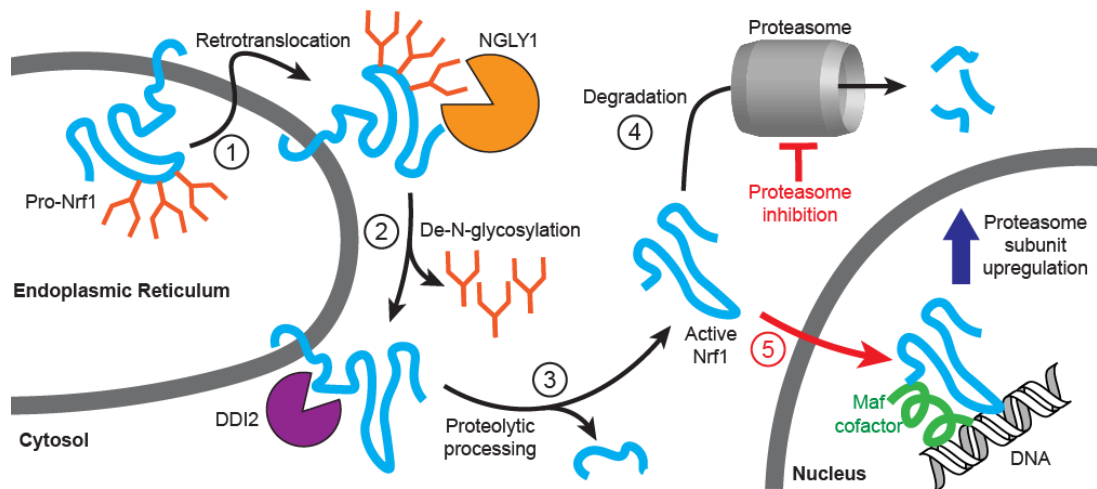


**Figure 6.19 Proposed action of NRF1 activation.** Open access article published under ACS AuthorChoice. Reprinted from (Tomlin et al. 2017).

Furthermore, a study of the transcriptome of *N*-glycanase KO *Drosophila* have shown an increase in stress response proteins such as heat shock proteins but a downregulation in oxidation-reduction, proteasome and lipid metabolism, concordant with a disruption of cap 'n' collar (Cnc) (Nrf1 *drosophila* homolog) function (Owings et al. 2018).

Nrf1 plays an important role in the proteasome recovery pathway (Radhakrishnan et al. 2010). However, in *N*-glycanase KO MEF cells Nrf1 was unable to translocate to the nucleus and proteolytic cleavage was inhibited (Tomlin et al. 2017). Under basal conditions there are no differences found in proteasome activity, however, under proteasome inhibition, PSM genes were not induced and *N*-glycanase KO sensitised cells to proteasome inhibition and increased cell death (Tomlin et al. 2017). This could also explain why Z-VAD-fmk or siRNA *N*-glycanase knockdown did not cause ER stress as these were performed under basal conditions. If Nrf1 cannot leave the ER due to its glycosylation halting further processing of the protein, therefore it cannot activate not just proteasome subunits, but other proteins involved in the antioxidant response and ER stress. In *C. elegans*, the NRF1 homolog, SKN-1, regulates UPR proteins including homologs of BiP, PERK, IRE1, XBP1, ATF4 and ATF6 under ER stress but not oxidative stress (Choe and Leung 2013, Digaleh et al. 2013, Cullinan et al. 2003, Pajares et al. 2017). In conclusion, inactivation of Nrf1 could affect activation of UPR and sensitise cells to a number of different stressors. This could also explain decreased levels of proteasome complex proteins; Nrf1 is identified as regulating PSMC1, PSMC3IP, PSMC4, PSMC5 and RAD23B (Rouillard et al. 2016b) as transcription of PSM genes may not be as efficient.

Nrf1 also regulates the expression of a number of mitochondrial proteins. Nrf1 and Nrf2 promotes expression of the transcription factor Tfam which controls mtDNA replication (Jornayvaz and Shulman 2010) and Nrf1 has been shown to directly regulate expression of mitochondrial proteins such as TOMM34, TOMM70 and TOMM20 (Blesa et al. 2008). A number of the roles of Nrf1 can be partially compensated for by Nrf2 but not completely (Digaleh et al. 2013, Cullinan et al. 2003). Nrf1 KO mice exhibits embryonic lethality at E13.5 (Ohtsuji et al. 2008) leading Nrf1 to be studied in conditional KO models. A mouse model of hepatocyte Nrf1 KO described liver damage which was absent in Nrf2 KO, and increases Nrf2 driven genes was found indicating Nrf2 cannot completely compensate for Nrf1 KO (Ohtsuji et al. 2008). This change in Nrf1 activation may also impact mitochondrial function and explain the dysregulation in mitochondria observed in (Kong et al. 2018).

To identify if other autophagy receptors were present in the dataset, comparison against the iLIR database was carried out. This retrieved proteins from the dataset containing an LC3 interaction domain (LIR), LC3 recognition sequence (LRS) or an Atg8-interacting motif (AIM) (Jacomin et al. 2016) which are summarised in Table 6.3. This method allowed the identification of proteins that are not necessarily known for, or where there is little literature about the role of the respective protein in autophagy. Proteins identified as enriched in each condition in Test 3 were analysed. A total of eighteen proteins with a putative LIR domain for found (although many of which were not identified across all conditions). FYCO1 was identified as significantly increased compared to the untreated control. FYCO1 links autophagosomes to the microtubule network to traffic them to lysosomes for cargo degradation. This increase may be due to increased autophagy in Z-VAD-fmk and N-glycanase KD which would require increased trafficking of autophagosome to lysosomes.

To identify if mitochondrial dysfunction leading to increased mitophagy is occurring, characterisation of mitochondrial function will be examined.

## 7.1 Introduction

The mitochondrial network is highly dynamic. Mitochondria are trafficked around the cell via the microtubule cytoskeleton and undergo multiple fission and fusion events (Tandler et al. 2018). Fusion is vital to allow distribution of mtDNA throughout the mitochondrial network and is mediated via Opa1 and mitofusin 1 and 2. Depolarisation of the membrane results in a loss of Opa1 and Mfn 1 and 2 which inhibits fusion and leads to mitochondrial fragmentation. Under different stress and environmental conditions, mitochondria adopt different morphologies (shown schematically in Figure 7.1). Mitochondria are also a major source of ROS, and are hence intrinsically linked to the homeostasis of the redox environment (Willems et al. 2015). Hydrogen ions are pumped from the matrix into the intermembrane space during oxidative phosphorylation generating a proton gradient and a highly positive environment, this drives the generation of energy in the form of ATP. Disruption in this membrane potential has been linked to decreased ATP production, increased ROS production and changes in the redox environment of the cell, mitochondrial morphology and signalling and the induction of mitophagy, the specific degradation of mitochondria via autophagy (Dimroth et al. 2000, Suski et al. 2012, Ding and Yin 2012, Willems et al. 2015).

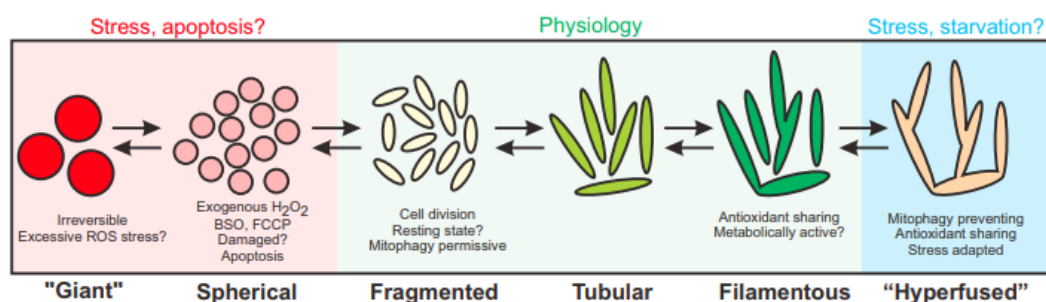


**Figure 7.1 Mitochondrial morphology under different environmental conditions. Reprinted from Cell Metabolism (Willems et al. 2015)**

Mitophagy is the specific removal of mitochondria via the autophagic machinery. Whole mitochondria are engulfed in double membrane vesicles and degraded via lysosomes. This process uses the same core machinery as canonical autophagy. The entire protein content of mitochondria is turned over every few days (Chan et al. 2015), which is suggestive of the regular bulk degradation of the organelles. There are two main types of mitophagy, ubiquitin

mediated mitophagy (involving the PINK1/Parkin system) and receptor mediated removal, which involves mitophagy adaptor proteins such as NIX, BNIP3 and FUNDC1 and the recruitment of autophagy membranes (Figure 7.2).

The ubiquitin kinase PINK1 is readily degraded under normal physiological conditions (Thomas et al. 2014). Upon mitochondrial membrane depolarisation PINK1 is stabilised on the mitochondrial outer membrane and phosphorylates ubiquitin at Ser65 (Kondapalli et al. 2012). Phospho-ubiquitin is structurally different from other ubiquitin chains, and activates parkin (Kondapalli et al. 2012), an ubiquitin ligase which attaches extra ubiquitin chains to the outer mitochondrial membrane (OMM) proteins like Mfn1 and Mfn2 to amplify the PINK1 signal (Rakovic et al. 2011). Damaged mitochondria are trafficked to the perinuclear region (Al-Mehdi et al. 2012) where adaptor proteins containing ubiquitin binding domains and LIR domains serve to target damaged mitochondria to the autophagic machinery. OPTN, NDP52 requires PINK1 activity (but not Parkin) for transport to the mitochondria (Michael Lazarou et al. 2015). OPTN, NDP52 (which has just a LIR domain and is also involved in xenophagy), NBR1 and P62 all have LIR and UB domains to further recruit autophagy machinery by binding of proteins with LIR domains to the cargo to recruit LC3 (M. Lazarou et al. 2015). However, the exact mechanism of which adaptors are recruited to damaged mitochondria is not completely understood and, p62 knockout studies have found no effect on mitophagy (Narendra et al. 2010).

There are two main mitochondrial receptor families which mediate mitophagy, NIX and BNIP3 family and FUNDC1 (Figure 7.2 panel B and C). NIX and BNIP3 are not highly expressed under normal conditions but are upregulated under hypoxic conditions and are localised to both mitochondrial and ER membranes (Zhang et al. 2008). One of the main functions of BNIP3 and NIX is to regulate cell death through ROS production by removing damaged mitochondria. Under hypoxic conditions hypoxia-inducible factor 1 (HIF-1) upregulates BNIP3 and NIX (Zhang et al. 2008) and under starvation conditions FOXO3 binds to BNIP3 and NIX promoter regions (Bakker et al. 2007). Both proteins contain a LIR domain, allowing recruitment of LC3. Mutations in these LIR domains inhibit LC3 binding and genetic knockout of NIX have shown defect in mitochondrial degradation in reticulocytes (Novak et al. 2010). Phosphorylation of BNIP3 at Ser17 and Ser24 promotes interaction with LC3B to increase mitophagy, although the kinase and phosphatase responsible is unknown (Rogov et al. 2017). BNIP3 is a Bcl-2 interacting protein and plays a role in apoptosis regulation. In response to hypoxic conditions it localises to the mitochondria and disrupts mitochondria function,

increasing ROS production, mitochondrial swelling and resulting in depolarisation of the membrane and induction of mitophagy to remove the damaged mitochondria. This is a survival mechanism, however if there are more damaged mitochondria than the cell can dispose of, BNIP3 will activate cell death cascades (Burton and Gibson 2009).

FUNDC1 is a transmembrane protein localised to the mitochondrial outer membrane. The N-terminus contains a LIR domain and faces the cytoplasm. Similarly to BNIP3 and NIX, removal of the LIR domain results in abolishment of LC3 binding and defects in mitophagy. FUNDC1 has been shown to mediate hypoxia induced mitophagy but interestingly, under hypoxic conditions, FUNDC1 mRNA and protein levels decrease as mitochondria are degraded. FUNDC1 is regulated by phosphorylation at Ser13 and Tyr18, by CK2 and Src kinase respectively under normal conditions. Under hypoxic conditions and decreased mitochondrial membrane potential FUNDC1 is dephosphorylated by PGAM5 which increases the binding affinity to LC3 (Kuang et al. 2016).

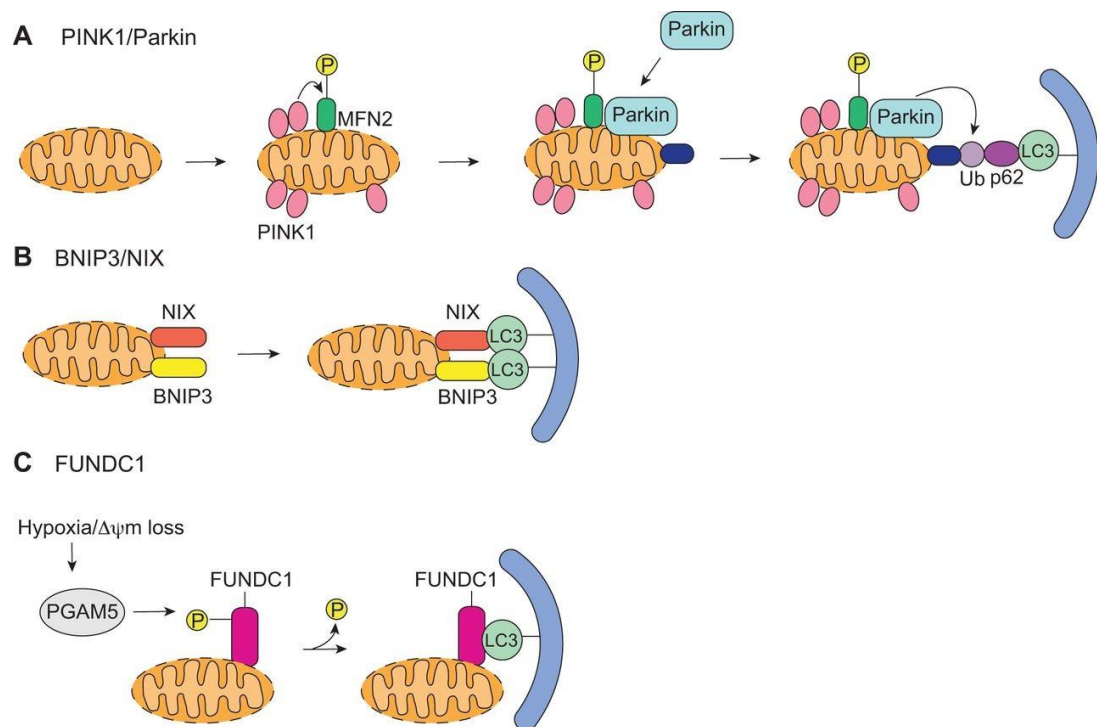


**Figure 7.2 Methods of autophagic recruitment to mitochondria. A shows PINK1/Parkin mediated removal. B shows BNIP3 and NIX mediated recruitment of LC3 and C shows FUNDC1 control of LC3 recruitment. Reprinted from The American Physiological Society (Moyzis et al. 2015)**



There are several ways in which levels of mitophagy can be assessed. A decrease in mitochondrial proteins can give an indication of mitochondrial degradation and can be measured by immunoblotting techniques, although methods such as these cannot distinguish between degradation pathways. Co-localisation of mitochondria and autophagic machinery using fluorescence microscopy and common markers such as TIMM/TOMM proteins and LC3 can also be employed (Kobayashi et al. 2016). In some cases, mitochondrial DNA can be used as a measure of mitochondrial density (Furda et al. 2014), however it should be noted that there are some known disorders that affect the copy number of mtDNA (Ding and Yin 2012).

#### 7.1.1 Clinical presentations of N-GLY1 deficiency disorder mirror those of mitochondrial disorders

A meta-analysis of eight transcriptome experiments of human respiratory chain disease samples identified *N*-glycanase as having consistently increased expression (Zhang and Falk 2014). Patients diagnosed with mitochondrial disorders such as respiratory chain disorders and, those diagnosed with NGLY1 also exhibit comparable phenotypic patterns (Enns et al. 2014, Ohtake et al. 2014). Despite this parity in clinical presentation, analysis of pyruvate dehydrogenase and pyruvate carboxylase activity (elements of the mitochondrial electron transfer chain and often measured as a marker of mitochondrial dysfunction (Kerr et al. 2012, Gray et al. 2014, Patel et al. 2012)) in skin fibroblasts, muscle or liver samples derived from NGLY1 patients showed no abnormalities (Enns et al. 2014). Conversely, two of the eight patients examined in the Enns et al. 2014 study did exhibit abnormal mitochondrial function. Patient 3 (c. 1205\_1207del and c.1570C>) showed a 39 % decrease in liver mtDNA while patient 7 (homozygous c.1201A>T) showed increased tricarboxylic acid cycle (TCA) intermediates (Enns et al. 2014). Another patient (c.1604G>A:c.1910delTT) showed abnormal liver mitochondrial morphology and proliferation and, a quadriceps muscle biopsy of this patient revealed five-fold increase in citrate synthase activity and 472% increase in mtDNA compared to age and tissue matched controls (Kong et al. 2018). These results are suggestive of tissue specific differences.

Mitochondrial dysfunction has also been observed in *N*-glycanase deficient *C. elegans*, MEFs and human fibroblasts derived from NGLY1 patients (Kong et al. 2018). *N*-glycanase KO *C. elegans* have been observed to have a stark decrease in lifespan (53 % reduction), and decreased (20 %) mitochondrial content (measured by Mitotracker). In addition, an 80 % decrease in mitochondrial membrane potential (measured by Tetramethylrhodamine ethyl

ester (TMRE) fluorescence intensity) and, a 20 % increased mitochondrial matrix oxidant burden (measured by MitoSOX<sup>TM</sup> fluorescence intensity) was also observed.

In comparison, *N*-glycanase KO MEFs and patient fibroblasts (FCL-M1; c.1205\_1207del:c.1570C>T and FCL-M2; homozygous c.1201A>T) showed no difference in Mitotracker<sup>TM</sup> fluorescence compared to that observed in WT cells under basal conditions. However, when grown under conditions which promotes OXPHOS (galactose supplemented media) and treated with the mitochondrial RC complex 1 inhibitor rotenone (25 nM, 72 h), patient fibroblasts FCL-M1 and FCL-M2 showed a significant reduction in cell viability (5 and 18 % respectively versus respective controls of 66 and 74 %, determined by CellTiter Glo<sup>TM</sup>). Furthermore, when patient fibroblasts were grown in galactose supplemented media, a 9 % decrease in TMRE fluorescence and a 65 % increase in ROS (measured by MitoSOX<sup>TM</sup> fluorescence intensity) (Kong et al. 2018) was observed. Differences were also noted in respiration levels. MEFs exhibited normal basal respiration but upon addition of the complex un-coupler FCCP to achieve maximal oxygen consumption there was a significant decrease in maximal oxygen consumption compared to the control. FCL-M2 fibroblasts showed a significant decrease (25.7 %) in basal respiration and a drop (22.6 %) in maximal respiration. Introduction of ectopic *N*-glycanase increased mitochondrial content, increased membrane potential and effected a reduction of the mitochondrial oxidant burden in MEF cells. In patient fibroblasts (FCL-M1) there was no change in mitochondrial content but there was an increase in TMRE fluorescence. FCL-M2 fibroblasts however, exhibited a 72 % increase in mitochondrial content, a 2.1-fold increase in TMRE fluorescence and, an 80% reduction in oxidant burden. Maximal oxygen consumption in both patient fibroblasts, FCL-M1 and FCL-M2 was rescued when cells were grown in galactose supplemented media (24.9 % and 79 % respectively) (Kong et al. 2018).

## 7.2 Aims and Objectives

As proteomics analysis indicated increased levels of mitochondrial proteins associated with autophagosomes, in this chapter mitochondrial function will be examined in HEK cells under both conditions of pharmacological inhibition and genetic ablation of *N*-glycanase. Mitochondrial health will be assessed by examination of the redox environment of the cell, mitochondrial membrane potential and determination of levels of mitophagy. Although there were no changes in overall lectin binding in whole cell lysates was observed, this does not exclude small changes in specific proteins or organelles. To this end, the mitochondria lectin binding profile was also examined.

### 7.3 Results

As many cells grown *in vitro* are grown under conditions of high glucose, they are adapted to be highly dependent upon glycolytic metabolism (using the breakdown of glucose for energy rather than via mitochondrial oxidative phosphorylation) (Marroquin et al. 2007, Diaz-Ruiz et al. 2011). This phenomenon is known as the Crabtree effect (Dell'Antone 2012, Diaz-Ruiz et al. 2011, Marroquin et al. 2007, Rodriguez-Enriquez et al. 2001). When studying whether a process or reagent influences mitochondrial function, if the cells are adapted to high aerobic glycolysis for energy production then they may be less sensitive to mitochondrial assault. Therefore, the conditions need to be adapted to increase mitochondrial dependency for energy production.

HEK cells grown in high glucose during exponential growth utilise glucose as the main carbon source and is mostly metabolised via glycolysis (Henry et al. 2011, Lin et al. 2014). In HEK 293 cells it was found most cellular pyruvate (77 %) is converted to lactate, whilst 22 % enters the TCA cycle for oxidation (Henry et al. 2011). These cells are therefore less susceptible to mitochondrial assault than cells which rely on mitochondrial oxidative phosphorylation for their energy needs. Evidence suggests cells switch between aerobic glycolysis and OXPHOS depending on glucose availability. Exchanging glucose for galactose changes cellular metabolism to rely more on mitochondrial OXPHOS for energy production (Marroquin et al. 2007). It has been found that several cell types, when grown in the presence of galactose instead of glucose, exhibit increased levels of oxidative phosphorylation (Aguer et al. 2011, Kase et al. 2013), increased mitochondrial protein expression (Rossignol et al. 2004), and contain mitochondria with increased numbers of cristae, but not increased mass (Rossignol et al. 2004). Galactose metabolism to pyruvate yields no net ATP and has been suggested to force cells to produce ATP via OXPHOS instead (Kase et al. 2013).

To study mitochondrial function in HEK cells under inhibition of *N*-glycanase and siRNA mediated knockdown of *N*-glycanase, cells were grown in high glucose (25 mM), representing standard cell culture conditions, or galactose (10 mM) supplemented media (Aguer et al. 2011, Kamalian et al. 2015) to increase dependence on mitochondrial oxidative phosphorylation for energy production. MTT reduction was measured under each culture condition to identify if *N*-glycanase inhibition or deficiency affected mitochondria. To confirm cell viability and proliferation, propidium iodide exclusion was measured and the number of cells under each condition were counted. Further investigation into mitochondrial function

was achieved by measurements of mitochondrial membrane potential via TMRE fluorescence. As autophagy activation has been identified under *N*-glycanase knockdown and inhibition and a number of mitophagy receptors were identified at low levels following proteomics analysis of autophagosomes, the level of mitophagy was examined using Mitotracker™ fluorescence, both before and after autophagy inhibition with Bafilomycin.

### 7.3.1 Galactose supplemented low glucose media does not affect HEK cell proliferation

To test whether HEK cells grown in media supplemented with galactose instead of glucose exhibited different growth patterns, cells were grown for six days in glucose (25 mM) or galactose (10 mM) supplemented media. Cells were sub-cultured at 2000 cells per well in a 48 well plate in either glucose (25 mM) or galactose (10 mM) supplemented media. Cells were also grown in media containing 1:1 glucose and galactose. Figure **7.3a** shows the growth curves of HEK cells in different media compositions. Cells were manually counted using a haemocytometer over 15 d.

The doubling times were calculated during the linear growth phase (between days 3 and 6). Figure **7.3b** shows the calculated doubling times for each media composition. There were no significant differences in cell doubling times. Cells exhibited an average doubling time of 21.3, 18.9 and 21.5 h for glucose, 1:1 glucose:galactose and galactose supplemented media respectively.

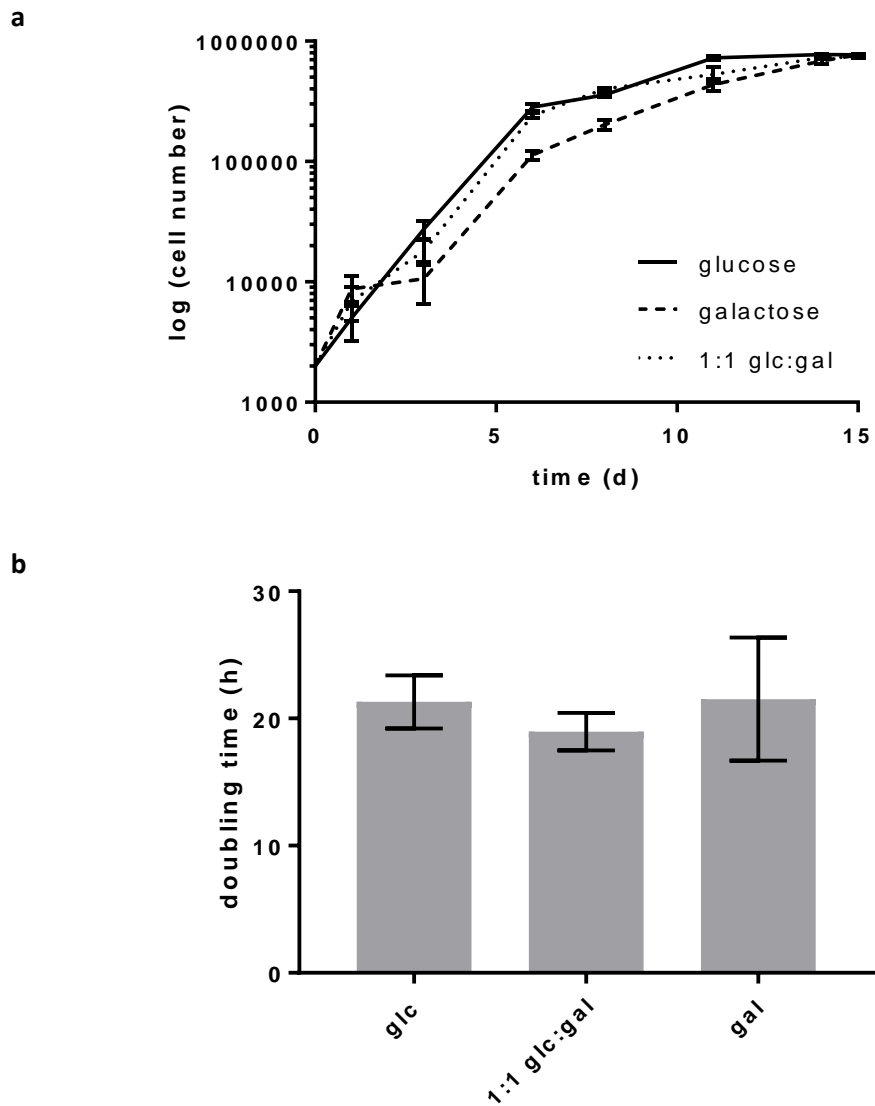


**Figure 7.3 Galactose does not affect HEK cell proliferation. a) growth curve of WT HEK cells grown in glucose (25 mM), glucose:galactose (12.5 mM:5 mM) and galactose (10 mM) b) calculated doubling time (h). Error bars indicate  $\pm$  SEM,  $n=4$ . One-way ANOVA.**

### 7.3.2 HEK cells grown in galactose show decreased MTT reduction when treated with Z-VAD-fmk for 72 h but no decrease in cell viability or proliferation

The MTT assay is commonly used for cell toxicity or proliferation studies (A. van Tonder et al. 2015). This is based on the reduction of MTT to coloured formazan by enzymes in actively metabolising cells. It is thought that most of the reducing power of metabolically active cells comes from the mitochondria (Alet van Tonder et al. 2015). In this study, cells were grown in glucose or galactose media and treated with 0-200  $\mu$ M Z-VAD-fmk or Q-VD-OPh to assess whether increased mitochondrial load causes decreased MTT reduction. Figure **7.4a** shows that cells grown in no glucose, galactose media treated with Z-VAD-fmk showed a significant decrease in MTT reduction compared to the vehicle control from just 1  $\mu$ M. To confirm this effect was not due to the effect of Z-VAD-fmk on caspase inhibition, this was repeated with Q-VD-OPh shown in Figure **7.4b**. There was no significant decrease in MTT reduction under Q-VD-OPh treatment.

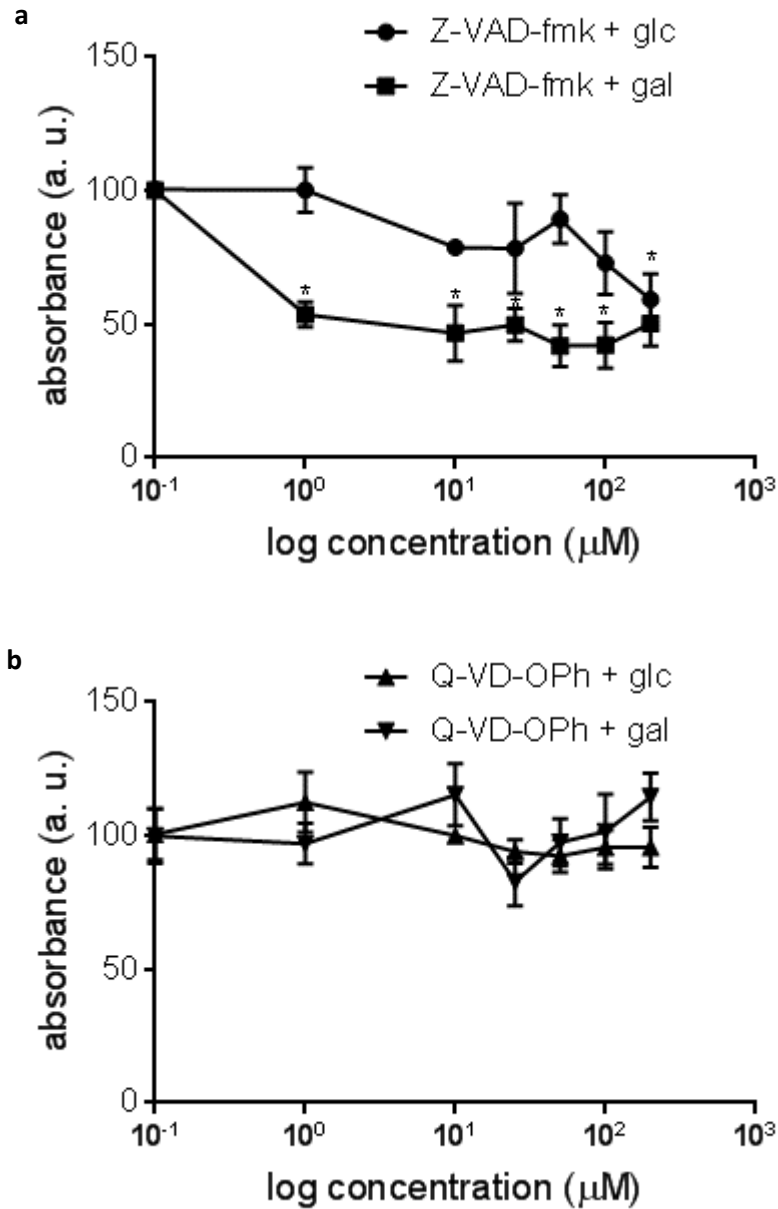


**Figure 7.4** MTT of HEK cells grown in DMEM high glucose media (4.5 g/L) or glucose-free DMEM supplemented with galactose (10 mM) and treated with a) Z-VAD-fmk (0-200 μM, 72 h) b) Q-VD-OPh (0-200 μM, 72 h). One-way ANOVA, Dunnett's multiple comparison, comparing samples to vehicle. Error bars ± SEM,  $n=3$ ,  $P < 0.05$ .

Lower levels of MTT reduction can result from decreased cell viability, decreased cell proliferation or decreased reduction potential. To confirm the reason of the reduced formazan absorbance, cell viability was confirmed by propidium iodide exclusion. Propidium iodide (PI) is a cell impermeant nuclear fluorescent dye. Dead cells have a disrupted plasma membrane allowing PI staining. Cells undergoing apoptosis have a distinct morphological phenotype as well as molecular markers such as Annexin V on the outer membrane of the

cell which occurs early in the apoptotic pathway whereas PI staining only occurs after a membrane has been damaged. To confirm changes in cell proliferation, the number of cells were counted per condition. Cells are plated at 40 000 cells per well and treated with Z-VAD-fmk or Q-VD-OPh (50  $\mu$ M, 24-72 h) and detached from wells and counted. Menadione, a potent inducer of apoptosis via increased ROS production (Loor et al. 2010) was used as a positive control.

Figure **7.5a** shows the percentage of cells with PI exclusion and therefore viable cells. There was no significant difference in Q-VD-OPh or Z-VAD-fmk treated cells to the vehicle control and all samples showed a > 80 % viability. Figure **7.5b** shows the annexin V staining, although there was an increase in staining in cells grown under galactose, there were no significant differences between Z-VAD-fmk, Q-VD-OPh and the vehicle. Figure **7.5c** shows the number of cells per mL counted. There were no significant differences in cell number, indicating that under growth in galactose media, Z-VAD-fmk or Q-VD-OPh does not affect cell proliferation. Due to no significant changes in cell viability and cell proliferation the decreased level of MTT reduction may suggest differences in the cellular redox environment.



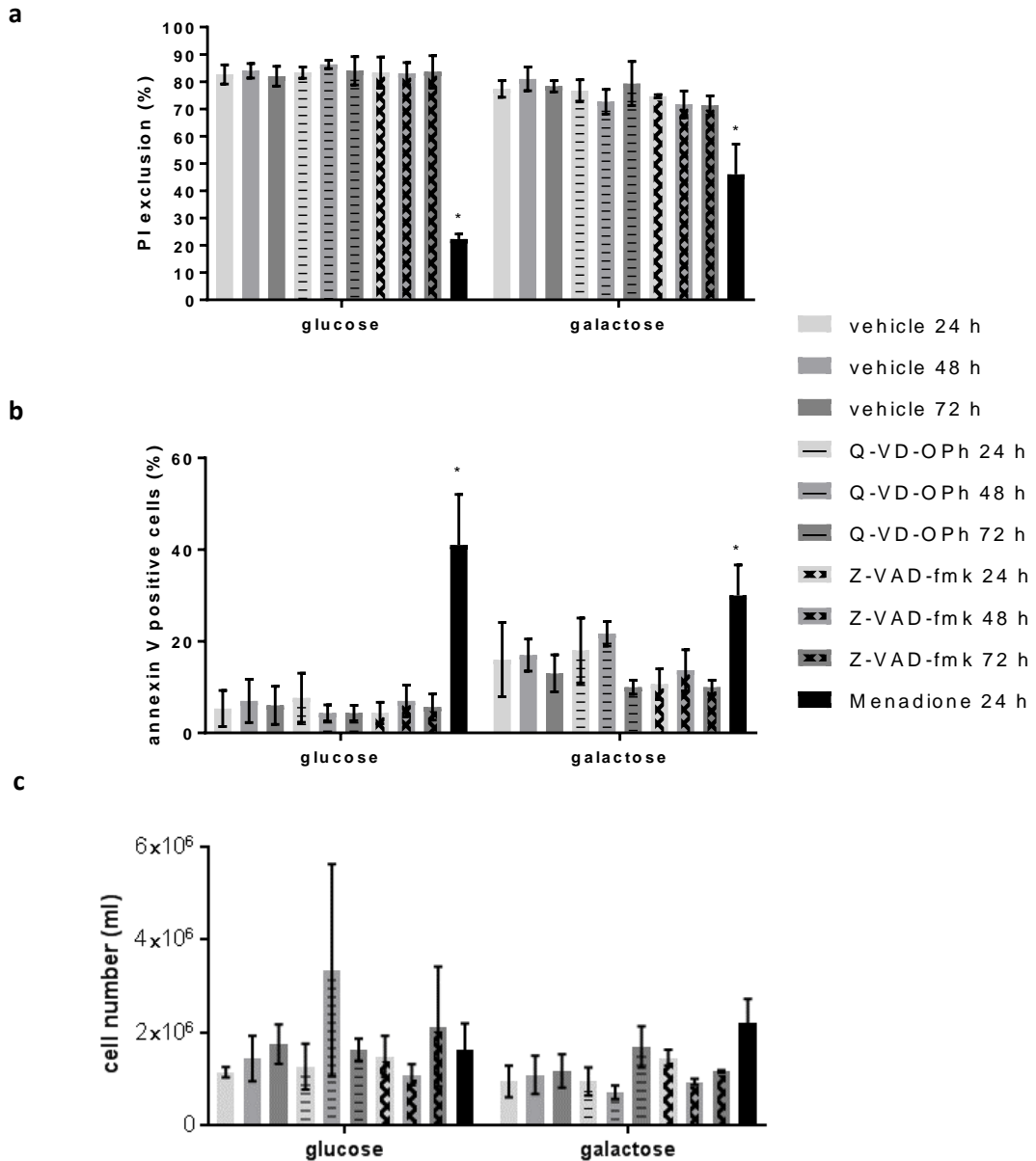


**Figure 7.5** There are no significant changes in PI exclusion, annexin V staining or cell number in WT HEK cells grown in high glucose (25 mM) or galactose (10 mM) DMEM. Cells were treated with Q-VD-OPh or Z-VAD-fmk (50  $\mu$ M, 72 h) or Menadione (100  $\mu$ M, 24 h) a) Percentage PI (10  $\mu$ g/ml 0.5 h) exclusion b) percentage of FITC annexin V positive cells c) cell number per mL. One-way ANOVA, Tukey's multiple comparison test within each condition. Error bars  $\pm$  SEM, n=3, P < 0.05.

### 7.3.3 Knockdown of *N*-glycanase in HEK cells grown in galactose show decreased MTT reduction but no decrease in cell viability or proliferation

To confirm the effects of Z-VAD-fmk on MTT reduction in galactose supplemented media HEK cells were transfected with *N*-glycanase siRNA. Figure 7.6 shows the formazan absorbance of HEK cells grown in either glucose or galactose supplemented DMEM transfected with *N*-glycanase or non-targeting control siRNA (siRNA absorbance normalised to percentage of the non-targeting control). As before, there is a significant decrease in MTT reduction in HEK cells with reduced *N*-glycanase activity when grown in galactose.

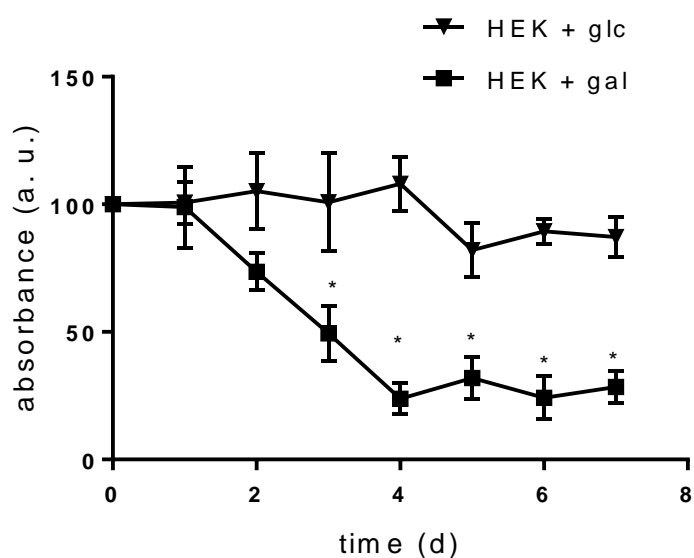


**Figure 7.6** MTT assay of HEK cells grown in high glucose DMEM (4.5 g/L) and galactose DMEM (10 mM) 7 d post-transfection with NGLY1 siRNA. One-way ANOVA, Dunnett's post hoc against the vehicle control at time 0. Error bars  $\pm$  SEM,  $n=3$ ,  $P < 0.05$ .

Cell viability and proliferation were assessed by PI exclusion and cell number. Unlike Z-VAD-fmk, *N*-glycanase siRNA has not been identified as targeting caspases and is does not thought to interfere in regulation of apoptosis. Annexin V was also measured to give an indication if cells were in the early apoptotic stages of cell death. Figure 7.7a shows the percentage of cells with PI exclusion, as with Z-VAD-fmk there was no decrease in cell viability in cells with decreased *N*-glycanase compared to the non-targeting control. Figure 7.7b shows there is no significant difference in the percentage of annexin V positive cells indicating cells are not undergoing apoptosis. Figure 7.7c shows that knockdown of *N*-glycanase does not affect proliferation in HEK cells grown in glucose or galactose media.

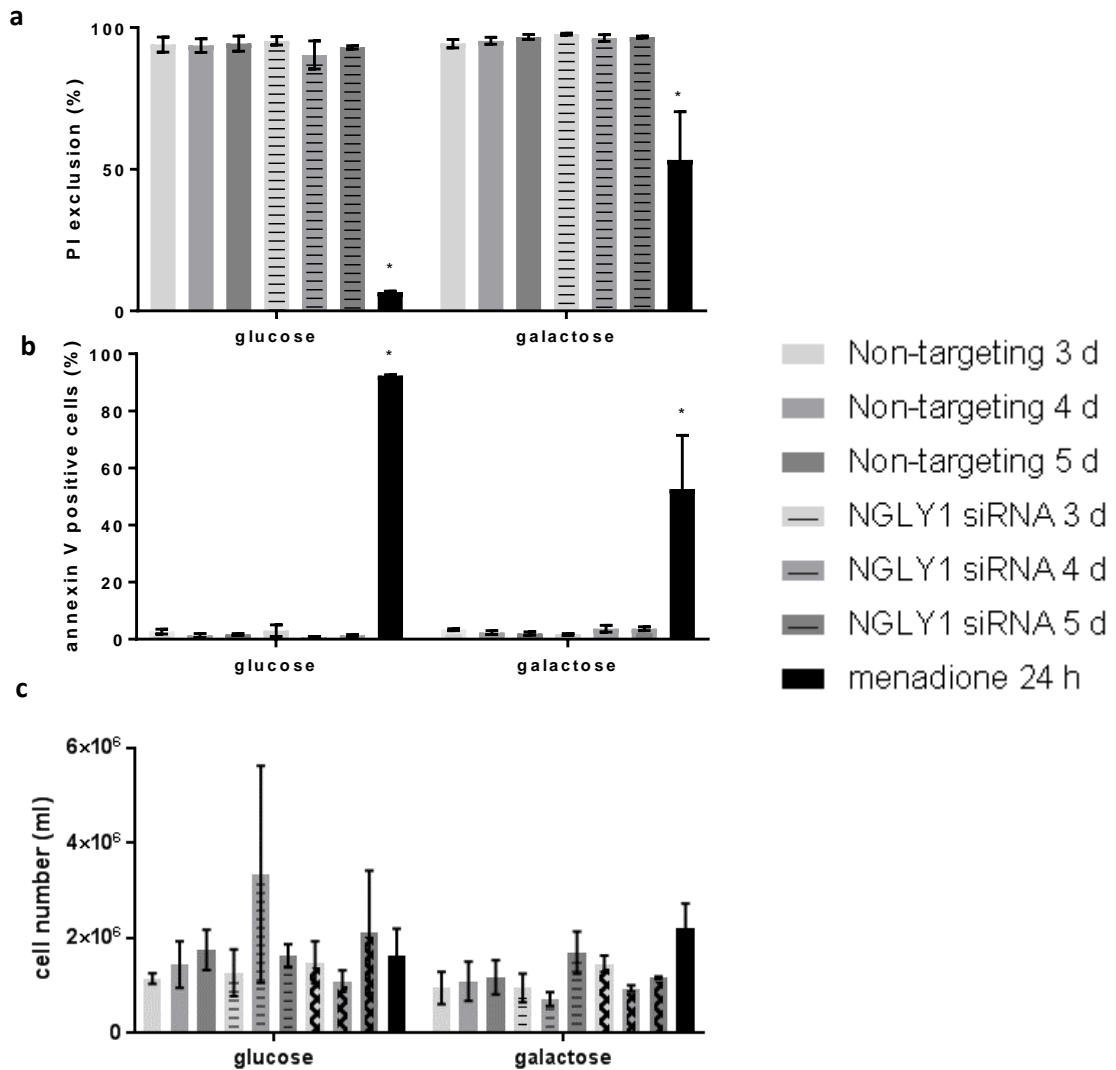


**Figure 7.7 Galactose does not affect viability in HEK cells transfected with NGLY1 siRNA.** There are no significant changes in propidium iodide exclusion as a measure of cell viability, annexin V staining or cell number in HEK cells grown in high glucose DMEM (4.5 g/L) or galactose DMEM (10 mM). Cells were transfected with NGLY1 siRNA or non-targeting siRNA and measured after 3-5 days a) percentage PI (10 µg/ml 0.5 h) exclusion. b) Percentage of FITC annexin V positive cells c) cell number per ml. One-way ANOVA, Tukey's multiple comparison test within each condition. Error bars ± SEM, n=3, P < 0.05.

### 7.3.4 Galactose, low glucose media does not affect ATG13 KO or WT MEF cell proliferation

Autophagy was identified as a protective measure in cells where *N*-glycanase activity was decreased and, ATG13 KO MEF cells showed decreased MTT reduction in the presence of Z-VAD-fmk or siRNA mediated *N*-glycanase knockdown. ATG13 KO MEF cells and WT MEFs were further examined to identify to the cause of decreased MTT reduction. To first identify if galactose supplemented media affects growth of ATG13 KO or WT MEFs, growth curves in glucose (25 mM), galactose (10 mM) or 1:1 glucose:galactose mix DMEM were measured. Figure 7.8a and b show the growth curves of WT MEFs and ATG13 KO MEFs respectively.

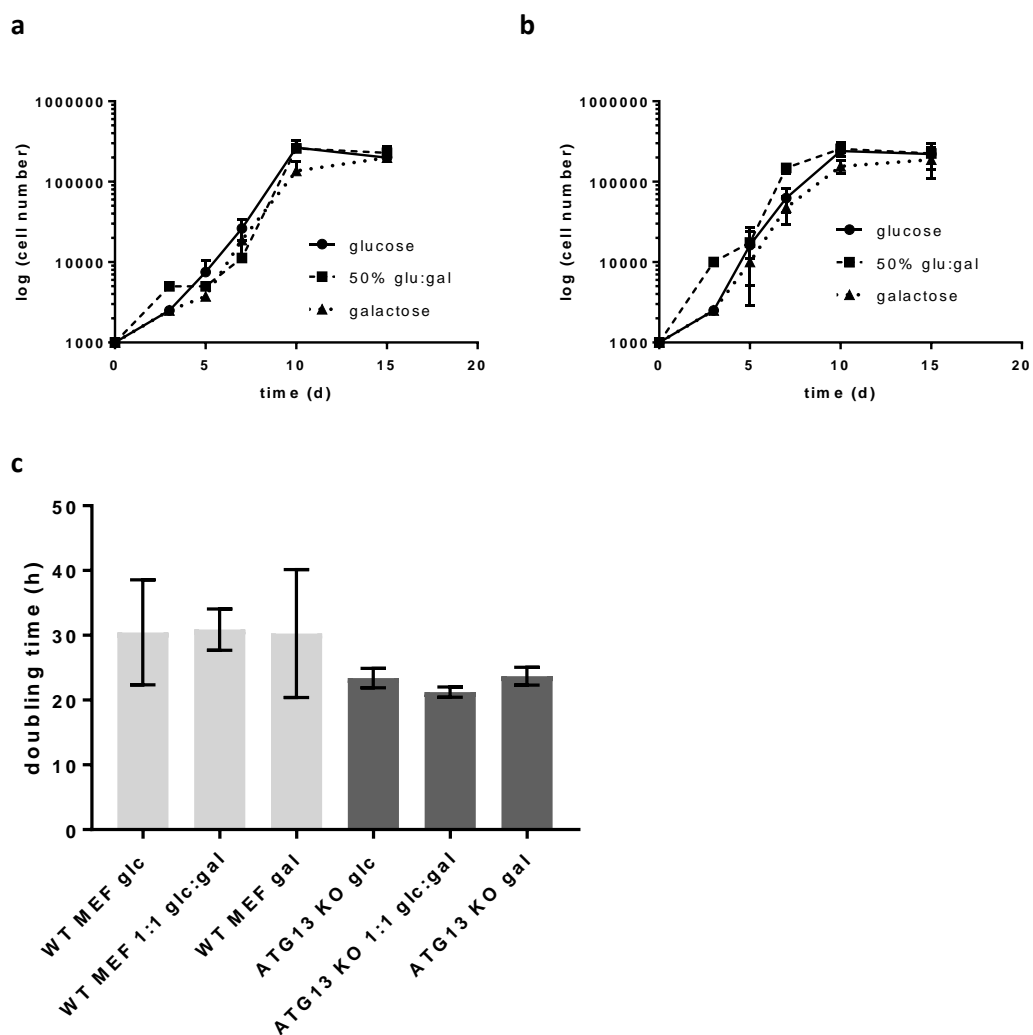


**Figure 7.8** There are no growth defects in WT MEF cells or ATG13 KO MEF cells in glucose or galactose media. a) WT MEFs or b) ATG13 KO MEFs grown in glucose (25 mM) glucose:galactose (12.5:5 mM) or galactose (10 mM) c) calculated doubling time (h). Error bars  $\pm$  SEM, n=4. Two-way ANOVA.

The doubling times were calculated during the linear growth phase. Figure **7.8c** shows the doubling times for WT and ATG13 KO MEF cells. There were no significant differences in growth rates between glucose or galactose media. Doubling times of 30.46, 30.88 and 30.48 h were recorded for WT MEF grown in glucose supplemented media, 50:50 glucose:galactose supplemented media and galactose. Doubling times of ATG13 deficient MEF cells were recorded as 23.38, 21.12 and 23.68 h respectively.

#### 7.3.5 ATG13 KO MEFs show decreased formazan reduction when grown in galactose with Z-VAD-fmk treatment

ATG13 KO MEFs were grown in high glucose DMEM and media supplemented with galactose (10 mM) and treated with Z-VAD-fmk (1-200  $\mu$ M) for 72 h. Similar to previous results (Figure **3.47**) of ATG13 KO MEFs grown in RPMI 1640 media (2 g/L glucose) there was a significant decrease in high glucose (4.5 g/L) DMEM at 200  $\mu$ M Z-VAD-fmk with an  $IC_{50}$  value of 63.2  $\mu$ M (versus an  $IC_{50}$  value of 12.98  $\mu$ M in glucose containing RPMI 1640). When ATG13 deficient MEF cells were grown in galactose supplemented DMEM there was a significant decrease in formazan absorbance following treatment with 50, 100 and 200  $\mu$ M Z-VAD-fmk compared to the vehiclecontrol with an  $IC_{50}$  of 40.9  $\mu$ M (1.5 fold increase) shown in Figure **7.9a**. Figure **7.9b** shows the effect of Q-VD-OPh in ATG13 KO MEFs grown in high glucose and galactose media. There was no significant decrease in formazan absorbance after treatment with Q-VD-OPh (1-200  $\mu$ M) for 72 h. This indicates that autophagy is indeed a protective measure and that the effects of decreased formazan reduction are due to a non-caspase inhibitory effect of Z-VAD-fmk.

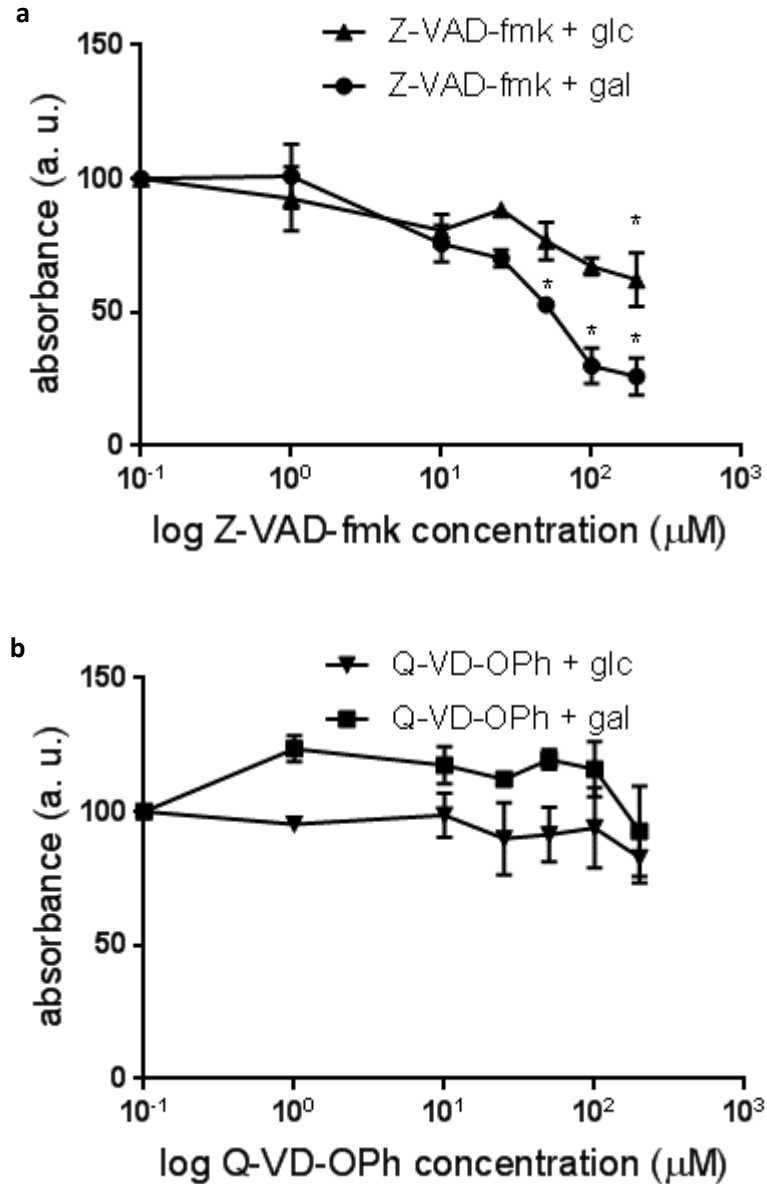


**Figure 7.9** MTT assay of ATG13 KO MEFs grown in DMEM high glucose media (4.5 g/L) or glucose free DMEM supplemented with galactose (10 mM) and treated with a) Z-VAD-fmk (0-200  $\mu\text{M}$ , 72 h) b) Q-VD-Oph (0-200  $\mu\text{M}$ , 72 h). One-way ANOVA, Dunnett's post hoc comparing samples to vehicle. Error bars  $\pm$  SEM, n=3.

Cell viability was confirmed using PI exclusion. ATG13 KO MEFs grown in glucose or galactose media had no significant differences in cell viability after treatment with Z-VAD-fmk (50  $\mu\text{M}$ ) or Q-VD-Oph (50  $\mu\text{M}$ , 24-72 h). Figure 7.10a shows that there were no significant differences in cell viability with PI exclusion > 80 %. As with HEK cells, there was a slight increase in Annexin V staining in cells grown in galactose but no difference between Z-VAD-fmk and vehicle or caspase control as shown in Figure 7.10b. Finally, there was no difference in cell

number between Z-VAD-fmk and vehicle and caspase control, indicating reduction in formazan absorbance was due to changes in the reduction potential of cells under *N*-glycanase inhibition.

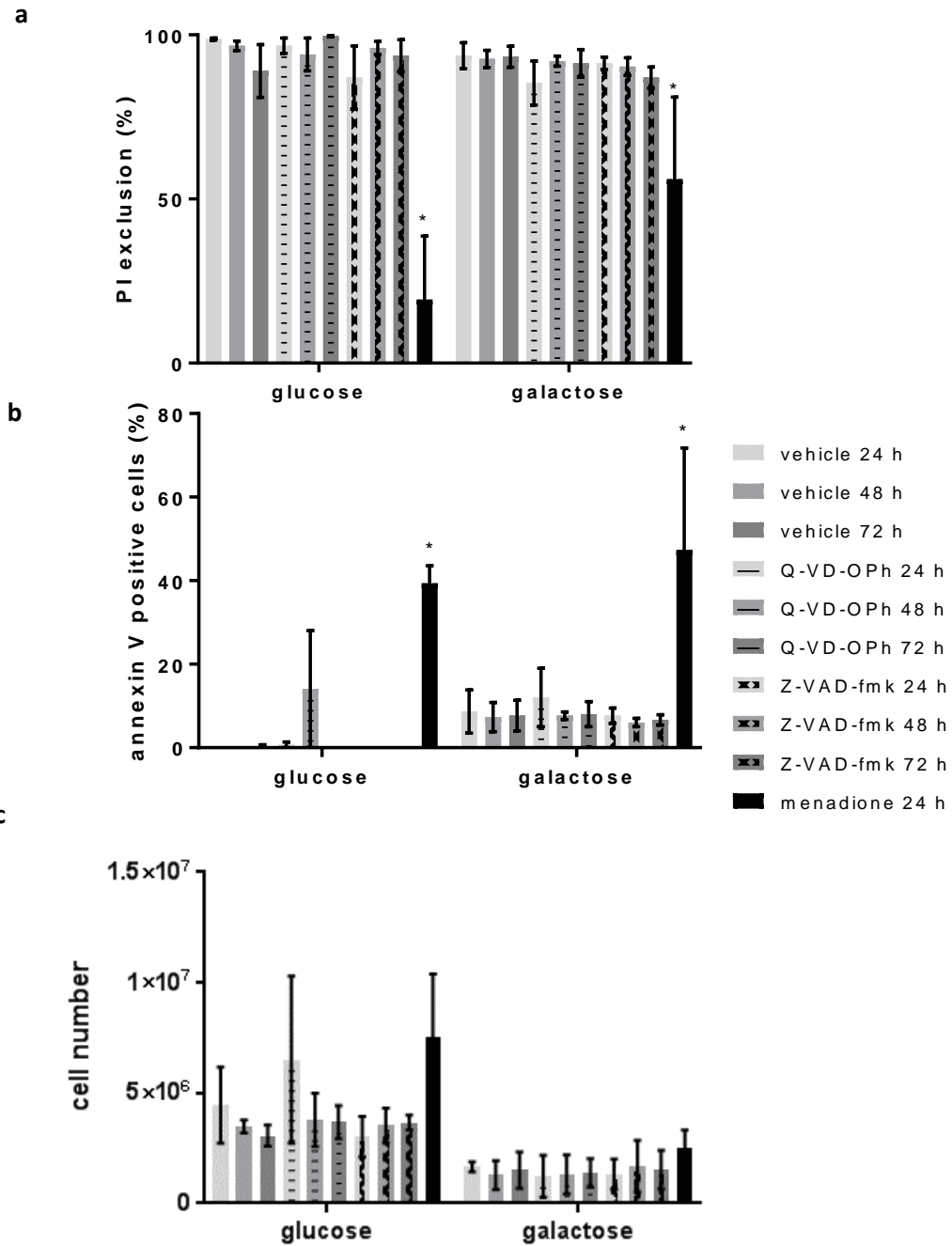


**Figure 7.10 Galactose does not affect viability of ATG13 KO MEFs treated with Z-VAD-fmk**  
 No significant changes in propidium iodide exclusion (as a measure of cell viability), annexin V staining or cell number in ATG13 KO MEFs grown in high glucose DMEM (4.5 g/L) or galactose DMEM (10 mM) were observed. Cells were treated with Q-VD-OPh or Z-VAD-fmk (50  $\mu$ M, 72 h), Menadione (100  $\mu$ M, 24 h) a) Percentage PI (10  $\mu$ g/ml 0.5 h) exclusion b) percentage of FITC annexin V positive cells c) Cell number per ml. One- way ANOVA, Tukey's post hoc. Error bars  $\pm$  SEM, n=3, P < 0.05.



### 7.3.6 WT MEFs show decreased formazan reduction when grown in galactose with Z-VAD-fmk treatment

WT MEF cells grown in RPMI 1640 media showed no significant decrease in formazan absorbance when treated with Z-VAD-fmk or Q-VD-OPh (1-200  $\mu\text{M}$ ). To confirm the effects observed in WT HEK and ATG13 KO MEF cells when grown in galactose, this was repeated in WT MEF cells. There was a significant decrease in formazan absorbance after 25, 50, 100 and 200  $\mu\text{M}$  Z-VAD-fmk after 72 h when WT MEF cells were grown in galactose media compared to the vehicle control ( $\text{IC}_{50}$  of 19.52  $\mu\text{M}$ ). There was no significant differences when grown in high glucose media (Figure **7.11a**). Figure **7.11b** shows WT MEF cells treated with Q-VD-OPh which showed no significant decreases in formazan absorbance in either high glucose or galactose media.

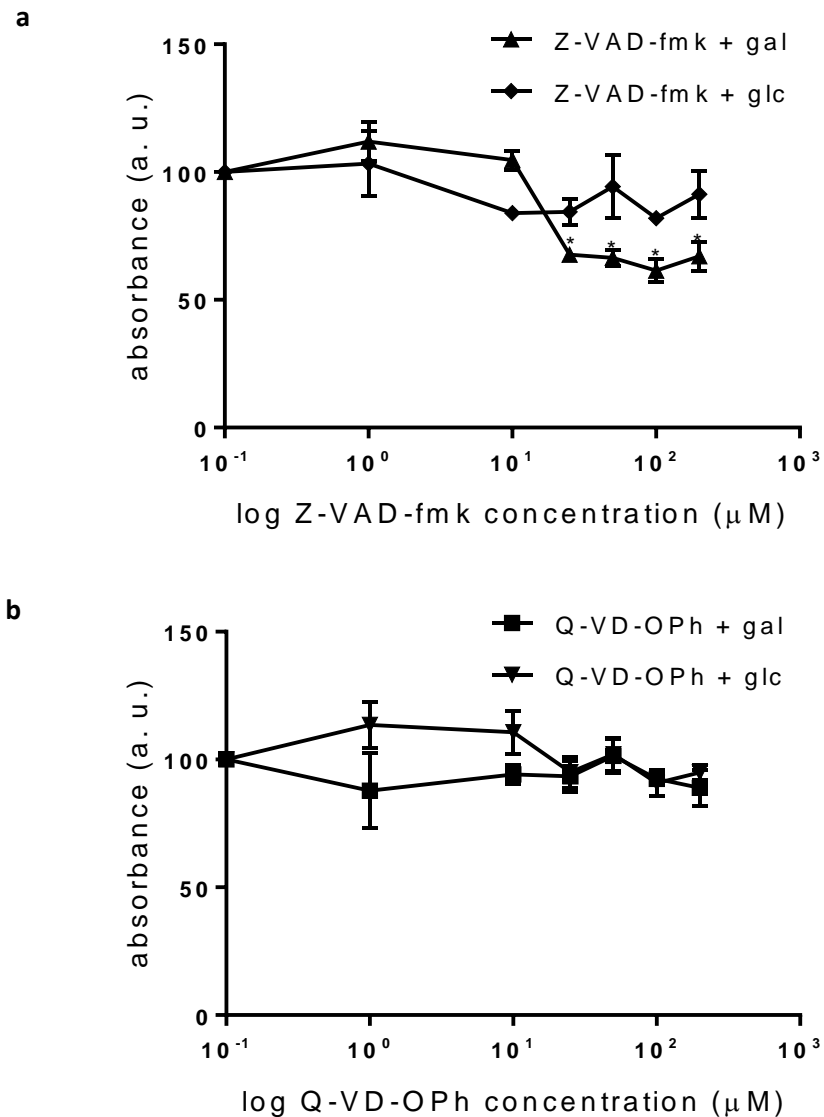


**Figure 7.11** MTT assay of WT MEF cells grown in DMEM high glucose media (4.5 g/L) or glucose free DMEM supplemented with galactose (10 mM) and treated with a) Z-VAD-fmk (0-200  $\mu\text{M}$ , 72 h) b. Q-VD-OPh (0-200  $\mu\text{M}$ , 72 h) One-way ANOVA, Dunnett's post hoc comparing samples to vehicle. Error bars  $\pm$  SEM,  $n=3$ ,  $P < 0.05$ .

Cell viability was tested by PI exclusion. Figure 7.12a indicates there were no significant decreases in cell viability in WT MEF cells treated with Z-VAD-fmk (50  $\mu\text{M}$ ) or Q-VD-OPh (50  $\mu\text{M}$ ) over 72 h when grown in either glucose or galactose containing media. Figure 7.12b shows that there were not significant changes in annexin V staining or (Figure 7.12c) cell number.

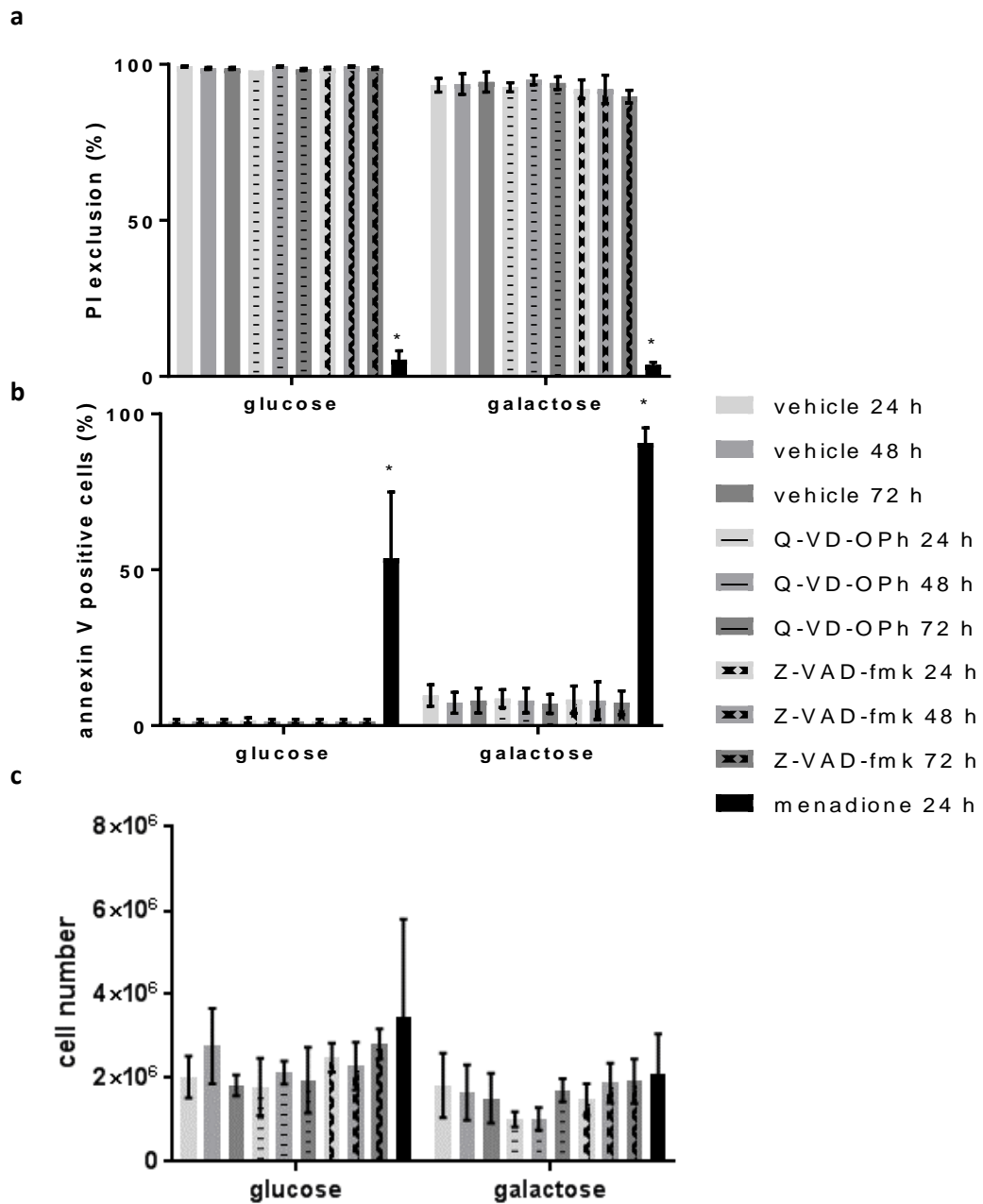


**Figure 7.12 Galactose does not affect viability of WT MEFs treated with Z-VAD-fmk. No significant changes in propidium iodide exclusion (as a measure of cell viability), annexin V staining or cell number in WT MEFs grown in high glucose DMEM (4.5 g/L) or galactose DMEM (10 mM) were observed. Cells were treated with Q-VD-OPh or Z-VAD-fmk (50  $\mu$ M) over 72 h. Menadione (100  $\mu$ M, 24 h) was used as a positive control a) Percentage PI (10  $\mu$ g/ml 0.5 h) exclusion b) percentage of FITC annexin V positive cells c) Cell number per ml. One-way ANOVA, Tukey's post hoc within each condition. Error bars  $\pm$  SEM, n=3, P < 0.05.**

### 7.3.7 Genetic knockdown of *N*-glycanase in ATG13 KO MEF and WT MEF cells in galactose supplemented DMEM reduced MTT reduction but not cell viability or proliferation

To confirm the effect of reduced formazan reduction under Z-VAD-fmk treatment was due to inhibition of *N*-glycanase and, that caspase inhibition was not influencing cell viability, ATG13 KO MEF and WT MEF cells were transfected with NGLY1 siRNA to reduce levels of *N*-glycanase. Figure 7.13a shows *N*-glycanase knockdown in ATG13 KO MEF cells with a significant reduction in formazan absorbance from day 2. Figure 7.13b shows the same treatment in WT MEF cells. When grown in galactose media there was a significant decrease in formazan absorbance from day 4.

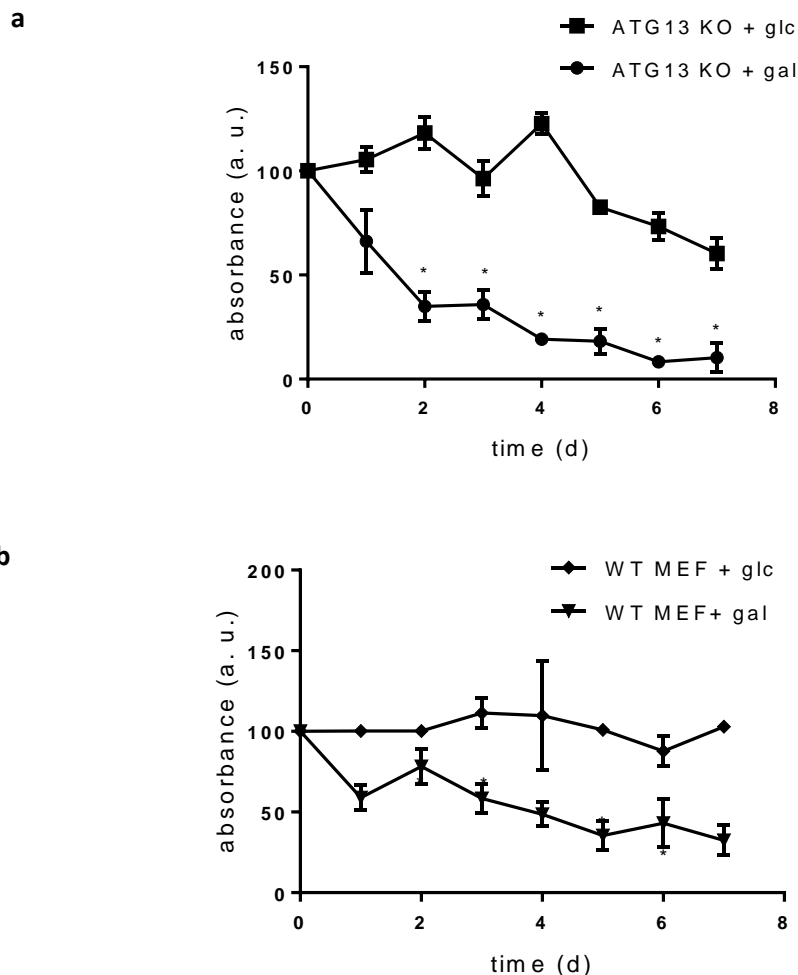
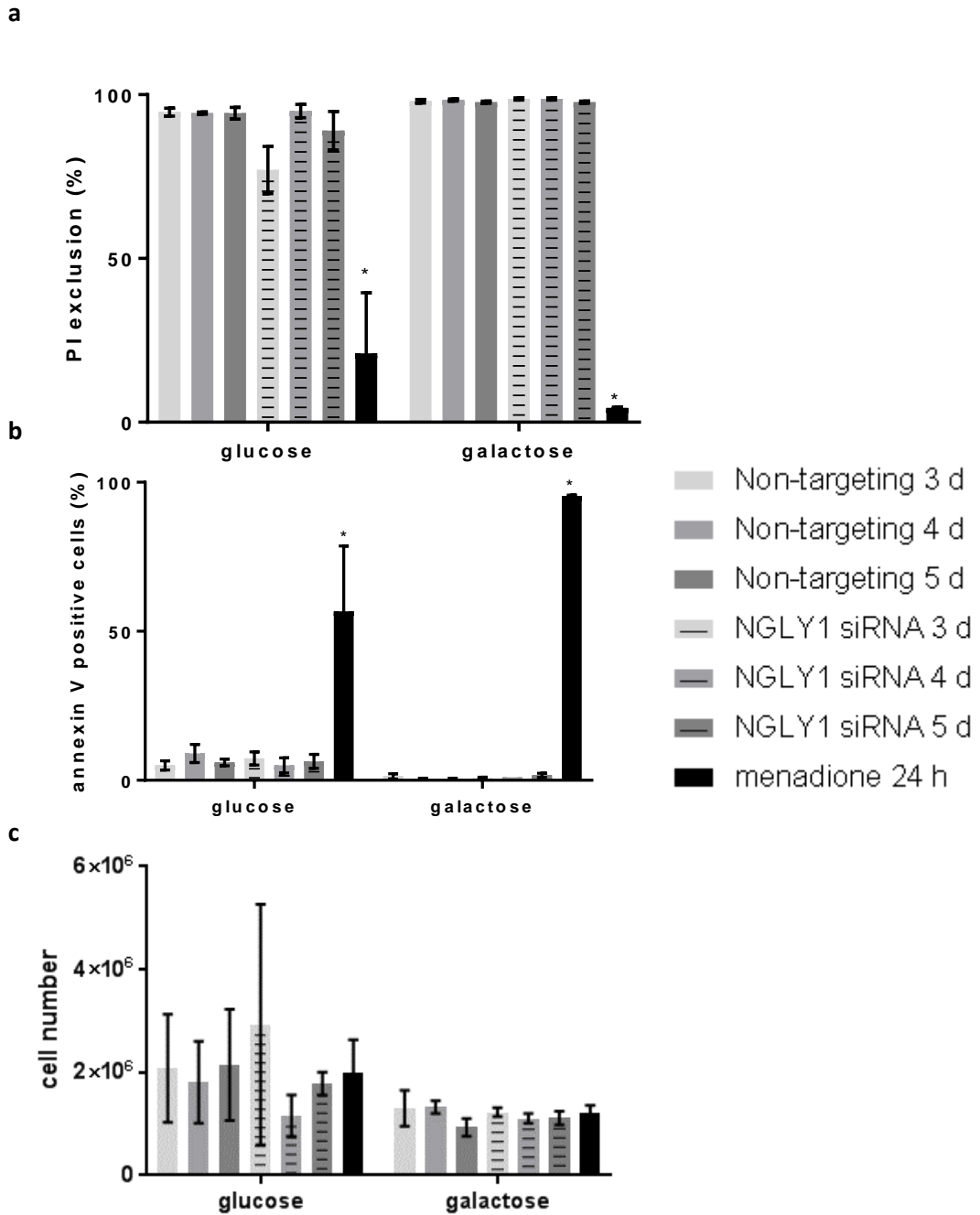


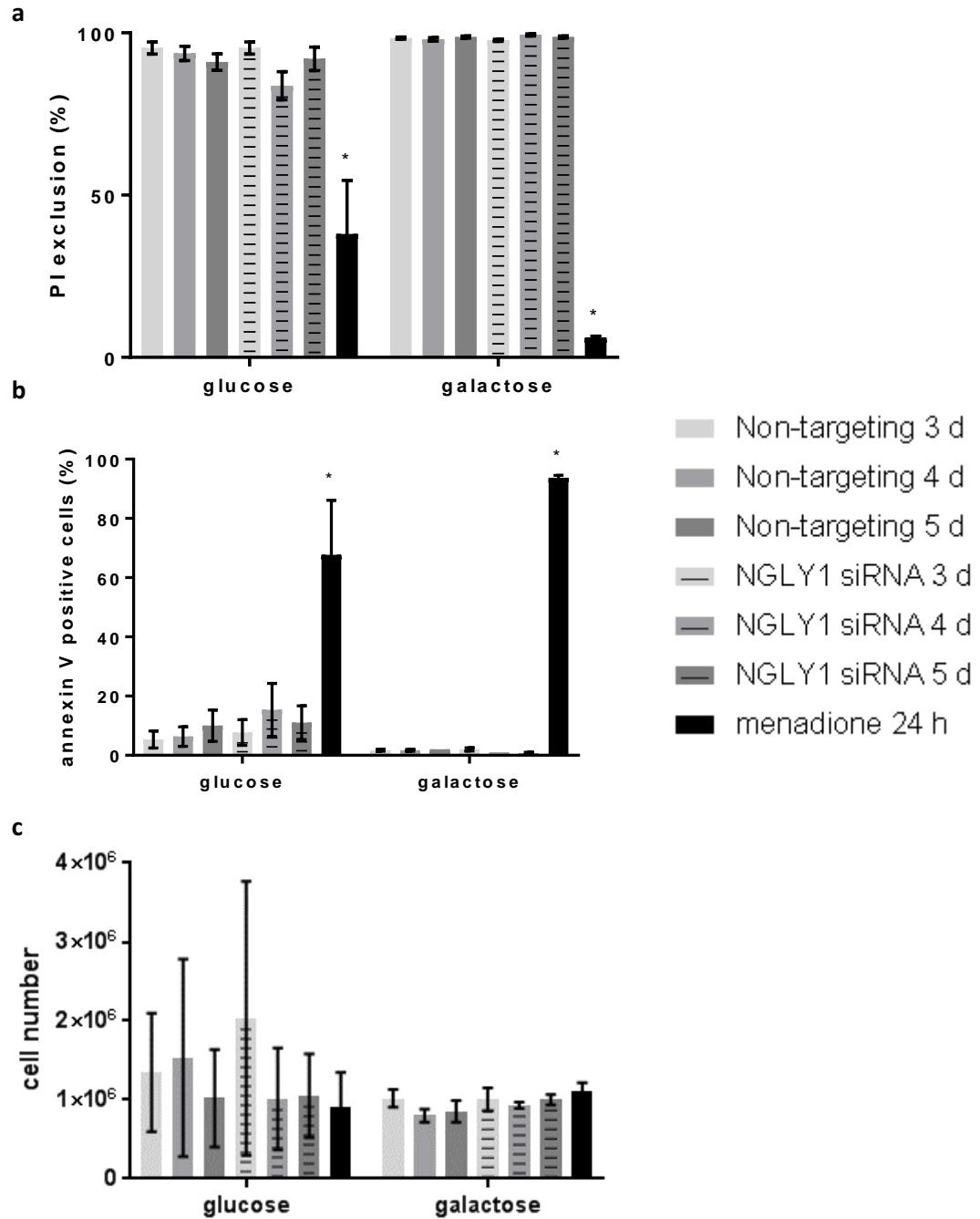
Figure 7.13 MTT assay of a) ATG13 KO MEF cells b) WT MEF cells grown in high glucose DMEM (4.5 g/L) and galactose DMEM (10 mM) 7 days post-transfection with NGLY1 siRNA. One-way ANOVA, Dunnett's post hoc against the vehicle control at time 0. Error bars  $\pm$  SEM,  $n=3$ ,  $P < 0.05$ .

Figure **7.14** shows the number of viable cells in ATG13 KO cells transfected with *N*-glycanase or non-targeting control siRNA. There were no significant decreases in cell viability (Figure **7.14a**), annexin V staining (Figure **7.14b**) or cell proliferation (Figure **7.14c**).



**Figure 7.14** Galactose does not affect viability of ATG13 KO MEFs transfected with NGLY1 siRNA. No significant changes in propidium iodide exclusion (as a measure of cell viability), annexin V staining or cell number in ATG13 KO MEFs grown in high glucose DMEM (4.5 g/L) or galactose DMEM (10 mM). Cells were transfected with NGLY1 siRNA or non-targeting siRNA and measured after 3-5 days. Menadione (100  $\mu$ M) for 24 h was used as a positive control a) percentage PI (10  $\mu$ g/ml 0.5 h) exclusion b) percentage of FITC annexin V positive cells c) cell number per ml. One-way ANOVA, Tukey's post hoc each condition. Error bars  $\pm$  SEM, n=3, P < 0.05.

Figure **7.15** shows the effect of *N*-glycanase siRNA knockdown on WT MEF cell viability, annexin V staining and cell number. There were no decreases in cell viability (Figure **7.15a**), annexin V staining (Figure **7.15b**) or in cell number (Figure **7.15c**).



**Figure 7.15 Galactose does not affect viability of WT MEFs transfected with NGLY1 siRNA.** No significant changes in propidium iodide exclusion (as a measure of cell viability), annexin V staining or cell number in WT MEF cells grown in high glucose DMEM (4.5 g/L) or galactose DMEM (10 mM). Cells were transfected with NGLY1 siRNA or non-targeting siRNA and measured after 3-5 days. Menadione (100  $\mu$ M) for 24 h was used as a positive control a) percentage PI (10  $\mu$ g/ml 0.5 h) exclusion b) percentage of FITC annexin V positive cells c) Cell number per ml. One-way ANOVA, Tukey's multiple comparison test within each condition. Error bars  $\pm$  SEM, n=3, P < 0.05.



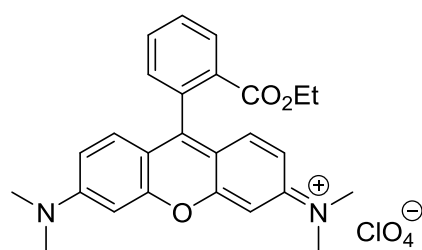
In summary, if cells were grown in either glucose or galactose supplemented media it was found that Z-VAD-fmk but not Q-VD-OPh decreased MTT reduction but did not reduce cell viability, increase early apoptotic features or affect cell proliferation. Therefore, the change in formazan absorbance can be attributed to redox activity in the cell. This trend was followed in WT MEF and ATG13 KO MEF cell lines. Furthermore, similar results were seen with knockdown of *N*-glycanase using siRNA, indicating a role for *N*-glycanase. Since there were no increases in annexin V staining in NGLY1 siRNA treated cells (indicating caspase inhibitors were not blocking apoptosis) cells were not preparing to undergo apoptosis, even in the ATG13 KO MEFs. This change could indicate decreased mitochondrial activity.

Although MTT was originally thought to be primarily reduced by mitochondrial enzymes, it is now known this is not always the case. Using confocal microscopy to examine the subcellular location of MTT reduced formazan (compared to TMRE and NAO labelled mitochondria) it was found only 25 % formazan signal overlapped labelled mitochondria. MTT fluorescence also shows a correlation with MTT reduction and, with glucose concentration in cell culture (Alet van Tonder et al. 2015). To further investigate the functionality of mitochondria under pharmacological *N*-glycanase inhibition and siRNA knockdown, mitochondrial polarisation was examined.

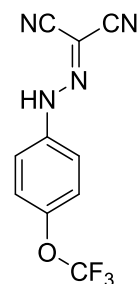
#### 7.3.8 Mitochondrial membrane potential is unaffected by inhibition and genetic ablation of *N*-glycanase

The mitochondrial membrane potential relates to the ATP production capacity of mitochondria. Changes in polarisation, whether hyperpolarisation or depolarisation, can be an indication of mitochondrial health (Lezi and Swerdlow 2012). Most of the dyes which are commonly used to measure mitochondrial membrane potential ( $\Delta\Psi_m$ ) are lipophilic cationic compounds. The more polarised, and therefore more negative, the mitochondrial matrix is, the more dye accumulates. Under high concentrations of dye, the fluorescence signal becomes quenched. In quenching mode, the concentrations of dye are high enough to accumulate in the mitochondrial matrix to an extent that it forms aggregates which results in lowered fluorescence emission. Depolarisation of the mitochondria under this condition results in an increase in fluorescence as the dye concentration drops and the fluorescence is unquenched. Hyperpolarisation in this case would result in a further decrease in fluorescence as even more dye accumulates in the mitochondrial matrix. This method is very difficult to analyse as the fluorescence is not linear compared to the polarisation of the mitochondria. In this study, mitochondrial potential was measured using tetramethylrhodamine ethyl ester

perchlorate (TMRE) **14** in non-quenching mode. In this case, lower polarisation will have lower fluorescence and hyperpolarised cells will have higher fluorescence. Cells are often treated with agents that rapidly decrease  $\Delta\Psi_m$  to ensure expected results with the dye of choice. Carbonyl cyanide-4-trifluoromethoxyphenylhydrazone (FCCP) **15** is an oxidative phosphorylation un-coupler used to decrease  $\Delta\Psi_m$ . Mitochondrial uncouplers transport protons across the inner membrane into the matrix, bypassing the normal route during respiration.



**14**



**15**

To confirm quenching and non-quenching concentrations of TMRE in HEK cells, cells were incubated with increasing concentrations of TMRE 0.5 h and the mean fluorescence was measured before and after treatment with FCCP (10  $\mu$ M, 5 min). Fluorescence was recorded using a TALI image based cytometer. The difference in fluorescence ( $\Delta$  fluorescence, equivalent to TMRE - TMRE fluorescence after FCCP treatment) was calculated. Figure **7.16** shows the  $\Delta$ TMRE fluorescence. For measurements recorded on the TALI image based cytometer, a concentration of 100 nM TMRE was selected. At concentrations below 100 nM the mitochondrial fluorescence is not quenched.

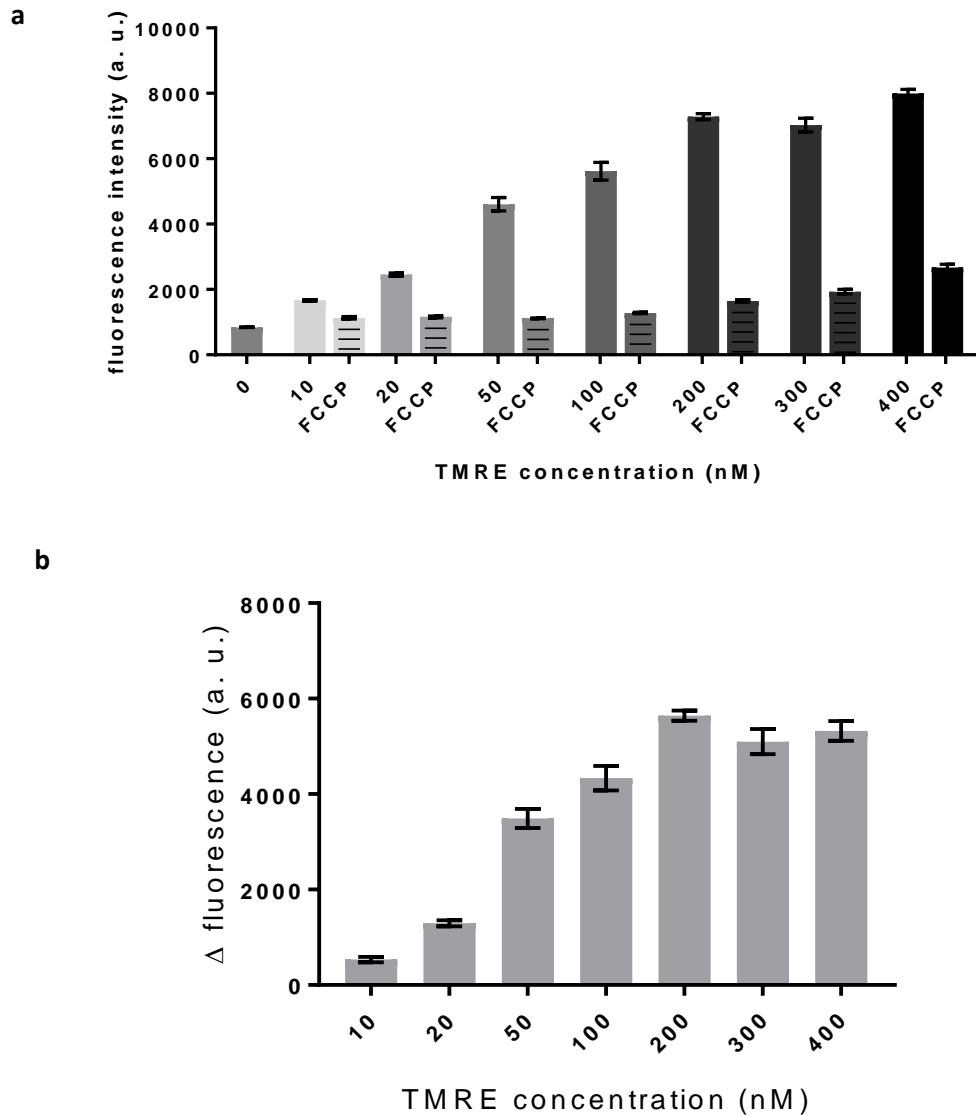


**Figure 7.16 a) Mean TMRE fluorescence in WT HEK cells measured on TALI image based cytometer. Error bars  $\pm$  SEM, 9 images taken per condition. b)  $\Delta$  TMRE levels.**

To measure the mitochondrial membrane potential, HEK cells were treated with Z-VAD-fmk or Q-VD-OPh (50  $\mu$ M, 24-72 h) and incubated with TMRE (100 nM, 0.5 h). To ensure TMRE accumulation in the mitochondria, cells treated in the same way were incubated with FCCP (10  $\mu$ M, 5 min) before TMRE incubation. Cells were trypsinised and washed twice in ice-cold PBS by centrifugation and re-suspended in PBS (500  $\mu$ L). Figure 7.17a shows the fluorescence intensity of TMRE measured using a TALI image based cytometer. There were no significant differences in starting TMRE fluorescence between the groups or by how much the FCCP

depolarised the samples. **Figure 7.17b** shows the  $\Delta$  fluorescence and there no significant differences were observed between groups.

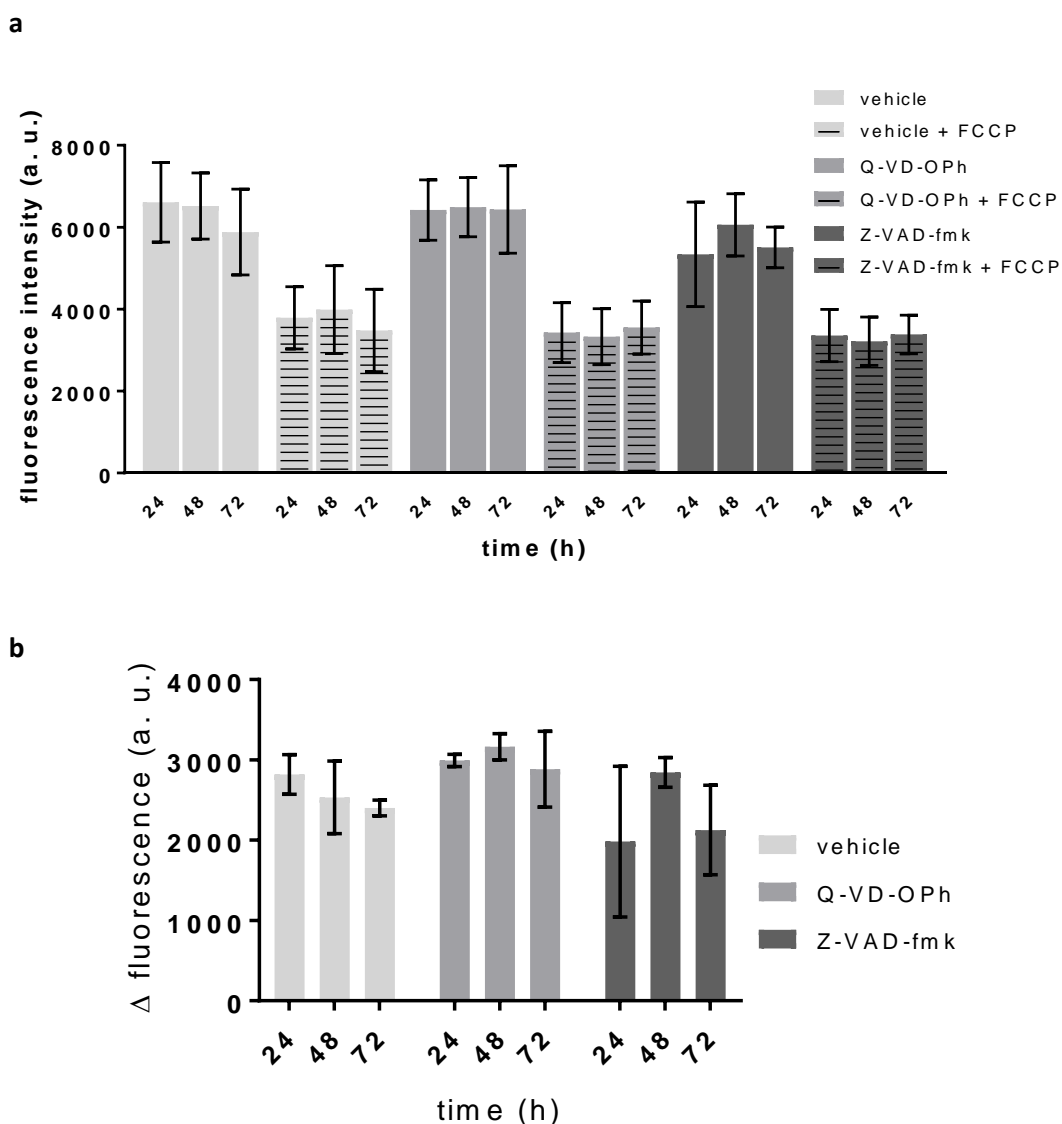


**Figure 7.17** Mean TMRE fluorescence of HEK 293 cells treated with Z-VAD-fmk or Q-VD-OPh (50  $\mu$ M, 24-72 h) with or without FCCP (10  $\mu$ M, 5 min) and stained with TMRE (100 nM, 30 min). **a)** Fluorescence intensity recorded on a TALI image based cytometer, 9 images were taken per condition. **b)** shows  $\Delta$  TMRE fluorescence (TMRE-(TMRE+FCCP)). Two-way ANOVA. Error bars  $\pm$  SEM,  $n=4$ .

To confirm this effect, HEK cells were also treated with *N*-glycanase siRNA and the membrane potential calculated. **Figure 7.18a** shows the mean fluorescence intensity of TMRE before and after FCCP treatment. **Figure 7.18b** shows  $\Delta$ TMRE fluorescence. There were no significant differences in mitochondria membrane potential after *N*-glycanase knockdown.

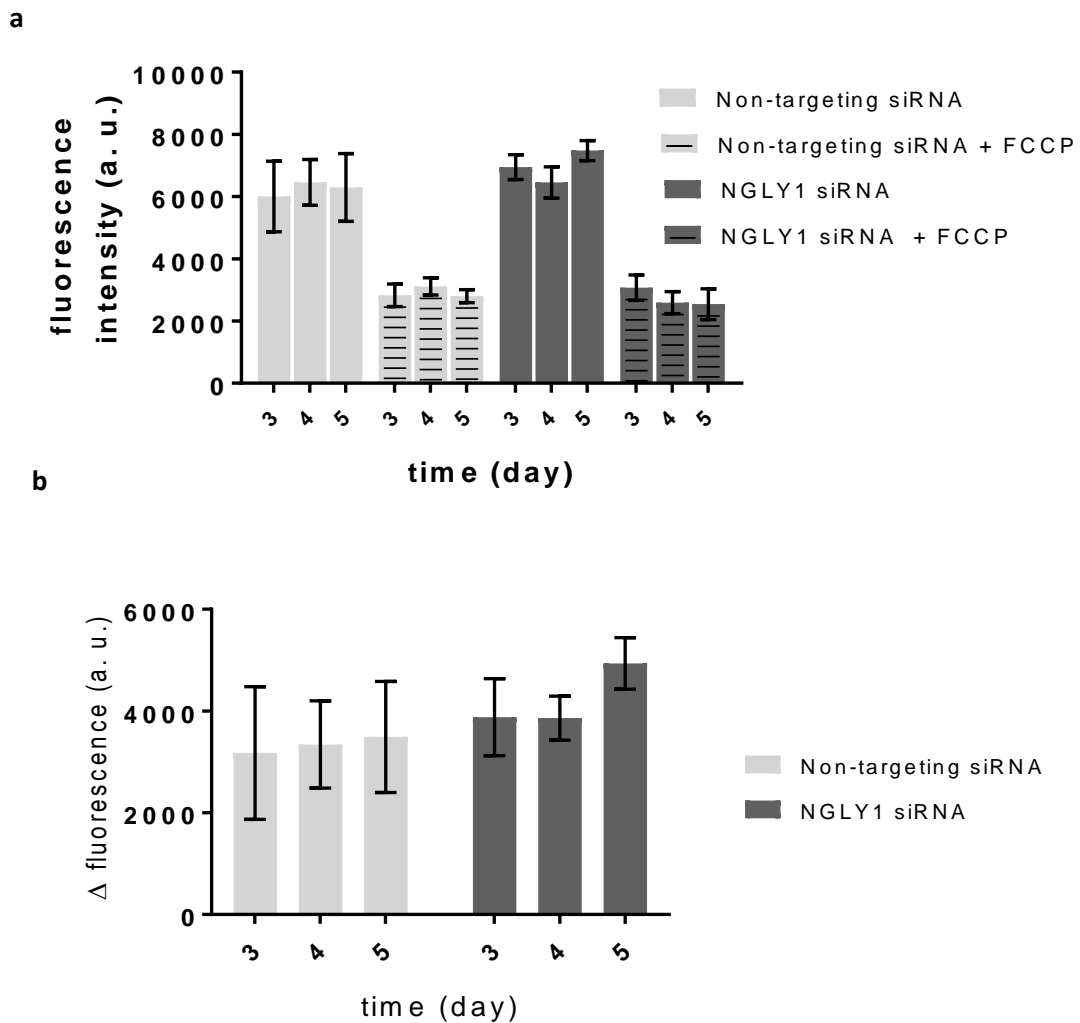


**Figure 7.18** a) mean TMRE fluorescence of HEK 293 cells transfected with NGLY1 siRNA or non-targeting siRNA over 3-5 days with or without FCCP (10  $\mu$ M, 5 min) and stained with TMRE (100 nM) for 0.5 h. Fluorescence intensity recorded on a TALI image based cytometer, 9 images were taken per condition b)  $\Delta$  TMRE fluorescence of HEK 293 cells. Two-way ANOVA found no significance. Error bars  $\pm$  SEM,  $n=4$ .

When cells were grown in glucose containing media, no changes in MTT reduction was observed. This could be because aerobic glycolysis is compensating for mitochondrial defects. To test this, cells were grown in zero glucose medium supplemented with 10 mM galactose. Again, cells were treated with Z-VAD-fmk or Q-VD-OPh (50  $\mu$ M, 24-72 h) and incubated with TMRE (100 nM) or FCCP (10  $\mu$ M, 5 min) before incubation with TMRE (100 nM, 30 min) prior to measurements. Cells were washed in PBS twice and placed on ice although the cells treated with FCCP were maintained with FCCP in the solution. Figure 7.19a shows the mean TMRE fluorescence intensity before and after FCCP treatment. Figure 7.19b

shows the  $\Delta$ TMRE fluorescence intensity. There was a trend for a slight decrease in in the Z-VAD-fmk treatment compared to vehicles and Q-VD-OPh with an average delta fluorescence reduction of 30 % over 72 h compared to the vehicle and 19 % compared to the Q-VD-OPh control; however this was found to be non-significant.

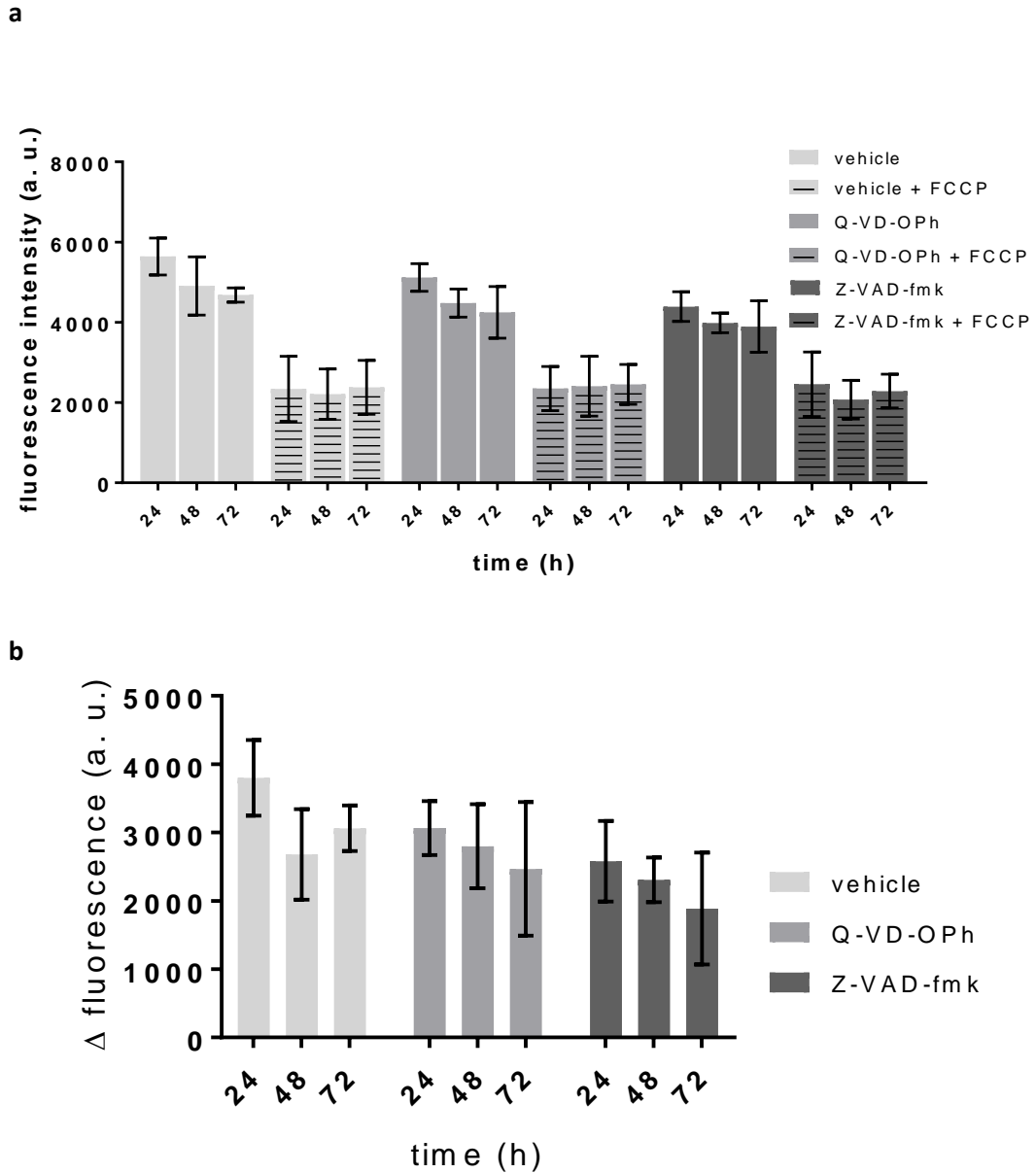


**Figure 7.19** There is no change in TMRE fluorescence in HEK cells grown in galactose. **a)** TMRE fluorescence of HEK 293 cells grown in galactose (10 mM) DMEM. Mean fluorescence of HEK 293 cells treated with Z-VAD-fmk or Q-VD-OPh (50  $\mu$ M, 24-72 h) with or without FCCP (10  $\mu$ M, 5 min) and stained with TMRE (100 nM, 0.5 h). FI calculated by TALI image based cytometer, 9 images were taken per condition **b)**  $\Delta$  TMRE fluorescence of HEK 293 cells. Two-way ANOVA found no significance. Error bars  $\pm$  SEM,  $n=3$ .

HEK cells were grown in galactose and transfected with *N*-glycanase siRNA as before and the mitochondrial membrane potential calculated. Figure **7.20a** shows the mean TMRE fluorescence before and after FCCP treatment. There were no significant differences in starting TMRE fluorescence compared to a non-targeting control. However, there was a small

significant decrease in fluorescence observed in *N*-glycanase knockdown cells after treatment with FCCP (compared to non-targeting siRNA control cells treated with FCCP) at day 5. Figure **7.20b** shows the  $\Delta$ TMRE fluorescence. This decreased fluorescence in knockdown cells compared to controls led to a significant increase in  $\Delta$ TMRE fluorescence at day 5. The opposite of the trend seen in Z-VAD-fmk treated cells which shows a small non-significant decrease in  $\Delta$ TMRE fluorescence. Although this is the same trend as siRNA treated cell when grown in glucose which showed an average increase of 70 % it was found not to be significant.



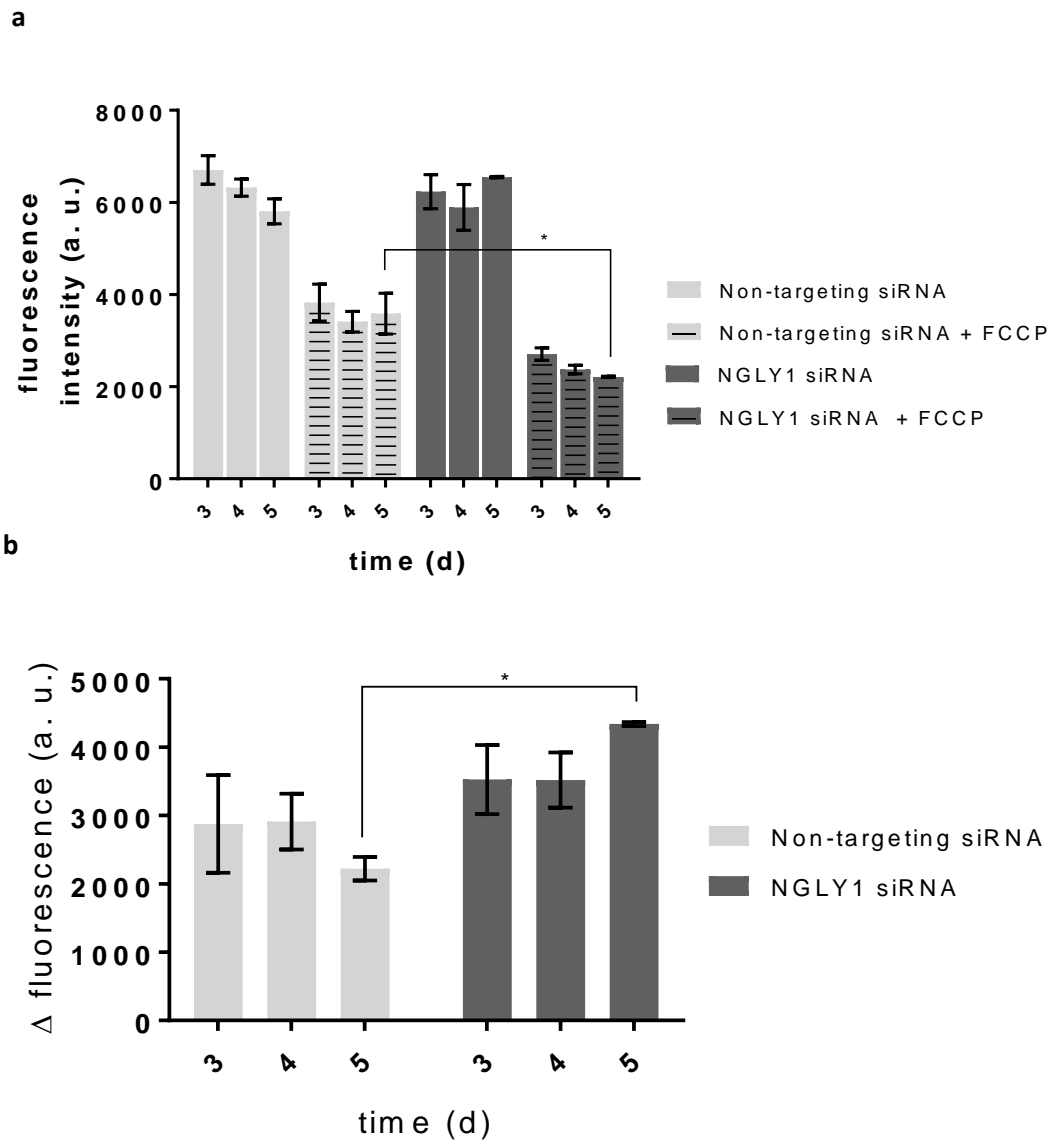


**Figure 7.20** a) TMRE fluorescence of HEK 293 cells grown in galactose (10 mM) supplemented DMEM. Mean fluorescence of HEK 293 cells transfected with NGLY1 siRNA or non-targeting siRNA over 3-5 days with or without 5 mM of FCCP (10  $\mu$ M) and stained with TMRE (100 nM) for 10 min b)  $\Delta$  TMRE fluorescence of HEK 293 cells. FI calculated by TALI image based cytometer, 9 images were taken per condition. Two-way ANOVA, Tukey's multiple comparison test. Error bars  $\pm$  SEM,  $n=2$ ,  $P < 0.05$ .

TALI based measurements of TMRE fluorescence lead to high variation between samples and high fluorescence under FCCP treatment. To confirm these changes in mitochondrial potential, TMRE fluorescence was measured using methods by flow cytometry. Figure 7.21 shows increasing concentration of TMRE stained HEK cells. Even at high concentrations the median fluorescence intensity continued to increase without showing indications of fluorescence quenching.

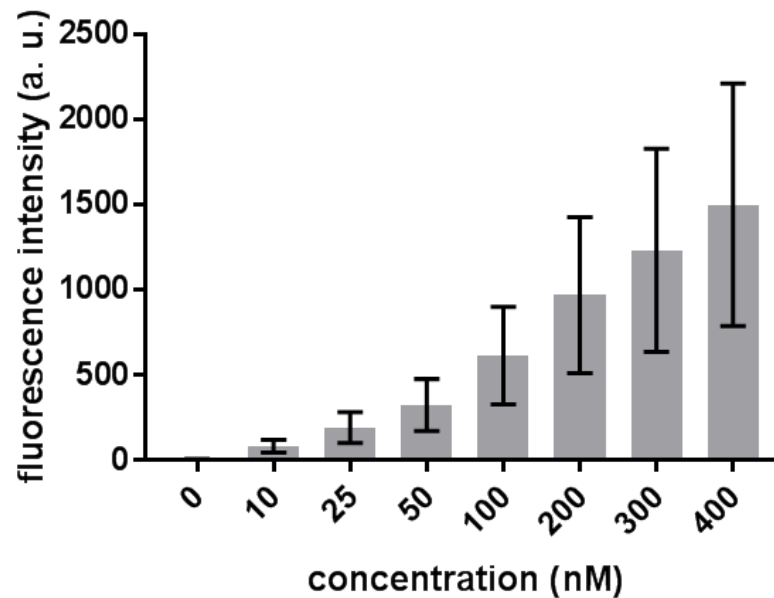


**Figure 7.21 Median TMRE fluorescence of HEK 293 measured by flow cytometry. Error bars  $\pm$  SEM,  $n=3$ .**

HEK cells were incubated in increasing concentrations of TMRE and imaged to confirm quenching concentrations. Cells were imaged every 20 s for 180 s to ensure an even baseline level of TMRE fluorescence before the addition of FCCP (10  $\mu$ M). Figure 7.22 shows the TMRE fluorescence of HEK cells loaded with 25-400 nM TMRE. TMRE levels above 100 nM showed an increase in fluorescence intensity after the addition of FCCP, indicating TMRE in quenched concentration in the mitochondria. Furthermore, the highest concentration, 400 nM, showed decreased starting fluorescence compared to lower concentrations (200 and 300 nM) indicating quenched fluorescence. To ensure the concentration of TMRE did not cause quenching, 50 nM was used in flow cytometry analysis of mitochondrial membrane potential.

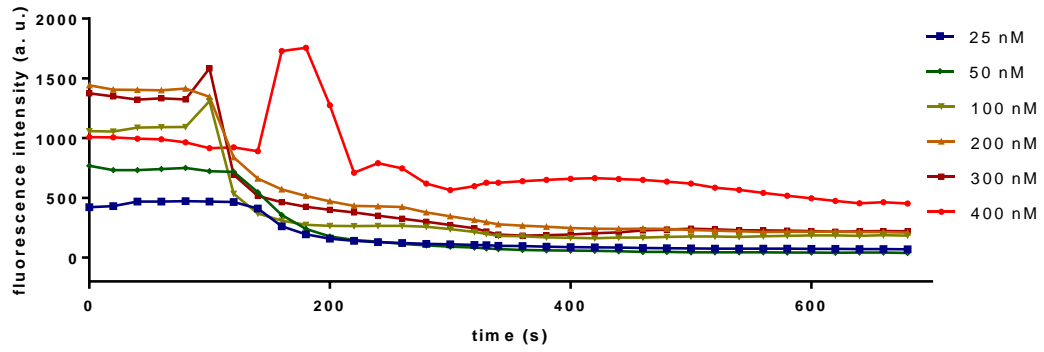


**Figure 7.22** TMRE fluorescence of HEK 293 cells treated with FCCP (10  $\mu$ M) as determined by microscopy. TMRE fluorescence was measured at 20 s intervals for 12 m. FCCP was added after 180 s. Data points show the average of 20 cells measured in one experiment.

As cells grown in galactose supplemented media exhibited the most different changes upon Z-VAD-fmk or *N*-glycanase knockdown, galactose media was used in the flow cytometry analysis of TMRE fluorescence. HEK cells were treated with Z-VAD-fmk and Q-VD-OPh (50  $\mu$ M, 24-72 h) as before in galactose supplemented media. Figure **7.23a** shows the median TMRE fluorescence before and after FCCP treatment. There were no significant differences between groups, FCCP treated and untreated conditions at the same time point, or within conditions or the  $\Delta$  TMRE fluorescence, shown in Figure **7.23b**.

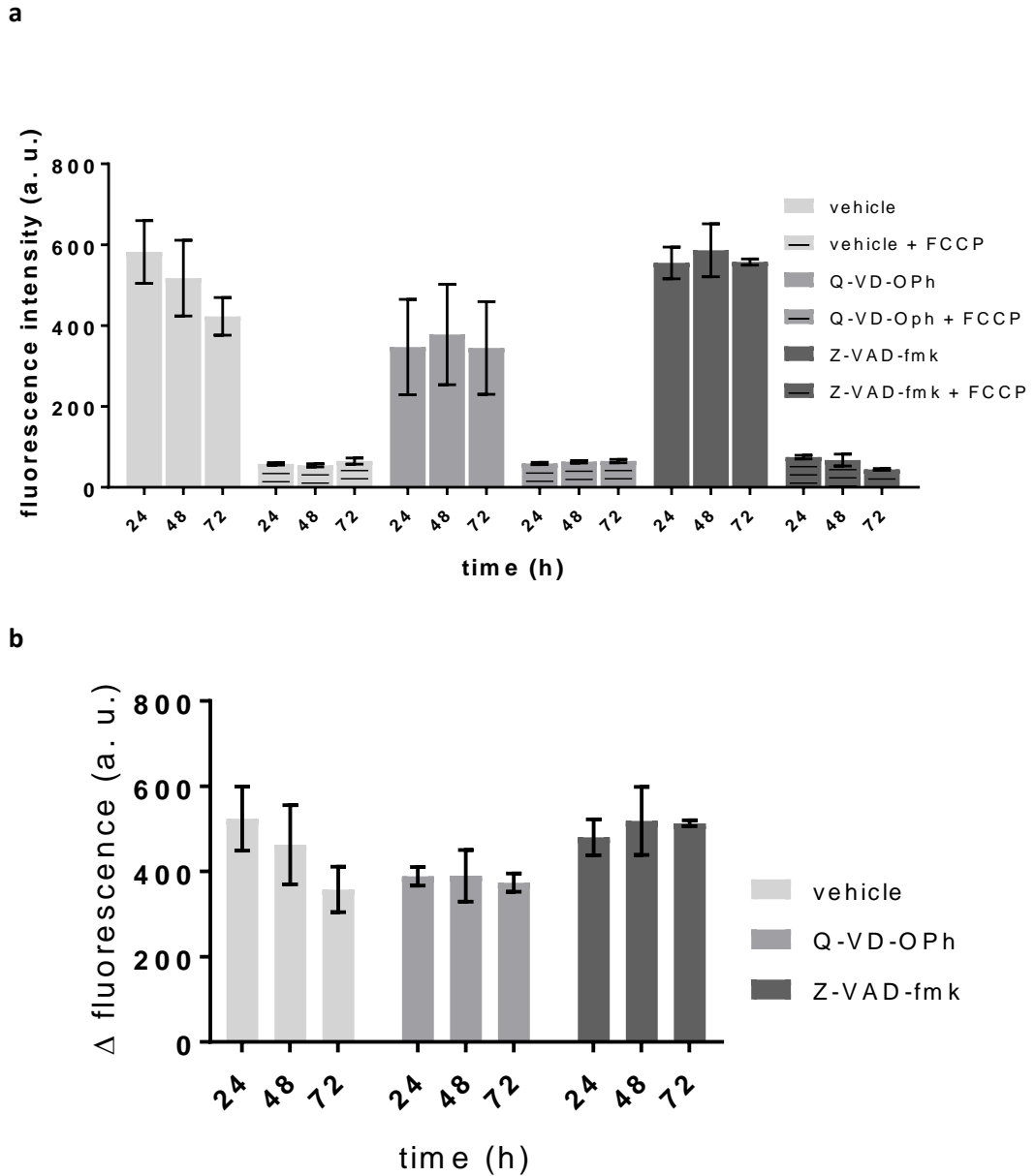


Figure 7.23 a) Median fluorescence of HEK cells treated with Z-VAD-fmk or Q-VD-OPh (50  $\mu$ M, 24-72 h) with or without FCCP (10  $\mu$ M, 5 min) and stained with TMRE (100 nM) for 30 m. Fluorescence intensity calculated by flow cytometry. Cells were grown in DMEM supplemented with galactose (10 mM) b)  $\Delta$  TMRE fluorescence of HEK 293 cells. Two-way ANOVA found no significance. Error bars  $\pm$  SEM,  $n=3$ .

The previously described experiment was repeated following genetic knockdown of *N*-glycanase using siRNA. No significant differences were identified (figure 7.24).

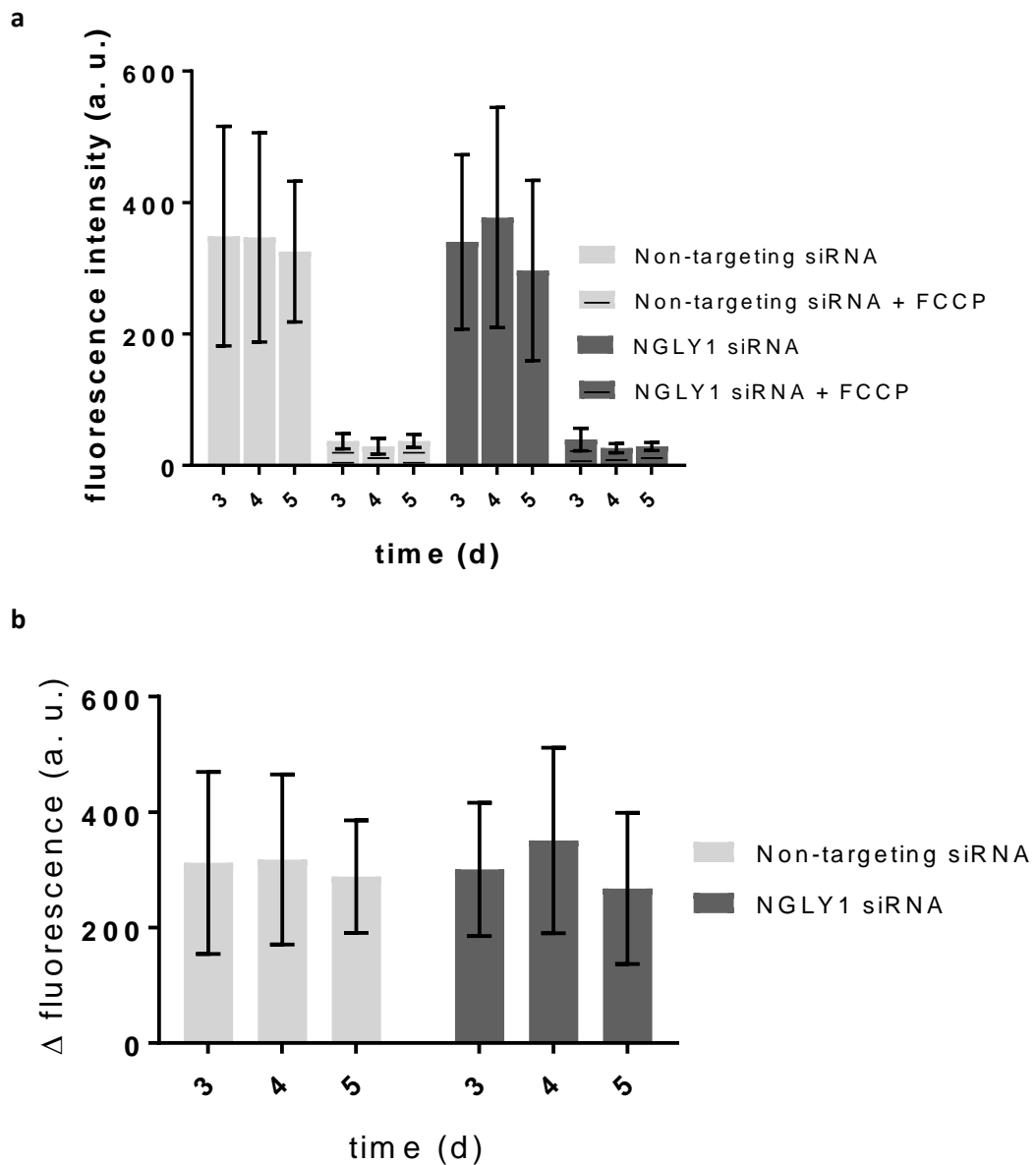


Figure 7.24 a) mean TMRE fluorescence of HEK 293 cells transfected with NGLY1 siRNA or non-targeting siRNA over 3-5 days with or without FCCP (10  $\mu$ M, 5 min) and stained with TMRE (100 nM) for 0.5 h. Fluorescence intensity determined by flow cytometry. Cells were grown in DMEM supplemented with galactose (10 mM) b)  $\Delta$  TMRE fluorescence of HEK 293 cells. Two-way ANOVA found no significance. Error bars  $\pm$  SEM,  $n=3$ .

### 7.3.9 Measurements of mitophagy by flow cytometry were variable between experiments

Several mitophagy factors (including PHB2 and p62) were identified in the proteomics screen, along with NBR1 and FAM134 in low abundance. The association between increased numbers of autophagosomes after treatment with Z-VAD-fmk (50  $\mu$ M, 72 h) and after 5 d post-transfection with *N*-glycanase siRNA (25 nM) and mitochondria were explored. Although no changes in mitochondria membrane potential have been identified in this study, there is a change in MTT reduction in galactose supplemented media which is commonly used to study mitochondrial function (Aguer et al. 2011, Dott et al. 2014, Kase et al. 2013, Marroquin et al. 2007, Rodriguez-Enriquez et al. 2001).

Mitophagy was assessed using the mitochondrial dye, MitoTracker<sup>®</sup> Deep Red, and analysed by flow cytometry in conjunction with the autophagy inhibitors, bafilomycin and 3-MA (Xiao et al. 2016). Under conditions of increased mitophagy, by inhibiting autophagy by either reduction of lysosomal degradation (Bafilomycin) or inhibition of autophagosome biogenesis (3-MA) it is expected to find increased MitoTracker<sup>®</sup> staining (Xiao et al. 2016).

To identify if the increased autophagy previously identified involved the specific removal of mitochondria, HEK cells were treated with the known inducer of autophagy, rapamycin (10  $\mu$ M, 4 h) and with Bafilomycin (100 nM, 4 h) or 3-MA (5 mM, 4 h) followed by incubation with MitoTracker<sup>®</sup> Deep Red (50 nM, 0.5 h). Figure **7.25a** shows the median mitotracker fluorescence intensity. Under basal conditions, inhibition of autophagy by bafilomycin or 3-MA did not increase MitoTracker<sup>®</sup> fluorescence intensity. However, in cells where autophagy is induced by rapamycin, there was an increase in fluorescent intensity after autophagy inhibition. Figure **7.25b** shows the fold change in fluorescence after autophagy inhibition. A significant increase in fluorescence intensity in rapamycin and 3-MA treated cells compared to 3-MA cells treated alone was found. For subsequent experiments, 3-MA was used to inhibit autophagy. 3-MA inhibits the formation of the autophagic membrane leaving mitochondria in the cytosol which may be more amenable to staining.

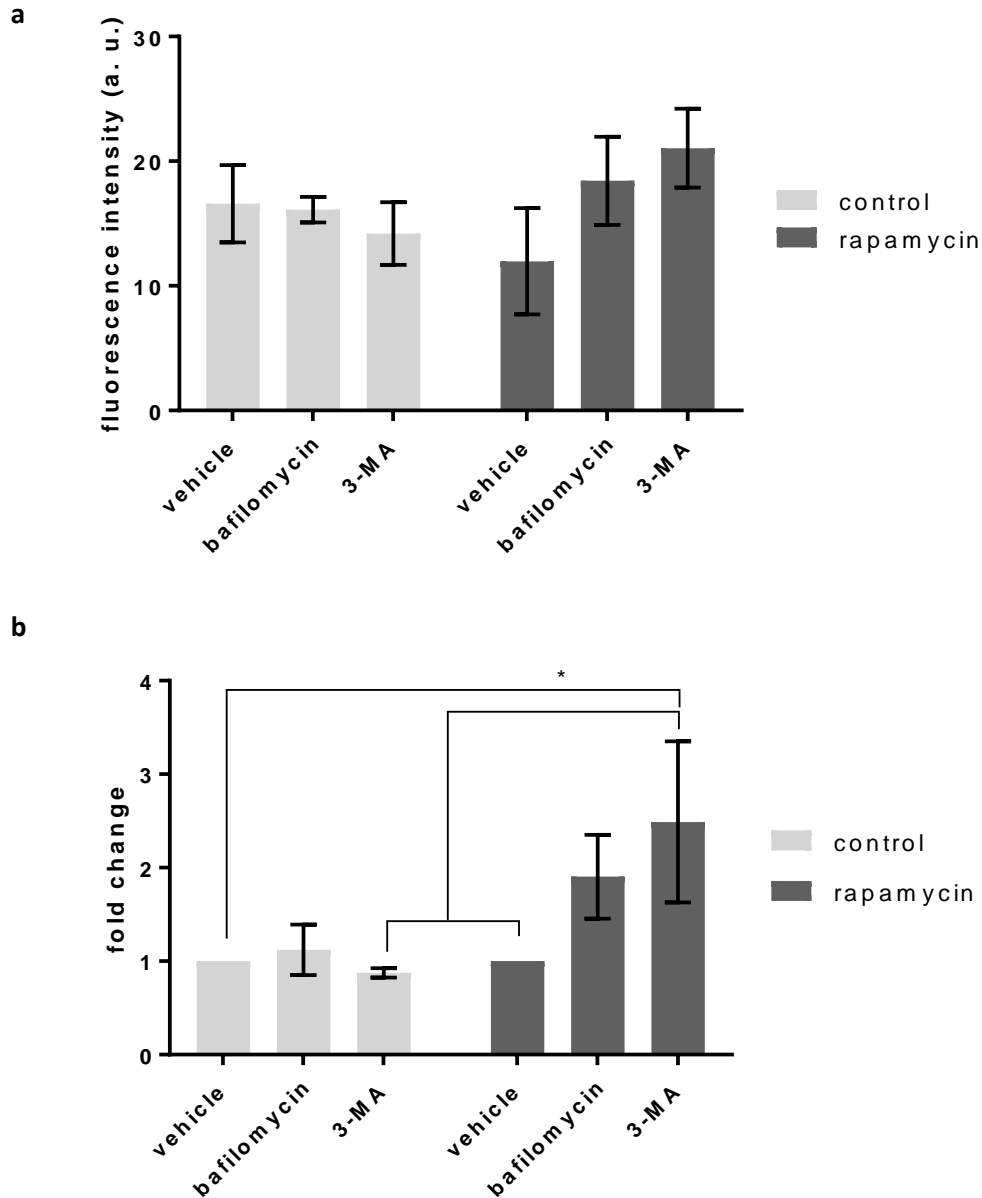


**Figure 7.25** a) mean MitoTracker<sup>TM</sup> Deep Red (50 nM, 0.5 h) fluorescence of HEK 293 cells treated with bafilomycin (100 nM, 4 h), 3-MA (5 mM, 4 h) in the presence or absence of rapamycin (10 μM, 4 h) b) fold change in MitoTracker fluorescence compared to vehicle after treatment with bafilomycin (100 nM) or 3-MA (5 mM, 4h). Two-way ANOVA, Tukey's post hoc test. Error bars  $\pm$  SEM,  $n=3$ .  $P < 0.05$ .

To identify if inhibition or knockdown of *N*-glycanase induced mitophagy specifically, HEK cells were treated with Z-VAD-fmk or Q-VD-OPh (50 μM, 24-72 h) and treated with or without 3-MA (5 mM, 4 h). **Figure 7.26a** shows the median Mitotracker<sup>TM</sup> fluorescence. There were no significant differences in Mitotracker staining before or after autophagy inhibition with 3-MA or in starting Mitotracker fluorescence. **Figure 7.26b** shows the fold change fluorescence

intensity was calculated following autophagy inhibition. There were no significant differences identified between the vehicle, Q-VD-OPh treated and Z-VAD-fmk treated cells.

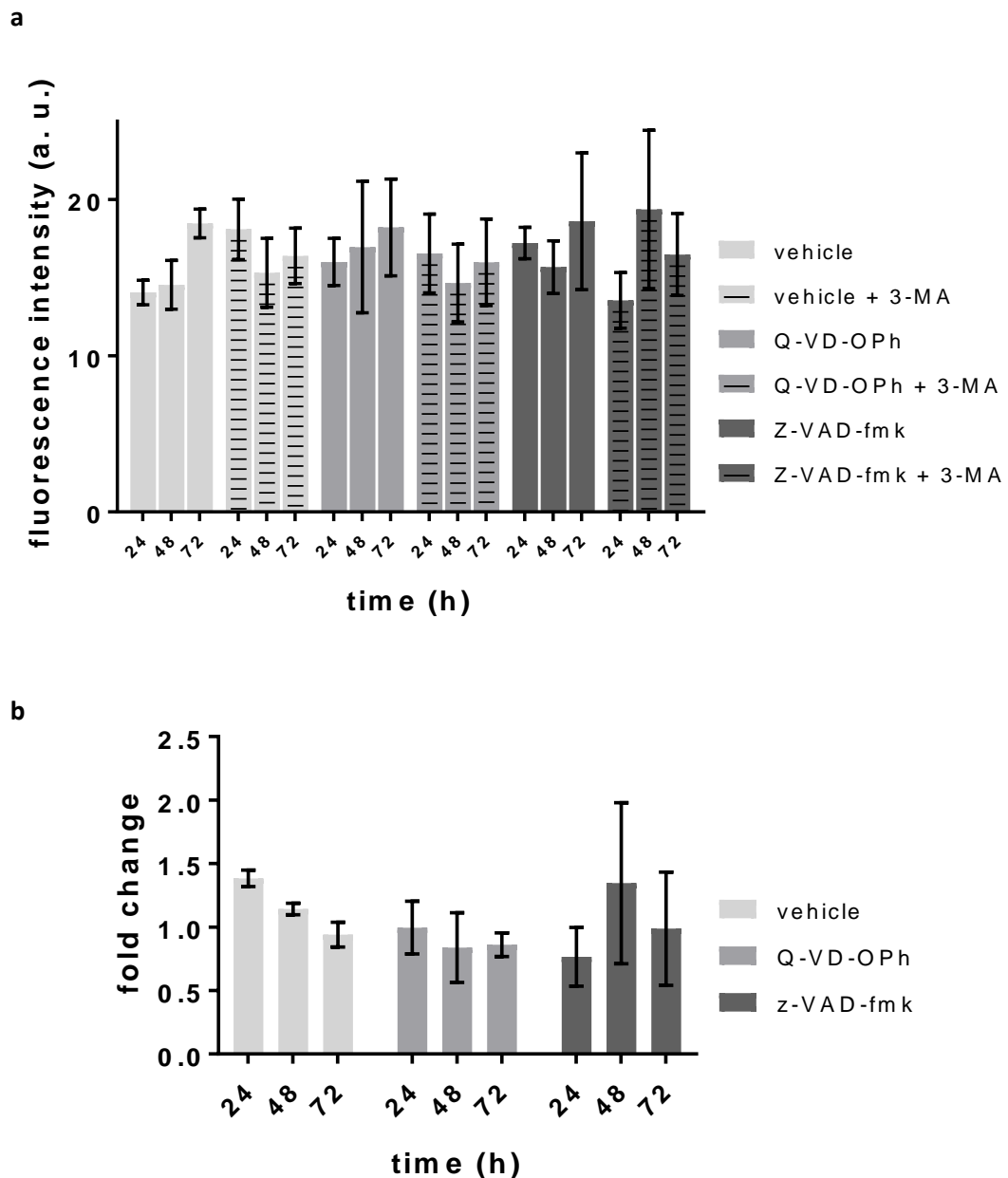


**Figure 7.26** No increase in MitoTracker™ fluorescence intensity after 3-MA treatment with Z-VAD-fmk or Q-VD-OPh was found a) mean MitoTracker™ (50 nM) fluorescence intensity in HEK 293 cells treated with vehicle, Z-VAD-fmk or Q-VD-OPh (50 μM, 24-72 h) with or without 3-MA (5 mM, 18 h). Fluorescence intensity measured by flow cytometry b) fold change in MitoTracker (50 nM) fluorescence intensity. Two-way ANOVA. Error bars ± SEM,  $n=4$ .



The experiment was repeated on cells transfected with *N*-glycanase siRNA. Figure 7.27a shows the median Mitotracker fluorescence. Similar to the observations in cases of pharmacological *N*-glycanase inhibition, there were no significant differences in Mitotracker™ fluorescence following genetic ablation before or after incubation with 3-MA shown (Figure 7.27).

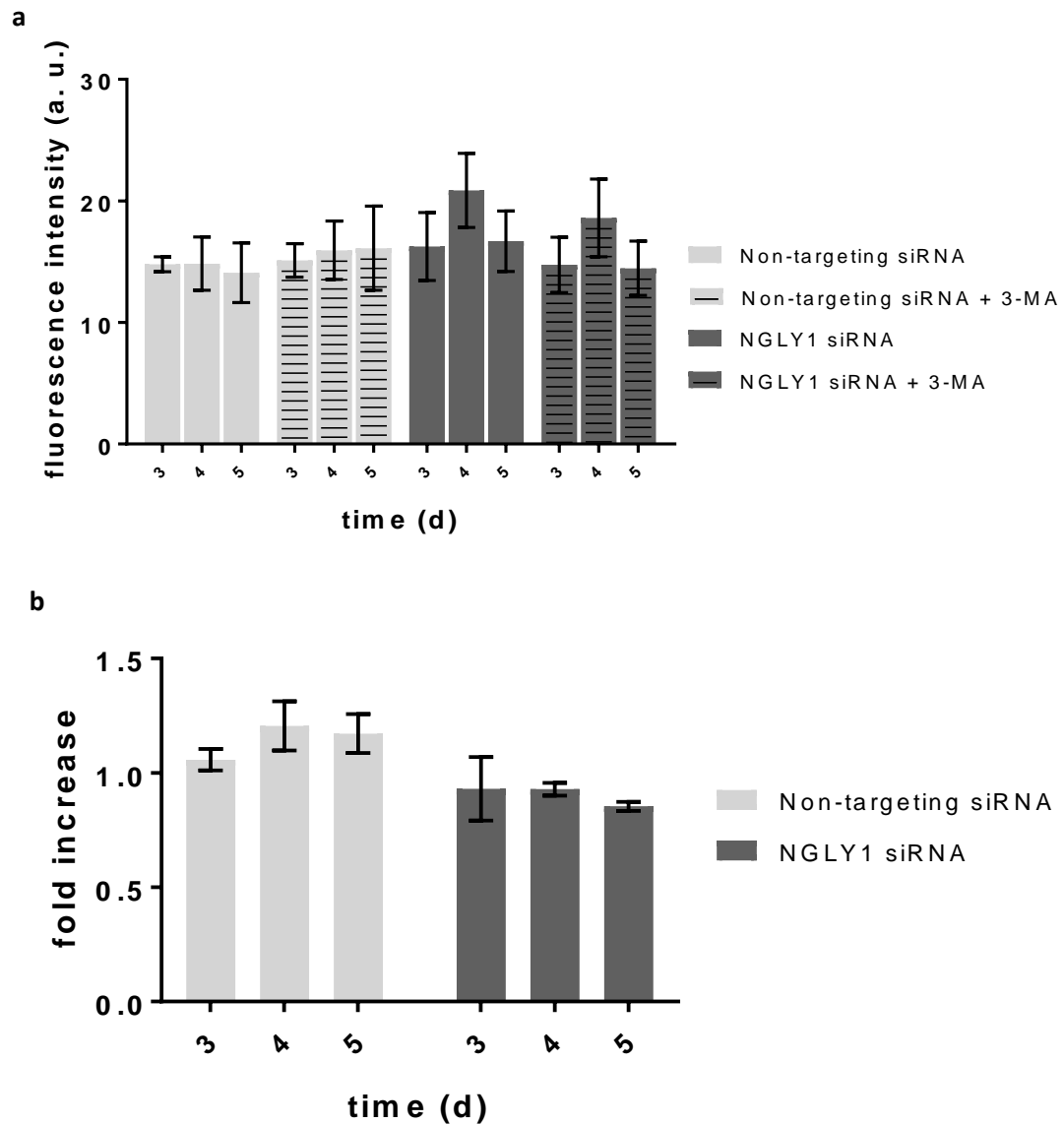


Figure 7.27 No increase in Mitotracker™ fluorescence intensity was found after 3-MA treatment in *N*-glycanase knockdown a) mean MitoTracker™ (50 nM) fluorescence intensity in HEK 293 cells transfected with NGLY1 siRNA or non-targeting control over 3-5 d with or without bafilomycin (50 nM) for 18 h. Fluorescence intensity measured by flow cytometry b) shows fold change in MitoTracker™ (50 nM) fluorescence intensity after Bafilomycin (50 nM) for 18 h. Two-way ANOVA. Error bars  $\pm$  SEM,  $n=3$ .

### 7.3.10 Pharmacological inhibition and genetic ablation of *N*-glycanase does not affect mitochondrial lectin profile

Mitochondria are regulated by developmental signals, at the tissue and organ level and intracellularly (Hüttemann et al. 2007). Many mitochondria proteins are regulated by PTMs including phosphorylation, acetylation, succinylation and *O*-GlcNAcylation. It has been shown that changes in the glycosylation of proteins can regulate their function and activity (Chen et al. 2010, Duan and Walther 2015, Edberg and Kimberly 1997, Fahie and Zachara 2016) and specifically deglycosylation in the case of Nrf1 activation (Tomlin et al. 2017). No study so far has looked at the effect of NGLY1 inhibition on the mitochondrial glycome. Many of these glycoproteins have been identified through high throughput proteomics screening without secondary verification (Burnham-Marusich and Berninsone 2012). With these, PDH E1 $\alpha$ , ATP synthase subunit d, OSCP subunit, NDUFS3 and ANT1 are expected to be *O*-GlcNAcyated as determined through prediction algorithms, with a potential *N*-glycosylation site identified on ATP synthase subunit d and ANT1, although this has not been confirmed (Burnham-Marusich and Berninsone 2012).

A number of hypotheses have suggested *N*-glycanase deficiency interferes with the regulation of glycoproteins. First, increased *N*-GlcNAc residues in the cell may disrupt *O*-GlcNAc signalling. In another instance mitochondrial proteins may be regulated in an *N*-glycanase deglycosylation dependent manner. Thirdly, a number of mitochondrial proteins are regulated by the UPS in which case degradation by this process may be halted or slowed for specific proteins. These differences could therefore cause changing levels in lectin staining profiles, for instance LCA and ConA for high mannose glycans or complex glycans with PHA-E.

To study if the mitochondrial proteins are regulated in this way, mitochondria were purified and lectin dot blots were performed to identify differences in mitochondrial glycosylation. Mitochondria were purified from HEK cells using the Thermofisher mitochondrial isolation kit for cultured cells (as per the manufacturer's protocol). Confirmation of increased mitochondrial proteins was assessed by western blot as shown in Figure **7.28a**. There was a

> 4 fold increase in TIM23, a mitochondrial import inner membrane protein in the mitochondrial fraction compared to the whole cell lysate (Figure 7.28b).

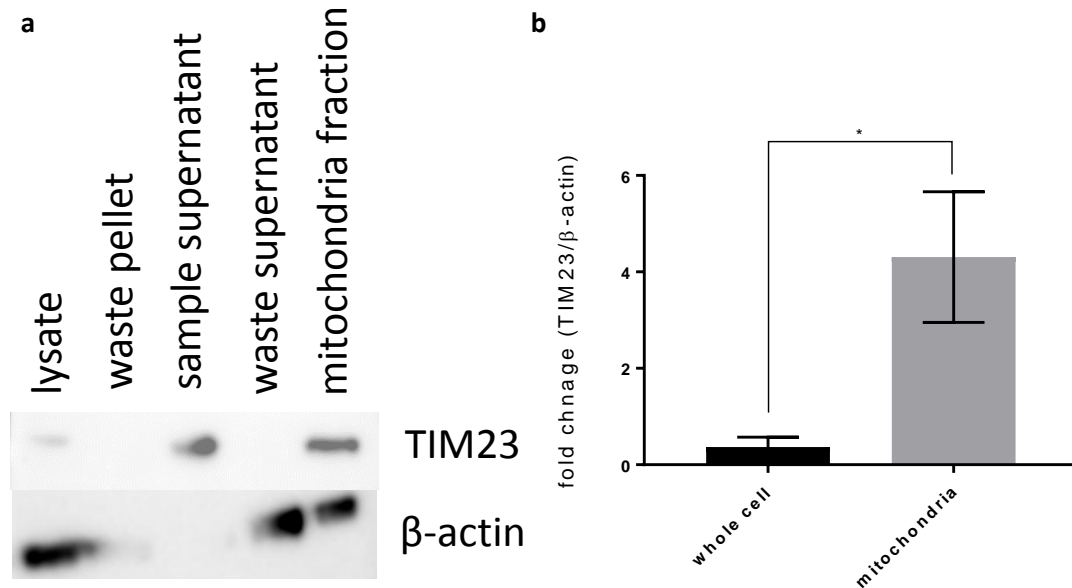


**Figure 7.28** Purification of mitochondria using the ThermoFisher Mitochondria isolation kit for cultured cells a) Mitochondria were purified, samples of the lysate, waste pellet, sample supernatant, waste supernatant and final mitochondrial sample were run on a 4.12% SDS-polyacrylamide gel. Immunoblotting was carried out against TIM23 (murine monoclonal antibody (SantaCruz, sc-514463) or  $\beta$ -actin murine monoclonal antibody (Santa Cruz, sc-58673), followed by incubation with the secondary antibody (Vector laboratories, HRP Horse anti-mouse IgG antibody peroxidase cat#PI-2000). Blots were visualised by Clarity ECL solution (BioRad) b) shows the quantitation of TIM23 abundance over  $\beta$ -actin abundance. Error bars  $\pm$  SEM, n=3, Student's T-test, \* P < 0.05.

HEK cells were treated with either Q-VD-Oph or Z-VAD-fmk (50  $\mu$ M, 72 h) or *N*-glycanase siRNA (25 nM, 5 d) and the mitochondria isolated. The purified mitochondria samples were lysed, 100 ng spotted onto nitrocellulose membrane and left to dry at room temperature for 1 h. Membranes were incubated with FITC-conjugated LCA, ConA, PHA-E, WGA and sWGA. Figure 7.29 shows the log fold change in lectin binding normalised to an untreated control.

ConA and LCA lectins typically bind to high mannose glycans associated with *N*-linked glycosylation. No significant changes in ConA or LCA staining were identified in any of the groups. PHA-E lectin also binds mannose, galactose and complex glycan structures. Again, there were no significant changes in lectin staining between samples. WGA staining is commonly used to probe for *O*-GlcNAc modified proteins. WGA binds GlcNAc, and has a preference for dimers and trimers but is also able to interact with glycans with terminal sialic acid residues. To confirm WGA staining to GlcNAc residues, succinylated WGA was also used, as this lectin does not bind sialic acid. No significant differences in WGA or sWGA staining was observed between conditions.

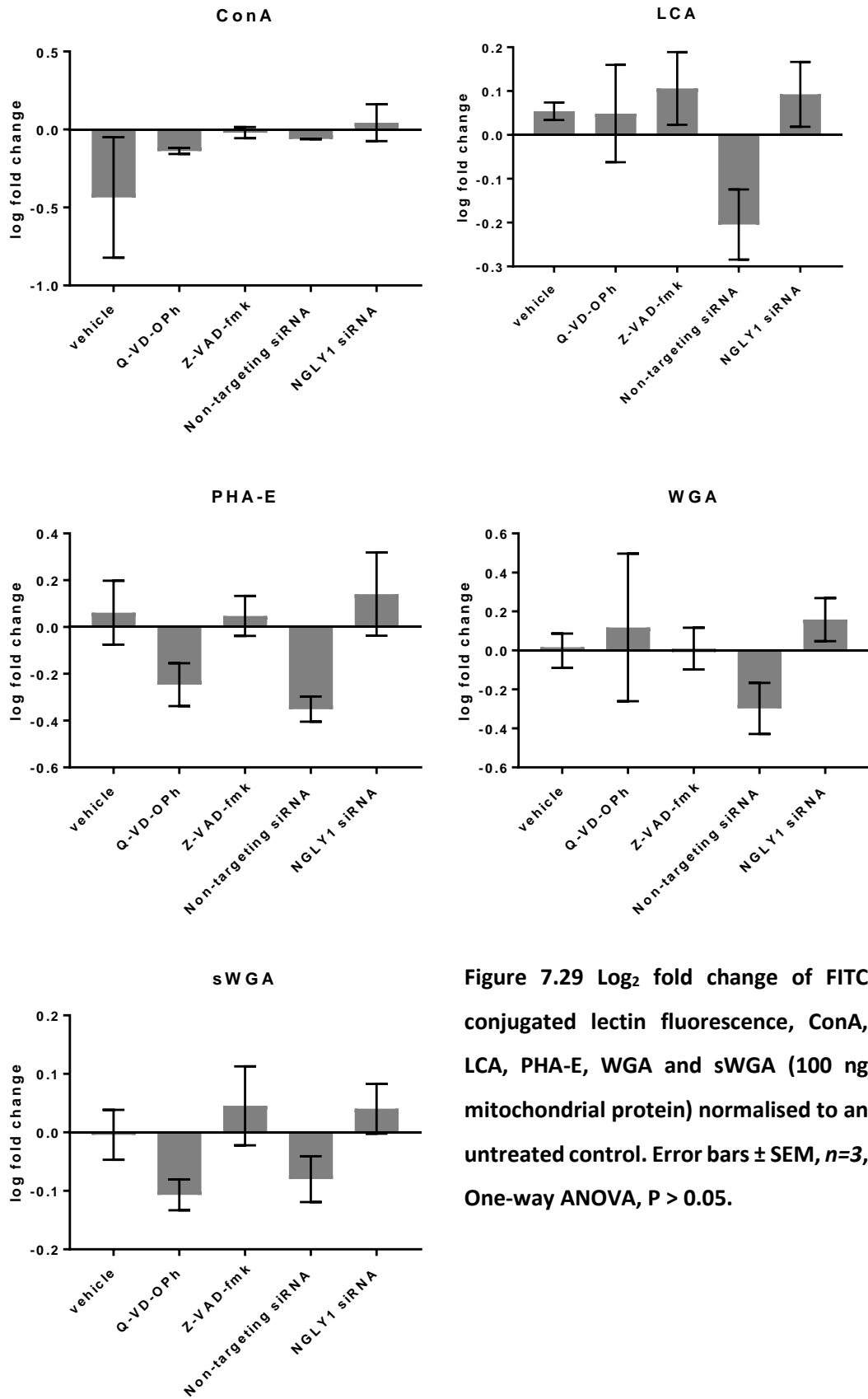


**Figure 7.29** Log<sub>2</sub> fold change of FITC conjugated lectin fluorescence, ConA, LCA, PHA-E, WGA and sWGA (100 ng mitochondrial protein) normalised to an untreated control. Error bars  $\pm$  SEM,  $n=3$ , One-way ANOVA,  $P > 0.05$ .

## 7.5 Discussion

*N*-glycanase deficiency often exhibits similar clinical presentations to mitochondrial respiratory chain (RC) disorders with symptoms including loss of muscle tone, seizures, developmental delays and heart and liver disease (Peng et al. 2015). Mitochondrial function has been identified as dysregulated in *N*-glycanase knockout cells and, in model organisms including mice and *C. elegans* (Kong et al. 2018). In this study mitochondrial function was examined by mitochondrial membrane potential and the analysis of mitophagy by the use of mitochondrial content dyes.

Mitochondria are linked to the redox environment of the cell and are a major source of reactive oxygen species and NAD is involved in the generation of energy and neutralisation of ROS and can be used as an indicator of the intracellular redox environment (Blacker and Duchen 2016) and therefore may cause an imbalance in ROS. Previously it was shown that under Z-VAD-fmk inhibition (Chapter 3) or *N*-glycanase knockdown HEK cells did not exhibit increased ROS levels. However, this experiment was undertaken in glucose containing media which may lessen any mitochondrial effects. In contrast, Kong *et al.* (2018) found increased ROS levels in *C. elegans*, MEFs and patient fibroblasts (c.1205\_1207del;c.1570C>T) compared to healthy controls when grown in standard cell culture conditions, with the MEF cells grown under 4.5 g/L glucose and the patient fibroblasts grown under 1 g/L glucose (Kong et al. 2018).

Cells grown in culture are highly adapted to aerobic glycolysis as the main source of energy. By switching cells to glucose free, galactose supplemented media forces cells to rely on oxidative phosphorylation for their energy needs. Cells grown in galactose and treated with the *N*-glycanase inhibitor, Z-VAD-fmk or in *N*-glycanase knockdown mediated by siRNA showed significantly decreased MTT reduction to formazan. Although usually a measure of cell toxicity or cell proliferation, there was no decrease in cell number or cell viability in conditions treated with Z-VAD-fmk or *N*-glycanase siRNA. Furthermore, there was no increase in annexin V staining compared to controls indicating cells were not in the early stages of apoptosis. The reduction of MTT is usually attributed to mitochondrial enzymes, therefore, less MTT reduction indicates mitochondrial dysfunction. However, there are a number of cytosolic reductases capable of MTT reduction. Therefore, changes in MTT reduction cannot be solely attributed to mitochondria function.

NADH is one of the main donors of electrons in the reduction of MTT and has a higher ratio of NADH in the cytosol, shown in Figure 7.30. Therefore, changes in NADH levels can lead to

increased MTT reduction. The ratio of NAD to NADH is an indicator of the intracellular redox environment.

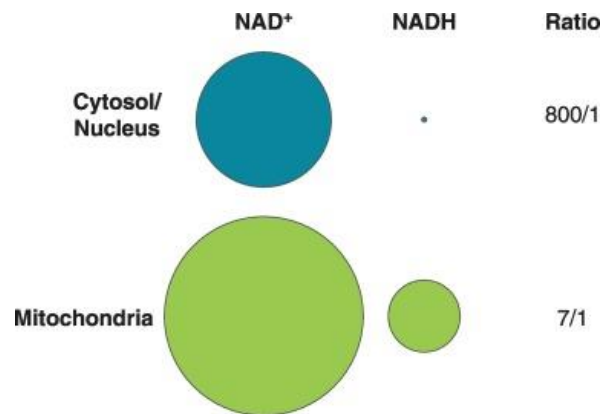


**Figure 7.30 Ratios of NAD and NADH in the cytosol and mitochondria. Open access article distributed under Creative Commons Attribution Licence (CC-BY) (Anderson et al. 2017).**

The ratio of NAD<sup>+</sup>/NADH is important in cellular function and homeostasis and regulates metabolic pathways. NADH and FADH are both substrates for electron transfer for MTT reduction and are needed to move protons into the mitochondrial inner membrane space and involved in the electron transport chain, producing the mitochondrial membrane potential and ATP for energy consumption (Srivastava 2016) (Figure 7.31).

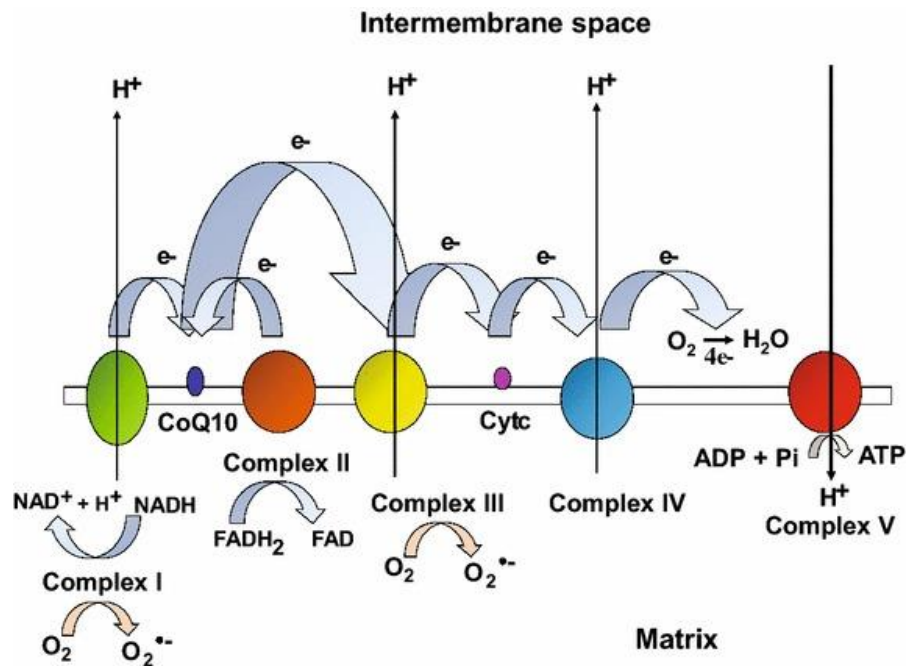


**Figure 7.31** Schematic representation of the mitochondrial electron transport chain. Open access article distributed under Creative Commons Attribution Licence (CC-BY). (Srivastava 2016)

Loss of MTT reduction may suggest an imbalance in NAD<sup>+</sup>/NADH homeostasis and possibly decreased levels of NADH. Decreased NAD<sup>+</sup>/NADH ratio has been associated with ageing and mitochondrial disorders (Srivastava 2016, Imai and Guarente 2016, Fang et al. 2017) and that supplementation of NAD<sup>+</sup> has alleviated symptoms of age related and mitochondrial diseases including AD in mice models (Fang et al. 2017) and in mitochondrial myopathies (Lightowlers and Chrzanowska-Lightowlers 2014).

Other than NAD<sup>+</sup>/NADH, NADP/NADPH can also influence MTT reduction and also play a role in antioxidant defences in the cell (Dey et al. 2016). NADPH can donate electrons to oxide radicals to neutralise its charge (Schieber and Chandel 2014). Therefore, changes in NADP/NADPH may interfere in the antioxidant pathway leading to increased superoxide found in *C. elegans*, MEFs and patient fibroblasts (Kong et al. 2018). In the autophagosome isolation a 3.9 fold increase in superoxide dismutase (SOD1) was identified under *N*-glycanase siRNA knockdown compared to basal cells and, an overall intensity of 2.6 fold and 1.55 fold increase oxidative stress associated proteins in *N*-glycanase siRNA and Z-VAD-fmk treated cells respectively, suggesting an increased need for antioxidants or increased mitochondria in autophagosomes. In this study, ROSBrite 570<sup>TM</sup> was used to determine increased levels of ROS. This probe preferentially picks up hydroxyl radicals, while Kong et al. 2018 used



MitoSOX™ which preferentially binds to superoxide. To identify if the generation of superoxide identified in (Kong et al. 2018) was associated in multiple cell models of *N*-glycanase deficiency it would be beneficial to look into HEK cells with a superoxide indicator. It is notable that superoxide is the ROS species most commonly associated with the initiation of autophagy (Chen et al. 2009, Slator et al. 2017, Parajuli and MacMillan-Crow 2012) which may help explain the increase in autophagy found in this study.

An autopsy of two NGLY1 patients (5 y and 9 m) were also noted to have hypoxic-ischemic encephalopathy (HIE), a common cause of mortality in neonates and is often found to be worsened under increased oxidative stress (Zhao et al. 2016). This symptom is not usually associated with mitochondrial disorders but has been associated with secondary mitochondrial dysfunction (Lu et al. 2015, Enns et al. 2014). Mitochondrial dysfunction was not further investigated in this case due to the absence of evidence of spongiform degeneration, which is most typically seen in mitochondrial disorders (Enns et al. 2014). This suggests, together with increased superoxide identified in patient fibroblasts, MEF cells and *C. elegans* (Kong et al. 2018) suggests that oxidative stress may play a role in NGLY1 pathogenesis. Changes in NAD<sup>+</sup>/NADH and NADP/NADPH may also be involved in the control of ROS (Srivastava 2016). It may be that *N*-glycanase deficiency is in some way linked to secondary mitochondrial dysfunction.

To further characterise mitochondrial function in HEK cells with reduced *N*-glycanase activity, mitochondrial membrane potential was measured. Initially this was studied using the mitochondria potential dependent indicator, TMRE and fluorescence intensity measured by TALI image based cytometer. No changes in starting TMRE of  $\Delta$  fluorescence was identified, whether grown in high glucose (aerobic glycolysis) or in galactose supplemented media to increase mitochondrial load. This method showed low sensitivity for TMRE fluorescence, with high fluorescence seen even in cells treated with an FCCP concentration designed to elicit maximum depolarisation and loss of fluorescence. To ensure the measurements of TMRE fluorescence were due to no change rather than a methodology with decreased sensitivity, TMRE fluorescence intensity was measured in HEK cells grown in galactose supplemented media and measured by flow cytometry. This method decreased the background fluorescence in FCCP treated cells. Again, no significant differences were seen in TMRE fluorescence intensity or  $\Delta$  intensity. In contrast to the findings in HEK cells in this study, there has been a decrease in mitochondrial membrane potential found in *N*-glycanase KO MEFs, patient fibroblasts and *N*-glycanase KO *C. elegans* compared to controls (Kong et

al. 2018). Decreased mitochondria membrane potential is associated with increased oxidative stress (Vayssier-Taussat et al. 2002). Although this seems to be cell dependent.

This study identified an increase in autophagy under both pharmacological inhibition and genetic knockdown of *N*-glycanase in HEK cells. Due to the changes in the redox environment found in HEK cells under galactose supplemented media. Autophagy is an essential process for the degradation and recycling of cellular components. Autophagy is regulated by nutrient availability and cellular stress pathways. Mitophagy, the selective degradation of mitochondria is important for maintaining a healthy pool of functioning mitochondria and therefore the redox environment of the cell, energy production, Ca<sup>2+</sup> homeostasis and control of apoptosis (Zhang 2015). In **Chapter 6** the proteins identified in the pull-down of autophagosomes in basal (Bafilomycin treated cells) and with Z-VAD-fmk inhibition of *N*-glycanase and siRNA mediated knockdown of *N*-glycanase found an average 1.44 and 1.51 fold increase in mitochondrial protein intensity. The theory that the increased autophagy was selective mitophagy was explored. Mitophagy was measured by looking at the fluorescence intensity of Mitotracker™ before and after autophagy inhibition which has been used to measure the mitophagy in mitochondrial membrane depolarisation and starvation in SH-SY5Y and HeLa cells (Xiao et al. 2016, Mauro-Lizcano et al. 2015). No significant changes were identified between Mitotracker™ staining before or after *N*-glycanase ablation or upon autophagy inhibition with 3-MA and HEK cells stained with Mitotracker™ deep red. It should be noted, however, that there was a high degree of variation within even the vehicle controls and therefore, it would be prudent to employ other methods of detecting mitophagy flux to fully investigate this process.

Mitophagy can be assessed by looking at specific mitochondrial protein abundance by western blotting, mtDNA abundance by PCR or microscopy techniques looking at co-localisation of mitochondrial proteins and autophagy markers like LC3. In other studies looking at Mitotracker™ staining in several models it was found there was no difference in Mitotracker™ intensity in *N*-glycanase KO MEF cells compared to WT control or in patient fibroblasts compared to healthy controls (Kong et al. 2018) which may indicate mitophagy is not active, although this does not take into account flux. However, there was a significant decrease in *C. elegans* with *N*-glycanase KO (Kong et al. 2018) although how this is related to degradation or mitochondrial biogenesis is not known.

Methods of measuring mitophagy can be difficult to interpret because of the dynamic nature and the heterogenous population within cells (Ogasawara et al. 2005, Chatre and

Ricchetti 2013). Mitochondria differ considerably between organ, tissue and cell type (Huang et al. 2004). Variations in levels of mtDNA have been observed in N-GLY1 patients (Enns et al. 2014). In one case, a 39 % decrease in liver mtDNA was observed while another patient exhibited a 472 % increase in quadricep muscle compared against age and tissue matched controls (Enns et al. 2014). How these differences relate to function are unclear. To date, there has been no study of mtDNA in cell culture models of *N*-glycanase deficiency. Kong et al. 2018 found increased levels of ROS in *C. elegans*, *N*-glycanase KO MEFs and patient fibroblasts (Kong et al. 2018). Mitochondrial DNA is reportedly ten times more susceptible to mutation and at increased risk from oxidative damage due to proximity of ROS production along with it not being protected by histone complexes (Guppy et al. 2002). Therefore, increased ROS may increase mitochondrial damage and promote selective mitochondrial removal.

Oxygen consumption rates (OCR) have also been studied in KO MEF cells and patient fibroblasts (Kong et al. 2018). In MEF cells there was no change in basal or leak but a reduction in maximal OCR in the KO cell, while patient fibroblasts showed a significant decrease in basal, leak and maximal OCR (Kong et al. 2018). The mitochondrial phenotypes exhibited in KO MEF cells, patient fibroblasts and *C. elegans* are often, although not always, associated with decreased ATP production (Salin et al. 2015). OCR and ATP production can be influenced by the type of reduction substrate used (succinate or pyruvate), proton slippage ('leak') and the membrane potential (Salin et al. 2015), and as such is not always a clear indication of energy metabolism. NAD<sup>+</sup>/NADH and NADP<sup>+</sup>/NADPH are also involved in a number of metabolic processes including glycolysis, TCA cycle and fatty acid oxidation (Wu et al. 2016). It would be beneficial to identify if these changes influenced the pathway of ATP production or the amount of ATP produced under *N*-glycanase deficiency. ATP deficiency is seen in a number of mitochondrial disorders characterised by decreased ATP synthase activity with 5-20 reduction in ATP in *ATP6* mutant in patient fibroblasts (Houšťek et al. 2006) with one of the key symptoms being muscle weakness (López-Gallardo et al. 2014) which is also seen in patients with NGLY1 (Enns et al. 2014, Caglayan et al. 2015).

Global quantification of Mitotracker<sup>TM</sup> fluorescence by flow cytometry does not give information about the morphology of the mitochondria, a common indicator of mitochondrial health and function (Xiao et al. 2016, Saunders et al. 2013, Mauro-Lizcano et al. 2015). Mitochondria are highly dynamic and morphology is altered depending on environment (Willems et al. 2015). Changes in mitochondrial morphology have been noted

in liver cells derived from a single patient with NGLY1 disorder (Enns et al. 2014), and it is therefore possible that consideration of changes in morphological features could potentially be investigated to provide insights into mitochondrial health. Morphological changes (such as mitochondrial swelling) can be studied using a variety of methods, including flow cytometry of isolated organelles. In such methods, isolated mitochondria are stained with fluorescent mitochondria probes (such as Mitotracker™ or TMRE) and examined using FSC and SSC to quantify features such as size and granularity of the mitochondria (Saunders et al. 2013). So, although in this study Mitotracker™ fluorescence was quantified, an in-depth analysis of morphology under these conditions would be advisable.

Results from this study suggest that in HEK cells where *N*-glycanase activity is reduced mitochondrial abundance does not change dramatically. This is in agreement with findings from studies in MEF cell and patient fibroblasts (Kong et al. 2018). In contrast, there was no significant change in membrane potential in HEK cells while *C. elegans*, MEF cells and patient fibroblasts showed decreased membrane potential (Kong et al. 2018). Additionally, changes in the redox environment in HEK cells under *N*-glycanase inhibition and knockdown were identified.

## 8.1 Introduction

Protein glycosylation is one of the most common post-translational modifications and endows proteins with additional structural and functional diversity beyond that which results from the protein structure alone. Disorders resulting from defects in the processing of cellular carbohydrates can have a broad and complex clinical presentation. As a result, they are often difficult to identify and diagnose with certainty.

The enzyme peptide:*N*-glycanase has been identified as a functional component of ERAD (Suzuki et al. 2000, Suzuki et al. 2001). Within the cell, this enzyme cleaves *N*-glycans from terminally misfolded proteins earmarked for degradation via the proteasome. Mutations in *N*-glycanase were found to be the cause of a genetic disorder, N-GLY1 deficiency, first identified in 2012. The importance of glycan processing is demonstrated by the severity and of symptoms of NGLY1 disorder (Enns et al. 2014, Caglayan et al. 2015, He et al. 2015, Fujihira et al. 2017, Suzuki 2015). Since the identification of N-GLY1 disorder in 2012 (Need et al. 2012) in the order of fifty people worldwide have been identified with this disorder. The aim of this study was to identify the effects of *N*-glycanase deficiency using pharmacological inhibition and genetic knockdown, in a well-characterised cellular model to examine the cellular effects of *N*-glycanase deficiency.

## 8.2 Findings

Previous studies using the ddVENUS assay (Grotzke et al. 2013) have confirmed that patients with mutations in the *NGLY1* gene exhibited decreased deglycosylation activity and reduced protein expression (He et al. 2015). In yeast Png1 KO, degradation of mutant carboxypeptidase Y protein (CPY) (an ERAD substrate) was delayed (Suzuki et al. 2000). In mammalian cells, contradictory evidence has been shown in different models using different ERAD substrates. In U373 astrocytoma cells with siRNA mediated knockdown of *N*-glycanase exhibited no change in degradation for TCR $\alpha$  or MHC I heavy chains (Hirsch et al. 2003, Blom et al. 2004). However, the rate of degradation of RTA $\Delta$ m was nearly doubled in NGLY1 KO MEFs (Huang et al. 2015) indicating a defect in protein degradation. Furthermore, increased RIPA insoluble *N*-GlcNAc linked proteins indicated the involvement of ENGase. In addition, it was hypothesised that *N*-glycanase deficiency caused ER stress, likely a result of a build-up of aggregated material (Misaghi et al. 2005, Martinet et al. 2006).

8.2.1 *N*-glycanase knockdown and inhibition does not cause protein aggregates or cellular stress in HEK cells.

To begin, basic cellular effects of pharmacological and genetic knockdown of *N*-glycanase were characterised in HEK cells (including viability and variation in glycan profile). *N*-glycanase activity was also quantified using the ddVENUS assay (Grotzke et al. 2013).

As the pan-caspase inhibitor Z-VAD-fmk has previously been identified to act as an inhibitor of *N*-glycanase, it was employed as a pharmacological inhibitor in this study. As a comparison, effects were compared to a pan-caspase inhibitor with a similar inhibition profile, called Q-VD-OPh (Chauvier et al. 2006) which lacks inhibitory activity against this target. Effects observed were also compared to *N*-glycanase KD using siRNA. HEK cells treated with either Z-VAD-fmk or *N*-glycanase siRNA found no decrease in cell viability or change in the glycoprotein profile. Both methods of inhibition resulted in a decrease in fluorescence of the deglycosylation dependent VENUS construct, suggestive of decreased *N*-glycanase activity. Q-VD-OPh exhibited no comparable effect on cell viability, glycoprotein profile or ddVENUS fluorescence.

Since *N*-glycanase is a component of ER-associated degradation, it follows that deficiency in this enzyme may influence the efficiency of the ERAD process. Previous studies have suggested that this may result in a change in the ability of the cell to effectively degrade misfolded proteins, leading to an accumulation of protein aggregates. Previous models using different model ERAD substrates have found contradictory evidence of the rate of protein degradation following *N*-glycanase KO. It should be noted that using model proteins can increase ER load and aggregation that is not related to the disorder studied. This can be due to constructs resulting in high levels of protein production based on strong promoters (Hussain et al. 2014).

In previous studies, using RTA $\Delta$ m as an ERAD substrate, detergent insoluble aggregates were identified bearing ENGase modified glycan chains resulting in a single *N*-GlcNAc in NGLY1 KO MEF cells (Huang et al. 2015). In this study, to examine protein aggregation a general stain (ThT) was used rather than a model protein to look only at endogenous proteins. ThT has been reported to stain cross- $\beta$ -sheets, a motif arising due to the hydrophobic nature of  $\beta$ -sheets and the readiness to interact with one another, hence often associated with protein aggregates. HEK cells treated with Z-VAD-fmk and siRNA mediated *N*-glycanase knockdown showed increases in ThT fluorescence, but no visible protein aggregates were observed. It is unknown whether these stimuli would have caused distinct cellular aggregates and, it should

be noted the protein concentration in detergent soluble/insoluble fractions was not studied in HEK cells under these conditions. The absence of distinct protein aggregates was later supported by a mouse KO study using histological staining by Congo red and PAS (Fujihira et al. 2017).

Autopsy results from of a patient with N-GLY1 disorder (homozygous R401X) presented ubiquitin positive nuclear and cytoplasmic aggregates in several areas of the brain; including the globus pallidus (fine motor control (Telford and Vattoth 2014)), red nucleus (gross motor function (Telford and Vattoth 2014)), sub-thalamic nucleus (pacemaker for basal ganglia (Telford and Vattoth 2014)), dentate nucleus in the cerebellum, cortex and spinal cord (Enns et al. 2014). Conversely, glial cells only showed diffuse nuclear ubiquitin staining (Enns et al. 2014). This is suggestive that cell type plays an important role in phenotype and, that non-proliferative cells will display a more severe phenotype. Glial cells are capable of mitosis, allowing diffusion of aggregates by division. Although the mitotic nature of neurons is still changing, it is typically thought that most are post-mitotic, meaning aggregates cannot be dispersed. This effect is common to other protein aggregation disorders, where increased cell death is observed in post-mitotic neurons compared to other cells types (Gundersen 2010, Joshi et al. 2014, Perry et al. 1987). There are a number of post-mitotic containing tissues in the body including neurons but also some cardiac cells (Siddiqi and Sussman 2014), skeletal muscle (Partridge 2002) and cells of the immune system including monocytes (Sugimoto et al. 2006). As well as the effect of *N*-glycanase deficiency in neurons, the study of other post-mitotic cells would also be interesting. A prion model of fatal spongiform encephalopathies found non-proliferative myotube cells accumulated more aggregates compared to proliferative myoblasts (Herbst et al. 2013). The lack of aggregation found in HEK cells may be due to their fast proliferation rate. To study this process in culture, non-dividing, neuronal cell lines could be used (such as ReNcell VM) which can be differentiated to form non-dividing neurons and glial cells (Donato et al. 2007).

#### 8.2.2 *N*-glycanase knockdown and inhibition increases autophagy

Previous studies using Z-VAD-fmk as a caspase inhibitor have found increased autophagic cell death or necrosis (Chen et al. 2011, Wu et al. 2008). The effect of *N*-glycanase deficiency on the other main degradation pathway, autophagy, was examined. This study identified an increase in autophagy under Z-VAD-fmk and *N*-glycanase knockdown which has not been identified in other models of *N*-glycanase deficiency. Autophagy can be attributed to the removal of protein aggregates and this was an attractive conclusion due to the correlation

between decreased ThT fluorescence and increase in autophagosomes under Z-VAD-fmk treatment at 72 h, although this pattern was not as correlational when *N*-glycanase was downregulated by siRNA. Autophagy occurs constitutively at basal levels, maintaining healthy level of organelles and proteins. Cellular stresses such as starvation, oxidative stress and activation of ER stress signalling induce autophagy to mediate stress and maintain homeostasis. ER and oxidative stress was examined. No increase in UPR markers was found, indicating no ER stress/protein aggregates in HEK cells. This supports the microscopy findings that no distinct protein aggregates were found in HEK cells treated with Z-VAD-fmk or *N*-glycanase siRNA. Measure of UPR markers have not been directly tested in other models of *N*-glycanase deficiency and is further supported by studies of a *Drosophila* *N*-glycanase KO model that found no increase in canonical ER stress markers in the transcriptome (Owings et al. 2018). Other adaptations allow cells to increase ERAD efficiency without activation of the UPR and costly and time-consuming upregulation of proteins. Misfolded proteins in the ER may delay turnover of ERAD proteins. Misfolded polypeptides in the ER can inhibit the removal of SEL1L and HRD1 complexes which auto-ubiquitinate. If more misfolded proteins are available as the preferred substrate, the E3 ligases are stabilised in the membrane (de Bie and Ciechanover 2011). This has not been explored under *N*-glycanase deficiency. ER Ca<sup>2+</sup> handling was also used as a measure of ER stress (Hammadi et al. 2013, Lomax et al. 2002). No change in ER Ca<sup>2+</sup> handling under Z-VAD-fmk or *N*-glycanase siRNA was found. No change in oxidative stress was measured by fluorescence intensity of reactive oxygen species indicators. This rules out a global effect of ER stress as the cause for increased autophagy. It also suggests that there is no severe level of mitochondrial dysfunction as the main cause of autophagy activation. The activation of autophagy is likely, at least in part, to be due to other factors.

To examine the role of autophagy further, ATG13 KO MEF cells were used, which found that Z-VAD-fmk and *N*-glycanase KD decreased MTT reduction. Initially this was thought to show decreased cell viability. Upon confirmation of viability with PI exclusion and cell number it was identified that no change in viability or cell number was identified. Changes in MTT reduction not due to cell proliferation or viability are typically attributed to mitochondrial function (Surin et al. 2017, Bernas and Dobrucki 2002). However, there are a number of cytosolic enzymes capable of this reaction and in some cases there is increased MTT reduction in the cytosol which is not affected by the respiratory inhibitor rotenone (Berridge et al. 2005). Therefore MTT reduction may come from glycolysis, supported by evidence of interference of MTT reduction by glycolysis inhibitors, 2-deoxyglucose and lonidamine (van



Tonder et al. 2015). However, mitochondrial involvement is further supported by exacerbation of this effect when cells are grown in glucose-free media supplemented with galactose used to increase energy production via mitochondria (Marroquin et al. 2007, Rodriguez-Enriquez et al. 2001).

Since ER stress and oxidative stress were not increased in HEK cells treated with Z-VAD-fmk or *N*-glycanase KD there must be another signal increasing autophagy. To identify the signal initiating autophagy in the system, the protein content of the autophagosomes was analysed by tandem LC-MS/MS. Autophagosomes were purified from *N*-glycanase KD and Z-VAD-fmk induced cells using GFP-LC3 immunoprecipitation. *N*-glycanase KD and Z-VAD-fmk showed increased numbers and intensities of mitochondrial proteins possibly indicative of increased mitochondrial uptake by autophagosomes. There was also an increase in vesicle trafficking proteins such as FYCO1 and MAP1A indicative of increased autophagosome trafficking.

Several of the proteins identified in a co-IP of host factors involved in HIV infection which included *N*-glycanase (Jäger et al. 2011) were also identified in autophagosome proteome under *N*-glycanase inhibition/KD study. These proteins were mainly related to the ER and proteasome, including ERAD ubiquitin ligases, ER chaperones and components of the 26S proteasome as expected during a viral hijacking of the protein production machinery of the cell (Inoue and Tsai 2013). However, the lysosomal protease cathepsin D and mitophagy receptor PHB2 which could indicate that *N*-glycanase may also be involved in the regulation of autophagy. There have been multiple studies displaying the crosstalk of the two degradation pathways, UPS and autophagy (Senft and Ronai 2015, Rashid et al. 2015, Song et al. 2018).

Previously a number of cell types have identified increased autophagic vesicles after treatment with Z-VAD-fmk (Martinet et al. 2006, Chen et al. 2011, Cheng et al. 2008) leading to a hypothesis that autophagy induction was due to inhibition of *N*-glycanase in these experiments. This may open further avenues as to why Z-VAD-fmk increased autophagic vesicles in different cell types and, depending on the cell type, whether it was pro- or anti-apoptotic (Chen et al. 2011, Wu et al. 2008).

### 8.2.3. Nrf1 is regulated by deglycosylation

Interestingly, in the autophagosomes isolation, a number of proteins identified as part of the proteasome complex were identified as significantly decreased in *N*-glycanase KD compared to the basal autophagy control. Recently, a study described the *N*-glycanase dependent activation of Nrf1 (Tomlin et al. 2017), a transcription factor regulating expression of proteasome genes. Under basal conditions Nrf1 is held in the ER, under proteasome inhibition, Nrf1 is flipped to face the cytosol which undergoes *N*-glycanase dependent deglycosylation and proteolytic cleavage to produce active Nrf1 which translocates to the nucleus to activate transcription of PSM genes (Tomlin et al. 2017). MEF cells deficient in *N*-glycanase halt proteolytic cleavage and translocation of Nrf1 to the nucleus, leading to cells sensitive to proteasome inhibition (Tomlin et al. 2017). Nrf1 inactivation could explain the decreased levels of proteins identified as part of the proteasome complex in both *N*-glycanase and Z-VAD-fmk compared to basal autophagy and amino acid starvation induced autophagy.

### 8.2.4 Mitochondrial involvement in N-GLY1 disorder

To investigate the role of mitochondria in *N*-glycanase deficiency, mitochondrial function was studied. Mitochondrial membrane potential was found to be unchanged while measurements of mitophagy require optimisation to draw any conclusions on this. However, a change in MTT reduction under cells grown in galactose supplemented media was found, which could indicate mitochondrial dysfunction. Mitochondrial dysfunction was considered as a potential cause of NGLY1 symptoms, however, the initial study of patients with N-GLY1 determined the most prominent symptoms associated with mitochondrial disorders were absent (Enns et al. 2014). Brain disease was noted during an autopsy of two related patients of N-GLY1, patients 5 and 6 with homozygous R401X mutation (Enns et al. 2014). Changes in brain structure were consistent with hypoxic-ischemic encephalopathy (HIE). This can be associated with secondary mitochondrial dysfunction but is not usual for inherited mitochondrial disorders (Lu et al. 2015, Enns et al. 2014).

Mitochondrial disease refers to a wide range of disorders that result in defective energy production via oxidative phosphorylation. Primary mitochondrial diseases usually result from mutations in mtDNA or nDNA that are required for oxidative phosphorylation (Niyazov et al. 2016). Disorders which have a similar phenotype to primary mitochondrial diseases but are not caused by a mutation in OXPHOS related proteins are classed as a secondary mitochondrial disease (SMD). SMD can be caused by germline mutations in other genes not

known to have a clinical implication in OXPHOS, can be caused by environment or by a pre-existing disorder (Niyazov, 2016). A study looking at the effect of *N*-glycanase deficiency in multiple models including *C. elegans*, MEF cultures and patient fibroblasts identified mitochondrial dysfunction (Kong et al. 2018). Mitochondrial function in *C. elegans*, MEFs and patient fibroblasts found no change in mitochondrial content measured by Mitotracker, but there was a significant decrease in mitochondrial membrane potential in all models (Kong et al. 2018). Furthermore, a significant decrease in basal, leak and maximal oxygen consumption rate was measured in patient fibroblasts (Kong et al. 2018). Indicating dysfunction in mitochondria. Basal OCR is typically controlled by ATP turnover but is not affected by maximal OCR or proton leak (Brand and Nicholls 2011), although the effect on ATP has not been studied in *N*-glycanase KO cells. A large increase in proton leak can indicate complete uncoupling, although a small change is likely due to a change in membrane potential, which was also confirmed to be decreased (Kong et al. 2018).

In HEK cells, no difference was found in TMRE fluorescence or Mitotracker stained content under Z-VAD-fmk or *N*-glycanase KD. It should be noted that short term inhibition/knockdown may not allow sufficient time for effects to be seen as these treatments only reduce the activity of *N*-glycanase and low levels of activity still remain. Furthermore, during inhibition the protein is still available in the cell perhaps maintaining non-deglycosylating roles of *N*-glycanase. In the stable KO models the protein is not translated.

#### 8.2.5 *N*-glycanase and Z-VAD-fmk alters the redox environment of cells grown in galactose

Increased mitochondrial proteins associated with autophagosomes can indicate increased mitochondrial degradation. This is usually triggered by some form of cellular stress or mitochondrial dysfunction. Mitochondrial function was examined by mitochondrial membrane potential and total content. No significant changes were identified in *N*-glycanase KD or Z-VAD-fmk compared to controls. However, a change in MTT reduction was identified in cells grown under glucose-free, galactose supplemented media. A change in MTT reduction indicates a change in the oxidation-reduction environment of the cell. As well as proteasome regulation, NRF1 is also involved in the antioxidant response pathway. The redox environment of the cell is vital during development. Changes in oxidation-reduction can change the fate of developing cells. Metabolism and ROS signalling are tightly controlled by redox pathways. Nrf1 and Nrf2 regulate the expression of enzymes involved in oxidative

stress such as glutathione, heme-oxygenase, glutathione peroxidase and superoxide dismutase (Biswas and Chan 2010, Sant et al. 2017, Reichard et al. 2007) all of which were identified in autophagosomes isolated from basal, Z-VAD-fmk and siRNA knockdown of *N*-glycanase induced autophagy. *N*-glycanase KO models of *C. elegans*, patient fibroblasts and KO MEF cells found increased ROS compared to controls (Kong et al. 2018). No increase in ROS was detected in HEK cells treated with Z-VAD-fmk or *N*-glycanase siRNA.

ROS are an important signalling pathway and are necessary for various growth factor signalling pathways (Schieber and Chandel 2014). However, dysregulation and an increase in ROS results in oxidative stress (Kong et al. 2018), the main source of which comes from the respiratory chain located on the inner mitochondrial membrane. This process oxidises hydrogen from pyruvate and fatty acids with oxygen to form water. Under normal conditions, 1-5% of oxygen is converted into ROS (Guo et al. 2013). Therefore, the main point of attack for ROS species is at the respiratory chain. Close proximity damages mtDNA leading to increased superoxide formation and further damage to the mitochondria and the cell. ROS damages proteins by adding oxygen to cysteine residues, changing the structure of the proteins. This can be reversed by reduction by thioredoxin and pererodoxin, both of which were identified in autophagosomes as part of the negative regulation of apoptosis under Z-VAD-fmk and *N*-glycanase KD. Inactivation of Nrf1 may increase cells' susceptibility to ROS. However, increased susceptibility was not explored in this study. Following proteasome inhibition, mitochondrial content usually increases in cells (Bragoszewski et al. 2017), similar to proteasome proteins. It would be interesting to see whether known mitochondrial targets of Nrf1 are still able to increase expression following this stress to identify the extent to which Nrf1 regulates mitochondrial proteins in this system.

As previously noted, Nrf1 regulates a high number of different processes including proteasome subunits, mitochondrial genes and the antioxidant response; 11289 targets have been identified by CHIP-seq datasets (Rouillard et al. 2016). NRF1 KO mice result in embryonic lethality indicating its importance in development, however, NGLY1 KO mice models and other models, *Drosophila* and *C. elegans* are not always lethal (Fujihira et al. 2017, Huang et al. 2015, Owings et al. 2018, Kong et al. 2018). This indicates that the symptoms caused by NGLY1 deficiency are not entirely due to Nrf1 inactivation. There may be other roles of Nrf1 that are not dependent on *N*-glycanase deglycosylation. However, Nrf1 conditional KO in mice brains exhibit age-dependent neurodegeneration similar to neurodegenerative models (Lieu et al. 2013) and NGLY1 KO mice models (Fujihira et al. 2017). Nrf1 KO also exhibited ubiquitin positive aggregates in the cortex and hippocampus and had

decreased proteasome function, mirroring aggregates found in NGLY1 patients (Enns et al. 2014). Nrf1 KO in HeLa cells also exhibited increased p62 and ubiquitin labelled aggregates and increased autophagosomes (Tsuchiya et al. 2013). All these symptoms point towards protein aggregate disorders, however, the contradiction in evidence may be due to experimental design and indicate that under basal conditions cells appear normal but exhibit increased sensitivity to stressors. However, in Nrf1 brain KO, no significant difference in GSH/GSSG ratios compared to controls indicating redox environment was normal. However, in NRF2 KO GSH/GSSG ratio was significantly changed (Lee et al. 2011) indicating Nrf1 is important to proteasome function but less so to redox state, indicating other factors are involved.

There is also the potential for crosstalk between Nrf1 function and autophagy. Several autophagy regulating pathways also regulate Nrf1. As regulators of the protein degradation pathway it follows under conditions that increase one protein degradation pathway also control the other. Nrf1 has been shown to increase proteasome expression via mTORC1, an inhibitor of autophagy, while increased AMPK activity activates Nrf1 activity and increases mitochondrial content (Bergeron et al. 2001) and increases autophagy via phosphorylation of BECN1 (Zhang et al. 2016). It is unknown how Nrf1 inactivation affects these systems.

Nrf2 is thought to be able to partially compensate for Nrf1 inactivation/KO (Ohtsuji et al. 2008, Sant et al. 2017, Leung et al. 2003, Xu et al. 2005, Chen et al. 2003, McMahon et al. 2001) especially as part of the antioxidant defence, more so than proteasome 'bounce-back'. Nrf2 is constitutively degraded by the UPS. KEAP1 is an adaptor for the ubiquitin ligase which targets Nrf2. During oxidative stress KEAP1 is inactivated, stabilising Nrf2 which moves to the nucleus to activate cyto-protective genes. P62 also interacts with the Nrf2 binding site of KEAP1, interfering with the KEAP1-Nrf2 interaction. p62 is also one of the genes translated during Nrf2 stabilisation. During increased p62, KEAP1 cannot ubiquitinate Nrf2 and the protein is stabilised. P62 binding affinity for KEAP1 is weak compared to Nrf2, however, when S351 is phosphorylated binding affinity is increased by 30 fold compared to non-phosphorylated p62 but still lower than Nrf2. Phosphorylated p62 is detectable under basal conditions but is significantly upregulated during oxidative stress as well as overall levels of p62 with KEAP1 being incorporated into the detergent insoluble fraction in the cell with levels dropping indicating KEAP1 is degraded by autophagy. This was confirmed when KEAP1 and p62 accumulate in ATG7 KO mice but not in a PSMC2 knockout, part of the 26S proteasome.

### 8.2.6 Regulation of proteins by deglycosylation

Nrf1 is not the first case of protein function noted as regulated by *N*-glycanase dependent deglycosylation. EDEM1 is regulated by deglycosylation as it is required for efficient removal, although not via the UPS. Deglycosylated EDEM1 forms triton insoluble aggregates that are ubiquitinated and degraded by autophagy via association with p62 and NBR1. Glycosylated EDEM1 is not ubiquitinated (Park et al. 2014). Z-VAD-fmk in HepG2 cells for 3 h (50  $\mu$ M) found a significant increase in glycosylated EDEM1 (Park et al. 2014). This may increase the amount of active EDEM1 in cells. Previously, this study found no increase in EDEM1 mRNA under Z-VAD-fmk or siRNA knockdown of *N*-glycanase, however, this does not measure stabilised protein concentrations (Park et al. 2014). Overexpression studies of EDEM1 have found that increased levels of EDEM1 allows cells to degrade proteins targeted to ERAD with or without the glycan and with increased speed of degradation (Shenkman et al. 2013, Molinari et al. 2003) which may also add to effect of non-delayed glycoprotein turnover identified in *N*-glycanase KO models. In *Drosophila*, upregulation of EDEMs, regardless of mannosidase activity resulted in protection against ER proteinopathies and extended lifespan with minimal toxicity (Sekiya et al. 2017). It has been shown that proteins can be regulated by deglycosylation, but how many are dependent on *N*-glycanase remains unknown.

### 8.2.7 Hexosamine Biosynthetic Pathway and *O*-GlcNAcylation

The transcriptome of an Ngly1 *Drosophila* KO was studied and found downregulation in oxidative-reduction process and UPS components which corresponds to Cnc (Nrf1 homolog) disruption (Owings et al. 2018). However, other hypotheses of the effects of *N*-glycanase deficiency have highlighted the possibility of a disruption of *O*-GlcNAc signalling due to stabilised *N*-GlcNAc containing proteins (Huang et al. 2015). An interesting protein that was found to be significantly downregulated by 1.7 fold was Gfat1 (homolog of human GFPT1). GFPT1 supplies the cell with UDP-GlcNAc, the rate limiting step in the hexosamine biosynthetic pathway (HBP) shown in Figure 8.1. UDP-GlcNAc is used as a substrate for glycan synthesis and *O*-GlcNAcylation as well as a coenzyme in a number of metabolic reactions (Ryczko et al. 2016). There was no change in other HBP pathway proteins including Gfat2 which plays a similar role and suggests compensation for Gfat1 does not occur.

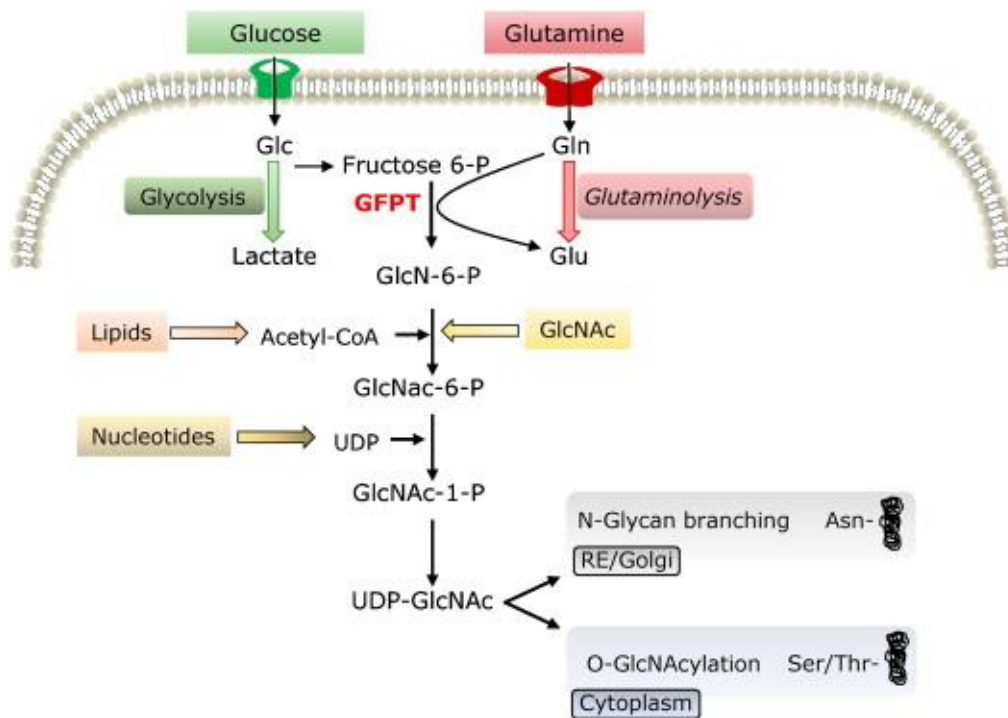


**Figure 8.1 Schematic representation of the hexosamine biosynthetic pathway (HBP). Reprinted from (Vasseur and Manié 2015) with permission from Elsevier.**

Unusually, *Ngly1* KO *Drosophila* showed increased levels of UDP-GlcNAc, the opposite of what would be expected with *Gfat1* reduction. Increased HBP flux has been shown to increase *O*-GlcNAc levels, oxidative stress and ER stress (Lombardi et al. 2012). Additional GlcNAc has been hypothesised to reprogram cellular metabolism via UDP-GlcNAc dependent glycosylation signalling (Ryczko et al. 2016) despite increasing GlcNAc in mice has shown to increase liver UDP-GlcNAc levels (Ryczko et al. 2016). GlcNAc supplementation in this *Drosophila* model decreased UDP-GlcNAc levels to normal and increased longevity at all stages of supplementation, but did not change transcriptome changes. Although there was an increase in UDP-GlcNAc levels, there were no global changes in *O*-GlcNAcylation in healthy or KO flies, with or without GlcNAc supplementation (Owings et al. 2018). Which also confirms the lack of changes in lectin binding in this and other studies (Huang et al. 2015). The human homolog of *Gfat1*, *GFPT1* is a target for *Nrf1* (Rouillard et al. 2016) indicating downregulation could be due to inactivity of *Nrf1*. Regulation via *Nrf1* rather than a negative feedback loop from UDP-GlcNAc would explain why GlcNAc supplementation does not change the transcriptome profile while it does normalise UDP-GlcNAc levels. However, this

does not explain the increase in UDP-GlcNAc. UDP-GlcNAc levels also regulate the *O*-GlcNAcylation homeostasis enzymes, OGA and, specifically OGT (Hanover et al. 2010). The OGT catalytic p110 subunit forms homotrimers which exhibit different binding affinities for UDP-GlcNAc. This is mediated by a tetratricopeptide repeat region motif (TPR) that is involved in the protein-protein interactions in multiprotein complexes. Using a peptide with a known *O*-GlcNAc site allowed kinetic measurements of OGT in response to different UDP-GlcNAc concentrations (Kreppel and Hart 1999). It was found that depending on the concentration of UDP-GlcNAc, OGT different multimerization states changes the affinity of OGT for UDP-GlcNAc (Kreppel and Hart 1999). Although no difference was identified in OGT mRNA expression levels, UDP-GlcNAc could have an effect on OGT affinity levels for its substrate. As well as controlling multimerization, the TPR domain has been shown to confer peptide specificity and that different multimeric states also change *O*-GlcNAcylation kinetics towards peptide substrates. (Iyer and Hart 2003). This could lead to substrate specific *O*-GlcNAc targeting rather than global changes that have not been evidenced in the literature.

OGA not only recognises the GlcNAc residue but also recognises the glycosylated hydroxyl residue from the serine or threonine to stabilise the protein. *N*-linked glycosylation presents an amide group at the site of glycosylation (Li et al. 2017). There is also evidence of OGA removing GlcNAc from different proteins at different rates, indicating a substrate specific difference (Li et al. 2017), and whether OGA would be able to recognise *N*-GlcNAc is unknown. However, the changes due to *N*-GlcNAc are more likely to be a biophysical effect. *O*-GlcNAc modifications can regulate proteins by blocking other PTMs, changing binding affinity or biophysical nature of the attached protein. The proteins containing *N*-GlcNAc have not been recognised to regulate protein function in the same way as *O*-GlcNAc. Despite this, however single *N*-GlcNAc residues may change the structure and physicochemical properties of the protein, making them more prone to aggregation.

### 8.3 Conclusion

This thesis describes experiments using short-term inhibition/KD in highly proliferative cells to identify the effects of *N*-glycanase inhibition in a previously unstudied cell culture model. Efforts were made to compare short-term inhibition with stable KO generated by CRISPR in the same model, although this was unsuccessful. The data provided along with new literature that due to the diverse substrates of *N*-glycanase disruption interferes with a number of different pathways including protein degradation pathways, glycosylation PTM regulated proteins, mitochondrial function and the hexosamine biosynthetic pathway, although the



complex interactions of these pathways are not fully understood. It is also clear many of these responses are dependent on cell type, and *N*-glycanase deficiency will effect different cells in different ways, such as the effect on post-mitotic cells that are more susceptible to cellular stress (Herbst et al. 2013). Mouse models of *N*-glycanase KO have shown how symptoms increase with age and show similar phenotypes to age-dependent neurodegeneration (Fujihira et al. 2017). Autophagy decreases with age in most cells, and autophagy has been targeted to alleviate neurodegenerative effects (Cuervo 2008). This study has identified autophagy as protective measure and without autophagy, although not toxic, *N*-glycanase inhibition/KD results in changes in the redox environment.

Together, this data indicates that there is no significant increase in ER stress or ROS in healthy dividing cells but dysfunction is most likely related to how cells respond to stress. It has been suggested that such effects may be related to the dysfunctional activation of Nrf1 (Tomlin et al. 2017). Under the system studied in these experiments, *N*-glycanase was reduced for only a short period of time using pharmacological or siRNA reduction while the majority of published studies described used stable KO of the enzyme, while only using Z-VAD-fmk to confirm decreased ddVENUS fluorescence, allowing the cell to adapt to the KO.

#### 8.4 Future perspectives

A number of possible targets have been suggested to alleviate N-GLY1 symptoms include the use of ENGase inhibitors (Huang et al. 2015, Bi et al. 2017) or GlcNAc dietary supplements (Owings et al. 2018). Autophagy has been identified as a protective measure under *N*-glycanase inhibition/KD. Furthermore, mitophagy may be involved in maintaining the health of the mitochondrial population in HEK cells. Autophagy has been an attractive target for protein degradation pathways especially in post-mitotic cells like neurons (Decressac et al. 2013, Rubinsztein 2007) and may be able to increase cell survival after inhibition of proteasome function following Nrf1 inactivation.

---

## APPENDIX

---

This appendix contains:

- A.1 Plasmid maps and construct sequences
- A.2 Sequence data confirming cloning of guide sequences into WT or Nickase variant CRISPR/Cas9 plasmids
- A.3 Sequences used for TIDE analysis
- A.4 FITC-labelling of RNase B

### A.1 Plasmid maps and construct sequences

Detailed in this section are:

- A.1.1 pOPH6 PNGase F plasmid map and sequence (Addgene #40315)
- A.1.2 GFP-LC3 plasmid sequence
- A.1.3 mAPPLE-N1 plasmid map (Addgene #54567)
- A.1.4 Sequence of bacterial PNGase mammalian expression construct BacPNG4\_pCMVF
- A.1.5 Sequence of bacterial PNGase mammalian expression construct BacPNG5\_pCMVF
- A.1.6 WT Cas9 CRISPR pSpCas9(BB)-2A-GFP (PX458) plasmid map and sequence (Addgene #48138)

### A.1.1 pOPH6 PNGase F plasmid (Addgene #40315)

Figure A1 shows the plasmid map of pOPH6 PNGase F plasmid (Addgene pOPH6 #40315). Sequencing data for this construct is also presented below.

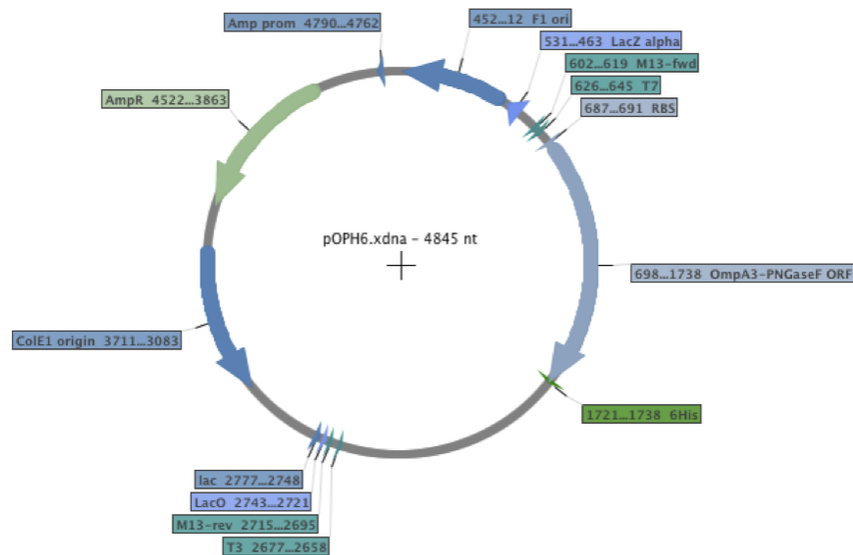


**Figure A1 Plasmid map of pOPH6 PNGase F plasmid (reproduced from Addgene, Addgene pOPH6 #40315)**

#### Sequencing of pOPH6 plasmid

##### > pOPH6 M13 Forward

```

ANNNCANNTACGGCGATGGAGCTCACCGCGGTGGCGGCCGCTCTAGATAACGAGGGCAAA
AAATGAAAAAGACAGCTATCGCGATAGCAGTGGCACTCGGCTGGTTTCGCTACCGTAGCG
CAGGCCGGAATTCCAGCTCCGGCAGATAATACCGTAAATATTTAAAACATTCGACAAAGTA
AAAAATGCCTTTGGTGACGGATTGTCCCAAAGTGCGGAAGGAACCTTTACATTTCCGGCC
GATGTAACAGCCGTA AAAACGATTAAGATGTTCAATTA AAAATGAATGTCCTAATAAACT
TGTGATGAATGGGATCGTTATGCCAATGTTTATGTA AAAAATAAAAACAACAGGTGAGTGG
TACGAAATAGGACGCTTTATTACTCCATATTGGGTGGGAACGGAAAAATTACCTCGTGGA
CTGGA AATTGATGTTACAGATTTCAAATCTTTACTATCCGGAATACAGA AACTTAAAATT
TATACGGAGACATGGCTGGCCAAAGGAAGAGAATACAGTGTAGATTTTCGATATTGTATAC
GGGACACCGGATTATAAATATTCGGCTGTAGTACCTGTAGTTCAGTATAACA AATCATCT
ATTGACGGAGTCCCTTATGGTAAAGCACATACATTGGCTTTGAAAAGAATATCCAGTTA
CCAACAACACAGAAAAAGCTTATCTTAAA AACTACTATTTCCGGATGGGGACATGCTAAG
CCATATGATGCGGGAAGCAGAGGTTGTGCAGAATGGTGCTTCAGAACACACACTATAGCA
ATAAATAATTCGAATACTTTCCAGCATCAGCTGGGTGCTTTAGGATGTTTCAGCAAACCT
ATCAATAATCAGAGTCCGGGAAATTGGACTCCCGACAGAGCCGGTGGTGCCCGGGAATG
GCAGTTC AACACGTATAGATGTA CTGAATAATTCTTTAATAGGCAGTACTTTTATGTTAT
GAATATAAATTCAGAACTGGACAAATAACGGAACCAATGGAGATGCTTTTTATGCAATT
TCCAGTTTTGTGATTGCAAAAAGTAATACCCCTATTAGTGCTCCGGTAGTTACAACTTG
GATCCGCATCACCATCACCACCATTGACGATCCGGCTGAACAACGACGTGAACGCATGCG
GTTCCGACGTTTCAGGCTGCTAAAGATGACGCAGCTCGTGCTAACCAGCGTCTGGACAAAA
TGGCTACTAAATACCGCAAGTAATAAAAACCTGGGAANTGAAAATGGGGCACATTGGGCGA
AATTTTTTTTTTGGCTGCCGTTTACCGCTAATGGGTCCCGCGTAACATAATC

```

### A.1.2 GFP-LC3 plasmid sequence

Sequencing data for this construct is presented below.

#### Sequencing of GFP-LC3 plasmid

##### >GFP-LC3\_pCMVF

```
CTCTCCGAGGANGTCATCAAGGAGTTCATGCGCTTCAAGGTGCGCATGGAGGGCTCCGTGAA
CGGCCACGAGTTCGAGATCGAGGGCGAGGGCGAGGGCCGCCCTACGAGGGCACCCAGACCG
CCAAGCTGAAGGTGACCAAGGGCGGCCCCCTGCCCTTCGCTGGGACATCCTGTCCCCTCAG
TTCCAGTACGGCTCCAAGGCTACGTGAAGCACCCCGCCGACATCCCCGACTACTTGAAGCT
GTCTTCCCCGAGGGCTTCAAGTGGGAGCGCGTGATGAACTTCGAGGACGGCGGCGTGGTGA
CCGTGACCCAGGACTCCTCCCTGCAGGACGGCGAGTTCATCTACAAGGTGAAGCTGCGCGGC
ACCAACTTCCCCTCCGACGGCCCCGTAATGCAGAAGAAGACCATGGGCTGGGAGGCCTCCAC
CGAGCGGATGTACCCCGAGGACGGCGCCCTGAAGGGCGAGATCAAGATGAGGCTGAAGCTGA
AGGACGGCGGCCACTACGACGCCGAGGTCAAGACCACCTACATGGCCAAGAAGCCCGTGCAG
CTGCCCGGCGCCTACAAGACCGACATCAAGCTGGACATCACCTCCCACAACGAGGACTACAC
CATCGTGGAACAGTACGAGCGCGCCGAGGGCCGCACTCCACCGGCGCCGGTGGACCGGTGCG
CCACCATGGTGAGCAAGGGCGAGGAGCTGTTACCGGGGTGGTGCCATCCTGGTCGAGCTG
GACGGCGACGTAAACGGCCACAAGTTCAGCGTGTCCGGCGAGGGCGAGGGCGATGCCACCTA
CGGCAAGCTGACCCTGAAGTTCATCTGCACCACCGCAAGCTGCCCCTGCCCTGGCCCACCC
TCGTGACCACCTGACCTACGGCGTGCAGTGCTTACGCCGCTACCCCGACCACATGAAGCAG
CACGACTTCTTCAAGTCCGCCATGCCCGAAGGCTACGTCCAGGAGCGCACCATCTTCTTCAA
GGACGACGGCAACTACAAGACCCGCGCCGAGGTGAAGTTCGAGGGCGACNCCTTGTNGAACC
GCATNNAGCTGAAGGGCATCGACTTTCAGGAAGGACGGNAACATCCTGGGGNCACAAGCTGG
AAGTANANCTT
```

### A.1.3 mAPPLE-N1 plasmid map and sequence (Addgene #54567)

Figure A2 shows the plasmid map of mAPPLE-N1 plasmid (Addgene mAPPLE-N1 #54567).

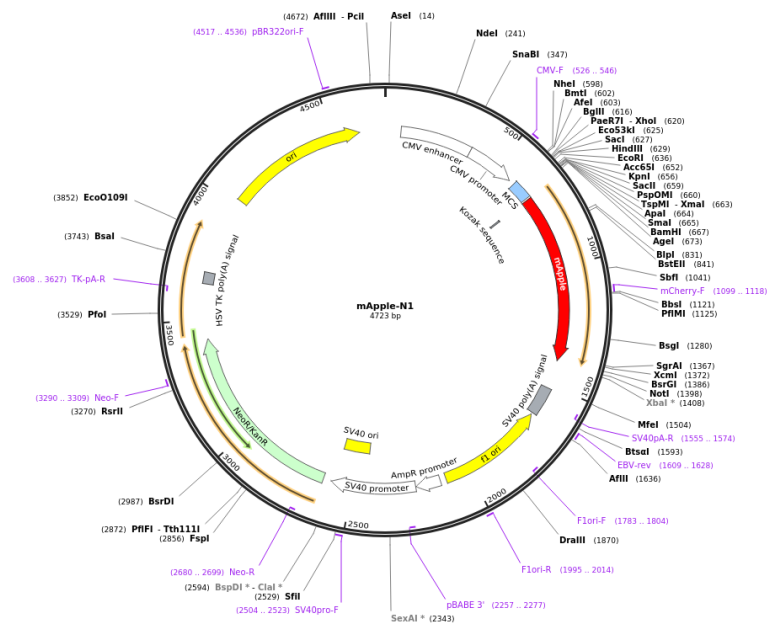


**Figure A2 mAPPLE-N1 plasmid map (reproduced from Addgene, Addgene mAPPLE-N1 #54567).**

### A.1.4 Sequence of bacterial PNGase mammalian expression construct BacPNG4\_pCMVF

Sequencing data for this construct is presented below.

#### Sequence of Bacterial PNGase mammalian expression construct, BacPNG4

> BacPNG4\_pCMVF

```
AAAGGGAAGTCTATATAGCAGAGCTGGTTTGTAGTGAACCGTCAGATCCGCTAGCGCTACCGGA
CTCAGATCTCGAGACCATGGCTCCGGCAGATAATACCGTAAATATTA AACATTTCGACAAAG
TAAAAAATGCCTTTGGTGACGGATTGTCCCAAAGTGC GGAAGGAACCTTTACATTTCCGGCC
GATGTAACAGCCGTAAAAACGATTAAGATGTTTATTAAAAATGAATGTCTTAATAAACTTG
TGATGAATGGGATCGTTATGCCAATGTTTATGTAAAAAATAAAACAACAGGTGAGTGGTACG
AAATAGGACGCTTTATTACTCCATATTGGGTGGGAACGGAAAAATTACCTCGTGGACTGGAA
ATTGATGTTACAGATTTCAAATCTTTACTATCCGGAATACAGAACTTAAAATTTATACGGA
GACATGGCTGGCCAAAGGAAGAGAATACAGTGTAGATTTTCGATATTGTATACGGGACACCGG
ATTATAAATATTCGGCTGTAGTACCTGTAGTTCAGTATAACAAATCATCTATTGACGGAGTC
CCTTATGGTAAAGCACATACATTTGGCTTTGAAAAAGAATATCCAGTTACCAACAAACACAGA
AAAAGCTTATCTTAGAACTACTATTTCCGGATGGGGACATGCTAAGCCATATGATGCGGGAA
GCAGAGGTTGTGCAGAATGGTGC TTCAGAACACACACTATAGCAATAAATAATTTCGAATACT
TTCCAGCATCAGCTGGGTGCTTTAGGATGTTT CAGCAAACCTATCAATAATCAGAGTCCGGG
AAATTGGACTCCCGACAGAGCCGGTTGGTGCCCGGGAATGGCAGTTCCAACACGTATAGATG
TACTGAATAATTTCTTTAATAGGCAGTACTTTT TAGTTATGAATATAAATTCAGAACTGGACA
AATAACGGAACCAATGGAGATGCTTTTTATGCAATTTCCAGTTTTGTGATTGCAAAAAGTAA
TACACCTATTAGTGCTCCGGTAGTTACAAACTTGGATCCACCGGTGCCACCATGGTGAGCA
AGGGCGAGGAGAATAACATGGCCATCATCAAGGAGTTCATGCGCTTCAAGGTGCACATGGAG
```

GGCTCCGTGAACGGCCACGAGTTCGAGATCGAAGGCAAGGGCGAGGGCCGCCCTACAAGGC  
CTTCAAACCGCTAAACTGAAGGTGACCAAGGGTGGCCCCCTGCCCTTCGCCTGGGAAATCC  
TGGCCCCTCAGTTCAGGTACGGGTCCAAGGTCTACTTTAAGCACCCAGCCGAAATCCCCGAA  
TAATTCAAGTTGTCCTTCCCCAAGGGCTTCAGGGGGGAAGCCGTGAAGAACTTCCAGGACGG  
GGGCTTTATTACGTTAACCAGNATTCCTCCCTGGAGGGAAGGGGGTTCTCTAAAAG

A.1.5 Sequence of bacterial PNGase mammalian expression construct  
BacPNG5\_pCMVF

Sequencing data for this construct is presented below.

**Sequence of Bacterial PNGase mammalian expression construct, BacPNG5**

**> BacPNG5\_pCMVF**

ATGGCTCCGGCAGATAATACCGTAAATATTTAAAACATTCGACAAAGTAAAAAATGCCTTTGG  
TGACGGATTGTCCCAAAGTGCGGAAGGAACCTTTACATTTCCGGCCGATGTAACAGCCGTAA  
AAACGATTAAGATGTTTCATTAATAAATGAATGTCCTAATAAACTTGTGATGAATGGGATCGT  
TATGCCAATGTTTATGTAAAAAATAAAACAACAGGTGAGTGGTACGAAATAGGACGCTTTAT  
TACTCCATATTGGGTGGGAACGGAAAAATTACCTCGTGGACTGGAAATTGATGTTACAGATT  
TCAAATCTTTACTATCCGGAAATACAGAACTTAAAATTTATACGGAGACATGGCTGGCCAAA  
GGAAGAGAATACAGTGTAGATTTTCGATATTGTATACGGGACACCGGATTATAAATATTCGGC  
TGTAGTACCTGTAGTTCAGTATAACAAATCATCTATTGACGGAGTCCCTTATGGTAAAGCAC  
ATACATTGGCTTTGAAAAAGAATATCCAGTTACCAACAAACACAGAAAAAGCTTATCTTAGA  
ACTACTATTTCCGGATGGGGACATGCTAAGCCATATGATGCGGGAAGCAGAGGTTGTGCAGA  
ATGGTGCTTCAGAACACACACTATAGCAATAAATAATTTCGAATACTTTCCAGCATCAGCTGG  
GTGCTTTAGGATGTTTCAGCAAACCCTATCAATAATCAGAGTCCGGGAAATTGGACTCCCGAC  
AGAGCCGGTTGGTGCCCGGGAATGGCAGTTCCAACACGTATAGATGTACTGAATAATTCTTT  
AATAGGCAGTACTTTTAGTTATGAATATAAATTCAGAACTGGACAAATAACGGAACCAATG  
GAGATGCTTTTTATGCAATTTCCAGTTTTGTGATTGCAAAAAGTAATACACCTATTAGTGCT  
CCGGTAGTTACAACTTGGATCCACCGGTGCCCACCATGTTGAGCAAGGGCGAGGAAAAATAA  
CATGCCCATCATCAAGGAGTTCATGCGCTTCAAGGTGCACATGGAAGGGCTCCGTGAACGGC  
CACGAGTTCAAAATCGAAGGCGAAGGGCGAGGGCCGCCCTAGAAGGCCTTTCAAACCGCTA  
AGCTGAAGGGGAACCAAGGGGGGGCCCCCTGGCCCTTCGCCTTGGGACATCCTGGCCCCCTC  
AGTTCATGTACGGCTTCCAAGGTCTACATTTAAGCACCCAGCCGAAATTTCCCCGAATAATTT  
CAAGTTGTCCTTTCCCCGAAGGGTTTCAGGGGGGAAACGCCTGGTTGAAATTTCCAGGAAGG  
GGGCATTAATTCAGTTTAACCAAGGAACCTCTCCCCTG

A.1.6 WT Cas9 CRISPR pSpCas9(BB)-2A-GFP (PX458) plasmid map and  
sequence (Addgene #48138)

Figure **A3** shows the plasmid map of WT Cas9 CRISPR pSpCas9(BB)-2A-GFP (PX458) plasmid  
map and sequence (Addgene #48138).

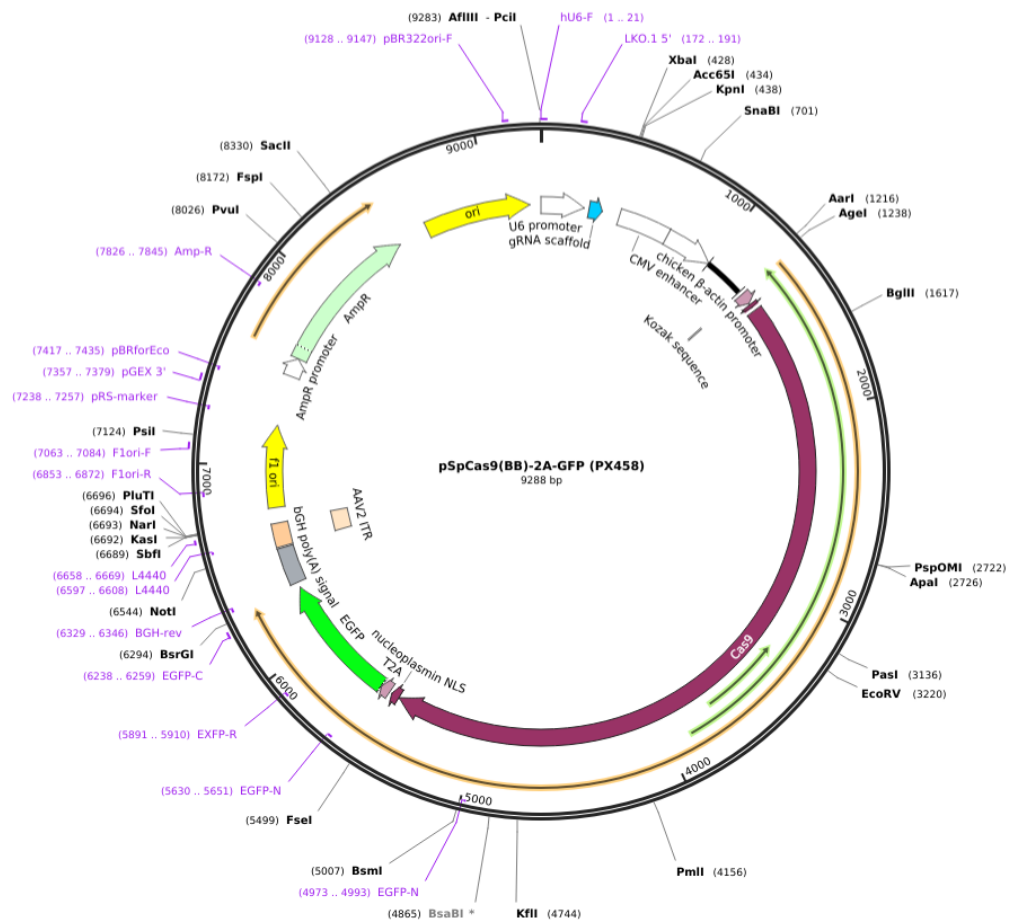


**Figure A3 WT Cas9 CRISPR pSpCas9(BB)-2A-GFP (PX458) plasmid map and sequence (Addgene #48138)**

Sequencing data for this construct is presented below.

**Sequence of WT CRISPR Cas9 plasmid**

**pSpCas9(BB)-2A-GFP (PX458) Sequence >U6sponge-F 5'-**

**GGACTATCATATGCTTACCGTAACTTGA-3' (Ran et al. 2013)**

```

tttcgatTTCTtGGCTTtAtATATCTTGTGGAAaAGGACGAAACACCGGGTCTTCGAGAAGAC
CTGTTTTAGAGCTAGAAATAGCAAGTTAAAATAAGGCTAGTCCGTTATCAACTTGAAAAAGT
GGCACCGAGTCGGTGCCTTTTTTGTTTTTAGAGCTAGAAATAGCAAGTTAAAATAAGGCTAGTC
CGTTTTTTAGCGCGTGCGCCAATTCTGCAGACAAATGGCTCTAGAGGTACCCGTTACATAACT
TACGGTAAATGGCCCGCCTGGCTGACCGCCAACGACCCCGCCATTGACGTCAATAGTAA
CGCCAATAGGGACTTTCCATTGACGTCAATGGGTGGAGTATTTACGGTAAACTGCCCACTTG
GCAGTACATCAAGTGTATCATATGCCAAGTACGCCCCCTATTGACGTCAATGACGGTAAATG
GCCCGCCTGGCATTGTGCCAGTACATGACCTTATGGGACTTTCCTACTTGGCAGTACATCT
ACGTATTAGTCATCGCTATTACCATGGTC
  
```

A.1.7 WT Cas9 CRISPR pSpCas9(BB)-2A-GFP (PX458) plasmid map and sequence (Addgene #48138)

Figure A4 shows the plasmid map of Nickase Cas9 CRISPR plasmid pSpCas9n(BB)-2A-GFP (PX461) (Addgene #48140)

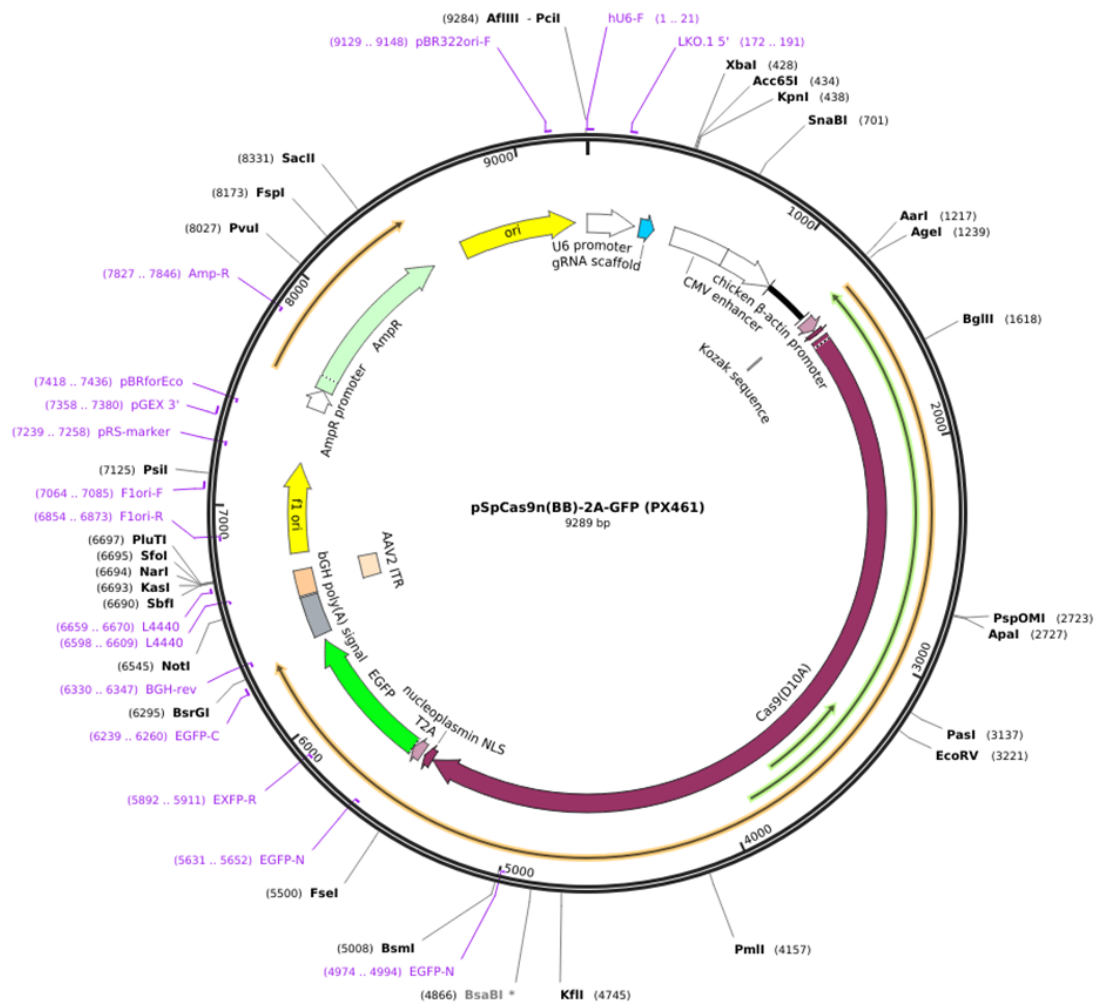


Figure A4 Nickase Cas9 CRISPR plasmid pSpCas9n(BB)-2A-GFP (PX461) (Addgene #48140)

Sequencing data for this construct is presented below.



**Sequence of Nickase CRISPR/Cas9 variant plasmid**

**pSpCas9n(BB)-2A-GFP (PX461) Sequence >U6sponge-F 5'-**

**GGACTATCATATGCTTACCGTAACTTGA-3' (Ran et al. 2013)**

tTTCGAtTTCTtGGCTTTaTaTATCTTGTGGAaAGGACGAAA**CACCG**GGTCTTCGAGAAGAC  
CT**GTTTTTA**GAGCTAGAAATAGCAAGTTAAAATAAGGCTAGTCCGTTATCAACTTGAAAAAGT  
GGCACCGAGTCGGTGCTTTTTTGTTTTAGAGCTAGAAATAGCAAGTTAAAATAAGGCTAGTC  
CGTTTTTAGCGCGTGCGCCAATTCTGCAGACAAATGGCTCTAGAGGTACCCGTTACATAACT  
TACGGTAAATGGCCCGCCTGGCTGACCGCCCAACGACCCCGCCATTGACGTCAATAGTAA  
CGCCAATAGGGACTTTCCATTGACGTCAATGGGTGGAGTATTTACGGTAAACTGCCCACTTG  
GCAGTACATCAAGTGTATCATATGCCAAGTACGCCCCCTATTGACGTCAATGACGGTAAATG  
GCCCGCCTGGCATTGTGCCCAGTACATGACCTTATGGGACTTTCCTACTTGGCAGTACATCT  
ACGTATTAGTCATCGCTATTACCATGGTCGAGGTGAGCCCCACGTTCTGCTTCACTCTCCCC  
ATCTCCCCCCCCCTCCCCACCCCAATTTTGTATTTATTTATTTTTTAATTATTTTGTGCagC  
GATGg

## A.2 Sequencing confirming cloning of guide sequence into WT or Nickase variant CRISPR/Cas9 plasmids

Sequencing confirming cloning of guide sequence into WT or Nickase variant CRISPR/Cas9 plasmids is presented below. ENGase WT A and PNGKO Nickase B were not successfully cloned into CRISPR plasmids.

### PNGKO WT A

```
CCCAAAGGCCTTGTTTACAGAAGAAATTGGATTAATTTGACTGTAAACACAAAGATATTAGT
ACAAAATACGTGACGTAGAAAAGTAATAATTTCTTGGGTAGTTTGCAGTTTTAAAATTATGTT
TTAAAATGGACTATCATATGCTTACCGTAACTTGAAAGTATTTTCGATTTCTTGGCTTTATAT
ATCTTGTGGAAAGGACGAAA CACCGGGCTGTGTTTCCAATCCGGAGTTT TAGAGCTAGAAAT
AGCAAGTTAAAATAAGGCTAGTCCGTTATCAACTTGAAAAAGTGGCACCAGTCGGTGCTTT
TTTGTTTTAGAGCTAGAAATAGCAAGTTAAAATAAGGCTAGTCCGTTTTTAGCGCGTGCGCC
AATTTCTGCAGACAAATGGCTCTAGAGGTACCCGTTACATAACTTACGGTAAATGGCCCGCCT
GGCTGACCGCCCAACGACCCCCGCCATTGACGTCAATAGTAACGCCAATAGGGACTTTCCA
TTGACGTCAATGGGTGGAGTATTTACGGTAAACTGCCCACTTGGCAGTACATCAAGTGTATC
ATATGCCAAGTACGCCCCCTATTGACGTCAATGACGGTAAATGGCCCGCCTGGCATTGTGCC
CAGTACATGACCTTATGGGACTTTCCTACTTGGCAGTACATCTACGTATTAGTCATCGCTAT
TACCATGGTCGAGGTGAGCCCCACGTTCTGCTTCACTCTCCCCATCTCCCCCCCCCTCCC
CACCACAGAAAGTATGGGATTAATTTAATTTTTTAATTAACCTAAGCACCACCACACAGGG
GGGCGGGGGGGGGGGCGGGGGC
```

### PNGKO WT B

```
CTTAAAACCGAAAACAACGCTGTTATAGAACACAACCTCGGAATTAATTTGACTGTAAACACA
AAGATATTAGTACAAAATACGTGACGTAGAAAAGTAATAATTTCTTGGGTAGTTTGCAGTTTT
AAAATTATGTTTTAAAATGGACTATCATATGCTTACCGTAACTTGAAAGTATTTTCGATTTCT
TGGCTTTATATATCTTGTGGAAAGGACGAAA CACCGACTAGACTCTTGCCGTGCAGGTTT TA
GAGCTAGAAATAGCAAGTTAAAATAAGGCTAGTCCGTTATCAACTTGAAAAAGTGGCACC GA
GTCGGTGCTTTTTTTGTTTTAGAGCTAGAAATAGCAAGTTAAAATAAGGCTAGTCCGTTTTTA
GCGCGTGCGCCAATTTCTGCAGACAAATGGCTCTAGAGGTACCCGTTACATAACTTACGGTAA
ATGGCCCGCCTGGCTGACCGCCCAACGACCCCCGCCATTGACGTCAATAGTAACGCCAATA
GGGACTTTCCATTGACGTCAATGGGTGGAGTATTTACGGTAAACTGCCCACTTGGCAGTACA
TCAAGTGTATCATATGCCAAGTACGCCCCCTATTGACGTCAATGACGGTAAATGGCCCGCCT
GGCATTGTGCCCAGTACATGACCTTATGGGACTTTCCTACTTGGCAGTACATCTACGTATTA
GTCATCGCTATTACCATGGTCGAGGTGAGCCCCACGTTCTGCTTCACTCTCCCCATCTCCCC
CCCTCCAACCCCCAATTTTTGTATATTATTTATTTTTTTTTTAATTTATTTTTTGTGCAACCGAA
TGGGGGGCGAGGGGTGGGGGGGCCCTCGCCGCGCCAAGCCGGGCGGGGGGGGGGACTAA
AGGTGTCGGTGCTGTGGCCGATGCCAAAAATGGACGCGCCAGCCAACCAACTCAGAAGGGG
GGGCGGTCCACAAAATTTTTTCTTTTTTAGGGGGGAAGGGCGGGCGTC
```

### PNGKO Nickase A

```
CAAAAGGGCCCTGGTTAGAGAGAAATTGGAATTAATTTGACTGTAAACACAAAGATATTAGT
ACAAAATACGTGACGTAGAAAAGTAATAATTTCTTGGGTAGTTTGCAGTTTTAAAATTATGTT
TTAAAATGGACTATCATATGCTTACCGTAACTTGAAAGTATTTTCGATTTCTTGGCTTTATAT
ATCTTGTGGAAAGGACGAAA CACCGGGCTGTGTTTCCAATCCGGAGTTT TAGAGCTAGAAAT
AGCAAGTTAAAATAAGGCTAGTCCGTTATCAACTTGAAAAAGTGGCACCAGTCGGTGCTTT
TTTGTTTTAGAGCTAGAAATAGCAAGTTAAAATAAGGCTAGTCCGTTTTTAGCGCGTGCGCC
AATTTCTGCAGACAAATGGCTCTAGAGGTACCCGTTACATAACTTACGGTAAATGGCCCGCCT
GGCTGACCGCCCAACGACCCCCGCCATTGACGTCAATAGTAACGCCAATAGGGACTTTCCA
```

TTGACGTCAATGGGTGGAGTATTTACGGTAAACTGCCCACTTGGCAGTACATCAAGTGTATC  
ATATGCCAAGTACGCCCCCTATTGACGTCAATGACGGTAAATGGCCCGCTGGCATTGTGCC  
CAGTACATGACCTTATGGGACTTTCCTACTTGGCAGTACATCTACGTATTAGTCATCGCTAT  
TACCATGGTTCGAGGTGAGCCCCACGTTCTGCTTCACTCTCCCCATCTCCCCCCCCCTCCCC  
ACCCCCAATTTTGGTATTTATTTATTTTTTTAATTATTTTGTGCCACAGATGGGGGGCGG  
AGGGGGGTGAGGGGGGCCA

#### PNGRX WT A

TATTGCAAACGATACAATGCTGTTAGAGAGAAATTGGAATTAATTTGACTGTAAACACAAAG  
ATATTAGTACAAAATACGTGACGTAGAAAGTAATAATTTCTTGGGTAGTTGCAGTTTTAAA  
ATTATGTTTTAAAATGGACTATCATATGCTTACCGTAACTTGAAAGTATTTTCGATTTCTGG  
CTTTATATATCTTGTGGAAAGGACGAAA **CACCGTTCTTTAACCTTAGTTCTTCGTTT** TAGAG  
CTAGAAATAGCAAGTTAAAATAAGGCTAGTCCGTTATCAACTTGAAAAAGTGGCACCGAGTC  
GGTGCTTTTTTGTTTTAGAGCTAGAAATAGCAAGTTAAAATAAGGCTAGTCCGTTTTTAGCG  
CGTGCGCCAATTCTGCAGACAAAATGGCTCTAGAGGTACCCGTTACATAACTTACGGTAAATG  
GCCCGCCTGGCTGACCGCCCAACGACCCCCGCCATTGACGTCAATAGTAACGCCAATAGGG  
ACTTTCCATTGACGTCAATGGGTGGAGTATTTACGGTAAACTGCCCACTTGGCAGTACATCA  
AGTGTATCATATGCCAAGTACGCCCCCTATTGACGTCAATGACGGTAAATGGCCCGCCTGGC  
ATTGTGCCCAGTACATGACCTTATGGGACTTTCCTACTTGGCAGTACATCTACGTATTAGTC  
ATCGCTATTACCATGGTCGAGGTGAGCCCCACGTTCTGCTTCACTCTCCCCATCTCCCCCCC  
CCTCCCCACCCCCAATTTTGTATTTATTTATTTTTTTAATTATTTTGTGCAGCGATGGTGG  
CG

#### PNGRX WT B

AAATGCAATACGATACACGCTGTTAGAGAGAAATTGGAATTAATTTGACTGTAAACACAAAG  
ATATTAGTACAAAATACGTGACGTAGAAAGTAATAATTTCTTGGGTAGTTTGCAGTTTTAAA  
ATTATGTTTTAAAATGGACTATCATATGCTTACCGTAACTTGAAAGTATTTTCGATTTCTTGG  
CTTTATATATCTTGTGGAAAGGACGAAA **CACCGTACTTCGAGACACTATTAATGTTT** TAGAG  
CTAGAAATAGCAAGTTAAAATAAGGCTAGTCCGTTATCAACTTGAAAAAGTGGCACCGAGTC  
GGTGCTTTTTTGTTTTAGAGCTAGAAATAGCAAGTTAAAATAAGGCTAGTCCGTTTTTAGCG  
CGTGCGCCAATTCTGCAGACAAAATGGCTCTAGAGGTACCCGTTACATAACTTACGGTAAATG  
GCCCGCCTGGCTGACCGCCCAACGACCCCCGCCATTGACGTCAATAGTAACGCCAATAGGG  
ACTTTCCATTGACGTCAATGGGTGGAGTATTTACGGTAAACTGCCCACTTGGCAGTACATCA  
AGTGTATCATATGCCAAGTACGCCCCCTATTGACGTCAATGACGGTAAATGGCCCGCCTGGC  
ATTGTGCCCAGTACATGACCTTATGGGACTTTCCTACTTGGCAGTACATCTACGTATTAGTC  
ATCGCTATTACCATGGTCGAGGTGAGCCCCACGTTCTGCTTCACTCTCCCCATCTCCCCCCC  
CATGGAGCACCCCCAATTTTGTATTTATTTATTTTTTTAATTATTTTGTGCAA

#### PNGRX Nickase A

CTGCCATACGATACATGCTGTTAGAGAGAAATTGGAATTAATTTGACTGTAAACACAAAGAT  
ATTAGTACAAAATACGTGACGTAGAAAGTAATAATTTCTTGGGTAGTTTGCAGTTTTAAAAT  
TATGTTTTAAAATGGACTATCATATGCTTACCGTAACTTGAAAGTATTTTCGATTTCTTGGCT  
TTATATATCTTGTGGAAAGGACGAAA **CACCGTTCTTTAACCTTAGTTCTTCGTTT** TAGAGCT  
AGAAATAGCAAGTTAAAATAAGGCTAGTCCGTTATCAACTTGAAAAAGTGGCACCGAGTCGG  
TGCTTTTTTTGTTTTAGAGCTAGAAATAGCAAGTTAAAATAAGGCTAGTCCGTTTTTAGCGG  
TGCGCCAATTCTGCAGACAAAATGGCTCTAGAGGTACCCGTTACATAACTTACGGTAAATGGC  
CCGCTGGCTGACCGCCCAACGACCCCCGCCATTGACGTCAATAGTAACGCCAATAGGGAC  
TTTCCATTGACGTCAATGGGTGGAGTATTTACGGTAAACTGCCCACTTGGCAGTACATCAAG  
TGTATCATATGCCAAGTACGCCCCCTATTGACGTCAATGACGGTAAATGGCCCGCCTGGCAT  
TGTGCCCAGTACATGACCTTATGGGACTTTCCTACTTGGCAGTACATCTACGTATTAGTCAT

CGCTATTACCATGGTCGAGGTGAGCCCCACGTTCTGCTTCACTCTCCCCATCTCCCCCCCCCT  
CCCCACCCCAATTTTGTATTTTATTTTATTTTTTTTAAATTATTTTGGGCAGCGATGGGGG  
GGGGGGGGGGGGGGGGGGACCCCCCCCCAGGGCGGGATCGGAGTCGGTAACGAATGGGCGG  
GTCTGAGCCTAAGCCAGAAAAGGGTGCCGGCGCAAGCCATTCCAAAAGTGGCCGCCTCTCC  
GAAAAGT

#### PNGRX Nickase B

ATACGTGACGTAGAAAAGTAATAATTTCTTGGGTAGTTTGCAGTTTTAAAATTATGTTTTAAA  
ATGGACTATCATATGCTTACCGTAACTTGAAAAGTATTTTCGATTTCTTGGCTTTATATATCTT  
GTGAAAGGACGAAA **CACCGTACTTCGAGACACTATTAATGTTT** TAGAGCTAGAAATAGCAA  
GTTAAAATAAGGCTAGTCCGTTATCAACTTGAAAAAGTGGCACCGAGTCGGTGCTTTTTTGT  
TTTAGAGCTAGAAATAGCAAGTTAAAATAAGGCTAGTCCGTTTTTAGCGCGTGCGCCAATTC  
TGCAGACAAATGGCTCTAGAGGTACCCGTTACATAACTTACGGTAAATGGCCCGCCTGGCTG  
ACCGCCCAACGACCCCCGCCCATTTGACGTCAATAGTAACGCCAATAGGGACTTTCCATTGAC  
GTCAATGGGTGGAGTATTTACGGTAACTGCCCACTTGGCAGTACATCAAGTGTATCATATG  
CCAAGTACGCCCCCTATTGACGTCAATGACGGTAAATGGCCCGCCTGGCATTGTGCCAGTA  
CATGACCTTATGGGACTTTTCTACTTGGCAGTACATCTACGTATTAGTCATCGCTATTACCA  
TGGTGAGGTGAGCCCCACGTTCTGCTTCACTCTCCCCATCTCCCCCCCCCTCCCCACCCCAA  
ATTTTGTATTTATTTATTTTTTTAATTTTTTTGGGGCCCCGTTGGGGGGGGGGGGGGGGGG  
GTTGTGTTTTATAAAAAAAAAAAGTCCCAAACCCTTCCGCACCAAAGCAAAAAAAGGGTT  
GAAAACAAAAAAGGGGGGGTAAAA

#### ENGase WT B

CAAAGGGCCTGTTAGAAGAGATAATTGGAATTAATTTGACTGTAAACACAAAGATATTAGTA  
CAAAATACGTGACGTAGAAAAGTAATAATTTCTTGGGTAGTTTGCAGTTTTAAAATTATGTTT  
TAAAATGGACTATCATATGCTTACCGTAACTTGAAAAGTATTTTCGATTTCTTGGCTTTATATA  
TCTTGTGAAAGGACGAAA **CACCGGGCGTGAAGCCCCGCTTGGGTTT** TAGAGCTAGAAATA  
GCAAGTTAAAATAAGGCTAGTCCGTTATCAACTTGAAAAAGTGGCACCGAGTCGGTGCTTTT  
TTGTTTTAGAGCTAGAAATAGCAAGTTAAAATAAGGCTAGTCCGTTTTTAGCGCGTGCGCCA  
ATTCTGCAGACAAATGGCTCTAGAGGTACCCGTTACATAACTTACGGTAAATGGCCCGCCTG  
GCTGACCGCCCAACGACCCCCGCCCATTTGACGTCAATAGTAACGCCAATAGGGACTTTCCAT  
TGACGTCAATGGGTGGAGTATTTACGGTAACTGCCCACTTGGCAGTACATCAAGTGTATCA  
TATGCCAAGTACGCCCCCTATTGACGTCAATGACGGTAAATGGCCCGCCTGGCATTGTGCC  
AGTACATGACCTTATGGGACTTTTCTACTTGGCAGTACATCTACGTATTAGTCATCGCTATT  
ACCATGGTCGAGGTGAGCCCCACGTTCTGCTTCACTCTCCCCATCTCCCCCCCCCTCCCCA  
CCCCCAAATTTTGTATTATATATTTTTTTTATATTATATTTTTTGTGCCCGGATGGGGGCGG  
GGGCGGGGTAACCTCTCGCCCCAATGACGACCCAACTGTCCAACGTCCGACCCGTCAAGCGA  
ATAGGTGCGCCGTCAACCAATCAGAAGGCGGCGCTTCCGAAAAG

#### ENGase Nickase A

ACGAACCACGGCCTGTTAGAGAGATAATTGGAATTAATTTGACTGTAAACACAAAGATATTA  
GTACAAAATACGTGACGTAGAAAAGTAATAATTTCTTGGGTAGTTTGCAGTTTTAAAATTATG  
TTTTAAAATGGACTATCATATGCTTACCGTAACTTGAAAAGTATTTTCGATTTCTTGGCTTTAT  
ATATCTTGTGAAAGGACGAAA **CACCGCAAGTAAAAGCTGATTGGTTGTTT** TAGAGCTAGAA  
ATAGCAAGTTAAAATAAGGCTAGTCCGTTATCAACTTGAAAAAGTGGCACCGAGTCGGTGCT  
TTTTTGTTTTTAGAGCTAGAAATAGCAAGTTAAAATAAGGCTAGTCCGTTTTTAGCGCGTGCG  
CCAATTCTGCAGACAAATGGCTCTAGAGGTACCCGTTACATAACTTACGGTAAATGGCCCGC  
CTGGCTGACCGCCCAACGACCCCCGCCCATTTGACGTCAATAGTAACGCCAATAGGGACTTTC  
CATTGACGTCAATGGGTGGAGTATTTACGGTAACTGCCCACTTGGCAGTACATCAAGTGT  
TCATATGCCAAGTACGCCCCCTATTGACGTCAATGACGGTAAATGGCCCGCCTGGCATTGTG

CCCAGTACATGACCTTATGGGACTTTCCTACTTGGCAGTACATCTACGTATTAGTCATCGCT  
ATTACCATGGTTCGAGGTGAGCCCCACGTTCTGCTTCACTCTCCCCATCTCCCCCCCCCTCCC  
ACCCCCAATTTTGTATTTATTTATTTTAAATTTTGTGCAGCGATGGGGGCGGGGGGG  
GGGAGCCCCGCGCCAAGCGGGGCGAGGCGGGGCGAGGGGCGGGCGGGCCGAAGCGAAAAG  
GTGCGGCCGCAGCCAATTCAAGAAGCGGCGGCGCTCCGAAAAGTTTCCCTTTTATGGGCAGAG  
G

### ENGase Nickase B

AGACAAACCCAAAACAATGGCTGTTAGAGAGATAAATTGGAATTAATTTGACTGTAAACACAA  
AGATATTAGTACAAAATACGTGACGTAGAAAGTAATAATTTCTTGGGTAGTTTGCAGTTTAA  
AAATTATGTTTTAAAATGGACTATCATATGCTTACCGTAACTTGAAAGTATTTTCGATTTCTT  
GGCTTTATATATCTTGTGAAAGGACGAAA **CACCGGGCGTGGAAAGCCCCGCTTGGGTTT** TAG  
AGCTAGAAATAGCAAGTTAAAATAAGGCTAGTCCGTTATCAACTTGAAAAAGTGGCACCGAG  
TCGGTGCCTTTTTTGTTTTAGAGCTAGAAATAGCAAGTTAAAATAAGGCTAGTCCGTTTTT  
CGCGTGCGCCAATTCTGCAGACAAATGGCTCTAGAGGTACCCGTTACATAACTTACGGTAAA  
TGGCCCGCCTGGCTGACCGCCCAACGACCCCCGCCATTGACGTCAATAGTAACGCCAATAG  
GGACTTTCCATTGACGTCAATGGGTGGAGTATTTACGGTAACTGCCCACTTGGCAGTACAT  
CAAGTGTATCATATGCCAAGTACGCCCCCTATTGACGTCAATGACGGTAAATGGCCCGCCTG  
GCATTGTGCCAGTACATGACCTTATGGGACTTTCCTACTTGGCAGTACATCTACGTATTAG  
TCATCGCTATTACCATGGTTCGAGGTGAGCCCCACGTTCTGCTTCACTCTCCCCATCTCCCC  
CCCCTCCCCACCCCAATTTTGTATTTATTTATTTTATTTTATTTTGTGCACCGATGGGGG  
CGGGGGGGGGGGGGGGGGCGCGCCCAAGCCGGGCGCGCCGGCCGAGGGTTCGGTTCGGTCT  
AGGCGAAAGTTGCGCGCACCCAATCAAGAGCGGCGGCGCTCCGAAAGTTTCTTTTATGGCGAG  
G

### A.3 Sequences used for TIDE analysis

The sequences used for TIDE analysis are presented below.

#### PNG KO predicted sequence

**GTACCTTAACAGCACAGAATG**TAATTTACTGTTTTTACTTATAGTAAAAACAACCATTGGTT  
TAGGGAAGAAAGAAAATCAGGTGACTATAAAGGTATACCTAGGTCATGTTTGTGAAAGTAA  
AGTCTTTGAAGAACTATGACCTGGTTTTTTTTATATATAATCAAACCTTTTGTTTTTTGTGAG  
AAACCCTAATGATGAAAAATATAGAT **CCATCCGGATTGGAAACACAGCC**TTTTCT**ACTAGAC**  
**TCTTGCCTGTGAGG**AGGAGCTGTTGAATGTTTATTTGAAATGGGCTTTGAAGAGGTAAGTATG  
TTCAAGGATTTCTCTCCCCTCTTCATGCACAAAGCAGCCATTATCATGTTGGTGAATAATT  
GTTTGAATAAGATAATGTTTTTAAATTTATCATTTTGGGAATCAGTAGAAGTAGTTATTTCT  
TCATTGATTGGACATTTAAAATCACAACAAGTATAGTTTAAAATTTAGTAAAATGTAACA  
ACGCTCCACAGAGAAATTTTACGAGTCTCAGTTCTTTAAAATAAGGGTCATACATGCAACC  
CAAGGACCAAATGTGGTTCACTTTAGGCTTTTAGCTAAAACCTGATTTGTGAGCACACATGA  
ATACTAATAGAGTCTA **GCTACCTGTCTGTAGTAGG**

#### WT gDNA >PNGF

CCATTGGTTTATAGGGAAGAAAGAAAATCAGGTGACTATAAAGGTATACCTAGGTCATGTTTGT  
TGAAAGTAAAGTCTTTGAAGAACTATGACCTGGTTTTTTTTTATATATAATCAAACCTTTTGT  
TTTTTGTGAGAAACC**TAATGATGAAAAATATAGATC** **CATCCGGATTGGAAACACAGCC**TTTT  
CT**ACTAGACTCTTGCCTGTGAGG**AGGAGCTGTTGAATGTTTATTTGAAATGGGCTTTGAAGAG  
GTAAGTATGTTCAAGGATTTCTCTCCCCTCTTCATGCACAAAGCAGCCATTATCATGTTGG  
TGAATAATTGTTTGAATAAGATAATGTTGTTTAAATTTATCATTTTGGGAATCAGTAGAAGTA  
GTTATTTCTTCATTGATTGCACATTTAAAATCACAACAAGTATAGCTTAACTTTCTGAAA  
AATGTATCAACGTTCAACAGAGAAATTTTACNGCTCAGTTCTTTAAAATAAAGGTCTACA

TGCAACCCAAGGACCAATTGTGGCTCACTTTAGGCTTTTACATAAACCTGATTTGTGAGCTC  
CATCAGTACTA

**PNGA Mixed population >PNGF**

CTTTTTCTTTAAGTAAACAACCATTTGGTTTAGGGAAGAAGAAAATCAGGTGACTATAAAGG  
TATACCTAGGTCATGTTTGTTGAAAGTAAAGTCTTTGAAGAACTATGACCTGGTTTTTTTTTA  
TATATAATCAAACCTTTGTTTTTGTTCAGAAACCCTAATGATGAAAAATATAGATCCA~~TCCG~~  
~~/GAATGGAAACCCCGCC~~TTTTCTCATAAACCCCTGGCTGGCCAAAGAACTTTTGTAAGGTTA  
ATTTAAAGGGGTTTTGAAAAAGTAATTAATTTCCCTGTTTTCCCCCCCCCTTTTCATGGAAA  
AATCGGGCCTTAACATGGTTGGGAATAAATGGTTTTATAATGTAATTGTTTTTAATTTAATC  
TTTTGGGGAACTATAAACTATGTTTTTCTTCGTTAATGAACTCTAAAAATCTAAAAATAG  
GT

**PNGB Mixed population >PNGF**

CTGCAGTCTTAAGTAAAACACCATTTGGTTTAGGGAGAAGAAAATCAGGTGACTATAAAGGTAT  
ACCTAGGTCATGTTTGTTGAAAGTAAAGTCTTTGAAGAACTATGACCTGGTTTTTTTTTATAT  
ATAATCAAACCTTTGTTTTTGTTCAGAAACCCTAATGATGAAAAATATAGATCCATCCGGAT  
TGGAAACACAGCCTTTTCT~~ACTAGACTCTTGCCTGT/TCAAAGG~~AGCTGTTGAATGTTTATT  
TGAAATGGGCTTTGAAAAGGTAAGTATGTTCAAGGATTTCTCTCCCCTCTTCATGCACAAA  
GCAGCATTATCATGTTGGGGAATAATTGTTTGAATAAGATAATGTTTTTTATTTTATCATT  
TTGGGAATCAGTAAAAGTAGTTATTTCTTCATTGATTGGACATTTAAAAATCACAACAAGTA  
TACTTTAAAATTTTCAAGTAAAATGCAACAACGCTCCACAAAAAATTTCTTACGAGTCTCATTT  
CTTTAAAATAAGGG

#### A.4 FITC-labelling of RNase B

RNaseB was conjugated with fluorescein isothiocyanate. The protein first was dissolved in sodium carbonate buffer (0.1 M, pH 9) to a final concentration of 2 mg/ml. Fluorescein isothiocyanate (CAS: 3326-32-7, Sigma-Aldrich, catalogue no: F4274) was dissolved in DMSO to a final concentration of 1 mg/ml. The solution of RNase B (1 mL) was agitated gently on a shaker plate, and the FITC solution (50  $\mu$ l) was added slowly in 5  $\mu$ l aliquots over 30 min. The reaction mixture was wrapped in foil to exclude light and incubated at 4 °C for 8 h. Following the incubation, ammonium chloride was added to a final concentration of 50 mM and the solution again left to incubate in the dark (4 °C, 2 h). Glycerol (50  $\mu$ l) was added, along with xylene cyanol FF (CAS: 2650-17-1, Sigma Aldrich, catalogue no: X4126). The labelled protein was separated from unconjugated protein and free label by elution in PBS on a PD10 column (GE Healthcare). The final concentration of protein was determined using a NanoDrop.

FITC-labelled RNase B was incubated with PNGase F using the conditions for the general RNase B deglycosylation assay previously described. The results are shown in Figure A5, and demonstrate that FITC-labelled RNase B acts as a suitable substrate for this assay.

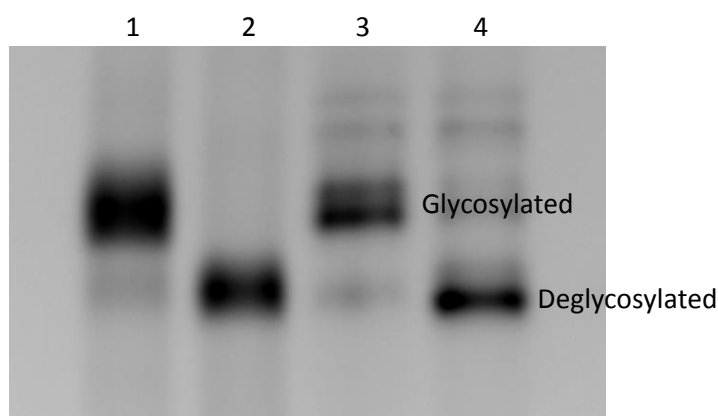


**Figure A5 RNase B labelled FITC incubated with PNGase F. Lane 1: denatured FITC labelled RNase B. Lane 2: denatured FITC labelled RNase B deglycosylated with PNGase F. Lane 3: FITC labelled RNase B. Lane 4: FITC labelled RNase B deglycosylated with PNGase F. Fluorescence Gel imaged using Syngene Gel:Doc.**

## Acknowledgment of Assistance

Sample preparation for LC-MS/MS of CRISPR generated clones and proteomics of autophagosome isolation studies were performed by Dr Holger Kramer (Head of Proteomics, MRC London Institute of Medical Sciences).

ATG13 KO MEFs and corresponding WT MEFs were a kind gift from Dr Nick Ktistakis (Babraham Institute, Cambridge).

GFP-RFP-LC3 plasmid was a kind gift from Professor Geert Bultynck (K. U. Leuven, Belgium)

The ddVENUS plasmid was a kind gift from Dr Jeff Grotzke (LAM Therapeutics, Connecticut) and Professor Peter Cresswell (Howard Hughes Medical Institute, Yale University).



## Bibliography

Aebi, M. (2013) 'N-linked protein glycosylation in the ER', *Biochimica et Biophysica Acta (BBA) - Molecular Cell Research*, 1833(11), 2430-2437.

Aguer, C., Gambarotta, D., Mailloux, R. J., Moffat, C., Dent, R., McPherson, R. and Harper, M.-E. (2011) 'Galactose Enhances Oxidative Metabolism and Reveals Mitochondrial Dysfunction in Human Primary Muscle Cells', *PLOS ONE*, 6(12), e28536.

Al-Mehdi, A.-B., Pastukh, V. M., Swiger, B. M., Reed, D. J., Patel, M. R., Bardwell, G. C., Pastukh, V. V., Alexeyev, M. F. and Gillespie, M. N. (2012) 'Perinuclear Mitochondrial Clustering Creates an Oxidant-Rich Nuclear Domain Required for Hypoxia-Induced Transcription', *Science signaling*, 5(231), ra47-ra47.

Alers, S., Löffler, A. S., Wesselborg, S. and Stork, B. (2012) 'Role of AMPK-mTOR-Ulk1/2 in the Regulation of Autophagy: Cross Talk, Shortcuts, and Feedbacks', *Molecular and Cellular Biology*, 32(1), 2-11.

Alonzi, D. S., Kukushkin, N. V., Allman, S. A., Hakki, Z., Williams, S. J., Pierce, L., Dwek, R. A. and Butters, T. D. (2013) 'Glycoprotein misfolding in the endoplasmic reticulum: identification of released oligosaccharides reveals a second ER-associated degradation pathway for Golgi-retrieved proteins', *Cell Mol Life Sci*, 70(15), 2799-814.

Alonzi, D. S., Neville, D. C., Lachmann, R. H., Dwek, R. A. and Butters, T. D. (2008) 'Glycosylated free oligosaccharides are biomarkers of endoplasmic- reticulum alpha-glucosidase inhibition', *Biochem J*, 409(2), 571-80.

Altrich-VanLith, M. L., Ostankovitch, M., Polefrone, J. M., Mosse, C. A., Shabanowitz, J., Hunt, D. F. and Engelhard, V. H. (2006) 'Processing of a class I-restricted epitope from tyrosinase requires peptide N-glycanase and the cooperative action of endoplasmic reticulum aminopeptidase 1 and cytosolic proteases', *Journal of Immunology*, 177(8), 5440-5450.

Amaya, C., Fader, C. M. and Colombo, M. I. (2015) 'Autophagy and proteins involved in vesicular trafficking', *FEBS Letters*, 589(22), 3343-3353.

Amerik, A. Y. and Hochstrasser, M. (2004) 'Mechanism and function of deubiquitinating enzymes', *Biochimica et Biophysica Acta (BBA) - Molecular Cell Research*, 1695(1), 189-207.

Anderson, K. A., Madsen, A. S., Olsen, C. A. and Hirschey, M. D. (2017) 'Metabolic control by sirtuins and other enzymes that sense NAD<sup>+</sup>, NADH, or their ratio', *Biochimica et Biophysica Acta (BBA) - Bioenergetics*, 1858(12), 991-998.

Arrasate, M. and Finkbeiner, S. (2012) 'Protein aggregates in Huntington's disease', *Exp Neurol*, 238(1), 1-11.

- Avezov, E., Frenkel, Z., Ehrlich, M., Herscovics, A. and Lederkremer, G. Z. (2008) 'Endoplasmic Reticulum (ER) Mannosidase I Is Compartmentalized and Required for N-Glycan Trimming to Man(5–6)GlcNAc(2) in Glycoprotein ER-associated Degradation', *Molecular Biology of the Cell*, 19(1), 216-225.
- Aynacioglu, A. S., Nacak, M., Filiz, A., Ekinci, E. and Roots, I. (2004) 'Protective role of glutathione S-transferase P1 (GSTP1) Val105Val genotype in patients with bronchial asthma', *British Journal of Clinical Pharmacology*, 57(2), 213-217.
- B'chir, W., Maurin, A.-C., Carraro, V., Averous, J., Jousse, C., Muranishi, Y., Parry, L., Stepien, G., Fafournoux, P. and Bruhat, A. (2013) 'The eIF2 $\alpha$ /ATF4 pathway is essential for stress-induced autophagy gene expression', *Nucleic Acids Research*, 41(16), 7683-7699.
- Bakker, W. J., Harris, I. S. and Mak, T. W. (2007) 'FOXO3a is activated in response to hypoxic stress and inhibits HIF1-induced apoptosis via regulation of CITED2', *Mol Cell*, 28(6), 941-53.
- Bao, Q. and Shi, Y. (2007) 'Apoptosome: a platform for the activation of initiator caspases', *Cell Death Differ*, 14(1), 56-65.
- Barrangou, R. and Marraffini, L. A. (2014) 'CRISPR-Cas systems: Prokaryotes upgrade to adaptive immunity', *Mol Cell*, 54(2), 234-44.
- Barth, S., Glick, D. and Macleod, K. F. (2010) 'Autophagy: assays and artifacts', *The Journal of pathology*, 221(2), 117-124.
- Bartlett, D. W. and Davis, M. E. (2006) 'Insights into the kinetics of siRNA-mediated gene silencing from live-cell and live-animal bioluminescent imaging', *Nucleic Acids Research*, 34(1), 322-333.
- Bartolomé, A., García-Aguilar, A., Asahara, S.-I., Kido, Y., Guillén, C., Pajvani, U. B. and Benito, M. (2017) 'MTORC1 Regulates both General Autophagy and Mitophagy Induction after Oxidative Phosphorylation Uncoupling', *Molecular and Cellular Biology*, 37(23).
- Behrends, C., Sowa, M. E., Gygi, S. P. and Harper, J. W. (2010) 'Network organization of the human autophagy system', *Nature*, 466(7302), 68-76.
- Berault, D. R. and Werstuck, G. H. (2013) 'Detection and quantification of endoplasmic reticulum stress in living cells using the fluorescent compound, Thioflavin T', *Biochimica et Biophysica Acta (BBA) - Molecular Cell Research*, 1833(10), 2293-2301.
- Berridge, M. V., Herst, P. M. and Tan, A. S. (2005) 'Tetrazolium dyes as tools in cell biology: New insights into their cellular reduction' in *Biotechnology Annual Review*, Elsevier, 127-152.
- Betteridge, D. J. (2000) 'What is oxidative stress?', *Metabolism*, 49(2 Suppl 1), 3-8.
- Bi, Y., Might, M., Vankayalapati, H. and Kuberan, B. (2017) 'Repurposing of Proton Pump Inhibitors as first identified small molecule inhibitors of endo-beta-N-acetylglucosaminidase

(ENGase) for the treatment of NGLY1 deficiency, a rare genetic disease', *Bioorg Med Chem Lett*, 27(13), 2962-2966.

Bi, Y., Might, M., Vankayalapati, H. and Kuberan, B. (2017) 'Repurposing of Proton Pump Inhibitors as first identified small molecule inhibitors of endo- $\beta$ -N-acetylglucosaminidase (ENGase) for the treatment of NGLY1 deficiency, a rare genetic disease', *Bioorganic & Medicinal Chemistry Letters*, 27(13), 2962-2966.

Biancalana, M. and Koide, S. (2010) 'Molecular Mechanism of Thioflavin-T Binding to Amyloid Fibrils', *Biochimica et biophysica acta*, 1804(7), 1405-1412.

Biswas, M. and Chan, J. Y. (2010) 'Role of Nrf1 in antioxidant response element-mediated gene expression and beyond', *Toxicol Appl Pharmacol*, 244(1), 16-20.

Bjørkøy, G., Lamark, T., Brech, A., Outzen, H., Perander, M., Øvervatn, A., Stenmark, H. and Johansen, T. (2005) 'p62/SQSTM1 forms protein aggregates degraded by autophagy and has a protective effect on huntingtin-induced cell death', *The Journal of Cell Biology*, 171(4), 603-614.

Blacker, T. S. and Duchen, M. R. (2016) 'Investigating mitochondrial redox state using NADH and NADPH autofluorescence', *Free Radic Biol Med*, 100, 53-65.

Blesa, J. R., Prieto-Ruiz, J. A., Abraham, B. A., Harrison, B. L., Hegde, A. A. and Hernández-Yago, J. (2008) 'NRF-1 is the major transcription factor regulating the expression of the human TOMM34 gene', *Biochemistry and Cell Biology*, 86(1), 46-56.

Bodaleo, F. J., Montenegro-Venegas, C., Henríquez, D. R., Court, F. A. and Gonzalez-Billault, C. (2016) 'Microtubule-associated protein 1B (MAP1B)-deficient neurons show structural presynaptic deficiencies in vitro and altered presynaptic physiology', *Scientific Reports*, 6, 30069.

Bond, M. R. and Hanover, J. A. (2015) 'A little sugar goes a long way: The cell biology of O-GlcNAc', *The Journal of Cell Biology*, 208(7), 869.

Brazelton, V. A., Jr., Zarecor, S., Wright, D. A., Wang, Y., Liu, J., Chen, K., Yang, B. and Lawrence-Dill, C. J. (2015) 'A quick guide to CRISPR sgRNA design tools', *GM Crops Food*, 6(4), 266-76.

Brentnall, M., Rodriguez-Menocal, L., De Guevara, R. L., Cepero, E. and Boise, L. H. (2013) 'Caspase-9, caspase-3 and caspase-7 have distinct roles during intrinsic apoptosis', *BMC Cell Biol*, 14, 32.

Brinkman, E. K., Chen, T., Amendola, M. and van Steensel, B. (2014) 'Easy quantitative assessment of genome editing by sequence trace decomposition', *Nucleic Acids Research*, 42(22), e168-e168.

Brinkmann, K., Schell, M., Hoppe, T. and Kashkar, H. (2015) 'Regulation of the DNA damage response by ubiquitin conjugation', *Front Genet*, 6, 98.

Brzostowski, J. A., Sawai, S., Rozov, O., Liao, X.-h., Imoto, D., Parent, C. A. and Kimmel, A. R. (2013) 'Phosphorylation of chemoattractant receptors regulates chemotaxis, actin reorganization and signal relay', *Journal of Cell Science*, 126(20), 4614-4626.

Burnham-Marusich, A. R. and Berninsone, P. M. (2012) 'Multiple proteins with essential mitochondrial functions have glycosylated isoforms', *Mitochondrion*, 12(4), 423-427.

Burton, T. R. and Gibson, S. B. (2009) 'The role of Bcl-2 family member BNIP3 in cell death and disease: NIPping at the heels of cell death', *Cell death and differentiation*, 16(4), 515-523.

Button, R. W., Luo, S. and Rubinsztein, D. C. (2015) 'Autophagic activity in neuronal cell death', *Neurosci Bull*, 31(4), 382-94.

Caffrey, D. R., Zhao, J., Song, Z., Schaffer, M. E., Haney, S. A., Subramanian, R. R., Seymour, A. B. and Hughes, J. D. (2011) 'siRNA Off-Target Effects Can Be Reduced at Concentrations That Match Their Individual Potency', *PLOS ONE*, 6(7), e21503.

Caglayan, A. O., Comu, S., Baranoski, J. F., Parman, Y., Kaymakçalan, H., Akgumus, G. T., Caglar, C., Dolen, D., Erson-Omay, E. Z., Harmanci, A. S., Mishra-Gorur, K., Freeze, H. H., Yasuno, K., Bilguvar, K. and Gunel, M. (2015) 'NGLY1 mutation causes neuromotor impairment, intellectual disability, and neuropathy', *European Journal of Medical Genetics*, 58(1), 39-43.

Cagnol, S. and Chambard, J.-C. (2010) 'ERK and cell death: Mechanisms of ERK-induced cell death – apoptosis, autophagy and senescence', *FEBS Journal*, 277(1), 2-21.

Caldecott, K. W. (2008) 'Single-strand break repair and genetic disease', *Nat Rev Genet*, 9(8), 619-31.

Callus, B. A. and Vaux, D. L. (2006) 'Caspase inhibitors: viral, cellular and chemical', *Cell death and differentiation*, 14, 73.

Cameron, M., Kékesi, O., Morley, J. W., Tapson, J., Breen, P. P., van Schaik, A. and Buskila, Y. (2016) 'Calcium Imaging of AM Dyes Following Prolonged Incubation in Acute Neuronal Tissue', *PLOS ONE*, 11(5), e0155468.

Cannino, G., El-Khoury, R., Pirinen, M., Hutz, B., Rustin, P., Jacobs, H. T. and Dufour, E. (2012) 'Glucose Modulates Respiratory Complex I Activity in Response to Acute Mitochondrial Dysfunction', *The Journal of Biological Chemistry*, 287(46), 38729-38740.

Cargnello, M. and Roux, P. P. (2011) 'Activation and function of the MAPKs and their substrates, the MAPK-activated protein kinases', *Microbiol Mol Biol Rev*, 75(1), 50-83.

Carter, J. and Wiedenheft, B. (2015) 'SnapShot: CRISPR-RNA-guided adaptive immune systems', *Cell*, 163(1), 260-260.e1.

- Caserta, T. M., Smith, A. N., Gultice, A. D., Reedy, M. A. and Brown, T. L. (2003) 'Q-VD-OPh, a broad spectrum caspase inhibitor with potent antiapoptotic properties', *Apoptosis*, 8(4), 345-52.
- Cebollero, E., Reggiori, F. and Kraft, C. (2012) 'Reticulophagy and Ribophagy: Regulated Degradation of Protein Production Factories', *International Journal of Cell Biology*, 2012, 9.
- Chan, X. a. C. Y., Black, C. M., Lin, A. J., Ping, P. and Lau, E. (2015) 'Mitochondrial protein turnover: methods to measure turnover rates on a large scale', *Journal of molecular and cellular cardiology*, 78, 54-61.
- Chang, H. Y. and Yang, X. (2000) 'Proteases for Cell Suicide: Functions and Regulation of Caspases', *Microbiology and Molecular Biology Reviews*, 64(4), 821-846.
- Chantret, I., Fasseu, M., Zaoui, K., Le Bizec, C., Sadou Yayé, H., Dupré, T. and Moore, S. E. H. (2010) 'Identification of Roles for Peptide: *N*-Glycanase and Endo- $\beta$ -*N*-Acetylglucosaminidase (Engase1p) during Protein *N*-Glycosylation in Human HepG2 Cells', *PLOS ONE*, 5(7), e11734.
- Chatre, L. and Ricchetti, M. (2013) 'Large heterogeneity of mitochondrial DNA transcription and initiation of replication exposed by single-cell imaging', *Journal of Cell Science*, 126(4), 914.
- Chauvier, D., Ankri, S., Charriaut-Marlangue, C., Casimir, R. and Jacotot, E. (2006) 'Broad-spectrum caspase inhibitors: from myth to reality?', *Cell death and differentiation*, 14, 387.
- Chen, Q., Miller, L. J. and Dong, M. (2010) 'Role of N-linked glycosylation in biosynthesis, trafficking, and function of the human glucagon-like peptide 1 receptor', *American Journal of Physiology - Endocrinology and Metabolism*, 299(1), E62-E68.
- Chen, R., Zou, Y., Mao, D., Sun, D., Gao, G., Shi, J., Liu, X., Zhu, C., Yang, M., Ye, W., Hao, Q., Li, R. and Yu, L. (2014) 'The general amino acid control pathway regulates mTOR and autophagy during serum/glutamine starvation', *J Cell Biol*, 206(2), 173-82.
- Chen, S.-y., Chiu, L.-Y., Maa, M.-C., Wang, J.-S., Chien, C.-L. and Lin, W.-W. (2011) 'zVAD-induced autophagic cell death requires c-Src-dependent ERK and JNK activation and reactive oxygen species generation', *Autophagy*, 7(2), 217-228.
- Chen, S., Zhou, L., Zhang, Y., Leng, Y., Pei, X. Y., Lin, H., Jones, R., Orlowski, R. Z., Dai, Y. and Grant, S. (2014) 'Targeting SQSTM1/p62 induces cargo loading failure and converts autophagy to apoptosis via NBK/Bik', *Mol Cell Biol*, 34(18), 3435-49.
- Chen, Y., Azad, M. B. and Gibson, S. B. (2009) 'Superoxide is the major reactive oxygen species regulating autophagy', *Cell Death Differ*, 16(7), 1040-52.
- Cheng, B., Martinez, A. A., Morado, J., Scofield, V., Roberts, J. L. and Maffi, S. K. (2013) 'Retinoic acid protects against proteasome inhibition associated cell death in SH-SY5Y cells via the AKT pathway', *Neurochem Int*, 62(1), 31-42.

- Cheng, Y., Qiu, F., Huang, J., Tashiro, S.-i., Onodera, S. and Ikejima, T. (2008) 'Apoptosis-suppressing and autophagy-promoting effects of calpain on oridonin-induced L929 cell death', *Archives of Biochemistry and Biophysics*, 475(2), 148-155.
- Cheong, H., Lindsten, T., Wu, J., Lu, C. and Thompson, C. B. (2011) 'Ammonia-induced autophagy is independent of ULK1/ULK2 kinases', *Proc Natl Acad Sci U S A*, 108(27), 11121-6.
- Choe, K. P. and Leung, C. K. (2013) 'SKN-1/Nrf, A New Unfolded Protein Response Factor?', *PLOS Genetics*, 9(9), e1003827.
- Christianson, J. C., Olzmann, J. A., Shaler, T. A., Sowa, M. E., Bennett, E. J., Richter, C. M., Tyler, R. E., Greenblatt, E. J., Harper, J. W. and Kopito, R. R. (2011) 'Defining human ERAD networks through an integrative mapping strategy', *Nat Cell Biol*, 14(1), 93-105.
- Christianson, J. C. and Ye, Y. (2014) 'Cleaning up in the endoplasmic reticulum: ubiquitin in charge', *Nature Structural & Molecular Biology*, 21, 325.
- Codogno, P., Mehrpour, M. and Proikas-Cezanne, T. (2011) 'Canonical and non-canonical autophagy: variations on a common theme of self-eating?', *Nature Reviews Molecular Cell Biology*, 13, 7.
- Confer, A. W. and Ayalew, S. (2013) 'The OmpA family of proteins: Roles in bacterial pathogenesis and immunity', *Veterinary Microbiology*, 163(3-4), 207-222.
- Cong, L., Ran, F. A., Cox, D., Lin, S., Barretto, R., Habib, N., Hsu, P. D., Wu, X., Jiang, W., Marraffini, L. A. and Zhang, F. (2013) 'Multiplex Genome Engineering Using CRISPR/Cas Systems', *Science*, 339(6121), 819.
- Cook, K. L., Soto-Pantoja, D. R., Abu-Asab, M., Clarke, P. A. G., Roberts, D. D. and Clarke, R. (2014) 'Mitochondria directly donate their membrane to form autophagosomes during a novel mechanism of parkin-associated mitophagy', *Cell & Bioscience*, 4, 16-16.
- Copp, J., Manning, G. and Hunter, T. (2009) 'TORC-specific phosphorylation of mammalian target of rapamycin (mTOR): phospho-Ser2481 is a marker for intact mTOR signaling complex 2', *Cancer Res*, 69(5), 1821-7.
- Cottrell, J. S. (2011) 'Protein identification using MS/MS data', *Journal of Proteomics*, 74(10), 1842-1851.
- Cowburn, White, J., Deighton, J., Walmsley, S. and Chilvers, E. (2005) 'z-VAD-fmk augmentation of TNF $\alpha$ -stimulated neutrophil apoptosis is compound specific and does not involve the generation of reactive oxygen species', *Blood*, 105(7), 2970.
- Criddle, D. N., Gillies, S., Baumgartner-Wilson, H. K., Jaffar, M., Chinje, E. C., Passmore, S., Chvanov, M., Barrow, S., Gerasimenko, O. V., Tepikin, A. V., Sutton, R. and Petersen, O. H.

(2006) 'Menadione-induced reactive oxygen species generation via redox cycling promotes apoptosis of murine pancreatic acinar cells', *J Biol Chem*, 281(52), 40485-92.

Cullinan, S. B., Zhang, D., Hannink, M., Arvisais, E., Kaufman, R. J. and Diehl, J. A. (2003) 'Nrf2 Is a Direct PERK Substrate and Effector of PERK-Dependent Cell Survival', *Molecular and Cellular Biology*, 23(20), 7198-7209.

Dandekar, A., Mendez, R. and Zhang, K. (2015) 'Cross talk between ER stress, oxidative stress, and inflammation in health and disease', *Methods Mol Biol*, 1292, 205-14.

Daniels, S. M., Melendez-Peña, C. E., Scarborough, R. J., Daher, A., Christensen, H. S., El Far, M., Purcell, D. F. J., Lainé, S. and Gatignol, A. (2009) 'Characterization of the TRBP domain required for Dicer interaction and function in RNA interference', *BMC Molecular Biology*, 10(1), 38.

del Alamo, M., Hogan, D. J., Pechmann, S., Albanese, V., Brown, P. O. and Frydman, J. (2011) 'Defining the specificity of cotranslationally acting chaperones by systematic analysis of mRNAs associated with ribosome-nascent chain complexes', *PLoS Biol*, 9(7), e1001100.

Dell'Antone, P. (2012) 'Energy metabolism in cancer cells: How to explain the Warburg and Crabtree effects?', *Medical Hypotheses*, 79(3), 388-392.

Dengjel, J., Høyer-Hansen, M., Nielsen, M. O., Eisenberg, T., Harder, L. M., Schandorff, S., Farkas, T., Kirkegaard, T., Becker, A. C., Schroeder, S., Vanselow, K., Lundberg, E., Nielsen, M. M., Kristensen, A. R., Akimov, V., Bunkenborg, J., Madeo, F., Jäättelä, M. and Andersen, J. S. (2012) 'Identification of Autophagosome-associated Proteins and Regulators by Quantitative Proteomic Analysis and Genetic Screens', *Mol Cell Proteomics*, 11(3), M111.014035.

Deszcz, L., Seipelt, J., Vassilieva, E., Roetzer, A. and Kuechler, E. (2004) 'Antiviral activity of caspase inhibitors: Effect on picornaviral 2A proteinase', *FEBS Letters*, 560(1-3), 51-55.

Dey, S., Sidor, A. and O'Rourke, B. (2016) 'Compartment-specific Control of Reactive Oxygen Species Scavenging by Antioxidant Pathway Enzymes', *The Journal of Biological Chemistry*, 291(21), 11185-11197.

Diaz-Ruiz, R., Rigoulet, M. and Devin, A. (2011) 'The Warburg and Crabtree effects: On the origin of cancer cell energy metabolism and of yeast glucose repression', *Biochimica et Biophysica Acta (BBA) - Bioenergetics*, 1807(6), 568-576.

Digaleh, H., Kiaei, M. and Khodagholi, F. (2013) 'Nrf2 and Nrf1 signaling and ER stress crosstalk: implication for proteasomal degradation and autophagy', *Cell Mol Life Sci*, 70(24), 4681-94.

Dimroth, P., Kaim, G. and Matthey, U. (2000) 'Crucial role of the membrane potential for ATP synthesis by F(1)F(o) ATP synthases', *J Exp Biol*, 203(Pt 1), 51-9.

- Ding, W.-X. and Eskelinen, E.-L. (2014) 'Do mitochondria donate membrane to form autophagosomes or undergo remodeling to form mitochondrial spheroids?', *Cell & Bioscience*, 4, 65.
- Ding, W.-X. and Yin, X.-M. (2012) 'Mitophagy: mechanisms, pathophysiological roles, and analysis', *Biol Chem*, 393(7), 547-564.
- Dong, K., Sun, X. and Ke, G. (2013) 'Involvement of Autophagy in z-VAD-FMK Induced Photoreceptor Necroptosis, a Caspase-Independent Cell Death, after Experimental Retinal Detachment', *Investigative Ophthalmology & Visual Science*, 54(15), 2854-2854.
- Dott, W., Mistry, P., Wright, J., Cain, K. and Herbert, K. E. (2014) 'Modulation of mitochondrial bioenergetics in a skeletal muscle cell line model of mitochondrial toxicity', *Redox Biology*, 2, 224-233.
- Du, H., Huang, Y., Zaghlula, M., Walters, E., Cox, T. C. and Massiah, M. A. (2013) 'The MID1 E3 Ligase Catalyzes the Polyubiquitination of Alpha4 ( $\alpha$ 4), a Regulatory Subunit of Protein Phosphatase 2A (PP2A): NOVEL INSIGHTS INTO MID1-MEDIATED REGULATION OF PP2A', *The Journal of Biological Chemistry*, 288(29), 21341-21350.
- Duan, G. and Walther, D. (2015) 'The Roles of Post-translational Modifications in the Context of Protein Interaction Networks', *PLoS Computational Biology*, 11(2), e1004049.
- Durnin, L., Lees, A., Manzoor, S., Sasse, K. C., Sanders, K. M. and Mutafova-Yambolieva, V. N. (2017) 'Loss of nitric oxide-mediated inhibition of purine neurotransmitter release in the colon in the absence of interstitial cells of Cajal', *Am J Physiol Gastrointest Liver Physiol*, 313(5), G419-g433.
- Edberg, J. C. and Kimberly, R. P. (1997) 'Cell type-specific glycoforms of Fc gamma R11a (CD16): differential ligand binding', *J Immunol*, 159(8), 3849-57.
- Eizirik, D. L., Miani, M. and Cardozo, A. K. (2013) 'Signalling danger: endoplasmic reticulum stress and the unfolded protein response in pancreatic islet inflammation', *Diabetologia*, 56(2), 234-41.
- Elia, Andrew E. H., Boardman, Alexander P., Wang, David C., Huttlin, Edward L., Everley, Robert A., Dephoure, N., Zhou, C., Koren, I., Gygi, Steven P. and Elledge, Stephen J. (2015) 'Quantitative Proteomic Atlas of Ubiquitination and Acetylation in the DNA Damage Response', *Mol Cell*, 59(5), 867-881.
- Ellgaard, L. and Helenius, A. (2003) 'Quality control in the endoplasmic reticulum', *Nature Reviews Molecular Cell Biology*, 4, 181.
- Ellgaard, L., McCaul, N., Chatsisvili, A. and Braakman, I. (2016) 'Co- and Post-Translational Protein Folding in the ER', *Traffic*, 17(6), 615-38.
- Enns, G. M., Shashi, V., Bainbridge, M., Gambello, M. J., Zahir, F. R., Bast, T., Crimian, R., Schoch, K., Platt, J., Cox, R., Bernstein, J. A., Scavina, M., Walter, R. S., Bibb, A., Jones, M.,



Hegde, M., Graham, B. H., Need, A. C., Oviedo, A., Schaaf, C. P., Boyle, S., Butte, A. J., Chen, R., Clark, M. J., Haraksingh, R., Cowan, T. M., He, P., Langlois, S., Zoghbi, H. Y., Snyder, M., Gibbs, R. A., Freeze, H. H. and Goldstein, D. B. (2014) 'Mutations in NGLY1 cause an inherited disorder of the endoplasmic reticulum-associated degradation pathway', *Genet Med*, 16(10), 751-758.

Fabbro, D., Cowan-Jacob, S. W. and Moebitz, H. (2015) 'Ten things you should know about protein kinases: IUPHAR Review 14', *British Journal of Pharmacology*, 172(11), 2675-2700.

Fahie, K. and Zachara, N. E. (2016) 'Molecular Functions of Glycoconjugates in Autophagy', *Journal of Molecular Biology*, 428(16), 3305-3324.

Fang, E. F., Lautrup, S., Hou, Y., Demarest, T. G., Croteau, D. L., Mattson, M. P. and Bohr, V. A. (2017) 'NAD<sup>+</sup> in Aging: Molecular Mechanisms and Translational Implications', *Trends in Molecular Medicine*, 23(10), 899-916.

Feng, Y., He, D., Yao, Z. and Klionsky, D. J. (2013) 'The machinery of macroautophagy', *Cell Research*, 24, 24.

Ferris, S. P., Kodali, V. K. and Kaufman, R. J. (2014) 'Glycoprotein folding and quality-control mechanisms in protein-folding diseases', *Disease Models & Mechanisms*, 7(3), 331.

Fischer, H., Polikarpov, I. and Craievich, A. F. (2004) 'Average protein density is a molecular-weight-dependent function', *Protein Science : A Publication of the Protein Society*, 13(10), 2825-2828.

Fischer-Kierzkowska, A., Vydra, N., Wysocka-Wycisk, A., Kronekova, Z., Jarzab, M., Lisowska, K. M. and Krawczyk, Z. (2011) 'Liposome-based DNA carriers may induce cellular stress response and change gene expression pattern in transfected cells', *BMC Molecular Biology*, 12(1), 27.

Fransolet, M., Henry, L., Labied, S., Noel, A., Nisolle, M. and Munaut, C. (2015) 'In vitro evaluation of the anti-apoptotic drug Z-VAD-FMK on human ovarian granulosa cell lines for further use in ovarian tissue transplantation', *J Assist Reprod Genet*, 32(10), 1551-9.

Freeze, Hudson H., Chong, Jessica X., Bamshad, Michael J. and Ng, Bobby G. (2014) 'Solving Glycosylation Disorders: Fundamental Approaches Reveal Complicated Pathways', *The American Journal of Human Genetics*, 94(2), 161-175.

Frottin, F., Bienvenut, W. V., Bignon, J., Jacquet, E., Jacome, A. S. V., Van Dorsselaer, A., Cianferani, S., Carapito, C., Meinel, T. and Giglione, C. (2016) 'MetAP1 and MetAP2 drive cell selectivity for a potent anti-cancer agent in synergy, by controlling glutathione redox state', *Oncotarget*, 7(39), 63306-63323.

Fu, H., Subramanian, R. R. and Masters, S. C. (2000) '14-3-3 Proteins: Structure, Function, and Regulation', *Annual Review of Pharmacology and Toxicology*, 40(1), 617-647.

Fujihira, H., Masahara-Negishi, Y., Tamura, M., Huang, C., Harada, Y., Wakana, S., Takakura, D., Kawasaki, N., Taniguchi, N., Kondoh, G., Yamashita, T., Funakoshi, Y. and Suzuki, T. (2017) 'Lethality of mice bearing a knockout of the Ngly1-gene is partially rescued by the additional deletion of the Engase gene', *PLOS Genetics*, 13(4), e1006696.

Fujita, M., Watanabe, R., Jaensch, N., Romanova-Michaelides, M., Satoh, T., Kato, M., Riezman, H., Yamaguchi, Y., Maeda, Y. and Kinoshita, T. (2011) 'Sorting of GPI-anchored proteins into ER exit sites by p24 proteins is dependent on remodeled GPI', *J Cell Biol*, 194(1), 61-75.

Funakoshi, Y., Negishi, Y., Gergen, J. P., Seino, J., Ishii, K., Lennarz, W. J., Matsuo, I., Ito, Y., Taniguchi, N. and Suzuki, T. (2010) 'Evidence for an Essential Deglycosylation-Independent Activity of PNGase in *Drosophila melanogaster*', *PLOS ONE*, 5(5), e10545.

Furda, A., Santos, J. H., Meyer, J. N. and Van Houten, B. (2014) 'Quantitative PCR-Based Measurement of Nuclear and Mitochondrial DNA Damage and Repair in Mammalian Cells', *Methods Mol Biol*, 1105, 419-437.

Galli, C., Bernasconi, R., Soldà, T., Calanca, V. and Molinari, M. (2011) 'Malectin Participates in a Backup Glycoprotein Quality Control Pathway in the Mammalian ER', *PLOS ONE*, 6(1), e16304.

Galluzzi, L., Baehrecke, E. H., Ballabio, A., Boya, P., Bravo-San Pedro, J. M., Cecconi, F., Choi, A. M., Chu, C. T., Codogno, P., Colombo, M. I., Cuervo, A. M., Debnath, J., Deretic, V., Dikic, I., Eskelinen, E. L., Fimia, G. M., Fulda, S., Gewirtz, D. A., Green, D. R., Hansen, M., Harper, J. W., Jaattela, M., Johansen, T., Juhasz, G., Kimmelman, A. C., Kraft, C., Ktistakis, N. T., Kumar, S., Levine, B., Lopez-Otin, C., Madeo, F., Martens, S., Martinez, J., Melendez, A., Mizushima, N., Munz, C., Murphy, L. O., Penninger, J. M., Piacentini, M., Reggiori, F., Rubinsztein, D. C., Ryan, K. M., Santambrogio, L., Scorrano, L., Simon, A. K., Simon, H. U., Simonsen, A., Tavernarakis, N., Tooze, S. A., Yoshimori, T., Yuan, J., Yue, Z., Zhong, Q. and Kroemer, G. (2017) 'Molecular definitions of autophagy and related processes', *Embo j*, 36(13), 1811-1836.

Gao, F., Chen, D., Si, J., Hu, Q., Qin, Z., Fang, M. and Wang, G. (2015) 'The mitochondrial protein BNIP3L is the substrate of PARK2 and mediates mitophagy in PINK1/PARK2 pathway', *Hum Mol Genet*, 24(9), 2528-38.

Gao, W., Chen, Z., Wang, W. and Stang, M. T. (2013) 'E1-Like Activating Enzyme Atg7 Is Preferentially Sequestered into p62 Aggregates via Its Interaction with LC3-I', *PLOS ONE*, 8(9), e73229.

Garcia-Calvo, M., Peterson, E. P., Leiting, B., Ruel, R., Nicholson, D. W. and Thornberry, N. A. (1998) 'Inhibition of human caspases by peptide-based and macromolecular inhibitors', *J Biol Chem*, 273(49), 32608-13.

Ge, L., Melville, D., Zhang, M. and Schekman, R. (2013) 'The ER-Golgi intermediate compartment is a key membrane source for the LC3 lipidation step of autophagosome biogenesis', *eLife*, 2, e00947.

- Ge, L. and Schekman, R. (2014) 'The ER-Golgi intermediate compartment feeds the phagophore membrane', *Autophagy*, 10(1), 170-2.
- Genereux, J. C. and Wiseman, R. L. (2015) 'Regulating extracellular proteostasis capacity through the unfolded protein response', *Prion*, 9(1), 10-21.
- Gerasimenko, J. V., Petersen, O. H. and Gerasimenko, O. V. (2014) 'Monitoring of intra-ER free Ca<sup>2+</sup>', *Wiley Interdisciplinary Reviews: Membrane Transport and Signaling*, 3(3), 63-71.
- Ghoshal, P., Rajendran, M., Odo, N. and Ikuta, T. (2014) 'Glycosylation inhibitors efficiently inhibit P-selectin-mediated cell adhesion to endothelial cells', *PLOS ONE*, 9(6), e99363.
- Gigout, A., Jolicoeur, M. and Buschmann, M. D. (2005) 'Low calcium levels in serum-free media maintain chondrocyte phenotype in monolayer culture and reduce chondrocyte aggregation in suspension culture', *Osteoarthritis and Cartilage*, 13(11), 1012-1024.
- Gitlin, I., Carbeck, J. D. and Whitesides, G. M. (2006) 'Why are proteins charged? Networks of charge-charge interactions in proteins measured by charge ladders and capillary electrophoresis', *Angew Chem Int Ed Engl*, 45(19), 3022-60.
- Gosain, A., Lohia, R., Shrivastava, A. and Saran, S. (2012) 'Identification and characterization of peptide: N- glycanase from *Dictyostelium discoideum*', *BMC Biochemistry*, 13, 9-9.
- Gray, L. R., Tompkins, S. C. and Taylor, E. B. (2014) 'Regulation of pyruvate metabolism and human disease', *Cellular and Molecular Life Sciences*, 71(14), 2577-2604.
- Greenbaum, D., Colangelo, C., Williams, K. and Gerstein, M. (2003) 'Comparing protein abundance and mRNA expression levels on a genomic scale', *Genome Biology*, 4(9), 117-117.
- Gregoire, S., Irwin, J. and Kwon, I. (2012) 'Techniques for Monitoring Protein Misfolding and Aggregation in Vitro and in Living Cells', *The Korean journal of chemical engineering*, 29(6), 693-702.
- Groenning, M., Olsen, L., van de Weert, M., Flink, J. M., Frokjaer, S. and Jorgensen, F. S. (2007) 'Study on the binding of Thioflavin T to beta-sheet-rich and non-beta-sheet cavities', *J Struct Biol*, 158(3), 358-69.
- Grotzke, J. E., Lu, Q. and Cresswell, P. (2013) 'Deglycosylation-dependent fluorescent proteins provide unique tools for the study of ER-associated degradation', *Proceedings of the National Academy of Sciences of the United States of America*, 110(9), 3393-3398.
- Grünewald, S. (2009) 'The clinical spectrum of phosphomannomutase 2 deficiency (CDG-1a)', *Biochimica et Biophysica Acta (BBA) - Molecular Basis of Disease*, 1792(9), 827-834.
- Gundersen, V. (2010) 'Protein aggregation in Parkinson's disease', *Acta Neurol Scand Suppl*, (190), 82-7.

- Guo, J. Y. and White, E. (2016) 'Autophagy, Metabolism, and Cancer', Cold Spring Harbor symposia on quantitative biology, 81, 73-78.
- Guo, Q., Mintier, G., Ma-Edmonds, M., Storton, D., Wang, X., Xiao, X., Kienzle, B., Zhao, D. and Feder, J. N. (2018) 'Cold shock' increases the frequency of homology directed repair gene editing in induced pluripotent stem cells', Scientific Reports, 8(1), 2080.
- Guppy, M., Leedman P Fau - Zu, X., Zu X Fau - Russell, V. and Russell, V. (2002) 'Contribution by different fuels and metabolic pathways to the total ATP turnover of proliferating MCF-7 breast cancer cells', (0264-6021 (Print)).
- Habibi-Babadi, N., Su, A., de Carvalho, C. E. and Colavita, A. (2010) 'The N-glycanase png-1 acts to limit axon branching during organ formation in *Caenorhabditis elegans*', J Neurosci, 30(5), 1766-76.
- Hadano, S., Hand, C. K., Osuga, H., Yanagisawa, Y., Otomo, A., Devon, R. S., Miyamoto, N., Showguchi-Miyata, J., Okada, Y., Singaraja, R., Figlewicz, D. A., Kwiatkowski, T., Hosler, B. A., Sagie, T., Skaug, J., Nasir, J., Brown, R. H., Jr., Scherer, S. W., Rouleau, G. A., Hayden, M. R. and Ikeda, J. E. (2001) 'A gene encoding a putative GTPase regulator is mutated in familial amyotrophic lateral sclerosis 2', Nat Genet, 29(2), 166-73.
- Hailey, D. W., Kim, P. K., Satpute-Krishnan, P., Rambold, A. S., Mitra, K., Sougrat, R. and Lippincott-Schwartz, J. (2010) 'Mitochondria supply membranes for autophagosome biogenesis during starvation', Cell, 141(4), 656-667.
- Hammadi, M., Oulidi, A., Gackiere, F., Katsogiannou, M., Slomianny, C., Roudbaraki, M., Dewailly, E., Delcourt, P., Lepage, G., Lotteau, S., Ducreux, S., Prevarskaya, N. and Van Coppenolle, F. (2013) 'Modulation of ER stress and apoptosis by endoplasmic reticulum calcium leak via translocon during unfolded protein response: involvement of GRP78', Faseb j, 27(4), 1600-9.
- Hanna, R. A., Quinsay, M. N., Orogo, A. M., Giang, K., Rikka, S. and Gustafsson, Å. B. (2012) 'Microtubule-associated Protein 1 Light Chain 3 (LC3) Interacts with Bnip3 Protein to Selectively Remove Endoplasmic Reticulum and Mitochondria via Autophagy', The Journal of Biological Chemistry, 287(23), 19094-19104.
- Hannus, M., Beitzinger, M., Engelmann, J. C., Weickert, M.-T., Spang, R., Hannus, S. and Meister, G. (2014) 'siPools: highly complex but accurately defined siRNA pools eliminate off-target effects', Nucleic Acids Research, 42(12), 8049-8061.
- Hanson, H. H., Kang, S., Fernández-Monreal, M., Oung, T., Yildirim, M., Lee, R., Suyama, K., Hazan, R. B. and Phillips, G. R. (2010) 'LC3-dependent Intracellular Membrane Tubules Induced by  $\gamma$ -Protocadherins A3 and B2: A ROLE FOR INTRALUMINAL INTERACTIONS', The Journal of Biological Chemistry, 285(27), 20982-20992.
- Hara, T., Nakamura, K., Matsui, M., Yamamoto, A., Nakahara, Y., Suzuki-Migishima, R., Yokoyama, M., Mishima, K., Saito, I., Okano, H. and Mizushima, N. (2006) 'Suppression of

- basal autophagy in neural cells causes neurodegenerative disease in mice', *Nature*, 441(7095), 885-889.
- Harayama, T. and Riezman, H. (2017) 'Detection of genome-edited mutant clones by a simple competition-based PCR method', *PLOS ONE*, 12(6), e0179165.
- Harder, L. M., Bunkenborg, J. and Andersen, J. S. (2014) 'Inducing autophagy: a comparative phosphoproteomic study of the cellular response to ammonia and rapamycin', *Autophagy*, 10(2), 339-55.
- Hartl, F. U., Bracher, A. and Hayer-Hartl, M. (2011) 'Molecular chaperones in protein folding and proteostasis', *Nature*, 475(7356), 324-332.
- Hartl, F. U. and Hayer-Hartl, M. (2009) 'Converging concepts of protein folding in vitro and in vivo', *Nature Structural & Molecular Biology*, 16, 574.
- Hashimoto, M., Rockenstein, E., Crews, L. and Masliah, E. (2003) 'Role of protein aggregation in mitochondrial dysfunction and neurodegeneration in Alzheimer's and Parkinson's diseases', *Neuromolecular Med*, 4(1-2), 21-36.
- Hassink, G., Kikkert, M., Voorden, Sjaak v., Lee, S.-J., Spaapen, R., Laar, Theo v., Coleman, Catherine S., Bartee, E., Früh, K., Chau, V. and Wiertz, E. (2005) 'TEB4 is a C4HC3 RING finger-containing ubiquitin ligase of the endoplasmic reticulum', *Biochemical Journal*, 388(Pt 2), 647-655.
- Hast, B. E., Goldfarb, D., Mulvaney, K. M., Hast, M. A., Siesser, P. F., Yan, F., Hayes, D. N. and Major, M. B. (2013) 'Proteomic analysis of ubiquitin ligase KEAP1 reveals associated proteins that inhibit NRF2 ubiquitination', *Cancer Research*, 73(7), 2199-2210.
- Haze, K., Yoshida, H., Yanagi, H., Yura, T. and Mori, K. (1999) 'Mammalian Transcription Factor ATF6 Is Synthesized as a Transmembrane Protein and Activated by Proteolysis in Response to Endoplasmic Reticulum Stress', *Molecular Biology of the Cell*, 10(11), 3787-3799.
- He, J., Yi, B., Chen, Y., Huang, Q., Wang, H., Lu, K. and Fu, W. (2017) 'The ET-1-mediated carbonylation and degradation of ANXA1 induce inflammatory phenotype and proliferation of pulmonary artery smooth muscle cells in HPS', *PLOS ONE*, 12(4), e0175443.
- He, M., Zhou, Z., Shah, A. A., Zou, H., Tao, J., Chen, Q. and Wan, Y. (2016) 'The emerging role of deubiquitinating enzymes in genomic integrity, diseases, and therapeutics', *Cell & Bioscience*, 6(1), 62.
- He, P., Grotzke, J. E., Ng, B. G., Gunel, M., Jafar-Nejad, H., Cresswell, P., Enns, G. M. and Freeze, H. H. (2015) 'A congenital disorder of deglycosylation: Biochemical characterization of N-glycanase 1 deficiency in patient fibroblasts', *Glycobiology*, 25(8), 836-844.
- Heinrichs, A. (2008) 'Ribophagy: selective ribosome eating', *Nature Reviews Molecular Cell Biology*, 9, 348.

- Helenius, A. and Aebi, M. (2001) 'Intracellular Functions of N-Linked Glycans', *Science*, 291(5512), 2364-2369.
- Henley, J. M., Craig, T. J. and Wilkinson, K. A. (2014) 'Neuronal SUMOylation: Mechanisms, Physiology, and Roles in Neuronal Dysfunction', *Physiological Reviews*, 94(4), 1249-1285.
- Henry, O., Jolicoeur, M. and Kamen, A. (2011) 'Unraveling the metabolism of HEK-293 cells using lactate isotopomer analysis', *Bioprocess and Biosystems Engineering*, 34(3), 263-273.
- Herzog, C., Yang, C., Holmes, A. and Kaushal, G. P. (2012) 'zVAD-fmk prevents cisplatin-induced cleavage of autophagy proteins but impairs autophagic flux and worsens renal function', *American Journal of Physiology - Renal Physiology*, 303(8), F1239-F1250.
- Hewitt, G. and Korolchuk, V. I. 'Repair, Reuse, Recycle: The Expanding Role of Autophagy in Genome Maintenance', *Trends in Cell Biology*, 27(5), 340-351.
- Hirayama, H., Hosomi, A. and Suzuki, T. (2014) 'Physiological and molecular functions of the cytosolic peptide:N-glycanase', *Seminars in cell & developmental biology*, (0).
- Hirsch, C., Blom, D. and Ploegh, H. L. (2003) 'A role for N-glycanase in the cytosolic turnover of glycoproteins', *The EMBO Journal*, 22(5), 1036-1046.
- Hirsch, C., Gauss, R., Horn, S. C., Neuber, O. and Sommer, T. (2009) 'The ubiquitylation machinery of the endoplasmic reticulum', *Nature*, 458(7237), 453-60.
- Hong, S. W., Jiang, Y., Kim, S., Li, C. J. and Lee, D.-k. (2014) 'Target Gene Abundance Contributes to the Efficiency of siRNA-Mediated Gene Silencing', *Nucleic Acid Therapeutics*, 24(3), 192-198.
- Hoogenraad, C. C. and van der Sluijs, P. (2010) 'GRASP-1 regulates endocytic receptor recycling and synaptic plasticity', *Communicative & Integrative Biology*, 3(5), 433-435.
- Hosomi, A. and Suzuki, T. (2015) 'Cytosolic peptide:N-glycanase cleaves N-glycans on a carboxypeptidase Y mutant during ERAD in *Saccharomyces cerevisiae*', *Biochimica et Biophysica Acta (BBA) - General Subjects*, 1850(4), 612-619.
- Hosomi, A., Tanabe K Fau - Hirayama, H., Hirayama H Fau - Kim, I., Kim I Fau - Rao, H., Rao H Fau - Suzuki, T. and Suzuki, T. (2010) 'Identification of an Htm1 (EDEM)-dependent, Mns1-independent Endoplasmic Reticulum-associated Degradation (ERAD) pathway in *Saccharomyces cerevisiae*: application of a novel assay for glycoprotein ERAD', (1083-351X (Electronic)).
- Hossler, P., Mulukutla, B. C. and Hu, W.-S. (2007) 'Systems Analysis of N-Glycan Processing in Mammalian Cells', *PLOS ONE*, 2(8), e713.

- Houštěk, J., Pícková, A., Vojtíšková, A., Mráček, T., Pecina, P. and Ješina, P. (2006) 'Mitochondrial diseases and genetic defects of ATP synthase', *Biochimica et Biophysica Acta (BBA) - Bioenergetics*, 1757(9), 1400-1405.
- Hu, B. H. (2016) 'Autophagy Signalling Interactive Pathway', CST Pathways [online], available: [accessed
- Hu, G., Xu, Y., Chen, W., Wang, J., Zhao, C. and Wang, M. (2016) 'RNA Interference of IQ Motif Containing GTPase-Activating Protein 3 (IQGAP3) Inhibits Cell Proliferation and Invasion in Breast Carcinoma Cells', *Oncol Res*, 24(6), 455-461.
- Huang, C., Harada, Y., Hosomi, A., Masahara-Negishi, Y., Seino, J., Fujihira, H., Funakoshi, Y., Suzuki, T., Dohmae, N. and Suzuki, T. (2015) 'Endo- $\beta$ -N-acetylglucosaminidase forms N-GlcNAc protein aggregates during ER-associated degradation in Ngly1-defective cells', *Proceedings of the National Academy of Sciences*, 112(5), 1398-1403.
- Huang, D. W., Sherman, B. T. and Lempicki, R. A. (2008) 'Systematic and integrative analysis of large gene lists using DAVID bioinformatics resources', *Nature protocols*, 4, 44.
- Huang, H.-C. and Briggs, J. M. (2002) 'The association between a negatively charged ligand and the electronegative binding pocket of its receptor', *Biopolymers*, 63(4), 247-260.
- Huang, H.-M., Fowler, C., Zhang, H. and Gibson, G. E. (2004) 'Mitochondrial Heterogeneity Within and Between Different Cell Types', *Neurochemical Research*, 29(3), 651-658.
- Huang, J. K., Chou, C. T., Chang, H. T., Shu, S. S., Kuo, C. C., Tsai, J. Y., Liao, W. C., Wang, J. L., Lin, K. L., Lu, Y. C., Chen, I. S., Liu, S. I., Ho, C. M. and Jan, C. R. (2011) 'Effect of thapsigargin on Ca(2)+ fluxes and viability in human prostate cancer cells', *J Recept Signal Transduct Res*, 31(3), 247-55.
- Huang, X., Luan, B., Wu, J. and Shi, Y. (2016) 'An atomic structure of the human 26S proteasome', *Nat Struct Mol Biol*, 23(9), 778-85.
- Hung, M.-C. and Link, W. (2011) 'Protein localization in disease and therapy', *Journal of Cell Science*, 124(20), 3381.
- Hüttemann, M., Lee, I., Samavati, L., Yu, H. and Doan, J. W. (2007) 'Regulation of mitochondrial oxidative phosphorylation through cell signaling', *Biochimica et Biophysica Acta (BBA) - Molecular Cell Research*, 1773(12), 1701-1720.
- Hyrskyluoto, A., Bruelle, C., Lundh, S. H., Do, H. T., Kivinen, J., Rappou, E., Reijonen, S., Waltimo, T., Petersen, A., Lindholm, D. and Korhonen, L. (2014) 'Ubiquitin-specific protease-14 reduces cellular aggregates and protects against mutant huntingtin-induced cell degeneration: involvement of the proteasome and ER stress-activated kinase IRE1 $\alpha$ ', *Hum Mol Genet*, 23(22), 5928-39.

Ichimura, Y., Kumanomidou, T., Sou, Y.-s., Mizushima, T., Ezaki, J., Ueno, T., Kominami, E., Yamane, T., Tanaka, K. and Komatsu, M. (2008) 'Structural Basis for Sorting Mechanism of p62 in Selective Autophagy', *Journal of Biological Chemistry*, 283(33), 22847-22857.

Imai, S.-i. and Guarente, L. (2016) 'It takes two to tango: NAD<sup>+</sup> and sirtuins in aging/longevity control', *Npj Aging And Mechanisms Of Disease*, 2, 16017.

Inobe, T. and Matouschek, A. (2014) 'Paradigms of protein degradation by the proteasome', *Current opinion in structural biology*, 0, 156-164.

Irvine, G. B., El-Agnaf, O. M., Shankar, G. M. and Walsh, D. M. (2008) 'Protein Aggregation in the Brain: The Molecular Basis for Alzheimer's and Parkinson's Diseases', *Molecular Medicine*, 14(7-8), 451-464.

Iwai, K., Fujita, H. and Sasaki, Y. (2014) 'Linear ubiquitin chains: NF-kappaB signalling, cell death and beyond', *Nat Rev Mol Cell Biol*, 15(8), 503-8.

Jackson, A. L. and Linsley, P. S. (2010) 'Recognizing and avoiding siRNA off-target effects for target identification and therapeutic application', *Nature Reviews Drug Discovery*, 9, 57.

Jacomin, A.-C., Samavedam, S., Promponas, V. and Nezis, I. P. (2016) 'iLIR database: A web resource for LIR motif-containing proteins in eukaryotes', *Autophagy*, 12(10), 1945-1953.

Jäger, S., Cimermancic, P., Gulbahce, N., Johnson, J. R., McGovern, K. E., Clarke, S. C., Shales, M., Mercenne, G., Pache, L., Li, K., Hernandez, H., Jang, G. M., Roth, S. L., Akiva, E., Marlett, J., Stephens, M., D'Orso, I., Fernandes, J., Fahey, M., Mahon, C., O'Donoghue, A. J., Todorovic, A., Morris, J. H., Maltby, D. A., Alber, T., Cagney, G., Bushman, F. D., Young, J. A., Chanda, S. K., Sundquist, W. I., Kortemme, T., Hernandez, R. D., Craik, C. S., Burlingame, A., Sali, A., Frankel, A. D. and Krogan, N. J. (2011) 'Global landscape of HIV-human protein complexes', *Nature*, 481(7381), 365-370.

Jakobsen, C. H., Størvold, G. L., Bremseth, H., Follestad, T., Sand, K., Mack, M., Olsen, K. S., Lundemo, A. G., Iversen, J. G., Krokan, H. E. and Schønberg, S. A. (2008) 'DHA induces ER stress and growth arrest in human colon cancer cells: associations with cholesterol and calcium homeostasis', *Journal of Lipid Research*, 49(10), 2089-2100.

Jantzen, S. G., Sutherland, B. J. G., Minkley, D. R. and Koop, B. F. (2011) 'GO Trimming: Systematically reducing redundancy in large Gene Ontology datasets', *BMC Research Notes*, 4, 267-267.

Jefferis, R. (2013) 'Review of Glycosylation Engineering of Biopharmaceuticals: Methods and Protocols: A book edited by Alain Beck', *mAbs*, 5(5), 638-640.

Jiménez-Mateos, E.-M., González-Billault, C., Dawson, Hana N., Vitek, Michael P. and Avila, J. (2006) 'Role of MAP1B in axonal retrograde transport of mitochondria', *Biochemical Journal*, 397(Pt 1), 53-59.



- Jimenez Fernandez, D. and Lamkanfi, M. (2015) 'Inflammatory caspases: key regulators of inflammation and cell death', *Biol Chem*, 396(3), 193-203.
- Jinek, M., Jiang, F., Taylor, D. W., Sternberg, S. H., Kaya, E., Ma, E., Anders, C., Hauer, M., Zhou, K., Lin, S., Kaplan, M., Iavarone, A. T., Charpentier, E., Nogales, E. and Doudna, J. A. (2014) 'Structures of Cas9 Endonucleases Reveal RNA-Mediated Conformational Activation', *Science (New York, N.Y.)*, 343(6176), 1247997-1247997.
- Johansen, T. and Lamark, T. (2011) 'Selective autophagy mediated by autophagic adapter proteins', *Autophagy*, 7(3), 279-296.
- Jornayvaz, F. R. and Shulman, G. I. (2010) 'Regulation of mitochondrial biogenesis', *Essays in biochemistry*, 47, 10.1042/bse0470069.
- Jung, C. H., Ro, S. H., Cao, J., Otto, N. M. and Kim, D. H. (2010) 'mTOR regulation of autophagy', *FEBS Lett*, 584(7), 1287-95.
- Jung, M., Lee, J., Seo, H.-Y., Lim, J. S. and Kim, E.-K. (2015) 'Cathepsin Inhibition-Induced Lysosomal Dysfunction Enhances Pancreatic Beta-Cell Apoptosis in High Glucose', *PLOS ONE*, 10(1), e0116972.
- Kageyama, S., Sou, Y.-s., Uemura, T., Kametaka, S., Saito, T., Ishimura, R., Kouno, T., Bedford, L., Mayer, R. J., Lee, M.-S., Yamamoto, M., Waguri, S., Tanaka, K. and Komatsu, M. (2014) 'Proteasome Dysfunction Activates Autophagy and the Keap1-Nrf2 Pathway', *The Journal of Biological Chemistry*, 289(36), 24944-24955.
- Kaizuka, T. and Mizushima, N. (2016) 'Atg13 Is Essential for Autophagy and Cardiac Development in Mice', *Molecular and Cellular Biology*, 36(4), 585-595.
- Kamalian, L., Chadwick, A. E., Bayliss, M., French, N. S., Monshouwer, M., Snoeys, J. and Park, B. K. (2015) 'The utility of HepG2 cells to identify direct mitochondrial dysfunction in the absence of cell death', *Toxicology in Vitro*, 29(4), 732-740.
- Kaneko, M., Iwase, I., Yamasaki, Y., Takai, T., Wu, Y., Kanemoto, S., Matsuhisa, K., Asada, R., Okuma, Y., Watanabe, T., Imaizumi, K. and Nomura, Y. (2016) 'Genome-wide identification and gene expression profiling of ubiquitin ligases for endoplasmic reticulum protein degradation', *Sci Rep*, 6, 30955.
- Kania, E., Pajak, B. and Orzechowski, A. (2015) 'Calcium homeostasis and ER stress in control of autophagy in cancer cells', *Biomed Res Int*, 2015, 352794.
- Karanasios, E., Walker, S. A., Okkenhaug, H., Manifava, M., Hummel, E., Zimmermann, H., Ahmed, Q., Domart, M.-C., Collinson, L. and Ktistakis, N. T. (2016) 'Autophagy initiation by ULK complex assembly on ER tubulovesicular regions marked by ATG9 vesicles', *Nature Communications*, 7, 12420.

- Karihaloo, A., Kale, S., Rosenblum, N. D. and Cantley, L. G. (2004) 'Hepatocyte growth factor-mediated renal epithelial branching morphogenesis is regulated by glypican-4 expression', *Mol Cell Biol*, 24(19), 8745-52.
- Karl, I., Jossberger-Werner, M., Schmidt, N., Horn, S., Goebeler, M., Leverkus, M., Wajant, H. and Giner, T. (2014) 'TRAF2 inhibits TRAIL- and CD95L-induced apoptosis and necroptosis', *Cell Death Dis*, 5, e1444.
- Kase, E. T., Nikolić, N., Bakke, S. S., Bogen, K. K., Aas, V., Thoresen, G. H. and Rustan, A. C. (2013) 'Remodeling of Oxidative Energy Metabolism by Galactose Improves Glucose Handling and Metabolic Switching in Human Skeletal Muscle Cells', *PLOS ONE*, 8(4), e59972.
- Kassim, A. A. and DeBaun, M. R. (2013) 'Sickle cell disease, vasculopathy, and therapeutics', *Annu Rev Med*, 64, 451-66.
- Kaushik, S., Bandyopadhyay, U., Sridhar, S., Kiffin, R., Martinez-Vicente, M., Kon, M., Orenstein, S. J., Wong, E. and Cuervo, A. M. (2011) 'Chaperone-mediated autophagy at a glance', *Journal of Cell Science*, 124(4), 495.
- Kennedy, D., Samali, A. and Jager, R. (2015) 'Methods for studying ER stress and UPR markers in human cells', *Methods Mol Biol*, 1292, 3-18.
- Kerr, D., Grahame, G. and Nakouzi, G. (2012) 'Assays of pyruvate dehydrogenase complex and pyruvate carboxylase activity', *Methods Mol Biol*, 837, 93-119.
- Kevei, É., Pokrzywa, W. and Hoppe, T. (2017) 'Repair or destruction—an intimate liaison between ubiquitin ligases and molecular chaperones in proteostasis', *FEBS Letters*, 591(17), 2616-2635.
- Kim, D. H. and Rossi, J. J. (2008) 'RNAi mechanisms and applications', *BioTechniques*, 44(5), 613-616.
- Kim, E. K. and Choi, E.-J. (2010) 'Pathological roles of MAPK signaling pathways in human diseases', *Biochimica et Biophysica Acta (BBA) - Molecular Basis of Disease*, 1802(4), 396-405.
- Kim, I., Ahn J Fau - Liu, C., Liu C Fau - Tanabe, K., Tanabe K Fau - Apodaca, J., Apodaca J Fau - Suzuki, T., Suzuki T Fau - Rao, H. and Rao, H. (2006 ) 'The Png1-Rad23 complex regulates glycoprotein turnover', (0021-9525 (Print)).
- Kim, J. J., Lee, S. B., Park, J. K. and Yoo, Y. D. (2010) 'TNF- $\alpha$ -induced ROS production triggering apoptosis is directly linked to Romo1 and Bcl-XL', *Cell death and differentiation*, 17, 1420.
- Kim, Y. J., Shin, Y. K., Sohn, D. S. and Lee, C. S. (2014) 'Menadione induces the formation of reactive oxygen species and depletion of GSH-mediated apoptosis and inhibits the FAK-mediated cell invasion', *Naunyn Schmiedebergs Arch Pharmacol*, 387(9), 799-809.

Kim, Y. M., Jang, W. H., Quezado, M. M., Oh, Y., Chung, K. C., Junn, E. and Mouradian, M. M. (2011) 'Proteasome inhibition induces alpha-synuclein SUMOylation and aggregate formation', *J Neurol Sci*, 307(1-2), 157-61.

Kimura, S., Noda, T. and Yoshimori, T. (2007) 'Dissection of the autophagosome maturation process by a novel reporter protein, tandem fluorescent-tagged LC3', *Autophagy*, 3(5), 452-60.

Kimura, T., Jain, A., Choi, S. W., Mandell, M. A., Schroder, K., Johansen, T. and Deretic, V. (2015) 'TRIM-mediated precision autophagy targets cytoplasmic regulators of innate immunity', *The Journal of Cell Biology*, 210(6), 973.

Kinoshita, T. (2016) 'Glycosylphosphatidylinositol (GPI) Anchors: Biochemistry and Cell Biology: Introduction to a Thematic Review Series', *Journal of Lipid Research*, 57(1), 4-5.

Kitajima, K., Suzuki, T., Kouchi, Z., Inoue, S. and Inoue, Y. (1995) 'Identification and Distribution of Peptide:N-Glycanase (PNGase) in Mouse Organs', *Archives of Biochemistry and Biophysics*, 319(2), 393-401.

Kobayashi, K., Araya, J., Minagawa, S., Hara, H., Saito, N., Kadota, T., Sato, N., Yoshida, M., Tsubouchi, K., Kurita, Y., Ito, S., Fujita, Y., Takasaka, N., Utsumi, H., Yanagisawa, H., Hashimoto, M., Wakui, H., Kojima, J., Shimizu, K., Numata, T., Kawaishi, M., Kaneko, Y., Asano, H., Yamashita, M., Odaka, M., Morikawa, T., Nakayama, K. and Kuwano, K. (2016) 'Involvement of PARK2-Mediated Mitophagy in Idiopathic Pulmonary Fibrosis Pathogenesis', *The Journal of Immunology*, 197(2), 504.

Komatsu, M., Waguri, S., Koike, M., Sou, Y.-s., Ueno, T., Hara, T., Mizushima, N., Iwata, J.-i., Ezaki, J., Murata, S., Hamazaki, J., Nishito, Y., Iemura, S.-i., Natsume, T., Yanagawa, T., Uwayama, J., Warabi, E., Yoshida, H., Ishii, T., Kobayashi, A., Yamamoto, M., Yue, Z., Uchiyama, Y., Kominami, E. and Tanaka, K. (2007) 'Homeostatic Levels of p62 Control Cytoplasmic Inclusion Body Formation in Autophagy-Deficient Mice', *Cell*, 131(6), 1149-1163.

Kondapalli, C., Kazlauskaitė A Fau - Zhang, N., Zhang N Fau - Woodroof, H. I., Woodroof Hi Fau - Campbell, D. G., Campbell Dg Fau - Gourlay, R., Gourlay R Fau - Burchell, L., Burchell L Fau - Walden, H., Walden H Fau - Macartney, T. J., Macartney Tj Fau - Deak, M., Deak M Fau - Knebel, A., Knebel A Fau - Alessi, D. R., Alessi Dr Fau - Muqit, M. M. K. and Muqit, M. M. (2012) 'PINK1 is activated by mitochondrial membrane potential depolarization and stimulates Parkin E3 ligase activity by phosphorylating Serine 65', (2046-2441 (Electronic)).

Kong, J., Peng, M., Ostrovsky, J., Kwon, Y. J., Oretsky, O., McCormick, E. M., He, M., Argon, Y. and Falk, M. J. (2018) 'Mitochondrial function requires NGLY1', *Mitochondrion*, 38, 6-16.

Kopach, O. V., Kruglikov, I. A., Kostyuk, P. G., Voitenko, N. V. and Fedirko, N. V. (2005) 'Mechanisms Underlying Leakage of Calcium from the Endoplasmic Reticulum of Acinar Cells of the Submandibular Salivary Gland', *Neurophysiology*, 37(4), 296-302.

Krushkal, J., Zhao, Y., Hose, C., Monks, A., Doroshow, J. H. and Simon, R. (2016) 'Concerted changes in transcriptional regulation of genes involved in DNA methylation, demethylation, and folate-mediated one-carbon metabolism pathways in the NCI-60 cancer cell line panel in response to cancer drug treatment', *Clinical Epigenetics*, 8, 73.

Ktistakis, N. T., Walker, S. A. and Karanasios, E. (2016) 'Assembly of early machinery for autophagy induction: novel insights from high resolution microscopy', *Oncotarget*, 7(52), 85678-85679.

Kuang, Y., Ma, K., Zhou, C., Ding, P., Zhu, Y., Chen, Q. and Xia, B. (2016) 'Structural basis for the phosphorylation of FUNDC1 LIR as a molecular switch of mitophagy', *Autophagy*, 12(12), 2363-2373.

Kuhn, R. M., Haussler, D. and Kent, W. J. (2013) 'The UCSC genome browser and associated tools', *Briefings in Bioinformatics*, 14(2), 144-161.

Lahiri, V. and Klionsky, D. J. (2017) 'PHB2/prohibitin 2: An inner membrane mitophagy receptor', *Cell Research*, 27, 311.

Lam, C., Ferreira, C., Krasnewich, D., Toro, C., Latham, L., Zein, W. M., Lehky, T., Brewer, C., Baker, E. H., Thurm, A., Farmer, C. A., Rosenzweig, S. D., Lyons, J. J., Schreiber, J. M., Gropman, A., Lingala, S., Ghany, M. G., Solomon, B., Macnamara, E., Davids, M., Stratakis, C. A., Kimonis, V., Gahl, W. A. and Wolfe, L. (2016) 'Prospective phenotyping of NGLY1-CDDG, the first congenital disorder of deglycosylation', *Genet Med*.

Lanctôt, P. M., Leclerc, P. C., Escher, E., Guillemette, G. and Leduc, R. (2006) 'Role of N-glycan-dependent quality control in the cell-surface expression of the AT1 receptor', *Biochemical and Biophysical Research Communications*, 340(2), 395-402.

Lanneau, D., Brunet, M., Frisan, E., Solary, E., Fontenay, M. and Garrido, C. (2008) 'Heat shock proteins: essential proteins for apoptosis regulation', *Journal of Cellular and Molecular Medicine*, 12(3), 743-761.

Lawless, M. W. and Greene, C. M. (2012) 'Toll-like receptor signalling in liver disease: ER stress the missing link?', *Cytokine*, 59(2), 195-202.

Lazarou, M., Sliter, D. A., Kane, L. A., Sarraf, S. A., Wang, C., Burman, J. L., Sideris, D. P., Fogel, A. I. and Youle, R. J. (2015) 'The ubiquitin kinase PINK1 recruits autophagy receptors to induce mitophagy', *Nature*, 524(7565), 309-314.

Lazarou, M., Sliter, D. A., Kane, L. A., Sarraf, S. A., Wang, C., Burman, J. L., Sideris, D. P., Fogel, A. I. and Youle, R. J. (2015) 'The ubiquitin kinase PINK1 recruits autophagy receptors to induce mitophagy', (1476-4687 (Electronic)).

Lefeber, D. J., Morava, E. and Jaeken, J. (2011) 'How to find and diagnose a CDG due to defective N-glycosylation', *Journal of Inherited Metabolic Disease*, 34(4), 849-852.

Lehrman, M. A. (2015) 'Flipping a Lipid-Linked Oligosaccharide? You Must Whip It!', *Trends in Biochemical Sciences*, 40(12), 715-717.

Lei, Y., Lu, L., Liu, H. Y., Li, S., Xing, F. and Chen, L. L. (2014) 'CRISPR-P: a web tool for synthetic single-guide RNA design of CRISPR-system in plants', *Mol Plant*, 7(9), 1494-1496.

Lezi, E. and Swerdlow, R. H. (2012) 'Mitochondria in Neurodegeneration', *Advances in experimental medicine and biology*, 942, 269-286.

Li, H., Wang, P., Sun, Q., Ding, W.-X., Yin, X.-M., Sobol, R. W., Stolz, D. B., Yu, J. and Zhang, L. (2011) 'Following cytochrome c release, autophagy is inhibited during chemotherapy-induced apoptosis by caspase-8-mediated cleavage of Beclin-1', *Cancer Research*, 71(10), 3625-3634.

Li, K., Gao, B., Li, J., Chen, H., Li, Y., Wei, Y., Gong, D., Gao, J., Zhang, J., Tan, W., Wen, T., Zhang, L., Huang, L., Xiang, R., Lin, P. and Wei, Y. (2015) 'ZNF32 protects against oxidative stress-induced apoptosis by modulating C1QBP transcription', *Oncotarget*, 6(35), 38107-38126.

Li, M. Y., Bruzzone, R. and Wang, P. G. (2015) 'New tricks for KDEL receptors', *Oncotarget*, 6(31), 30425-30426.

Li, W. W., Li, J. and Bao, J. K. (2012) 'Microautophagy: lesser-known self-eating', *Cell Mol Life Sci*, 69(7), 1125-36.

Li, X., Wu, X.-Q., Deng, R., Li, D.-D., Tang, J., Chen, W.-D., Chen, J.-H., Ji, J., Jiao, L., Jiang, S., Yang, F., Feng, G.-K., Senthilkumar, R., Yue, F., Zhang, H.-L., Wu, R.-Y., Yu, Y., Xu, X.-L., Mai, J., Li, Z.-L., Peng, X.-D., Huang, Y., Huang, X., Ma, N.-F., Tao, Q., Zeng, Y.-X. and Zhu, X.-F. (2017) 'CaMKII-mediated Beclin 1 phosphorylation regulates autophagy that promotes degradation of Id and neuroblastoma cell differentiation', *Nature Communications*, 8(1), 1159.

Li, Y., Guo, Y., Tang, J., Jiang, J. and Chen, Z. (2014) 'New insights into the roles of CHOP-induced apoptosis in ER stress', *Acta Biochim Biophys Sin (Shanghai)*, 46(8), 629-40.

Li, Y., Pan, S., Zhang, Y., Ren, M., Feng, M., Peng, N., Chen, L., Liang, Y. X. and She, Q. (2016) 'Harnessing Type I and Type III CRISPR-Cas systems for genome editing', *Nucleic Acids Research*, 44(4), e34-e34.

Liang, R. Y., Chen, L., Ko, B. T., Shen, Y. H., Li, Y. T., Chen, B. R., Lin, K. T., Madura, K. and Chuang, S. M. (2014) 'Rad23 interaction with the proteasome is regulated by phosphorylation of its ubiquitin-like (Ubl) domain', *J Mol Biol*, 426(24), 4049-60.

Liang, X., Potter, J., Kumar, S., Zou, Y., Quintanilla, R., Sridharan, M., Carte, J., Chen, W., Roark, N., Ranganathan, S., Ravinder, N. and Chesnut, J. D. (2015) 'Rapid and highly efficient mammalian cell engineering via Cas9 protein transfection', *Journal of Biotechnology*, 208, 44-53.

- Lightowlers, R. N. and Chrzanowska-Lightowlers, Z. M. A. (2014) 'Salvaging hope: Is increasing NAD(+) a key to treating mitochondrial myopathy?', *EMBO Molecular Medicine*, 6(6), 705-707.
- Lilienbaum, A. (2013) 'Relationship between the proteasomal system and autophagy', *International Journal of Biochemistry and Molecular Biology*, 4(1), 1-26.
- Lin, Y.-C., Boone, M., Meuris, L., Lemmens, I., Van Roy, N., Soete, A., Reumers, J., Moisse, M., Plaisance, S., Drmanac, R., Chen, J., Speleman, F., Lambrechts, D., Van de Peer, Y., Tavernier, J. and Callewaert, N. (2014) 'Genome dynamics of the human embryonic kidney 293 lineage in response to cell biology manipulations', *Nature Communications*, 5, 4767.
- Lin, Y., Choksi, S., Shen, H. M., Yang, Q. F., Hur, G. M., Kim, Y. S., Tran, J. H., Nedospasov, S. A. and Liu, Z. G. (2004) 'Tumor necrosis factor-induced nonapoptotic cell death requires receptor-interacting protein-mediated cellular reactive oxygen species accumulation', *J Biol Chem*, 279(11), 10822-8.
- Lindberg, D. J., Wranne, M. S., Gilbert Gatty, M., Westerlund, F. and Esbjörner, E. K. (2015) 'Steady-state and time-resolved Thioflavin-T fluorescence can report on morphological differences in amyloid fibrils formed by A $\beta$ (1-40) and A $\beta$ (1-42)', *Biochemical and Biophysical Research Communications*, 458(2), 418-423.
- Little, A. S., Smith, P. D. and Cook, S. J. (2013) 'Mechanisms of acquired resistance to ERK1/2 pathway inhibitors', *Oncogene*, 32(10), 1207-15.
- Lodish H, B. A., Zipursky SL, et al. (2000) ' Hierarchical Structure of Proteins' in *Molecular Cell Biology*, 4th Edition ed., New York: W. H. Freeman.
- Lomax, R. B., Camello, C., Van Coppenolle, F., Petersen, O. H. and Tepikin, A. V. (2002) 'Basal and Physiological Ca<sup>2+</sup> Leak from the Endoplasmic Reticulum of Pancreatic Acinar Cells: SECOND MESSENGER-ACTIVATED CHANNELS AND TRANSLOCONS', *Journal of Biological Chemistry*, 277(29), 26479-26485.
- Loor, G., Kondapalli, J., Schriewer, J. M., Chandel, N. S., Vanden Hoek, T. L. and Schumacker, P. T. (2010) 'Menadione triggers cell death through ROS-dependent mechanisms involving PARP activation without requiring apoptosis', *Free Radic Biol Med*, 49(12), 1925-36.
- López-Gallardo, E., Emperador, S., Solano, A., Llobet, L., Martín-Navarro, A., López-Pérez, M. J., Briones, P., Pineda, M., Artuch, R., Barraquer, E., Jericó, I., Ruiz-Pesini, E. and Montoya, J. (2014) 'Expanding the clinical phenotypes of MT-ATP6 mutations', *Human Molecular Genetics*, 23(23), 6191-6200.
- Louwen, R., Staals, R. H. J., Endtz, H. P., van Baarlen, P. and van der Oost, J. (2014) 'The Role of CRISPR-Cas Systems in Virulence of Pathogenic Bacteria', *Microbiol Mol Biol Rev*, 78(1), 74-88.

- Lu, Y., Tucker, D., Dong, Y., Zhao, N., Zhuo, X. and Zhang, Q. (2015) 'Role of Mitochondria in Neonatal Hypoxic-Ischemic Brain Injury', *Journal of neuroscience and rehabilitation*, 2(1), 1-14.
- Maclaine, N. J. and Hupp, T. R. (2009) 'The regulation of p53 by phosphorylation: a model for how distinct signals integrate into the p53 pathway', *Aging*, 1(5), 490-502.
- Maeda, M. and Kimura, Y. (2014) 'Structural features of free N-glycans occurring in plants and functional features of de-N-glycosylation enzymes, ENGase, and PNGase: the presence of unusual plant complex type N-glycans', *Frontiers in Plant Science*, 5, 429.
- Maerz, S., Funakoshi, Y., Negishi, Y., Suzuki, T. and Seiler, S. (2010) 'The Neurospora peptide:N-glycanase ortholog PNG1 is essential for cell polarity despite its lack of enzymatic activity', *J Biol Chem*, 285(4), 2326-32.
- Maes, M. E., Schlamp, C. L. and Nickells, R. W. (2017) 'Live-cell imaging to measure BAX recruitment kinetics to mitochondria during apoptosis', *PLOS ONE*, 12(9), e0184434.
- Malhotra, J. D. and Kaufman, R. J. (2011) 'ER Stress and Its Functional Link to Mitochondria: Role in Cell Survival and Death', *Cold Spring Harbor Perspectives in Biology*, 3(9), a004424.
- Malm, D. and Nilssen, Ø. (2008) 'Alpha-mannosidosis', *Orphanet Journal of Rare Diseases*, 3(1), 21.
- Man, S. M. and Kanneganti, T.-D. (2016) 'Regulation of lysosomal dynamics and autophagy by CTSB/cathepsin B', *Autophagy*, 12(12), 2504-2505.
- Mancias, J. D., Wang, X., Gygi, S. P., Harper, J. W. and Kimmelman, A. C. (2014) 'Quantitative proteomics identifies NCOA4 as the cargo receptor mediating ferritinophagy', *Nature*, 509(7498), 105-9.
- Manifava, M., Smith, M., Rotondo, S., Walker, S., Niewczas, I., Zoncu, R., Clark, J. and Ktistakis, N. T. (2016) 'Dynamics of mTORC1 activation in response to amino acids', *eLife*, 5.
- Marchi, S., Patergnani, S. and Pinton, P. (2014) 'The endoplasmic reticulum–mitochondria connection: One touch, multiple functions', *Biochimica et Biophysica Acta (BBA) - Bioenergetics*, 1837(4), 461-469.
- Marcinowski, M., Rosam, M., Seitz, C., Elferich, J., Behnke, J., Bello, C., Feige, M. J., Becker, C. F., Antes, I. and Buchner, J. (2013) 'Conformational selection in substrate recognition by Hsp70 chaperones', *J Mol Biol*, 425(3), 466-74.
- Marroquin, L. D., Hynes, J., Dykens, J. A., Jamieson, J. D. and Will, Y. (2007) 'Circumventing the Crabtree Effect: Replacing Media Glucose with Galactose Increases Susceptibility of HepG2 Cells to Mitochondrial Toxicants', *Toxicological Sciences*, 97(2), 539-547.
- Martinet, W., De Meyer, G. R. Y., Timmermans, J.-P., Herman, A. G. and Kockx, M. M. (2006a) 'Macrophages but Not Smooth Muscle Cells Undergo Benzyloxycarbonyl-Val-Ala-

'z-VAD-fmk-Induced Non-Apoptotic Cell Death Depending on Receptor-Interacting Protein 1 Expression: Implications for the Stabilization of Macrophage-Rich Atherosclerotic Plaques', *Journal of Pharmacology and Experimental Therapeutics*, 317(3), 1356.

Martinet, W., Schrijvers, D. M., Herman, A. G. and Meyer, G. R. Y. D. (2006b) 'z-VAD-fmk-Induced Non-Apoptotic Cell Death of Macrophages: Possibilities and Limitations for Atherosclerotic Plaque Stabilization', *Autophagy*, 2(4), 312-314.

Martinez-Lopez, N., Athonvarangkul, D., Mishall, P., Sahu, S. and Singh, R. (2013) 'Autophagy proteins regulate ERK phosphorylation', *Nature Communications*, 4, 2799.

Martinez-Vicente, M., Tallozy, Z., Wong, E., Tang, G., Koga, H., Kaushik, S., de Vries, R., Arias, E., Harris, S., Sulzer, D. and Cuervo, A. M. (2010) 'CARGO RECOGNITION FAILURE IS RESPONSIBLE FOR INEFFICIENT AUTOPHAGY IN HUNTINGTON'S DISEASE', *Nature neuroscience*, 13(5), 567-576.

Maruyama, T., Dougan, S. K., Truttmann, M., Bilate, A. M., Ingram, J. R. and Ploegh, H. L. (2015) 'Inhibition of non-homologous end joining increases the efficiency of CRISPR/Cas9-mediated precise [TM: inserted] genome editing', *Nature biotechnology*, 33(5), 538-542.

Mason, N., Ciuffo, L. F. and Brown, J. D. (2000) 'Elongation arrest is a physiologically important function of signal recognition particle', *Embo j*, 19(15), 4164-74.

Mathew, R., Khor, S., Hackett, S. R., Rabinowitz, J. D., Perlman, D. H. and White, E. (2014) 'Functional Role of Autophagy-mediated Proteome Remodeling in Cell Survival Signaling and Innate Immunity', *Mol Cell*, 55(6), 916-930.

Mathews, E. S., Mawdsley, D. J., Walker, M., Hines, J. H., Pozzoli, M. and Appel, B. (2014) 'Mutation of 3-Hydroxy-3-Methylglutaryl CoA Synthase I Reveals Requirements for Isoprenoid and Cholesterol Synthesis in Oligodendrocyte Migration Arrest, Axon Wrapping, and Myelin Gene Expression', *The Journal of Neuroscience*, 34(9), 3402-3412.

Mathupala, S. P. and Sloan, A. E. (2009) 'An agarose-based cloning-ring anchoring method for isolation of viable cell clones', *BioTechniques*, 46(4), 305-307.

Mauro-Lizcano, M., Esteban-Martínez, L., Seco, E., Serrano-Puebla, A., Garcia-Ledo, L., Figueiredo-Pereira, C., Vieira, H. L. A. and Boya, P. (2015) 'New method to assess mitophagy flux by flow cytometry', *Autophagy*, 11(5), 833-843.

Mauvezin, C. and Neufeld, T. P. (2015) 'Bafilomycin A1 disrupts autophagic flux by inhibiting both V-ATPase-dependent acidification and Ca-P60A/SERCA-dependent autophagosome-lysosome fusion', *Autophagy*, 11(8), 1437-1438.

McCourt, J. L., Talsness, D. M., Lindsay, A., Arpke, R. W., Chatterton, P. D., Nelson, D. M., Chamberlain, C. M., Olthoff, J. T., Belanto, J. J., McCourt, P. M., Kyba, M., Lowe, D. A. and Ervasti, J. M. (2018) 'Mouse models of two missense mutations in actin-binding domain 1 of



- dystrophin associated with Duchenne or Becker muscular dystrophy', *Hum Mol Genet*, 27(3), 451-462.
- McIlwain, D. R., Berger, T. and Mak, T. W. (2013) 'Caspase functions in cell death and disease', *Cold Spring Harb Perspect Biol*, 5(4), a008656.
- Medzihradzky, K. F. (2008) 'Characterization of site-specific N-glycosylation', *Methods Mol Biol*, 446, 293-316.
- Mekahli, D., Bultynck, G., Parys, J. B., De Smedt, H. and Missiaen, L. (2011) 'Endoplasmic-Reticulum Calcium Depletion and Disease', *Cold Spring Harbor Perspectives in Biology*, 3(6), a004317.
- Merkulova, E. A., Guiboileau, A., Naya, L., Masclaux-Daubresse, C. and Yoshimoto, K. (2014) 'Assessment and Optimization of Autophagy Monitoring Methods in Arabidopsis Roots Indicate Direct Fusion of Autophagosomes with Vacuoles', *Plant and Cell Physiology*, 55(4), 715-726.
- Meusser, B., Hirsch, C., Jarosch, E. and Sommer, T. (2005) 'ERAD: the long road to destruction', *Nat Cell Biol*, 7(8), 766-772.
- Misaghi, S., Korbel, G. A., Kessler, B., Spooner, E. and Ploegh, H. L. (2005) 'z-VAD-fmk inhibits peptide:N-glycanase and may result in ER stress', *Cell Death Differ*, 13(1), 163-165.
- Misaghi, S., Pacold, M. E., Blom, D., Ploegh, H. L. and Korbel, G. A. (2004) 'Using a Small Molecule Inhibitor of Peptide: N-Glycanase to Probe Its Role in Glycoprotein Turnover', *Chemistry & Biology*, 11(12), 1677-1687.
- Missiakas, D. and Raina, S. (1997) 'Protein folding in the bacterial periplasm', *Journal of Bacteriology*, 179(8), 2465.
- Monteiro, J. P., Martins, A. F., Nunes, C., Morais, C. M., Lúcio, M., Reis, S., Pinheiro, T. J. T., Geraldes, C. F. G. C., Oliveira, P. J. and Jurado, A. S. (2013) 'A biophysical approach to menadione membrane interactions: Relevance for menadione-induced mitochondria dysfunction and related deleterious/therapeutic effects', *Biochimica et Biophysica Acta (BBA) - Biomembranes*, 1828(8), 1899-1908.
- Mota, S. I., Costa, R. O., Ferreira, I. L., Santana, I., Caldeira, G. L., Padovano, C., Fonseca, A. C., Baldeiras, I., Cunha, C., Letra, L., Oliveira, C. R., Pereira, C. M. and Rego, A. C. (2015) 'Oxidative stress involving changes in Nrf2 and ER stress in early stages of Alzheimer's disease', *Biochim Biophys Acta*, 1852(7), 1428-41.
- Moyzis, A. G., Sadoshima, J. and Gustafsson, A. B. (2015) 'Mending a broken heart: the role of mitophagy in cardioprotection', *Am J Physiol Heart Circ Physiol*, 308(3), H183-92.
- Nair, P., Lu, M., Petersen, S. and Ashkenazi, A. (2014) 'Apoptosis initiation through the cell-extrinsic pathway', *Methods Enzymol*, 544, 99-128.

Nakajima, S., Kato, H., Takahashi, S., Johno, H. and Kitamura, M. (2011) 'Inhibition of NF- $\kappa$ B by MG132 through ER stress-mediated induction of LAP and LIP', *FEBS Letters*, 585(14), 2249-2254.

Nam, J. H., Zhang, F., Ermonval, M., Linhardt, R. J. and Sharfstein, S. T. (2008) 'The Effects of Culture Conditions on the Glycosylation of Secreted Human Placental Alkaline Phosphatase Produced in Chinese Hamster Ovary Cells', *Biotechnol Bioeng*, 100(6), 1178-1192.

Narendra, D. P., Kane, L. A., Hauser, D. N., Fearnley, I. M. and Youle, R. J. (2010) 'p62/SQSTM1 is required for Parkin-induced mitochondrial clustering but not mitophagy; VDAC1 is dispensable for both', *Autophagy*, 6(8), 1090-1106.

Nascimbeni, A. C., Giordano, F., Dupont, N., Grasso, D., Vaccaro, M. I., Codogno, P. and Morel, E. (2017) 'ER-plasma membrane contact sites contribute to autophagosome biogenesis by regulation of local PI3P synthesis', *Embo j*, 36(14), 2018-2033.

Nath, K. A. and Hebbel, R. P. (2015) 'Sickle cell disease: renal manifestations and mechanisms', *Nature reviews. Nephrology*, 11(3), 161-171.

Nath, S., Dancourt, J., Shteyn, V., Puente, G., Fong, W. M., Nag, S., Bewersdorf, J., Yamamoto, A., Antony, B. and Melia, T. J. (2014) 'Lipidation of the LC3/GABARAP family of autophagy proteins relies upon a membrane curvature-sensing domain in Atg3', *Nature Cell Biology*, 16(5), 415-424.

Nathan, J. A., Kim, H. T., Ting, L., Gygi, S. P. and Goldberg, A. L. (2013) 'Why do cell proteins linked to K63-polyubiquitin chains not associate with proteasomes?', *The EMBO Journal*, 32(4), 552-565.

Nault, L., Vendrely, C., Bréchet, Y., Bruckert, F. and Weidenhaupt, M. (2013) 'Peptides that form  $\beta$ -sheets on hydrophobic surfaces accelerate surface-induced insulin amyloid aggregation', *FEBS Letters*, 587(9), 1281-1286.

Nazio, F., Strappazon, F., Antonioli, M., Bielli, P., Cianfanelli, V., Bordi, M., Gretzmeier, C., Dengjel, J., Piacentini, M., Fimia, G. M. and Cecconi, F. (2013) 'mTOR inhibits autophagy by controlling ULK1 ubiquitylation, self-association and function through AMBRA1 and TRAF6', *Nat Cell Biol*, 15(4), 406-416.

Need, A. C., Shashi, V., Hitomi, Y., Schoch, K., Shianna, K. V., McDonald, M. T., Meisler, M. H. and Goldstein, D. B. (2012) 'Clinical application of exome sequencing in undiagnosed genetic conditions', *Journal of Medical Genetics*.

Nishi, H., Hashimoto, K. and Panchenko, A. R. (2011) 'Phosphorylation in protein-protein binding: effect on stability and function', *Structure (London, England : 1993)*, 19(12), 1807-1815.

Nishitoh, H. (2012) 'CHOP is a multifunctional transcription factor in the ER stress response', *J Biochem*, 151(3), 217-9.

Niu, Y., Dai, J., Chen, Y., Wu, C., Zhang, S. and Zhang, D. (2016) 'Positive effect of apoptotic inhibitor z-vad-fmk on vitrified-thawed porcine mii stage oocytes', *Cryo Letters*, 37(3), 188-95.

Nixon, R. A. (2013a) 'The role of autophagy in neurodegenerative disease', *Nat Med*, 19(8), 983-997.

Nixon, R. A. (2013b) 'The role of autophagy in neurodegenerative disease', *Nat Med*, 19, 983.

Noda, T. (2017) 'Autophagy in the context of the cellular membrane-trafficking system: the enigma of Atg9 vesicles', *Biochemical Society Transactions*.

Nojima, H., Adachi, M., Matsui, T., Okawa, K., Tsukita, S. and Tsukita, S. (2008) 'IQGAP3 regulates cell proliferation through the Ras/ERK signalling cascade', *Nature Cell Biology*, 10, 971.

NORD (2015) 'Congenital Disorders of Glycosylation', for Patients and Families [online], available: [accessed 17/01/2018] <https://rarediseases.org/rare-diseases/congenital-disorders-of-glycosylation/>

Novak, I., Kirkin, V., McEwan, D. G., Zhang, J., Wild, P., Rozenknop, A., Rogov, V., Löhr, F., Popovic, D., Occhipinti, A., Reichert, A. S., Terzic, J., Dötsch, V., Ney, P. A. and Dikic, I. (2010) 'Nix is a selective autophagy receptor for mitochondrial clearance', *EMBO Reports*, 11(1), 45-51.

Nyathi, Y., Wilkinson, B. M. and Pool, M. R. (2013) 'Co-translational targeting and translocation of proteins to the endoplasmic reticulum', *Biochimica et Biophysica Acta (BBA) - Molecular Cell Research*, 1833(11), 2392-2402.

Obeng, E. A., Carlson, L. M., Gutman, D. M., Harrington, W. J., Lee, K. P. and Boise, L. H. (2006) 'Proteasome inhibitors induce a terminal unfolded protein response in multiple myeloma cells', *Blood*, 107(12), 4907-4916.

Ogasawara, Y., Nakayama, K., Tarnowka, M., McCoy, J. P., Kajigaya, S., Levin, B. C. and Young, N. S. (2005) 'Mitochondrial DNA spectra of single human CD34(+) cells, T cells, B cells, and granulocytes', *Blood*, 106(9), 3271-3284.

Ogen-Shtern, N., Ben David, T. and Lederkremer, G. Z. (2016) 'Protein aggregation and ER stress', *Brain Research*, 1648(Part B), 658-666.

Ohtake, A., Murayama, K., Mori, M., Harashima, H., Yamazaki, T., Tamaru, S., Yamashita, Y., Kishita, Y., Nakachi, Y., Kohda, M., Tokuzawa, Y., Mizuno, Y., Moriyama, Y., Kato, H. and Okazaki, Y. (2014) 'Diagnosis and molecular basis of mitochondrial respiratory chain disorders: Exome sequencing for disease gene identification', *Biochimica et Biophysica Acta (BBA) - General Subjects*, 1840(4), 1355-1359.

- Ohtsuji, M., Katsuoka F Fau - Kobayashi, A., Kobayashi A Fau - Aburatani, H., Aburatani H Fau - Hayes, J. D., Hayes Jd Fau - Yamamoto, M. and Yamamoto, M. (2008) 'Nrf1 and Nrf2 play distinct roles in activation of antioxidant response element-dependent genes', (0021-9258 (Print)).
- Olsen, J. V., Blagoev, B., Gnad, F., Macek, B., Kumar, C., Mortensen, P. and Mann, M. (2006) 'Global, In Vivo, and Site-Specific Phosphorylation Dynamics in Signaling Networks', *Cell*, 127(3), 635-648.
- Olzmann, J. A., Kopito, R. R. and Christianson, J. C. (2013) 'The Mammalian Endoplasmic Reticulum-Associated Degradation System', *Cold Spring Harbor Perspectives in Biology*, 5(9), 10.1101/cshperspect.a013185 a013185.
- Oue, N., Yamamoto, Y., Oshima, T., Asai, R., Ishikawa, A., Uraoka, N., Sakamoto, N., Sentani, K. and Yasui, W. (2017) 'Overexpression of the Transmembrane Protein IQGAP3 Is Associated with Poor Survival of Patients with Gastric Cancer', *Pathobiology*.
- Overbye, A., Fengsrud, M. and Seglen, P. O. (2007) 'Proteomic analysis of membrane-associated proteins from rat liver autophagosomes', *Autophagy*, 3(4), 300-22.
- Owings, K. G., Lowry, J. B., Bi, Y., Might, M. and Chow, C. Y. (2018) 'Transcriptome and functional analysis in a Drosophila model of NGLY1 deficiency provides insight into therapeutic approaches', *Hum Mol Genet*.
- Pace, C. N., Scholtz, J. M. and Grimsley, G. R. (2014) 'Forces Stabilizing Proteins', *FEBS Letters*, 588(14), 2177-2184.
- Pajares, M., Cuadrado, A. and Rojo, A. I. (2017) 'Modulation of proteostasis by transcription factor NRF2 and impact in neurodegenerative diseases', *Redox Biology*, 11, 543-553.
- Pankiv, S., Clausen Th Fau - Lamark, T., Lamark T Fau - Brech, A., Brech A Fau - Bruun, J.-A., Bruun Ja Fau - Outzen, H., Outzen H Fau - Overvatn, A., Overvatn A Fau - Bjorkoy, G., Bjorkoy G Fau - Johansen, T. and Johansen, T. (2007) 'p62/SQSTM1 binds directly to Atg8/LC3 to facilitate degradation of ubiquitinated protein aggregates by autophagy', (0021-9258 (Print)).
- Pant, V. and Lozano, G. (2014) 'Limiting the power of p53 through the ubiquitin proteasome pathway', *Genes & Development*, 28(16), 1739-1751.
- Papanikolaou, N., Pavlopoulos, G. A., Theodosiou, T. and Iliopoulos, I. (2015) 'Protein-protein interaction predictions using text mining methods', *Methods*, 74, 47-53.
- Parajuli, N. and MacMillan-Crow, L. A. (2012) 'Role of reduced manganese superoxide dismutase in ischemia-reperfusion injury: a possible trigger for autophagy and mitochondrial biogenesis?', *American Journal of Physiology-Renal Physiology*, 304(3), F257-F267.

Patel, K. P., O'Brien, T. W., Subramony, S. H., Shuster, J. and Stacpoole, P. W. (2012) 'The spectrum of pyruvate dehydrogenase complex deficiency: Clinical, biochemical and genetic features in 371 patients', *Molecular genetics and metabolism*, 106(3), 385-394.

Patrice Codogno, M. M. T. P.-C. (2012) 'Canonical and non-canonical autophagy: variations on a common theme of self-eating?', *Nature Reviews Molecular Cell Biology*, 13, 7-12.

Peng, H., Yang, J., Li, G., You, Q., Han, W., Li, T., Gao, D., Xie, X., Lee, B.-H., Du, J., Hou, J., Zhang, T., Rao, H., Huang, Y., Li, Q., Zeng, R., Hui, L., Wang, H., Xia, Q., Zhang, X., He, Y., Komatsu, M., Dikic, I., Finley, D. and Hu, R. (2017) 'Ubiquitylation of p62/sequestosome1 activates its autophagy receptor function and controls selective autophagy upon ubiquitin stress', *Cell Research*, 27, 657.

Peng, M., Ostrovsky, J., Kwon, Y. J., Polyak, E., Licata, J., Tsukikawa, M., Marty, E., Thomas, J., Felix, C. A., Xiao, R., Zhang, Z., Gasser, D. L., Argon, Y. and Falk, M. J. (2015) 'Inhibiting cytosolic translation and autophagy improves health in mitochondrial disease', *Human Molecular Genetics*, 24(17), 4829-4847.

Percicote, A. P., Mardegan, G. L., Gugelmim, E. S., Ioshii, S. O., Kuczynski, A. P., Nagashima, S. and de Noronha, L. (2018) 'Tissue expression of retinoic acid receptor alpha and CRABP2 in metastatic neuroblastomas', *Diagn Pathol*, 13(1), 9.

Perzlsmaier, A. F., Richter, F. and Seufert, W. (2013) 'Translation Initiation Requires Cell Division Cycle 123 (Cdc123) to Facilitate Biogenesis of the Eukaryotic Initiation Factor 2 (eIF2)', *The Journal of Biological Chemistry*, 288(30), 21537-21546.

Pham, J. W. and Sontheimer, E. J. (2005) 'Molecular requirements for RNA-induced silencing complex assembly in the Drosophila RNA interference pathway', *J Biol Chem*, 280(47), 39278-83.

Pizarro, L. and Norambuena, L. (2014) 'Regulation of protein trafficking: posttranslational mechanisms and the unexplored transcriptional control', *Plant Sci*, 225, 24-33.

Plotnikov, A., Zehorai, E., Procaccia, S. and Seger, R. (2011) 'The MAPK cascades: Signaling components, nuclear roles and mechanisms of nuclear translocation', *Biochimica et Biophysica Acta (BBA) - Molecular Cell Research*, 1813(9), 1619-1633.

Pop, C., Timmer, J., Sperandio, S. and Salvesen, G. S. (2006) 'The apoptosome activates caspase-9 by dimerization', *Mol Cell*, 22(2), 269-75.

Prien, J. M., Ashline, D. J., Lapadula, A. J., Zhang, H. and Reinhold, V. N. (2009) 'The High Mannose Glycans from Bovine Ribonuclease B Isomer Characterization by Ion Trap MS', *Journal of the American Society for Mass Spectrometry*, 20(4), 539-556.

Pugsley, H. R. (2017) 'Assessing Autophagic Flux by Measuring LC3, p62, and LAMP1 Co-localization Using Multispectral Imaging Flow Cytometry', *J Vis Exp*, (125).

- Qian, E. N., Han, S. Y., Ding, S. Z. and Lv, X. (2016) 'Expression and diagnostic value of CCT3 and IQGAP3 in hepatocellular carcinoma', *Cancer Cell Int*, 16, 55.
- Radhakrishnan, S. K., den Besten, W. and Deshaies, R. J. (2014) 'p97-dependent retrotranslocation and proteolytic processing govern formation of active Nrf1 upon proteasome inhibition', *eLife*, 3, e01856.
- Radhakrishnan, S. K., Lee, C. S., Young, P., Beskow, A., Chan, J. Y. and Deshaies, R. J. (2010) 'Transcription factor Nrf1 mediates the proteasome recovery pathway after proteasome inhibition in mammalian cells', *Mol Cell*, 38(1), 17-28.
- Raju, T. S., Briggs, J. B., Borge, S. M. and Jones, A. J. S. (2000) 'Species-specific variation in glycosylation of IgG: evidence for the species-specific sialylation and branch-specific galactosylation and importance for engineering recombinant glycoprotein therapeutics', *Glycobiology*, 10(5), 477-486.
- Rakovic, A., Grunewald, A., Kottwitz, J., Bruggemann, N., Pramstaller, P. P., Lohmann, K. and Klein, C. (2011) 'Mutations in PINK1 and Parkin impair ubiquitination of Mitofusins in human fibroblasts', *PLOS ONE*, 6(3), e16746.
- Ran, F. A., Hsu, P. D., Wright, J., Agarwala, V., Scott, D. A. and Zhang, F. (2013) 'Genome engineering using the CRISPR-Cas9 system', *Nature protocols*, 8(11), 2281-2308.
- Rath, D., Amlinger, L., Rath, A. and Lundgren, M. (2015a) 'The CRISPR-Cas immune system: Biology, mechanisms and applications', *Biochimie*, 117(Supplement C), 119-128.
- Rath, D., Amlinger, L., Rath, A. and Lundgren, M. (2015b) 'The CRISPR-Cas immune system: Biology, mechanisms and applications', *Biochimie*, 117, 119-128.
- Ravid, T. and Hochstrasser, M. (2008) 'Degradation signal diversity in the ubiquitin-proteasome system', *Nature reviews. Molecular cell biology*, 9(9), 679-690.
- Redfern, A. D., Colley, S. M., Beveridge, D. J., Ikeda, N., Epis, M. R., Li, X., Foulds, C. E., Stuart, L. M., Barker, A., Russell, V. J., Ramsay, K., Kobelke, S. J., Li, X., Hatchell, E. C., Payne, C., Giles, K. M., Messineo, A., Gatignol, A., Lanz, R. B., O'Malley, B. W. and Leedman, P. J. (2013) 'RNA-induced silencing complex (RISC) Proteins PACT, TRBP, and Dicer are SRA binding nuclear receptor coregulators', *Proceedings of the National Academy of Sciences of the United States of America*, 110(16), 6536-6541.
- Richardson, C. D., Ray, G. J., Bray, N. L. and Corn, J. E. (2016) 'Non-homologous DNA increases gene disruption efficiency by altering DNA repair outcomes', *Nature Communications*, 7, 12463.
- Rinnerthaler, M., Bischof, J., Streubel, M. K., Trost, A. and Richter, K. (2015) 'Oxidative stress in aging human skin', *Biomolecules*, 5(2), 545-89.

Ritter, C., Quirin, K., Kowarik, M. and Helenius, A. (2005) 'Minor folding defects trigger local modification of glycoproteins by the ER folding sensor GT', *The EMBO Journal*, 24(9), 1730-1738.

Rizzo, W. B. (2014) 'Fatty Aldehyde and Fatty Alcohol Metabolism: Review and Importance for Epidermal Structure and Function', *Biochimica et biophysica acta*, 1841(3), 377-389.

Roberts, T. M., Rudolf, F., Meyer, A., Pellaux, R., Whitehead, E., Panke, S. and Held, M. (2016) 'Identification and Characterisation of a pH-stable GFP', *Scientific Reports*, 6, 28166.

Rodríguez-Enfedaque, A., Delmas, E., Guillaume, A., Gaumer, S., Mignotte, B., Vayssière, J.-L. and Renaud, F. (2012) 'zVAD-fmk upregulates caspase-9 cleavage and activity in etoposide-induced cell death of mouse embryonic fibroblasts', *Biochimica et Biophysica Acta (BBA) - Molecular Cell Research*, 1823(8), 1343-1352.

Rodriguez-Enriquez, S., Juarez O Fau - Rodriguez-Zavala, J. S., Rodriguez-Zavala Js Fau - Moreno-Sanchez, R. and Moreno-Sanchez, R. (2001 ) 'Multisite control of the Crabtree effect in ascites hepatoma cells', (0014-2956 (Print)).

Rogov, V. V., Suzuki, H., Marinković, M., Lang, V., Kato, R., Kawasaki, M., Buljubašić, M., Šprung, M., Rogova, N., Wakatsuki, S., Hamacher-Brady, A., Dötsch, V., Dikic, I., Brady, N. R. and Novak, I. (2017) 'Phosphorylation of the mitochondrial autophagy receptor Nix enhances its interaction with LC3 proteins', *Scientific Reports*, 7(1), 1131.

Rolland, T., Tasan, M., Charlotheaux, B., Pevzner, S. J., Zhong, Q., Sahni, N., Yi, S., Lemmens, I., Fontanillo, C., Mosca, R., Kamburov, A., Ghiassian, S. D., Yang, X., Ghamsari, L., Balcha, D., Begg, B. E., Braun, P., Brehme, M., Broly, M. P., Carvunis, A. R., Convery-Zupan, D., Corominas, R., Coulombe-Huntington, J., Dann, E., Dreze, M., Dricot, A., Fan, C., Franzosa, E., Gebreab, F., Gutierrez, B. J., Hardy, M. F., Jin, M., Kang, S., Kiros, R., Lin, G. N., Luck, K., MacWilliams, A., Menche, J., Murray, R. R., Palagi, A., Poulin, M. M., Rambout, X., Rasla, J., Reichert, P., Romero, V., Ruysinck, E., Sahalie, J. M., Scholz, A., Shah, A. A., Sharma, A., Shen, Y., Spirohn, K., Tam, S., Tejada, A. O., Trigg, S. A., Twizere, J. C., Vega, K., Walsh, J., Cusick, M. E., Xia, Y., Barabasi, A. L., Iakoucheva, L. M., Aloy, P., De Las Rivas, J., Tavernier, J., Calderwood, M. A., Hill, D. E., Hao, T., Roth, F. P. and Vidal, M. (2014) 'A proteome-scale map of the human interactome network', *Cell*, 159(5), 1212-1226.

Rossignol, R., Gilkerson, R., Aggeler, R., Yamagata, K., Remington, S. J. and Capaldi, R. A. (2004) 'Energy Substrate Modulates Mitochondrial Structure and Oxidative Capacity in Cancer Cells', *Cancer Research*, 64(3), 985.

Rouillard, A. D., Gundersen, G. W., Fernandez, N. F., Wang, Z., Monteiro, C. D., McDermott, M. G. and Ma'ayan, A. (2016a) 'The harmonizome: a collection of processed datasets gathered to serve and mine knowledge about genes and proteins', *Database*, 2016, baw100-baw100.

Rouillard, A. D., Gundersen, G. W., Fernandez, N. F., Wang, Z., Monteiro, C. D., McDermott, M. G. and Ma'ayan, A. (2016b) 'The harmonizome: a collection of processed datasets

gathered to serve and mine knowledge about genes and proteins', Database: The Journal of Biological Databases and Curation, 2016, baw100.

Rozman-Pungerčar, J., Kopitar-Jerala, N., Bogyo, M., Turk, D., Vasiljeva, O., Štefe, I., Vandenabeele, P., Brömme, D., Puizdar, V., Fonović, M., Trstenjak-Prebanda, M., Dolenc, I., Turk, V. and Turk, B. (2003) 'Inhibition of papain-like cysteine proteases and legumain by caspase-specific inhibitors: when reaction mechanism is more important than specificity', Cell death and differentiation, 10, 881.

Rudd, P. M. and Dwek, R. A. (1997) 'Glycosylation: heterogeneity and the 3D structure of proteins', Crit Rev Biochem Mol Biol, 32(1), 1-100.

Ruggiano, A., Foresti, O. and Carvalho, P. (2014) 'Quality control: ER-associated degradation: protein quality control and beyond', J Cell Biol, 204(6), 869-79.

Ryan, N. S. and Rossor, M. N. (2010) 'Correlating familial Alzheimer's disease gene mutations with clinical phenotype', Biomarkers in medicine, 4(1), 99-112.

Sadhukhan, R., Leone, J. W., Lull, J., Wang, Z., Kletzien, R. F., Heinrikson, R. L. and Tomasselli, A. G. (2006) 'An efficient method to express and refold a truncated human procaspase-9: A caspase with activity toward Glu-X bonds', Protein Expression and Purification, 46(2), 299-308.

Sadowski, M. I. and Jones, D. T. (2009) 'The sequence-structure relationship and protein function prediction', Curr Opin Struct Biol, 19(3), 357-62.

Saeki, Y. (2017) 'Ubiquitin recognition by the proteasome', The Journal of Biochemistry, 161(2), 113-124.

Salin, K., Auer, S. K., Rey, B., Selman, C. and Metcalfe, N. B. (2015) 'Variation in the link between oxygen consumption and ATP production, and its relevance for animal performance', Proceedings of the Royal Society B: Biological Sciences, 282(1812), 20151028.

Sander, J. D. and Joung, J. K. (2014) 'CRISPR-Cas systems for editing, regulating and targeting genomes', Nat Biotech, 32(4), 347-355.

Saunders, J. E., Beeson, C. C. and Schnellmann, R. G. (2013) 'Characterization of Functionally Distinct Mitochondrial Subpopulations', Journal of bioenergetics and biomembranes, 45(0), 87-99.

Schieber, M. and Chandel, N. S. (2014) 'ROS Function in Redox Signaling and Oxidative Stress', Current biology : CB, 24(10), R453-R462.

Schlick, T. (2002) 'Protein Structure Hierarchy' in Schlick, T., ed. Molecular Modeling and Simulation: An Interdisciplinary Guide, New York, NY: Springer New York, 91-112.



Schotte, P., Declercq, W., Van Huffel, S., Vandenabeele, P. and Beyaert, R. (1999) 'Non-specific effects of methyl ketone peptide inhibitors of caspases', *FEBS Letters*, 442(1), 117-121.

Schwarz, F. and Aebi, M. (2011) 'Mechanisms and principles of N-linked protein glycosylation', *Current opinion in structural biology*, 21(5), 576-582.

Scott, D., Oldham, N. J., Strachan, J., Searle, M. S. and Layfield, R. (2015) 'Ubiquitin-binding domains: Mechanisms of ubiquitin recognition and use as tools to investigate ubiquitin-modified proteomes', *PROTEOMICS*, 15(5-6), 844-861.

Scott, D. W., Dunn, T. S., Ballestas, M. E., Litovsky, S. H. and Patel, R. P. (2013) 'Identification of a high-mannose ICAM-1 glycoform: effects of ICAM-1 hypoglycosylation on monocyte adhesion and outside in signaling', *American Journal of Physiology - Cell Physiology*, 305(2), C228-C237.

Scott, H. and Panin, V. M. (2014) 'The role of protein N-glycosylation in neural transmission', *Glycobiology*, 24(5), 407-17.

Senft, D. and Ronai, Z. A. (2015) 'UPR, autophagy, and mitochondria crosstalk underlies the ER stress response', *Trends Biochem Sci*, 40(3), 141-8.

Shapiro, D. J., Livezey, M., Yu, L., Zheng, X. and Andruska, N. (2016) 'Anticipatory UPR Activation: A Protective Pathway and Target in Cancer', *Trends Endocrinol Metab*, 27(10), 731-741.

Shenoy, S. R. and Jayaram, B. (2010) 'Proteins: sequence to structure and function--current status', *Curr Protein Pept Sci*, 11(7), 498-514.

Shi, Y. (2004) 'Caspase activation, inhibition, and reactivation: A mechanistic view', *Protein Science : A Publication of the Protein Society*, 13(8), 1979-1987.

Skibinski, G. A. and Boyd, L. (2012) 'Ubiquitination is involved in secondary growth, not initial formation of polyglutamine protein aggregates in *C. elegans*', *BMC Cell Biol*, 13(1), 1-16.

Slator, C., Molphy, Z., McKee, V. and Kellett, A. (2017) 'Triggering autophagic cell death with a di-manganese(II) developmental therapeutic', *Redox Biology*, 12, 150-161.

Smith, M. D., Harley, M. E., Kemp, A. J., Wills, J., Lee, M., Arends, M., von Kriegsheim, A., Behrends, C. and Wilkinson, S. (2018) 'CCPG1 Is a Non-canonical Autophagy Cargo Receptor Essential for ER-Phagy and Pancreatic ER Proteostasis', *Dev Cell*, 44(2), 217-232.e11.

Song, M., Wang, Y., Zhang, Z. and Wang, S. (2017) 'PSMC2 is up-regulated in osteosarcoma and regulates osteosarcoma cell proliferation, apoptosis and migration', *Oncotarget*, 8(1), 933-953.

- Song, S., Tan, J., Miao, Y. and Zhang, Q. (2018) 'Crosstalk of ER stress-mediated autophagy and ER-phagy: Involvement of UPR and the core autophagy machinery', *Journal of Cellular Physiology*, 233(5), 3867-3874.
- Sousa, M. and Parodi, A. J. (1995) 'The molecular basis for the recognition of misfolded glycoproteins by the UDP-Glc:glycoprotein glucosyltransferase', *The EMBO Journal*, 14(17), 4196-4203.
- Sovolyova, N., Healy, S., Samali, A. and Logue, S. E. (2014) 'Stressed to death - mechanisms of ER stress-induced cell death', *Biol Chem*, 395(1), 1-13.
- Srivastava, S. (2016) 'Emerging therapeutic roles for NAD(+) metabolism in mitochondrial and age-related disorders', *Clinical and Translational Medicine*, 5, 25.
- Stanley, P. (2011) 'Golgi Glycosylation'. *Cold Spring Harbour Perspectives in Biology*. 1;3(4).
- Streeter, A., Menzies, F. M. and Rubinsztein, D. C. (2016) 'LC3-II Tagging and Western Blotting for Monitoring Autophagic Activity in Mammalian Cells', *Methods Mol Biol*, 1303, 161-70.
- Su, T. W., Yang, C. Y., Kao, W. P., Kuo, B. J., Lin, S. M., Lin, J. Y., Lo, Y. C. and Lin, S. C. (2017) 'Structural Insights into DD-Fold Assembly and Caspase-9 Activation by the Apaf-1 Apoptosome', *Structure*, 25(3), 407-420.
- Suski, J. M., Lebiezinska, M., Bonora, M., Pinton, P., Duszynski, J. and Wieckowski, M. R. (2012) 'Relation between mitochondrial membrane potential and ROS formation', *Methods Mol Biol*, 810, 183-205.
- Suzuki, H., Osawa, T., Fujioka, Y. and Noda, N. N. (2017) 'Structural biology of the core autophagy machinery', *Current opinion in structural biology*, 43, 10-17.
- Suzuki, H., Tabata, K., Morita, E., Kawasaki, M., Kato, R., Dobson, Renwick C. J., Yoshimori, T. and Wakatsuki, S. (2003) 'Structural Basis of the Autophagy-Related LC3/Atg13 LIR Complex: Recognition and Interaction Mechanism', *Structure*, 22(1), 47-58.
- Suzuki, T. (2005) 'A simple, sensitive in vitro assay for cytoplasmic deglycosylation by peptide: N-glycanase', *Methods*, 35(4), 360-365.
- Suzuki, T. (2015) 'The cytoplasmic peptide:N-glycanase (Ngly1)—basic science encounters a human genetic disorder', *The Journal of Biochemistry*, 157(1), 23-34.
- Suzuki, T., Huang, C. and Fujihira, H. (2016) 'The cytoplasmic peptide:N-glycanase (NGLY1) — Structure, expression and cellular functions', *Gene*, 577(1), 1-7.
- Suzuki, T., Park, H., Hollingsworth, N. M., Sternglanz, R. and Lennarz, W. J. (2000) 'PNG1, a Yeast Gene Encoding a Highly Conserved Peptide:N-Glycanase', *The Journal of Cell Biology*, 149(5), 1039-1052.

Suzuki, T., Park, H., Kwofie, M. A. and Lennarz, W. J. (2001) 'Rad23 Provides a Link between the Png1 Deglycosylating Enzyme and the 26 S Proteasome in Yeast', *Journal of Biological Chemistry*, 276(24), 21601-21607.

Swatek, K. N. and Komander, D. (2016) 'Ubiquitin modifications', *Cell Research*, 26(4), 399-422.

Szklarczyk, D., Morris, J. H., Cook, H., Kuhn, M., Wyder, S., Simonovic, M., Santos, A., Doncheva, N. T., Roth, A., Bork, P., Jensen, L. J. and von Mering, C. (2017) 'The STRING database in 2017: quality-controlled protein-protein association networks, made broadly accessible', *Nucleic Acids Res*, 45(D1), D362-d368.

Taipa, R., Pereira, C., Reis, I., Alonso, I., Bastos-Lima, A., Melo-Pires, M. and Magalhães, M. (2016) 'DJ-1 linked parkinsonism (PARK7) is associated with Lewy body pathology', *Brain*, 139(6), 1680-1687.

Takamura, A., Komatsu, M., Hara, T., Sakamoto, A., Kishi, C., Waguri, S., Eishi, Y., Hino, O., Tanaka, K. and Mizushima, N. (2011) 'Autophagy-deficient mice develop multiple liver tumors', *Genes & Development*, 25(8), 795-800.

Tan, G. S., Garchow, B. G., Liu, X., Metzler, D. and Kiriakidou, M. (2011) 'Clarifying mammalian RISC assembly in vitro', *BMC Molecular Biology*, 12, 19-19.

Tandler, B., Hoppel, C. L. and Mears, J. A. (2018) 'Morphological Pathways of Mitochondrial Division', *Antioxidants (Basel)*, 7(2).

Tang, G. and Sulzer, D. (2014) 'Chapter 10 - Cargo Recognition Failure Underlies Macroautophagy Defects in Huntington's Disease A2 - Hayat, M.A' in *Autophagy: Cancer, Other Pathologies, Inflammation, Immunity, Infection, and Aging*, Amsterdam: Academic Press, 147-162.

Tanida, I., Tanida-Miyake, E., Ueno, T. and Kominami, E. (2001) 'The human homolog of *Saccharomyces cerevisiae* Apg7p is a Protein-activating enzyme for multiple substrates including human Apg12p, GATE-16, GABARAP, and MAP-LC3', *J Biol Chem*, 276(3), 1701-6.

Tannous, A., Pisoni, G. B., Hebert, D. N. and Molinari, M. (2015) 'N-linked sugar-regulated protein folding and quality control in the ER', *Seminars in cell & developmental biology*, 41, 79-89.

Taylor, R. C. (2016) 'Aging and the UPR(ER)', *Brain Res*, 1648(Pt B), 588-593.

Teixeira, P. F., Cerca, F., Santos, S. D. and Saraiva, M. J. (2006) 'Endoplasmic reticulum stress associated with extracellular aggregates. Evidence from transthyretin deposition in familial amyloid polyneuropathy', *J Biol Chem*, 281(31), 21998-2003.

Thom, C. S., Dickson, C. F., Gell, D. A. and Weiss, M. J. (2013) 'Hemoglobin Variants: Biochemical Properties and Clinical Correlates', *Cold Spring Harbor Perspectives in Medicine*, 3(3), a011858.

Thomas, R. E., Andrews, L. A., Burman, J. L., Lin, W. Y. and Pallanck, L. J. (2014) 'PINK1-Parkin pathway activity is regulated by degradation of PINK1 in the mitochondrial matrix', (1553-7404 (Electronic)).

Tomlin, F. M., Gerling-Driessen, U. I. M., Liu, Y.-C., Flynn, R. A., Vangala, J. R., Lentz, C. S., Clauder-Muenster, S., Jakob, P., Mueller, W. F., Ordoñez-Rueda, D., Paulsen, M., Matsui, N., Foley, D., Rafalko, A., Suzuki, T., Bogyo, M., Steinmetz, L. M., Radhakrishnan, S. K. and Bertozzi, C. R. (2017) 'Inhibition of NGLY1 Inactivates the Transcription Factor Nrf1 and Potentiates Proteasome Inhibitor Cytotoxicity', *ACS Central Science*, 3(11), 1143-1155.

Turk, V., Stoka, V., Vasiljeva, O., Renko, M., Sun, T., Turk, B. and Turk, D. (2012) 'Cysteine cathepsins: From structure, function and regulation to new frontiers', *Biochimica et Biophysica Acta (BBA) - Proteins and Proteomics*, 1824(1), 68-88.

Tyedmers, J., Mogk, A. and Bukau, B. (2010) 'Cellular strategies for controlling protein aggregation', *Nat Rev Mol Cell Biol*, 11(11), 777-788.

Udeshi, N. D., Mertins, P., Svinkina, T. and Carr, S. A. (2013) 'Large-Scale Identification of Ubiquitination Sites by Mass Spectrometry', *Nature protocols*, 8(10), 1950-1960.

Ullmark, T., Montano, G., Jarvstrat, L., Jernmark Nilsson, H., Hakansson, E., Drott, K., Nilsson, B., Vidovic, K. and Gullberg, U. (2017) 'Anti-apoptotic quinolinate phosphoribosyltransferase (QPRT) is a target gene of Wilms' tumor gene 1 (WT1) protein in leukemic cells', *Biochem Biophys Res Commun*, 482(4), 802-807.

van Tonder, A., Joubert, A. M. and Cromarty, A. D. (2015) 'Limitations of the 3-(4,5-dimethylthiazol-2-yl)-2,5-diphenyl-2H-tetrazolium bromide (MTT) assay when compared to three commonly used cell enumeration assays', *BMC Research Notes*, 8, 47.

van Tonder, A., Joubert, A. M. and Cromarty, A. D. (2015) 'Limitations of the 3-(4,5-dimethylthiazol-2-yl)-2,5-diphenyl-2H-tetrazolium bromide (MTT) assay when compared to three commonly used cell enumeration assays', *BMC Res Notes*, 8, 47.

Vayssier-Taussat, M., Kreps, S. E., Adrie, C., Dall'Ava, J., Christiani, D. and Polla, B. S. (2002) 'Mitochondrial membrane potential: a novel biomarker of oxidative environmental stress', *Environmental Health Perspectives*, 110(3), 301-305.

Velentzas, P. D., Velentzas, A. D., Mpakou, V. E., Antonelou, M. H., Margaritis, L. H., Papassideri, I. S. and Stravopodis, D. J. (2013) 'Detrimental effects of proteasome inhibition activity in *Drosophila melanogaster*: implication of ER stress, autophagy, and apoptosis', *Cell Biol Toxicol*, 29(1), 13-37.

Veloso, A. and Kerman, K. (2013) 'Advances in electrochemical detection for study of neurodegenerative disorders', *Anal Bioanal Chem*, 405(17), 5725-41.

- Verlhac, P., Grégoire, Isabel P., Azocar, O., Petkova, Denitsa S., Baguet, J., Viret, C. and Faure, M. 'Autophagy Receptor NDP52 Regulates Pathogen-Containing Autophagosome Maturation', *Cell Host & Microbe*, 17(4), 515-525.
- Wade, S. L. and Auble, D. T. (2010) 'The Rad23 ubiquitin receptor, the proteasome and functional specificity in transcriptional control', *Transcription*, 1(1), 22-26.
- Wahle, E. and Winkler, G. S. (2013) 'RNA decay machines: deadenylation by the Ccr4-not and Pan2-Pan3 complexes', *Biochim Biophys Acta*, 1829(6-7), 561-70.
- Waite, K. A., De-La Mota-Peynado, A., Vontz, G. and Roelofs, J. (2016) 'Starvation Induces Proteasome Autophagy with Different Pathways for Core and Regulatory Particles', *J Biol Chem*, 291(7), 3239-53.
- Wang, C. and Youle, R. J. (2009) 'The Role of Mitochondria in Apoptosis()', *Annual review of genetics*, 43, 95-118.
- Wang, F., Canadeo, L. A. and Huibregtse, J. M. (2015) 'Ubiquitination of newly synthesized proteins at the ribosome', *Biochimie*, 114, 127-33.
- Wang, J., Lu, Z., Wientjes, M. G. and Au, J. L. S. (2010) 'Delivery of siRNA Therapeutics: Barriers and Carriers', *The AAPS Journal*, 12(4), 492-503.
- Wang, L., Chen, M., Yang, J. and Zhang, Z. (2013) 'LC3 fluorescent puncta in autophagosomes or in protein aggregates can be distinguished by FRAP analysis in living cells', *Autophagy*, 9(5), 756-69.
- Wang, L. Q., Cheng, X. S., Huang, C. H., Huang, B. and Liang, Q. (2015) 'Rapamycin protects cardiomyocytes against anoxia/reoxygenation injury by inducing autophagy through the PI3k/Akt pathway', *J Huazhong Univ Sci Technolog Med Sci*, 35(1), 10-5.
- Wang, M., Wey, S., Zhang, Y., Ye, R. and Lee, A. S. (2009) 'Role of the Unfolded Protein Response Regulator GRP78/BiP in Development, Cancer, and Neurological Disorders', *Antioxidants & Redox Signaling*, 11(9), 2307-2316.
- Wang, P., Li, J. and Sha, B. (2016) 'The ER stress sensor PERK luminal domain functions as a molecular chaperone to interact with misfolded proteins', *Acta Crystallogr D Struct Biol*, 72(Pt 12), 1290-1297.
- Wang, Y.-C., Peterson, S. E. and Loring, J. F. (2013) 'Protein post-translational modifications and regulation of pluripotency in human stem cells', *Cell Research*, 24, 143.
- Wang, Z., Watt, W., Brooks, N. A., Harris, M. S., Urban, J., Boatman, D., McMillan, M., Kahn, M., Henrikson, R. L., Finzel, B. C., Wittwer, A. J., Blinn, J., Kamtekar, S. and Tomasselli, A. G. (2010) 'Kinetic and structural characterization of caspase-3 and caspase-8 inhibition by a novel class of irreversible inhibitors', *Biochimica et Biophysica Acta (BBA) - Proteins and Proteomics*, 1804(9), 1817-1831.

- Wani, W. Y., Chatham, J. C., Darley-Usmar, V., McMahon, L. L. and Zhang, J. (2017) 'O-GlcNAcylation and neurodegeneration', *Brain Res Bull*, 133, 80-87.
- Wei, Y., Chiang, W. C., Sumpter, R., Jr., Mishra, P. and Levine, B. (2017) 'Prohibitin 2 Is an Inner Mitochondrial Membrane Mitophagy Receptor', *Cell*, 168(1-2), 224-238.e10.
- Werthmoller, N., Frey, B., Wunderlich, R., Fietkau, R. and Gaipl, U. S. (2015) 'Modulation of radiochemoimmunotherapy-induced B16 melanoma cell death by the pan-caspase inhibitor zVAD-fmk induces anti-tumor immunity in a HMGB1-, nucleotide- and T-cell-dependent manner', *Cell Death Dis*, 6, e1761.
- Willems, Peter H. G. M., Rossignol, R., Dieteren, Cindy E. J., Murphy, Michael P. and Koopman, Werner J. H. (2015) 'Redox Homeostasis and Mitochondrial Dynamics', *Cell Metabolism*, 22(2), 207-218.
- Williams, G. J., Hammel, M., Radhakrishnan, S. K., Ramsden, D., Lees-Miller, S. P. and Tainer, J. A. (2014) 'Structural insights into NHEJ: building up an integrated picture of the dynamic DSB repair super complex, one component and interaction at a time', *DNA repair*, 17, 110-120.
- Wilson, G. G., Pascual, J. M., Brooijmans, N., Murray, D. and Karlin, A. (2000) 'The Intrinsic Electrostatic Potential and the Intermediate Ring of Charge in the Acetylcholine Receptor Channel', *The Journal of General Physiology*, 115(2), 93-106.
- Wilson, R. C., Tambe, A., Kidwell, M. A., Noland, C. L., Schneider, C. P. and Doudna, J. A. (2015) 'Dicer-TRBP complex formation ensures accurate mammalian microRNA biogenesis', *Mol Cell*, 57(3), 397-407.
- Wirawan, E., Vande Walle, L., Kersse, K., Cornelis, S., Claerhout, S., Vanoverberghe, I., Roelandt, R., De Rycke, R., Verspurten, J., Declercq, W., Agostinis, P., Vanden Berghe, T., Lippens, S. and Vandenabeele, P. (2010) 'Caspase-mediated cleavage of Beclin-1 inactivates Beclin-1-induced autophagy and enhances apoptosis by promoting the release of proapoptotic factors from mitochondria', *Cell Death & Disease*, 1(1), e18.
- Wisniewski, J. R., Zougman, A., Nagaraj, N. and Mann, M. (2009) 'Universal sample preparation method for proteome analysis', *Nat Methods*, 6(5), 359-62.
- Witte, M. D., Horst, D., Wiertz, E. J. H. J., van der Marel, G. A. and Overkleeft, H. S. (2009) 'Synthesis and Biological Evaluation of a Chitobiose-Based Peptide N-Glycanase Inhibitor Library', *The Journal of Organic Chemistry*, 74(2), 605-616.
- Wonder, E., Simón-Gracia, L., Scodeller, P., Majzoub, R., Ramana Kotamraju, V., Ewert, K. K., Teesalu, T. and Safinya, C. (2017) 'Role of Charge and Ligand-Receptor Binding in Specific Targeting of Peptide-Tagged Cationic Liposome Nanoparticles for Gene Delivery', *Biophysical Journal*, 112(3), 591a.

- Wong, Y. C. and Holzbaur, E. L. (2014) 'Optineurin is an autophagy receptor for damaged mitochondria in parkin-mediated mitophagy that is disrupted by an ALS-linked mutation', *Proc Natl Acad Sci U S A*, 111(42), E4439-48.
- Wu, J., Jin, Z., Zheng, H. and Yan, L.-J. (2016) 'Sources and implications of NADH/NAD(+) redox imbalance in diabetes and its complications', *Diabetes, Metabolic Syndrome and Obesity: Targets and Therapy*, 9, 145-153.
- Wu, Y.-T., Tan, H.-L., Shui, G., Bauvy, C., Huang, Q., Wenk, M. R., Ong, C.-N., Codogno, P. and Shen, H.-M. (2010) 'Dual Role of 3-Methyladenine in Modulation of Autophagy via Different Temporal Patterns of Inhibition on Class I and III Phosphoinositide 3-Kinase', *Journal of Biological Chemistry*, 285(14), 10850-10861.
- Wu, Y. T., Tan Hl Fau - Huang, Q., Huang Q Fau - Kim, Y.-S., Kim Ys Fau - Pan, N., Pan N Fau - Ong, W.-Y., Ong Wy Fau - Liu, Z.-G., Liu Zg Fau - Ong, C.-N., Ong Cn Fau - Shen, H.-M. and Shen, H. M. (2008a) 'Autophagy plays a protective role during zVAD-induced necrotic cell death', (1554-8635 (Electronic)).
- Wu, Y. T., Tan, H. L., Huang, Q., Kim, Y. S., Pan, N., Ong, W. Y., Liu, Z. G., Ong, C. N. and Shen, H. M. (2008b) 'Autophagy plays a protective role during zVAD-induced necrotic cell death', *Autophagy*, 4(4), 457-66.
- Wu, Y. T., Tan, H. L., Huang, Q., Sun, X. J., Zhu, X. and Shen, H. M. (2011) 'zVAD-induced necroptosis in L929 cells depends on autocrine production of TNF[alpha] mediated by the PKC-MAPKs-AP-1 pathway', *Cell Death Differ*, 18(1), 26-37.
- Xiao, B., Deng, X., Zhou, W. and Tan, E.-K. (2016) 'Flow Cytometry-Based Assessment of Mitophagy Using MitoTracker', *Frontiers in Cellular Neuroscience*, 10, 76.
- Xu, L., Yang, L., Hashimoto, K., Anderson, M., Kohlhagen, G., Pommier, Y. and D'Arpa, P. (2002) 'Characterization of BTBD1 and BTBD2, two similar BTB-domain-containing Kelch-like proteins that interact with Topoisomerase I', *BMC Genomics*, 3, 1.
- Xu, W., Xu, B., Yao, Y., Yu, X., Cao, H., Zhang, J., Liu, J. and Sheng, H. (2016) 'Overexpression and biological function of IQGAP3 in human pancreatic cancer', *Am J Transl Res*, 8(12), 5421-5432.
- Yang, B., El Nahas, A. M., Fisher, M., Wagner, B., Huang, L., Storie, I., Barnett, D., Barratt, J., Smith, A. C. and Johnson, T. S. (2004) 'Inhibitors directed towards caspase-1 and -3 are less effective than pan caspase inhibition in preventing renal proximal tubular cell apoptosis', *Nephron Exp Nephrol*, 96(2), e39-51.
- Yang, L., Biswas, M. E. and Chen, P. (2003) 'Study of Binding between Protein A and Immunoglobulin G Using a Surface Tension Probe', *Biophysical Journal*, 84(1), 509-522.
- Yang, W. H., Kim, J. E., Nam, H. W., Ju, J. W., Kim, H. S., Kim, Y. S. and Cho, J. W. (2006) 'Modification of p53 with O-linked N-acetylglucosamine regulates p53 activity and stability', *Nature Cell Biology*, 8, 1074.

- Ye, B., Liao, D., Zhang, X., Zhang, P., Dong, H. and Huganir, R. L. (2000) 'GRASP-1: A Neuronal RasGEF Associated with the AMPA Receptor/GRIP Complex', *Neuron*, 26(3), 603-617.
- Yerbury, J. J., Ooi, L., Dillin, A., Saunders, D. N., Hatters, D. M., Beart, P. M., Cashman, N. R., Wilson, M. R. and Ecroyd, H. (2016) 'Walking the tightrope: proteostasis and neurodegenerative disease', *Journal of Neurochemistry*, 137(4), 489-505.
- Yoshii, Saori R., Kuma, A., Akashi, T., Hara, T., Yamamoto, A., Kurikawa, Y., Itakura, E., Tsukamoto, S., Shitara, H., Eishi, Y. and Mizushima, N. (2016) 'Systemic Analysis of *Atg5*-Null Mice Rescued from Neonatal Lethality by Transgenic ATG5 Expression in Neurons', *Developmental Cell*, 39(1), 116-130.
- Zaffagnini, G. and Martens, S. (2016) 'Mechanisms of Selective Autophagy', *Journal of Molecular Biology*, 428(9Part A), 1714-1724.
- Zhang, H., Bosch-Marce, M., Shimoda, L. A., Tan, Y. S., Baek, J. H., Wesley, J. B., Gonzalez, F. J. and Semenza, G. L. (2008) 'Mitochondrial autophagy is an HIF-1-dependent adaptive metabolic response to hypoxia', *J Biol Chem*, 283(16), 10892-903.
- Zhang, J. (2015) 'Teaching the basics of autophagy and mitophagy to redox biologists—Mechanisms and experimental approaches', *Redox Biology*, 4, 242-259.
- Zhang, Z. and Falk, M. J. (2014) 'Integrated transcriptome analysis across mitochondrial disease etiologies and tissues improves understanding of common cellular adaptations to respiratory chain dysfunction', *Int J Biochem Cell Biol*, 50, 106-11.
- Zhang, Z., Tan, E. P., VandenHull, N. J., Peterson, K. R. and Slawson, C. (2014) 'O-GlcNAcase Expression is Sensitive to Changes in O-GlcNAc Homeostasis', *Frontiers in Endocrinology*, 5, 206.
- Zhao, G., Li, G., Zhou, X., Matsuo, I., Ito, Y., Suzuki, T., Lennarz, W. J. and Schindelin, H. (2009) 'Structural and mutational studies on the importance of oligosaccharide binding for the activity of yeast PNGase', *Glycobiology*, 19(2), 118-25.
- Zhao, G., Zhou X Fau - Wang, L., Wang L Fau - Li, G., Li G Fau - Schindelin, H., Schindelin H Fau - Lennarz, W. J. and Lennarz, W. J. (2007) 'Studies on peptide:N-glycanase-p97 interaction suggest that p97 phosphorylation modulates endoplasmic reticulum-associated degradation', (0027-8424 (Print)).
- Zhao, M., Zhu, P., Fujino, M., Zhuang, J., Guo, H., Sheikh, I., Zhao, L. and Li, X.-K. (2016) 'Oxidative Stress in Hypoxic-Ischemic Encephalopathy: Molecular Mechanisms and Therapeutic Strategies', *International Journal of Molecular Sciences*, 17(12), 2078.
- Zhu, Y., Zhao, L., Liu, L., Gao, P., Tian, W., Wang, X., Jin, H., Xu, H. and Chen, Q. (2010) 'Beclin 1 cleavage by caspase-3 inactivates autophagy and promotes apoptosis', *Protein Cell*, 1(5), 468-77.



Zielinska, Dorota F., Gnad, F., Schropp, K., Wiśniewski, Jacek R. and Mann, M. (2012) 'Mapping N-Glycosylation Sites across Seven Evolutionarily Distant Species Reveals a Divergent Substrate Proteome Despite a Common Core Machinery', *Mol Cell*, 46(4), 542-548.

Zimmermann, A. C., Zarei, M., Eiselein, S. and Dengjel, J. (2010) 'Quantitative proteomics for the analysis of spatio-temporal protein dynamics during autophagy', *Autophagy*, 6(8), 1009-16.

Zoltewicz, J. S., Ashique, A. M., Choe, Y., Lee, G., Taylor, S., Phamluong, K., Solloway, M. and Peterson, A. S. (2009) 'Wnt Signaling Is Regulated by Endoplasmic Reticulum Retention', *PLOS ONE*, 4(7), e6191.

Zorov, D. B., Juhaszova, M. and Sollott, S. J. (2014) 'Mitochondrial Reactive Oxygen Species (ROS) and ROS-Induced ROS Release', *Physiological Reviews*, 94(3), 909-950.

**SPRINGER NATURE LICENSE  
TERMS AND CONDITIONS**

Feb 13, 2018

---

**This Agreement between Sarah Needs ("You") and Springer Nature ("Springer Nature") consists of your license details and the terms and conditions provided by Springer Nature and Copyright Clearance Center.**

License Number	4287100760383
License date	Feb 13, 2018
Licensed Content Publisher	Springer Nature
Licensed Content Publication	Oncogene
Licensed Content Title	Mechanisms of acquired resistance to ERK1/2 pathway inhibitors
Licensed Content Author	A S Little, P D Smith, S J Cook
Licensed Content Date	May 7, 2012
Licensed Content Volume	32
Licensed Content Issue	10
Type of Use	Thesis/Dissertation
Requestor type	academic/university or research institute
Format	print and electronic
Portion	figures/tables/illustrations
Number of figures/tables/illustrations	1
High-res required	no
Will you be translating?	no
Circulation/distribution	<501
Author of this Springer Nature content	no
Title	Biochemical basis of congenital disorders of glycosylation
Instructor name	n/a
Institution name	n/a
Expected presentation date	Feb 2018
Portions	1
Requestor Location	Sarah Needs LHCS Venables Walton Hall, Open University Milton Keynes, MK7 6AA United Kingdom Attn: Sarah Needs
Billing Type	Invoice
Billing Address	Sarah Needs LHCS Venables Walton Hall, Open University Milton Keynes, United Kingdom MK7 6AA Attn: Sarah Needs
Total	0.00 GBP
Terms and Conditions	

**ELSEVIER LICENSE  
TERMS AND CONDITIONS**

Feb 13, 2018

This Agreement between Sarah Needs ("You") and Elsevier ("Elsevier") consists of your license details and the terms and conditions provided by Elsevier and Copyright Clearance Center.

License Number	4287000904608
License date	Feb 13, 2018
Licensed Content Publisher	Elsevier
Licensed Content Publication	The American Journal of Human Genetics
Licensed Content Title	Solving Glycosylation Disorders: Fundamental Approaches Reveal Complicated Pathways
Licensed Content Author	Hudson H. Freeze, Jessica X. Chong, Michael J. Bamshad, Bobby G. Ng
Licensed Content Date	Feb 6, 2014
Licensed Content Volume	94
Licensed Content Issue	2
Licensed Content Pages	15
Start Page	161
End Page	175
Type of Use	reuse in a thesis/dissertation
Portion	figures/tables/illustrations
Number of figures/tables/illustrations	1
Format	both print and electronic
Are you the author of this Elsevier article?	No
Will you be translating?	No
Original figure numbers	1
Title of your thesis/dissertation	Biochemical basis of congenital disorders of glycosylation
Expected completion date	Feb 2018
Estimated size (number of pages)	250
Requestor Location	Sarah Needs LHCS Venables Walton Hall, Open University Milton Keynes, MK7 6AA United Kingdom Attn: Sarah Needs
Publisher Tax ID	GB 494 6272 12
Total	0.00 GBP
Terms and Conditions	

**INTRODUCTION**

1. The publisher for this copyrighted material is Elsevier. By clicking "accept" in connection with completing this licensing transaction, you agree that the following terms and conditions

**SPRINGER NATURE LICENSE  
TERMS AND CONDITIONS**

Jan 21, 2018

This Agreement between Sarah Needs ("You") and Springer Nature ("Springer Nature") consists of your license details and the terms and conditions provided by Springer Nature and Copyright Clearance Center.

License Number	4273810701128
License date	Jan 21, 2018
Licensed Content Publisher	Springer Nature
Licensed Content Publication	Nature Structural & Molecular Biology
Licensed Content Title	Cleaning up in the endoplasmic reticulum: ubiquitin in charge
Licensed Content Author	John C Christianson, Yihong Ye
Licensed Content Date	Apr 4, 2014
Licensed Content Volume	21
Licensed Content Issue	4
Type of Use	Thesis/Dissertation
Requestor type	academic/university or research institute
Format	print and electronic
Portion	figures/tables/illustrations
Number of figures/tables/illustrations	1
High-res required	no
Will you be translating?	no
Circulation/distribution	<501
Author of this Springer Nature content	no
Title	Biochemical basis of congenital disorders of glycosylation
Instructor name	n/a
Institution name	n/a
Expected presentation date	Feb 2018
Portions	2
Requestor Location	Sarah Needs LHCS Venables Walton Hall, Open University Milton Keynes, MK7 6AA United Kingdom Attn: Sarah Needs
Billing Type	Invoice
Billing Address	Sarah Needs LHCS Venables Walton Hall, Open University Milton Keynes, United Kingdom MK7 6AA Attn: Sarah Needs
Total	0.00 GBP
Terms and Conditions	

JOHN WILEY AND SONS LICENSE  
TERMS AND CONDITIONS

Feb 09, 2018

This Agreement between Sarah Needs ("You") and John Wiley and Sons ("John Wiley and Sons") consists of your license details and the terms and conditions provided by John Wiley and Sons and Copyright Clearance Center.

License Number	4284810214767
License date	Feb 09, 2018
Licensed Content Publisher	John Wiley and Sons
Licensed Content Publication	Proteomics
Licensed Content Title	Ubiquitin-binding domains: Mechanisms of ubiquitin recognition and use as tools to investigate ubiquitin-modified proteomes
Licensed Content Author	Daniel Scott, Neil J. Oldham, Jo Strachan, Mark S. Searle, Robert Layfield
Licensed Content Date	Dec 28, 2014
Licensed Content Pages	18
Type of use	Dissertation/Thesis
Requestor type	University/Academic
Format	Print and electronic
Portion	Figure/table
Number of figures/tables	1
Original Wiley figure/table number(s)	2
Will you be translating?	No
Title of your thesis / dissertation	Biochemical basis of congenital disorders of glycosylation
Expected completion date	Feb 2018
Expected size (number of pages)	250
Requestor Location	Sarah Needs LHCS Venables Walton Hall, Open University Milton Keynes, MK7 6AA United Kingdom Attn: Sarah Needs
Publisher Tax ID	EU826007151
Total	0.00 GBP
Terms and Conditions	

TERMS AND CONDITIONS

This copyrighted material is owned by or exclusively licensed to John Wiley & Sons, Inc. or one of its group companies (each a "Wiley Company") or handled on behalf of a society with which a Wiley Company has exclusive publishing rights in relation to a particular work (collectively "WILEY"). By clicking "accept" in connection with completing this licensing transaction, you agree that the following terms and conditions apply to this transaction (along with the billing and payment terms and conditions established by the Copyright Clearance Center Inc., ("CCC's Billing and Payment terms and conditions"), at the time that

JOHN WILEY AND SONS LICENSE  
TERMS AND CONDITIONS

Feb 13, 2018

This Agreement between Sarah Needs ("You") and John Wiley and Sons ("John Wiley and Sons") consists of your license details and the terms and conditions provided by John Wiley and Sons and Copyright Clearance Center.

License Number	4287040637038
License date	Feb 13, 2018
Licensed Content Publisher	John Wiley and Sons
Licensed Content Publication	Journal of Neurochemistry
Licensed Content Title	Walking the tightrope: proteostasis and neurodegenerative disease
Licensed Content Author	Justin J. Yerbury, Lezanne Ooi, Andrew Dillin, Darren N. Saunders, Danny M. Hatters, Phillip M. Beart, Neil R. Cashman, Mark R. Wilson, Heath Ecroyd
Licensed Content Date	Mar 8, 2016
Licensed Content Pages	17
Type of use	Dissertation/Thesis
Requestor type	University/Academic
Format	Print and electronic
Portion	Figure/table
Number of figures/tables	1
Original Wiley figure/table number(s)	1
Will you be translating?	No
Title of your thesis / dissertation	Biochemical basis of congenital disorders of glycosylation
Expected completion date	Feb 2018
Expected size (number of pages)	250
Requestor Location	Sarah Needs LHCS Venables Walton Hall, Open University Milton Keynes, MK7 6AA United Kingdom Attn: Sarah Needs
Publisher Tax ID	EU826007151
Total	0.00 GBP
Terms and Conditions	

TERMS AND CONDITIONS

This copyrighted material is owned by or exclusively licensed to John Wiley & Sons, Inc. or one of its group companies (each a "Wiley Company") or handled on behalf of a society with which a Wiley Company has exclusive publishing rights in relation to a particular work (collectively "WILEY"). By clicking "accept" in connection with completing this licensing transaction, you agree that the following terms and conditions apply to this transaction (along with the billing and payment terms and conditions established by the Copyright Clearance Center Inc., ("CCC's Billing and Payment terms and conditions"), at the time that

**ELSEVIER LICENSE  
TERMS AND CONDITIONS**

Jan 21, 2018

---

**This Agreement between Sarah Needs ("You") and Elsevier ("Elsevier") consists of your license details and the terms and conditions provided by Elsevier and Copyright Clearance Center.**

License Number	4273741389847
License date	Jan 21, 2018
Licensed Content Publisher	Elsevier
Licensed Content Publication	Gene
Licensed Content Title	The cytoplasmic peptide:N-glycanase (NGLY1) — Structure, expression and cellular functions
Licensed Content Author	Tadashi Suzuki, Chengcheng Huang, Haruhiko Fujihira
Licensed Content Date	Feb 10, 2016
Licensed Content Volume	577
Licensed Content Issue	1
Licensed Content Pages	7
Start Page	1
End Page	7
Type of Use	reuse in a thesis/dissertation
Portion	figures/tables/illustrations
Number of figures/tables/illustrations	1
Format	both print and electronic
Are you the author of this Elsevier article?	No
Will you be translating?	No
Original figure numbers	2
Title of your thesis/dissertation	Biochemical basis of congenital disorders of glycosylation
Expected completion date	Feb 2018
Estimated size (number of pages)	250
Requestor Location	Sarah Needs LHCS Venables Walton Hall, Open University

-  
**NATURE PUBLISHING GROUP LICENSE  
TERMS AND CONDITIONS**

Oct 03, 2017

---

This Agreement between Sarah Needs ("You") and Nature Publishing Group ("Nature Publishing Group") consists of your license details and the terms and conditions provided by Nature Publishing Group and Copyright Clearance Center.

License Number	4201560128056
License date	Oct 03, 2017
Licensed Content Publisher	Nature Publishing Group
Licensed Content Publication	Genetics in Medicine
Licensed Content Title	Mutations in NGLY1 cause an inherited disorder of the endoplasmic reticulum-associated degradation pathway
Licensed Content Author	Gregory M. Enns, Vandana Shashi, Matthew Bainbridge, Michael J. Gambello, Farah R. Zahir, Thomas Bast
Licensed Content Date	Mar 20, 2014
Licensed Content Volume	16
Licensed Content Issue	10
Type of Use	reuse in a dissertation / thesis
Requestor type	academic/educational
Format	print and electronic
Portion	figures/tables/illustrations
Number of figures/tables/illustrations	1
High-res required	no
Figures	Figure 1
Author of this NPG article	no
Your reference number	
Title of your thesis / dissertation	Biochemical basis of congenital disorders of glycosylation
Expected completion date	Feb 2018
Estimated size (number of pages)	250
Requestor Location	Sarah Needs LHCS Venables Walton Hall, Open University Milton Keynes, MK7 6AA United Kingdom Attn: Sarah Needs
Billing Type	Invoice
Billing Address	Sarah Needs LHCS Venables Walton Hall, Open University Milton Keynes, United Kingdom MK7 6AA Attn: Sarah Needs
Total	0.00 GBP
Terms and Conditions	



ELSEVIER LICENSE  
TERMS AND CONDITIONS

Jan 04, 2018

This Agreement between Sarah Needs ("You") and Elsevier ("Elsevier") consists of your license details and the terms and conditions provided by Elsevier and Copyright Clearance Center.

License Number	4261870780497
License date	Jan 04, 2018
Licensed Content Publisher	Elsevier
Licensed Content Publication	Chemistry & Biology
Licensed Content Title	Using a Small Molecule Inhibitor of Peptide: N-Glycanase to Probe Its Role in Glycoprotein Turnover
Licensed Content Author	Shahram Misaghi, Michael E. Pacold, Daniël Blom, Hidde L. Ploegh, Gregory Alan Korbel
Licensed Content Date	Dec 1, 2004
Licensed Content Volume	11
Licensed Content Issue	12
Licensed Content Pages	11
Start Page	1677
End Page	1687
Type of Use	reuse in a thesis/dissertation
Portion	figures/tables/illustrations
Number of figures/tables/illustrations	1
Format	both print and electronic
Are you the author of this Elsevier article?	No
Will you be translating?	No
Original figure numbers	1
Title of your thesis/dissertation	Biochemical basis of congenital disorders of glycosylation
Expected completion date	Feb 2018
Estimated size (number of pages)	250
Requestor Location	Sarah Needs LHCS Venables Walton Hall, Open University Milton Keynes, MK7 6AA United Kingdom Attn: Sarah Needs
Publisher Tax ID	GB 494 6272 12
Total	0.00 GBP
Terms and Conditions	

ELSEVIER LICENSE  
TERMS AND CONDITIONS

Jan 31, 2018

This Agreement between Sarah Needs ("You") and Elsevier ("Elsevier") consists of your license details and the terms and conditions provided by Elsevier and Copyright Clearance Center.

License Number	4261870780497
License date	Jan 04, 2018
Licensed Content Publisher	Elsevier
Licensed Content Publication	Chemistry & Biology
Licensed Content Title	Using a Small Molecule Inhibitor of Peptide: N-Glycanase to Probe Its Role in Glycoprotein Turnover
Licensed Content Author	Shahram Misaghi, Michael E. Pacold, Daniël Blom, Hidde L. Ploegh, Gregory Alan Korb
Licensed Content Date	Dec 1, 2004
Licensed Content Volume	11
Licensed Content Issue	12
Licensed Content Pages	11
Start Page	1677
End Page	1687
Type of Use	reuse in a thesis/dissertation
Portion	figures/tables/illustrations
Number of figures/tables/illustrations	1
Format	both print and electronic
Are you the author of this Elsevier article?	No
Will you be translating?	No
Original figure numbers	1
Title of your thesis/dissertation	Biochemical basis of congenital disorders of glycosylation
Expected completion date	Feb 2018
Estimated size (number of pages)	250
Requestor Location	Sarah Needs LHCS Venables Walton Hall, Open University Milton Keynes, MK7 6AA United Kingdom Attn: Sarah Needs
Publisher Tax ID	GB 494 6272 12
Total	0.00 GBP
Terms and Conditions	

OXFORD UNIVERSITY PRESS LICENSE  
TERMS AND CONDITIONS

Nov 30, 2017

---

This Agreement between Sarah Needs ("You") and Oxford University Press ("Oxford University Press") consists of your license details and the terms and conditions provided by Oxford University Press and Copyright Clearance Center.

License Number	4238830291282
License date	Nov 30, 2017
Licensed content publisher	Oxford University Press
Licensed content publication	Glycobiology
Licensed content title	A congenital disorder of deglycosylation: Biochemical characterization of <i>N</i> -glycanase 1 deficiency in patient fibroblasts
Licensed content author	He, Ping; Grotzke, Jeff E
Licensed content date	Apr 21, 2015
Type of Use	Thesis/Dissertation
Institution name	
Title of your work	Biochemical basis of congenital disorders of glycosylation
Publisher of your work	n/a
Expected publication date	Feb 2018
Permissions cost	0.00 GBP
Value added tax	0.00 GBP
Total	0.00 GBP
Requestor Location	Sarah Needs LHCS Venables Walton Hall, Open University Milton Keynes, MK7 6AA United Kingdom Attn: Sarah Needs
Publisher Tax ID	GB125506730
Billing Type	Invoice
Billing Address	Sarah Needs LHCS Venables Walton Hall, Open University Milton Keynes, United Kingdom MK7 6AA Attn: Sarah Needs
Total	0.00 GBP
Terms and Conditions	

SPRINGER NATURE LICENSE  
TERMS AND CONDITIONS

Jan 31, 2018

This Agreement between Sarah Needs ("You") and Springer Nature ("Springer Nature") consists of your license details and the terms and conditions provided by Springer Nature and Copyright Clearance Center.

License Number	4261510323060
License date	Jan 03, 2018
Licensed Content Publisher	Springer Nature
Licensed Content Publication	Diabetologia
Licensed Content Title	Signalling danger: endoplasmic reticulum stress and the unfolded protein response in pancreatic islet inflammation
Licensed Content Author	D. L. Eizirik, M. Miani, A. K. Cardozo
Licensed Content Date	Jan 1, 2012
Licensed Content Volume	56
Licensed Content Issue	2
Type of Use	Thesis/Dissertation
Requestor type	academic/university or research institute
Format	print and electronic
Portion	figures/tables/illustrations
Number of figures/tables/illustrations	1
Will you be translating?	no
Circulation/distribution	<501
Author of this Springer Nature content	no
Title	Biochemical basis of congenital disorders of glycosylation
Instructor name	n/a
Institution name	n/a
Expected presentation date	Feb 2018
Portions	1
Requestor Location	Sarah Needs LHCS Venables Walton Hall, Open University Milton Keynes, MK7 6AA United Kingdom Attn: Sarah Needs
Billing Type	Invoice
Billing Address	Sarah Needs LHCS Venables Walton Hall, Open University Milton Keynes, United Kingdom MK7 6AA Attn: Sarah Needs
Total	0.00 USD
Terms and Conditions	

# JOHN WILEY AND SONS LICENSE TERMS AND CONDITIONS

Dec 18, 2017

This Agreement between Sarah Needs ("You") and John Wiley and Sons ("John Wiley and Sons") consists of your license details and the terms and conditions provided by John Wiley and Sons and Copyright Clearance Center.

License Number	4232590452764
License date	Nov 19, 2017
Licensed Content Publisher	John Wiley and Sons
Licensed Content Publication	Protein Science
Licensed Content Title	Caspase activation, inhibition, and reactivation: A mechanistic view
Licensed Content Author	Yigong Shi
Licensed Content Date	Aug 1, 2004
Licensed Content Pages	9
Type of Use	Dissertation/Thesis
Requestor type	University/Academic
Format	Print and electronic
Portion	Figure/table
Number of figures/tables	1
Original Wiley figure/table number(s)	4
Will you be translating?	No
Title of your thesis / dissertation	Biochemical basis of congenital disorders of glycosylation
Expected completion date	Feb 2018
Expected size (number of pages)	250
Requestor Location	Sarah Needs LHCS Venables Walton Hall, Open University Milton Keynes, MK7 6AA United Kingdom Attn: Sarah Needs
Publisher Tax ID	EU826007151
Billing Type	Invoice
Billing Address	Sarah Needs LHCS Venables Walton Hall, Open University Milton Keynes, United Kingdom MK7 6AA Attn: Sarah Needs
Total	0.00 GBP
Terms and Conditions	

## TERMS AND CONDITIONS

This copyrighted material is owned by or exclusively licensed to John Wiley & Sons, Inc. or one of its group companies (each a "Wiley Company") or handed on behalf of a society with which a Wiley Company has exclusive publishing rights in relation to a particular work (collectively "WILEY"). By clicking "accept" in connection with completing this licensing transaction, you agree that the following terms and conditions apply to this transaction (along with the billing and payment terms and conditions established by the Copyright Clearance Center Inc., ("CCC's Billing and Payment terms and conditions"), at the time that you opened your RightsLink account (these are available at any time at <http://myaccount.copyright.com>).

**NATURE PUBLISHING GROUP LICENSE  
TERMS AND CONDITIONS**

Dec 03, 2017

---

This Agreement between Sarah Needs ("You") and Nature Publishing Group ("Nature Publishing Group") consists of your license details and the terms and conditions provided by Nature Publishing Group and Copyright Clearance Center.

License Number	4241430518177
License date	Dec 03, 2017
Licensed Content Publisher	Nature Publishing Group
Licensed Content Publication	Nature Protocols
Licensed Content Title	Genome engineering using the CRISPR-Cas9 system
Licensed Content Author	F Ann Ran, Patrick D Hsu, Jason Wright, Vineeta Agarwala, David A Scott et al.
Licensed Content Date	Oct 24, 2013
Licensed Content Volume	8
Licensed Content Issue	11
Type of Use	reuse in a dissertation / thesis
Requestor type	academic/educational
Format	print and electronic
Portion	figures/tables/illustrations
Number of figures/tables/illustrations	1
High-res required	no
Figures	3
Author of this NPG article	no
Your reference number	
Title of your thesis / dissertation	Biochemical basis of congenital disorders of glycosylation
Expected completion date	Feb 2018
Estimated size (number of pages)	250
Requestor Location	Sarah Needs LHCS Venables Walton Hall, Open University Milton Keynes, MK7 6AA United Kingdom Attn: Sarah Needs
Billing Type	Invoice
Billing Address	Sarah Needs LHCS Venables Walton Hall, Open University Milton Keynes, United Kingdom MK7 6AA Attn: Sarah Needs
Total	0.00 GBP
Terms and Conditions	

ELSEVIER LICENSE  
TERMS AND CONDITIONS

Feb 27, 2018

This Agreement between Sarah Needs ("You") and Elsevier ("Elsevier") consists of your license details and the terms and conditions provided by Elsevier and Copyright Clearance Center.

License Number	4297031238024
License date	Feb 27, 2018
Licensed Content Publisher	Elsevier
Licensed Content Publication	Cell Metabolism
Licensed Content Title	Redox Homeostasis and Mitochondrial Dynamics
Licensed Content Author	Peter H.G.M. Willems,Rodrigue Rossignol,Cindy E.J. Dieteren,Michael P. Murphy,Werner J.H. Koopman
Licensed Content Date	Aug 4, 2015
Licensed Content Volume	22
Licensed Content Issue	2
Licensed Content Pages	12
Start Page	207
End Page	218
Type of Use	reuse in a thesis/dissertation
Portion	figures/tables/illustrations
Number of figures/tables/illustrations	1
Format	both print and electronic
Are you the author of this Elsevier article?	No
Will you be translating?	No
Original figure numbers	1
Title of your thesis/dissertation	Biochemical basis of congenital disorders of glycosylation
Expected completion date	Feb 2018
Estimated size (number of pages)	250
Requestor Location	Sarah Needs LHCS Venables Walton Hall, Open University Milton Keynes, MK7 6AA United Kingdom Attn: Sarah Needs
Publisher Tax ID	GB 494 6272 12
Total	0.00 GBP
Terms and Conditions	

ELSEVIER LICENSE  
TERMS AND CONDITIONS

Feb 16, 2018

This Agreement between Sarah Needs ("You") and Elsevier ("Elsevier") consists of your license details and the terms and conditions provided by Elsevier and Copyright Clearance Center.

License Number	4290740412678
License date	Feb 16, 2018
Licensed Content Publisher	Elsevier
Licensed Content Publication	Biochimica et Biophysica Acta (BBA) - Bioenergetics
Licensed Content Title	Metabolic control by sirtuins and other enzymes that sense NAD+, NADH, or their ratio
Licensed Content Author	Kristin A. Anderson, Andreas S. Madsen, Christian A. Olsen, Matthew D. Hirschey
Licensed Content Date	Dec 1, 2017
Licensed Content Volume	1858
Licensed Content Issue	12
Licensed Content Pages	8
Start Page	991
End Page	998
Type of Use	reuse in a thesis/dissertation
Portion	figures/tables/illustrations
Number of figures/tables/illustrations	1
Format	both print and electronic
Are you the author of this Elsevier article?	No
Will you be translating?	No
Original figure numbers	2
Title of your thesis/dissertation	Biochemical basis of congenital disorders of glycosylation
Expected completion date	Feb 2018
Estimated size (number of pages)	250
Requestor Location	Sarah Needs LHCS Venables Walton Hall, Open University Milton Keynes, MK7 6AA United Kingdom Attn: Sarah Needs
Publisher Tax ID	GB 494 6272 12
Total	0.00 GBP
Terms and Conditions	



ELSEVIER LICENSE  
TERMS AND CONDITIONS

Mar 28, 2018

This Agreement between Sarah Needs ("You") and Elsevier ("Elsevier") consists of your license details and the terms and conditions provided by Elsevier and Copyright Clearance Center.

License Number	4317591037890
License date	Mar 28, 2018
Licensed Content Publisher	Elsevier
Licensed Content Publication	Seminars in Cancer Biology
Licensed Content Title	ER stress and hexosamine pathway during tumourigenesis: A pas de deux?
Licensed Content Author	Sophie Vasseur, Serge N. Manié
Licensed Content Date	Aug 1, 2015
Licensed Content Volume	33
Licensed Content Issue	n/a
Licensed Content Pages	6
Start Page	34
End Page	39
Type of Use	reuse in a thesis/dissertation
Portion	figures/tables/illustrations
Number of figures/tables/illustrations	1
Format	both print and electronic
Are you the author of this Elsevier article?	No
Will you be translating?	No
Original figure numbers	1
Title of your thesis/dissertation	Biochemical basis of congenital disorders of glycosylation
Expected completion date	Apr 2018
Estimated size (number of pages)	250
Requestor Location	Sarah Needs LHCS Venables Walton Hall, Open University Milton Keynes, MK7 6AA United Kingdom Attn: Sarah Needs
Publisher Tax ID	GB 494 6272 12
Total	0.00 GBP
Terms and Conditions	